Human Plasma Adsorption to Biomaterials: Fundamental Level Chemical Modifications and Their Effects on Biocompatibility

by

Markian Stephen Bahniuk

A thesis submitted in partial fulfillment of the requirements for the degree of

Doctor of Philosophy

Department of Biomedical Engineering
University of Alberta

Abstract

The non-specific adsorption of proteins to biomaterials is a process that begins instantly upon implantation and results in the formation of a protein-rich layer coating the biomaterial surface. The consequences of this complex phenomenon are far-reaching and may affect both the biomaterial performance and the health of the host. Though this phenomenon has been studied for 50 years, our understanding is far from complete. The difficulty lies in the myriad of biomaterials designed for various applications along with the complexity of the adsorption event given the hundreds of proteins found in blood, their complex structure-function relationships and their potential interactions with one another.

Protein-biomaterial interactions are too complex and the materials involved too varied to study on a case-by-case basis. Studies of protein adsorption to biomaterials with well characterized chemical modifications can be used to elucidate how molecular level modifications may impact protein adsorption, from which a generalized model of protein adsorption can be developed in addition to broad design strategies for future biomaterials. To this end, platelet poor human plasma was exposed to a variety of biomaterials, each with specific variations in their chemistry, and the composition of the adsorbed protein corona was evaluated using the highly sensitive and specific Western blotting method.

Studies demonstrated that varying the level of carboxyl group substitution in a thermosensitive poly(ethylene glycol) and poly(ε-caprolactone) triblock copolymer hydrogel resulted in significantly different adsorbed proteomes.

Increasing carboxyl substitution from 30% to 54% eliminated the presence of immunoglobulin G (IgG) and alpha$_1$ antitrypsin while greatly increasing the presence of fibrinogen, prothrombin and antithrombin.

In order to better understand the mechanism behind bioactive glass osseointegration and expand upon their successful clinical application, human plasma protein adsorption to bioactive glass 45S5 with varying crystallinities and/or manufacturing methods were evaluated. Increased crystallization did not affect the amount of protein adsorption, but did reduce the levels of deleterious proteins. Sol-gel manufacturing resulted in greater adsorption overall, particularly of fibrinogen and immunoglobulin G.

An analysis of the proteomes adsorbed to poly(acrylic acid) nanoparticles containing various metal oxide cores indicated some significant variations in proteome composition including large differences in levels of complement factor 3 (C3), IgG, fibrinogen and fibronectin. The clotting response of human plasma in the presence of these particles tended to indicate varying degrees of inhibition, again depending upon the metal oxide core composition.

A novel family of leucine-containing, short, marginally soluble elastin-like polypeptides (ELPs) were designed and produced in order to systematically examine the effects of chain length, guest amino acid chemistry and particle size on plasma protein adsorption as well as macrophage viability and phagocytosis. Given the unique combination of short lengths and hydrophobic guest amino acid, a novel purification method needed to be developed in order to successfully

express and purify these ELPs which resulted in yields 10-20 times greater than reported yields for comparable constructs.

A comprehensive, systematic examination of the leucine-containing ELP assembly and disassembly demonstrated previously unreported observations regarding ELP behaviour including how chain length, concentration and hydrophobicity may influence irreversible sub-micron particle formation as well as multi-micron, colloidally unstable aggregates. Hydrophobicity may have also influenced the zeta potential and packing density upon ELP assembly as well as particle stability upon dilution.

Studies examining the adsorbed proteome as a function of ELP amino acid content, length and particle size found minor variations in plasma protein content and clotting response regardless of ELP composition or nanoparticle size. Moderate levels of adsorbed protein were found with the primary protein being albumin. These results suggest a generally favourable host response to these materials.

ELP nanoparticles were found to have minimal impact on the viability of murine RAW 264.7 macrophage cells, regardless of the nanoparticle compositions or physical characteristics. Phagocytosis in this cell line was found to be mildly repressed in some instances as a function of nanoparticle diameter, amino acid hydrophobicity or ELP chain length.

The studies reported herein contribute to the development of a generalized model of biomaterial-protein adsorption and demonstrate the utility of short, marginally soluble ELPs as biocompatible nanoscale delivery vehicles.

Preface

Chapter 3 of the thesis has been published as Nikouei NS, Vakili MR, Bahniuk MS, Unsworth L, Akbari A, Wu J, Lavasanifar A. Thermoreversible hydrogels based on triblock copolymers of poly (ethylene glycol) and carboxyl functionalized poly (ε-caprolactone): the effect of carboxyl group substitution on the transition temperature and biocompatibility in plasma. Acta biomaterialia. 2015 Jan 15;12:81-92. I was responsible for the plasma incubation, Western blotting and clotting data collection, analysis and manuscript composition. NS Nikouei, MR Vakili and A Akbari were involved in material synthesis and physical characterization in addition to composing the corresponding portions of the manuscript. L Unsworth, J Wu and A Lavasanifar were the supervising authors and were involved with the study design and the writing and editing of the manuscript.

Chapter 4 of this thesis has been published as Bahniuk MS, Pirayesh H, Singh HD, Nychka JA, Unsworth LD. Bioactive glass 45S5 powders: effect of synthesis route and resultant surface chemistry and crystallinity on protein adsorption from human plasma. Biointerphases. 2012 Dec 1;7(1-4):1-5. I was responsible for X-ray photoelectron spectroscopy, plasma adsorption, protein assay and Western blotting experimental design, data collection, analysis and

manuscript composition. H Pirayesh and HD Singh were responsible for material synthesis and physical characterization data collection and analysis. JA Nychka and LD Unsworth were the supervising authors and were involved in the study design and manuscript composition.

Chapter 6 of the thesis has been published as Bahniuk MS, Alshememry AK, Unsworth LD. High-yield recombinant expression and purification of marginally soluble, short elastin-like polypeptides. BioTechniques. 2016 Dec;61(6):297-304. © 2009 BioTechniques. Used by Permission. I was responsible for the study design, development, analysis and manuscript composition. AK Alshememry was involved in the study development, analysis and composition. LD Unsworth was a supervising author and was involved in the study design and manuscript composition.

Appendix 1 has been published as a supplementary protocol to Chapter 6 as Bahniuk MS, Alshememry AK, Unsworth LD. A Detailed and High-Yield Protocol for the Concatemerization, Expression and Purification of Marginally Soluble, Short Elastin-Like Polypeptides. BioTechniques. 2016 Dec;61(6):297-304. © 2009 BioTechniques. Used by Permission. Author responsibilities are identical to those for Chapter 6.

Appendix 2 has been published as Yogasundaram H, Bahniuk MS, Singh HD, Aliabadi HM, Uludağ H, Unsworth LD. BSA nanoparticles for siRNA delivery: coating effects on nanoparticle properties, plasma protein adsorption, and in vitro siRNA delivery. International journal of biomaterials. 2012 Aug

7;2012. © 2012 Haran Yogasundaram et al. under the Creative Commons Attribution License. I was responsible for the plasma incubation, elution and immunoblotting data collection, analysis and corresponding manuscript creation. H Yogasundaram, HD Singh and HM Aliabadi were involved in the material synthesis, characterization and cell uptake studies as well as composing the corresponding manuscript sections. H Uludağ and LD Unsworth were the supervising authors and were involved with the design of the study, its implementation and the creation of the manuscript.

Some of the research conducted for this thesis forms part of a research collaboration between Van A Ortega, myself and our supervisors Drs. G Goss, J Stafford and LD Unsworth. Chapters 5 and 9 are results from this collaboration. I was responsible for elastin-like polypeptide experimental design, synthesis and characterization in addition to all plasma adsorption, elution, Western blotting and clotting data collection and analysis as well as the composition of corresponding sections in the manuscripts. VA Ortega was responsible for poly(acrylic acid) nanoparticle experimental design and characterization as well as all cell assay data collection and analysis as well as the composition of corresponding manuscript sections. G Goss, J Stafford and LD Unsworth were supervising authors and were involved with the design of the studies and the creation of the manuscripts.

All other portions of this thesis are original works.

Dedication

While mine may be the name on the front of this thesis, I would never have been able to complete it without the endless support, encouragement, food and love, as well as the occasional percussive motivation from Markdullah, Hogrobah, my inner ninja Daria, my parents and my dear wife. Thank you, truly.

Acknowledgements

I would like to acknowledge the friends and colleagues I have made throughout my time at the University of Alberta and NINT, namely Wayne, Valentyna, Cathy and Angela for sharing their years of expertise in order to help a young untested scientist start off on the right foot.

I would like to recognize the numerous collaborating researchers with whom I've had the pleasure to work with over the course of my graduate program. It was an invigorating experience to learn from and work with experts from other fields.

I also thank the other members of the Unsworth group, past and present, undergrad or graduate student. The long days spent in the lab were all the more pleasant for their company and all the more productive for the insights we shared.

I am grateful to my supervisory committee, Dr. Hasan Uludağ and Dr. Robert Burrell, for their support and guidance, for constantly challenging me, always asking the unexpected questions and reminding me of the big picture.

I'm very appreciative of my supervisor, Dr. Larry Unsworth, for seeing me through my graduate studies and fostering my growth as a scientist and researcher. He introduced me to the fascinating crossroads of biology and engineering. He encouraged me to pursue lofty goals and was there to help figure out how to work past each stumbling block. It was because of his patient and persistent guidance that I am the capable, independent researcher I am today.

Table of Contents

List of Tables

List of Figures

1. Introduction

Immediately upon implantation of a biomaterial the interface undergoes countless interactions with the surrounding tissue environment. Almost instantly, the biomaterial will come into contact with blood and the hundreds of types of components contained therein (1). The primary species which interacts with the biomaterial at such an early time scale is the milieu of proteins found in blood. The sum of the interactions between blood proteins and biomaterial is complex and dynamic. Some of these interactions are intended and central to the biomaterial design and function, and some are unintended and, as of yet, unpredictable with the consequences of the initial adsorption process taking days or weeks to be fully realized. Some of these unintended consequences can negatively affect the biomaterial durability and function, while some can affect the host directly. These host responses may include altering the coagulation/fibrinolytic balance, chronic inflammation, immune response and impaired wound healing.

The non-specific adsorption of proteins to biomaterial surfaces is an important phenomenon as it has far-reaching potential consequences for biomaterial performance and host health. It is a complex series of interactions which have been studied since proteins were first observed adsorbing to biomaterial surfaces 50 years ago (2). While some progress has been made, as of yet the picture is far from complete. Part of the complexity is due to the variety of materials designed to interact with a host, while another part lies with the breadth of proteins found in blood and their complex structure-function relationships.

Additionally, the composition of the adsorbed proteome on a biomaterial surface is not static. The Vroman Effect describes the changes in adsorbed protein composition over time wherein high concentration proteins adsorb quickly but are replaced over time with less abundant but stronger binding species (3). Lastly, as proteins adsorb to surfaces, they can undergo changes in their tertiary conformations which can expose occult epitopes within the protein that can lead to a variety of biological responses, like cell signalling or binding sequences that can trigger further deleterious host responses.

It is unrealistic to expect to understand the complexities of protein-biomaterial interactions by studying them on a case-by-case basis. Knowledge about the underlying forces that drive the interactions between protein and biomaterial and the downstream consequences of their adsorption must be gathered to create a generalized model for protein adsorption to surfaces. This may be accomplished in part by systematically introducing specific modifications in biomaterial chemistries and observing corresponding changes in the adsorbed proteome.

1.1. Protein-Surface Interactions & Their Host Response Consequences

As mentioned previously, the adsorption of proteins from blood is an inevitable response to biomaterial implantation. It is a very complex phenomenon due to the wide variety of biomaterial in use, coupled with the hundreds of biological components that may adsorb and interact with one another and the

surrounding biological environment. The adsorbed proteome directs the cellular and host response toward the biomaterial and, in essence, dictates its therapeutic efficacy and the success or failure of the medical intervention. The following discussion details some of the protein-level biological responses to biomaterial surfaces as mediated by the adsorbed proteome. An understanding of these pathways, their initiation, amplification, regulatory mechanisms and interplay as well as methods to downregulate, inactivate or circumvent them entirely are critical for the successful design and implementation of biocompatible biomaterials.

1.1.1. Immune Response to Biomaterials

The immune system is responsible for defending the host from the infiltration of foreign bodies including microbes, viruses, parasites and foreign materials such as biomaterials. It is a complex, layered set of structures, processes and reactions and is generally broken down into two categories: the innate immune response and the adaptive immune response. Innate immunity in a generalized response toward all foreign bodies and occurs rapidly upon detection of the foreign entity and is comprised of physical barriers, inflammation, protein-based humoral elements and cells neutrophils and macrophages. Adaptive immune responses occur later than those of the innate response, but are specific for the type of foreign body. Moreover, adaptive immunity retains the knowledge of all previous foreign entities in order to mount a faster response upon their re-introduction into the host.

1.1.1.1. Innate Immunity

Of the two branches of the immune system, innate immunity is the faster acting of the two, mounting a generalized defense response within hours of the introduction of an antigen. The innate immune response is made up of various components including inflammation, blood proteins such as complement, cells such as natural killer cells, neutrophils and macrophages, the cytokines produced by these cells and finally physical barriers made up of skin and other epithelia (4-6). The entirety of innate immunity is a complex system and beyond the scope of this discussion. As the focus of this body of work is on blood protein adsorption, the primary focus herein will be on this component of innate immunity.

Inflammation, as part of the innate immune response, is an unavoidable consequence of biomaterial implantation and is triggered near-instantaneously by the tissue damage associated with the act of implantation. The degree and duration of the response depends upon the extent of tissue injury, the location of the implant and the physical characteristics of the biomaterial itself. Acute inflammation is characterized by the infiltration of neutrophils and macrophages as well as mast cell degranulation. This type of inflammation has a duration of less than one week and is not considered harmful to the host (7). Chronic inflammation is typically the result of sustained stimulation of the inflammatory response and, unlike acute inflammation, can have a much longer duration and have deleterious host responses, with the potential for severe tissue damage. The presence of monocytes and lymphocytes are the key differentiating factor between acute and chronic inflammation (7).

A critical, protein-based component of innate immunity is the complement system. Complement is made up of roughly 35 individual proteins, some of which are soluble and some which are membrane bound. Complement is a primitive, fast-acting system by which the body can distinguish invaders such as pathogens and foreign materials from the host. When a "non-self" entity is detected, primarily by adsorption of complement proteins, activation of this response can lead to opsonisation, activation of inflammation, the formation of a cell lysing protein complex and/or upregulated responses by the adaptive immune system. There are three major pathways by which complement can be activated, with varying degrees of relevance for protein-biomaterial interactions.

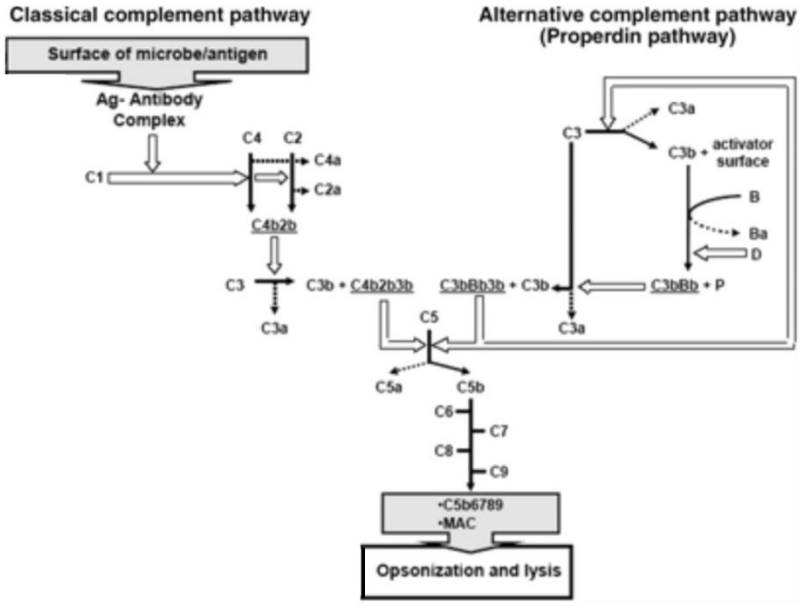

Figure 1.1. Classical and alternative pathways of complement activation. Image modified from Bonvini *et. al.*(8) © The European Society of Cardiology 2005

The classical activation pathway is of some relevance for the field of biomaterials and is schematically represented in Figure 1.1. This pathway is primarily activated by the recognition and binding of antibodies to their corresponding antigens. This complex is recognized, then bound to by complement component 1 (C1). This activates C1 and leads to a series of proteolytic reactions which form and activate a complex that bind and cleaves complement component 3 (C3). The presence of C3 on a surface acts as a signal for phagocytosis (9, 10). The cleavage of C3 is a point of convergence between the classical and alternative pathways within complement and such is an important point at which to monitor and/or modulate the activation of complement. Upon cleavage of C3, two different components are created which each contribute to an immune response in different fashions. C3a is a small portion of C3 and binds to various cell receptors to stimulate inflammatory responses such as increased vasodilation and permeability as well as histamine release (11). C3b is also formed and can bind with the complex that cleaved it in order to allow it to cleave complement component 5 (C5). Similarly to C3, upon C5 cleavage a mediator of the inflammatory response (C5a) is created as well as C5b. The creation of C5b leads to the formation of a membrane attack complex composed of various complement proteins which can form pores in lipid bilayers through which small molecules can pass through and cell lysis and death may occur (12).

The second method of complement activation is known as the lectin pathway. In this case, complement is activated by the recognition of certain

carbohydrates by the mannose-binding protein. This protein complexes with a corresponding serine protease and the complex behaves analogously to C1 and follows the same mechanism as the classical activation pathway (13). The activating carbohydrates are commonly found on various bacteria, viruses or fungi and, provided biomaterials are not designed with these activating sugars, do not play a significant role in immune responses toward biomaterials (14).

The complement activation pathway most relevant for the biomaterials field is the alternative pathway. It has been found that while the classical pathway has some role in activating complement in response to the presence of biomaterials, most of the activation occurs through the alternative pathway (15). What sets this pathway apart from the classical or lectin pathways is that the alternative pathway activation is nonspecific. It does not depend upon the recognition of specific antigens or carbohydrates, but rather the accumulation of spontaneously formed C3b on a material surface. Thus, in addition to C3 being a key component of the classical and lectin pathways, it is critical to this activation method as well. The alternative pathway of complement activation is shown in Figure 1.1. A small proportion of C3 is continually cleaved into C3a and C3b by a solution-phase convertase enzyme. Under normal regulatory conditions the C3b is hydrolyzed and inactivated and no complement activation is observed. However, the C3b can be stabilized by binding to a surface where amino or hydroxyl groups are available. These surface-stabilized C3b molecules cannot be inactivated by standard regulatory methods. Stabilized C3b will accumulate on the material surface over time and eventually form an alternative C5-cleaving complex. The

subsequent steps in the alternative complement pathway are identical to those of the classical and lectin pathways.

The consequences of non-specific complement activation on host health have been readily observed in cases where patients have been subjected to cardiopulmonary bypass or hemodialysis. The medical devices employed during these procedures have, in the past, had a tendency to activate complement *via* the alternative pathway. As such, the implications of these reactions are relevant for all biomaterial development. Symptoms resulting from deleterious host responses to hemodialysis include neutropenia, hypertension, fever, vomiting, tachycardia and cardiac arrest (16). Complement activation as a result of cardiovascular bypass is known as "post-perfusion" syndrome and can include fever, blood loss and impaired organ function. It was demonstrated that application of a single antibody that binds and inhibits C5a was enough to significantly decrease the severity of post-perfusion syndrome and reduced mortality rates (17, 18).

Given the severity of potential consequences to complement activation, it is of critical importance to prevent and/or modulate complement in response to the presence of a biomaterial. Research in the field, including the aforementioned studies, has yielded many of the details behind complement activation and as such, there are multiple routes by which to minimize or completely avoid complement activation in the presence of biomaterials (19, 20). Controlling the surface chemistry of biomaterials to minimize the presence of nucleophilic groups such as amines, hydroxyl and carboxylic group has been shown to be an effective way to decrease the adsorption and stabilization of C3b (21). Systemic inhibition

of complement has been achieved by the application of various protein therapeutics such as a recombinant C1 inhibitor (Ruconest®) or an anti-C5 antibody (Soliris®) (22, 23). Local regulation by recruiting complement regulatory proteins such as Factor H has also been a successful way to modulate non-specific complement activation by either directly immobilizing the regulator directly to the surface, or by coating the biomaterial with a Factor H-binding peptide (24-26).

1.1.1.2. Adaptive Immunity

This arm of the immune response is a more specific but a slower acting response compared to innate immunity. Adaptive immunity is also more sophisticated and can be primed by the presence of a foreign body in order to respond sooner and more vigorously to the reintroduction of the same foreign body. This type of immunity is made up of circulating proteins, cellular components and the cytokines produced by the cells. A complete discussion on the adaptive immune response is beyond the scope of this document and the topic herein will be limited to the blood protein component of adaptive immunity.

The principal humoral protein component of adaptive immunity is a family of proteins known as antibodies or immunoglobulins. Of the five major groups of immunoglobulins, immunoglobulin G (IgG) is by far the most common. IgG is a Y-shaped protein composed of four polypeptide chains, two pairs of identical protein sequences known as light and heavy chains. The N-termini of these chains make up the ends of the Y structure and are the sites whereby the

antibody binds to an antigen, known as the antigen-binding fragment, F_{ab}. This region shows tremendous genetically-encoded amino acid sequence and structural variability and is the reason why antibodies can bind to millions of unique antigens. Upon binding to an antigen, IgGs function by recruiting macrophage or natural killer cells to opsonize and break down the pathogen, prevent the toxin from binding and/or entering host tissues and can activate the complement portion of the innate immune response *via* the classical activation pathway (4). Should IgGs adsorb to biomaterial surfaces and initiate these responses, this could result in impaired device performance or complete failure. Furthermore, the host could experience local tissue damage, inflammation and scarring (7).

There is ongoing research in the field looking to understand and control immunoglobulin adsorption to biomaterials in order to mitigate its potentially deleterious consequences. Research from our lab has shown that the preparation method of bioactive glass 45S5 can modulate non-specific IgG adsorption, with the both amorphous and cast crystalline bioglasses not exhibiting any bound IgG while a sol-gel derived bioglass showed moderate IgG levels (27). Nikouei *et al.* found that increased carboxylation of a thermoresponsive triblock copolymer hydrogel could eliminate IgG adsorption after incubation in platelet poor human plasma (28). Changes in elastomer crosslinking as well as surface hydration were shown to have a significant effect on IgG adsorption wherein a greater stiffness resulted in corresponding increases in IgG adsorption (29). Surface passivation by treatment with copolymers of poly(2-(dimethylamino)ethylmethacrylate) and poly(oligo(ethylene glycol) methylether methacrylate) have been shown to resist

nonspecific adsorption of IgG significantly more than a commercial blocking agent or bovine serum albumin, with complete resistance observed for copolymers with small cationic and large hydrophilic segments (30). Carboxymethylation and sulfonation of anion-substituted poly(vinyl alcohol) both reduced non-specific IgG adsorption from human plasma, with the sulfonated variant adsorbing the least (31). Kurosawa *et al.* examined IgG adsorption to plasma-polymerized films made up of various monomers and found that increased IgG adsorption correlated with the cationic character of the polymer with maximal IgG adsorption found with tetrafluoroethylene or allymide monomers while polymerized acrylic acid adsorbed the least (32).

1.1.2. Coagulation and Fibrinolysis

Coagulation and fibrinolysis are diametrically opposed processes which work together to ensure that, when necessary, the blood is able to clot in order to stop bleeding and allow for repair to damaged blood vessels and tissues. The clotting response must be limited to only the damaged area and only for as long as necessary as an uncontrolled response could result in various serious complications including hemophilia, heart attack or stroke. As such, there must be a fine balance between clot formation and breakdown. This balance can be disturbed by the presence of various biomaterials. While there may be instances where pro- or anti-coagulant activity may be necessary in a biomaterial, most applications strive for no net effect regarding clotting and its regulation (33-35). Platelets also play a very significant role in clotting, however given that the subsequent materials testing was done specifically in platelet poor human plasma,

the discussion will limit itself to protein factors involved in coagulation and fibrinolysis.

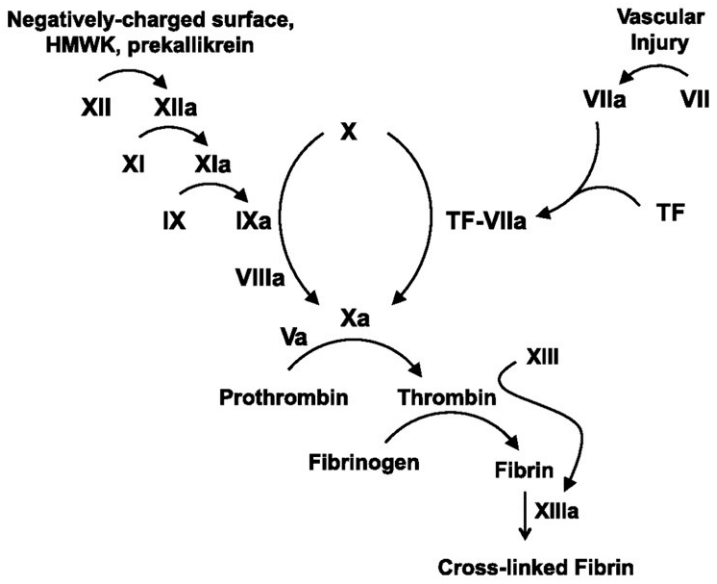

Figure 1.2. Intrinsic and extrinsic pathways for coagulation activation. Image modified from Kumar *et. al.* (36) © 2011 The American Physiological Society

There are two different biochemical pathways for the activation of coagulation, the extrinsic and intrinsic pathways, which converge at the point of activation of Factor X to form the common pathway as shown in Figure 1.2. Extrinsic activation of coagulation is typically thought to be a consequence of tissue injury. The instigator in this pathway is known as the Tissue Factor (TF) and is found on the surface of damaged cells. Upon instances of structural damage to the vasculature, Plasma Factor VII binds to the now-accessible Tissue Factor and forms a complex which is capable of cleaving and activating Factor X and leads to the common pathway. The intrinsic pathway begins by the adsorption of

specific proteins onto a foreign surface. This process is known as contact activation. It is generally thought that the initial adsorption event involves Factor XII activation after contact with an anionic or hydrophilic surface (37, 38). Activated Factor XII then converts prekallikrein to kallikrein and activates Factor XI with the assistance of high molecular weight kininogen (HMWK), which acts as a cofactor for the reaction by binding to the surface and stabilizing the other factors. Activated Factor XI activates Factor IX which itself activates Factor X which leads to the common pathway. Despite *in vitro* experiments clearly showing it to be the initiator of the intrinsic pathway, the role of Factor XII *in vivo* is not clear as a deficiency in it does not give rise to a bleeding disorder (39). A more detailed discussion of the role of Factor XII can be found in reviews by Vogler or de Maat (40, 41). In the field of biomaterials, the contact activation pathway is generally considered to be more relevant, though there is some evidence that Tissue Factor-initiated coagulation may have a larger role to play than currently thought (42).

The common pathway of coagulation begins with the activation of Factor X by either the extrinsic or intrinsic pathways-derived complexes. Activated Factor X binds with a cofactor and then can convert prothrombin to thrombin. Thrombin is the enzyme directly responsible for the cleavage and activation of fibrin from fibrinogen which polymerizes along with platelets and fibrin stabilizing Factor XIII to form an insoluble clot (43).

Plasminogen is another protein which is incorporated into the fibrin clot. It is the inactive form of the enzyme plasmin, which is responsible for the

breakdown of fibrin clots-a process known as fibrinolysis. Soluble circulating factors such as tissue plasminogen activator and urokinase catalyze the activation of plasmin. Plasmin degrades the polymeric fibrin clot into short chains known as fibrin degradation products which are carried away in the blood (43).

While the processes of coagulation and fibrinolysis initially appear to be contradictory in nature, they work together to ensure the swift generation of a clot to halt bleeding which, as the wound heals, is broken down to restore the vasculature to its pristine state. This balance is carefully maintained through the use of multiple activators and regulating factors throughout the various pathways. If an outside force acts to disrupt the balance, there may be dire consequences for the host. Unfortunately many biomaterials have been shown to disrupt this system and push it towards aberrant coagulation. These materials include vascular grafts, hemodialyzers, catheters, membrane oxygenators and other polymeric biomaterials (44-49). Improper, uncontrolled coagulation can lead to the degradation and impaired functioning of the implanted biomaterial as well as the generation of occluding thrombi or free flowing emboli which may fatally disrupt the flow of blood.

Biomaterial modifications are being developed in order to attempt to prevent aberrant thrombus formation in the first place, surface coatings of poly(ethylene oxide) polymer result in significantly lower protein and cell adsorption to materials and may be a promising method by which to address biomaterial-induced thrombosis (50). Surface coatings composed of albumin protein have also been shown to reduce material platelet and leukocyte adhesion

(51). A biomaterial can be coated with albumin or with molecules which bind endogenous albumin with high affinity in order to passivate the surface (52). While the two preceeding examples act to inhibit protein and cell adsorption to the surface of a biomaterial, the use of thrombomodulin as a surface coating works to inhibit thrombin and the activation of fibrin. This protein works by binding and sequestering thrombin and activating endogenous Protein C-activated anticoagulant functions (53).

1.1.3. Cell Binding

Another event resulting from biomaterial implantation into a host is the adhesion of cells to the material. There are a wide variety of cells capable of binding to a biomaterial surface including platelets, leukocytes, macrophages and red blood cells (7, 54). The binding event can lead to a number of deleterious host responses including platelet activation and clot formation, degranulation, activation of Tissue Factor expression and chemoattractant release leading to further macrophage recruitment (54-56). In some instances this may even lead to the formation of foreign body giant cells which can result in biomaterial degradation and eventual device failure (7).

Like the other processes mentioned previously, the attachment of cells is governed by the adsorbed proteome present on the biomaterial surface with some of the major proteins involved in this being fibrinogen, fibronectin and vitronectin (1, 57). For instance, platelets contain a cell surface receptor known as glycoprotein IIb/IIIa (also known as integrin $\alpha_{IIb}\beta_3$) on their surface which

mediates the cell adhesion to these and other adhesive plasma proteins (57). Fibrinogen is of particular importance for cell adhesion events and the foreign body response to biomaterials given that it also facilitates macrophage adhesion *via* the $\alpha_M\beta_2$ integrin (58). One of the most common current strategies to reduce instances of cellular adhesion and the resulting deleterious host responses is to functionalize biomaterial surfaces with non-fouling polymers such as poly(ethylene glycol) to reduce overall levels of protein adsorption from blood however this strategy, while promising *in vitro*, does not necessarily translate to improved host responses (59). These seemingly contradictory results highlight an important factor in plasma protein-mediated cell adhesion: the conformation of the adsorbed cell binding protein. While it has been known that protein adsorption to surfaces may alter their conformation, that these conformational changes may result in the activation of host responses such as cell binding and platelet activation is a relatively recent discovery (56, 60-62). This has been demonstrated through extensive studies with fibrinogen. For instance, measuring the total amount of fibrinogen adsorption to various surfaces was found to correlate poorly with platelet activation, but a strong relationship was found when platelet binding site availability was compared with adhesion levels (63). Another study showed that platelet adhesion levels did not correlate to adsorbed amounts of fibrinogen on self-assembled monolayers but that the adhesion correlated well with loss of alpha-helical structure in the fibrinogen (64). These and other studies have demonstrated that the structure of fibrinogen must be altered to expose sequences on normally hidden parts of the protein in order to achieve integrin-mediated cell

binding (65). Ultimately, prevention and control of cellular adhesion to biomaterial surfaces must take both the adsorbed proteome content and conformation into account and as the understanding of these factors grows so too does our ability to control and direct cellular adhesion (66, 67).

1.2. Biomaterials for Drug Delivery

The field of biomaterials has been under constant flux for some 70 years. Early biomaterials were designed to replace tissues without eliciting a negative host response. The second generation of biomaterials were designed to move beyond being bioinert and bioactivity was introduced in forms such as resorbability and controlled release. The latest iteration aims to move even further and add regenerative, stimulus-responsive and biological interfacing capacities to their designs. As the field evolves, so do the types of employed materials-from silicone rubber to biomimetic, stimulus-responsive self-assembling nanoparticles. This evolution must still take into account one of the earliest principles of biomaterials-that they do not elicit a negative host response. For reasons explained earlier, developing a complete understanding of biocompatibility is a complex task and while our understanding has grown, a generalized model of biocompatibility and host response still does not exist. Even the first step, the adsorption of proteins onto the biomaterial surface, is still not completely understood. The research that follows is an attempt to contribute to the understanding of this initial event. The drug delivery biomaterials under

examination will undergo systematic alterations and the effects these changes have on the adsorbed proteome will be characterized. What follows are overviews of the materials under study, their relevance for sophisticated delivery applications and how they may be systematically modified in order to better understand the protein-driven underpinnings of biocompatibility and host response.

1.2.1. Thermoresponsive Hydrogels

Thermogelling materials are a fascinating, highly customizable class of biomaterial with many potential applications. Composed of a careful arrangement of natural and/or synthetic polymers, these solutions will undergo a rapid soluble-to-gel transition in reaction to an increase in temperature-usually from room temperature to 37°C. These materials are, in essence, a minimally invasive, injectable, stimulus responsive, rapid-forming hydrogel depot for drug delivery and tissue engineering that is capable of molding to fit the area into which it is injected (68). Various drugs or protein-based therapeutic agents can readily be incorporated into the material before gelation and in some instances can improve the solubility of drugs such as paclitaxel more than 400-fold (69, 70). Thermogelling materials can be made out of numerous synthetic and/or natural polymers including, but not limited to: N-isopropyl acrylamide, poly(ethylene glycol), polycaprolactone, poly(lactic acid), poly(glycolic acid), poly(urethane), chitosan and elastin-like polypeptides. A more detailed list can be found in a review by Moon H.J. *et al.* (71). The choice, architecture and proportion of polymer in a thermogelling material can greatly influence the final physical

characteristics of the hydrogel making this a very flexible and customizable platform suitable for a variety of applications including localized and/or sustained release of therapeutics, ocular treatments and tissue engineering (72). Given all the benefits of a flexible, modular system such as this, it comes as no surprise that thermogelling polymer research is a popular field. While much effort is being expended on developing the biomaterials themselves, the biocompatibility of these materials is not as vigorously investigated. The controlled, well-characterized alterations made in the polymer chains during the material development present an excellent opportunity to examine protein adsorption effects as a direct result of the alterations to the materials. Biocompatibility can be a concern for thermogelling materials in that a negative response could result in encapsulation of the hydrogel, thus altering the pharmacokinetics or even completely negating any therapeutic benefits of the biomaterial. Material degradation may be altered by the host response as well and not progress as observed under the controlled conditions during their development. When designed for tissue engineering, thermogelling biomaterials obviously undergo some biological testing, though usually under simplified experimental conditions. Without thorough testing in complex media there is the risk that *in vivo*, the biomaterial may not perform as observed *in vitro*.

1.2.2. Bioactive Glass

Bioactive glasses are a type of biomaterial employed heavily in clinical applications involving large bone or dental defects. One formulation in particular, known as Bioglass® 45S5 and composed of 45% SiO_2, 24.5% CaO, 24.5% Na_2O

and 6% P_2O_5 by weight, has been shown to have excellent osseointegrative and osteoconductive properties (73, 74). Studies have demonstrated that bioactive glass can bind strongly to endogenous bone to provide structural support while also serving as a support onto which stem cells can attach and differentiate to facilitate tissue repair (75-78). In addition to bone defect repair, bioactive glasses have been used as ossicular implants to restore hearing and as a method to enhance dental repair in instances of periodontal disease (79). Further applications of bioactive glasses are limited by the mechanical properties of the material and manufacturing methods and research into the devitrification of bioactive glasses is ongoing. Studies have shown that crystallization can result in improved mechanical properties and allow for powder sintering but the crystalline bioactive glass also become less soluble in biological fluids (80-83). This decreased solubility may seriously affect protein adsorption and the resulting cellular response and as such, the bioactivity of the biomaterial as a whole. Protein adsorption to bioactive glasses and the role they play in the cellular response to these materials is not well understood for neither amorphous nor crystalline glasses and this omission may be part of the reason there are numerous conflicting cell studies in the literature (84-87). Most studies focused upon the interactions between bioactive glasses and the host environment do so using a solution known as Simulated Body Fluid which is, in essence, a buffer containing various elements at physiological ionic concentrations but lacking all other plasma components like cholesterols, triglycerides or proteins (88). Studies examining protein adsorption to bioactive glasses of various preparations are crucial for

determining the consequences of various manufacturing methods and the viability of crystalline bioactive glasses. Furthermore, studies on the clinically successful 45S5 formulation would provide valuable insight for the development of a generalized model of biomaterial protein adsorption.

1.2.3. Poly(acrylic acid) Nanoparticles

Polymers are not only used as thermogelling biomaterials, but see a number of other uses including as fluorescent agents for medical and cell imaging, additives in paints and cosmetics, water purification reagents and nanocarriers for therapeutic purposes (89). Most relevant for the discussion herein is the use of polymers for nanoscale delivery systems of pharmaceuticals. There are a number of advantages to systems on this scale including protection from premature drug degradation, enhanced drug penetration, adsorption and distribution, improved drug solubility and stability (90, 91). The carriers can also be modified to introduce sophisticated functionalities including specific release patterns, targeting and localization behaviours and stimulus-responsive release (92, 93). A thorough review of the myriad of polymer nanocarriers is well beyond of the scope of this discussion. Polymers such as poly(acrylic acid) (PAA) can also be used to enhance the function of existing metal nanoparticles by reducing their tendency to aggregate and precipitate out of solution and decrease the potential for free metal ions to leech into solution (94, 95). As PAA nanoparticle coatings become more common as drug delivery vehicles and in non-medicinal fields such as agricultural pesticide dispersion, it is undeniable that their biocompatibility needs to be well understood (96). Studies of polymer-coated

nanoparticles in particular can yield some interesting information in regards to how much, if at all, the core of the nanoparticle may influence biological phenomena such as protein adsorption and the downstream host response. This information is invaluable for evaluating PAA-nanoparticle biomaterial safety and the use of PAA as a polymer for passivation of other blood-contacting devices.

1.2.4. Elastin-Like Polypeptides

Elastin-like polypeptides (ELPs) are a protein-based biomaterial currently undergoing much research and development. ELPs are a versatile, customizable, stimulus-responding and self-assembling biopolymer that is being developed for use in a variety of applications including: recombinant protein purification, nanoparticle-based passive and targeted drug delivery, hydrogel drug depots and tissue scaffolds. ELPs are derived from mammalian elastin-a common extracellular matrix protein (97). Elastin itself possesses some very interesting characteristics: it is formed from tropoelastin precursors which self-assemble by transitioning from soluble to insoluble and are crosslinked with one another, forming a highly flexible, elastic and durable material which undergoes countless expansions and contractions over its 70 year half-life (98). It can be organized in various fashions depending on the tissue-in the lung elastin forms an intricate lattice, in cartilage it forms a honeycomb structure, in ligaments and tendons they adopt woven-fiber structure and around arteries they form ring structures (99). In addition to being a major structural protein, elastin has been shown to promote attachment of skin fibroblasts, stimulate endothelial cells to form vasculature and

cause fibroblast cells to differentiate into contracting cells to aid in wound closure (100-102).

The research lab of Dr. Dan Urry is largely considered responsible for the development of the first elastin-like polypeptide from tropoelastin. The amino acid monomer sequence of this ELP is valine-proline-glycine-valine-glycine (VPGVG) and was shown to undergo coacervation as a result of a reversible phase change of the individual protein chains (103). Further studies indicated that the fourth residue of this "pentapeptide" could be substituted for any other amino acid with the exception of proline while retaining the sequences' ability to undergo a phase transition, though the conditions at which the ELP undergoes its phase transition are affected (104). Thus the sequence for a prototypical ELP can be expressed as $(VPGXG)_n$ where X is any amino acid with the exception of proline and n represents the number of repeats of the pentapeptide. Alanine mutations in the first, third and fifth positions of this sequence have been studied and have been shown to alter the phase transition behaviour. $(APGVG)_n$ and $(VPGVA)_n$ show no reversible elasticity while $(IPGVG)_n$ is unaffected (105-107). $(VPGAG)_n$ sequences have been shows to have significantly strong hysteresis behaviours which have led some researchers to consider these sequences more plastic than elastomeric (108). Other related ELP-like monomer sequences including VPGG, GVGVP and VAPGVG have been studied (109).

As mentioned above, the transition temperature for ELPs can be reliably modified without otherwise altering its ability to undergo a reversible phase change by altering the amino acid in the fourth position of the VPGXG sequence.

Generally speaking, the more hydrophobic the amino acid in the X position, the lower the transition temperature (104). Urry took this concept so far as to create an entirely new hydrophobicity scale for amino acids based upon this phenomenon (104). The total chain length of an ELP can also affect the constructs transition temperature. While not as influential on ELPs composed of ≥100 repeats, the shorter the ELP sequence, the higher the transition temperature (110). In addition to characteristics intrinsic to ELPs, the environmental conditions around the ELP can also influence its phase-changing behaviour. Salts have been shown to have a strong influence over ELP transitions with increasing salt concentrations decreasing the transition temperature and different types of salts having greater or lesser effects consistent with their position in the Hofmeister series (111). The concentration of the ELP in solution can also influence the transition point, with more concentrated solutions lowering the required temperature though some sources suggest this relationship may not exist under all circumstances (110, 112, 113). Though not as common as temperature and salt concentration, other methods of triggering ELP phase transitions have been studied and include changes in pH, ligand binding and light as reviewed by Franco *et al.* (114).

Applying these numerous and varied customization methods toward ELPs is a relatively straightforward procedure owing to the protein-based nature of ELPs. That is, these biopolymers can be designed and manufactured using recombinant methods. This type of synthesis allows for an unprecedented level of control over the chemistry and position of every amino acid in an ELP chain,

results in the creation of a monodisperse polymeric product and various biofunctional moieties can be appended quite simply.

DNA sequences encoding for ELPs are by their very nature highly repetitive and are often rich with G-C base pairs. These two characteristics makes it difficult to work with these types of sequences in the lab and also prohibitively expensive to synthesize large ELP genes commercially. Techniques such as PCR, which depends on the melting and re-annealing of double stranded DNA, may not function well, if at all, for ELP-encoding DNA sequences. Fortunately, through the clever application of specific restriction enzymes, short commercially sourced ELP genes can be concatemerized together. This process is known as recursive directional ligation (RDL) (115). In the forthcoming protocol will be a method to create DNA sequences for marginally soluble, short ELPs using a modified method for RDL addressing some technical issues experienced during their production including inefficient restriction enzyme cleavage due to DNA methylation, significant numbers of incorrect vector-only clones during attempted ELP sequence concatemerization, and minimal SfiI restriction enzyme cleavage when using only one cleavage site in the expression vector modifying sequence. The modifications greatly increase the overall efficiency of the RDL process while minimizing time- and reagent-intensive steps, such as modified expression-vector linearization and mass colony screening.

The purification of recombinantly produced proteins is typically the largest bottleneck in their production, but with ELPs, their reversible solubility can be exploited to partially simplify purification under the correct conditions.

This approach is known as inverse temperature cycling (ITC) and was demonstrated by Meyer and Chilkoti (116). When ELPs have been purified successfully, for the most part the guest amino acids in these constructs fall toward the middle of Urry's ELP hydrophobicity scale (104). While ITC purification has been sufficient for these types of constructs, it is not applicable to all ELPs. Successfully employing an ITC-only purification procedure means the ELP construct and its expression have to meet certain criteria: The ELP must not end up in the insoluble fraction of the cell lysate during the lysis procedure; the ELP must be in its soluble monomer form in the cell lysate; the phase transition needs to be triggered in the cell lysate under reasonable temperature and salinity conditions; and the protein must be expressed at a concentration high enough for a phase transition to be possible under reasonable conditions but must also be low enough to avoid significant depression of the transition temperature as well as the formation of inclusion bodies. Not all ELP purifications meet these criteria. If an ELP is poorly expressed, or if it contains guest amino acids that are significantly more hydrophilic or hydrophobic than those commonly employed in the literature, or if the ELPs are significantly longer or shorter than what is commonly used, the transition temperature of the ELP construct may be too high or too low for an ITC-only approach.

ELP constructs that can successfully be purified using an ITC only approach, that is those with longer chain lengths (~120 repeats) and only moderately hydrophobic guest amino acids, have been developed for use as purification tags for recombinantly-produced therapeutic proteins. The advantages

of ITC-only purifications for ELPs are applied to ELP-therapeutic fusion proteins. Given the complexities and expenses of standard large scale protein purification "ELPylation," as it is sometimes referred to, could prove to be critical for wide-scale production of recombinantly-produced therapeutics. One of the first demonstrations of this strategy was published in 2001 and showed that thioredoxin purification from *Escherechia coli* using an appended ELP tag produced a statistically similar amount of protein as a standard immobilized metal affinity chromatography method (117). ELP tags have also been used to purify an 18 amino acid antimicrobial peptide produced in *E. coli* with a final yield ~2.4X greater than a comparable purification using a polyhistidine tag (118). ELP tags have also been used in recombinant production from tobacco leaves. A potential therapeutic known as Glycoprotein 130 was fused to an ELP sequence and ITC was successfully used to purify the final product from the plant debris (119). At the moment there have not been any successful applications of "ELPylation" technologies to mammalian expression systems, though these types of cells are the preferred method for biological therapeutic production. An examination of this and other potential issues surrounding the industrial applications of ELP protein purification tags is summarized in the literature by Yeboah *et al.* (120).

While there are abundant proposed applications for self-assembling ELPs, our understanding of their behaviour is not complete, with multiple models of ELP assembly being proposed over the years. Early studies suggested that below their transition temperature, ELPs existed as random coils and underwent a widespread conformational change in conjunction with self-assembly. This has

been disproven with more advanced studies using molecular dynamics simulations and nuclear magnetic resonance. The current understanding of ELPs is that they are well hydrated, intrinsically disordered proteins and contain transient local beta turn and/or polyproline structures (121-123). Their assembly is thought to be entropically driven and triggered by a sudden decreased solvation of the protein backbone (124, 125). This assembly does not affect the transient structural tendencies of individual ELP chains (126-127).

Debate surrounding ELP phase transition behaviours have not hampered their development as a biomaterial for numerous applications. Drug delivery is one of the areas in which ELPs are undergoing vigorous development. As ELPs can be engineered to form nanoparticles, as a delivery system they have the same advantages as polymer nanoparticles discussed earlier. Given that they are made of proteins, ELPs also have advantages of biocompatibility and biofunctionality as discussed in the albumin nanoparticle section above. Given that ELPs have tunable stimulus-responsive phase transition behaviour, are easily engineered *via* their DNA sequence and can have a variety of biofunctionalities appended to them, there are clearly countless ways in which ELPs as a platform can be customized for a variety of drug delivery strategies and applications. This is evident given the numerous review articles in the literature focused exclusively on ELPs and drug delivery (113, 128-135). The following discussion will be an overview of some of the different ways ELPs can be used for drug delivery.

Delivery has been demonstrated using monoblock ELPs in conjunction with penetrating or targeting moieties. One of the earliest proofs of principle for

engineered delivery involved a 120-mer ELP with a 1:7:8 ratio of valine, glycine and alanine in the guest amino acid position which was fused with a variety of cell penetrating peptides (136). These constructs were shown to successfully enter cervical and ovarian carcinoma cells and, when appended to a kinase inhibitor, slowed cell growth. Tumor targeting capabilities were demonstrated by fusing valine-containing ELP sequences with the tumor homing peptide AP1 (137). This study showed successful binding of the constructs to the interleukin 4 receptor on the surface of cancer cell lines *in vitro* as well as homing capabilities and enhanced retention times in tumour-containing mouse models. ELP block copolymers are commonly used to generate nanoscale drug delivery vehicles. Constructs include, at minimum, two distinct ELP blocks where one incorporates hydrophobic guest amino acids and the other block hydrophilic and/or charged residues. This results in a protein with two distinct transition temperatures which, at physiological conditions, contains an insoluble, hydrophobic, drug-containing core and a soluble, hydrated shell. Dreher *et al.* conducted a systematic analysis of the roles of ELP molecular weight and hydrophobic;hydrophilic ratios on diblock ELPs composed of hydrophobic valine-containing domains and hydrophilic domains with 1:7:8 ratios of valine:alanine:glycine in the guest amino acid position (138). The drug rapamycin was incorporated into a different ELP block copolymer made of a serine-containing hydrophilic segment and an isoleucine-containing hydrophobic segment (139). This construct enhanced the solubility, drug loading and half-life of the rapamycin significantly which lead to decreased toxicity and a reduction in tumor growth in mouse models.

While the aforementioned drug delivery constructs typically encapsulate their payloads, there are also strategies where drugs are conjugated directly to ELP molecules. This can lead to the generation of nanoparticles by virtue of the presence of a hydrophobic drug and hydrophilic protein sequence or to soluble conjugates which can be subjected to targeted accumulation by localized heating. The covalent addition of doxorubicin to the end of an ELP with a 1:7:8 ratio of valine:alanine:glycine guest amino acids resulted in the spontaneous formation of nanoparticles with diameters of approximately 40nm (140). This particular ELP had a transition temperature well above physiological conditions and as such, the nanoparticle formation was driven exclusively by the presence of multiple hydrophobic drug molecules localized on one end of the ELP chains. A simple adjustment of the guest amino acid ratio from 1:7:8 to 5:2:3 resulted in a construct with a transition temperature of 41°C. This construct was also conjugated to doxorubicin and was targeted to accumulate in solid surface tumors by simply heating the area to 41-42°C (141, 142). The localized increase in temperature caused the ELP-doxorubicin conjugates to transition from soluble to insoluble exclusively in the tumor and resulted in a 2-fold increase in drug accumulation in the tumor compared to a temperature-insensitive control.

While the preceding examples of ELP use in drug delivery make use of rather simple constructs, they serve to clearly illustrate various ways in which ELPs can be used for nanoscale drug delivery and how their programmability and unique phase transition behaviour can be exploited. These experiments open the door for more complex ELP constructs composed of combinations of targeting

sequences, enzymatic cleavage sites, biological therapeutics as well as hybrid systems made up of ELP-liposomes, ELP-silica micelles or ELP-chitosan-alginate capsules (143-145).

In addition to nanoscale drug delivery systems, ELPs are also finding use as hydrogel-based biomaterials for localized drug delivery. Given their ability to spontaneously self-assemble and that ELPs can be programmed means researchers can tune the physical properties of the hydrogel to control their porosity, mechanical properties and degradability (146). As with nanoscale drug delivery applications, there exist numerous review articles focused on the use of ELPs as hydrogels and the following examples serve to provide an illustration of the potential for these proteins in the field of hydrogel biomaterials (129, 130).

ELPs have been used as drug depots for antibiotics in order to reduce their systemic toxicity. Adams *et al.* created a hydrogel made of crosslinked ELP sequences with 102 repeats of $VPGKG(VPGVG)_{16}$ and used it to deliver the antibiotics cefazolin and vancomycin (147). This construct was able to release the antibiotics in a sustained fashion for about 25 hours for the cefazolin and roughly 500 hours for the vancomycin.

ELPs have also been used to create depots to treat dry eye disease by fusing a 96-mer of VPGVG to the prosecretory eye protein lacritin (148). This construct was injected into the lacrimal glands of mice and was shown to stimulate tear production *in vivo* and enhanced the retention of the lacritin six-fold. This is a significant development given that the presence of tears means it

can be very challenging to create drug depots in a high clearance environment like the eye.

Tissue engineering is another application for which ELPs are being applied. Given the ability to exactly control their sequence, program in biological moieties with ease and control the resulting viscoelastic properties by engineering the amino acids means ELPs overcome some of the shortcomings of both synthetic polymer and naturally-derived scaffolds for tissue engineering. Lim *et al.* developed a family of ELP-based tissue scaffolds that were able to undergo rapid *in situ* crosslinking and support fibroblast cell growth (149). The scaffolds were made using ELPs with guest amino acid ratios of either 1:7:1 or 1:2:1 of lysine:valine:phenylalanine of lengths ranging from 32-144 repeats. The lysine residues were used in conjunction with β-[tris(hydroxymethyl)phosphino]-propionic acid in order to improve the mechanical properties of the scaffold. The matrices derived from these studies were then used to repair osteochondral defects in goats and it was found that after 3 months the defects treated with the ELP scaffold healed faster than the controls, though after 6 months the ELP had been completely degraded (150).

ELP scaffolds supporting endothelial cells have been developed for vascular grafts with diameters under 5 mm by Heilshorn *et al*. (151). They were engineered to use 60-125 repeats of ELP sequences primarily containing isoleucine resides in the guest position with some constructs containing lysine residues for crosslinking purposes. A fibronectin-derived cell binding motif CS5 was also included. It was found that human umbilical vein endothelial cells

adhered and were retained on the crosslinked ELP scaffolds in comparable levels to a fibronectin-only scaffold. Further studies showed that the placement of the crosslinking lysine resides can alter cell binding efficiency and confining the crosslinking regions to the protein termini enhanced cell binding (152).

While there has been an explosion in the development of ELP-based biomaterials, there has not been an accompanying increase in data regarding the biocompatibility for these materials. Given that these medical devices are intended to eventually be used in clinical situations, the lack of information regarding the potential host response seems like an oversight. This knowledge gap is misrepresented in the literature as the assumed biocompatibility of ELPs is frequently mentioned in publications. Throughout the literature there are numerous allusions to the fact that ELPs are protein based, should degrade into amino acids, and have been shown to possess superior biocompatibility but, when referencing publications focused on ELP biocompatibility, always end up referencing the same 2-3 papers. Most mentions of biocompatibility of ELP materials in the literature are based on incidental observations made during other testing involving mammalian cells (153, 154). While the observations may be valid, given that they are made using different constructs with differing cell lines under non-identical conditions, means the information cannot be combined and is of limited use in developing a greater overall understanding of ELP biocompatibility. Another factor lending credence to the assumed biocompatibility of every ELP-containing construct is a publication from Urry which reports the results of a series of generic biocompatibility testing on a

crosslinked VPGVG-composed ELP (155). The report finds that this particular ELP is very biocompatible and many researchers assume that this biocompatibility extends to all other ELP constructs. Further testing on the same class of constructs confirmed the biocompatibility of the material unless the ELPs were of 200 repeats or more-in those cases aberrant calcification was observed (156). Biocompatibility testing of microparticles of poly(VPAVG) ELPs for ocular applications showed some inflammation after intraocular injection (157). This result indicates that the chemistry of the third amino acid of the sequence and/or the morphology of the ELP may have a role to play in ELP biocompatibility. Another study demonstrated that the guest amino acid position may affect the material biocompatibility (158). While a construct composed exclusively of VPGVG did not show any inflammation, a comparable device with a guest amino acid ratio of 3:1 of valine:phenylalanine caused some inflammation and the formation of a fibrous membrane around the implant. A paper by Sallach *et al.* examined the short and long-term responses to an ABA block copolymer composed of repeats of the sequence VPAVG[$(IPAVG)_4(VPAVG)]_{16}$IPAVG in the A block and VPGVG[$(VPGVG)_2$VPGEG(VPGVG)$2]_{48}$VPGVG in the B block (159). This study found there to be no inflammatory response or calcification in their mouse model and that the implant retained its shape, architecture and mechanical properties for more than a year. Taken together, the results above suggest that it cannot be assumed all ELPs, particularly complex hybrids made up of more than the prototypical VPGXG sequence, are equally biocompatible. Systematic testing must be done to determine what influence the

guest amino acids, chain length and overall morphology have on ELP biomaterial biocompatibility. An understanding of ELP biocompatibility and the effects of amino acid additions or substitutions is of immediate critical importance. Otherwise many promising ELP biomaterials may, after much time and effort spent in development, find themselves unusable due to deleterious host responses.

ELPs represent a rare opportunity for a systematic examination of plasma protein adsorption to protein materials as a function of guest amino acid chemistry, overall chain length or overall morphology. Because of their reliable programmability and synthesis, systematic alterations to the ELP sequence can be made with precision otherwise unheard of in the biomaterials field. This information will help elucidate the amino-acid level effects on biocompatibility for all protein-based biomaterials. ELPs are also a very intriguing vehicle by which to test protein adsorption and biocompatibility because, with proper sample prep, the confounding factors of subunit chemistry and resulting morphology can be delineated from one another. Typically when alterations are made to the basic units of a biomaterial, a polymer chain for instance, this results in some changes in constructs overall physical characteristics. Thus, when comparative biocompatibility studies are carried out, they cannot control for the differences in appearance of the materials and the variations in host response those may produce. ELPs, with proper sample preparation, can allow for variations in the chain length and chemistry without significant alterations in their morphology. This would allow for direct observations of amino acid-level consequences on protein adsorption and biocompatibility. Additionally, identical ELP constructs

can be used to create a variety of morphologies such as microparticles, nanoparticle and hydrogels which would allow for a direct survey of the morphological consequences on protein adsorption and biocompatibility.

1.3. Research Proposal

1.3.1. Rationale

Understanding the host response to a biomaterial is a complex yet critical issue. For any biomaterial to be employed clinically it must be shown to not negatively impact the host. That is, it must be biocompatible. Complicating the issue is that there are a myriad of biomaterials designed for a variety of applications that are made from a number of materials. Host responses to biomaterials are not uniform and can vary depending on the material and environment in question. From the standpoint of the host, the reactions to biomaterials can be varied and are only partially understood. The basis for a biological response to an implant depends upon the near instantaneous adsorption of proteins onto the biomaterial surface. There are hundreds of proteins which may or may not be involved in a single adsorption event. Several techniques are used to probe the protein adsorption to material surfaces including immunoblotting assays, radiolabelling and, more recently, high-throughput mass spectroscopy-based proteome analysis. This thesis will examine how molecular-level modifications to a variety of biomaterials affect human plasma protein

adsorption to their surfaces by using immunoblotting methods. The materials under study herein represent a wide cross-section of biomaterials which can be easily and reliably modified so that the downstream consequences of these modifications can be characterized. This information can be used to help develop an overall understanding of the process of protein adsorption and generalized guidelines for future biomaterial design to decrease the likelihood of deleterious host responses.

1.3.2. Objectives

The thesis will endeavour to answer the following questions:

- Can stimulus-responsive, self-assembling protein nanoparticles be made using novel short, marginally-soluble elastin-like polypeptides and how do factors such as chain length, guest amino acid chemistry and concentration affect nanoparticle formation?

- What role do various fundamental level chemical modifications have on the biocompatibility of biomaterials for drug delivery as primarily evaluated by plasma protein adsorption to material surfaces?
    - What role does carboxylation play in the plasma protein adsorption to block copolymers of poly(ethylene glycol) and poly(ε-caprolactone)?

- What plasma proteins adsorb to clinically successful bioactive glass 45S5? What effect does altering crystallinity or manufacturing method have on surface protein adsorption?
- How do ELP nanoparticle diameter, protein chain length and chemistry alter the adsorption of plasma proteins, plasma clotting rates, survivability and phagocytic response from macrophage cells?

1.4. References

1. Horbett TA. Chapter II.1.2 - Adsorbed Proteins on Biomaterials A2 - Ratner, Buddy D. In: Hoffman AS, Schoen FJ, Lemons JE, editors. Biomaterials Science (Third Edition): Academic Press; 2013. p. 394-408.

2. Vroman L. Effect of Adsorbed Proteins on the Wettability of Hydrophilic and Hydrophobic Solids. Nature. 1962;196(4853):476-7.

3. Vroman L, Adams A, Fischer G, Munoz P. Interaction of high molecular weight kininogen, factor XII, and fibrinogen in plasma at interfaces. Blood. 1980;55(1):156-9.

4. Abbas AK. Cellular and molecular immunology. In: Lichtman AH, Pillai S, editors. 6th ed. ed. Philadelphia :: Saunders Elsevier; 2007.

5. Medzhitov R, Janeway Jr C. Innate immunity. New England Journal of Medicine. 2000;343(5):338-44.

6. Medzhitov R. Recognition of microorganisms and activation of the immune response. Nature. 2007;449(7164):819-26.

7. Anderson JM, Rodriguez A, Chang DT. Foreign body reaction to biomaterials. Seminars in immunology. 2008;20(2):86-100.

8. Bonvini RF. Inflammatory response post-myocardial infarction and reperfusion: a new therapeutic target? European Heart Journal Supplements. 2005;7(Suppl I):I27-I36.

9. Hamad OA, Ekdahl KN, Nilsson B, editors. Non-proteolytically activated C3 promotes binding of activated platelets and platelet-derived microparticles to leukocytes via CD11b/CD18. Immunobiology; 2012.

10. Hamad OA, Nilsson PH, Wouters D, Lambris JD, Ekdahl KN, Nilsson B. Complement component C3 binds to activated normal platelets without preceding proteolytic activation and promotes binding to complement receptor 1. The journal of immunology. 2010;184(5):2686-92.

11. Klos A, Tenner AJ, Johswich K-O, Ager RR, Reis ES, Köhl J. The role of the anaphylatoxins in health and disease. Molecular immunology. 2009;46(14):2753-66.

12. Walport MJ. Complement. First of two parts. The New England journal of medicine. 2001;344(14):1058-66.

13. Wong N, Kojima M, Dobo J, Ambrus G, Sim R. Activities of the MBL-associated serine proteases (MASPs) and their regulation by natural inhibitors. Molecular immunology. 1999;36(13):853-61.

14. Matsushita M. The lectin pathway of the complement system. Microbiology and immunology. 1996;40(12):887-93.

15. Andersson J, Ekdahl KN, Lambris JD, Nilsson B. Binding of C3 fragments on top of adsorbed plasma proteins during complement activation on a model biomaterial surface. Biomaterials. 2005;26(13):1477-85.

16. Craddock PR, Fehr J, Brigham KL, Kronenberg RS, Jacob HS. Complement and leukocyte-mediated pulmonary dysfunction in hemodialysis. New England Journal of Medicine. 1977;296(14):769-74.

17. Fitch JC, Rollins S, Matis L, Alford B, Aranki S, Collard CD, et al. Pharmacology and biological efficacy of a recombinant, humanized, single-chain

antibody C5 complement inhibitor in patients undergoing coronary artery bypass graft surgery with cardiopulmonary bypass. Circulation. 1999;100(25):2499-506.

18. Haverich A, Shernan SK, Levy JH, Chen JC, Carrier M, Taylor KM, et al. Pexelizumab reduces death and myocardial infarction in higher risk cardiac surgical patients. The Annals of thoracic surgery. 2006;82(2):486-92.

19. Gemmell CH, Black JP, Yeo EL, Sefton MV. Material-induced up-regulation of leukocyte CD11b during whole blood contact: Material differences and a role for complement. Journal of Biomedical Materials Research Part A. 1996;32(1):29-35.

20. Tang L, Liu L, Elwing HB. Complement activation and inflammation triggered by model biomaterial surfaces. Journal of biomedical materials research. 1998;41:333-40.

21. Salvador-Morales C, Flahaut E, Sim E, Sloan J, Green ML, Sim RB. Complement activation and protein adsorption by carbon nanotubes. Molecular immunology. 2006;43(3):193-201.

22. Ricklin D, Lambris JD. Complement in immune and inflammatory disorders: therapeutic interventions. The Journal of Immunology. 2013;190(8):3839-47.

23. Tillou X, Poirier N, Le Bas-Bernardet S, Hervouet J, Minault D, Renaudin K, et al. Recombinant human C1-inhibitor prevents acute antibody-mediated rejection in alloimmunized baboons. Kidney international. 2010;78(2):152-9.

24. Andersson J, Larsson R, Richter R, Ekdahl KN, Nilsson B. Binding of a model regulator of complement activation (RCA) to a biomaterial surface:

surface-bound factor H inhibits complement activation. Biomaterials. 2001;22(17):2435-43.

25. Andersson J, Bexborn F, Klinth J, Nilsson B, Ekdahl KN. Surface-attached PEO in the form of activated pluronic with immobilized factor H reduces both coagulation and complement activation in a whole-blood model. Journal of Biomedical Materials Research Part A. 2006;76(1):25-34.

26. Wu Y-Q, Qu H, Sfyroera G, Tzekou A, Kay BK, Nilsson B, et al. Protection of nonself surfaces from complement attack by factor H-binding peptides: implications for therapeutic medicine. The Journal of Immunology. 2011;186(7):4269-77.

27. Bahniuk MS, Pirayesh H, Singh HD, Nychka Ja, Unsworth LD. Bioactive glass 45S5 powders: effect of synthesis route and resultant surface chemistry and crystallinity on protein adsorption from human plasma. Biointerphases. 2012;7(1-4):41-.

28. Nikouei NS, Vakili MR, Bahniuk MS, Unsworth L, Akbari A, Wu J, et al. Thermoreversible hydrogels based on triblock copolymers of poly(ethylene glycol) and carboxyl functionalized poly(ε-caprolactone): The effect of carboxyl group substitution on the transition temperature and biocompatibility in plasma. Acta biomaterialia. 2014;12:81-92.

29. Vyner MC, Liu L, Sheardown HD, Amsden BG. The effect of elastomer chain flexibility on protein adsorption. Biomaterials. 2013;34(37):9287-94.

30. Vuoriluoto M, Orelma H, Zhu B, Johansson LS, Rojas OJ. Control of Protein Affinity of Bioactive Nanocellulose and Passivation Using Engineered Block and Random Copolymers. ACS Appl Mater Interfaces. 2016;8(8):5668-78.

31. Ryu KE, Rhim H, Park CW, Chun HJ, Hong SH, Kim JJ, et al. Plasma protein adsorption to anion substituted poly (vinyl alcohol) membranes. Macromolecular research. 2003;11(6):451-7.

32. Kurosawa S, Kamo N, Aizawa H, Muratsugu M. Adsorption of 125I-labeled immunoglobulin G, its F(ab')2 and Fc fragments onto plasma-polymerized films. Biosens Bioelectron. 2007;22(11):2598-603.

33. Neuffer MC, McDivitt J, Rose D, King K. Hemostatic dressings for the first responder: a review. Military medicine. 2004;169(9):716.

34. Waner M, editor Novel hemostatic alternatives in reconstructive surgery. Seminars in hematology; 2004: Elsevier.

35. Banerjee R, Nageswari K, Puniyani R. Hematological aspects of biocompatibility-review article. Journal of biomaterials applications. 1997;12(1):57-76.

36. Kumar A, Kar S, Fay WP. Thrombosis, physical activity, and acute coronary syndromes. J Appl Physiol (1985). 2011;111(2):599-605.

37. Griep MA, Fujikawa K, Nelsestuen GL. Possible basis for the apparent surface selectivity of the contact activation of human blood coagulation factor XII. Biochemistry. 1986;25(21):6688-94.

38. Zhuo R, Miller R, Bussard KM, Siedlecki CA, Vogler EA. Procoagulant stimulus processing by the intrinsic pathway of blood plasma coagulation. Biomaterials. 2005;26(16):2965-73.

39. Renné T, Pozgajová M, Grüner S, Schuh K, Pauer H-U, Burfeind P, et al. Defective thrombus formation in mice lacking coagulation factor XII. Journal of Experimental Medicine. 2005;202(2):271-81.

40. Vogler EA, Siedlecki CA. Contact activation of blood-plasma coagulation. Biomaterials. 2009;30(10):1857-69.

41. de Maat S, Maas C. Factor XII: form determines function. J Thromb Haemost. 2016;14(8):1498-506.

42. Gorbet MB, Sefton MV. Biomaterial-associated thrombosis: roles of coagulation factors, complement, platelets and leukocytes. Biomaterials. 2004;25(26):5681-703.

43. Hemostasis and thrombosis : practical guidelines in clinical management. In: Roberts HR, Saba HI, editors.

44. Ziats NP, Pankowsky D, Tierney B, Ratnoff O, Anderson JM. Adsorption of Hageman factor (factor XII) and other human plasma proteins to biomedical polymers. The Journal of laboratory and clinical medicine. 1990;116(5):687-96.

45. Mulzer SR, Brash JL. Identification of plasma proteins adsorbed to hemodialyzers during clinical use. Journal of biomedical materials research. 1989;23(12):1483-504.

46. Yau JW, Stafford AR, Liao P, Fredenburgh JC, Roberts R, Weitz JI. Mechanism of catheter thrombosis: comparison of the antithrombotic activities of

fondaparinux, enoxaparin, and heparin in vitro and in vivo. Blood. 2011;118(25):6667-74.

47. Larsson M, Rayzman V, Nolte MW, Nickel KF, Björkqvist J, Jämsä A, et al. A factor XIIa inhibitory antibody provides thromboprotection in extracorporeal circulation without increasing bleeding risk. Science translational medicine. 2014;6(222):222ra17-ra17.

48. Elam J-H, Nygren H. Adsorption of coagulation proteins from whole blood on to polymer materials: relation to platelet activation. Biomaterials. 1992;13(1):3-8.

49. Van der Kamp K, Van Oeveren W. Factor XII fragment and kallikrein generation in plasma during incubation with biomaterials. Journal of Biomedical Materials Research Part A. 1994;28(3):349-52.

50. Lee JH, Lee HB, Andrade JD. Blood compatibility of polyethylene oxide surfaces. Progress in Polymer Science. 1995;20(6):1043-79.

51. Park K, Mosher DF, Cooper SL. Acute surface-induced thrombosis in the canine ex vivo model: Importance of protein composition of the initial monolayer and platelet activation. Journal of Biomedical Materials Research Part A. 1986;20(5):589-612.

52. Eberhart R, Munro M, Frautschi J, Lubin M, Clubb F, Miller C, et al. Influence of Endogenous Albumin Binding on Blood-Material Interactionsa. Annals of the New York Academy of Sciences. 1987;516(1):78-95.

53. Yeh H-Y, Lin J-C. Bioactivity and platelet adhesion study of a human thrombomodulin-immobilized nitinol surface. Journal of Biomaterials Science, Polymer Edition. 2009;20(5-6):807-19.

54. Jaffer IH, Fredenburgh JC, Hirsh J, Weitz JI. Medical device-induced thrombosis: what causes it and how can we prevent it? J Thromb Haemost. 2015;13 Suppl 1:S72-81.

55. Tang L, Jennings TA, Eaton JW. Mast cells mediate acute inflammatory responses to implanted biomaterials. Proceedings of the National Academy of Sciences. 1998;95(15):8841-6.

56. Sivaraman B, Latour Ra. The adherence of platelets to adsorbed albumin by receptor-mediated recognition of binding sites exposed by adsorption-induced unfolding. Biomaterials. 2010;31(6):1036-44.

57. Gresele P, Page C, Fuster V, Vermylen J. Platelets in Thrombotic and Non-Thrombotic Disorders. Transfusion Medicine. 2003;13(1):57-8.

58. Shen M, Horbett TA. The effects of surface chemistry and adsorbed proteins on monocyte/macrophage adhesion to chemically modified polystyrene surfaces. Journal of biomedical materials research. 2001;57(3):336-45.

59. Shen M, Martinson L, Wagner MS, Castner DG, Ratner BD, Horbett TA. PEO-like plasma polymerized tetraglyme surface interactions with leukocytes and proteins: in vitro and in vivo studies. Journal of Biomaterials Science, Polymer Edition. 2002;13(4):367-90.

60. Kondo A, Oku S, Murakami F, Higashitani K. Conformational changes in protein molecules upon adsorption on ultrafine particles. Colloids and Surfaces B: Biointerfaces. 1993;1(3):197-201.

61. Karlsson M, Mårtensson L-G, Jonsson B-H, Carlsson U. Adsorption of human carbonic anhydrase II variants to silica nanoparticles occur stepwise: binding is followed by successive conformational changes to a molten-globule-like state. Langmuir. 2000;16(22):8470-9.

62. Abraham S, So A, Unsworth LD. Poly(carboxybetaine methacrylamide)-modified nanoparticles: a model system for studying the effect of chain chemistry on film properties, adsorbed protein conformation, and clot formation kinetics. Biomacromolecules. 2011;12(10):3567-80.

63. Tsai WB, Grunkemeier JM, Horbett TA. Variations in the ability of adsorbed fibrinogen to mediate platelet adhesion to polystyrene-based materials: A multivariate statistical analysis of antibody binding to the platelet binding sites of fibrinogen. Journal of Biomedical Materials Research Part A. 2003;67(4):1255-68.

64. Sivaraman B, Latour RA. The relationship between platelet adhesion on surfaces and the structure versus the amount of adsorbed fibrinogen. Biomaterials. 2010;31(5):832-9.

65. Forsyth CB, Solovjov DA, Ugarova TP, Plow EF. Integrin αMβ2-mediated cell migration to fibrinogen and its recognition peptides. The Journal of experimental medicine. 2001;193(10):1123-34.

66. Bacakova L, Filova E, Parizek M, Ruml T, Svorcik V. Modulation of cell adhesion, proliferation and differentiation on materials designed for body implants. Biotechnol Adv. 2011;29(6):739-67.

67. Di Cio S, Gautrot JE. Cell sensing of physical properties at the nanoscale: Mechanisms and control of cell adhesion and phenotype. Acta Biomater. 2016;30:26-48.

68. Hoffman AS. Stimuli-responsive polymers: Biomedical applications and challenges for clinical translation. Advanced drug delivery reviews. 2013;65(1):10-6.

69. Ruel-Gariepy E, Leroux J-C. In situ-forming hydrogels—review of temperature-sensitive systems. European Journal of Pharmaceutics and Biopharmaceutics. 2004;58(2):409-26.

70. Loh XJ, Li J. Biodegradable thermosensitive copolymer hydrogels for drug delivery. Expert Opinion on Therapeutic Patents. 2007;17(8):965-77.

71. Moon HJ, Park MH, Joo MK, Jeong B. Temperature-responsive compounds as in situ gelling biomedical materials. Chemical Society Reviews. 2012;41(14):4860-83.

72. Dou QQ, Liow SS, Ye E, Lakshminarayanan R, Loh XJ. Biodegradable thermogelling polymers: working towards clinical applications. Adv Healthc Mater. 2014;3(7):977-88.

73. Hench LL, Splinter RJ, Allen WC, Greenlee TK. Bonding mechanisms at the interface of ceramic prosthetic materials. Journal of Biomedical Materials Research. 1971;5(6):117-41.

74. Hench LL, Paschall Ha. Direct chemical bond of bioactive glass-ceramic materials to bone and muscle. Journal of biomedical materials research. 1973;7(3):25-42.

75. Xynos ID, Edgar aJ, Buttery LD, Hench LL, Polak JM. Ionic products of bioactive glass dissolution increase proliferation of human osteoblasts and induce insulin-like growth factor II mRNA expression and protein synthesis. Biochemical and biophysical research communications. 2000;276(2):461-5.

76. Gough JE, Notingher I, Hench LL. Osteoblast attachment and mineralized nodule formation on rough and smooth 45S5 bioactive glass monoliths. Journal of biomedical materials research Part A. 2004;68(4):640-50.

77. Christodoulou I, Buttery LDK, Saravanapavan P, Tai G, Hench LL, Polak JM. Dose- and time-dependent effect of bioactive gel-glass ionic-dissolution products on human fetal osteoblast-specific gene expression. Journal of biomedical materials research Part B, Applied biomaterials. 2005;74(1):529-37.

78. Christodoulou I, Buttery LDK, Tai G, Hench LL, Polak JM. Characterization of human fetal osteoblasts by microarray analysis following stimulation with 58S bioactive gel-glass ionic dissolution products. Journal of biomedical materials research Part B, Applied biomaterials. 2006;77(2):431-46.

79. Hench LL. Bioceramics. Journal of the American Ceramic Society. 1998;81(7):1705-28.

80. Peitl Filho O, Latorre GP, Hench L. Effect of crystallization on apatite-layer formation of bioactive glass 45%. J Biomed Mater Res. 1996;30:509-14.

81. Peitl O, Dutra E, Hench LL. Highly bioactive P 2 O 5 ± Na 2 O ± CaO ± SiO 2 glass-ceramics. Time. 2001;292.

82. Lefebvre L, Gremillard L, Chevalier J, Bernache-Assollant D, editors. Sintering Behavior of 45S5 Bioglass®. Key Engineering Materials; 2008: Trans Tech Publ.

83. Lefebvre L, Chevalier J, Gremillard L, Zenati R, Thollet G, Bernache-Assolant D, et al. Structural transformations of bioactive glass 45S5 with thermal treatments. Acta Materialia. 2007;55(10):3305-13.

84. El-Ghannam A, Ducheyne P, Shapiro IM. Formation of surface reaction products on bioactive glass and their effects on the expression of the osteoblastic phenotype and the deposition of mineralized extracellular matrix. Biomaterials. 1997;18(4):295-303.

85. Wilson J, Pigott GH, Schoen FJ, Hench LL. Toxicology and biocompatibility of bioglasses. Journal of biomedical materials research. 1981;15(6):805-17.

86. Vrouwenvelder W, Groot C. Histological and biochemical evaluation of osteoblasts cultured on bioactive glass, hydroxylapatite, titanium alloy, and stainless steel. Journal of biomedical. 1993;27:465-75.

87. Matsuda T, Yamauchi K, Ito G. The influence of bioglass on the growth of fibroblasts. Journal of biomedical materials research. 1987;21(4):499-507.

88. Kokubo T, Kushitani H, Sakka S, Kitsugi T, Yamamuro T. Solutions able to reproduce in vivo surface-structure changes in bioactive glass-ceramic A-W3. Journal of Biomedical Materials Research. 1990;24(6):721-34.

89. Lai DY. Toward toxicity testing of nanomaterials in the 21st century: a paradigm for moving forward. Wiley Interdisciplinary Reviews: Nanomedicine and Nanobiotechnology. 2012;4(1):1-15.

90. Suri SS, Fenniri H, Singh B. Nanotechnology-based drug delivery systems. Journal of occupational medicine and toxicology. 2007;2(1):16.

91. Nanotechnology and drug delivery. In: Arias JL, editor.

92. Couvreur P, Vauthier C. Nanotechnology: intelligent design to treat complex disease. Pharmaceutical research. 2006;23(7):1417-50.

93. Sahoo SK, Labhasetwar V. Nanotech approaches to drug delivery and imaging. Drug discovery today. 2003;8(24):1112-20.

94. Ortega VA, Ede JD, Boyle D, Stafford JL, Goss GG. Polymer-Coated Metal-Oxide Nanoparticles Inhibit IgE Receptor Binding, Cellular Signaling, and Degranulation in a Mast Cell-like Cell Line. Advanced Science. 2015;2(11).

95. Wiench K, Wohlleben W, Hisgen V, Radke K, Salinas E, Zok S, et al. Acute and chronic effects of nano-and non-nano-scale TiO 2 and ZnO particles on mobility and reproduction of the freshwater invertebrate Daphnia magna. Chemosphere. 2009;76(10):1356-65.

96. Molnar RM, Bodnar M, Hartmann JF, Borbely J. Preparation and characterization of poly (acrylic acid)-based nanoparticles. Colloid and Polymer Science. 2009;287(6):739-44.

97. Urry DW. Entropic elastic processes in protein mechanisms. I. Elastic structure due to an inverse temperature transition and elasticity due to internal chain dynamics. Journal of protein chemistry. 1988;7:1-34.

98. Daamen WF, Veerkamp JH, Van Hest JCM, Van Kuppevelt TH. Elastin as a biomaterial for tissue engineering. Biomaterials. 2007;28(30):4378-98.

99. Mithieux SM, Weiss AS. Elastin. Advances in protein chemistry. 2005;70:437-61.

100. Bax DV, Rodgers UR, Bilek MM, Weiss AS. Cell adhesion to tropoelastin is mediated via the C-terminal GRKRK motif and integrin αVβ3. Journal of biological chemistry. 2009;284(42):28616-23.

101. Robinet A, Fahem A, Cauchard J-H, Huet E, Vincent L, Lorimier S, et al. Elastin-derived peptides enhance angiogenesis by promoting endothelial cell migration and tubulogenesis through upregulation of MT1-MMP. Journal of cell science. 2005;118(2):343-56.

102. De Vries HJ, Middelkoop E, Mekkes JR, Dutrieux RP, Wildevuur CH, Westerhof W. Dermal regeneration in native non-cross-linked collagen sponges with different extracellular matrix molecules. Wound Repair and Regeneration. 1994;2(1):37-47.

103. Urry D, Long M, Cox B, Ohnishi T, Mitchell L, Jacobs M. The synthetic polypentapeptide of elastin coacervates and forms filamentous aggregates. Biochimica et Biophysica Acta (BBA)-Protein Structure. 1974;371(2):597-602.

104. Urry DW, Gowda DC, Parker TM, Luan CH, Reid MC, Harris CM, et al. Hydrophobicity scale for proteins based on inverse temperature transitions. Biopolymers. 1992;32:1243-50.

105. Vrhovski B, Jensen S, Weiss AS. Coacervation characteristics of recombinant human tropoelastin. European Journal of Biochemistry. 1997;250(1):92-8.

106. Urry DW, Trapane TL, Long MM, Prasad KU. Test of the librational entropy mechanism of elasticity of the polypentapeptide of elastin. Effect of introducing a methyl group at residue 5. Journal of the Chemical Society, Faraday Transactions 1: Physical Chemistry in Condensed Phases. 1983;79(4):853-68.

107. Urry DW, Luan CH, Parker TM, Gowda DC, Prasad KU, Reid MC, et al. Temperature of polypeptide inverse temperature transition depends on mean residue hydrophobicity. Journal of the American Chemical Society. 1991;113(11):4346-8.

108. Reguera J, Calvo B. Thermal Behavior and Kinetic Analysis of the Chain Unfolding and Refolding and of the Concomitant Nonpolar Solvation and Desolvation of Two Elastin-like Polymers. Macromolecules. 2003:8470-6.

109. Girotti A, Fernandez-Colino A, Lopez IM, Rodriguez-Cabello JC, Arias FJ. Elastin-like recombinamers: biosynthetic strategies and biotechnological applications. Biotechnol J. 2011;6(10):1174-86.

110. Chilkoti A, Dreher MR, Meyer DE. Design of thermally responsive, recombinant polypeptide carriers for targeted drug delivery. Cancer. 2002;54:1093-111.

111. Cho Y, Zhang Y, Christensen T, Sagle LB, Chilkoti A, Cremer PS. Effects of Hofmeister anions on the phase transition temperature of elastin-like polypeptides. J Phys Chem B. 2008;112(44):13765-71.

112. McDaniel JR, Radford DC, Chilkoti A. A unified model for de novo design of elastin-like polypeptides with tunable inverse transition temperatures. Biomacromolecules. 2013;14(8):2866-72.

113. Navon Y, Bitton R. Elastin-Like Peptides (ELPs) - Building Blocks for Stimuli-Responsive Self-Assembled Materials. Israel Journal of Chemistry. 2016;56(8):581-9.

114. Puiggalí J, Franco L, J. del Valle L. Smart systems related to polypeptide sequences. AIMS Materials Science. 2016;3(1):289-323.

115. Meyer DE, Chilkoti A. Genetically Encoded Synthesis of Protein-Based Polymers with Precisely Specified Molecular Weight and Sequence by Recursive Directional Ligation: Examples from the Elastin-like Polypeptide System. Biomacromolecules. 2002:357-67.

116. Meyer DE, Chilkoti A. Purification of recombinant proteins by fusion with thermally-responsive polypeptides. Nature Biotechnology. 1999;17(November).

117. Meyer DE, Trabbic-Carlson K, Chilkoti a. Protein purification by fusion with an environmentally responsive elastin-like polypeptide: effect of polypeptide length on the purification of thioredoxin. Biotechnology progress. 2001;17(4):720-8.

118. Hu F, Ke T, Li X, Mao PH, Jin X, Hui FL, et al. Expression and purification of an antimicrobial peptide by fusion with elastin-like polypeptides in Escherichia coli. Applied biochemistry and biotechnology. 2010;160(8):2377-87.

119. Lin M, Rose-John S, Grötzinger J, Conrad U, Scheller J. Functional expression of a biologically active fragment of soluble gp130 as an ELP-fusion

protein in transgenic plants: purification via inverse transition cycling. Biochemical Journal. 2006;398(3):577-83.

120. Yeboah A, Cohen RI, Rabolli C, Yarmush ML, Berthiaume F. Elastin-like polypeptides: A strategic fusion partner for biologics. Biotechnol Bioeng. 2016;113(8):1617-27.

121. Li NK, Garcia Quiroz F, Hall CK, Chilkoti A, Yingling YG. Molecular description of the LCST behavior of an elastin-like polypeptide. Biomacromolecules. 2014;15(10):3522-30.

122. Hong M, Isailovic D, McMillan R, Conticello V. Structure of an elastin-mimetic polypeptide by solid-state NMR chemical shift analysis. Biopolymers. 2003;70(2):158-68.

123. Yao X, Hong M. Structure distribution in an elastin-mimetic peptide (VPGVG) 3 investigated by solid-state NMR. Journal of the American Chemical Society. 2004;126(13):4199-210.

124. Rauscher S, Baud S, Miao M, Keeley FW, Pomes R. Proline and glycine control protein self-organization into elastomeric or amyloid fibrils. Structure. 2006 Nov 30;14(11):1667-76.

125. Muiznieks LD, Keeley FW. Proline periodicity modulates the self-assembly properties of elastin-like polypeptides. Journal of Biological Chemistry. 2010 Dec 17;285(51):39779-89.

126. Kumashiro KK, Ohgo K, Elliott DW, Kagawa TF, Niemczura WP. Backbone motion in elastin's hydrophobic domains as detected by 2H NMR spectroscopy. Biopolymers. 2012 Nov 1;97(11):882-8.

127. Reichheld SE, Muiznieks LD, Keeley FW, Sharpe S. Direct observation of structure and dynamics during phase separation of an elastomeric protein. Proceedings of the National Academy of Sciences. 2017 May 15:201701877.

128. MacEwan SR, Chilkoti A. Applications of elastin-like polypeptides in drug delivery. Journal of controlled release : official journal of the Controlled Release Society. 2014;190:314-30.

129. Rodriguez-Cabello JC, Pina MJ, Ibanez-Fonseca A, Fernandez-Colino A, Arias FJ. Nanotechnological Approaches to Therapeutic Delivery Using Elastin-Like Recombinamers. Bioconjug Chem. 2015;26(7):1252-65.

130. Rodriguez-Cabello JC, Arias FJ, Rodrigo MA, Girotti A. Elastin-like polypeptides in drug delivery. Adv Drug Deliv Rev. 2016;97:85-100.

131. Saxena R, Nanjan MJ. Elastin-like polypeptides and their applications in anticancer drug delivery systems: a review. Drug Deliv. 2015;22(2):156-67.

132. Herrera Estrada LP, Champion JA. Protein nanoparticles for therapeutic protein delivery. Biomater Sci. 2015;3(6):787-99.

133. Germershaus O, Lühmann T, Rybak JC, Ritzer J, Meinel L. Application of natural and semi-synthetic polymers for the delivery of sensitive drugs. International Materials Reviews. 2014;60(2):101-31.

134. Ryu JS, Raucher D. Elastin-like polypeptide for improved drug delivery for anticancer therapy: preclinical studies and future applications. Expert Opin Drug Deliv. 2015;12(4):653-67.

135. Price R, Poursaid A, Ghandehari H. Controlled release from recombinant polymers. J Control Release. 2014;190:304-13.

136. Massodi I, Bidwell GL, 3rd, Raucher D. Evaluation of cell penetrating peptides fused to elastin-like polypeptide for drug delivery. J Control Release. 2005;108(2-3):396-408.

137. Sarangthem V, Cho Ea, Bae SM, Singh TD, Kim SJ, Kim S, et al. Construction and application of elastin like polypeptide containing IL-4 receptor targeting peptide. PLoS ONE. 2013;8(12):1-12.

138. Dreher MR, Simnick AJ, Fischer K, Smith RJ, Patel A, Schmidt M, et al. Temperature triggered self-assembly of polypeptides into multivalent spherical micelles. Journal of the American Chemical Society. 2008;130(2):687-94.

139. Shi P, Aluri S, Lin YA, Shah M, Edman M, Dhandhukia J, et al. Elastin-based protein polymer nanoparticles carrying drug at both corona and core suppress tumor growth in vivo. Journal of Controlled Release. 2013;171(3):330-8.

140. MacKay JA, Chen M, McDaniel JR, Liu W, Simnick AJ, Chilkoti A. Self-assembling chimeric polypeptide-doxorubicin conjugate nanoparticles that abolish tumours after a single injection. Nature materials. 2009;8(12):993-9.

141. Meyer DE, Kong GA, Dewhirst MW, Zalutsky MR, Chilkoti A. Targeting a Genetically Engineered Elastin-like Polypeptide to Solid Tumors by Local Hyperthermia 1. In Vitro. 2001;42745:1548-54.

142. Meyer DE, Shin B, Kong G, Dewhirst M, Chilkoti A. Drug targeting using thermally responsive polymers and local hyperthermia. Journal of controlled release. 2001;74(1):213-24.

143. Park SM, Cha JM, Nam J, Kim MS, Park S-J, Park ES, et al. Formulation optimization and in vivo proof-of-concept study of thermosensitive liposomes

balanced by phospholipid, elastin-like polypeptide, and cholesterol. PloS one. 2014;9(7):e103116.

144. Han W, MacEwan SR, Chilkoti A, López GP. Bio-inspired synthesis of hybrid silica nanoparticles templated from elastin-like polypeptide micelles. Nanoscale. 2015;7(28):12038-44.

145. Costa RR, Castro E, Arias FJ, Rodríguez-Cabello JC, Mano JoF. Multifunctional compartmentalized capsules with a hierarchical organization from the nano to the macro scales. Biomacromolecules. 2013;14(7):2403-10.

146. Koetting MC, Peters JT, Steichen SD, Peppas NA. Stimulus-responsive hydrogels: Theory, modern advances, and applications. Materials Science and Engineering: R: Reports. 2015;93:1-49.

147. Adams SB, Jr., Shamji MF, Nettles DL, Hwang P, Setton LA. Sustained release of antibiotics from injectable and thermally responsive polypeptide depots. J Biomed Mater Res B Appl Biomater. 2009;90(1):67-74.

148. Wang W, Jashnani A, Aluri SR, Gustafson JA, Hsueh PY, Yarber F, et al. A thermo-responsive protein treatment for dry eyes. J Control Release. 2015;199:156-67.

149. Lim DW, Nettles DL, Setton La, Chilkoti A. Rapid Cross-Linking of Elastin-like Polypeptides with (Hydroxymethyl) phosphines in Aqueous Solution Rapid Cross-Linking of Elastin-like Polypeptides with (Hydroxymethyl) phosphines in Aqueous Solution. Construction. 2007:1463-70.

150. Nettles DL, Kitaoka K, Hanson NA, Flahiff CM, Mata BA, Hsu EW, et al. In situ crosslinking elastin-like polypeptide gels for application to articular

cartilage repair in a goat osteochondral defect model. Tissue Eng Part A. 2008;14(7):1133-40.

151. Heilshorn S. Endothelial cell adhesion to the fibronectin CS5 domain in artificial extracellular matrix proteins. Biomaterials. 2003;24(23):4245-52.

152. Heilshorn SC, Liu JC, Tirrell DA. Cell-binding domain context affects cell behavior on engineered proteins. Biomacromolecules. 2005;6(1):318-23.

153. Hsueh YS, Savitha S, Sadhasivam S, Lin FH, Shieh MJ. Design and synthesis of elastin-like polypeptides for an ideal nerve conduit in peripheral nerve regeneration. Mater Sci Eng C Mater Biol Appl. 2014;38:119-26.

154. Yigit S, Dinjaski N, Kaplan DL. Fibrous proteins: At the crossroads of genetic engineering and biotechnological applications. Biotechnol Bioeng. 2016;113(5):913-29.

155. Urry DW, Parker TM, Reid MC, Gowda DC. Biocompatibility of the Bioelastic Materials, Poly(GVGVP) and Its γ-Irradiation Cross-Linked Matrix: Summary of Generic Biological Test Results. Journal of Bioactive and Compatible Polymers. 1991;6(3):263-82.

156. Wood S, Lemons J, Prasad K, Urry D. In vitro calcification and in vivo biocompatibility of the cross-linked polypentapeptide of elastin. Journal of biomedical materials research. 1986;20(3):315-35.

157. Rincon AC, Molina-Martinez IT, de Las Heras B, Alonso M, Bailez C, Rodriguez-Cabello JC, et al. Biocompatibility of elastin-like polymer poly(VPAVG) microparticles: in vitro and in vivo studies. J Biomed Mater Res A. 2006;78(2):343-51.

158. Elsas FJ, Gowda DC, Urry DW. Synthetic polypeptide sleeve for strabismus surgery. Journal of pediatric ophthalmology and strabismus. 1992;29(5):284-6.

159. Sallach RE, Cui W, Balderrama F, Martinez AW, Wen J, Haller Ca, et al. Long-term biostability of self-assembling protein polymers in the absence of covalent crosslinking. Biomaterials. 2010;31(4):779-91.

2. Materials and Methods

2.1. Plasma Incubation, Protein Assay and Western Blot Procedure

2.1.1. Day 1: Plasma Incubations

Incubation of Wafers

The incubation protocol is modified from Unsworth *et al.* (1).

1. For each system, consider running at least 3 samples. In a multiwell plate, place all samples in individual wells. Use soft tweezers (or put 1 µL to 10 µL pipet tip on normal tweezers) when handling the wafers.

   Choice of plate depends on wafer size. Generally, the greater the available volume for plasma, the better.
2. Inject enough 37°C plasma into each well to fill it to the top and incubate them for 2 hours at 37°C.
3. In different wells, incubate the wafers separately in 200 µL of 1X (0.15M) PBS pH 7.4 solution 3 times for 5 minutes each at room temperature. Use fresh PBS for each wash.
4. In inverted, cut 1.5 mL tubes, place all the samples of the same system in the same well. For example, 3 samples of CBMA-1 in well 1, 3 samples of CBMA-5 in well 2 etc. Place the wafers vertically, and make sure the samples do not touch. Combining the wafers in this step concentrates the eluted proteome.

5. Pipet enough 2% SDS solution to cover the wafers. Incubate them at room temperature for 24 hours.

Nanoparticle Plasma Incubation

Protocol adapted from Kim HR *et al.* (2).

6. In centrifuge tubes, measure out certain amount of nanoparticles for the incubation. In the case of bioglass 45S5, 50 mg of the sample was used.
7. Add 1.25 mL of 37°C plasma to each centrifuge tube. Place the tubes in a plastic container, put tissue paper in the container to make sure the tubes won't move in the container. Place the container in the rocking hot water bath for 2 hours at 37°C and speed of 150 rpm. Make sure the tubes are placed in the direction of motion.
8. Centrifuge at 13000 rpm for 10 minutes at room temperature.
9. Remove the plasma from the tubes and add 1 mL of 1X (0.15M) PBS pH 7.4 into the tube. Incubate by rocking for 30 minutes at room temperature. After 30 minutes, centrifuge at 13000 rpm for 10 minutes at room temperature. The PBS incubation is done twice, using fresh PBS each time.
10. Remove PBS solution from the tubes and add 1 mL of 2% SDS in PBS. In later instances 10% SDS in PBS was used with the DC assay standard curve modified to match. Place into the container same way as step 7, and

place in the rocking hot water bath for 2 hours at 50°C and speed of 150 rpm.

11. Centrifuge at 13000 rpm for 10 minutes at room temperature. Pipet out the sample solutions in new centrifuge tubes and store at 4°C. Note that if no overnight elution step is required, the day 2 protein assay may be completed now.

2.1.2. Day 2: Detergent Compatible (DC) Protein Assay

D.C. Microplate Protein Assay

12. Firstly, prepare reagent A' fresh every time DC protein assay is performed. For every mL of reagent A added, 20 µL of reagent S is added to make reagent A'. Vortex for 10 seconds at max intensity to mix.
13. In a 96 well multiplate dispense each of the following solutions in triplicate to form the standard curve and samples for measurement. Use 5 µL of 2% SDS (or 10% SDS if that was used in the elution step) in PBS to act as the blank. Add 5 µL of BSA standards of 0.2 mg/mL, 0.5 mg/mL, 0.75 mg/mL, 1.0 mg/mL, 1.25 mg/mL, and 1.5 mg/mL for the standard curve. Finally, add 5 µL of each.
14. Add 25 µL of reagent A' to each well.
15. Add 200 µL of reagent B to each well and pipette up and down to mix.

    After 15 minutes, absorbance can be read at 740 nm using a plate reader or spectrophotometer.

2.1.3. Day 3: Gel Electrophoresis, Transfer and Blocking

16. Make transfer buffer first thing on day 3, so it will have time to cool in the 4°C fridge.

Transfer Buffer: (ref: Mini-Protein® Tetra Cell Instruction Manual)

3 g	Tris base
14.4 g	Glycine
200 mL	Methanol

Fill it to 1L with Milli-Q Water.

Make and stored in 4°C fridge until use.

Gel Electrophoresis and Western Blots

17. Prepare gels as per Bio-Rad Mini-Protein® Tetra Cell Instruction Manual

12% Separating gel:

6 mL	40% Acrylamide
5 mL	1.5M Tris-HCl pH 8.8
200 µL	10% SDS
8.6 mL	Milli-Q distilled Water
200 µL	10% Ammonium Persulfate
10 µL	TEMED

The 10% APS and TEMED are the last things to add to the solution. Invert to mix after adding APS solution. After adding TEMED and gently inverted (to avoid creating air bubbles), the gel plate are IMMEDIATELY filled with solution. After

2 minutes, add a small amount of distilled water over gel. Allow the gel to solidify for 30 minutes.

4% Stacking gel:

938 µL	40% Acrylamide
938 µL	0.5M Tris-HCl pH 6.8
75 µL	10% SDS
5.5 mL	Milli-Q distilled Water
75 µL	10% Ammonium Persulfate
10 µL	TEMED

Fill the gel plate to the top with the 4% gel. Add the Western blotting combs (ie. Those with lanes 2-9 covered with packing tape). Allow the gel to solidify for 30 minutes.

18. Prepare sample. Add amount of the sample that gives 30 µg of protein according to the protein assay. Add a volume of sample buffer (4X) that is 1/3 the volume of the sample. The total of the final sample depends on the concentration of the eluted proteome and may end up being >100 µL. (ref: Mini-Protein® Tetra Cell Instruction Manual)

Sample buffer (4X):

3 mL	100% Glycerol
600 µL	β-Mercaptoethanol

50 µL	10% Coomassie R250
750 µL	2M Tris pH 7.0
1.2 g	SDS
6.35 mL	Milli-Q Water

Aliquot into 1 mL centrifuge tubes and store in -20°C freezer.

19. After mixing the sample buffer into the sample, heat the mixture for 5 minutes at 95°C.

Gel Electrophoresis:

20. Remove gel from casting stand and place into the electrophoresis clamp with the shorter plate facing the inside of the chamber. Place clamp into the buffer chamber. Fill the chamber with 1X electrophoresis running buffer until the level indicated on the chamber. Load 5 µL of ladder solution in lane 1 of the gel. Load sample in the large middle lane of the gel. Put the lid on and run electrophoresis at 200 V and 400 mA until the dye just runs off the bottom of the gel. It will approximately take 40-50 minutes.

Electrophoresis Buffer (5X):

15 g	Tris Base
72 g	Glycine
5 g	SDS

Fill to 1L with Milli-Q water.

Dilute to 1X by mixing 200 mL of 5X buffer with 800 mL of Milli-Q water before use.

21. After gel electrophoresis is done, place the gel in transfer buffer for 20 minutes with rocking.
22. Cut Immobilon PVDF transfer membrane to size, pre-wet in 100% methanol for 3 seconds, water for 1 minute, and soak in transfer buffer for 15 minutes. Place gel and membrane into the transfer cell according to instructions, ensuring no air bubbles are trapped between the gel and membrane. Fill the transfer chamber with transfer buffer to the very top. Transfer for 1 hour at 100 V and 200 mA.

    Note: Never touch PVDF membrane with either bare or gloved fingers as protein from your hand may be adsorbed and interfere with the blot.
23. After transfer, draw a line on the very bottom of the blot for orientation (vertical and blot face) and identification (if working with 2 blots at once) purposes. Use a pen, NOT a felt marker.
24. Cut a 1.5 cm piece from the edge of the membrane that contains the ladder and 5 mm of normal sample lane for gold staining. Do not block this strip. Save it for gold staining on Day 4.
25. Inject 2 mL of blocking solution (10% nonfat dry milk in TTBS) into each of the 23 wells of the Western plate. Cut remaining membrane into 2.5 mm strips, pre-wet in methanol for 3 seconds, water for 10 seconds, and

place into the 23 wells of blocking solution. Seal cassette with parafilm, place extra Western blotting strip cassette on top, and then incubate overnight at room temperature with rocking.

Blocking solution:

7.5 g nonfat dry milk

Fill to 75 mL with 1X TTBS

2.1.4. Day 4: Western Blotting and Gold Staining

26. Remove the blocking solution. Replace with 2 mL of washing solution. (0.1% nonfat dry milk in TBS). Incubate for 5 minutes. Repeat the washing procedure two more times with fresh wash solution each time.

Wash solution:

0.5 g milk

500 mL 1X TBS

27. Incubate the strips in 500 µL of primary antibodies (1:1000 dilution) for 1 hour on rocking platform at room temperature sealed with parafilm.
28. Wash away the loosely bound antibodies by incubating in 2 mL washing solution for 5 minutes. This is done a total of 3 times with fresh wash solution each time.
29. Incubate with 500 µL of secondary antibodies (1:1000 dilution) for 1 hour on rocking platform at room temperature sealed with parafilm.

30. Wash away loosely bound secondary antibodies by incubating in 2 mL of washing solution for 5 minutes. This washing procedure is done 3 times with fresh wash solution each time.
31. Add 350 µL of TMB-stabilized HRP substrate solution to each well of the Western blotting cassette. Incubate with rocking at room temperature until precipitate begins to form. If comparing the results of multiple Western blotting procedures, ensure the colour-development reaction time is consistent between blots.
32. Remove the TMB solution. Replace with 2 mL of Milli-Q water for 10 minutes to stop the reaction.
33. As soon as strips are dry, reassemble the blot(s) and scan them.

Gold Staining:

34. Briefly rehydrate the membrane strips by incubating in methanol for 3 seconds then Milli-Q water for 10 seconds.
35. Place the ladder strip in a petri dish and incubate in enough TTBS solution to cover the bottom of the dish for 20 minutes on the rocking platform to block the membrane. This is done a total of 3 times using fresh TTBS each time.
36. Incubate in Milli-Q water 3 times for 2 minutes each.
37. Incubate in enough Colloidal Gold solution to cover the bottom of the dish for approximately 40-50 minutes depending on the intensity of gold

nanoparticle in the gold solution. Stop the reaction when protein bands are clearly shown on the samples lane. Save the gold solution for reuse.

38. Wash with Milli-Q water 3 times for 1 minute each. Allow the membrane to dry then add it to the western blot strips.

Miscellaneous Solutions

10X TBS:

60.57 g (500 M) Tris Base

87.66 g (1.5 M) NaCl

Add Milli-Q water to a final volume of ~900 mL. Adjust pH to 7.4

Fill to 1 L and filter sterilize.

1X TTBS:

100 mL 10X TBS

300 µL Tween 20

Fill to 1 L with Milli-Q Water

Antibody Dilution Solution

1 g/100 mL milk powder

0.05% Tween20

TBS to final volume

For typical Western procedures make 100 mL of dilution solution. Combine 1 g milk powder with 50 µL Tween 20 and dilute to 100 mL using 1X TBS.

All primary antibodies as well as the anti-mouse and anti-rabbit secondary antibodies are diluted from 2 µL up to 2 mL. The anti-sheep and anti-goat secondary antibodies are diluted from 10 µL to 10 mL.

2.2. Plasma Recalcification Turbidimetric Assay Details

Procedure based on McClung *et al.* (3).

The basic experimental setup for one sample involves setting up four separate sets of reactions with each reaction repeated 5 times. Those reactions are: plasma-only positive control, plasma-only negative control, sample reaction, sample negative control reaction. This allows for a real time clotting comparison while also allowing corrections for reaction baselines and sample background scattering. As more samples are needed, more sample reaction and sample negative control reactions can be added-all of which may be compared to the one positive control.

Sample contents:

Positive control: 100 µL plasma + 25 µL PBS + 100 µL $CaCl_2$

Corresponding negative control: 100 µL plasma + 25 µL PBS +100 µL PBS

The timing for this step is critical as clotting may occur within minutes of adding $CaCl_2$ and the assay must detect the onset of clotting.

Samples: 100 µL plasma + 25 µL sample +100 µL $CaCl_2$

Sample negative control: 100 µL plasma + 25 µL sample +100 µL PBS

Assay Protocol:

1. Preheat plasma, PBS, $CaCl_2$ and (if possible) sample solutions at 37°C for 30-60 minutes.
2. Activate plate reader, allowing ~20 minutes for the instrument to warm up then ~10 minutes for it to preheat to 37°C.
3. Aliquot plasma, PBS and samples as required. Use a multichannel pipettor to minimize pipetting time and solution cooling. Minimize solution cooling by aliquoting onto a multiwell plate on a heated surface such as a heat block or incubator.
4. Start plate reader program (detailed below) and ensure instrument is standing by with tray out, ready to receive multiwell plate.
5. Using a multichannel pipettor, add the $CaCl_2$ solution as needed and immediately place multiwell plate in plate reader and begin the assay.

Immediately after placing plate in reader, one 10 second shake is performed. The assay is run at 37°C for 1 hour with spectrophotometric monitoring at 405nm every minute.

Assay program details (as input for BioTek Synergy H1 plate reader):

Temperature setpoint: 37°C

Shake: linear, 10 seconds

Start kinetic test: duration 1 hour, 1 minute measurement intervals, 405 nm

Assay data processing details:

1. Calculate average and standard deviations of each sample or control at each time point from the 5 repeated measurements.
2. Subtract the average negative control value for a given time point from the corresponding raw data in the sample reaction. This will correct for any background absorbance.
3. Calculate the averages and standard deviations of the samples from the background corrected raw data.

4. To correct for different baseline values, calculate the average baseline absorbance for a given sample from the first 3-5 measurements (ie. The ones taken before clotting begins) and subtract that value from all A_{405} values for the sample. This will ensure all datasets start with zero absorbance.
5. Generate a graph of the plasma recalcification turbidimetric assay with time on the x-axis and A_{405} on the y-axis. Error bars may be included but tend to make the graphs more difficult to interpret.

2.3. Summarized Method of ELP Gene Synthesis, Expression and Purification

Procedure published by Bahniuk *et al.* (4).

Note that this is only a very brief summary. A complete, detailed protocol may be found in Appendix 1.

Recursive Directional Ligation for ELP Gene Concatemerization

1. After obtaining synthetic ELP gene, clone it into a pUC19 vector and into XL10-Gold *Escherichia coli* (*E. coli*) for larger scale replication via mini/midi plasmid preps.
2. Digest the ELP-pUC19 plasmid with both BglI and PflMI in order to obtain an ELP insert. Collect the insert by DNA gel electrophoresis and gel extraction.
3. Digest the ELP pUC19 plasmid with PflMI only to yield a linearized vector. Purify with gel electrophoresis and extraction then repeat the linearization and dephosphorylate the cut vector with Antarctic phosphatase.
4. Ligate the ELP insert and vector together at a 50:10 fmol ratio of insert to vector and transform into XL-10 *E. coli*.
5. Colony screening is performed by digesting purified plasmids with BglI and PflMI enzymes. Upon successful concatemerization the ELP gene should have doubled in length.

6. Repeat as needed. Note that any ELP gene can be inserted using this protocol, not only those which would further lengthen a monomeric ELP gene.

Expression Vector Modification and ELP Gene Insertion

7. Insert a synthetic expression vector modification gene (containing the N and C-terminal ELP sequences as well as two appropriately spaced SfiI restriction enzyme cut sites) into the pET-25b(+) vector via EcoRI and NdeI-mediated cloning with a 20:10 fmol insert:vector ratio.
8. Screen for successful vector modification by looking for successful SfiI digestion and unsuccessful BamHI linearization.
9. Linearize the modified vector with SfiI at 50°C, gel purify, redigest with SfiI and dephosphorylate.
10. Ligate the ELP gene into the linearized, modified pET-25b(+) using a 5-:10 fmol insert:vector ratio.
11. Confirm successful ligation by double digestion reactions with NdeI and EcoRI.
12. Send the ELP-containing expression vector away for DNA sequencing at the T7 promoter and terminator sites.
13. Transform *E. coli* BL21(DE3) with the ELP expression plasmid.

ELP Expression

14. A 50 mL starter culture of ELP-expressing *E. coli* BL21(DE3) can be grown up in terrific broth supplemented with 10mM proline and 100 μg/mL ampicillin overnight at 37°C, 225 rpm.
15. Add the starter culture to a 1 L terrific broth liquid culture with the same supplements.
16. When OD_{600} reaches 0.8, add isopropyl β-D-1-thiogalactopyranoside to a final concentration of 2 mM then incubate at 37°C, 225 rpm for 24 hours.
17. Collect the cells by centrifugation and store at -80°C.

ELP Purification

18. The first purification method is denaturing metal affinity chromatography. Cells are lysed in buffered 8M urea, centrifuged to remove insoluble contaminants, and then the soluble lysate is incubated with Ni-NTA beads for ~16 hours at 4°C. This extended binding incubation is critical for high ELP yields.
19. Ni-NTA beads are washed with 8M urea wash solution then in copious amounts of 25mM Tris, 50mM NaCl buffer.
20. ELPs are eluted using a buffered imidazole step gradient ranging from 31-500 mM imidazole.
21. If necessary, eluents can be visualized on SDS-PAGE gels with a $CuCl_2$ negative stain to determine where the ELPs were eluted.

22. ELP eluents can then be further purified using inverse temperature cycling. Specific temperature and NaCl concentrations may vary depending upon the ELP construct.
23. Combine all ELP-containing imidazole eluents then heat to 37°C for 5-15 minutes. Solutions should turn cloudy indicating ELP phase transition.
24. Centrifuge the warm solution at 37°C to collect ELPs in the pellet.
25. Resuspend the ELP pellet in cold PBS pH 7.4 with bath sonication on ice for 30 minutes.
26. Centrifuge the resuspended ELP solution at 4°C to remove any remaining insoluble contaminants.
27. ELP purification can be assessed by SDS-PAGE and $CuCl_2$ staining.
28. Purified ELP solutions should have their concentrations measured and be aliquoted and flash frozen the day of their purification to prevent potential protein precipitation. Protein absorbance at 280 nm along with a theoretical ELP extinction coefficient calculated using ProtParam from ExPASy can be used to determine the final ELP concentration.
29. If ELPs are forming particles while the A_{280} is being measured, this will impact the reading and 2-4M urea may be included in the ELP sample in order to prevent temperature-triggered ELP assembly during spectrophotometric measurements.

References

1.) Unsworth LD, Sheardown H, Brash JL. Polyethylene oxide surfaces of variable chain density by chemisorption of PEO-thiol on gold: adsorption of proteins from plasma studied by radiolabelling and immunoblotting. Biomaterials. 2005 Oct 31;26(30):5927-33.

2.) Kim HR, Andrieux K, Gil S, Taverna M, Chacun H, Desmaële D, Taran F, Georgin D, Couvreur P. Translocation of poly (ethylene glycol-co-hexadecyl) cyanoacrylate nanoparticles into rat brain endothelial cells: role of apolipoproteins in receptor-mediated endocytosis. Biomacromolecules. 2007 Mar 12;8(3):793-9.

3.) McClung WG, Babcock DE, Brash JL. Fibrinolytic properties of lysine-derivatized polyethylene in contact with flowing whole blood (Chandler loop model). Journal of Biomedical Materials Research Part A. 2007 Jun 1;81(3):644-51.

4.) Bahniuk MS, Alshememry AK, Unsworth LD. High-yield recombinant expression and purification of marginally soluble, short elastin-like polypeptides. BioTechniques. 2016 Dec;61(6):297-304.

3. Thermoreversible hydrogels based on triblock copolymers of poly(ethylene glycol) and carboxyl functionalized poly(ε-caprolactone): The effect of carboxyl group substitution on the transition temperature and biocompatibility in plasma

Published as "Nikouei NS, Vakili MR, Bahniuk MS, Unsworth L, Akbari A, Wu J, Lavasanifar A. Thermoreversible hydrogels based on triblock copolymers of poly (ethylene glycol) and carboxyl functionalized poly (ε-caprolactone): the effect of carboxyl group substitution on the transition temperature and biocompatibility in plasma. Acta biomaterialia. 2015 Jan 15;12:81-92."

3.1. Abstract

In this study we report on the development, characterization and plasma protein interaction of novel thermoresponsive in situ hydrogels based on triblock copolymers of poly(ethylene glycol) (PEG) and poly(α-carboxyl-co-benzyl carboxylate)-ε-caprolactone (PCBCL) having two different degrees of carboxyl group substitution on the PCBCL block. Block copolymers were synthesized through ring-opening polymerization of α-benzyl carboxylate-ε-caprolactone by dihydroxy PEG, leading to the production of poly(α-benzyl carboxylate-ε-caprolactone)–PEG–poly(α-benzyl carboxylate-ε-caprolactone) (PBCL–PEG–PBCL). This was followed by partial debenzylation of PBCL blocks under controlled conditions, leading to the preparation of PCBCL–PEG–PCBCL triblock copolymers with 30 and 54 mol.% carboxyl group substitution. Prepared PCBCL–PEG–PCBCL block copolymers have been shown to have a concentration-dependent sol to gel transition as a result of an increase in temperature above ~29 °C, as evidenced by the inverse flow method, differential scanning calorimetry and dynamic mechanical analysis. The sol–gel transition temperature/concentration and dynamic mechanical properties of the gel were found to be dependent on the level of carboxyl group substitution. Both hydrogels (30 and 54 mol.% carboxyl group substitution) showed similar amounts of protein adsorption but striking differences in the profiles of the adsorbed proteome. Additionally, the two systems showed similarities in their clot formation kinetics but substantial differences in clot endpoints. The results show great promise for

the above-mentioned thermoreversible in situ hydrogels as biocompatible materials for biomedical applications.

3.2. Graphical abstract

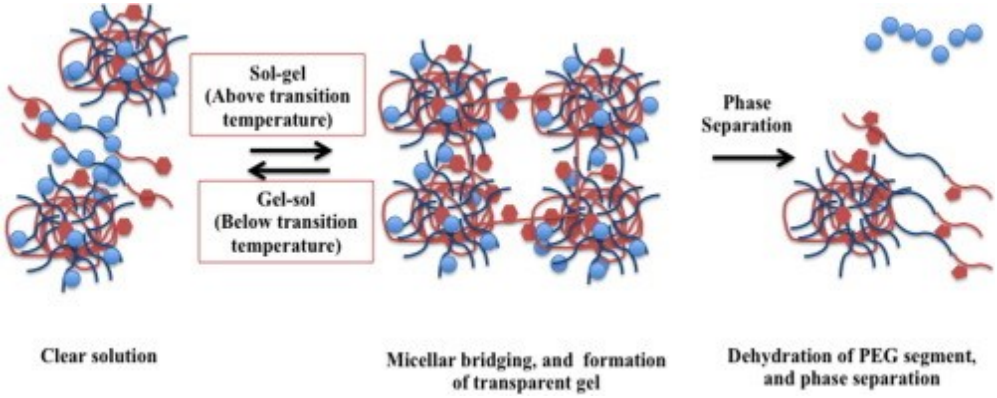

3.3. Keywords

In situ hydrogel; Thermoresponsive; Protein adsorption; Biodegradable gel; Biocompatibility

3.4. Introduction

Thermogelling polymers that undergo a sol-to-gel transition in aqueous media at temperatures a few degrees below the normal physiological temperature of 37 °C are of great interest as vehicles for regional drug delivery or tissue engineering applications (1). Thermogelling materials are injectable at room temperature, but immediately transform into standing in situ hydrogels when exposed to physiological temperature upon administration. This unique characteristic provides for the minimally invasive application of these materials.

In addition, the in situ forming hydrogel will be able to take the shape of the body cavity in which it is inserted. Small molecule drugs or macromolecular therapeutic agents such as peptides and proteins can easily be incorporated into the gel in the sol state at room temperature (2, 3). At body temperature, however, the in situ forming hydrogels can provide sustained or stimulus-controlled delivery of the incorporated therapeutic.

A common problem associated with the use of existing thermogelling materials, as in situ hydrogels, for biomedical applications are concerns over their inadequate safety and/or degradation profile. One of the first examples of relatively safe and degradable thermogelling materials was reported in 1990s. This in situ gel-forming material was based on a poly(lactide-co-glycolide)–*block*–poly(ethylene glycol)–*block*–poly(lactide-co-glycolide) (PLGA–*b*–PEG–*b*–PLGA) triblock copolymer (4) that was water soluble at room temperature but formed a gel at concentrations of 5–30 wt.% and elevated temperatures (5, 6). This block copolymer, which was later given the trade name of ReGel®, was also shown to enhance the solubility of poorly soluble drugs like paclitaxel and cyclosporine A by 400 to >2000-fold. The gel was used for depot drug delivery, with release times ranging from 1 to 6 weeks. For instance, excellent control over the release of paclitaxel was achieved using ReGel® for approximately 50 days, while proteins like pGH, G-CSF, insulin and rHbsAg showed a continuous release for up to 10–14 days without any signs of burst release when incorporated in ReGel® (7). Block copolymers consisting of PEG and a more hydrophobic

polyester, poly(ε-caprolactone) (PCL) (8, 9), have also been widely studied for drug delivery or tissue engineering applications (8, 10-14).

Our research group has developed a new family of biodegradable di- and triblock copolymers based on PEG and carboxyl-functionalized PCL (15, 16). The current manuscript describes the results of our investigations on the potential of triblock copolymers based on PEG and carboxyl-functionalized PCL for the formation of thermoresponsive and biocompatible in situ hydrogels. In this context, we defined the sol–gel transition temperature of the aqueous solutions of triblock copolymers as a function of polymer concentration by different methods and investigated the mechanism of thermoresponsive gel formation. We then assessed the potential biocompatibility of the gels using human platelet-poor plasma for the express purpose of studying protein adsorption and plasma clotting kinetics. This adsorbed protein layer has been shown to direct numerous responses, including coagulation, immune, complement and platelet activation, in addition to directing the interactions between the hydrogels and host cells (17). A kinetic study of the clotting response of recalcified human plasma in response to the polymer hydrogel material will build upon the information gleaned from the adsorption experiments and further discern the biocompatibility of this system.

3.5. Materials and Methods

3.5.1. Materials

Dihydroxy poly(ethylene glycol) (PEG, MW = 1450 Da) and palladium, 10% on activated charcoal, were purchased from Sigma, St. Louis, MO. α-Benzyl carboxylate-ε-caprolactone (BCL) was synthesized by Alberta Research Chemicals Inc (ARCI), Edmonton, Canada. Cyclosporine A was purchased from LC laboratories, USA. All other chemicals and reagents were analytical grade.

3.5.2. Synthesis of triblock copolymers

Synthesis of triblock copolymer was carried out following a previously reported two-step procedure (16) with some modifications. First, triblock copolymers composed of PEG in the middle and poly(α-benzyl carboxylate)-ε-caprolactone (PBCL) on the sides were synthesized through ring-opening polymerization of BCL in the absence of any catalyst. The polymerization was completed with 3 h of preheating at 140 °C followed by 15 h of heating at 160 °C. The product was purified by dissolving the polymer in dichloromethane and precipitation in ether followed by repeated washing with ether. The PBCL–*b*–PEG–*b*–PBCL block copolymer was then reduced using continuous hydrogen gas in the presence of palladium on activated charcoal at a concentration of 5 wt.% of the polymer. Dry tetrahydrofuran was used as the solvent. The degree of reduction was controlled by keeping the hydrogen gas flow rate to 19–20 ml min^{-1} and

changing the reaction time between 30 to 90 min. For purification, the product was dissolved in dichloromethane and precipitated in hexane three times. The degree of polymerization and the number of carboxyl groups for each copolymer was measured by ^{1}H NMR spectroscopy, as described before (16). As a result, poly[(α-carboxyl-co-α-benzylcaboxylate)-ε-caprolactone]–*b*–PEG–*b*–poly[(α-carboxyl-co-α-benzylcaboxylate)-ε-caprolactone] (PCBCL–b–PEG–b–PCBCL) triblock copolymers with 30 and 54% carboxyl substitution on the lateral blocks were produced.

3.5.3. Characterization of sol–gel transition temperature of triblock copolymer solutions in water

3.5.3.1. Visual observation of sol–gel transition by tube inversion method

The sol-to-gel transition of the synthesized triblock copolymer solutions was first determined by the tube inversion method (13) ; (18). For this purpose, PCBCL–*b*–PEG–*b*–PCBCL block copolymers were dissolved in distilled water at concentrations of 7, 10 and 15 wt.%. Vials containing 1 ml of polymer solution were immersed in a water bath at a temperature of 25 °C. The temperature was allowed to increase by 1 °C every 5 min up to 60 °C. The phase transition (flow/no flow) was assessed by inverting the tube vertically to allow a visual assessment of the aqueous polymer sample. The copolymer solution was

considered to be a gel when the solution did not flow for 1 min upon inversion of the vial. The incubation temperature at which this phenomenon was observed, was recorded as the sol-to-gel transition temperature.

3.5.4. Modulated differential scanning calorimetry

Thermal analysis was performed with a Q series™ 2000 modulated differential scanning calorimeter. Triblock copolymer solutions in deionized water at concentrations of 7, 10 and 15 wt.% were prepared and kept in a refrigerator overnight. Each sample (10 mg) was hermetically sealed in an aluminum pan. The samples were first heated to 70 °C, then kept at this temperature for 5 min to eliminate their thermal history. Heating thermograms were recorded using a modulated mode with an amplitude of 0.2 °C in 60 s and a ramping of 0.5 °C per min. Scans were conducted from 8 to 10 °C. This was followed by holding the sample at 10 °C for 15 min, then increasing the temperature to 70 °C with the same rate under nitrogen gas. A pan filled with distilled water was used as a reference.

3.5.5. Dynamic mechanical analysis (DMA)

The storage and loss moduli were determined for polymer solutions as a function of temperature using a Physica MCR xx0 rheometer equipped with a Peltier heating/cooling plate. Polymer solutions in distilled water (7, 10 and 15

wt.%) were placed between two parallel plates. Temperature sweeps (20–60 °C) were conducted at a fixed strain of 1% using an angular frequency of 10 rad s^{-1}. Sweeps were conducted at 1 °C min^{-1}. The changes in the storage and loss moduli as a function of temperature were plotted. The transition temperature of a solution was estimated by dividing the loss modulus value by the storage modulus value. The sol-to-gel transition temperature was calculated as the temperature at which the ratio of loss modulus to storage modulus fell below one (graph not shown).

3.5.6. Assessing the mechanism of gel formation using ^{1}H NMR spectroscopy

The ^{1}H NMR spectra of PCBCL–*b*–PEG–*b*–PCBCLs (30 and 54% reduced) in D_2O (1 wt.%) were obtained as a function of temperature rising from 7 to 60 °C. The temperature was raised at a rate of 2 °C every 6 min. The ratio of the integration of certain peaks of the copolymer, i.e. PEG protons (δ = 3.65 ppm), methylene protons of the PCBCL backbone (–CH2–CH2–CH2–, δ = 1.2, 1.4 and 1.9 ppm), phenyl protons (δ = 7.4 ppm) or methylene protons of the benzyl carboxylate substituent (δ = 5.15 ppm), to the integration of the peak of dimethyl sulfone protons (δ = 3.2 ppm) (external standard) were plotted as a function of temperature.

3.5.7. Zeta potential measurement

The surface charge of the copolymers (1 mg ml^{-1} concentration) in Tris-buffered saline (20 mM Tris, pH 7.4) was investigated using a Nano-ZS Zetasizer (Malvern Instruments Ltd., UK) at 25 °C.

3.5.8. Characterization of gel biocompatibility in human plasma

3.5.9. Protein adsorption to hydrogel following incubation in plasma

To ensure any plasma protein interactions were due to the presence of the hydrogels only and not the containers, the 24-well tissue culture plates (Corning Life Sciences, Corning NY) to be used for adsorption experiments were first blocked using 10% w/v milk powder (Carnation, Markham ON) in 0.3% Tween 20 in Tris-buffered saline (20 mM Tris and 500 mM NaCl) at room temperature overnight with rocking agitation. The following morning the blocking solution was removed and 200 µl of 10% w/v hydrogel solution was added to form a uniform layer on the bottom of the well. All remaining steps involved maintained a temperature of 37 °C for all solutions. The multiwell plates were then incubated at 37 °C for 30 min to allow for complete gelation. Platelet-poor human plasma (2 ml, Research Division of Canadian Blood Services) was added to each well. In accordance with Canadian Blood Services policy, samples were pooled to preserve donor anonymity and the donors provided informed consent. The non-

plasma-contacting samples had equivalent volumes of Tris-buffered saline (20 mM Tris and 500 mM NaCl; TBS) added in lieu of plasma. Hydrogel samples equilibrated with the plasma or TBS for 2 h with rocking agitation. The plasma or TBS was then aspirated and the hydrogels washed three times with 2 ml of TBS for 30 min to remove any loosely bound protein.

The remaining adsorbed plasma proteins were eluted from the hydrogels using a 2% w/v sodium dodecyl sulfate (SDS) solution (200 μl, 37 °C Bio-Rad, Hercules, CA) in TBS and incubated at 50 °C for 2 h with rocking agitation. After incubation it was found that the hydrogels had reverted to their liquid form and would no longer form gels. As such, the solutions used for subsequent protein assays, gel electrophoresis and Western blotting contained both the adsorbed plasma protein and the polymer originally used to form the hydrogels.

The microplate protocol for the DC Protein Assay (Bio-Rad, Hercules, CA) was used to determine the plasma protein concentration eluted from the hydrogels. Briefly, standard curves were generated using bovine serum albumin (BSA) protein in 2% SDS in TBS at concentrations ranging from 0.20 to 1.50 mg ml^{-1}. Aliquots of the BSA standard (5 μl) and each of the TBS and plasma-incubated hydrogel samples were analyzed using the components provided in the assay kit. The absorbance at 740 nm was measured using a DU 730 Life Sciences

UV/Vis spectrophotometer (Beckman Coulter, Mississauga, ON). Each sample was assayed in triplicate, and reported as average and standard deviation.

3.5.10. SDS–polyacrylamide gel electrophoresis (SDS–PAGE) and Western blotting

SDS–PAGE and Western blotting techniques were used to identify the adsorbed protein, as described in Ref. (19). In order to compare the results of specific proteins between samples, a total of 30 μg of protein (or, in the case of the non plasma-contacting control samples, the volumetric equivalent of) was run on each electrophoresis gel. Briefly, a sample buffer was added to the protein samples containing 0.5 M β-mercaptoethanol and 2% SDS in order to completely reduce and denature the samples. This process was further enhanced by heating the samples at 95 °C for 5 min before running them on 12% SDS–polyacrylamide gels. The proteins were then transferred to 0.2 μm Immuno-Blot PVDF membranes (Bio-Rad, Hercules, CA). All consumables had been purchased from Bio-Rad (Hercules, CA). Each membrane was then divided into 23 strips for Western blotting, with the remainder being used for total protein staining using colloidal gold. The antibodies were used at a 1:1000 concentration without any further purification. Protein–antibody complexes were visualized using 350 μl of stabilized TMB substrate (Promega, Madison, WI) per membrane strip. The color-developing reactions were allowed to advance until generalized precipitation of the colored product was seen (approximately 10 min for each sample). The color-developing reaction was then quenched and, as soon as the membrane strips were completely dry, the blots were reassembled and digitized.

Copolymer	Carboxyl substitution (mol.%) [a]	M_n [b]	number of pendent groups per functionalized PCL chain [b]		Zeta potential of copolymers in Tris-buffered saline (mV)
			Carboxyl	Benzyl carboxylate	
PCBCL–PEG–PCBCL	30	3882	3.3	7.7	- 7.77 ± 0.59
PCBCL–PEG–PCBCL	54	3648	5.9	5.1	- 14.3 ± 0.91

Table 3.1. Characteristic of synthesized triblock copolymers. [a] The number shown indicates the percentage of reduction of benzyl carboxylate to carboxyl group in each block copolymer determined by ^{1}H NMR spectroscopy. [b] Based on data from ^{1}H NMR.

3.5.11. Plasma recalcification turbidimetric assay

Clot formation in the presence of the hydrogels was evaluated using a plasma recalcification turbidimetric assay as described previously (20). Briefly, 25 µl of hydrogel solution or TBS was used to coat the bottom of the wells of a 96-well multiwell plate. They were allowed to gel at 37 °C for 30 min, then 100 µl of 37 °C human plasma was added to each well. Immediately before the multiwell plate was placed into the preheated 37 °C plate reader, 100 µl of 25 µM $CaCl_2$ or TBS was added to each well. A Beckman Coulter AD 340 plate reader (Beckman Coulter, Mississauga ON) was set to maintain a temperature of 37 °C and to read at a wavelength of 405 nm. Measurements were taken for each well every minute for 1 h. All samples were repeated five times and the results reported as the average and standard deviation.

3.5.12. Statistical analysis

The significance of differences between results was assessed using an unpaired Student's *t*-test. The level of significance was set at $\alpha = 0.05$.

3.6. Results

3.6.1. Thermoresponsive transition of block copolymer solutions in water

3.6.2. Inverse flow method

The characteristics of the triblock copolymers under study are summarized in Table 3.1. Fig. 3.1 shows the temperature-dependent phase transition behavior of aqueous solutions of PCBCL–PEG–PCBCL triblock copolymers with 30 and 54% carboxyl substitution at 7, 10 and 15 wt.% polymer concentrations as determined by the inverse flow method. The PCBCL–PEG–PCBCL triblock copolymer having 54% COOH substitution formed a transparent gel at 7 wt.% as the temperature was raised above 31 °C. This is the temperature used to identify the lower transition temperature of the block copolymer solution in Fig. 3.1. With further increasing temperature, the transparent gel became turbid. Upon further heating at 41 °C, phase separation occurred and a turbid solution was achieved. The latter temperature was used to plot the upper transition curve in Fig. 3.1. Similar behavior was observed for the PCBCL–PEG–PCBCL block copolymer with 30% COOH substitution. At a concentration of 7 wt.%, the lower and upper

transition temperatures for this block copolymer were measured at 35 and 45 °C, respectively. It is noteworthy that, at this concentration (7 wt.%), the copolymer with the lower degree of COOH substitution showed a slightly higher sol-to-gel transition temperature.

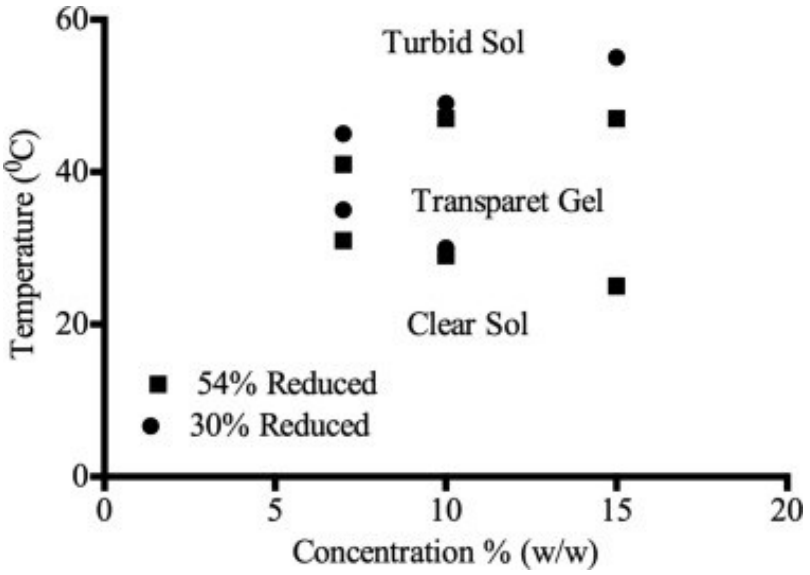

Figure 1.1. Phase transition diagrams of PCBCL-PEG-PCBCL block copolymers with 30 and 54% COOH substitution at different polymer concentrations in distilled water as determined by inverse flow method.

For both copolymers, the lower transition temperature decreased as the polymer concentration increased. For the copolymer with 54% COOH substitution, the lower transition temperature decreased from 31 to 25 °C as the concentration of the polymer increased from 7 to 15 wt.%. For the copolymer with 30% COOH substitution, the lower transition temperature decreased from 35

to 25 °C as the concentration of the polymer was increased from 7 to 15 wt.%. The upper transition temperature, however, was increased by increasing the concentration of block copolymer. An increase in polymer concentration from 7 to 15 wt.%, led to an increase in the upper transition temperature from 45 to 55 °C and from 41 to 47 °C for copolymers with 30 and 54% COOH substitution, respectively.

3.6.3. DMA

Fig. 3.2A and B shows changes in the storage modulus, G′ of triblock copolymer solutions as a function of temperature at 7–15 wt.% polymer concentrations. For both block copolymers, we observed a sharp increase in G′ at a certain temperature. In addition, the temperature at which a sharp rise in G′ was observed decreased as the concentration of the triblock copolymer was increased. For the block copolymer with 30% COOH substitution, the storage modulus reached its maximum value at around 45 °C and started to decline after. For the block copolymer with 54% COOH substitution, the storage modulus reached its maximum value at 30–41 °C (depending on polymer concentration) and remained at that level up to 60 °C. This indicated the formation of more stable and robust gels from 54% COOH-substituted block copolymer above the corresponding transition temperatures (21).

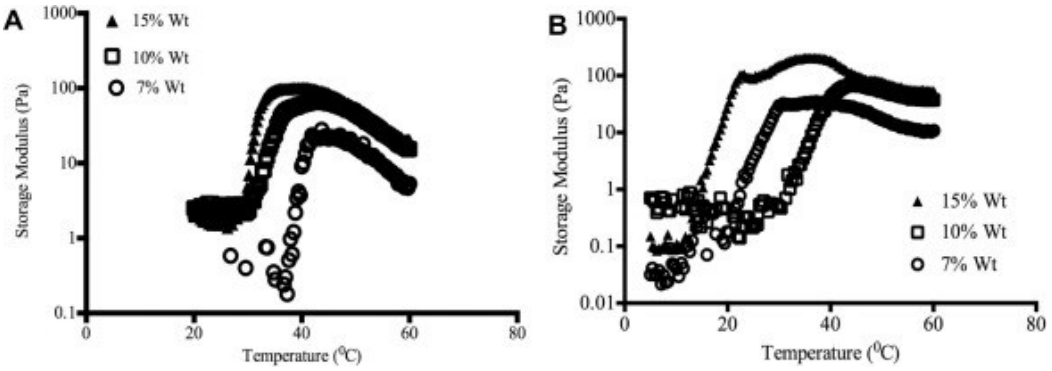

Figure 3.2. Changes in the storage modulus, G', as a function of temperature for aqueous soltutions of PCBCL-PEG-PCBCL block copolymer having (A) 30 %, and (B) 54% carboxyl substitution at different polymer concentrations (n = 3).

The change in the ratio of the storage modulus, G′ to the loss modulus, G″ as a function of temperature for block copolymers of different COOH substitution was used to measure their sol-to-gel transition temperatures (Fig. 3.3A and B). As can be seen in both figures, at low temperatures, the loss modulus and storage modulus of polymer solutions were similar, indicating a typical liquid state. Both storage and loss moduli increased at a certain temperature, but the level of increase in the loss modulus (reflecting resistance to flow) was lower than that in the storage modulus (reflecting resistance to deformation) (22). This indicated gel formation, and the temperature for the onset of this change was considered as the sol-to-gel transition temperature (21).

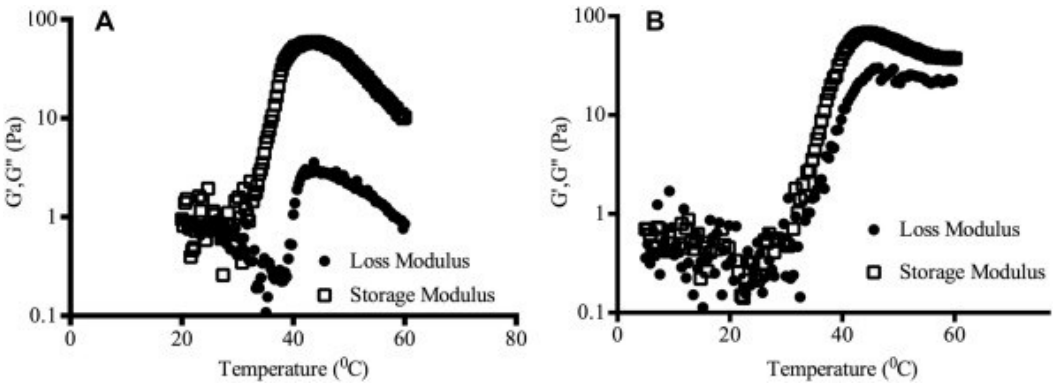

Figure 3.3. Increases in storage modulus (G') and loss modulus (G'') of PCBCL-PEG-PCBCL block copolymers with (A) 30%, and (B) 54% COOH substitution at 10 wt.% polymer concentration as a function of rising temperature (n = 3).

Similar graphs were obtained for the block copolymer at 7 and 15 wt.% polymer concentrations and used to determine the sol-to-gel transition temperature of block copolymers by DMA (Table 2). In line with our earlier results, the sol-to-gel transition temperature of block copolymers showed a decreasing trend as a function of an increase in block copolymer concentration in water. Similar to previous results, at a polymer concentration of 7%, the polymer with the 30% COOH substitution formed gel at a slightly higher transition temperature. Of the two block copolymers, the one with the 54% COOH substitution formed a more stable gel at temperatures above its transition temperature, but the sol-to-gel transition for this polymer was not as rapid as the polymer with the 30% COOH substitution.

COOH substitution level (%)	Polymer concentration (wt.%)	Sol-to-gel transition temperature (°C) ± SD
30	7	38 ± 0.60
	10	30 ± 0.45
	15	27 ± 0.75
54	7	33 ± 0.43
	10	33 ± 0.55
	15	28 ± 0.43

Table 3.2. Transition temperatures of PCBCL–PEG–PCBCL block copolymers with different levels of COOH substitution at different concentrations in water as measured by DMA (n = 3).

3.6.4. DSC

Fig. 3.4 illustrates the modulated DSC thermograms of aqueous solutions of block copolymers at a concentration of 10 wt.%. The block copolymer with 30% carboxyl substitution showed two endothermic peaks. The first peak appeared at 35.05 °C, which coincides with the sol-to-gel transition temperature of this block copolymer solution in water as measured by the inverse flow method. The second peak appeared at 45.71 °C, which coincides with the phase separation of this copolymer. The modulated DSC thermograms of the block copolymer with 54% COOH substitution also showed two endothermic transition peaks, at 33.57 and 45.21 °C. These temperatures are also close to the sol-to-gel transition and phase separation temperatures, respectively, of this polymer as measured by the inverse flow method (Fig. 3.1).

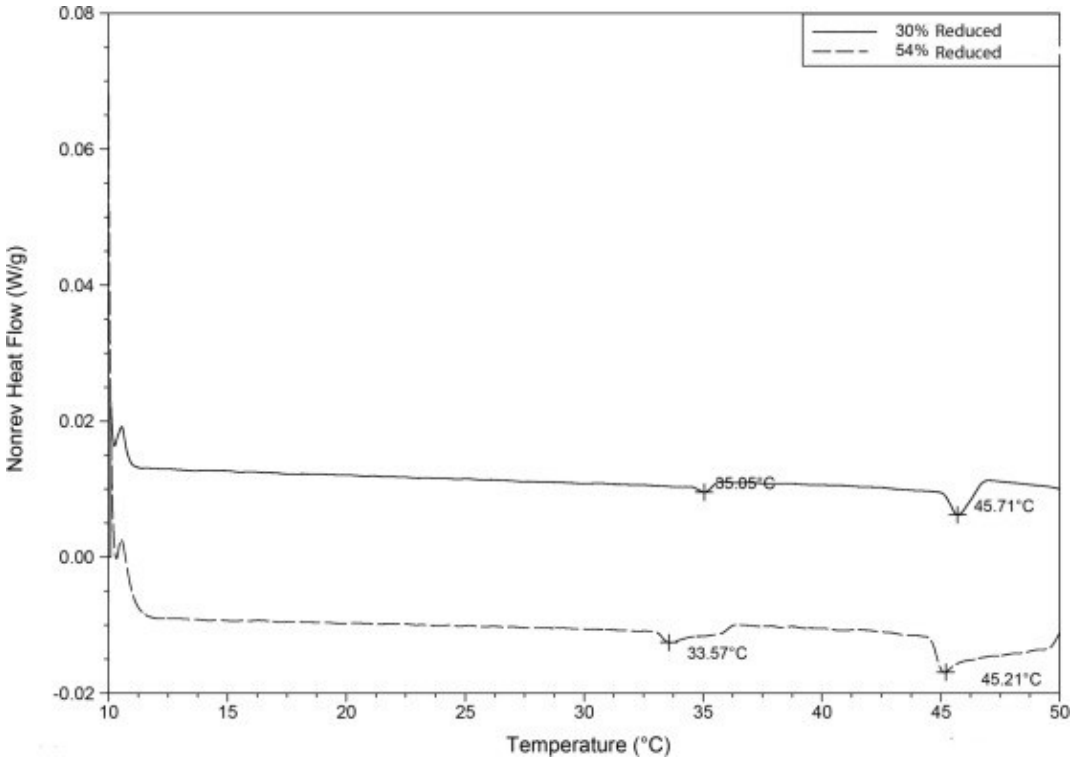

Figure 3.4. Modulated DSC thermograms of block copolymers with 30 and 54 % reduction (i.e., level of COOH substitution) in distilled water at 10 wt.% copolymer concentrations.

The first and second transition enthalpies of the copolymer with 30% COOH substitution were 0.07 and 0.44 J g^{-1}, respectively. These values were 0.31 and 1.58 J g^{-1} for the block copolymer with 54% COOH substitution. The endothermic nature of the peaks and their comparative enthalpy values imply a role for the breaking of hydrogen bonds in the thermoresponsive transition processes. The first transition (around 33 and 35 °C) more likely reflects the breaking of inter- or intra polymer chain hydrogen bonds between pendent COOH groups and/or breaking of hydrogen bonds between water and COOH groups (23), followed by the association of micelles through inter-micellar bridging of the hydrophobic parts of the triblock copolymers. This assumption is in line with our

observation on the lower enthalpy of transition for block copolymer with 30% compared to those with 54% COOH substitution. Polymers with higher degree of COOH substitution showed a higher enthalpy of transition (0.07 vs. 0.31 J g^{-1} for 30 and 54% COOH substituted block copolymers, respectively), perhaps due to breaking of more inter- or intramicellar hydrogen bounds. The second endothermic peak, on the other hand, may reflect the dehydration of the PEG and/or the PCBCL segment, leading to a change in micellar conformation and phase separation (24).

3.6.5. Assessing the mechanism of temperature responsive gelation of block copolymers by ^{1}H NMR

Fig. 3.5 shows ^{1}H NMR spectra of PCBCL–PEG–PCBCL block copolymer solution and dimethyl sulfone (as external standard) in D_2O (10 mg ml^{-1} polymer) at 7 and 29 °C, respectively. At 7 °C, the peaks related to the PCBCL block (hydrophobic block) of copolymer showed lowered intensity because of the restricted mobility of the protons in the solid-like structure of the core in PCBCL–*b*–PEG–*b*–PCBCL micelles. This was expected and is in line with previous observations from our group and others (28). Interestingly, the ^{1}H NMR spectrum of the block copolymer exhibited a marked increase in the integration of the methylene protons of the benzyl group (–CH_2–O–C=O, δ = 5.15), the phenyl protons of the benzyl group (–C_6H_5, δ = 7.2 ppm) and the methylene protons on the PCBCL backbone (–CH_2–CH_2–CH_2–CH_2–O, δ = 1.2,

1.4 and 1.9 ppm) at 29 °C compared to 7 °C. We have calculated the ratio of the integration of the above-mentioned peaks to the peak related to the standard for the same sample at different temperatures to get an insight into the conformational changes occurring in the polymer solution and the involved chemical groups that can lead to the formation of three-dimensional networks in PCBCL–*b*–PEG–*b*–PCBCL gels. It should be noted that these studies were conducted at a polymer concentration of 1 wt.%, which is below the critical gelation concentration of the block copolymers under study. Fig. 3.6A–D shows the temperature dependence of the ratio of the area under the peak for the protons on the phenyl ring, the methylene of the benzylcarboxylate group, the methylene groups related to the PCBCL backbone as well as the methylene groups of PEG to that of dimethyl sulfone ($–CH_3$, δ = 3.2 ppm), respectively, for both copolymers under study (PCBCL–PEG–PCBCL with 30 and 54% COOH substitution) in D_2O. Temperature dependency in peak integration was only observed for the protons related to the PCBCL block (i.e. phenyl ring, methylene of benzylcarboxylate group, methylene groups related to PCBCL backbone). In contrast, the ratio for the integration of peaks related to PEG protons to the peaks related to dimethyl sulfone protons did not show any significant change as a function of increasing temperature. This reflects the better mobility of the PCBCL block at elevated temperatures that can lead to the formation of a gel network.

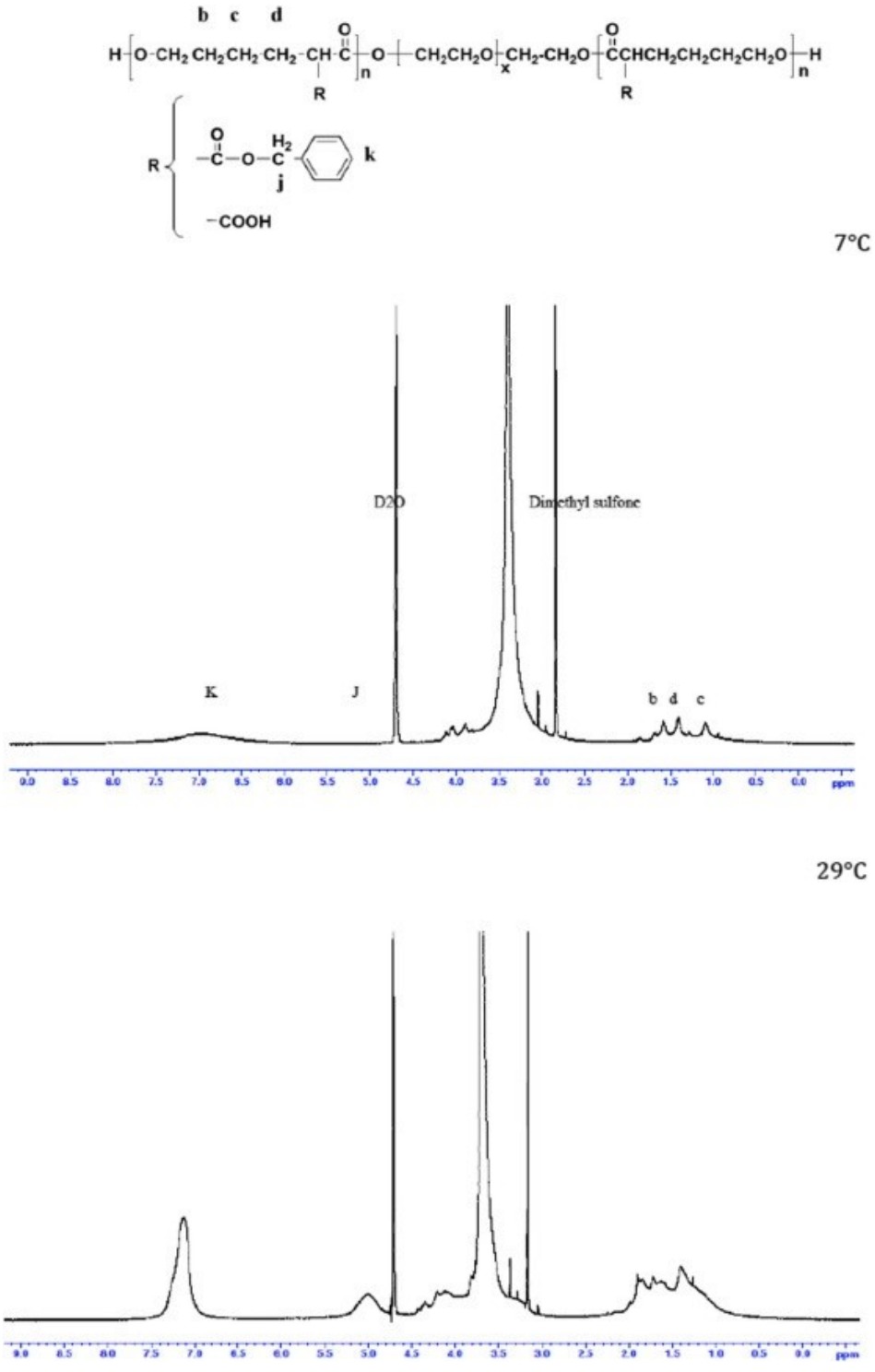

Figure 3.5. ^{1}H NMR spectra of PCBCL-PEG-PCBCL block copolymer (54% COOH substitution) solution in D_2O (1 wt.% concentration) at 7 and 29 °C.

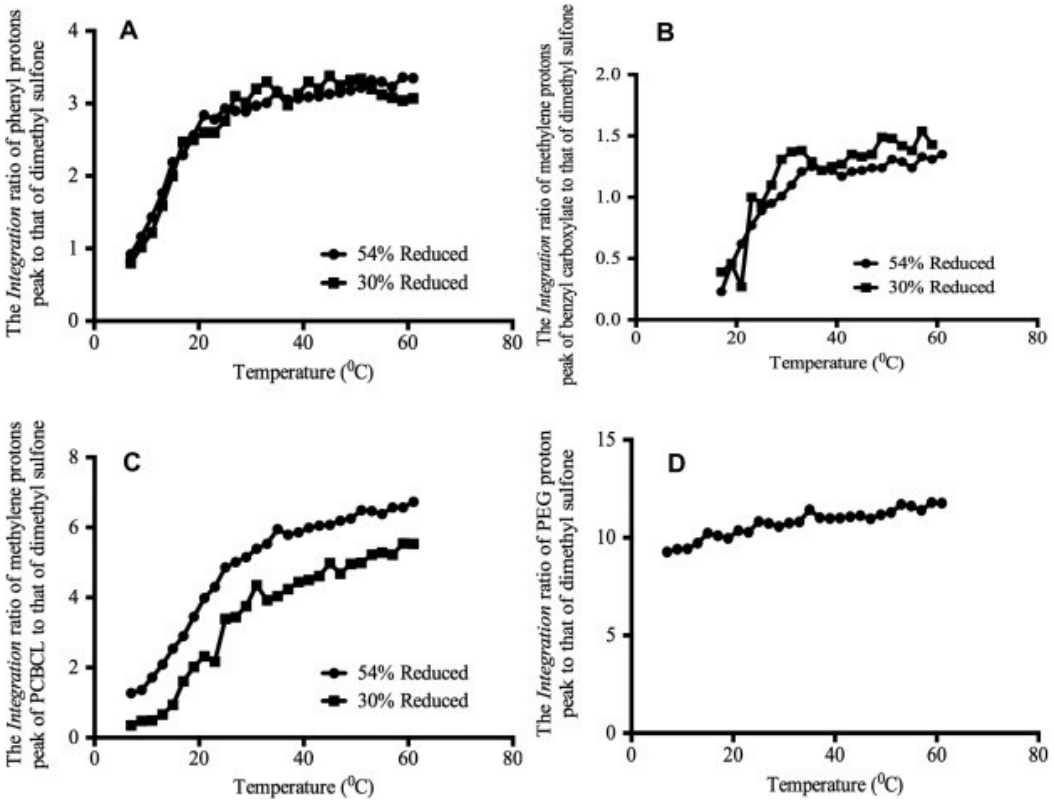

Figure 3.6. The change in the ratio of the integration of peaks related to the protons of (A) phenyl, (B) methylene benzyl carboxylate, (C) methylene of the PCBCL backbone and (D) PEG to the integration of peaks related to dimethyl sulfone protons as a function of temperature in ^{1}H NMR spectroscopy of PCBCL-PEG-PCBCL block copolymers conducted in D_2O.

3.6.6. Characterization of the hydrogel for its surface charge

Both copolymers exhibited negative surface charges (Table 3.1), −7.7 and −14.3 mV for 30 and 54% COOH substituted block copolymers, respectively. A Student's *t*-test for significance showed that these two block copolymers were statistically different in terms of their zeta potential (unpaired Student's *t*-test, $p < 0.05$).

3.6.7. Characterization of the hydrogel for plasma protein interactions

In order to assess hydrogel biocompatibility, specifically their interactions with plasma proteins, both the 30 and 54% substituted hydrogels were incubated with human plasma at 37 °C for a period of 2 h. PBS was used afterwards to remove any proteins that were only loosely bound. After washing, the adsorbed proteome was eluted using a 2% SDS solution. This incubation with detergent resulted in a permanent eradication of the hydrogel structure. Consequently, the polymer was rendered inseparable from the eluted proteins and its presence was accounted for in subsequent analysis.

The DC protein assay was employed to quantify the amount of protein eluted from all hydrogel samples (Table 3). Of note is the fact that the non-plasma-contacting negative control samples elicited non-zero responses from the protein assay. The protein concentration values for the plasma contacting samples were adjusted accordingly.

System	Apparent Amount of Adsorbed Protein (μg/μL)	Corrected Amount of Adsorbed Protein (μg/μL)	Total Protein Processed on Western Blot (μg)
30% Negative Control	0.15 ± 0.02	0	N/A
30% Plasma Incubated	5.1 ± 0.3	5.0 ± 0.3	30.3 ± 1.8
54% Negative Control	0.40 ± 0.01	0	N/A
54% Plasma Incubated	4.5 ± 0.3	4.1 ± 0.3	30.1 ± 2.2

Table 3.3. Amounts of adsorbed protein determined using the DC protein assay. Values represent average ± SD (n = 3). For the negative control samples, volumes equivalent to those used for the corresponding plasma incubated samples were processed on the Western blots.

SDS–PAGE and Western blotting analysis were employed in order to identify individual protein species from the adsorbed proteome. A constant amount of protein (30 μg) and a consistent developing time for color-producing reactions was used for all samples in order to allow for the comparison of band intensities between like proteins found in the various copolymer hydrogel samples. However, this does not allow for direct comparisons of band intensities between different proteins as each primary antibody may bind differently, resulting in variations in their "labeling efficiency". The protein band intensity data is summarized in Table 3.4. Intensities were quantified using a 13-step grayscale. A zero value designates no visible band was present. A value of 12 indicates a completely black band, with values decreasing as the band intensities decrease. While Western blotting techniques allow for the identification of various proteins, they do not provide any information regarding their conformations. This is worth noting because it has been shown that the conformation of adsorbed proteins can cause further cellular reactions (25). The banding patterns for the various adsorbed protein samples after SDS–PAGE and colloidal gold staining show some similarities between samples (results not shown). Both the 30 and 54% hydrogels show intense banding centered at ~66 kDa, as well as some moderate banding extending down to ~50 kDa. These bands are at least partially made up of albumin and Immunoglobulin G (IgG) or

fibrinogen, respectively. Another moderately intense protein band can be seen at ~25 kDa in both samples. The polymer itself also presents as a band at ~30 kDa, as seen in the non-plasma-contacting negative control samples (results not shown). In addition to these bands, the proteome adsorbed to the 54% polymer hydrogel showed a variety of bands ranging in molecular weight from 25 to 50 kDa, suggesting a greater variety of proteins were adsorbed to this sample.

Plasma protein	Fragment size (kDa)	Fragment name	System			
			30% Negative Control	30%	54% Negative Control	54%
Albumin	66		0	12	1	12
C3	42	Activation	0	3	0	4
	70	β	0	10	0	10
	115	α	0	7	0	8
IgG	27	Light	0	5	0	0
	55	Heavy	0	7	0	0
$Alpha_1$ antitrypsin	47		0	1	0	12
Fibrinogen	<48	Cleavage	0	0	0	0
	48	γ	0	0	0	6
	56	β	0	0	0	6
	68	α	0	0	0	10
Transferrin	77		0	12	0	12
Prothrombin	70		0	0	0	8
$Alpha_2$ macroglobulin	163		0	0	0	2
Antithrombin	53		0	1	0	11

Table 3.4. Relative intensities for Western blots of plasma proteins adsorbed to the investigated hydrogels and non-plasma contacting hydrogel negative controls. 0 indicates no band intensity; 12 indicates maximum band intensity, with lower numbers signifying lower intensity.

3.6.8. Characterization of hydrogels for plasma clotting time

To determine what effect the polymer hydrogel material has on blood clotting, a plasma recalcification turbidimetric assay was employed. The hydrogels were incubated with platelet-poor human plasma in the presence of calcium at 37 °C for 1 h. A positive control sample using TBS in the place of the hydrogel was used in order to be able to directly compare the clotting time as a function of hydrogel presence and percent carboxyl substitution. To account for

any baseline turbidity, negative control samples for the 30 and 54% hydrogels and the previously mentioned positive control were employed. TBS was used in place of calcium, so no clotting would occur over the course of the assay. The rate and intensity of turbidity as a function of clotting time were measured by looking at the increase in apparent absorbance, in effect the reduced transmission, at 405 nm (Fig. 3.7). The results of the clotting assay were corrected for any turbidity associated with the plasma and/or hydrogels. Each assay sample was repeated five times and the average results are reported. In the presence of either the 30 or 54% hydrogel, the clotting reaction started approximately 5 min into the assay and began to plateau at ~10 min. In contrast, the positive control sample began to clot after ~10 min and stabilized at ~30 min. The 30% hydrogel sample reached a final turbidity comparable to that of the positive control, while the 54% sample stabilized at a lower overall value.

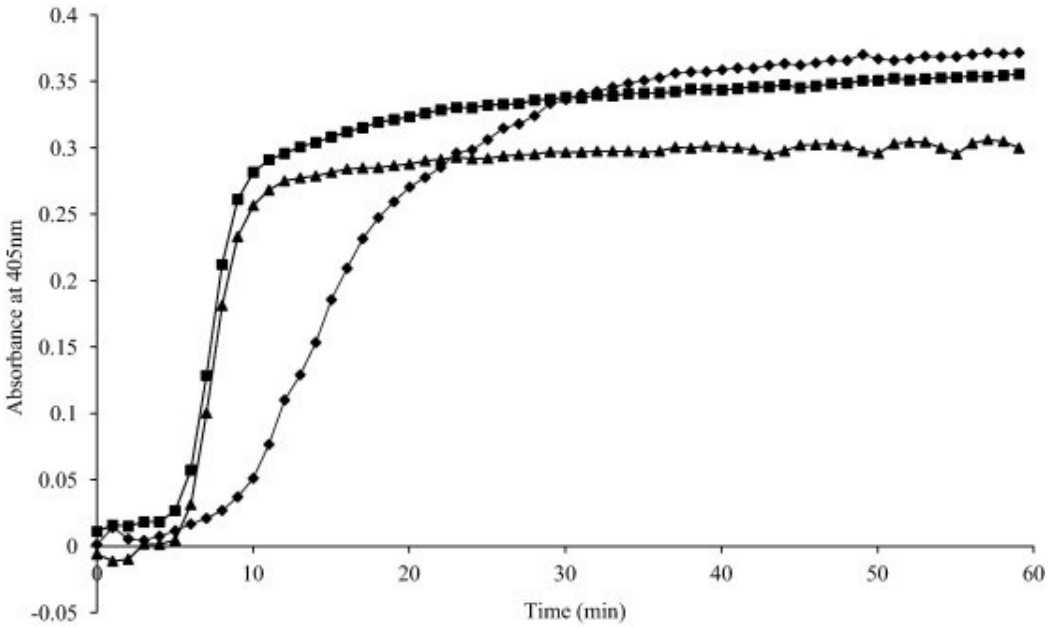

Figure 3.7. Background corrected clot formation in human platelet poor plasma over time in the presence of the 30% and 54% hydrogel. The absorbance profiles represent human plasma (♦), human plasma with 30% hydrogel (■) and human plasma with 54% hydrogel (▲) after correcting for background absorbance. Error is considered to be ± 10%.

3.7. Discussion

This manuscript describes the preparation and characterization of a novel thermoreversible hydrogel based on triblock copolymers of PEG and COOH-functionalized PCL. Both polymers under study (Table 3.1) showed thermoreversible sol-to-gel transitions (Fig. 3.2, Fig. 3.3 ; Fig. 3.4), as evidenced by different methods of measurement (26). In general, different methods used to characterize the sol-to-gel transition of the block copolymer solution showed similar results: a transition temperature around 30–35 °C for block copolymer with 30% COOH substitution and around 29–34 °C for the block copolymers with 54% COOH substitution, depending on polymer concentration in water. This

indicates a sol-to-gel transition above room temperature (>25 °C) and below body temperature (<37 °C) for both copolymers under study. Second, for both copolymers, the sol-to-gel transition decreased as the polymer concentration increased. Finally, both copolymers illustrated phase separation at temperatures around 45 °C.

Based on the results of the DSC (Fig. 3.4) and D_2O NMR (Fig. 3.5 ; Fig. 3.6), formation of a micellar network through intermicellar hydrophobic bridging is proposed to be responsible for gel formation. The micellar network formation was speculated to be initiated by the breaking of hydrogen bonds between COOH groups of one or different polymer chains within the micellar structure, allowing mobilization of the PCBCL segment of the block copolymer out of the micelles. This process was assumed to be followed by micellar bridging through hydrophobic interactions between the hydrophobic segments of the PCBCL blocks (i.e. benzyl side groups or CH2 groups of the PCBCL backbone). At higher temperatures (above the second transition temperature) dehydration of the PEG and/or PCBCL segment may lead to the formation of turbid gels. This will eventually lead to phase separation (Fig. 3.8). The proposed mechanism can explain the endothermic nature of two peaks observed in modulated DSC thermograms as the dehydration of hydrophobic chains and PEG segments are both heat-absorbing processes. The changes in the NMR spectra as a function of temperature are an indirect indication of the changes in the related protons with respect to the hydrogel's environment and viscosity. These conformational

changes precede any physical change in the physical appearance of the biomaterial from sol to gel, for example. Therefore, the temperatures for the onset of the rise in NMR integration ratios are much lower than those measured using inverse flow or DSC methods.

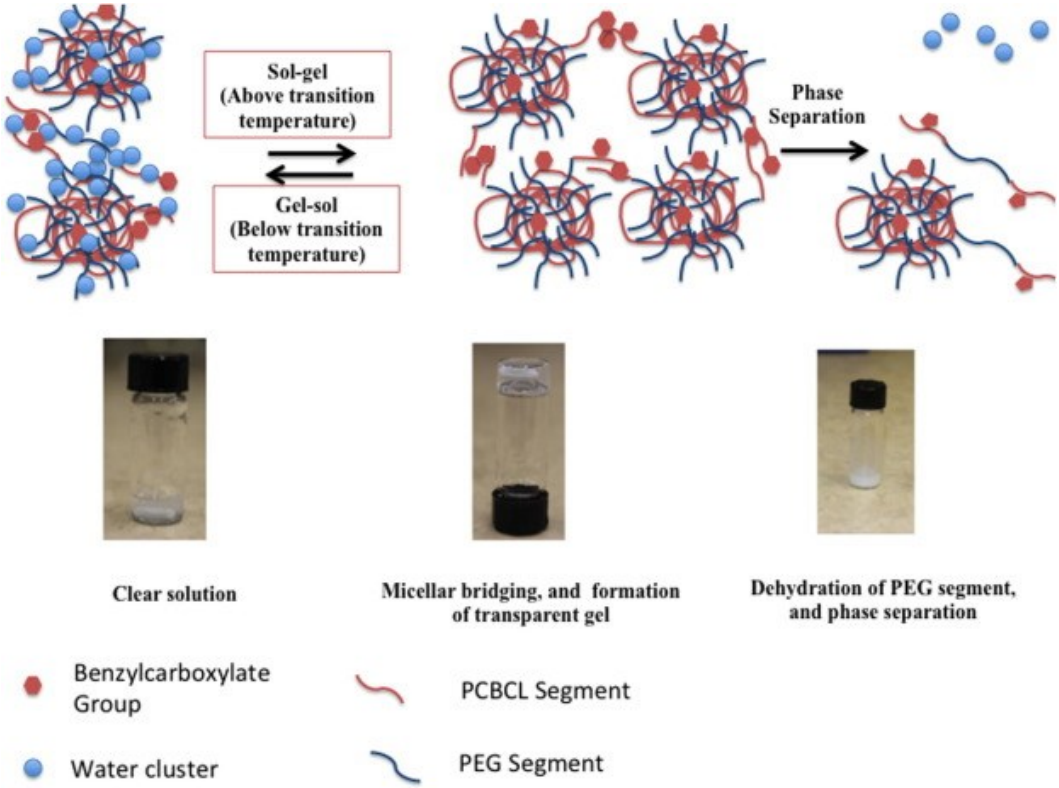

Figure 3.8. Schematic diagram for the sol-to-gel and gel-to-sol transition mechanisms of prepared triblock copolymers in aqueous solution as a function of increasing temperature.

We then tried to assess the biocompatibility of prepared hydrogels in terms of plasma protein interactions and define the role of COOH substitution

level in this process. Given that the polymer hydrogels used for plasma protein adsorption lost their structural integrity after incubation with the SDS-containing elution solution, it was determined that the polymers had an effect on the DC assay. While the responses of the individual polymers differ slightly, they represent, at most, one-tenth of the total signal elicited from the plasma-incubated samples. The 30% polymer causes less of a false positive signal than the 54%, which suggests that an increase in the degree of carboxyl substitution may cause an increase in reactivity to the DC assay. The unpaired Student's *t*-test used to compare the corrected values of adsorbed protein to the 30 and 54% hydrogels gave a *p*-value of 0.0213, indicating a significant difference between the two hydrogels. Given that the 30% reduced polymer has a greater proportion of benzyl carboxylate side groups, the increase in observed protein adsorption may, in part, be attributed to the greater hydrophobic character of the material or the lower overall negative charge, as measured by the zeta potential.

The adsorption of plasma proteins to a surface is a complex and dynamic process. Plasma is made up of hundreds of individual components, each of which may interact with the surface with various kinetics and binding strengths (i.e. the Vroman effect) (27). Furthermore, adsorbed proteins may then help facilitate the adsorption of other protein species from the plasma. The surfaces to which the proteins are adsorbing are also rarely simple and further complicate the task of determining the reasons behind the presence of specific plasma proteins as identified using Western blotting methods. The most reasonable approach to

examining such a convoluted series of events is to examine the types and relative intensities of the proteins present, as well as the potential biological responses that may result from hydrogel implantation.

The Western blot intensity data in Table 3.4 shows that, while there are some similarities in their adsorbed proteome, the difference in degree of carboxyl substitution can have a pronounced effect on the presence of certain plasma proteins. Given the high sensitivity of Western blotting, it is unlikely that the protein signal would have been too weak to detect. As such, the differences in the adsorbed proteomes found on the hydrogels are likely to be due to the variation in carboxyl substitution and subsequent differences in charge and/or hydrogel morphology. Moreover, it could be that there are proteins that diffuse into the hydrogel structure that do not tightly interact with the hydrogel complex and, because they are sheltered within the hydrogel, are not removed during the wash process. This is likely not the case because if general diffusion of proteins were to occur there should be an abundance of plasma proteins found present on the Western blots. Furthermore, it would be unlikely for one hydrogel to show large amounts of a particular protein while the other hydrogel had none, as can be seen for IgG, fibrinogen, prothrombin and alpha$_2$-macroglobulin (Table 4).

Both hydrogel samples showed a large amount of adsorbed albumin (Table 4). Given that albumin is present in high concentrations in plasma, it is not

unusual for it to be found strongly adsorbed to the hydrogel samples. However, albumin's presence may be far from innocuous. Denatured albumin has been shown to potentially lead to platelet adsorption and activation (25). While Western blotting is only able to discern the presence of albumin, not its conformation, from a biocompatibility standpoint it is still important to recognize that there is the potential for a deleterious host response in this case.

The complement system is part of the innate immunity that can cause cell lysis, opsonization and an increased antibody response upon activation (28). This is of particular importance for biomaterial effectiveness and host health as complement activation serves as a response to foreign materials (29). There are three activation pathways for complement, all of which heavily involve complement component 3 (C3) (28). An activation fragment can be seen with SDS–PAGE at 42 kDa when C3 is cleaved and complement is activated (28). Given the intensities of the Western blotting bands, it appears that both the 30 and 54% carboxyl-substituted hydrogels adsorb moderate to moderately large amounts of both C3 chains. Both samples also appear to activate complement, as evidenced by the detection of the C3 activation fragment. Given the carboxyl substitutions on the polymer side chains, C3 activation via the alternative pathway would not be unusual. This may imply that both the 30 and 54% hydrogels have enough exposed carboxyl groups to elicit an immune response. Furthermore, increasing the amount of carboxyl side chain substitution from 30 to 54% appears to have a limited apparent increase in complement activation. Compared to plasma

adsorption studies in the literature using polyethylene oxide (PEO), a well-known biocompatible system, the amounts of adsorbed C3 for this system approximately match those seen previously (30). IgG is an antibody. As such, it is involved in the host immune response, and may also contribute to C3 activation via the classical pathway (28), phagocytosis and opsonization. This protein was found in moderate amounts on the 30% carboxyl-substituted polymer hydrogel based on the band intensity values in Table 3.4. The presence of IgG suggests that opsonization and phagocytosis or fibrous capsule-based isolation may occur for the 30% substituted hydrogel. IgG was not detected at all on the 54% carboxyl-substituted hydrogel sample. The amount of IgG adsorbed to the 30% substituted hydrogel appears to be slightly larger than the amounts seen adsorbed to PEO in the literature (30).

Alpha$_1$-antitrypsin is one of the most important serine proteases and maintains the body's anti-inflammatory response (31). This protein was found to adsorb in large amounts to the 54% hydrogel sample and minimally to the 30% sample. At pH 7.0 this protein is expected to have 12.0 negatively charged amino acid residues, so it is expected that this protein would not adsorb directly to either negatively charged polymer. It is possible, however, that the protein is present on the surface because it interacts with other adsorbed proteins, or alters its conformation in order to adsorb. The degree of carboxyl substitution seems to also influence the level of alpha$_1$-antitrypsin adsorption. Transferrin's primary role is the transport of iron (32), but it has recently been shown to also be an

activating molecule for macrophages (33). Transferrin was found in large amounts on both the 30 and 54% hydrogels. As transferrin does not contain a large number of charged residues, it is most likely adsorbing through hydrophobic-based interactions and not charge–charge interactions. Its presence on both hydrogel systems could potentially cause macrophage activation.

If fibrinogen is cleaved, further banding at molecular weights below 48 kDa may be observed. Moderate to moderately large amounts of fibrinogen was found on the 54% hydrogel but no cleavage fragments were seen, which suggests that the hydrogel does not encourage fibrin activation. However, it is possible for adsorbed fibrinogen to denature enough to resemble either fibrin or its degradation products (34), and adsorbed fibrinogen can activate platelets (35) and/or potentially attract phagocytes (36). No fibrinogen was found adsorbed to the 30% hydrogel. When compared to PEO, it appears the 54% substituted hydrogel adsorbs larger amounts of the α chain and comparable amounts of the β and γ chains (30). Prothrombin is the 70 kDa inactive precursor of the enzyme thrombin and was found at moderately high levels on the 54% carboxyl-substituted hydrogel. It is possible that this accumulation of prothrombin may lead to an increase in clot formation if the prothrombin is activated. This protein was not found to be associated with the 30% hydrogel. Antithrombin is a serine protease inhibitor that, among other things, is capable of down-regulating thrombin-mediated coagulation and is one of the more significant proteins tasked with regulating thrombosis (37). This protein was found in large amounts on the

54% substituted hydrogel and minimally on the 30% sample. This may mean that the degree of carboxyl substitution may affect its adsorption. It is possible that the presence of antithrombin on both hydrogel surfaces may result in decreased thrombin procoagulant activity. Alpha$_2$-macroglobulin is a proteinase inhibitor found in abundance in plasma (31) that is able to inhibit both clotting and fibrinolysis. This protein was found in small amounts on the 54% substituted hydrogel. Western blotting alone cannot predict whether its presence will have a pro- or anticoagulant effect.

Inasmuch as proteins found adsorbed to the hydrogel surfaces yield useful information, the lack of specific proteins in the adsorbed proteome can also provide insight into the hydrogel biocompatibility. When comparing the complete list of proteins which were screened for (Table 1S) with the list of proteins found in the adsorbed proteome (Table 4), it is clear that a number of important proteins are not found to be adsorbed to the hydrogels. For instance, the lack of both fibronectin and vitronectin is an indicator that these hydrogels may not promote cellular adhesion. The complete lack of contact phase coagulation proteins, namely high molecular weight kininogen, prekallikrein, Factor XI and Factor XII, implies that the hydrogel materials may not cause coagulation through the extrinsic pathway of the coagulation cascade. The lack of adsorbed plasminogen suggests that these materials may not stimulate fibrinolysis. Furthermore, the absence of Protein C and Protein S further strengthens the idea that the polymer hydrogels do not exhibit significant anticoagulant behavior.

The results of the plasma recalcification turbidimetric assay (Fig. 3.7) clearly demonstrate that the 30 and 54% carboxyl-substituted hydrogels affected clot formation. Given that the clotting reaction began after 5 min for the 30 and 54% samples and after 10 min for the control sample containing TBS in place of hydrogel, it appears that the presence of the hydrogel material does encourage clotting. Both hydrogel samples also reached stable absorbance plateaus after only about 5 min. Conversely, the positive control clotting reaction took around 20 min to form a stable clot mass. Thus, not only do the 30 and 54% hydrogels encourage a clotting reaction, but they also increase the overall rate of clot formation compared to the negative control. One part of the clotting assay that shows that there is a difference between the 30 and 54% substituted hydrogels in the final overall absorbance. The 54% sample shows a significantly lower turbidity (higher absorbance) than both the 30% sample ($p < 0.005$) and the control ($p < 0.0005$). This distinction between the 30 and 54% samples may be due to the variation in their adsorbed proteomes. Unlike the 30% hydrogel, the 54% sample showed large amounts of adsorbed antithrombin as well as some alpha$_2$-macroglobulin. These two proteins may have inhibited thrombin activity such that there was less overall.

3.8. Conclusions

Triblock copolymers formed from PEG as the middle block and PCBCL with 30 and 54% COOH group substitution on the PCBCL block showed a concentration-dependent sol-to-gel transition at temperatures a few degrees below body temperature (~30–35 °C). The transition temperature of polymer solutions, the kinetics of gel formation and the viscoelastic properties of hydrogels were found to be dependent on the level of carboxyl substitution on the PCBCL backbone as well as the triblock copolymer concentration. Block copolymers with 54% COOH substitution formed more stable gels above their transition temperature, but their sol-to-gel transition was not as rapid as the polymer with 30% COOH substitution. Plasma protein adsorption studies and turbidimetric clotting assays also demonstrated that the degree of carboxyl substitution can affect the adsorbed proteome and the degree of clotting, and thus the host response to implantation of these hydrogels. The presence of activated C3 suggests that some complement reaction may occur in both hydrogels. The 54% hydrogel sample lacked the IgG adsorption seen in the 30% sample. This, in conjunction with the significantly lower clotting result, implies that 54% carboxyl substitution may show a less deleterious host response in reaction to the hydrogel implantation. In general, the results of this study illustrated a great potential for PCBCL–PEG–PCBCL block copolymers as in situ gel-forming materials for biomedical applications. In addition to responsiveness to temperature, the developed materials are expected to show pH sensitivity owing to the presence of pending COOH groups. Characterization of the pH responsive behavior of these

block copolymers is beyond the scope of current work and is the subject of a separate manuscript.

3.9. Acknowledgements

The authors acknowledge financial support from Natural Science and Engineering Council of Canada (NSERC). M.S.B. also acknowledges the support of the Alberta Innovates Graduate Scholarship. L.D.U. acknowledges the support of the National Research Council of Canada, and the National Institute for Nanotechnology.

Appendix A. Figures with essential colour discrimination

Certain figures in this article, particularly Figs. 3.5 and 3.8, are difficult to interpret in black and white. The full colour images can be found in the on-line version, at http://dx.doi.org/10.1016/j.actbio.2014.09.050.

3.10. References

1. Hoffman AS. Stimuli-responsive polymers: biomedical applications and challenges for clinical translation. Adv Drug Deliv Rev 2012;65:10–6

2. Li Z, Zhang Z, Liu KL, Ni X, Li J. Biodegradable hyperbranched amphiphilic

polyurethane multiblock copolymers consisting of poly (propylene glycol), poly (ethylene glycol), and polycaprolactone as in situ thermogels. Biomacromolecules 2012;13:3977–89

3. Ruel-Gariepy E, Leroux J-C. In situ-forming hydrogels – review of temperature-sensitive systems. Eur J Pharm Biopharm 2004;58:409–26

4. Rathi RC, Zentner GM. Biodegradable low molecular weight triblock poly (lactide-co-glycolide) polyethylene glycol copolymers having reverse thermal gelation properties. U.S. Patent No. 6,004,573, 21 December 1999

5. Shim MS, Lee HT, Shim WS, Park I, Lee H, Chang T, et al. Poly (D, L-lactic acid- co-glycolic acid)-b-poly (ethylene glycol)-b-poly (D, L-lactic acid-co-glycolic acid) triblock copolymer and thermoreversible phase transition in water. J Biomed Mater Res 2002;61:188–96

6. Loh XJ, Li J. Biodegradable thermosensitive copolymer hydrogels for drug delivery. Expert Opin 2007;17:3977–89

7. Zentner GM, Rathi R, Shih C, McRea JC, Seo M-H, Oh H, et al. Biodegradable block copolymers for delivery of proteins and water-insoluble drugs. J Control Release 2001;72:203–15

8. Yin HB, Gong CY, Shi S, Liu XY, Wei YQ, Qian ZY. Toxicity evaluation of biodegradable and thermosensitive PEG-PCL-PEG hydrogel as a potential in

situ sustained ophthalmic drug delivery system. J Biomed Mater Res B Appl Biomater 2010;92:129–37

9. Gong C, Shi S, Dong P, Kan B, Gou M, Wang X, et al. Synthesis and characterization of PEG-PCL-PEG thermosensitive hydrogel. Int J Pharm 2009;365:89–99

10. Ni PY, Fan M, Qian ZY, Luo JC, Gong CY, Fu SZ, et al. Synthesis and characterization of injectable, thermosensitive, and biocompatible acellular bone matrix/poly (ethylene glycol)-poly (ε-caprolactone)-poly (ethylene glycol) hydrogel composite. J Biomed Mater Res, Part A 2012;100:171–9

11. Jiang ZQ, Deng XM, Hao JY. Novel thermogelling poly (ε -caprolactone-co-lactide)-poly (ethylene glycol)-poly (ε -caprolactone-co-lactide) aqueous solutions. Chin Chem Lett 2007;18:747–9

12. Bae SJ, Joo MK, Jeong Y, Kim SW, Lee W-K, Sohn YS, et al. Gelation behavior of poly (ethylene glycol) and polycaprolactone triblock and multiblock copolymer aqueous solutions. Macromolecules 2006;39:4873–9

13. Bae SJ, Suh JM, Sohn YS, Bae YH, Kim SW, Jeong B. Thermogelling poly (caprolactone-b-ethylene glycol-b-caprolactone) aqueous solutions. Macromolecules 2005;38:5260–5

14. Gong C, Shi S, Wu L, Gou M, Yin Q, Guo Q, et al. Biodegradable in situ gel-forming controlled drug delivery system based on thermosensitive PCL-PEG-PCL hydrogel. Part 2: sol-gel-sol transition and drug delivery behavior. Acta Biomater 2009;5:3358–70

15. Mahmud A, Xiong XB, Lavasanifar A. Novel self-associating poly (ethylene oxide)-block-poly (ε -caprolactone) block copolymers with functional side groups on the polyester block for drug delivery. Macromolecules 2006;39:9419–28

16. Safaei Nikouei N, Lavasanifar A. Characterization of the thermo- and pH-responsive assembly of triblock copolymers based on poly(ethylene glycol) and functionalized poly(ε -caprolactone). Acta Biomater 2011;7:3708–18

17. Brash JL. Exploiting the current paradigm of blood material interactions for the rational design of blood-compatible materials. J Biomater Sci Polym Ed 2000;11:1135–46

18. Loh XJ, Tan YX, Li Z, Teo LS, Goh SH, Li J. Biodegradable thermogelling poly(ester urethane) s consisting of poly (lactic acid) – thermodynamics of micellization and hydrolytic degradation. Biomaterials 2008;29:2164–72

19. Bahniuk MS, Pirayesh H, Singh HD, Nychka JA, Unsworth LD. Bioactive glass 45S5 powders: effect of synthesis route and resultant surface chemistry and

crystallinity on protein adsorption from human plasma. Biointerphases 2012;7:1–15

20. Abraham S, So A, Unsworth LD. Poly(carboxybetaine methacrylamide)-modified nanoparticles: a model system for studying the effect of chain chemistry on film properties, adsorbed protein conformation, and clot formation kinetics. Biomacromolecules 2011;12:3567–80

21. Cheng Y, He C, Ding J, Xiao C, Zhuang X, Chen X. Thermosensitive hydrogels based on polypeptides for localized and sustained delivery of anticancer drugs. Biomaterials 2013;34(38):10338–47

22. Hou Y, Matthews AR, Smitherman AM, Bulick AS, Hahn MS, Hou H, et al. Thermoresponsive nanocomposite hydrogels with cell-releasing behavior. Biomaterials 2008;29:3175–84

23. Liu YY, Shao YH, Lu J. Preparation, properties and controlled release behaviors of pH-induced thermosensitive amphiphilic gels. Biomaterials 2006;27:4016–24

24. Wang Q, Li L, Jiang S. Effects of a PPO-PEO-PPO triblock copolymer on micellization and gelation of a PEO-PPO-PEO triblock copolymer in aqueous solution. Langmuir 2005;21:9068–75

25. Sivaraman B, Latour RA. The adherence of platelets to adsorbed albumin by

receptor-mediated recognition of binding sites exposed by adsorption-induced unfolding. Biomaterials 2010;31:1036–44

26. Takeuchi Y, Tsujimoto T, Uyama H. Thermogelation of amphiphilic poly (asparagine) derivatives. Polym Adv Technol 2011;22:620–6

27. Wojciechowski P, Ten Hove P, Brash JL. Phenomenology and mechanism of the transient adsorption of fibrinogen from plasma (Vroman effect). J Colloid Interface Sci 1986;111:455–65

28. Molina H. Complement and immunity. Rheum Dis Clin North Am 2004;30:1–18

29. Tang L, Liu L, Elwing HB. Complement activation and inflammation triggered by model biomaterial surfaces. J Biomed Mater Res 1998;41:333–40

30. Unsworth LD, Sheardown H, Brash JL. Polyethylene oxide surfaces of variable chain density by chemisorption of PEO-thiol on gold: adsorption of proteins from plasma studied by radiolabelling and immunoblotting. Biomaterials 2005;26:5927–33

31. Gettins PGW. Serpin structure, mechanism, and function. Chem Rev 2002;102:4751–804

32. Moos T, Morgan EH. Transferrin and transferrin receptor function in brain barrier systems. Cell Mol Neurobiol 2000;20:77–95

33. Stafford JL, Belosevic M. Transferrin and the innate immune response of fish: identification of a novel mechanism of macrophage activation. Dev Comp Immunol 2003;27:539–54

34. Mosesson MW. Fibrinogen and fibrin structure and functions. J Thromb Hemost 2005;3:1894–904

35. Massa TM, Yang ML, Ho JYC, Brash JL, Santerre JP. Fibrinogen surface distribution correlates to platelet adhesion pattern on fluorinated surface-modified polyetherurethane. Biomaterials 2005;26:7367–76

36. Tang L, Eaton JW. Natural responses to unnatural materials: a molecular mechanism for foreign body reactions. Mol Med 1999;5:351

37. El-Ghannam A, Ducheyne P. Shapiro, I.M. Effect of serum proteins on osteoblast adhesion to surface-modified bioactive glass and hydroxyapatite. J Orthop Res 1999;17:340–5

4. Bioactive Glass 45S5 Powders: Effect of Synthesis Route and Resultant Surface Chemistry and Crystallinity on Protein Adsorption from Human Plasma

Published as "Bahniuk MS, Pirayesh H, Singh HD, Nychka JA, Unsworth LD. Bioactive glass 45S5 powders: effect of synthesis route and resultant surface chemistry and crystallinity on protein adsorption from human plasma. Biointerphases. 2012 Dec 1;7(1-4):1-5."

4.1. Abstract

Despite its medical applications, the mechanisms responsible for the osseointegration of bioactive glass (45S5) have yet to be fully understood. Evidence suggests that the strongest predictor for osseointegration of bioactive glasses, and ceramics, with bone tissue as the formation of an apatitic calcium phosphate layer atop the implanted material, with osteoblasts being the main mediator for new bone formation. Most have tried to understand the formation of this apatitic calcium phosphate layer, and other bioresponses between the host and bioactive glass 45S5 using Simulated Body Fluid; a solution containing ion concentrations similar to that found in human plasma without the presence of proteins. However, it is likely that cell attachment is probably largely mediated via the adsorbed protein layer. Plasma protein adsorption at the tissue bioactive glass interface has been largely overlooked. Herein, we compare crystalline and amorphous bioactive glass 45S5, in both melt-derived as well as sol–gel forms. Thus, allowing for a detailed understanding of both the role of crystallinity and powder morphology on surface ions, and plasma protein adsorption. It was found that sol–gel 45S5 powders, regardless of crystallinity, adsorbed 3–5 times as much protein as the crystalline melt-derived counterpart, as well as a greater variety of plasma proteins. The devitrification of melt-cast 45S5 resulted in only small differences in the amount and variety of the adsorbed proteome. Surface properties, and not material crystallinity, play a role in directing protein

adsorption phenomena for bioactive glasses given the differences found between crystalline melt-cast 45S5 and sol–gel derived 45S5.

4.2. Introduction

Bioactive glasses, specifically ceramic Bioglass® formulation 45S5 (45 %SiO_2, 24.5 %Na_2O, 24.5 %CaO, and 6 % P_2O_5 by weight), have garnered serious attention as a functional biomaterial due to its ability to integrate with bone. Previous work has shown that bioactive glass 45S5 can be inserted into areas of large scale bone damage to help augment its repair, while providing structural support by binding strongly to endogenous bone (1-3). This material is capable of interacting with the surrounding tissue milieu, and has been shown to serve as a substrate on which osteogenic stem cells can attach and differentiate (2-8). Moreover, bioactive glasses have been used for several clinical applications, such as ossicular implantation for alleviating conductive hearing loss, as dental implants for maintaining the endosseous ridge before dentures are fitted, and as a particulate for augmenting the natural repair process in patients with periodontal disease (9). Besides improving the mechanical properties of the final material, leading to its application to a broader range of clinical applications, inducing crystallinity in bioactive glasses may affect the mineral formation rate and bone integration at the tissue-material interface (10-12). Nonetheless, clear evidence implicates the strongest predictor for osseointegration of bioactive glasses and ceramics with bone tissue as the formation of an apatitic calcium phosphate layer

atop the implanted material, as aptly reviewed elsewhere (13). Wherein, strong in vivo evidence suggests that osteoblasts, in the presence of an apatitic calcium phosphate layer, attach and proliferate to form new bone. Most work in the field has tried to model the interaction between the host and bioactive glass 45S5 using Simulated Body Fluid (SBF) rather than in vivo testing. Kokubo and Takadama posit that a particular concentration of ions in a simulated body fluid (SBF, with ion concentrations similar to those found in human plasma) may be useful in predicting in vivo bone formation if an apatitic calcium phosphate layer forms on the surface of the bioactive glass after immersion in the SBF (13). The situation is of course more complicated: cells may not directly attach to these surfaces, rather cell attachment may largely be mediated via adsorbed proteins, and SBF contains no proteins. It appears that the adsorption of proteins at the tissue bioactive glass interface has been largely overlooked regarding proxy tests for in vivo animal implantation and histology.

The crystallinity and the manufacturing method of 45S5 are thought to have significant effects on this material (11, 12). Many studies have investigated the effect of devitrifying bioactive glasses, to move from an amorphous to ceramic glass (crystalline or semi-crystalline), so as to optimize the required parameters of bioactive materials for application in the medical industry: with a special emphasis on bone growth (14-16). Bioactive glass 45S5 transforms to a glass ceramic with crystalline phase $Na_2Ca_2Si_3O_9$ (combeite) by heating the material at 700 °C for more than 0.5 h (17, 18). Crystallization of the bioactive glass results in improved mechanical properties and allows for powder sintering.

Despite these benefits, glass ceramics (crystalline or semi-crystalline) can show less solubility in body fluid and, thus, may dramatically affect the protein adsorption profile. Various mechanisms for such in vitro and in vivo behavioural differences have been proposed. A common argument is that the phosphorous concentration and distribution changes upon crystallization of a glass, and thus the phosphorous dissolution profile changes, which ultimately affects the time to form a mineral phase suitable for tissue integration (i.e., hydroxycarbonate apatite, HCA). For example, crystalline ceramics of the same starting composition require three times as much time to form HCA compared to amorphous counterparts (12). Such a time limitation to form HCA for crystalline ceramics can be overcome by increasing the surface area of the material by using an alternate manufacturing method (19) in order to change the "texture" of the ceramic (20). As opposed to the dense surface structure created via traditional melt casting methods, the sol–gel method is a widely used production technique that yields a highly porous material structure, which could lead to higher apparent dissolution rates (higher surface area to volume ratio) (21).

The interactions of bioactive glass ceramics with the host environment have been characterized using either SBF or cell studies. SBF is an acellular solution designed to mimic the ionic concentrations of various elements found in human plasma including Na^+, Mg^{2+}, Ca^{2+}, Cl^-, HCO_3^- and HPO_4^{2-} (22). However, it lacks other plasma components such as dissolved nutrients, vitamins, triglycerides, cholesterols and proteins. This omission may be why cell studies with bioactive glasses show results ranging from enhancement of bone repair to

inhibition of the same process (23-27). While proteins make up less than 10 % of human plasma, their effects on host response can outweigh any effect elicited by a change in ion concentration. The adsorption of a protein layer to a biomaterial surface takes mere seconds, but this adsorbed layer directs any host responses such as platelet activation, coagulation, complement and immune responses as well as any interactions between cells and the biomaterial (28).

It has been shown in the literature that the presence of proteins can affect 45S5 bioactive glass reactions yet the interactions of plasma proteins with 45S5 bioactive glass have not been studied in depth. Most studies make use of either single or double protein solutions or do not attempt to identify which proteins adsorb to the bioactive glass surface (23, 29, 30). Understanding the complex adsorption phenomena and their effects on host response is critical to our understanding of all bioactive glasses, including 45S5. To this end, this study will examine the adsorption of proteins from platelet-poor human plasma to most accurately simulate the adsorption effects seen when the bioactive glass is used in medical applications. Furthermore, immunoblots will be used to reliably identify the types of proteins found eluted off of the surfaces down to picomolar concentrations. The consequences of changes in bioactive glass formulations as well as any underlying crystalline domains may alter plasma protein adsorption and also need to be understood. This knowledge is important not only for the development of bioactive glasses, but because of 45S5's clinical successes, the plasma adsorption information can be used in the development of a generalized model of plasma protein adsorption to all biomaterial surfaces.

In this study a comparison of the protein absorption from human blood plasma to melt-cast 45S5 (amorphous and crystalline), with gel-derived 45S5 (crystalline), has been carried out. It was found that the gel-derived glass had about twice the specific surface area (using BET-N_2 adsorption techniques) of the cast samples due to the submicron porosity demonstrated by SEM. XPS analysis showed there was a difference in surface compositions between the amorphous and crystalline samples but the surface charges for each sample were all around −15 mV. The sol–gel bioactive glass eluted 3–5 times more protein than the cast samples and also showed a greater variety of plasma proteins in the adsorbed proteome. It appears that the atomic surface composition of the materials has a greater effect on protein adsorption than net charge, as well as material crystallinity.

4.3. Materials and Methods

4.3.1. Materials

Bioactive glass 45S5 prepared by two separate manufacturing routes (melt and sol–gel derived) was used in this study. Melt-derived bioactive glass 45S5 powder (<20 μm) was furnished by Mo-Sci Corporation (Missouri, USA). Two versions of melt-derived 45S5 were used: amorphous (as received) and crystalline (devitrified). Crystalline 45S5 was prepared by heat treating amorphous glass powder at 720 °C for 20 min which resulted in 100 % crystalline 45S5.

Sol–gel derived glasses were prepared according to the following procedure to prepare 20 g of powder. 3.26 mL of 69 % nitric acid was added to 47.6 mL of water to create a 1 M nitric acid solution. 0.15 mol (33.5 mL) tetraethylorthosilicate (TEOS, Sigma Aldrich, US) was added to the 1 M nitric acid for a final H_2O: TEOS molar ratio equal to 18. The precursor hydrolysis was performed for 60 min with stirring. The following reagents were allowed to react for 45 min during stirring in the following sequence: 0.017 mol (2.9 mL) triethylphosphate (TEP, Sigma Aldrich, US), 0.085 mol (20.13 g) calcium nitrate tetrahydrate (Sigma Aldrich, US), and 0.16 mol (13.52 g) sodium nitrate (Sigma Aldrich, US). The prepared transparent solution was stored in a sealed Teflon container for 5 days at ambient temperature to allow gel formation. The gel was aged for 24 h at 70 °C then dried at 120 °C for 24 h. Finally the dried sample was stabilized in a high alumina crucible at 700 °C using a benchtop muffle furnace (Thermo scientific, F48055-60) for 24 h to remove residual nitrates. The prepared powder was ground using a planetary ball-mill at 500 rpm for 10 min with a spherical zirconia media (2 mm dia.) in ethanol to reduce the particle size to 5–15 μm in order to be comparable to that of the melt-cast powders. Measurement of particle size was carried out by photon correlation spectroscopy (31). The average median diameter of melt cast and gel-derived powders were 8.0 and 11.8 μm, respectively.

4.3.2. Surface Area Measurement

The surface areas of the powders were measured using a Quantochrome Autosorb MP1 (Florida, USA) automatic gas absorption system. The measurements were carried out using nitrogen isotherms at 77 K. The point BET method (0.05, 0.075, 0.1, 0.15, 0.25 and 0.3 mm Hg) was used to analyze data. All the samples were degassed at 200 °C, under vacuum, for 3–4 h prior to the tests. All values returned using the BET method have an associated error of 5 %.

4.3.3. Scanning Electron Microscopy

A JEOL 6301F scanning electron microscope (SEM, Tokyo, Japan) was used to image the morphology of the powder particles. Samples were coated with chromium to achieve the highest conductivity with the least charging (Edwards XE200, Xenosput, Australia). A 5 kV accelerating voltage was also used to minimize charging.

4.3.4. X-ray Diffraction

A Rigaku Rotaflex Diffractometer (Woodlands, TX, USA) was used to carry out X-ray diffraction (XRD) to characterize the powder morphology and identify the presence of crystalline phases after devitrification of bioactive glass. The diffractometer was operated at 40 kV and 110 mA (Cu target) at 2θ range of 10–110° with a step size of 0.02°.

4.3.5. Zeta-Potential Analysis

The electrophoretic mobility of the bioactive glass samples was measured using the Nano-ZS instrument (Malvern Instruments Ltd., UK) at 25 °C in order to determine their surface charges. If necessary, samples were diluted with 1 mM NaCl solution.

4.3.6. X-ray Photoelectron (XPS) Analysis

The XPS measurements were performed using an AXIS 165 spectrometer (Kratos Analytical) at the Alberta Centre for Surface Engineering and Science (University of Alberta). The base pressure in the analytical chamber was lower than 3×10^{-8} Pa. A monochromatic Al K α source ($h\nu = 1486.6$ eV) was used at a power of 210 W. The analysis spot was 400 × 700 μm. The instrument resolution was 0.55 eV for Ag 3d and 0.70 eV for Au 4f peaks. Survey scans were collected for binding energy from 1100 eV to 0 with analyzer pass energy of 160 eV and a step of 0.35 eV. High-resolution spectra pass-energy was 20 eV with steps of 0.1 eV. The number of scans varied from 8 to 60. Electron flooding was applied to compensate for sample charging. The binding energies of all samples were corrected using 284.8 eV for the C1 s peak.

High-resolution Si spectra were modeled using CasaXPS (version 2.3.15, Casa Software Ltd.). The Si model contained two components: one component

representing SiO, where the peak position, but not full-width at half maximum (fwhm), was fixed at a value of 102.7 eV (32). A second component was represented via the addition of another peak; this peak was left unconstrained and was identified using data from the National Institute of Standards and Technology (NIST) X-ray Photoelectron Spectroscopy Database (http://srdata.nist.gov/xps/Default.aspx).

4.3.7. Plasma Adsorption

Platelet poor human plasma was obtained from the Research Division of Canadian Blood Services and stored at −80 °C prior to its use. Bioactive glass materials were added to 0.15 M phosphate buffered saline (PBS). In order to compare protein adsorption results between the various bioactive glass samples, surface area values for each system were characterized using BET analysis (as outlined above). That said, it should be recognized that (esp. for sol–gel samples) BET results for surface area is directly relative to the size of nitrogen and may significantly overestimate how much surface area is accessible to protein for adsorption. 250 μL of each bioactive glass solution were mixed with 1.25 mL human plasma for a final plasma concentration of 83 %. Protein adsorption was conducted at 37 °C for 2 h under rocking agitation. Samples were spun down at 13,000 rpm (VWR galaxy 16DH, Mississauga, ON) for 10 min. Supernatant was replaced with 1 mL 0.15 M PBS, left at room temperature for 30 min so as to remove loosely bound proteins. This wash step was carried out twice.

Adsorbed protein was eluted from the bioactive glass surface by incubating rinsed samples in 2 % w/v sodium dodecyl sulfate (SDS) (J.T. Baker, Phillipsburg NJ) in 0.15 M PBS at 50 °C for 2 h as described in (33). Conditions that yielded consistent and optimal protein removal included looking at temperature variation (room temperature to 50 °C) and solution SDS concentration (2–10 %). The above strategy was found to be optimal (results not shown). Eluent containing removed protein was collected by centrifuging the samples, as described above. Finally, all blood donors were fully informed (according to Canadian Blood Services policy) and samples were pooled to anonymize the donors.

4.3.8. Total Protein Assays

The DC Protein Assay from Bio-Rad (Hercules, CA) was used to determine the concentration of eluted protein from the bioactive glass samples. Recommended manufacturer's protocols were followed. Briefly, bovine serum albumin (BSA) was used to generate standard curves in 2 % SDS and 0.15 M PBS. The BSA control and 100 μL aliquots of each solution of protein eluted from the bioactive glass sample were analyzed using the protein assay kit components, and a DU 730 Life Sciences UV/Vis spectrophotometer (Beckman Coulter, Mississauga, ON) was used to read the absorbances at 740 nm. Each sample was assayed in duplicate.

However, for some samples the total protein values returned from this assay were near the assay's lower limit, questioning their accuracy. Thus, an alternative method was developed based on colloidal gold staining (23), which should have a significantly greater sensitivity to the protein. 3 μL from each bioactive glass sample was pipetted onto a PVDF membrane (0.2 μm, Bio-Rad, Hercules, CA) and allowed to air dry. The same was done with various known quantities of BSA in the same buffer as the samples. The membranes were then processed according to the Colloidal Gold Total Protein Stain instructions (Bio-Rad, Hercules CA). Briefly, the membranes were blocked with 0.3 % Tween 20 in Tris-buffered saline (20 mM Tris and 500 mM NaCl) three times for 20 min each, rinsed with Milli-Q Synthesis purified water (Billerica, MA) 3 times for 2 min each, stained with colloidal gold solution (Bio-Rad, Hercules, CA) for 1 h and finally rinsed again with purified water 3 times for 1 min each. The membranes were then scanned and the stain intensities, less background intensities, quantified using Adobe Photoshop (Version 9, Adobe Systems Inc, San Jose CA USA). This information, coupled with the calibration curve intensities, yielded the total protein per sample.

4.3.9. SDS-PAGE and Western Blotting

As described previously (34), 30 μg of total eluted protein from each bioactive glass sample was analyzed using reducing SDS polyacrylamide gel electrophoresis (SDS-PAGE) and Western blotting techniques. Briefly, protein

samples were reduced and denatured by the addition of sample buffer which, when diluted, contained 0.5 M β-mercaptoethanol and 2 % SDS. The sample and sample buffer mixtures were then heated at 95 °C for 5 min before being run on 12 % SDS polyacrylamide gels at 200 V and 400 mA. Proteins were transferred from these gels to 0.2 μm Immuno-Blot PVDF membrane (Bio-Rad, Hercules, CA) for 1 h at 100 V, 200 mA. All consumables and equipment were purchased from Bio-Rad (Hercules, CA). The membranes were then divided into strips for colloidal gold staining or Western blotting. Table 4.1 lists the primary and secondary antibodies used for Western analysis. The antibodies were used without further purification at concentrations of 1:1000. 350 μL of stabilized TMB substrate (Promega, Madison, WI) was used to visualize all protein-antibody complexes. The colour developing reactions were allowed to progress until precipitation of the coloured compound was observed (20 min for cast amorphous and cast crystalline and 10 min for sol–gel). The reaction was then quenched for 10 min with 2 mL of water from a MilliQ Synthesis water purification system (Billerica, MA).

Antibody	Plasma protein MW (kDa)	Plasma protein pI	Host	Source
Kininogen (light chain)	50	6.6	Mouse	US Biological, Swampscott, MA, USA
Kininogen (heavy chain)	88–120	6.8	Mouse	US Biological, Swampscott, MA, USA
Factor I	88	7.6	Mouse	Cedarlane Laboratories, Hornby, ON, CAN
Fibrinogen	340	6.6	Rabbit	Calbiochem, Gibbstown, NJ, USA
Fibronectin	440	5.7	Rabbit	Cedarlane Laboratories, Hornby, ON, CAN
Hemoglobin	68	8.0	Rabbit	Sigma-Aldrich, St. Louis, MO, USA
α_1-Antitrypsin	47	5.6	Sheep	Cedarlane Laboratories, Hornby, ON, CAN
Thrombin	36	5.4	Sheep	Cedarlane Laboratories, ON, CAN
Prothrombin	72	5.9	Sheep	Cedarlane Laboratories, ON, CAN
Protein C	62	6.3	Sheep	Cedarlane Laboratories, ON, CAN
Vitronectin	75	5.8	Sheep	Cedarlane Laboratories, ON, CAN
Protein S	69	5.7	Sheep	Cedarlane Laboratories, ON, CAN
Prekallikrein	85	8.2	Sheep	Cedarlane Laboratories, ON, CAN
Antithrombin	53	6.7	Sheep	Cedarlane Laboratories, ON, CAN
IgG	174	8.4	Goat	Sigma-Aldrich, St. Louis, MO, USA
Human albumin	66	6.8	Goat	OEM Concepts, Saco, ME, USA
Plasminogen	90	7.3	Goat	Cedarlane Laboratories, ON, CAN
Complement factor 3 (C3)	185	6.4	Goat	Calbiochem, Gibbstown, NJ, USA
Factor XII	80	7.7	Goat	Cedarlane Laboratories, ON, CAN
Factor XI	160	8.1	Goat	Cedarlane Laboratories, ON, CAN
Apolipoprotein A1	28	7.1	Goat	Sigma-Aldrich, St. Louis, MO, USA
Transferrin	77	7.1	Goat	Sigma-Aldrich, St. Louis, MO, USA
α_2-Macroglobulin	718	6.4	Goat	Sigma-Aldrich, St. Louis, MO, USA

Table 4.1. Primary antibodies used for immunoblotting of plasma proteins adsorbed to bioactive glass as well as plasma protein physical characteristics

4.4. Results

4.4.1. Surface Area

Surface area measurements were performed on both the melt-cast and sol–gel derived bioactive glasses in order to determine if the surface areas per gram changed as a function of the manufacturing method. It was found that the melt-cast bioactive glass had a surface area of 5.9 m^2/g and the sol–gel has a surface area of 11.1 m^2/g (95 % reproducibility limit). That is to say, using the sol–gel manufacturing method increased the surface area of the bioactive glass by about a factor of 2. For the purposes of this experiment it was assumed that devitrification

of melt-cast bioglass should not significantly change the surface area of the material, relative to the factor of two change in surface area realized for severe morphological differences that exist between the sol–gel and melt-cast derived materials.

4.4.2. SEM

The morphologies of the bioactive glasses are illustrated in Fig. 4.1. Gel-derived 45S5 powder appears as agglomerates of fine sub-micron particles and exhibits submicron porosity (Fig. 4.1a). This leads to a higher surface area for the gel-derived 45S5 compared to the other powders as shown with the surface area results. Melt-cast samples show similar particle morphology in either amorphous or crystalline states (Fig. 4.1b, c), with crystalline powder having slightly smoother surfaces and edges due to glass softening at relatively high temperatures.

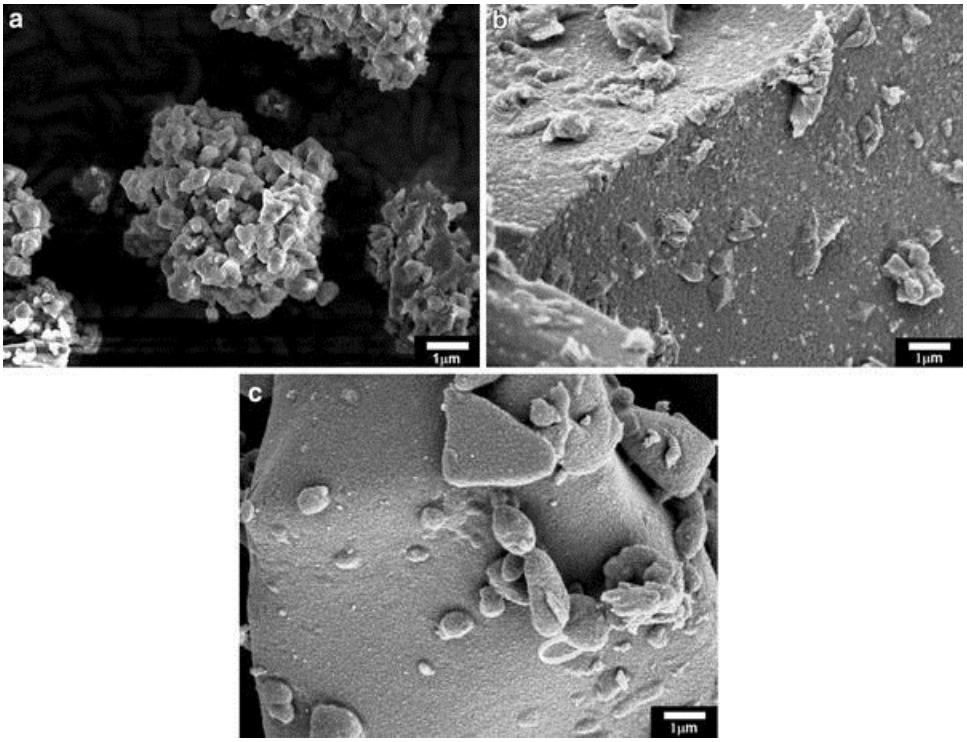

Figure 4.1. Secondary electron SEM micrographs of (a) crystalline gel-derived 45S5, (b) amorphous melt-cast 45S5, and (c) crystalline (devitrified) melt-cast 45S5. Notice the agglomerated particles in the gel-derived specimen (a) which gives rise to submicron porosity, whereas the melt-cast glasses in (b) and (c) have much smoother surfaces. Upon heat treatment to change from state (b) to (c) the glass devitrifies and the sharp angular fractured surfaces smoothen slightly due to glass softening at 720 °C

4.4.3. XRD

X-ray diffraction patterns are shown in Fig. 4.2. As expected, no sharp peaks were detected on the amorphous 45S5 given its structure; confirmed by the presence of a broad peak at ~32° 2θ. The XRD patterns of the crystalline samples matched that of combeite—a crystalline sodium-calcium-silicate phase ($Na_2Ca_2Si_3O_9$, PDF#075-1687) commonly formed upon devitrification of 45S5 bioactive glass.

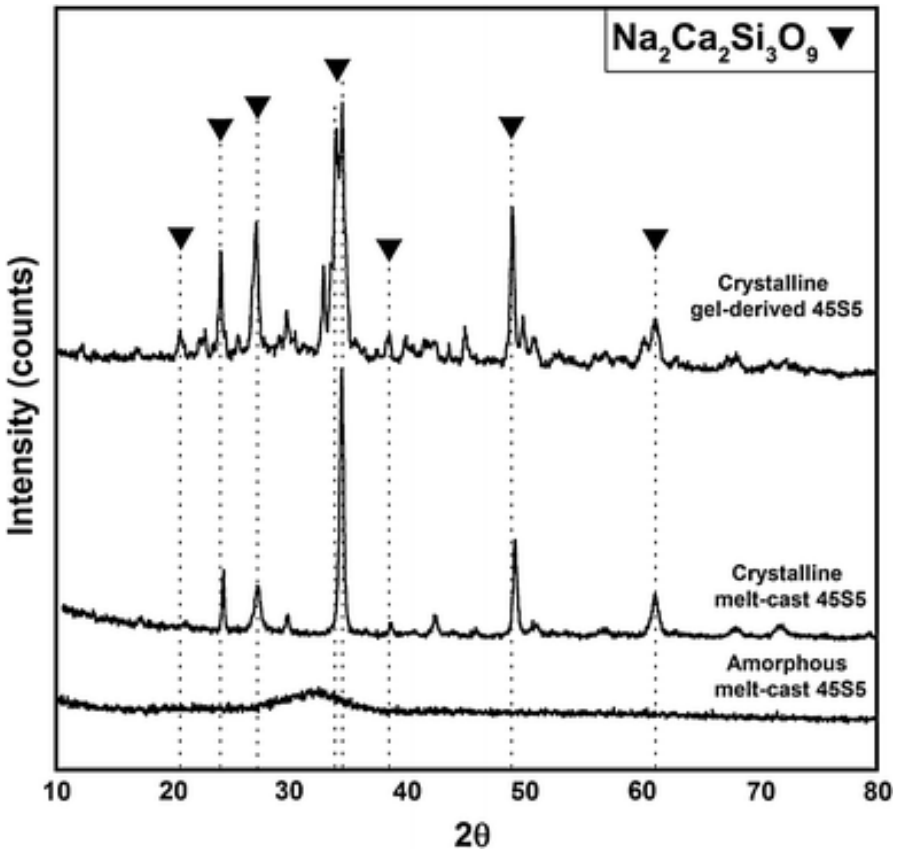

Figure 4.2. XRD patterns of melt-cast and gel-derived 45S5 powders. The as cast melt-cast glass is amorphous (showing a broad bump at ~32° 2θ and no sharp peaks corresponding to crystallographic planes). When the cast glass is intentionally crystallized the peaks that are observed match those of combeite ($Na_2Ca_2Si_3O_9$), the same phase which is observed after gel-derived 45S5 is thermally stabilized and crystallized

4.4.4. Surface Charge

Zeta potential measurements were conducted on pristine samples to determine the surface charges of the various bioactive glass materials (Table 2). It was observed that all of these materials, regardless of crystallinity or manufacturing conditions,

exhibited similar surface charges ranging from −14 to −17 mV. A Student's *t* test for significance showed that these systems were not statistically different although cast crystalline sample appears to have a difference in surface charge compared to the sol–gel and cast amorphous.

System	Surface charge (mV)
Sol–gel	−14.3 ± 3.5
Cast amorphous	−14.8 ± 2.9
Cast crystalline	−17.1 ± 1.5

Table 4.2. Surface charges of bioactive glass constructs before incubation with human plasma (n = 3). Data represent mean ± 1 SD.

4.4.5. Surface Properties: X-ray Photoelectron Spectroscopy (XPS) Results

XPS was performed on all systems, both prior to and after incubation in platelet poor human plasma (Table 3). Pristine bioactive glass samples showed high levels of carbonaceous contamination, a situation that has previously been reported in the literature for similar systems (35). The ill-defined layer of contaminating carbon ultimately decreases the atomic percentages of all the other elements, a trend observed for all pristine samples when compared to the theoretical composition. It has been previously shown that carbonaceous contamination may contain oxygen as well, so in order to better understand the

bioactive glass surface, the atomic percentages of both carbon and oxygen were removed and the remaining values normalized (Table 4).

System	Na	O	Ca	P	Si	N	C	S
Theoretical (atomic %)	*17.3*	*55.2*	*9.5*	*1.8*	*16.3*			
Before solution incubation								
Sol–gel	9.5	45.7	3.2	0.5	10.7		30.1	
Cast amorphous	8.9	40.9	2.7	1.3	6.1		39.8	
Cast crystalline	7.8	49.1	4.8	0.5	12.3		25.3	
After solution incubation								
Sol–gel	4.5	46.9	7.7	3.6	7.0		29.1	1.1
Cast amorphous	10.7	34.2	2.9	0.8	2.1	1.4	46.6	1.4
Cast crystalline	6.8	53.8	8.9	4.7	8.0		17.3	

Table 4.3. Summary of the atomic percentages of bioactive glass systems before and after incubation with human plasma. Values are accurate to less than ±10 %.

System	Na	Ca	P	Si	N	S
Theoretical (atomic %)	*38.5*	*21.2*	*3.9*	*36.4*		
Before solution incubation						
Sol–gel	39.7	13.5	2.1	44.7		
Cast amorphous	46.8	14.2	6.8	32.2		
Cast crystalline	30.6	18.8	2.0	48.6		
After solution incubation						
Sol–gel	18.8	32.0	15.0	29.1		4.7
Cast amorphous	55.5	15.0	4.1	10.9	7.3	7.2
Cast crystalline	23.5	30.8	16.1	27.8		

Table 4.4. Summary of the atomic percentages of various bioactive glass systems before and after incubation with human plasma after removing C and O values and normalizing. Values are accurate to less than ±10 %.

High resolution XPS for both Si and P were analyzed. However, the variety of binding energies present for P made it impossible to independently determine its binding environment. A similar issue existed for Si, whereby a plethora of SiOx binding energies have been reported in the literature (ranging from 99.3 to 103.6 eV) (36). However, the binding energy for SiO was 102.0 eV specifically. Therefore, elucidation of the Si (2p) binding energies was possible; one peak was constrained to represent SiO and a second peak was used to represent the general SiOx binding energies (Table 5). Complimentary to this, a minimum number of peaks were used to fit the high resolution Si data; the reduction of the degrees of freedom in the model, while returning similar fits, being thought to be the most accurate means of modeling this data. Using this strategy for peak fitting of the high resolution Si data, it was observed that all pristine bioactive glass surfaces had virtually no SiO present. The entire Si (2p) peak could be fit using binding energies relative to SiOx. This might be expected, as it has been discussed in the literature that SiO may be formed only transiently during the early stages of biomineralization (37). After incubation in plasma both the cast crystalline and sol–gel samples did show some SiO on their surfaces. The presence of SiO on these surfaces but not on the amorphous bioglass suggests that the crystalline samples undergo biomineralization at a slower rate than the amorphous bioactive glass. This increase in reaction time of crystallized bioactive glass is consistent with the literature (10-12).

Sample ID	% SiO (102.0 eV)	SiO curve FWHM	% SiO_x	SiO_x position (eV)	SiO_x curve FWHM	Possible chemistry	SiO_x references
Before plasma incubation							
Sol–gel	0	0	100	99.8	1.8	Si	[38]
Cast amorphous	0	0	100	99.8	2.0	SiO_x/Si	[38]
Cast crystalline	0	0	100	100.9	3.0	SiO_x	[39]
After plasma incubation							
Sol–gel	5.5	1.7	94.5	100.2	1.9	SiO_x	[39]
Cast amorphous	0	0	100	100.7	2.1	SiO_x	[39]
Cast crystalline	25.4	3.1	74.6	100.5	2.0	SiO_x	[39]

Table 4.5. Summary of high resolution modeling of Si (2p) for bioactive glass samples before and after incubation in plasma. Values are accurate to less than ±10 %.

4.4.6. Protein Adsorption: Amount Adsorbed

Bioactive glass samples were incubated with platelet-poor human plasma for 2 h at 37 °C and any loosely bound proteins were removed by washing twice with PBS. Rinsed bioactive 45S5 powders were incubated in SDS solutions (final 2 % concentration) and eluents were analyzed for total protein concentration. From the XPS results summarized in Table 4.3, after incubation in plasma, multiple buffer rinses and the SDS elution step, it was evident that there were only trace amounts of residual N and S on some of the samples.

The total amount of plasma proteins adsorbed to the various bioactive glass systems were determined using two independent methods: the common DC protein assay and an in-house nanogold based assay. DC and nanogold protein assay results are summarized in Table 4.6 and Table 4.7, respectively. The nanogold assay was specifically developed to utilize the nanogram sensitivity that Au nanoparticles exhibit for protein, facilitating the quantification of low concentration protein solutions. It is well known that although the DC assay

overcomes the issues associated with the presence of SDS in a protein solution, protein concentrations below ~0.2 mg/mL (2 % SDS) cannot be accurately detected. Although complicated strategies can be employed for concentrating the protein in solution, a more direct and convenient methodology for directly measuring protein concentration has been employed (23). Herein, this nanogold assay was shown to be appropriate for quantifying the amount of protein in a concentration range almost five times less that of the minimum detectable concentration of the DC assay, viz., ~0.04 mg/mL.

System	Concentration of eluted protein (μg/μL)	Eluted protein per Surface area (mg/m^2)
Cast amorphous	0.157 ± 0.004	0.53 ± 0.01
Cast crystalline	0.169 ± 0.01	0.57 ± 0.03
Sol–gel	0.082 ± 0.005	2.46 ± 0.2

Table 4.6. Protein adsorbed amounts determined using the DC protein assay. Values represent average ± 1 SD (n = 3).

System	Concentration of eluted protein (μg/μL)	Eluted protein per surface area (mg/m^2)
Cast amorphous	0.140 ± 0.007	0.47 ± 0.02
Cast crystalline	0.151 ± 0.007	0.51 ± 0.02
Sol–gel	0.045 ± 0.007	1.35 ± 0.2

Table 4.7. Protein adsorbed amounts determined using nanogold colourimetric assay. Values represent average ± 1 SD (n = 3).

4.4.7. Protein Adsorption: Adsorbed Proteome

Eluted protein solutions from the various bioactive glass samples were subject to SDS-PAGE and immunoblotting analysis in order to identify the composition of the adsorbed protein layer. In order to facilitate the comparison of band intensities between different systems, a constant quantity of protein (30 μg), as well as constant times for all colour development steps, were used for all systems. This also removes any specific surface area variations when comparing samples. By keeping these conditions constant between samples it is possible to compare the intensities of the immunoblot bands between samples, for the same protein, to determine the relative amount of each protein that was eluted from the bioactive glass surfaces. Table 4.7 summarizes the band intensity data for all samples. A 13 step grayscale was used to quantify the band intensity. The number 12 indicate a fully black band, or the highest intensity band, and lower numbers mean decreased band intensity. A value of zero indicates no band was present. Moreover, it is not possible to compare between band intensities of different proteins, as each protein may 'label' differently. Thus, only comparisons can be drawn between the intensities of like proteins. It should also be highlighted that although these techniques can detail the composition of the adsorbed protein layer, they do not provide insight into the *conformation* of the adsorbed proteins themselves. Recently, it has been shown that it is not only the adsorbed protein content, but also the conformation of the adsorbed proteins that can facilitate further cellular interactions (40).

The results of the SDS-PAGE of the eluted plasma proteins for each bioactive glass sample seemed quite similar (results not shown). Each of the samples yielded a very intense band at ~66 kDa and a moderately intense band at ~50 kDa. These bands are thought to be at least partially made up of albumin and alpha$_1$ antitrypsin, respectively. A band at ~25 kDa was also visible for each sample, being most intense for the sol–gel system, then the cast amorphous and least for the cast crystalline systems. Faint banding was also visible at ~35 kDa. In general though, the degree of banding and their intensities in the SDS-PAGE results imply that there were comparable varieties of protein found eluted off of each of the three bioactive glass samples.

4.5. Discussion

4.5.1. Surface Area

Surface area measurements indicate twice the surface area per unit mass of powder for sol–gel derived powders compared to melt-cast powders. Based on the manufacturing route, a higher surface area for sol–gels, as their structure is built through condensation of Si–O bonds, leaving behind precursor chemicals which then evaporate leaving pores. The higher specific surface area values for sol–gel powders indicates that the surfaces of such powders should be more tortuous, or more porous than their cast counterparts, which is indeed what was observed in microscopy.

4.5.2. SEM

SEM confirmed that the powder surface morphology, at least on a micron length scale, was very different between sol–gel and cast powders. The sol–gel powders appear to be agglomerates of submicron particles that have not fully come into contact, thus leaving an internal pore structure on the submicron length scale. The larger melt-cast particles in Fig. 4.1b and c have smaller powder particles stuck to their surfaces, which also generate regions resembling pores.

With respect to the melt-cast amorphous powder, the weak interaction of smaller powder particles to the surface may or may not be stable in solution, so it is not possible to predict if the specific surface area changes upon immersion. The devitrified melt-cast and stabilized sol–gel powders were exposed to relatively high temperatures (close to the softening temperature/point) so it is reasonable to assume that the powders have fused together with sufficient strength to withstand immersion.

The SEM micrographs also indicate that there is as associated surface roughness on all powder particles. The roughness was not quantified, but judging from the micrographs in Fig. 4.1 it is possible to see variations in surface roughness of individual particles between the powders; devitrified melt-cast appears smoother than as cast melt-cast powder, and similar to sol–gel powder. Again the thermal treatments likely play a role in the similarity between

devitrified melt-cast and sol–gel powders. Interpretation of fine scale roughness, or smoothness, is not a simple task, and was not undertaken in this work. However, it should be noted that a smoother looking surface could potentially have higher microporosity than a rougher looking surface at low magnifications—the fine scale surface morphology would need to be quantified in order to make any claims about differences between all the powders studied herein in order to shed light on potential implications for porosity on the length scale relevant for proteome adsorption (i.e., nanometer scale). Nonetheless, based on surface area measurements, with gas molecules small enough to penetrate nanometer scale pores, the differences between the powders do not seem great enough to imply large differences in fine scale microporosity on the surfaces of the powders, hence our limited investigation of small scale surface properties.

4.5.3. XRD

XRD was used to verify the structure of the various powders. The broad peak of the amorphous melt-cast powder indicates that there is no repeating long range order within the glass, and hence there will necessarily be a distribution of bond lengths within the material. For crystalline powders such as devitrified melt-cast powder and sol–gel derived powder the patterns match combeite ($Na_2Ca_2Si_3O_9$), which has a trigonal-trapezohedral class symmetry. A major implication in the formation of combeite crystals in both devitrified powders is that combeite is a calcium sodium silicate and should not contain any

phosphorous. If phosphorous was rejected from the combeite crystals as they grew, then a gradient in phosphorous could be generated between the crystals and their grain boundaries, or the phosphorous could volatilize. Previous work has suggested that some phosphorous is still present in a grain boundary phase with different aqueous solubility (17). XPS analysis suggests that phosphorous content is lower in the crystallized powders (Table 4), which could imply that some of the phosphorous has volatilized, and that some remains in the grain boundary phase. Regardless, the phosphorous effect is likely not significant; similar XRD patterns and surface chemistry (XPS) between crystalline powders does not result in similar protein adsorption profiles, thus the surface morphology, or more subtle variations in surface chemistry may play a more dominant role.

4.5.4. Surface Charge: Zeta Potential

The zeta potential results differ from those reported by El-Ghannam et al. (41) where they show that for cast amorphous 45S5 bioactive glass as little as 5 % crystallization of cast amorphous bioactive glass leads to a statistically significant change in zeta potential. It should be noted that in the study performed by El-Ghannam et al. the bioactive glass particulates were suspended in simulated body fluid, which may alter the surface properties.

4.5.5. Surface Properties: XPS

It is apparent that substantial differences existed between the fractional amount of various elements predicted by the overall atomic composition of the bioactive glass samples and the atomic compositions determined at the surface region using XPS techniques. Theoretically, all bioactive glass samples should have similar surface compositions; however, it was observed that the surface regions had somewhat unique atomic profiles. In general, the pristine sol–gel surface was enriched by ~23 % in Si, compared to the theoretical content, while being depleted by ~36 and 46 % in Ca and P, respectively (Table 4). These are obviously substantial differences in the surface content of the sol–gel materials. The surface of the pristine cast amorphous sample showed an enrichment of ~22 and 74 % in Na and P specifically, while exhibiting a reduction of ~33 % in Ca. Upon crystallization, however, cast crystalline samples were observed to be enriched by ~34 % in Si and reduced by ~20 and 49 % in Na, and P, respectively.

The crystallization of 45S5 bioactive glass seemed to have dramatic effects upon the atomic composition of the surfaces. For example, when comparing the cast amorphous to cast crystalline it is apparent that the levels of Na and Si are almost exactly reversed. The cast crystalline having ~49 % of the surface composed of Si, while the amorphous material exhibiting ~47 % of the surface being Na. Also of interest is the apparent difference in P, where the amorphous layers had more than three times the P than either crystalline material. Moreover, it seems that the surface compositions of the cast crystalline and crystalline sol–gel were somewhat similar: both showed enriched amounts of Si,

and similar amounts of P. The only substantial differences being that the sol–gel surfaces retained more Na and less Ca than the cast crystalline samples. Currently there are very few XPS measurements for the sol–gel derived bioactive glass, making it difficult to compare these results to the literature.

The pristine bioactive glass elemental composition data only somewhat resembles the XPS data for the cast amorphous 45S5 bioactive glass found in the literature (35, 42) most likely due to the differences in the amounts and thicknesses of C and O contamination and their effects on the atomic concentration calculations and the penetrating power of the XPS itself. Chen et al. had C and O levels of 49.6 % and 24.8 % respectively and Mladenovic et al. found C levels of 12.3 % and O levels of 66.05 % on their respective cast amorphous 45S5 bioactive glass. Not only are these values different from those shown in Table 4.3 and from one another, the levels of Na, Ca, P and Si reported in (35, 42) also vary a considerable degree. Chen et al. report atomic concentrations of 0.88, 4.63 and 4.03 % for Na, Ca and P respectively while Mladenovic et al. found their surfaces composed of 16.27, 2.91 and 0.25 % Na, Ca and P.

It is well known that the incubation of bioactive glass samples (amorphous) in various 'physiologically relevant' solutions (i.e., simulated body fluid) leads to the first steps of biomineralization, as aptly reviewed elsewhere (9). From this work, it is also apparent that incubation in platelet-poor human plasma affected the surface composition of each of the bioactive glass samples. Upon comparing the pristine sol–gel with the same samples after incubation in plasma it

is apparent that drastic differences in all atomic concentrations occurred. After incubation the sol–gel surface layers experienced respective reductions of ~52 and 35 % in Na and Si content. Conversely, the sol–gel surfaces experienced drastic increases of ~2 and 7 times for Ca and P content. These changes in surface chemistry correlate with the sequence of events which occur on bioactive glass surfaces during bone bonding (9). The apparent reduction in Na^+ is more accurately described as an exchange of cations with H^+ or H_3O^+ from solution. The decrease in Si is consistent with the loss of soluble SiO_2 species and the large increases in surface Ca and P match the composition of naturally grown apatites and indicate the first step of hydroxyapatite formation (9). Lastly, the presence of S atoms was most likely due to remaining sodium dodecyl sulfate (SDS), which was used as a detergent to strip proteins off of these surfaces. Cast amorphous surfaces, however, did not exhibit a drastic alteration in atomic concentrations. Only moderate changes in Na and decrease in P were observed, most likely within the error of the characterization technique. However, a Si decrease of ~60 % occurred. Again this is consistent with the dissolution of SiO_2 seen in the sol–gel sample but could also indicate that the XPS is not penetrating far enough into the material to reach the Si rich layer as shown in (9). This could be explained by the presence of an N and S signal for these samples, suggesting the presence of protein and the potential presence of SDS. This adsorbed layer of biomolecules could inhibit the signal intensity of the bioactive glass surface atoms. Cast crystalline surface alterations were very similar to those observed for the sol–gel surface, showing drastic increases of ~2 and 7 times the amount of Ca and P,

respectively, and a decrease of ~43 % in Si as well. As with the sol–gel bioactive glass, the decrease in Si may be indicative of the loss of soluble SiO_2 species and the large increases in Ca and P suggest the accumulation of the chemical moieties necessary for hydroxyapatite formation (9). Although not guaranteed, in this case it would seem a complete removal of SDS and protein occurred, as evidenced by the lack of N and S signal. Moreover, it was apparent that the two crystalline materials underwent very similar changes in their surface chemistry and those changes were not consistent with those seen for the cast amorphous bioactive glass.

In order to further understand the state of the surface, it is important to consider the steps of interfacial reactions that are thought to occur in solution after 3 h incubation in platelet poor human plasma. Previous work has detailed the sequence of reactions at the bioactive glass surface (9). Briefly, bioactive glasses first experience dissolution of Na^+ and/or K^+ with H^+ or H_3O^+ in solution. Silanol (SiH_3OH) formation is thought to occur next, in conjunction with the release of soluble SiO_2. These silanol groups undergo further polycondensation, and the material begins to adsorb amorphous phosphates, calcium and carbonate groups from solution. These groups then undergo crystallization to form hydroxyl carbonate apatite. These first steps taking place within the first 2 h of solution incubation for amorphous 45S5 bioactive glass (9). The next step is adsorption of biological moieties to the newly formed hydroxyl carbonate apatite layer. This step is thought to occur as early as the polycondensation of silanol groups and

continues throughout crystallization until the action of macrophages is observed after ~15 h solution incubation.

Upon comparison of the changes in surface composition data of the cast crystalline and sol–gel samples as well as the results of the Si modeling to the same timeline of surface reaction it can be said that the increases in surface Ca and P suggest that the first steps of biomineralization have been completed and the materials were most likely adsorbing amorphous Ca, PO_4 and CO_3 (9). Furthermore, the SiO found on the same surfaces means that both the sol–gel and cast crystalline samples are still undergoing polycondensation of SiOH and adsorption of Ca and P as discussed above. Determining the position of the cast amorphous bioactive glass on the timeline was more difficult in that the XPS data only showed a decrease in Si and increases in S and N after incubation in plasma. The lack of detectable SiO on the surface of the cast amorphous sample could mean that the sample has not undergone any surface biomineralization reactions or that is has moved beyond the polycondensation step. As discussed above, the decrease in Si could be attributed to SiO_2 dissolution or may be a result of changes in the surface profile of the sample as adsorption of hydroxyl carbonyl apatite components occurred. At hour 3 of the interfacial reaction timeline the adsorption of the components of hydroxyl carbonyl apatite has ceased and the crystallization of these components is complete. The primary active process is the adsorption of various biological entities, such as proteins, to the newly formed hydroxyl carbonyl apatite layer. This may be reflected in the results by the presence of N and S, elements indicative of proteins. Furthermore, the similarity

of the Si signals for cast amorphous bioactive glass before and after incubation is consistent with what has been observed the literature (43).

When the positions of the three bioactive glass samples on the interfacial reaction timeline are compared to each other it is clear that this series of experiments demonstrates that all bioactive glass samples have begun biomineralization with the cast amorphous sample progressing at the rate predicted in the timeline for a 3 h incubation and the cast crystalline and sol–gel samples lagging behind. This is consistent with the findings of Filho et al., which state that crystallization of 45S5 bioactive glass slows the rate of surface reactions but does not completely halt them (44).

4.5.6. Protein Adsorption: Amount Adsorbed

When considering the adsorbed amounts calculated, it is imperative that the surfaces areas were determined using B.E.T. gas (N_2) adsorption. Given the probability that surfaces accessible to this gas may not be accessible to proteins, makes it very difficult to accurately determine the amount adsorbed per unity surface area. Nevertheless, this strategy was adopted due to the fact that it is unknown how much of this surface area is accessible to the solvent and available for protein interactions. In general, when near the lower concentration limit of the DC assay (~0.2 mg/mL), both the DC and colloidal gold assays yielded similar concentrations. However, a large difference occurred when attempting to quantify protein concentrations lower than the suggested minimum for the DC assay. The

DC assay showed, for the sol–gel prepared surfaces, a total protein concentration almost twice as large as the nanogold assay technique. It is thought that this difference was largely due to the inaccuracy of the DC assay at this concentration. Nevertheless, it is apparent that the cast amorphous and cast crystalline samples had similar amounts of protein removed from their surfaces and that these values were at least double that of the amount adsorbed to the sol–gel sample before considering the specific surface area of the samples. When the amount of surface area of each sample is taken into account, the relationship is then inverted and the sol–gel bioactive glass eluted more protein per unit mass than the cast samples. These results show that the devitrification of melt-cast 45S5 does not play a significant role in the adsorption of plasma proteins as both the cast amorphous and cast crystalline samples eluted similar quantities of protein. Data in Table 4.3 suggests the elution procedure may not have been 100 % complete as based on the atomic percentages of nitrogen and sulphur. Despite these values being only approximately 1 %, it is probable that they represent both retained protein (N and S) and/or SDS (S) on the material surface. However, due to their low levels and the lack of consistent trend in the C or O amounts, the amount of trace protein left at the powder surface was thought to be minimal.

4.5.7. Protein Adsorption: Adsorbed Proteome

Elucidating the underlying reasons for the presence of different proteins screened for using immunoblot techniques is not a trivial task. The complexity of

the surface, relative to the diversity of the proteins in solution makes it almost impossible to attribute a proteins presence at the interface due to charge differences between the protein and surface only. In reality, proteins adsorbed to the interface may facilitate further protein adsorption. This is compounded further due to the fact that bioactive glass, upon immersion into plasma, has been shown to have a transient interfacial composition. Thus, the best that can be done is to understand the types of proteins present, their relative amounts, and potential influence for the various bioactive glass preparations.

The data in Table 4.8 shows a clear difference in the identities of the proteins adsorbed to either crystalline 45S5 samples. This change in protein profile cannot be attributed to the difference in specific surface area as identical amounts of eluted protein were used in the Western analysis. Furthermore, given the very high sensitivity of the Western blotting technique it is unlikely that any plasma proteins present would not be detected. Thus the only reason for such a large variation in plasma protein adsorption between crystalline 45S5 samples would be their surface compositions, or surface morphology, both of which could affect protein conformation.

Plasma protein	Fragment size (kDa)	Fragment name	System		
			Cast amorphous	Cast crystalline	Sol–gel
Albumin	66		9	12	12
C3	42	Activation	4	0	9
	70	β	8	1	12
	115	α	3	0	12
IgG	27	Light	0	0	4
	55	Heavy	0	0	1
$Alpha_1$ antitrypsin	47		6	1	11
Fibrinogen	48	γ	0	0	0
	56	β	0	0	9
	68	α	0	0	9
	<48	Cleavage	0	0	0
Transferrin	77		0	0	11
Antithrombin	53		0	0	9

Table 4.8. Relative intensities for immunoblots of plasma proteins eluted from all of the bioactive glass systems investigated. 0 indicates zero band intensity. The number 12 indicates the highest intensity band, with lower numbers indicating lower intensity.

After albumin has been denatured and reduced during sample preparation for SDS-PAGE the protein runs as a single band with a molecular weight of 66 kDa. Albumin was found to be in the eluted protein solutions for all samples. Moreover, the band intensities indicated that albumin was present at a similar amount for all samples studied; with the cast amorphous sample potentially adsorbing less than both cast crystalline and sol–gel samples. From this data, it is also apparent that even though there was more protein adsorbed in total to the cast samples, the protein layer present for these systems was largely composed of albumin. In the case of cast crystalline this was the only protein that was observed to be present, and cast amorphous this was one of only two proteins observed: out of the 23 proteins screened. The presence of albumin is somewhat expected due to its high plasma concentration, but it is of particular interest due to the fact that it

has been reported that denatured albumin can lead to platelet adsorption and activation (40). This is particularly important, as activated platelets are commonly used for bone formation strategies (45).

Complement refers to a portion of innate immunity that when activated can cause opsonization, an increased antibody response and lysis of cells (46). As it is a response to foreign bodies and materials, complement activation can have serious consequences for biomaterial effectiveness and overall host health (47). Central to each of the three complement activation pathways is complement Factor 3 (C3) (46). It is composed of α (115 kDa) and β (72 kDa) peptide chains, respectively. If complement is activated and C3 cleaved, a band at 42 kDa becomes apparent (46). Given this, it was apparent that the different surfaces adsorbed varying amounts of C3 and showed differences in activation of the complement pathway. The sol–gel sample showed high levels of all of the C3 fragments, indicating that this surface strongly adsorbed and activated C3; possibly indicating this surface may elicit a strong immune response. The cast amorphous system showed less amounts of adsorbed and activated C3, but more than cast crystalline samples. The cast crystalline sample was found to have almost no detectable C3 on its surface. Only a small amount of the β chain was found. This information may imply that the cast crystalline samples will not strongly activate complement in vivo, while the other two samples may.

Immunoglobulin G (IgG) is an antibody involved in host immune response that, upon binding to an antigen, can cause opsonization and phagocytosis and complement activation via the classical pathway (46). IgG normally runs as two

bands: the heavy chain at 55 kDa and the light chain at 27 kDa. Neither the cast amorphous nor cast crystalline samples appeared to have any IgG on their surfaces. However, this protein was found eluted off of the surface of the sol–gel system. Although IgG was detected, other critical molecular markers for indicating a potential immune response were not observed to be present. For example, the lack of Factor I may indicate that although IgG was present, the classical activation pathway may not be initiated (Table 7). Of course, this does not rule out the possibility of IgG opsonization, and potential phagocytosis or fibrous capsule formation occurring due to the presence of IgG; as previously observed for cast 45S5 bioactive glass systems implanted into the thigh muscles of Sprague–Dawley rats (48).

Alpha$_1$-antitrypsin is considered to be one of the most important serine proteases in the body (49) and is responsible for maintaining anti-inflammatory response (especially in protecting connective tissues). Normally, alpha$_1$-antitrypsin appears as a single band at ~52 kDa. In general, this plasma protein was found to elute off of all of the tested samples. The cast crystalline sample showed the least amount of the protein, followed by the cast amorphous. The sol–gel sample had the highest amount of alpha$_1$-antitrypsin found in the adsorbed protein layer. Given that alpha$_1$-antitrypsin has a charge of −12 at a pH of 7.0, it might not be expected that its adsorption to negatively charged bioactive glass should be observed. However, two possible mechanisms may allow for this to occur. Firstly, this protein is a part of the adsorbed protein layer, and may interact with already adsorbed protein as opposed to directly interacting with the surface.

Secondly, the composition of the surface of the bioactive glass is transient as it incubates within the plasma solution.

Fibrinogen's α, β and γ chains appear as three bands with molecular weights of 68, 56 and 48 kDa, respectively. Bands at lower molecular weights can appear when fibrinogen is cleaved. The sol–gel bioactive glass is the only sample from which any fibrinogen was eluted. While the lack of fibrinogen degradation products may seem to be a positive sign in that the surface does not appear to stimulate fibrin formation, adsorbed fibrinogen has been shown to denature to the point where it resembles fibrin or fibrinogen degradation products (50). Additionally adsorbed fibrinogen can activate platelets (51) and has been shown to cause the accumulation of phagocytes (52), which fight infection.

Transferrin is primarily responsible for the transport of iron (53), and when run on a reduced SDS-PAGE gel it forms a single band with an approximate molecular weight of 75 kDa (53). Transferrin was found exclusively on the surface of the sol–gel sample. Based on its relative band intensity, a large amount of transferrin was removed from the bioactive glass surface. Given that the protein does not contain a large number of charged residues it can be presumed that the transferrin was not adsorbed due to charge–charge interactions.

Antithrombin is a serine protease inhibitor and while not limited to acting on thrombin it is one of the most important proteins responsible for limiting irregular clotting (54). This protein appears as a single band at approximately 53 kDa when run on an SDS-PAGE gel. It was found on the sol–gel bioactive glass

in fairly high amounts as determined by the relative band intensity. As was the case with transferrin this protein is not charged and was only found on the sol–gel bioactive glass. Given that both the sol–gel and cast crystalline bioactive glass samples are crystalline and have similar surface compositions (Table 3) some characteristic imposed upon the sol–gel sample during its manufacturing appears to be the cause of antithrombin adsorption. When comparing to the XPS data, it seems that antithrombin's adsorption differences between these samples cannot be due to the biomineralization process, for if it were it should be found on both the cast crystalline and sol–gel samples as they are at roughly the same place in their maturation.

The absence of proteins from the bioactive glass surfaces can provide just as much information as the proteins found on the surface. When comparing the list of proteins found on the various bioactive glass surfaces (Table 4.7) to the table listing all of the proteins which were scanned for (Table 4.1) there are a large number of important plasma proteins which were not found on any of the surfaces. Of significance is the lack of any common cell adhesive proteins (i.e., fibronectin and vitronectin) being present on the surfaces. The presence of fibronectin has never been found on the surfaces of pristine bioactive glasses (55). As for clot formation, Factor XI, Factor XII, prekallikrein and high molecular weight kininogen are all absent. These contact phase coagulation proteins are involved in the initiation of the extrinsic coagulation cascade. Their lack of detection may indicate that none of the samples may activate coagulation through the contact phase. Neither prothrombin nor thrombin was found on the surfaces of

any of the bioactive glass samples. This is another strong indication that these surfaces do not stimulate coagulation given thrombin's central role in this process (54). Furthermore, the lack of these proteins in conjunction with protein C and protein S indicates there is no strong anticoagulant activity caused by the bioactive glass samples. Also, the absence of α_2-macroglobulin, a potent inhibitor for both clotting and fibrinolysis, further strengthens the hypothesis that the bioactive glass surfaces do not stimulate either clot formation or breakdown. These are generally considered a positive attribute for implanted biomaterials to have, as the lack of these molecular level markers for the activation of the coagulation cascade may indicate a lack of clot formation.

While the consequences of the adsorption of specific plasma proteins on cellular responses such as osteoblast differentiation, viability and proliferation are beyond the scope of this study, it has been demonstrated that a multitude of factors influence plasma protein adsorption and, by extension, host response. This has been unwittingly demonstrated in the literature by the varied responses of osteoblasts to Class A bioactive materials. The effects of these materials have ranged from very positive to inhibitory (23-27). Given that these studies did not use identical circumstances or times, they also would not have elicited identical responses from the plasma proteins directing host responses.

4.6. Conclusions

In this study bioactive glass 45S5 was produced in various forms using differing methods and evaluated for their physical characteristics and interactions with platelet poor human plasma. Commercially and medically employed melt-cast 45S5 was compared with devitrifed crystalline melt-cast 45S5 as well as sol–gel produced crystalline 45S5. These modifications in bioactive glass synthesis were imparted to produce glasses with better physical properties. Devitrification of melt-cast 45S5 leads to improved mechanical properties while enabling powder sintering and using the sol–gel method produces a porous crystalline glass with a higher specific surface area to encourage interactions with the surrounding environment.

It was found that sol–gel derived 45S5 showed higher surface area and submicron porosity in the structure compared to either of the melt-derived glasses. This in turn led to increased plasma protein adsorption both in terms of quantity and in variety of the adsorbed proteome. The presence of IgG and fibrinogen on the sol-gel glass suggest that this manufacturing method may lead to negative host responses, namely immune and clotting responses. The devitrification of melt-cast 45S5 changed the surface composition as shown by XPS analysis but did not change the amount of plasma protein adsorption; devitrification did, however decrease the presence of C3 and $alpha_1$ antitrypsin on the surface which may decrease any tendency toward deleterious host responses. These differences in surface structure obviously affect the adsorbed proteome and may influence bone integration via mediating cell attachment.

4.7. Acknowledgments

LDU and JAN gratefully acknowledge the support of NSERC-Discovery Grants and MSB acknowledges the support of Alberta Innovates Graduate Scholarship.

4.8. References

1. Hench LL, Splinter RJ, Allen WC, Greenlee TK. Bonding mechanisms at the interface of ceramic prosthetic materials. Journal of Biomedical Materials Research Part A. 1971 Nov 1;5(6):117-41.

2. Hench LL, Paschall HA. Direct chemical bond of bioactive glass-ceramic materials to bone and muscle. Journal of Biomedical Materials Research Part A. 1973 May 1;7(3):25-42.

3. Sarkisov PD, Mikhailenko NY, Khavala VM. Biological activity of glass-and sitall-based materials. Glass and ceramics. 1993 Sep 1;50(9):372-9.

4. Hench LL. Bioactive materials: the potential for tissue regeneration. Journal of Biomedical Materials Research Part A. 1998 Sep 15;41(4):511-8.

5. Xynos ID, Hukkanen MV, Batten JJ, Buttery LD, Hench LL, Polak JM. Bioglass® 45S5 stimulates osteoblast turnover and enhances bone formation in vitro: implications and applications for bone tissue engineering. Calcified Tissue International. 2000 Oct 24;67(4):321-9.

6. Gough JE, Notingher I, Hench LL. Osteoblast attachment and mineralized nodule formation on rough and smooth 45S5 bioactive glass monoliths. Journal of Biomedical Materials Research Part A. 2004 Mar 15;68(4):640-50.

7. Christodoulou I, Buttery LD, Saravanapavan P, Tai G, Hench LL, Polak JM. Dose-and time-dependent effect of bioactive gel-glass ionic-dissolution products on human fetal osteoblast-specific gene expression. Journal of Biomedical Materials Research Part B: Applied Biomaterials. 2005 Jul 1;74(1):529-37.

8. Christodoulou I, Buttery LD, Tai G, Hench LL, Polak JM. Characterization of human fetal osteoblasts by microarray analysis following stimulation with 58S bioactive gel-glass ionic dissolution products. Journal of Biomedical Materials Research Part B: Applied Biomaterials. 2006 May 1;77(2):431-46.

9. Hench LL Bioceramics. Journal of the American Ceramic Society. 1998 Jul 1;81:1705–1728

10. Greenlee TK, Beckham CA, Crebo AR, Malmorg JC. Glass ceramic bone implants. A light microscopic study. Journal of Biomedical Materials Research Part A. 1972 May 1;6(3):235-44.

11. Peitl Filho O, Latorre GP, Hench L. Effect of crystallization on apatite-layer formation of bioactive glass 45%. J Biomed Mater Res. 1996;30:509-14.

12. Peitl O, Zanotto ED, Hench LL. Highly bioactive P 2 O 5–Na 2 O–CaO–SiO 2 glass-ceramics. Journal of Non-Crystalline Solids. 2001 Nov 30;292(1):115-26.

13. Kokubo T, Takadama H. How useful is SBF in predicting in vivo bone bioactivity?. Biomaterials. 2006 May 31;27(15):2907-15.

14. Hench LL, Jones JR, Sepulveda P. Bioactive materials for tissue engineering scaffolds. In Future strategies for tissue and organ replacement 2002 (pp. 3-24).

15. Lefebvre L, Gremillard L, Chevalier J, Bernache-Assollant D. Sintering Behavior of 45S5 Bioglass®. InKey Engineering Materials 2008 (Vol. 361, pp. 265-268). Trans Tech Publications.

16. Lefebvre L, Chevalier J, Gremillard L, Zenati R, Thollet G, Bernache-Assolant D, Govin A. Structural transformations of bioactive glass 45S5 with thermal treatments. Acta Materialia. 2007 Jun 30;55(10):3305-13.

17. Nychka JA, Mazur SL, Kashyap S, Li D, Yang F. Dissolution of bioactive glasses: The effects of crystallinity coupled with stress. JOM Journal of the Minerals, Metals and Materials Society. 2009 Sep 1;61(9):45-51.

18. Chen QZ, Thompson ID, Boccaccini AR. 45S5 Bioglass®-derived glass–ceramic scaffolds for bone tissue engineering. Biomaterials. 2006 Apr 30;27(11):2414-25.

19. Li R, Clark AE, Hench LL. An investigation of bioactive glass powders by sol-gel processing. Journal of Applied Biomaterials. 1991 Dec 1;2(4):231-9.

20. Jones JR, Sepulveda P, Hench LL. Dose-dependent behavior of bioactive glass dissolution. Journal of Biomedical Materials Research Part A. 2001 Jan 1;58(6):720-6.

21. Pirayesh H. Effects manufacturing method on surface mineralization of bioactive glasses.

22. Kokubo T, Kushitani H, Sakka S, Kitsugi T, Yamamuro T. Solutions able to reproduce in vivo surface-structure changes in bioactive glass-ceramic A-W3. Journal of Biomedical Materials Research Part A. 1990 Jun 1;24(6):721-34.

23. El-Ghannam A, Ducheyne P, Shapiro IM. Formation of surface reaction products on bioactive glass and their effects on the expression of the osteoblastic phenotype and the deposition of mineralized extracellular matrix. Biomaterials. 1997 Jan 1;18(4):295-303.

24. Wilson J, Pigott GH, Schoen FJ, Hench LL. Toxicology and biocompatibility of bioglasses. Journal of Biomedical Materials Research Part A. 1981 Nov 1;15(6):805-17.

25. Vrouwenvelder WC, Groot CG, De Groot K. Behaviour of fetal rat osteoblasts cultured in vitro on bioactive glass and nonreactive glasses. Biomaterials. 1992 Jan 1;13(6):382-92.

26. Matsuda T, Yamauchi K, Ito G. The influence of bioglass on the growth of fibroblasts. Journal of Biomedical Materials Research Part A. 1987 Apr 1;21(4):499-507.

27. Vrouwenvelder WC, Groot CG, De Groot K. Histological and biochemical evaluation of osteoblasts cultured on bioactive glass, hydroxylapatite, titanium

alloy, and stainless steel. Journal of Biomedical Materials Research Part A. 1993 Apr 1;27(4):465-75.

28. Brash JL. Exploiting the current paradigm of blood–material interactions for the rational design of blood-compatible materials. Journal of Biomaterials Science, Polymer Edition. 2000 Jan 1;11(11):1135-46.

29. Kaufmann EA, Ducheyne P, Radin S, Bonnell DA, Composto R. Initial events at the bioactive glass surface in contact with protein-containing solutions. Journal of Biomedical Materials Research Part A. 2000 Dec 15;52(4):825-30.

30. Buchanan LA, El-Ghannam A. Effect of bioactive glass crystallization on the conformation and bioactivity of adsorbed proteins. Journal of Biomedical Materials Research Part A. 2010 May 1;93(2):537-46.

31. Singh HD, Wang G, Uludağ H, Unsworth LD. Poly-L-lysine-coated albumin nanoparticles: stability, mechanism for increasing in vitro enzymatic resilience, and siRNA release characteristics. Acta biomaterialia. 2010 Nov 30;6(11):4277-84.

32. Taylor JA, Lancaster GM, Ignatiev A, Rabalais JW. Interactions of ion beams with surfaces. Reactions of nitrogen with silicon and its oxides. The Journal of Chemical Physics. 1978 Feb 15;68(4):1776-84.

33. Kim HR, Andrieux K, Gil S, Taverna M, Chacun H, Desmaële D, Taran F, Georgin D, Couvreur P. Translocation of poly (ethylene glycol-co-hexadecyl)

cyanoacrylate nanoparticles into rat brain endothelial cells: role of apolipoproteins in receptor-mediated endocytosis. Biomacromolecules. 2007 Mar 12;8(3):793-9.

34. Unsworth LD, Sheardown H, Brash JL. Polyethylene oxide surfaces of variable chain density by chemisorption of PEO-thiol on gold: adsorption of proteins from plasma studied by radiolabelling and immunoblotting. Biomaterials. 2005 Oct 31;26(30):5927-33.

35. Chen QZ, Rezwan K, Armitage D, Nazhat SN, Boccaccini AR. The surface functionalization of 45S5 Bioglass®-based glass-ceramic scaffolds and its impact on bioactivity. Journal of Materials Science: Materials in Medicine. 2006 Nov 1;17(11):979-87.

36. NIST (2003) X-ray Photoelectron spectroscopy database (database on the Internet) (cited November 2010). Available from: http://srdata.nist.gov/xps/

37. Hench LL. Bioceramics: from concept to clinic. Journal of the american ceramic society. 1991 Jul 1;74(7):1487-510.

38. Cros A, Saoudi R, Hollinger G, Hewett CA, Lau SS. An x-ray photoemission spectroscopy investigation of oxides grown on Au x Si1− x layers. Journal of Applied Physics. 1990 Feb 15;67(4):1826-30.

39. Aoyama T, Sugii T, Ito T. Determination of band line-up in β-SiC/Si heterojunction for Si-HBT's. Applied surface science. 1990 Jan 1;41:584-6.

40. Sivaraman B, Latour RA. The adherence of platelets to adsorbed albumin by receptor-mediated recognition of binding sites exposed by adsorption-induced unfolding. Biomaterials. 2010 Feb 28;31(6):1036-44.

41. El-Ghannam A, Hamazawy E, Yehia A. Effect of thermal treatment on bioactive glass microstructure, corrosion behavior, ζ potential, and protein adsorption. Journal of Biomedical Materials Research Part A. 2001 Jun 5;55(3):387-95.

42. Mladenovic Z, Sahlin-Platt A, Bengtsson Å, Ransjö M, Shchukarev A. Surface characterization of bone graft substitute materials conditioned in cell culture medium. Surface and Interface Analysis. 2010 Jun 1;42(6-7):452-6.

43. Cerruti M, Bianchi CL, Bonino F, Damin A, Perardi A, Morterra C. Surface modifications of bioglass immersed in TRIS-buffered solution. A multitechnical spectroscopic study. The Journal of Physical Chemistry B. 2005 Aug 4;109(30):14496-505.

44. Peitl Filho O, Latorre GP, Hench L. Effect of crystallization on apatite-layer formation of bioactive glass 45%. J Biomed Mater Res. 1996;30:509-14.

45. Anitua E, Andia I, Ardanza B, Nurden P, Nurden AT. Autologous platelets as a source of proteins for healing and tissue regeneration. Thrombosis and haemostasis. 2004 Jan 1;91(1):4-15.

46. Molina H. Complement and immunity. Rheumatic Disease Clinics of North America. 2004 Feb 29;30(1):1-8.

47. Tang L, Liu L, Elwing HB. Complement activation and inflammation triggered by model biomaterial surfaces. Journal of Biomedical Materials Research Part A. 1998 Aug 1;41(2):333-40.

48. Clark AE, Hench LL, Paschall HA. The influence of surface chemistry on implant interface histology: a theoretical basis for implant materials selection. Journal of Biomedical Materials Research Part A. 1976 Mar 1;10(2):161-74.

49. Gettins PG. Serpin structure, mechanism, and function. Chemical reviews. 2002 Dec 11;102(12):4751-804.

50. Mosesson MW. Fibrinogen and fibrin structure and functions. Journal of Thrombosis and Haemostasis. 2005 Aug 1;3(8):1894-904.

51. Massa TM, Yang ML, Ho JY, Brash JL, Santerre JP. Fibrinogen surface distribution correlates to platelet adhesion pattern on fluorinated surface-modified polyetherurethane. Biomaterials. 2005 Dec 31;26(35):7367-76.

52. Tang L, Eaton JW. Natural responses to unnatural materials: A molecular mechanism for foreign body reactions. Molecular medicine. 1999 Jun;5(6):351.

53. Moos T, Morgan EH. Transferrin and transferrin receptor function in brain barrier systems. Cellular and molecular neurobiology. 2000 Feb 1;20(1):77-95.

54. Davie EW, Kulman JD. An overview of the structure and function of thrombin. In Seminars in thrombosis and hemostasis 2006 Feb (Vol. 32, No. S 1, pp. 003-015). Copyright© 2006 by Thieme Medical Publishers, Inc., 333 Seventh Avenue, New York, NY 10001, USA..

55. El-Ghannam A, Ducheyne P, Shapiro IM. Effect of serum proteins on osteoblast adhesion to surface-modified bioactive glass and hydroxyapatite. Journal of orthopaedic research. 1999 May 1;17(3):340-5.

5. Nanoparticle Protein Corona Formation in Human Blood and Effects on *E. coli* Opsonisation, Phagocytosis and Coagulation

5.1. Abstract

Upon exposure to biological environments, nanoparticles are immediately coated with proteins and this adsorbed corona establishes the biological response to the nanoparticle. This protein corona is often overlooked during toxicological studies and accurate assessments of the biological outcomes to nanoparticle exposure, including contact activation of coagulation, opsonization and phagocytosis, must take this adsorbed proteome into account. This study will employ both murine macrophage and rat mast cell-like cell lines to investigate the effects of metal-oxide poly(acrylic acid) nanoparticles on the phagocytosis of transformed *Escherichia coli* with green fluorescent protein, taking into account the adsorbed proteomes, as assessed using Western blotting and clotting assays. Across all five tested metal core-PAA nanoparticles, proteins including albumin, activated complement Factor 3, immunoglobulin G, fibrinogen and transferrin were detected while various other pro and anti-coagulant and cell binding proteins were found adsorbed to only some nanoparticle systems. Each nanoparticle system was shown to inhibit human plasma coagulation to various degrees, with the zinc oxide sample completely eliminating any clotting. Pre-exposure of titanium dioxide nanoparticles to fetal bovine serum resulted in a 50% increase in phagocytic activity of mast cells, and a 12.5% increase in macrophages, as assessed by both flow cytometry and confocal microscopy. Overall, this study identified numerous structural, coagulation and immune proteins in the adsorbed coronae of metal-oxide poly(acrylic acid) nanoparticles. Phagocytosis

assessments showed that the presence of an adsorbed protein layer resulted in enhanced phagocytosis in two distinct immune cell lines.

Keywords: Macrophage, mast cell, metal oxide poly(acrylic acid) nanoparticle, protein adsorption, opsonization, phagocytosis, coagulation

5.2. Introduction

When nanoparticles breach protective external barriers and infiltrate biological compartments, such as blood vessels, they quickly acquire a diverse mixture of blood proteins and other biomolecules that bind to the nanoparticle to form the biomolecular protein corona. Nano properties such as charge, surface area and size are key characteristics that likely dictate the profile of proteins that are present, however, it is the protein corona itself that establishes the "biological identity" of the nanoparticle and encodes important information about the interface that forms between the nanoparticle and a cell surface (1). Biological responses to nanoparticles would therefore be a function of this interface and could be traced to the corona profile. However, in most *in vitro* nanotoxicology studies, the corona is not evaluated nor considered when interpreting toxicological outcomes, and instead focus on nanoparticle properties that were characterized post-synthesis, when the particles lacked a protein corona. Therefore, it would be more precise to evaluate the biological and toxicological outcomes of nanoparticle exposures from the bio-corona perspective, rather than simply from its original synthesized form. Indeed, recent studies have shown that the same nanoparticle can induce different biological outcomes, depending on the presence or

composition of the protein corona (2). For example, it has been shown that cytotoxicity is corona-dependent, whereby the presence of a protein corona reduced reactive oxygen species production in monocytes compared to nanoparticles without a corona (3). Maiorano *et al.* also showed that protein coronas composed from Dulbecco's Minimal Essential Medium cell culture media were more protective to HeLa cells from nanoparticle damage than coronas sourced from Roswell Park Memorial Institute media (4).

The contact activation pathway in blood (an axis of coagulation) is a protein cascade system that could be susceptible to interference from PAA-nanoparticles. Its activation is triggered when coagulation Factor XII makes contact with negatively charged surfaces or molecules, which leads to a cascade of protein interactions and catalytic conversions that ultimately terminates with fibrin polymerization that creates the stable clot surrounding an open wound (5). The high negative charge of poly(acrylic acid) (PAA) nanoparticles could activate the contact pathway and interfere with clot formation in unknown ways.

Cell uptake has also been shown to be sensitive to corona composition since uptake mechanisms, including phagocytosis, are ligand-mediated processes. Therefore, the presence of immunoglobulins (e.g. IgG) or complement proteins in the corona could stimulate phagocytic cells, including macrophages and mast cells, to take up nanoparticles. This process is known as opsonisation whereby the coating of foreign particles (e.g. pathogen or a nanoparticle) with opsonins promotes the recognition and phagocytic uptake of the foreign particle inside the cell. Thus, an opsonin is any protein that promotes phagocytosis by associating

with an antigen. Indeed, recent studies have shown that macrophages and dendritic cells increasingly take up nanoparticles that are coated with complement or other Ig molecules, and nanoparticles that lack a protein corona tend to adhere to the cell membrane without being internalized (2, 6, 7). Moreover, studies examining serum protein coronas have consistently found that it is composed of many types of opsonins and other immune-activating proteins (8). Therefore, understanding the composition of corona proteins is key to understanding the effects that nanoparticles impart on immune cells. While these recent studies show interesting roles that protein coronas can have on the recognition and internalization of opsonized nanoparticles, what has not been examined to date are the effects that nanoparticle-protein coronas have on the opsonisation process and subsequent phagocytosis of opsonized pathogens by immune cells.

Phagocytosis is an ancient component of the innate immune system that is utilized by many animals, including invertebrates and mammals (9-11). The recognition and engulfment of extracellular targets, like bacteria, or damaged or dying host cells, requires the engagement of different phagocytic receptor types (12). Therefore, phagocytosis is vital for maintaining organismal health. Two well-studied phagocytic receptor models include the antibody receptor, FcR, which binds IgG, and the complement receptor, CR3 (also called the macrophage integrin $\alpha_M\beta_2$), which binds complement C3 and C4 proteins. These receptor-target complexes selectively regulate intracellular signaling to facilitate the destruction of harmful pathogens by utilizing inflammatory processes, or can remove apoptotic host cells without an inflammatory response. Mast cells and

macrophages are two types of innate immune cells that possess phagocytic receptors to remove pathogens and other opsonized targets, via phagocytosis. However, while macrophages are generally considered "professional" phagocytes because of their principle role in targeting and removing invaders, mast cells are not, since they are more commonly associated with degranulatory effector functions. However, they can still effectively phagocytize when necessary.

For this study, we utilized two innate immune cell lines, the murine macrophage RAW 264.7 cell line and the rat mast cell-like RBL-2H3 cell line to examine and compare their phagocytic response for fluorescent green fluorescent protein-*Escherichia coli* (GFP-*E. coli*). We investigated the effects that metal oxide-PAA-nanoparticles (TiO_2, CeO_2, Fe_2O_3, ZnO and Capsules) have on the opsonization and phagocytosis of GFP-*E. coli* when exposed to serum proteins. Secondly, we also measured the effects on coagulation given that it is susceptible to interference from negatively-charged colloids in circulation. Finally, we profiled the serum proteins that form part the protein corona to bio-characterize these nanoparticles and correlate their presence or specific proteins associated with the nanoparticle with potential biological effects.

5.3. Materials and Methods

5.3.1. RAW 264.7 and RBL-2H3 cell line culture conditions

RAW 264.7 and RBL-2H3 cells were grown to confluence at 37°C with 5% CO_2 in culture media consisting of either Dulbecco's Minimal Essential

Medium (DMEM) for RAW-264.7, or Minimal Essential Eagles Medium (MEM) for RBL-2H3, both with Earle's balanced salt solution (Sigma-Aldrich, Canada) and supplemented with 1 % 2 mM L-glutamine, 1% penicillin/streptomycin, and 10 % heat-inactivated FBS. Cells were passed every third day by harvesting cells in a harvest buffer medium (1.5 mM EDTA, 135 mM NaCl, 20 mM HEPES, 5 mM KCl, pH 7.4) at 37^{o}C with 5 % CO_2 for 10 minutes, followed by pipetting to detach cells from cell culture plate (BD Biosciences, Mississauga, Canada). Cells were seeded into new flasks at a sub-cultivation ratio of 1:10.

5.3.2. GFP-Escherichia coli bacteria

Green fluorescent protein (GFP)-expressing *E. coli* were a kind gift from Dr. M. Belosevic (University of Alberta) and were cultured by streaking frozen cells onto an ampicillin (Amp)-containing Luria broth (LB) agar plate (1% Bacto-agar (BD), 0.5% yeast extract, 85.55 mM NaCl, 5% ampicillin pH 7) using a heat-sterilized sterilized inoculating loop, and incubated overnight at 37^{o}C. Single isolated colonies were then used to inoculate 5 mL of LB-Amp solution. The culture was grown overnight in a shaker at 37^{o}C.

5.3.3. PAA-nanoparticle incubation in human plasma

200 µL of 10 g/L nanoparticle solutions were combined with 1.8 mL of 37°C platelet-poor human plasma (Research Division of Canadian Blood Services). Donors provided informed consent and samples were pooled in order to preserve donor anonymity, in accordance with policies from Canadian Blood Services. Nanoparticle-plasma solutions were incubated at 37°C for 2 hours with

rocking agitation. Samples were then centrifuged at 20000 x g for 10 minutes to collect the nanoparticles and the associated adsorbed proteome. In order to remove loosely bound proteins, samples were first washed by resuspending in 1 mL of phosphate buffered saline (PBS) at pH 7.4 (ThermoFisher, Waltham, Massachusetts) and incubated at room temperature with rocking for 30 minutes. This wash procedure was performed twice. After the second wash, the adsorbed proteome was removed by resuspending the nanoparticles in 100 μL of 10% sodium dodecyl sulfate (SDS) (ThermoFisher, Waltham, Massachusetts) in PBS and incubating the samples at 50°C for 2 hours with rocking agitation. Samples were then centrifuged as above and the soluble fractions were retained for subsequent analysis.

5.3.4. SDS-polyacrylamide gel electrophoresis and Western blotting

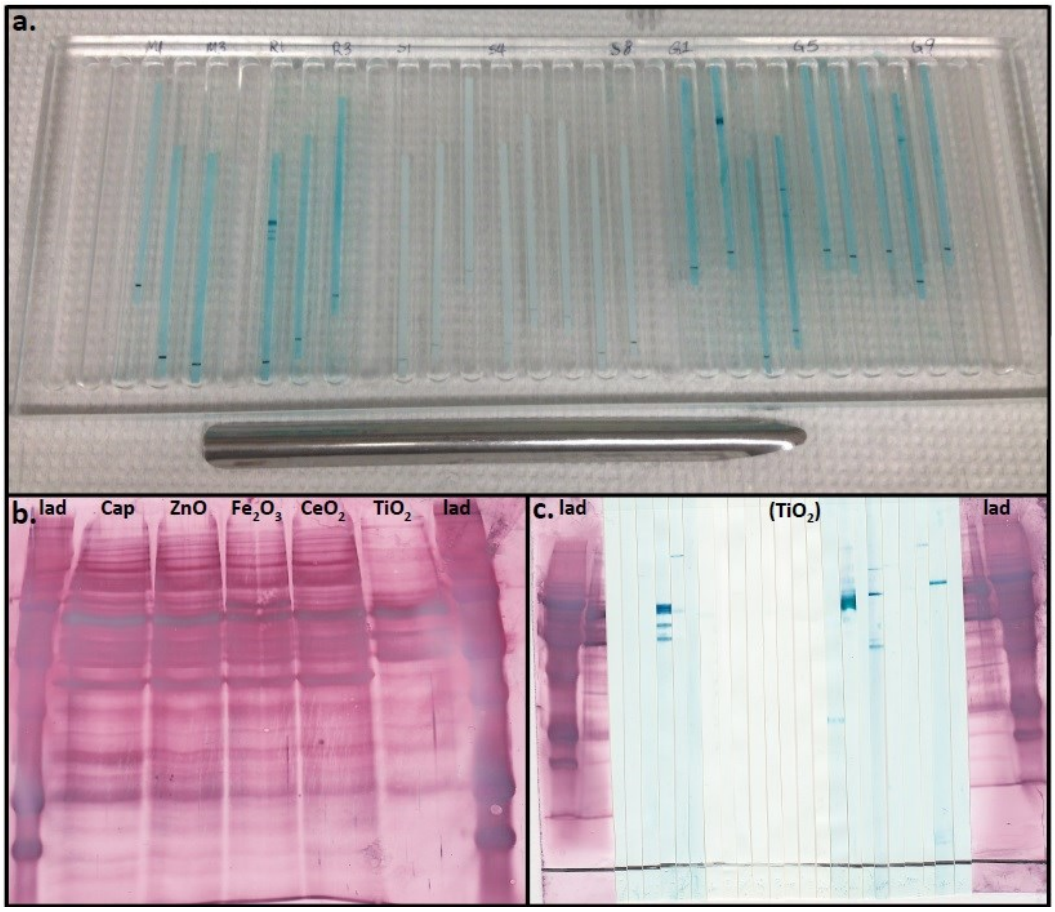

Figure 5.1. (a) Plasma protein Western Blot development tray showing stripped membrane inside individual wells each with unique antibodies. (b) Colloidal gold stained adhered-proteome for each tested PAA-NP (left - right: Ladder, PAA-Caps, PAA-ZnO, PAA-Fe_2O_3, PAA-CeO_2, PAA-TiO_2, Ladder). (c) Reassembled PAA-TiO_2 Western blot membrane post immunoblot development with the outer-most protein lanes stained with colloidal gold.

Antibody	Protein MW (kDa)	Protein pI	Grand Average of Hydropathicity	Host	Source
Albumin	66	6.8	-0.395	Goat	OEM Concepts, Saco, ME, USA
Antithrombin	53	6.7	-0.278	Sheep	Cedarlane Laboratories, Hornby, Ontario, Canada
Beta-lipoprotein	516	7.1	-0.296	Goat	Sigma-Aldrich, St. Louis, MO, USA
Complement Factor 3	185	6.4	-0.32	Goat	Calbiochem, Gibbstown, NJ, USA
Factor I	88	7.6	-0.577	Mouse	Cedarlane Laboratories, Hornby, Ontario, Canada
Factor XI	160	8.1	-0.263	Goat	Cedarlane Laboratories, Hornby, Ontario, Canada
Factor XII	80	7.7	-0.411	Goat	Cedarlane Laboratories, Hornby, Ontario, Canada
Fibrinogen	340	6.6	-0.723	Rabbit	Calbiochem, Gibbstown, NJ, USA
Fibronectin	440	5.7	-0.538	Rabbit	Cedarlane Laboratories, Hornby, Ontario, Canada
Hemoglobin	68	8	0.031	Rabbit	Sigma-Aldrich, St. Louis, MO, USA
IgG	174	8.4	-0.282	Goat	Sigma-Aldrich, St. Louis, MO, USA
Kininogen (heavy chain)	72	6.8	-0.757	Mouse	US Biological, Swampscott, MA, USA
Kininogen (light chain)	50	6.6	-0.473	Mouse	US Biological, Swampscott, MA, USA
Plasminogen	90	7.3	-0.688	Goat	Cedarlane Laboratories, Hornby, Ontario, Canada
Prekallikrein	85	8.2	-0.263	Sheep	Cedarlane Laboratories, Hornby, Ontario, Canada
Protein C	62	6.3	-0.349	Sheep	Cedarlane Laboratories, Hornby, Ontario, Canada
Protein S	69	5.7	-0.295	Sheep	Cedarlane Laboratories, Hornby, Ontario, Canada
Prothrombin	72	5.9	-0.539	Sheep	Cedarlane Laboratories, Hornby, Ontario, Canada
Thrombin	36	5.4	-0.606	Sheep	Cedarlane Laboratories, Hornby, Ontario, Canada
Transferrin	77	7.1	-0.337	Goat	Sigma-Aldrich, St. Louis, MO, USA
Vitronectin	75	5.8	-0.723	Sheep	Cedarlane Laboratories, Hornby, Ontario, Canada
α_1-Antitrypsin	47	5.6	-0.183	Sheep	Cedarlane Laboratories, Hornby, Ontario, Canada
α_2-Macroglobulin	718	6.4	-0.195	Goat	Sigma-Aldrich, St. Louis, MO, USA

Table 5.1. Primary antibodies against human plasma proteins used for immunoblotting nanoparticle eluents and their physical properties. The Kyte-Doolittle scale of hydrophobicity was used to calculate the grand average of hydropathicity where the more positive the score, the more hydrophobic the protein sequence.

Denaturing SDS-polyacrylamide gel electrophoresis (SDS-PAGE) and Western blotting was used to identify the proteome eluted from the various nanoparticles as described previously (13-15). A constant 40 μL volume of eluent was analyzed for each nanoparticle system to compare the results of specific proteins between samples. Briefly, a denaturing sample buffer containing additional SDS as well as 0.5 M β-mercaptoethanol (Bioshop Canada Inc., Burlington, ON) were added to the samples in order to completely denature and reduce the samples. This was supplemented by heating the samples at 95°C for 5 minutes before running them on denaturing 12% polyacrylamide gels. The proteins were then transferred onto 0.2 μm Immuno-Blot polyvinylidene difluoride (PVDF) membranes (Bio-Rad, Hercules, CA) using standard methods. All consumables were purchased from Bio-Rad (Hercules, CA) and used as provided. Each membrane was divided into 25 total strips with 23 used for Western blotting and the remaining two used for colloidal gold total protein staining (Figure 5.1a). A complete listing of the primary antibodies used for Western blotting as well as some physical properties of the corresponding plasma proteins can be found in Table 5.1. Colloidal gold staining was carried out as per the included instructions. An example of the gold-stained proteome for each PAA-nanoparticle is presented in Figure 5.1b. The antibodies used for Western blotting were used at 1:1000 dilutions without additional purification. Protein-antibody complexes were visualized by using horseradish peroxidase (HRP)-conjugated secondary antibodies in conjunction with 350 μL of TMB-stabilized HRP substrate (Promega, Madison, WI) per membrane strip. The colour-

development reactions were allowed to proceed until precipitation of the coloured product was observed (~20 minutes for each sample), after which the reaction was quenched with water. As soon as the membrane strips dried, the blots were reassembled and digitized for analysis (Figure 5.1c).

5.3.5. Human plasma recalcification assay

The plasma recalcification turbidimetric assay was used to discern the formation of clots in platelet-poor human plasma in the presence of PAA-nanoparticles as described previously (15, 16). Briefly, 25 μL of 10 g/L nanoparticle solutions were combined with 100 μL of 37°C platelet-poor plasma in a 96-well multiwall plate. Immediately before placing the plate in a preheated 37°C plate reader, 100 μL of 25 μM $CaCl_2$ (EMD Millipore, Etobicoke, Ontario) or PBS was added to each well. PBS was used as a non-clotting control for each system. A Synergy H1 plate reader (Biotek Instruments Inc., Winooski, VT) was set to a temperature of 37°C and programmed to read the sample turbidities at 405 nm each minute for an hour. Final values underwent both background correction as well as an artificial baseline correction so that all samples had the same arbitrary A_{405} value at time zero. Five replicates were used for each sample and the results were reported as the average and standard deviation.

5.3.6. Cell phagocytosis flow cytometry assay development

GFP-*E. coli* Multiplicity of Infection	Opsonization treatment
RBL-2H3	PBS
0:1	
	ΔFBS (20%)
5:1	
10:1	
100:1	
	FBS (20%)
500:1	
1000:1	
RAW 264.7	PBS
0:1	
	ΔFBS (20%)
1:1	
10:1	
100:1	
	FBS (20%)
500:1	
1000:1	

Table 5.2. Experimental set up for phagocytosis assay development

A phagocytosis assay was developed to examine uptake of GFP-*E. coli* by RBL-2H3 and RAW 264.7 cells under three opsonisation conditions to determine whether opsonizing GFP- *E. coli* with FBS proteins increased phagocytosis assay efficacy. These conditions included, 1. Phosphate buffered saline (PBS), without opsonizing proteins 2. 20% heated FBS (ΔFBS) to heat-inactivate opsonizing proteins and 3. 20% unheated FBS. In addition, various multiplicities of infections (MOI) were tested to determine the optimal the uptake of GFP- *E. coli* for each cell type. For RBL-2H3 cells, the MOIs (*E. coli* to cell) included; 0:1 5:1, 10:1, 100:1, 500:1 and 1000:1, while for RAW 264.7 cells they were 0:1, 1:1, 10:1, 100:1, 500:1 and 1000:1 (Table 5.2). Cell culture-suspended RBL-2H3 and RAW 264.7 cells were seeded (2.5 x 10^5 cells per well) into a 96-well flat bottom plate (Costar) and incubated at 37^{o}C for 1 h to allow for cells to settle and re-attach to plate surface. GFP-*E. coli* stock concentrations were determined using spectrophotometry (optical density 600 nm) and then prepared for each treatment condition by washing in PBS, centrifuging at 3000 x g for 7 min and resuspending in PBS, 20% ΔFBS or 20% FBS at appropriate MOI concentrations. 20% FBS and 20% ΔFBS was previously determined to be optimal for opsonizing GFP-*E. coli*. The cells were then incubated for 2 h at 37^{o}C with GFP-*E. coli* at each of the MOIs described above. Following phagocytosis, non-internalized GFP-*E. coli* were aspirated from wells and the cells were washed three times by gently rocking with PBS and mechanically detached from the culture plate using warmed harvest buffer, transferred to corresponding 1.5 mL centrifuge tubes, centrifuged for 6 min. at 400 x g and resuspended with PBS supplemented with 0.5 % fetal

bovine serum (FBS) (Sigma, Canada) (herein known as PBS-FBS). The percent of phagocytized GFP-*E. coli* (Ex/Em = 395/509 nm) in each sample was determined using the FL1 detector (533/30 nm) on the flow cytometor (Beckman Coulter Quanta SC, Mississauga, Canada).

5.3.7. Effects of nanoparticle-exposed serum proteins on the phagocytosis of GFP-*E. coli*

GFP-*E. coli* Multiplicity of Infection	**Opsonization treatment**	**nanoparticle Treatment (200 µg/mL) (±)**	
RBL-2H3 1000:1	PBS	$PAA\text{-}TiO_2$	PAA-Cap
	ΔFBS (20%)	$PAA\text{-}TiO_2$	PAA-Cap
	FBS (20%)	$PAA\text{-}TiO_2$	PAA-Cap
RAW 264.7 10:1	PBS	$PAA\text{-}TiO_2$	PAA-Cap
	ΔFBS (20%)	$PAA\text{-}TiO_2$	PAA-Cap
	FBS (20%)	$PAA\text{-}TiO_2$	PAA-Cap

Table 5.3. Experimental set up for phagocytosis assay measuring effects of PAA-nanoparticle-exposed serum on the opsonisation and phagocytosis of GFP-*E. coli*

The phagocytosis assay was used to examine whether protein coronas formed on PAA-nanoparticle surfaces affected the opsonization and phagocytosis of GFP-*E. coli* by RAW 264.7 and RBL-2H3 cells. The cells were enumerated and seeded as described above and experimental treatment groups were designed as summarized in Table 5.3.

To perform the experiment, 20 µL of PAA-TiO_2, PAA-Caps or ddH_2O (as a vehicle control) were combined with 180 µL of ΔFBS, FBS or PBS to make final test concentrations of 200 µg/mL nanoparticles and 20% ΔFBS, 20% FBS or PBS. The solutions were incubated at 37°C for 2 h with rocking agitation to allow serum proteins to adhere to the nanoparticles.

Following nanoparticle incubation, the control and nanoparticle-exposed solutions were added to pelleted GFP-*E.coli* that were previously prepared at each MOI concentration and incubated as a suspension for 1 h at 37°C. Following GFP-*E. coli* opsonisation, 1 mL of PBS was added to each solution and centrifuged at 3000 x g for 7 min as a wash step to removed excess nanoparticles. Pelleted GFP-*E.coli* were then resuspended in 200 µL of PBS and added to corresponding RBL-2H3 and RAW 264.7 treatment wells to stimulate phagocytosis for 2 h at 37°C. Following phagocytosis, cells were processed as above and GFP fluorescence in each sample treatment was measured by flow cytometry (FL1 gate).

5.3.8. Effects of nanoparticle-exposed serum proteins on the phagocytosis of Yellow-Green-bead carboxylate beads

To validate whether phagocytosis is affected by nanoparticle-bound serum proteins, fluorescent 2µm Yellow-Green(YG) carboxylate microspears (YG-beads) (Polysciences, Inc, USA) were used in a follow-up phagocytosis experiment to eliminate immune cell recognition of pathogen associated

molecular pattern (PAMP) molecules present on GFP-*E. coli* by pattern recognition receptors (PRRs) found on immune cells. Unlike GFP-*E. coli*, YG-beads do not stimulate phagocytosis unless opsonized with serum proteins. Therefore, phagocytosis is eliminated when non-opsonizing solutions like PBS are used, and thus, the effect of a nanoparticle-protein corona on cell phagocytosis can be confirmed without interference from background uptake of beads.

To perform this experiment, YG-beads were prepared by washing an appropriate volume of beads in PBS, pelleting (400 x g for 7 min.) and resuspending in 20% FBS with or without PAA-TiO_2 at 200 μg/mL, or in PBS as a negative control for 1 h at 37^{o}C at an MOI of 100:1. After opsonizing, the YG-bead solutions were added to previously seeded RBL-2H3 cells (2.5 x 10^5 cells/well) for 2 h to stimulate phagocytosis. Following this step, non-phagocytized YG-beads were aspirated from wells and cells were washed 3 times with PBS and harvested as before and YG-bead fluorescence measured by flow cytometry as described earlier. Phagocytic activity was reported in two ways. First, as the percentage of cells that had phagocytized YG-beads (i.e. % phagocytic-positive cells), and second, as the mean fluorescence intensity (MFI) of the phagocytic-positive cells. Percent phagocytosis is a measure of whether a cell has successfully internalized a YG-bead, while MFI is a proxy measure of the phagocytic index (i.e. the number of YG-bead that have been consumed per cell).

5.3.9. Laser scanning confocal microscopy imaging and quantitation of cell phagocytosis

Glass slide coverslips (Fisher Scientific) were sterilized with 70 % ethanol, washed with sterile H_2O, UV irradiated and placed into the bottom of 6 well flat-bottom plates (Corning Costar, USA). Cells were seeded overtop of the cover slips, at a density of 1.0 x 10^5 cells in cell culture media, and incubated for 2 days at 37 °C. Following 2 days of growth, culture media was removed, cover slips containing adhered RBL 2H3 or RAW-264.7 cells were washed twice in PBS and then incubated with GFP-*E. coli* that had been opsonized with 20% FBS, 20% ΔFBS, or PBS solutions with, or without pre-exposure to PAA-TiO_2 (200 μg/mL) to stimulate phagocytosis.

After exposure, cells were washed twice with PBS-FBS and once with PBS and coverslips were removed from wells and inverted on parafilm containing 5.0 μg/mL CellMask Deep Red in PBS (Ex/Em = 649/666 nm, Molecular Probes) for 10 min. at RT in the dark to stain the plasma membrane (magenta). Coverslips were then washed twice with PBS-FBS and fixed at room temperature in the dark with 4% paraformaldehyde, followed by washing with PBS and mounted on glass slides using mounting medium containing 1.0 μg/mL of 4',6-diamidino-2-phenylindole (DAPI; Ex/Em = 358/461 nm) as a nuclear stain (blue). Fixed cells were imaged with a Zeiss LSCM, LSM 710 AxioObserver Laser Scanning Confocal Microscope (objective 40x 1.3 oil plan-Apochromat, Carl Zeiss Microscopy, Jena, Germany), data collected with Zen 2011 software and processed with LSM Image Browser (v. 4.2.0.121, Carl Zeiss). Adobe Photoshop

(version 18.0) was used to colour-correct confocal images, while three-dimensional z-stack images were surface rendered and animated using Imaris software (v. 8.1, Bitplane, Zurich, Switzerland) to visualize the phagocytosis of GFP-*E. coli*. Imaris software was also used to quantitate the number of phagocytized GFP-*E. coli* inside each cell. The average of three images per treatment was used to determine the phagocytic index of each treatment group. The number of cells per image varied between 11 – 22 cells for RBL-2H3 cells, and between 11 – 14 cells for RAW 264.7 cells.

5.3.10. Statistics

Statistical analysis was performed using GraphPad Prism 6.0 Statistical Software. To analyze effects of MOI on phagocytosis, a one-way analysis of variance (ANOVA) with a Tukey multiple comparison test was performed for comparisons between MOI at each opsonisation condition (i.e. PBS, ΔFBS, FBS). A one-way ANOVA with a pairwise Tukey test was also used to analyze comparisons between opsonisation treatments at each MOI.

To analyze the effects of PAA-TiO_2 and PAA-Caps on phagocytosis, similar one-way ANOVA comparisons with Tukey multiple comparison test were made between opsonisation treatments (i.e. PBS, ΔFBS, FBS) for each nanoparticle treatment group (i.e. Controls, PAA-TiO_2, PAA-Caps). Differences within an opsonisation treatment were analyzed with an unpaired t test. A probability of $p < 0.05$ was considered significant. Data values are presented as mean ± standard error on the mean (SEM).

5.4. Results

5.4.1. Characterization of the nanoparticle plasma protein corona

Plasma protein	Fragment size (kDa)	Fragment name	System				
			PAA-TiO_2	PAA-CeO_2	PAA-Fe_2O_3	PAA-ZnO	PAA-Capsule
Albumin	66		12	12	12	12	12
C3	42	Activation	8	2	3	6	3
	70	β	12	9	10	12	12
	115	α	8	0	0	6	5
	187	Whole	0	0	0	2	0
IgG	27	Light Chain	5	7	3	6	8
	55	Heavy Chain	2	7	1	4	5
$Alpha_1$ antitrypsin	47		1	1	1	3	2
Fibrinogen	48	γ	9	6	6	6	3
	56	β	10	6	7	9	5
	68	α	12	7	9	11	8
	< 48	Cleavage	0	0	0	0	0
Vitronectin	54		1	0	0	0	0
Fibronectin	259		10	0	0	1	1
Prothrombin	70		1	0	0	2	2
Antithrombin	53		0	0	0	1	1
Plasminogen	91		0	0	0	1	1
Factor XI	70		3	0	10	0	0
Factor XII	68		1	0	0	0	0
Transferrin	77		11	8	8	12	12
Beta-lipoprotein	516		7	2	1	0	1

Table 5.4. Relative intensities for Western blots of plasma proteins adsorbed to the various PAA nanoparticle systems. 0 indicates no detectable band intensity. 12 indicates maximum band intensity and lower values denote lower intensities.

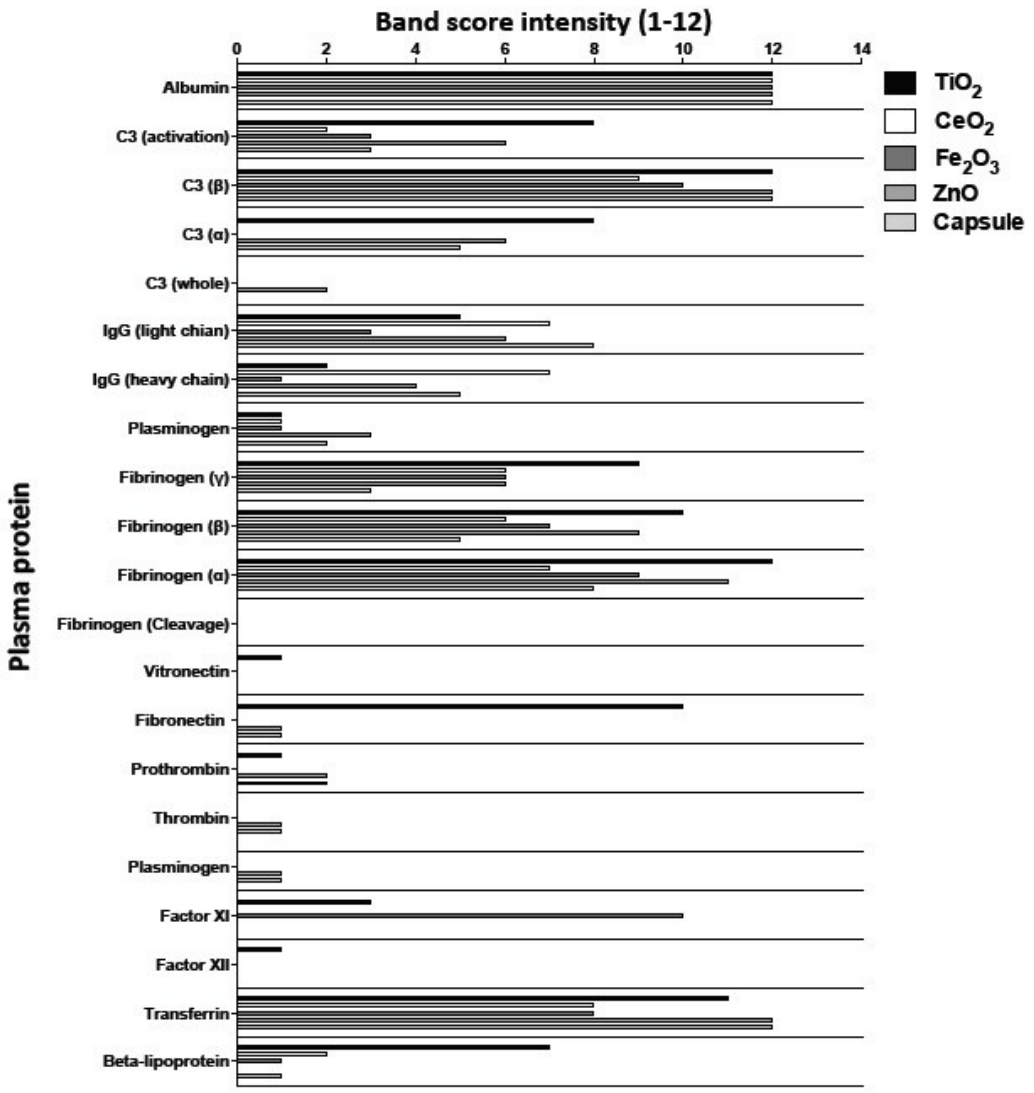

Figure 5.2. Relative intensities for Western blots of human plasma proteins adsorbed to the various polyacrylic acid (PAA) (PAA-TiO_2, PAA-CeO_2, PAA-Fe_2O_3, PAA-ZnO, PAA-Caps). 0 indicates no detectable band intensity. 12 indicates maximum band intensity and smaller values denote decreased intensities.

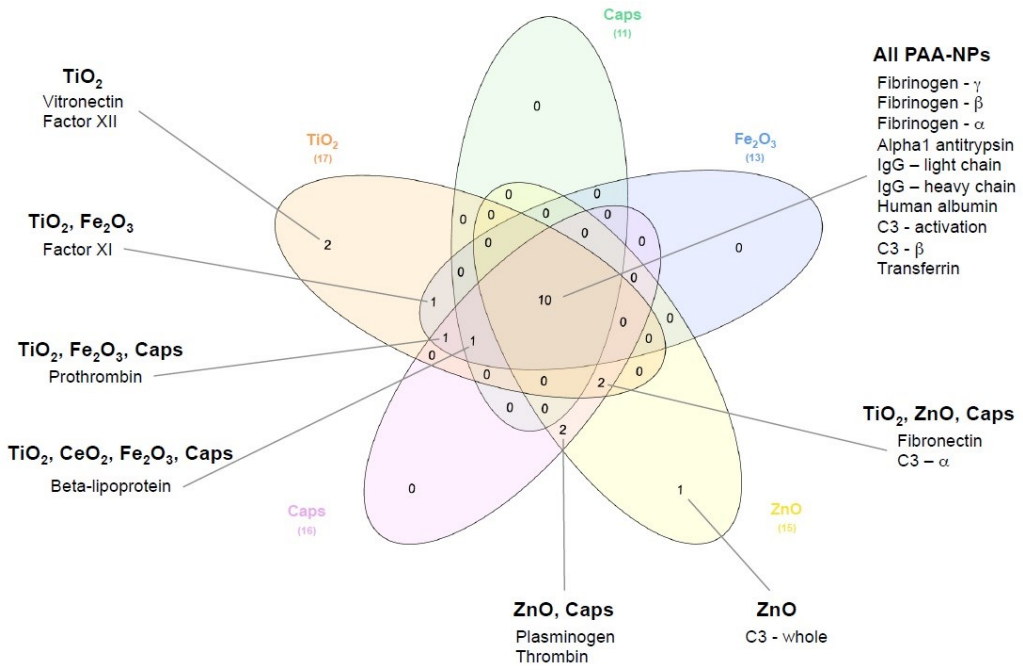

Figure 5.3. Venn diagram of human plasma proteins adsorbed to various polyacrylic acid (PAA) nanoparticles (PAA-TiO2, PAA-CeO2, PAA-Fe2O3, PAA-ZnO, PAA-Caps) that were identified using Western blot techniques. NPs with common proteins are enclosed in regions of overlapping ellipsoids.

To compare the Western blot band intensities between various nanoparticle proteomes, constant volumes of eluent and consistent development time for colour-producing reactions were used. While this allows for comparison of individual protein bands between samples, it does not allow for the direct comparison of band intensities between different protein species as there may be variations in binding moieties and/or affinities for different antibodies. Table 5.4 summarizes the intensities of the different protein bands for each nanoparticle sample. Figure 5.2 presents this data as a histogram in order to visualize these differences more clearly. A 13-step grayscale was used to quantify the Western blotting band intensities whereby a value of 12 indicates a completely saturated black band and lower values indicate correspondingly lower band intensities.

Table 5.4 does not list all of the proteins, which were tested for, but only those that were detected. A list of all 23 plasma protein antibodies used, including physical characteristics and purchasing source can be found in Table 5.1. While the Western blotting technique allows for the detection and identification of various proteins, no conformational information can be discerned. As such, any role that the tertiary protein structure may have in the cellular and host response would be in addition to the responses elicited by the protein adsorption discussed herein (17). The overall protein banding patterns for each PAA nanoparticle sample indicate some similarities, but differences in protein type or intensity of protein are apparent. The Venn diagram in Figure 5.3 displays the protein corona relatedness for each PAA-nanoparticle. All samples show strong banding at roughly 66 kDa in addition to a number of moderately strong bands in the range of ~45-50 kDa. Albumin, IgG and/or fibrinogen are likely major components of these bands. Another moderately strong band can be seen in all samples at 25 kDa, which is likely the light chain of IgG. The PAA-CeO_2, PAA-Fe_2O_3, PAA-ZnO and PAA-Capsule proteomes all had very similar banding patterns. There were only minor variations observed such as a stronger band at ~32 kDa for the PAA-Capsule, or more intense banding at ~75 kDa for PAA-Fe_2O_3, which may represent clotting Factor XI (70 kDa). The PAA-TiO_2 proteome, however, was shown to have numerous dissimilarities from the other samples. Overall, there were noticeably more bands for the PAA-TiO_2, primarily at molecular weights of either >100 kDa or 25-50 kDa. Also of note was the significantly reduced band

intensity at ~43 kDa along with a much stronger banding at 50 kDa compared to the other four PAA-nanoparticles.

5.4.2. Plasma clotting kinetics in the presence of PAA nanoparticles

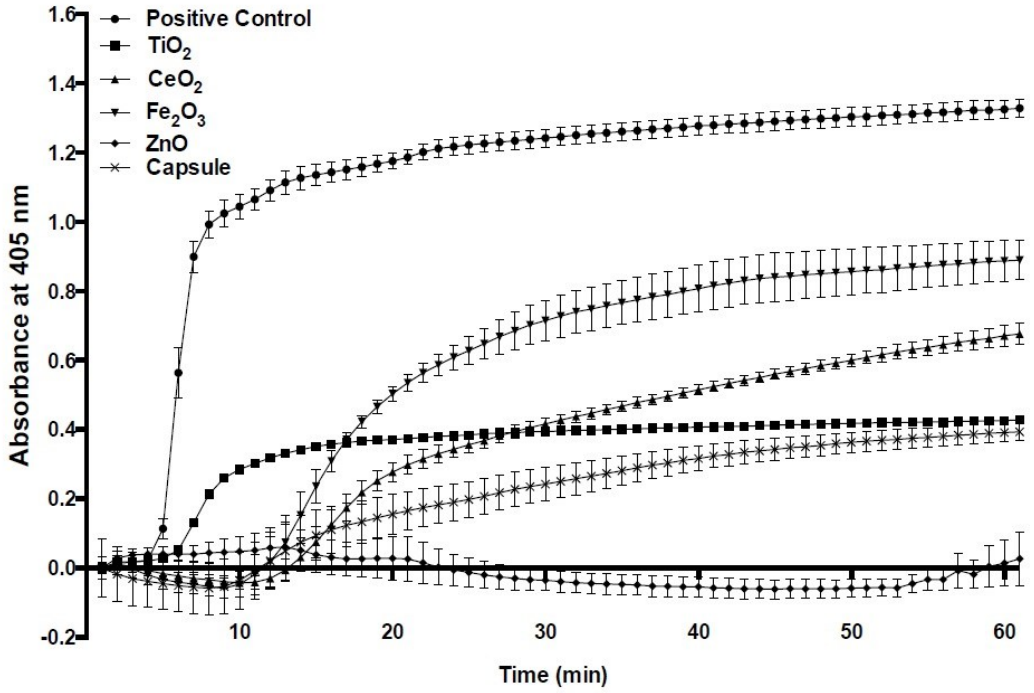

Figure 5.4. Plasma recalcification turbidimetric assay. Background and baseline corrected clot formation in human platelet poor plasma over time in the presence of various PAA nanoparticles. The absorbance profiles represent human plasma (●), PAA-TiO2 (■), PAA-CeO2 (▲), PAA-Fe2O3 (▼), PAA-ZnO (♦) and PAA-Capsule (x) after correcting for background absorbance. Error is considered to be ± 10%.

A plasma recalcification turbidimetric assay was employed in order to evaluate what effect PAA-nanoparticles may have on blood clotting. Nanoparticles were incubated with platelet-poor human plasma and calcium at

37°C for 1 hour alongside a positive control where PBS was used in place of the nanoparticle solution. Negative controls for each of the PAA-nanoparticles as well as the positive control were made by substituting PBS for the calcium solution. This allowed for correction of any turbidity occurring due to the presence of the baseline nanoparticles or plasma solutions. The reduced transmission or apparent increased absorbance at 405 nm due to the onset of solution turbidity as a function of clot formation was monitored over the course of an hour (Figure 5.4). The results are the means (± SEM) of 5 separate clotting reactions per sample after correcting for background turbidity. The positive control reaction began to clot within 5 minutes of the beginning of the assay and began to plateau within 10 minutes. The PAA-TiO_2 sample began to clot and plateau at roughly the same times but the final turbidity was much lower than the control. Clotting in the presence of PAA-CeO_2 nanoparticles began and plateaued later, at 10 and 20 minutes, respectively. PAA-Fe_2O_3 also caused a delayed onset of clotting at ~10 minutes, and a plateau was reached after 30 minutes. No apparent change in turbidity was observed for clotting reaction containing PAA-ZnO nanoparticles. PAA-Capsules prompted a gentle, minor increase in turbidity between 10-30 minutes of the clotting experiment duration. With the exception of PAA-Fe_2O_3, all other samples had much lower final turbidity values compared to the control sample, although all 5 PAA-nanoparticles inhibited clotting over the 60 minute period.

5.4.3. Cell phagocytosis flow cytometry assay development

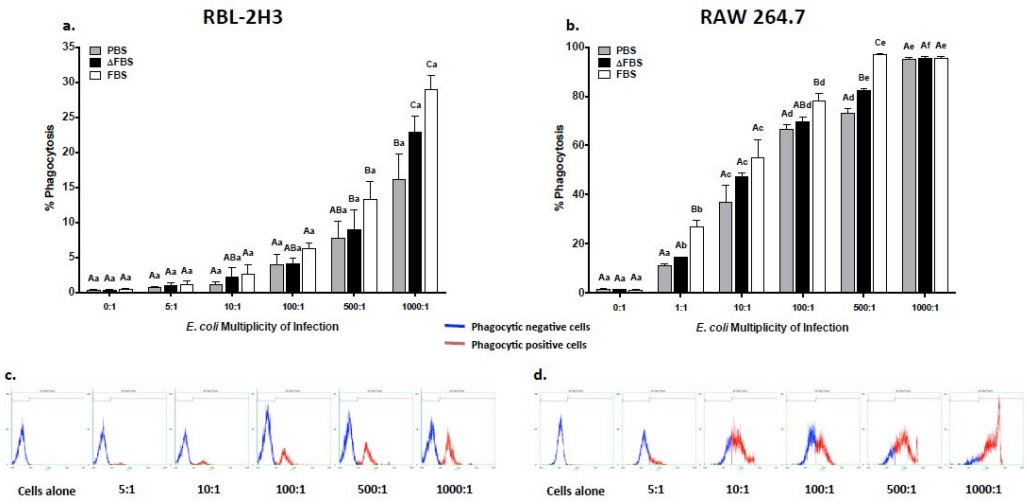

Figure 5.5. Percent phagocytosis of GFP- *E. coli* by (a) RBL-2H3 and (b) RAW 264.7 cells as measured by flow cytometry (FL1 detector). The cells were incubated for 2 h at 37°C with GFP- *E. coli* that was opsonized with either PBS (grey bars), 20% heated FBS (ΔFBS; black bars) or 20% FBS (white bars) solutions at various multiplicity of infections (MOI). Representative flow cytometry histogram plots display percent phagocytic negative (blue) and phagocytic positive (red) cells for (c) RBL-2H3 and (d) RAW 264.7 cells. Data are means ± SEM, n = 8-10. Different upper-case letters denote significant differences between MOI within an opsonization treatment (i.e. PBS, ΔFBS, FBS) (one-way ANOVA, $p < 0.05$). Different lower-case letters denote significant differences between opsonization treatments (i.e. PBS, ΔFBS, FBS) with in an MOI (one-way ANOVA, $p < 0.05$).

Results from the GFP-*E. coli* flow cytometry assay development clearly demonstrated that while both RAW 264.7 and RBL-2H3 cells were capable of phagocytosis, the macrophage cell line (RAW 264.7) was a superior at phagocytosis as it had much higher percent phagocytic positive cells than did the mast cell-like cell line (RBL-2H3) (Figure 5.5**)**. For example, at an MOI of 10:1, percent phagocytosis for RBL-2H3 when incubated in PBS, ΔFBS or FBS, were 1.13 ± 0.32%, 2.12 ± 1.42% and 2.56 ± 1.44%, respectively (Figure 5.5a), while for RAW 264.7 cells, percent phagocytosis were 36.83 ± 7.14%, 47.36 ± 1.45% and 54.86 ± 7.48%, respectively (Figure 5.5b). At an MOI of 1000:1, phagocytic positive cells for RBL-2H3 were, 16.07 ± 3.65%, 22.83 ± 2.26%, 28.95 ± 2.02%,

respectively, while for RAW 264.7 cells they were, 94.93 ± 0.79%, 95.49 ± 0.66 and 95.53 ± 0.63%, respectively.

Although a clear statistical increase in phagocytic positive cells was observed as the MOI increased, there were less significant differences between the opsonization treatments for both cell types. An exception was observed when percent phagocytosis was between 15 – 20%. For RBL-2H3 cells, this occurred at an MOI of 1000:1, while for RAW 264.7 cells, this occurred at 1:1 (PBS: 11.01 ± 0.83%, ΔFBS: 14.37 ± 0.33%, FBS: 27.02 ± 2.40%), and also at 10:1, where percent phagocytosis was (PBS: 36.83 ± 7.14%, ΔFBS: 47.36 ± 1.49%, FBS: 54.86 ± 7.48%. At MOIs > 100:1, percent phagocytosis for RAW 264.7 approached saturation, where at 1000:1, less than 5% of the cell sample was phagocytic negative (Figure 5.5b)

5.4.4. Effect of nanoparticle-protein corona on RBL-2H3 phagocytosis of GFP-*E. coli*

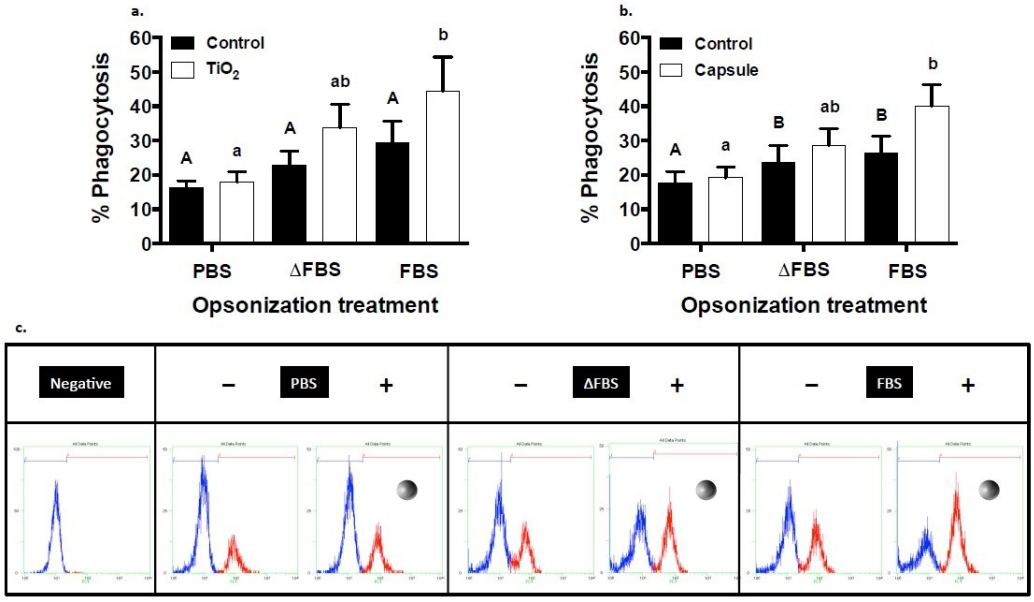

Figure 5.6. Percent phagocytosis of GFP- E. coli by RBL-2H3 cells as measured by flow cytometry (FL1 detector). The cells were incubated for 2 h at 37°C with GFP- *E. coli* (multiplicity of infection: 1000:1) that was opsonized with either PBS, 20% heated FBS (ΔFBS), or 20% FBS solutions with either prior exposure for 2 h to (a) PAA-TiO_2 or (b) PAA-Caps (white bars), or to an equivalent volume of ddH_2O as a vehicle control (black bars). Representative flow cytometry histogram plots (c) display percent phagocytic positive (red) and phagocytic negative (blue) cells for each opsonization treatment with (+) or without (-) prior PAA-TiO_2 exposure. Data are means ± SEM, n = 8-10. Different upper-case letters denote significant differences between opsonization treatments (i.e. PBS, ΔFBS, FBS) for the control group (one-way ANOVA, $p < 0.05$). Different lower-case letters denote significant differences between opsonization treatments (i.e. PBS, ΔFBS, FBS) for the PAA-NP group (i.e. PAA-TiO_2, PAA-Caps (one-way ANOVA, $p < 0.05$). * denote significant differences (ANOVA, $p < 0.05$) between control and PAA-NP exposures within each opsonization treatment.

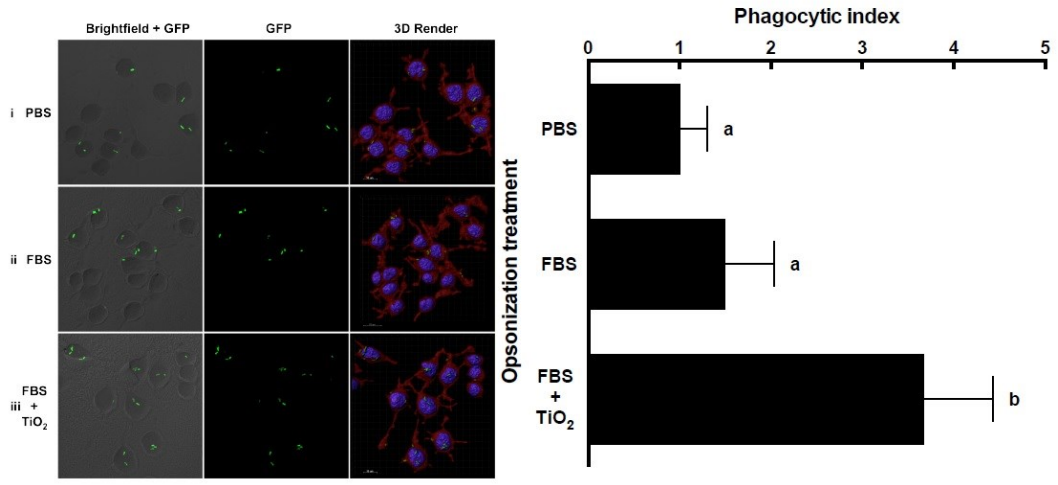

Figure 5.7. Confocal microscopy (Objective 40x, 1.3 oil plan-Apochromat) images of GFP-*E. coli* phagocytosis by RBL-2H3 cells (multiplicity of infection: 1000:1) under three experimental conditions whereby the cells were incubated for 2 h at 37°C with GFP- *E. coli* that were previously opsonized for 1 h with either (i) PBS, (ii) 20% FBS, or (iii) 20% FBS solution that was pre-exposed to PAA-TiO_2 (200 µg/mL) for 2 h. An equivalent volume of ddH_2O was used a vehicle control for treatments (i) and (ii). Representative bright field optical micrographs with fluorescent GFP-*E. coli* after differential interference contrast (a, d, g), GFP-*E. coli* fluorescence micrographs (b, e, h), and three-dimensional surface rendering of RBL-2H3 cells (c, f, i). DAPI (Blue) and CellMask Deep red (Red; 75% transparent surface for three-dimensional reconstruction) were used as probes for cell nucleus and plasma membrane, respectively. Scale bars for three-dimensional images are 15 µm. Imaris software (v. 8.1, Bitplane, Zurich, Switzerland) was used to quantitate the number of phagocytized GFP-*E. coli* inside each cell. The average of three images per treatment was used to determine the phagocytic index, which is summarized in the bar graph. Data are means ± SEM, n = 3. Different lower-case letters denote significant differences between treatment groups (one-way ANOVA, $p < 0.05$).

With the development of the GFP-*E. coli* phagocytosis assay, the effects of nanoparticle-bound plasma proteins (i.e. the protein corona) on RBL-2H3 phagocytosis were tested using PAA-TiO_2 given that it strongly interacted with a broad suite of immune-activating plasma proteins, including complement, IgG and transferrin. PAA-Caps were also tested since these nanoparticles represent a coating control for metal-based PAA-nanoparticle, but also have their own

nanoparticle-based properties and also bind immune-activating proteins (see Figure 5.2).

Results demonstrated that when ΔFBS and FBS were pre-exposed to PAA-TiO_2 and PAA-Caps, percent phagocytosis was elevated for RBL-2H3 cells, despite not being statistically significant, likely a result of dataset variability (Figure 5.6). Nevertheless, there was a 50% increase in percent phagocytosis when FBS was pre-exposed to PAA-TiO_2 prior to opsonizing GFP- *E. coli* (control: 29.49 ± 6.11%, PAA-TiO_2: 44.45 ± 9.95%) (Figure 5.6a). A similar 50% increase was observed for FBS when PAA-Caps were used (control: 26.52 ± 4.71%, PAA-Caps: 40.01 ± 6.25%) (Figure 5.6b). No differences in phagocytosis were observed when PBS was pre-exposed to either PAA-TiO_2 or PAA-Caps.

Confocal microscopy imaging results clearly show that RBL-2H3 cells successfully phagocytized GFP- *E. coli* (Figure 5.7). Bright field confocal images display GFP-*E. coli* in close association with RBL-2H3 cells (Figure 5.7a, d, g), and three-dimensional surface rendering from z stack images confirmed that the GFP-*E. coli* were inside the cells (Figure 5.7c, f, i). Quantitative analysis of z stacks images showed that pre-exposing FBS to PAA-TiO_2 significantly increased the number of GFP-*E. coli* inside each cell (3.67 ± 0.76%) (i.e. increased phagocytic index) when compared to PBS (1.0 ± 0.30%) or FBS alone (1.50 ± 0.53%) (Figure 5.7).

5.4.5. Effect of nanoparticle-protein corona on RAW 264.7 phagocytosis of GFP-*E. coli*

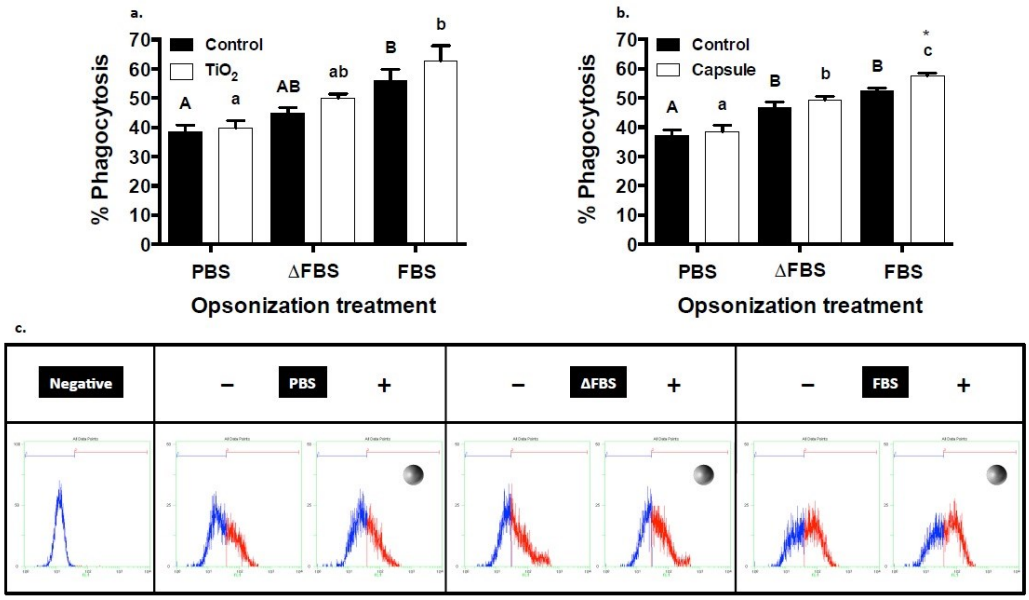

Figure 5.8. Percent phagocytosis of GFP- *E. coli* by RAW 264.7 cells as measured by flow cytometry (FL1 detector). The cells were incubated for 2 h at 37°C with GFP- *E. coli* (multiplicity of infection: 10:1) that was opsonized with either PBS, 20% heated FBS (ΔFBS), or 20% FBS solutions with either prior exposure for 2 h to (a) PAA-TiO_2 or (b) PAA-Caps (white bars), or to an equivalent volume of ddH_2O as a vehicle control (black bars). Representative flow cytometry histogram plots (c) display percent phagocytic positive (red) and phagocytic negative (blue) cells for each opsonization treatment with (+) or without (-) prior PAA-TiO_2 exposure. Data are means ± SEM, n = 8-10. Different upper-case letters denote significant differences between opsonization treatments (i.e. PBS, ΔFBS, FBS) for the control group (one-way ANOVA, $p < 0.05$). Different lower-case letters denote significant differences between opsonization treatments (i.e. PBS, ΔFBS, FBS) for the PAA-NP group (i.e. PAA-TiO_2, PAA-Caps) (one-way ANOVA, $p < 0.05$). * denote significant differences (ANOVA, $p < 0.05$) between control and PAA-NP exposures within each opsonization treatment.

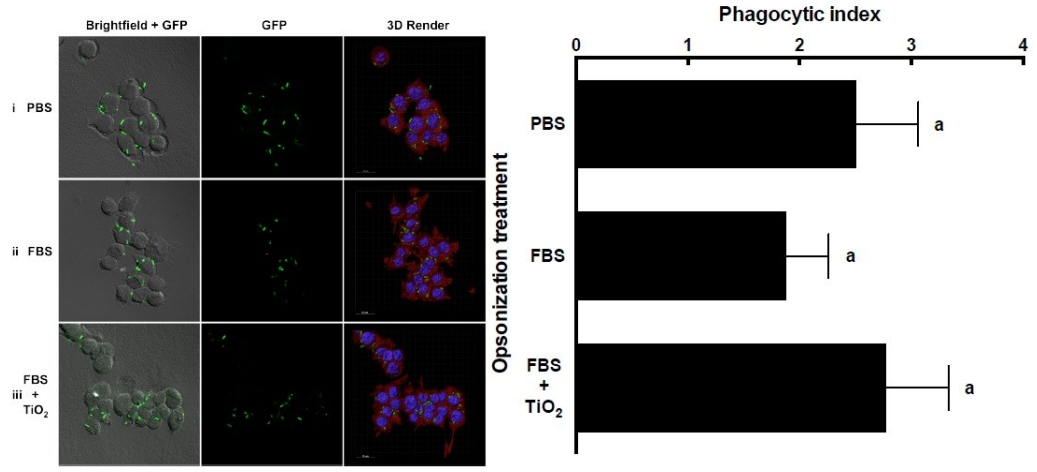

Figure 5.9. Confocal microscopy (Objective 40x, 1.3 oil plan-Apochromat) images of GFP-*E. coli* phagocytosis by RAW 264.7 cells (multiplicity of infection: 10:1) under three experimental conditions whereby the cells were incubated for 2 h at 37°C with GFP- *E. coli* that were previously opsonized for 1 h with either (i) PBS, (ii) 20% FBS, or (iii) 20% FBS solution that was pre-exposed to PAA-TiO_2 (200 µg/mL) for 2 h. An equivalent volume of ddH_2O was used a vehicle control for treatments (i) and (ii). Representative bright field optical micrographs with fluorescent GFP-*E. coli* after differential interference contrast (a, d, g), GFP-*E. coli* fluorescence micrographs (b, e, h), and three-dimensional surface rendering of RAW 264.7 cells (c, f, i). DAPI (Blue) and CellMask Deep red (Red; 75% transparent surface for three-dimensional reconstruction) were used as probes for cell nucleus and plasma membrane, respectively. Scale bars for three-dimensional images are 15 µm. Imaris software (v. 8.1, Bitplane, Zurich, Switzerland) was used to quantitate the number of phagocytized GFP-*E. coli* inside each cell. The average of three images per treatment was used to determine the phagocytic index, which is summarized in the bar graph. Data are means ± SEM, n = 3. Different lower-case letters denote significant differences between treatment groups (one-way ANOVA, $p < 0.05$).

Percent phagocytosis of GFP-*E. coli* was not significantly affected for RAW 264.7 cells when ΔFBS and FBS were pre-exposed to PAA-TiO_2 (ΔFBS: 50.01 ± 1.41%, FBS: 62.87 ± 5.07%) compared to control exposures (ΔFBS: 45.02 ± 1.65%, FBS: 55.86 ± 3.82%) (Figure 5.8a), despite small increases in nanoparticle-exposed opsonization treatments. Percent phagocytosis was also similarly not affected when ΔFBS or FBS were pre-exposed to PAA-Caps (ΔFBS:

49.19 ± 1.42%, FBS: 57.49 ± 1.01%), compared to control exposures (ΔFBS: 46.86 ± 1.79%, FBS: 52.53 ± 0.96%), despite a significant increase in phagocytosis for the FBS treatment, which is likely a result of very small standard errors values (Figure 5.8b).

Confocal imaging also confirmed that GFP-*E. coli* were readily phagocytized by RAW 264.7 cells (Figure 5.9). Bright field images show the GFP- *E. coli* localized within the cell (Figure 5.9a, d, g), which was confirmed by three-dimensional surface rendering (Figure 5.9c, f, i). Quantitative image analysis showed that GFP- *E. coli* phagocytic index was not significantly affected when FBS was pre-exposed to PAA-TiO_2 (2.77 ± 0.56%), compared to PBS (2.5 ± 0.56%) or FBS alone (1.88 ± 0.39%).

5.4.6. Effect of nanoparticle-protein corona on RBL-2H3 phagocytosis of YG-beads

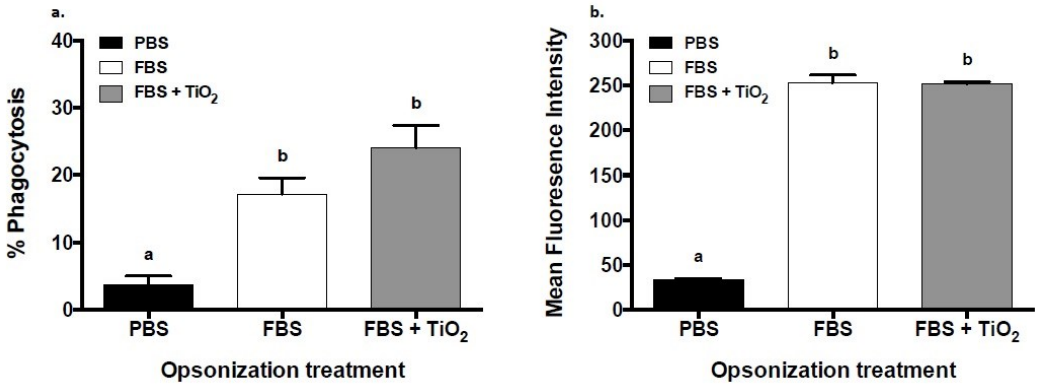

Figure 5.10. Percent phagocytosis of GFP latex beads by RBL-2H3 cells as measured by flow cytometry (FL1 detector). The cells were incubated for 2 h at

37^{o}C with 2 μm GFP latex beads (100:1) that were previously opsonized for 1 h with either PBS (black bars), 20% FBS (white bars), or 20% FBS solution that was pre-exposed to PAA-TiO_2 (200 μg/mL) for 2 h (grey bars). An equivalent volume of ddH_2O was used a vehicle control for PBS and 20% FBS treatments. Data are means ± SEM, n = 3 are presented as (a) % phagocytosis and (b) mean fluorescence intensity. Different lower-case letters denote significant differences between treatment groups for each graph (one-way ANOVA, $p < 0.05$).

Percent phagocytosis was significantly increased, compared to PBS, when YG-beads were opsonized with either FBS or FBS that had been pre-exposed to PAA-TiO_2 (Figure 5.10a). PBS opsonization resulted in only background levels of phagocytosis. Furthermore, opsonizing YG-beads with PAA-TiO_2-exposed FBS stimulated a larger increase in percent phagocytosis than FBS alone. Despite this result not being significant, it supports similar outcomes obtained in Figures 5.6 and 5.7 that used GFP-*E. coli*.

The MFI was also elevated when FBS (253 ± 8.53%) or PAA-TiO_2-exposed FBS (252 ± 2.73%) were used to opsonize YG-beads, compared to PBS, which had trace MFI levels (33.73 ± 1.39%) (Figure 5.10b). There was no significant difference in MFI between FBS or TiO_2-exposed FBS.

5.5. Discussion

General summary of results

Delineating the exact series of events leading to the adsorption of a particular plasma protein species to a material surface is highly complicated and

not fully understood (18). Plasma is composed of a myriad of different components, each of which may potentially interact with the complex material surface in different ways and with varying affinities (19). Additionally, the adsorbed proteome composition is not static, but shifts over time from high-concentration species to those which are less common, but have higher binding affinities in a phenomenon known as the Vroman Effect (20). Adsorbed proteins can also serve to facilitate further protein adsorption, further convoluting the sequence of events of protein adsorption to a material's surface (21). One logical and reasonable method to approaching this convoluted phenomenon is to identify the proteins that are present, their relative intensities on the nanoparticle surface and the potential biological responses the proteome may elicit as a function of the physical properties of the various PAA-nanoparticles.

The Western blot data in Table 5.4 demonstrates significant variations in the eluted proteomes of each different PAA-nanoparticle. Given the high sensitivity of the Western blotting method, it is unlikely that the corresponding antibodies did not detect an eluted protein. Moreover, since identical sample volumes and colour-development times were used, the differences between Western blotting signals can therefore likely be attributed to differences in the eluted proteome, which themselves are products of varying nanoparticle compositions, morphologies and/or other physicochemical characteristics. These proteome differences could result in variations in biological outcomes for each PAA-nanoparticle, and so, understanding the role of each eluted protein is an

important first-step for making logical interpretations of biological responses in blood, such as coagulation and phagocytosis.

Transporting and maintenance proteins

Albumin is a large ubiquitous blood protein found in high concentrations in plasma and thus, detecting it in the eluted PAA-nanoparticle proteomes was not unexpected. Albumin helps maintain intravascular osmotic pressure (i.e. blood volume) by keeping fluid within the vasculature instead of leaking into tissues (22). It also serves as an important carrier of molecules with low water solubility, including bile, bilirubin, calcium, and possibly nanoparticles as well, since many are indispersible (23). Therefore, given its role and abundance in blood, albumin was found in substantial amounts on all PAA-nanoparticle preparations, similar to previous studies on clinically employed bioactive glass (14, 15). Despite albumin generally considered innocuous, to the point of it being employed in biomaterial passivation strategies (24), evidence suggests that conformational changes associated with albumin denaturation can lead to platelet adsorption and activation (17). Western blotting on its own cannot discern the conformation of the protein and whether the presence of albumin is innocuous or not. As such, the potential for a deleterious host response must be considered.

Beta-lipoprotein, also known as apolipoprotein B, is a major structural component of low and very low-density lipoproteins (25). While their role in atherogenesis,

that is the development of atherosclerotic plaques, is well known, they are only recently being evaluated as thrombus-forming agents upon contact with biomaterials (25, 26). This protein was found eluted in moderate amounts from PAA-TiO_2 samples and low amounts from PAA-CeO_2, PAA-Fe_2O_3 and PAA-Capsules. Its presence on the surfaces of nanoparticles suggests that it may influence the formation of thrombi or potentially affect the transport and accumulation of these nanoparticles throughout a host.

Clot-associated proteins

Coagulation is a complex, multifaceted and highly conserved physiological process that is used to seal an open wound by creating a blood clot (27, 28). It involves numerous cellular (platelets) and protein (coagulation factor) components that interact in a sequential process to form a tangled fibrin mesh that becomes the clot (29, 30). Coagulation is initiated when the endothelium and/or the blood vessel wall is damaged, which starts primary hemostasis involving blood vessel constriction (vasoconstriction) and platelet aggregation at the injured site to reduce blood flow and form a temporary plug, respectively (30, 31). Platelets are activated when exposed collagen and other proteins (kininogen, prekallikrein) outside the vessel walls, makes contact with the platelets to start the clot formation process. To secure the clot, secondary hemostasis is activated and involves two separate but related pathways, including the intrinsic, or contact activation pathway, and the extrinsic, or tissue factor pathway. The extrinsic

pathway is generally the first pathway that is activated and occurs when the vessel is externally damaged (i.e. a wound), while the intrinsic pathway is activated when blood circulates over damaged internal surfaces of the vessel endothelium (for ex. exposure to a reactive nanoparticle) (29, 30). The extrinsic pathway axis is started when an external protein called, tissue factor, enters the damaged vessel through the open wound to activate coagulation Factor VII. Factor VII then activates Factor X, which is also the final factor activated from intrinsic pathway axis. The intrinsic pathway starts when internal vessel injury activates Factor XII (Hageman Factor), which activates Factor XI, then Factor IX and finally Factor X (30). The converged amplified production of Factor X from both the extrinsic and intrinsic axis causes the cleavage of prothrombin (Factor II) to thrombin (Factor IIa), which in turn catalyzes the conversion of fibrinogen (Factor I) to fibrin (Factor Ia); the terminal point of coagulation. Fibrin molecules then polymerize to create long insoluble adhesive threads that create a sticky mesh surrounding the platelet plug to permanently seal the open wound and form the final clot (30).

Factors XI and XII are key components of the intrinsic contact activation pathway of coagulation. Both of these pro-coagulant proteins were found in low amounts in the eluent from PAA-TiO_2, but a large amount of Factor XI was associated with PAA-Fe_2O_3. Both of these factors would have moderately strong positive charges at physiological conditions and could conceivably associate with the strongly negative PAA-nanoparticles, however, given that they are not found in all of the eluent PAA-nanoparticle samples suggests that there is a more specific mechanism behind Factor XI and Factor XII adsorption to these

nanoparticles than simple charge-charge interactions. Moreover, given that these pro-coagulant factors were found in only two of the five tested samples, plus the lack of detectable kininogen, prekallikrein or thrombin in all five samples, suggests that these PAA-nanoparticles likely do not elicit a pro-coagulant response *via* the contact activation pathway, even with low-levels of prothrombin, the inactive precursor of thrombin, detected in the eluted proteomes of PAA-TiO_2, PAA-ZnO and PAA-Capsules.

Fibrinogen is another protein found in copious amounts in plasma. It is detected by Western blotting as four bands: the α (68 kDa), β (56 kDa) and γ (48 kDa) chains, while bands below 48 kDa may be detected when fibrinogen is activated/cleaved. Fibrinogen was detected in the eluents from all PAA-nanoparticles, with intensities ranging almost the entire 12-step scale. Fibrinogen has also been identified in abundant amounts in several previous metal nanoparticle corona studies (32-34). As with C3, PAA-TiO_2 and PAA-ZnO had the highest and second highest amounts of fibrinogen eluted from their surfaces. Critically, fibrinogen cleavage bands were not detected in the eluent from any samples. This implies that while fibrinogen does adsorb to all PAA-nanoparticles, it is not being converted to active fibrin. This may still mean however, that with sufficient denaturation it may resemble fibrin and attract and activate platelets and/or phagocytes (35-37). Along with fibrinogen, fibronectin and vitronectin are some of the major plasma proteins capable of governing the attachment of cells to material surfaces (38). Vitronectin was detected in low levels in the PAA-TiO_2 eluent, while fibronectin was found in low levels from PAA-ZnO and PAA-

Capsule samples and in high levels in the PAA-TiO_2 eluent. These in combination with the moderate to high levels of eluted fibrinogen could mean significant protein-mediated attachment by various cell types including platelets, leukocytes and macrophages, with PAA-TiO_2 potentially having the strongest propensity for cell binding relative to the other tested PAA-nanoparticles.

Antithrombin is a powerful inhibitor of thrombin-mediated coagulation and has been characterized as one of the most important proteins for controlling irregular clotting (39). It was minimally detected in the eluted proteomes of PAA-ZnO and PAA-Capsule samples. An identical distribution was observed for plasminogen, another type of anti-coagulant protein. Plasminogen is a key component in fibrinolysis, or clot breakdown. $Alpha_1$-antitrypsin, another physiological inhibitor of coagulation was found eluted from each PAA-nanoparticle system at low levels. It was found most prominently alongside antithrombin and plasminogen in PAA-ZnO and PAA-Capsule eluents. Taken together, the presence of these anti-coagulant or fibrinolytic proteins suggests that PAA-nanoparticles, in particular those with ZnO in their core or those with no metal oxide core at all, may explain the inhibitory effect on coagulation noted in the coagulation assay.

The results of the plasma recalcification turbidimetric assay shown in Figure 5.4 demonstrate that the tested PAA-nanoparticles have varying inhibitory effects on coagulation. PAA-TiO_2 had clotting onset and plateau times consistent with the control sample though the clot endpoint absorbance was greatly reduced. In addition to lower endpoint absorbance values, PAA-CeO_2, PAA-Fe_2O_3 and

PAA-Capsule samples all show delayed onsets of clotting as well as delayed plateaus in turbidity which suggests impaired clot formation kinetics. Altered clotting kinetics and endpoint values may be explained by the presence of various clot-regulating (antithrombin) or fibrinolytic (plasminogen, alpha$_1$-antitrypsin) proteins in eluted proteomes. PAA-Capsule PAA-ZnO, for instance, were found to have alpha$_1$-antitrypsin, antithrombin and plasminogen in the eluent, all of which would contribute to reduced clotting, as seen in Figure 5.4. Higher clot endpoints for PAA-CeO_2 and PAA-Fe_2O_3 may be explained by the presence of only alpha$_1$-antitrypsin in their eluted proteomes, with large amounts of pro-coagulant Factor XI in the PAA-Fe_2O_3 eluent potentially being responsible for the increased clotting endpoint absorbance. The unimpaired clot kinetics of PAA-TiO_2 may be explained in part by the very large amounts of fibrinogen, the key penultimate substrate for clot formation, together with even small amounts of prothrombin, could produce a normal, but reduced kinetic coagulation plot.

The complete abrogation of clotting by PAA-ZnO illustrates another key aspect of PAA-nanoparticle influence on clot formation and host biocompatibility. Clotting requires calcium, and PAA has been shown to be a potent chelator of calcium (40). The chelation ability of PAA depends on numerous parameters including molar ratios of polymer to calcium, the PAA synthesis method, hydration state of the polymer and overall molecular weight (41, 42). The PAA-ZnO nanoparticles may possess a combination of characteristics, which cause it to have strong chelation properties, essentially eliminating the ability of the plasma

to clot. It may be possible that all of the PAA-nanoparticle samples chelate calcium to some degree, which would contribute to their inhibition of coagulation.

Finally, given that these PAA-nanoparticles can strongly inhibit or even eliminate the plasma clotting response through a possible combination of adsorbed proteins and calcium chelation, prompts significant concerns about host health in the presence of these materials in circulation.

Immunological proteins

Complement is another prominent protein cascade system in the blood and is a critical component of the innate immune response. It is utilized in the body to opsonize infectious bacteria, foreign agents and damaged host cells for phagocytosis, and can also be used to lysis cells. Complement can also initiate inflammatory processes, and/or trigger adaptive immune responses (43).

Although there are three separate pathways (classical, alternative and mannose-binding lectin) responsible for activating complement, all of them converge on complement component 3 (C3), cleaving it into C3b, which acts as an opsonin by binding to the pathogen surface, and C3a, which promotes inflammation by stimulating mast cells to degranulate and release histamine (44-46). Activated C3 triggers the common lytic pathway, which terminates with the assembly of the membrane attack complex (MAC) that is used to lyse bacteria and other cells by damaging their membranes. C5a, which is produced during the lytic pathway, attracts macrophages, neutrophils and mast cells to also propagate

inflammation (44). Therefore, C3 is one of the more critical proteins in the cascade. The classical pathway is initiated when antigen-bound antibodies (IgG) on pathogen surfaces are themselves bound by complement C1 proteins (44). The mannose-binding lectin pathway is antibody-independent and is instead activated when lectin or ficolin, bind to mannose or oligosaccharides (i.e. carbohydrates) on the bacterial surface, respectively (47, 48). Both classical and mannose-binding lectin pathways create a C3 convertase enzyme that cleaves and activates C3. The alternative pathway enhances the classical and mannose-binding lectin pathways by creating more C3 convertase to amplify the conversion of C3 (44). The alternative activation pathway is the most common source of complement activation in instances of host-material interactions and thus, is most relevant for the discussion herein (49).

C3 is detected in four distinct bands when characterized by Western blot: whole C3 (187 kDa), α chain (115 kDa), β chain (a 70 kDa) and an activation fragment (42 kDa). Data from Table 5.4 clearly indicates that two to four bands from C3 were found in the eluted proteome from all of the PAA-nanoparticle samples. Moderately high amounts of the α chain were detected from the PAA-TiO_2, PAA-ZnO and PAA-Capsule samples while high amounts of the β chain were eluted from all PAA-nanoparticle samples. Critically, the activation fragment of C3 was also detected in all of the eluted samples though the levels were low for PAA-CeO_2, PAA-Fe_2O_3 and PAA-Capsule, suggesting low levels of complement activation for these PAA-nanoparticles. PAA-ZnO and PAA-TiO_2 eluents contained moderate and moderately high levels of the activation fragment,

respectively, implying these nanoparticle samples were stronger activators of complement. Past studies have also shown complement proteins bind strongly to several types of nanoparticles, including polymers, liposomes and metals (8, 50-55). Binding to nanoparticles has also consistently shown that complement proteins become activated, which can subsequently activate the contact system (50, 52, 55). Furthermore, these studies have also demonstrated that phagocytic cells take up complement-bound nanoparticles more efficiently than when not opsonized, a finding that is logical given that complement proteins bind to complement receptors (CR1, CR3) on phagocytes to stimulate phagocytosis, even when denatured on the surface of a nanoparticle (52-54, 56).

IgG is another prominent plasma protein and is the most common circulating antibody isotype of the immunoglobulin super family. IgGs are major components of humoral adaptive immunity, and function by binding to perceived pathogenic antigens to opsonize them *via* agglutination. The opsonisation process isolates the pathogen and increases the efficiency of recognition and ingestion by phagocytic immune cells (macrophages, mast cells and neutrophils) so the pathogen can be consumed and eliminated (57). IgGs can also activate complement, part of innate immunity, by the classical activation pathway, as described earlier (58). Therefore, the presence of IgGs in a nanoparticle protein corona could have significant impacts on the activation of phagocytic cells and several components of the adaptive and innate immune system. On a denaturing Western blot, IgG will be present as two bands corresponding to both the light (27 kDa) and heavy (55 kDa) chains. All PAA-nanoparticles had IgG in their eluted

proteomes with levels ranging from low (PAA-Fe_2O_3) to moderate (PAA-TiO_2, and PAA-ZnO) to moderately high (PAA-Capsule and PAA-CeO_2). These levels of IgG adsorption are comparable or slightly higher than those previously found on several of the most-common metal and metal nanoparticles, polymers, poly(ethylene oxide) coatings and slightly higher than what was found eluted off of sol-gel manufactures bioactive glass(8, 50, 59). However, despite significant levels of IgG detected in all the PAA-nanoparticle eluents, thrombin was not detected in any, suggesting that the complement cascade may not be activated by IgG *via* the classical activation pathway. Although, it remains possible that nanoparticle-bound IgG could still participate in the opsonisation of pathogens and alter phagocytic responses of innate immune cells. Previous work has shown that TiO_2 nanoparticles are phagocytized by macrophages via FcR surface receptors, for which IgG are ligands (60).

Although transferrin is primarily known as an iron transport protein, recent studies have demonstrated it also has a role in macrophage activation (61, 62). Transferrin was found in moderately high to high amounts on all of the PAA-nanoparticles. As transferrin is relatively uncharged it is unlikely that charge interactions, with the highly negatively charged PAA-nanoparticles, were a major role in their adsorption and elution (63). The detection of large amounts of this protein in the eluent suggests these nanoparticles may strongly activate macrophages, and together with the significant amount of IgG also detected presents a mechanism by which protein coronas stimulate phagocytic activity in activated macrophages, and/or other phagocytes.

Indeed, results from the phagocytic assay support this theory. The pre-exposure of serum to PAA-TiO_2 or PAA-Caps, prior to opsonizing GFP-*E. coli*, resulted in elevated percent phagocytosis (i.e. # of phagocytic cells) and especially phagocytic index (# of GFP-*E. coli* consumed per cell) in RBL-2H3 cells. These effects were much less pronounced in RAW 264.7 cells, possibly because of the potency that RAW 264.7 cells phagocytize materials, compared to RBL-2H3. Figure 5.5 clearly showed RAW 264.7 cells to be superior at phagocytizing GFP- *E. coli*, and phagocytic saturation was attained at much lower MOIs than for RBL-2H3 cells. Therefore, potentiating phagocytosis in RAW 264.7 cells would be more difficult since saturation is attained much faster. It is still an interesting finding that mast cells could be triggered to phagocytize more material than would normally occur without the presence of PAA-nanoparticles. As mentioned earlier, other studies have also shown that phagocytosis can be triggered by nanoparticles that are coated with complement or Ig proteins, and Binnemars-Postma *et al.* recently showed that nanoparticles exposed to serum are increasingly taken up by macrophages than nanoparticles without serum exposure (2, 53). However, our findings appear to be the first to suggest that pathogen opsonisation, as it relates to phagocytosis, is also affected from pre-exposure of nanoparticles to serum.

Results from Figure 5.10 provide a second line of evidence to support these phagocytic findings. YG-beads were used as a follow up experiment to the GFP-*E. coli* experiments because when YG-beads are not opsonized with serum proteins (i.e. PBS treatments), phagocytosis will not occur, while YG-*E. coli*

would still be consumed because of the PAMPs on pathogen surfaces. RBL-2H3 percent phagocytosis for PBS-opsonized YG-*E. coli* was nearly 16%, while for YG-beads, it was at 3.5%. Therefore, the potentiated phagocytosis of YG-beads when opsonized with FBS-exposed PAA-TiO_2 compared to FBS alone would likely be a result of the nanoparticles and the proteins contained in the corona, including high levels of IgG.

Undetected proteins

While the presence of proteins in material eluents may yield useful information, so too can the absence of proteins. Of the proteins tested for in Table 5.1, notable proteins not detected include kininogen, prekallikrein, thrombin, protein C and protein S. The absence of kininogen and prekallikrein in conjunction with the limited presence of Factors XI and XII suggest contact activation of coagulation in the presence of the tested PAA-nanoparticles is not a likely occurrence. The limited presence of prothrombin and complete lack of detected thrombin also suggest pro-coagulant stimulation is an unlikely host response to the presence of these materials. A lack of detectable protein C and protein S suggest that these PAA-nanoparticles also do not stimulate a strong fibrinolytic response, though detected antithrombin, plasminogen and $alpha_1$-antitrypsin mean the possibility of a fibrinolytic response cannot be completely discounted.

5.6. Conclusion

In this work, we have shown significant structural, clot-associated and immune-related plasma proteins in the protein corona of size-uniform PAA-nanoparticles. There were considerable differences in the composition and relative intensities of the proteins in each nanoparticle proteome, which may be related to charge differences between the nanoparticles, or to some other physicochemical property. Nevertheless, the combination of proteins resulted in significant inhibition in plasma coagulation relative to positive control by all the PAA-nanoparticles, with a complete abrogation by PAA-ZnO. The kinetic profile of each PAA-nanoparticle suggested that different aspects of the coagulation cascade were affected since in some cases the profile onset and plateau times were consistent with control (PAA-TiO_2), while in others (PAA-CeO_2, PAA-Fe_2O_3 and PAA-Caps), the onset was greatly reduced. Phagocytosis results suggested that plasma protein-bound nanoparticles enhanced the opsonisation of a pathogenic target, which potentiated phagocytosis in two immune cell types. The implications of this novel finding provide a new perspective from which to consider the impact of nanoparticles on immune responses. Not only can opsonized nanoparticles be taken up more easily but they can also cause the enhanced uptake of other circulating targets.

5.7. References

1. Walkey CD, Olsen JB, Song F, Liu R, Guo H, Olsen DWH, et al. Protein corona fingerprinting predicts the cellular interaction of gold and silver nanoparticles. ACS nano. 2014;8(3):2439-55.

2. Lee YK, Choi EJ, Webster TJ, Kim SH, Khang D. Effect of the protein corona on nanoparticles for modulating cytotoxicity and immunotoxicity. Int J Nanomedicine. 2015;10:97-113.

3. Casals E, Pfaller T, Duschl A, Oostingh GJ, Puntes VF. Hardening of the nanoparticle–protein corona in metal (Au, Ag) and oxide (Fe3O4, CoO, and CeO2) nanoparticles. Small. 2011;7(24):3479-86.

4. Maiorano G, Sabella S, Sorce B, Brunetti V, Malvindi MA, Cingolani R, et al. Effects of cell culture media on the dynamic formation of protein−nanoparticle complexes and influence on the cellular response. ACS nano. 2010;4(12):7481-91.

5. Colman RW. Are hemostasis and thrombosis two sides of the same coin? Journal of Experimental Medicine. 2006;203(3):493-5.

6. Pondman KM, Tsolaki AG, Paudyal B, Shamji MH, Switzer A, Pathan AA, et al. Complement deposition on nanoparticles can modulate immune responses by macrophage, B and T cells. Journal of biomedical nanotechnology. 2016;12(1):197-216.

7. Reddy ST, van der Vlies AJ, Simeoni E, Angeli V, Randolph GJ, O'Neil CP, et al. Exploiting lymphatic transport and complement activation in nanoparticle vaccines. Nature biotechnology. 2007;25(10):1159-64.

8. Deng ZJ, Mortimer G, Schiller T, Musumeci A, Martin D, Minchin RF. Differential plasma protein binding to metal oxide nanoparticles. Nanotechnology. 2009;20(45):455101.

9. Gordy MA, Pila EA, Hanington PC. The role of fibrinogen-related proteins in the gastropod immune response. Fish & shellfish immunology. 2015;46(1):39-49.

10. Couleau N, Techer D, Pagnout C, Jomini S, Foucaud L, Laval-Gilly P, et al. Hemocyte responses of Dreissena polymorpha following a short-term in vivo exposure to titanium dioxide nanoparticles: preliminary investigations. Science of the Total Environment. 2012;438:490-7.

11. Gagné F, Auclair J, Turcotte P, Fournier M, Gagnon C, Sauvé S, et al. Ecotoxicity of CdTe quantum dots to freshwater mussels: impacts on immune system, oxidative stress and genotoxicity. Aquatic toxicology. 2008;86(3):333-40.

12. Lillico DM, Zwozdesky MA, Pemberton JG, Deutscher JM, Jones LO, Chang JP, et al. Teleost leukocyte immune-type receptors activate distinct phagocytic modes for target acquisition and engulfment. Journal of leukocyte biology. 2015;98(2):235-48.

13. Yogasundaram H, Bahniuk MS, Singh H-D, Aliabadi HM, Uludağ H, Unsworth LD. BSA Nanoparticles for siRNA Delivery: Coating Effects on Nanoparticle Properties, Plasma Protein Adsorption, and In Vitro siRNA Delivery. International journal of biomaterials. 2012;2012:584060-.

14. Bahniuk MS, Pirayesh H, Singh HD, Nychka Ja, Unsworth LD. Bioactive glass 45S5 powders: effect of synthesis route and resultant surface chemistry and

crystallinity on protein adsorption from human plasma. Biointerphases. 2012;7(1-4):1-5.

15. Nikouei NS, Vakili MR, Bahniuk MS, Unsworth L, Akbari A, Wu J, et al. Thermoreversible hydrogels based on triblock copolymers of poly(ethylene glycol) and carboxyl functionalized poly(ε-caprolactone): The effect of carboxyl group substitution on the transition temperature and biocompatibility in plasma. Acta biomaterialia. 2014;12:81-92.

16. Abraham S, So A, Unsworth LD. Poly(carboxybetaine methacrylamide)-modified nanoparticles: a model system for studying the effect of chain chemistry on film properties, adsorbed protein conformation, and clot formation kinetics. Biomacromolecules. 2011;12(10):3567-80.

17. Sivaraman B, Latour Ra. The adherence of platelets to adsorbed albumin by receptor-mediated recognition of binding sites exposed by adsorption-induced unfolding. Biomaterials. 2010;31(6):1036-44.

18. Anderson J, Bonfield T, Ziats N. Protein adsorption and cellular adhesion and activation on biomedical polymers. The International journal of artificial organs. 1990;13(6):375-82.

19. Collier T, Anderson J. Protein and surface effects on monocyte and macrophage adhesion, maturation, and survival. Journal of Biomedical Materials Research Part A. 2002;60(3):487-96.

20. Wojciechowski P, Ten Hove P, Brash JL. Phenomenology and mechanism of the transient adsorption of fibrinogen from plasma (Vroman effect). Journal of Colloid and Interface Science. 1986;111(2):455-65.

21. Cedervall T, Lynch I, Lindman S, Berggård T, Thulin E, Nilsson H, et al. Understanding the nanoparticle–protein corona using methods to quantify exchange rates and affinities of proteins for nanoparticles. Proceedings of the National Academy of Sciences. 2007;104(7):2050-5.

22. Lu J, Stewart AJ, Sadler PJ, Pinheiro TJ, Blindauer CA. Albumin as a zinc carrier: properties of its high-affinity zinc-binding site. Portland Press Limited; 2008.

23. Farrugia A. Albumin usage in clinical medicine: tradition or therapeutic? Transfusion medicine reviews. 2010;24(1):53-63.

24. Lyman D, Klein KG, Brash J, Fritzinger B, Andrade J, Bonomo F. Platelet interaction with protein-coated surfaces: an approach to thrombo-resistant surfaces. Platelet Adhesion and Aggregation in Thrombosis: Countermeasures. 1970.

25. Cornelius R, Macri J, Cornelius K, Brash J. Interactions of Apolipoproteins AI, AII, B and HDL, LDL, VLDL with Polyurethane and Polyurethane-PEO Surfaces. Langmuir. 2015;31(44):12087-95.

26. Cornelius RM, Macri J, Cornelius KM, Brash JL. Lipoprotein interactions with a polyurethane and a polyethylene oxide-modified polyurethane at the plasma–material interface. Biointerphases. 2016;11(2):029810.

27. Macfarlane R. An enzyme cascade in the blood clotting mechanism and its function as a biochemical amplifier. Nature. 1964;202(4931):498-9.

28. Davie EW, Ratnoff OD. Waterfall sequence for intrinsic blood clotting. Science. 1964;145(3638):1310-2.

29. Romney G, Glick M. An updated concept of coagulation with clinical implications. The Journal of the American Dental Association. 2009;140(5):567-74.

30. Hoffman M. Remodeling the blood coagulation cascade. Journal of thrombosis and thrombolysis. 2003;16(1):17-20.

31. Proença-Ferreira R, Franco-Penteado CF, Traina F, Saad ST, Costa FF, Conran N. Increased adhesive properties of platelets in sickle cell disease: roles for αIIbβ3-mediated ligand binding, diminished cAMP signalling and increased phosphodiesterase 3A activity. British journal of haematology. 2010;149(2):280-8.

32. Kelly PM, Åberg C, Polo E, O'connell A, Cookman J, Fallon J, et al. Mapping protein binding sites on the biomolecular corona of nanoparticles. Nature nanotechnology. 2015;10(5):472-9.

33. Vogt C, Pernemalm M, Kohonen P, Laurent S, Hultenby K, Vahter M, et al. Proteomics analysis reveals distinct corona composition on magnetic nanoparticles with different surface coatings: Implications for interactions with primary human macrophages. PloS one. 2015;10(10):e0129008.

34. Landgraf L, Christner C, Storck W, Schick I, Krumbein I, Dähring H, et al. A plasma protein corona enhances the biocompatibility of Au@ Fe 3 O 4 Janus particles. Biomaterials. 2015;68:77-88.

35. Mosesson MW. Fibrinogen and fibrin structure and functions. Journal of thrombosis and haemostasis : JTH. 2005;3(8):1894-904.

36. Tang L, Eaton JW. Natural responses to unnatural materials: A molecular mechanism for foreign body reactions. Molecular Medicine. 1999;5(6):351-.

37. Massa TM, Yang ML, Ho JYC, Brash JL, Santerre JP. Fibrinogen surface distribution correlates to platelet adhesion pattern on fluorinated surface-modified polyetherurethane. Biomaterials. 2005;26(35):7367-76.

38. Gresele P, Page C, Fuster V, Vermylen J. Platelets in Thrombotic and Non-Thrombotic Disorders. Transfusion Medicine. 2003;13(1):57-8.

39. Davie EW, D P, Kulman JD. An Overview of the Structure and Function of Thrombin. Seminars In Thrombosis And Hemostasis. 2006;32(suppl 1):3-15.

40. Changa D. The binding of free calcium ions in aqueous solution using chelating agents, phosphates and poly (acrylic acid). Journal of the American Oil Chemists' Society. 1983;60(3):618-22.

41. Kuila D, Blay GA, Borjas RE, Hughes S, Maddox P, Rice K, et al. Polyacrylic acid (poly-A) as a chelant and dispersant. Journal of applied polymer science. 1999;73(7):1097-115.

42. Wang Q, Prigiobbe V, Huh C, Bryant SL. Alkaline Earth Element Adsorption onto PAA-Coated Magnetic Nanoparticles. Energies. 2017;10(2):223.

43. Molina H. Complement and immunity. Rheumatic Disease Clinics of North America. 2004;30(1):1-18.

44. Janeway Jr CA, Medzhitov R. Innate immune recognition. Annual review of immunology. 2002;20(1):197-216.

45. Medzhitov R, Janeway C, editors. Innate immune induction of the adaptive immune response. Cold Spring Harbor symposia on quantitative biology; 1999: Cold Spring Harbor Laboratory Press.

46. Iwasaki A, Medzhitov R. Control of adaptive immunity by the innate immune system. Nature immunology. 2015;16(4):343-53.

47. Holmskov U, Thiel S, Jensenius JC. Collectins and ficolins: humoral lectins of the innate immune defense. Annual review of immunology. 2003;21(1):547-78.

48. Endo Y, Takahashi M, Fujita T. Lectin complement system and pattern recognition. Immunobiology. 2006;211(4):283-93.

49. Andersson J, Ekdahl KN, Lambris JD, Nilsson B. Binding of C3 fragments on top of adsorbed plasma proteins during complement activation on a model biomaterial surface. Biomaterials. 2005;26(13):1477-85.

50. Engberg AE, Rosengren-Holmberg JP, Chen H, Nilsson B, Lambris JD, Nicholls IA, et al. Blood protein-polymer adsorption: Implications for understanding complement-mediated hemoincompatibility. Journal of Biomedical Materials Research Part A. 2011;97(1):74-84.

51. Chen F, Wang G, Griffin JI, Brenneman B, Banda NK, Holers VM, et al. Complement proteins bind to nanoparticle protein corona and undergo dynamic exchange in vivo. Nature nanotechnology. 2017;12(4):387-93.

52. Klapper Y, Hamad OA, Teramura Y, Leneweit G, Nienhaus GU, Ricklin D, et al. Mediation of a non-proteolytic activation of complement component C3 by phospholipid vesicles. Biomaterials. 2014;35(11):3688-96.

53. Binnemars-Postma KA, ten Hoopen HW, Storm G, Prakash J. Differential uptake of nanoparticles by human M1 and M2 polarized macrophages: protein corona as a critical determinant. Nanomedicine. 2016;11(22):2889-902.

54. Inturi S, Wang G, Chen F, Banda NK, Holers VM, Wu L, et al. Modulatory role of surface coating of superparamagnetic iron oxide nanoworms in complement opsonization and leukocyte uptake. ACS nano. 2015;9(11):10758-68.

55. Ekstrand-Hammarström B, Hong J, Davoodpour P, Sandholm K, Ekdahl KN, Bucht A, et al. TiO 2 nanoparticles tested in a novel screening whole human blood model of toxicity trigger adverse activation of the kallikrein system at low concentrations. Biomaterials. 2015;51:58-68.

56. Hamad OA, Nilsson PH, Wouters D, Lambris JD, Ekdahl KN, Nilsson B. Complement component C3 binds to activated normal platelets without preceding proteolytic activation and promotes binding to complement receptor 1. The journal of immunology. 2010;184(5):2686-92.

57. Anderson JM, Rodriguez A, Chang DT. Foreign body reaction to biomaterials. Seminars in immunology. 2008;20(2):86-100.

58. Abbas AK. Cellular and molecular immunology. In: Lichtman AH, Pillai S, editors. 6th ed. ed. Philadelphia :: Saunders Elsevier; 2007.

59. Unsworth LD, Sheardown H, Brash JL. Polyethylene oxide surfaces of variable chain density by chemisorption of PEO-thiol on gold: Adsorption of proteins from plasma studied by radiolabelling and immunoblotting. Biomaterials. 2005;26(30):5927-33.

60. Scherbart AM, Langer J, Bushmelev A, van Berlo D, Haberzettl P, van Schooten F-J, et al. Contrasting macrophage activation by fine and ultrafine titanium dioxide particles is associated with different uptake mechanisms. Particle and fibre toxicology. 2011;8(1):31.

61. Moos T, Morgan EH. Transferrin and transferrin receptor function in brain barrier systems. Cellular and molecular neurobiology. 2000;20(1):77-95.

62. Stafford JL, Belosevic M. Transferrin and the innate immune response of fish: identification of a novel mechanism of macrophage activation. Developmental and comparative immunology. 2003;27(6-7):539-54.

63. Ortega V, Katzenback B, Stafford J, Belosevic M, Goss G. Effects of polymer-coated metal oxide nanoparticles on goldfish (Carassius auratus L.) neutrophil viability and function. Nanotoxicology. 2015;9(1):23-33.

6. High-yield recombinant expression and purification of marginally soluble, short elastin-like polypeptides

Published as “Bahniuk MS, Alshememry AK, Unsworth LD. High-yield recombinant expression and purification of marginally soluble, short elastin-like polypeptides. BioTechniques. 2016 Dec;61(6):297-304.”

Abstract

The protocol described here is designed as an extension of existing techniques for creating elastin-like polypeptides. It allows for the expression and purification of elastin-like polypeptide (ELP) constructs that are poorly expressed or have very low transition temperatures. DNA concatemerization has been modified to reduce issues caused by methylation sensitivity and inefficient cloning. Linearization of the modified expression vector has been altered to greatly increase cleavage efficiency. The purification regimen is based upon using denaturing metal affinity chromatography to fully solubilize and, if necessary, pre-concentrate the target peptide before purification by inverse temperature cycling (ITC). This protocol has been used to express multiple leucine-containing elastin-like polypeptides, with final yields of 250–660 mg per liter of cells, depending on the specific construct. This was considerably greater than previously reported yields for similar ELPs. Due to the relative hydrophobicity of the tested constructs, even compared with commonly employed ELPs, conventional methods would not have been able to be purify these peptides.

6.1. Introduction

Elastin-like polypeptides (ELPs) are protein-based biopolymer analogs of mammalian elastin (1). The general architecture of an ELP sequence is any number of repeats of the amino acid sequence valine-proline-glycine-X-glycine (VPGXG), where X can be any amino acid except proline (2). In elastin, this

guest amino acid is typically valine. What makes this particular sequence of amino acids distinct is that it can reversibly undergo self-assembly in reaction to changes in local environmental factors such as temperature and salinity (1). The ELP amino acid chain typically exists in a random coil conformation in solution, but upon heating, it undergoes a conformational change, adopting a β-spiral conformation (3). These spirals then self-associate to form aggregates. Upon cooling, it is thought that ELPs revert to a random coil conformation and regain solubility.

The exact environmental conditions under which ELPs change their conformation and solubility depend greatly upon the number of repeats of the VPGXG sequence and the side chain chemistry of the amino acid in the guest amino acid position (2). This effectively means that ELPs can be customized to aggregate under very specific conditions and can be employed in a variety of situations. ELPs are being used in a number of applications, including protein purification, environmental sensing, customizable drug delivery vehicles, and as a method of targeting the delivery of drugs to specific areas (4,–7). In addition to their flexibility, the preliminary biocompatibility of ELPs has been favorable and because they are made up of amino acids, there are few concerns about toxic degradation products (8). Another advantage of using protein-based polymers such as ELPs is that they can be produced recombinantly by inserting a DNA gene encoding an ELP into *Escherichia coli*, using the bacteria as molecular factories. Making these types of molecules using recombinant methods allows for an unprecedented level of control over the final product compared with traditional

polymer synthesis and can allow for the straightforward incorporation of various biofunctional moieties, including targeting, cell penetrating, and enzymatically cleavable sequences.

The purification of recombinantly produced proteins is typically the largest bottleneck in their production, but with ELPs, their reversible solubility can be exploited to partially simplify purification under the correct conditions. This approach is known as inverse temperature cycling (ITC) and was first demonstrated by Meyer and Chilkoti (9). While ELPs and their potential applications are attractive and worth pursuing, there has until now been no published systematic protocol for expressing and purifying marginally soluble, short ELPs, and in our experience, standard protocols are inadequate for this subset of ELPs.

DNA sequences encoding for ELPs are by their very nature highly repetitive and are often rich with G-C base pairs. These two characteristics makes it difficult to work with these types of sequences in the lab and also prohibitively expensive to synthesize large ELP genes commercially. Techniques such as PCR, which depends on the melting and re-annealing of double-stranded DNA, may not function well, if at all, for ELP-encoding DNA sequences. Fortunately, through the clever application of specific restriction enzymes, short commercially sourced ELP genes can be concatemerized together. This process is known as recursive directional ligation (RDL) (10). Here, we describe a protocol featuring modifications to RDL designed to address technical bottlenecks experienced in our lab, including inefficient restriction enzyme cleavage due to DNA

methylation, significant numbers of incorrect vector-only clones during attempted ELP sequence concatemerization, and minimal *Sfi*I cleavage when using only one cleavage site in the expression vector modifying sequence. Our modifications greatly increase the overall efficiency of the RDL process while minimizing time- and reagent-intensive steps, such as modified-expression-vector linearization and mass colony screening.

The protein sequences created from these difficult-to-process DNA sequences can also be troublesome to deal with. Given that ELPs are generally hydrophobic regardless of their conformation, even routine lab procedures such as spin concentration, dialysis, and long-term storage become more complicated. Care must also be taken to not lose ELPs due to non-specific adsorption to sample tubes during routine handling. The ELPs covered here are highly repetitive, typically uncharged, relatively hydrophobic, and can spontaneously precipitate out of solution when stored at high concentrations at temperatures as low as 4°C for long periods of time. While these characteristics are integral to the unique reversible solubilization of ELPs, they also make their purification and downstream sample handling a delicate affair.

When ELPs have been purified successfully, for the most part the guest amino acids in these constructs fall toward the middle of Urry's ELP hydrophobicity scale (11). While ITC purification has been sufficient for these types of constructs, it is not applicable to all ELPs. Successfully employing an ITC-only purification procedure means the ELP construct and its expression have to meet certain criteria: The ELP must not end up in the insoluble fraction of the

cell lysate during the lysis procedure; the ELP must be in its soluble monomer form in the cell lysate; the phase transition needs to be triggered in the cell lysate under reasonable temperature and salinity conditions; and the protein must be expressed at a concentration high enough for a phase transition to be possible under reasonable conditions but must also be low enough to avoid significant depression of the transition temperature as well as the formation of inclusion bodies. Not all ELP purifications meet these criteria. If an ELP is poorly expressed, or if it contains guest amino acids that are significantly more hydrophilic or hydrophobic than those commonly employed in the literature, or if the ELPs are significantly longer or shorter than what is commonly used, the transition temperature of the ELP construct may be too high or too low for an ITC-only approach.

Some work has been carried out on shorter, hydrophobic ELPs using maltose binding protein (MBP) as a solubility and affinity-purification partner as a way to circumvent the above issues (12). This has, however, introduced another complication in that the MBP must then be separated from the hydrophobic ELP, an approach with varying levels of success depending on the ELP construct in question (12). More recently an ITC-only purification approach has been used to produce the ELPs without the interfering MBP, but the yields of purified protein severely limit the applications of such an approach (13).

6.2. Method summary

This efficient and dependable method for the high-yield production and purification of short, marginally soluble, elastin-like polypeptides (ELPs) involves increasing the reliability of DNA concatemerization procedures and utilizing denaturing metal affinity chromatography to ensure these ELPs are fully soluble and recoverable from insoluble cell debris. If the ELPs are poorly expressed, this also serves as a pre-concentration step to maximize the ELP concentration before temperature cycling purification.

6.3. Materials and Methods

A complete listing of the materials used in this study and a detailed protocol are provided in the Supplementary Material.

6.3.1. ELP gene concatemerization and cloning

A synthetic oligonucleotide encoding for 10 repeats of VPGLG (L_{10}) was purchased from Integrated DNA Technologies (Coralville, IA). Due to its length the oligonucleotide was provided in a pIDT-blue plasmid. This plasmid was transformed into XL10 Gold competent *E. coli* cells (Agilent Technologies, Santa Clara, CA), and the cells were grown in liquid culture to produce large amounts of the ELP-containing plasmid. The ELP gene was obtained from the plasmid by double digesting it with the *EcoR*I and *HinD*III restriction enzymes (all restriction enzymes were purchased from New England BioLabs, Ipswich, MA) and purified

by agarose gel electrophoresis. The gene was ligated into a pUC19 vector (Bio Basic, Ontario, Canada) that was also digested by the same restriction enzymes. Correct gene insertion was confirmed by double digestion with restriction enzymes *Bgl*I and *Nde*I.

Oligomerization of the ELP gene was carried out using a modified recursive directional ligation (RDL) scheme. Vector DNA was linearized using *PflM*I, purified using gel electrophoresis, digested again with *PflM*I, and dephosphorylated using Antarctic phosphatase (New England Biolabs). Insert DNA was double-digested with *PflM*I and *Bgl*I and purified using gel electrophoresis. The two ELP-containing genes were ligated together and transformed into XL10 Gold cells. A double digest using *PflM*I and *Bgl*I confirmed successful gene concatemerization. This RDL process was repeated to generate ELP genes with increasing numbers of repeats.

For the RDL-generated ELP genes to be inserted into a pET-25b(+) expression vector (EMD Millipore, Ontario, Canada), a short modifying sequence containing two *Sfi*I cleavage sites along with the N- and C-terminal sequences of the ELP was first added. As with the L_{10} gene above, the synthetic oligonucleotide was purchased commercially (Integrated DNA Technologies), supplied in a vector, transformed into XL10 *E. coli*, and the sequence of interest was isolated using the *EcoR*I and *Nde*I restriction enzymes. The expression vector was similarly linearized and then ligated with the isolated modifying sequence. A post-ligation digest with *BamH*I before transformation was used to greatly reduce

the number of vector-only clones. Vector modification was confirmed by single digests with either *BamH*I or *Sfi*I.

To prepare for insertion of the ELP gene into the modified expression vector, the vector was digested with *Sfi*I, purified by gel electrophoresis, digested again, and then dephosphorylated. The insert was prepared in the same manner as the inserts for RDL. The two were ligated together, and a post-ligation *Sfi*I digest was performed before transformation to reduce the number of incorrect colonies observed after cloning. Restriction enzyme digestions and DNA sequencing confirmed the final plasmid sequences.

6.3.2. Expression and purification

ELP expression vectors were transformed into OneTouch BL21 (DE3) *E. coli* (Invitrogen, Carlsbad, CA) cells, and 1 L cultures of these cells were grown in Terrific Broth (TB) (Thermo Fisher Scientific, Waltham, MA) supplemented with 100 μg/mL ampicillin (Thermo Fisher Scientific) and 10 mM L-proline (Sigma-Aldrich, St. Louis, MO). Expression was induced for 24 h using 2 mM isopropyl β-D-1-thiogalactopyranoside (Thermo Fisher Scientific).

Purification was achieved by first performing denaturing metal-affinity chromatography and eluting the ELPs using an imidazole step gradient. Buffered 8 M urea (Thermo Fisher Scientific) was used to lyse the cells and ensure the ELPs were fully soluble and free from any inclusion bodies. The urea was removed during the extensive column washing. Eluents were screened for the

presence of ELPs by gel electrophoresis or by heating them to room temperature or 37°C, depending on the construct, and observing which samples turned reversibly cloudy. Samples confirmed to contain ELPs were combined and then subjected to one round of ITC for final purification. The temperature used to cause ELP aggregation varied depending on the construct. The purification was confirmed with denaturing PAGE (SDS-PAGE) and the ELP concentrations were measured by sample absorbance at 280 nm.

6.4. Results and Discussion

Many of the design considerations for new ELP sequences have been discussed in detail previously (10). Briefly, the design of the initial DNA sequences should take into account *E. coli* codon bias; that is, the frequency of the employed triplet codons should reflect the naturally occurring frequency of their corresponding tRNAs. The ends of the ELP DNA sequences should be designed such that oligomerization of the DNA eliminates the *Pfl*MI and *Bgl*I cleavage sites without introducing another cut site for a restriction enzyme employed downstream. While these restriction enzymes are used here to facilitate ELP gene oligomerization, they are not the only two that could be used. In addition to the published guidelines, if individual oligonucleotides are being used, rather than genes already contained in plasmids, the oligonucleotides should be ordered in a semi-purified state. If the oligonucleotides are ordered with only standard

desalting as the purification method, there is a high probability that an undesirable heterogeneous product will be obtained because of the highly repeated sequence.

The basic workflow of RDL has been based on the work of Meyer and Chilkoti (10). Modifications have been introduced to both maximize restriction enzyme digest efficiency by minimizing interference by methylation and significantly decrease the likelihood of incorrect background colonies by maximizing vector linearization and purity. This drastically reduces the number of colonies that must be screened in order to find the correct RDL product. We found that methylation was less of a concern when using XL10-Gold *E. coli* as opposed to the XL1-Blue strain. Before switching host cell lines, restriction enzyme digests were usually only 30%–40% efficient. This drastically reduced the yield of linearized vector and correctly digested inserts necessary for RDL. The number of background colonies was decreased by gel purifying the digested vectors, repeating the linearization procedure, and then dephosphorylating the vector. These additional steps help to reduce the number of background colonies resulting from both uncut vector DNA and re-closed empty vectors. Without this additional effort, the number of clones containing only the vector completely eclipsed the number of correctly ligated clones. These precautions reduced the proportion of incorrect clones from ~95% to <5%. Figure 6.1 shows the results of an RDL colony screening procedure and clearly demonstrates the complete lack of empty vector clones. The time required to screen clones to find a correct ligation is greatly reduced by performing all of the steps above to reduce both uncut vector and religated DNA. Useful controls for the RDL cloning procedure

consisting of DNA ligation reactions where the ELP insert and/or ligase enzyme are replaced by water can be used to assess the amount of empty vector that makes it through the ligation procedure.

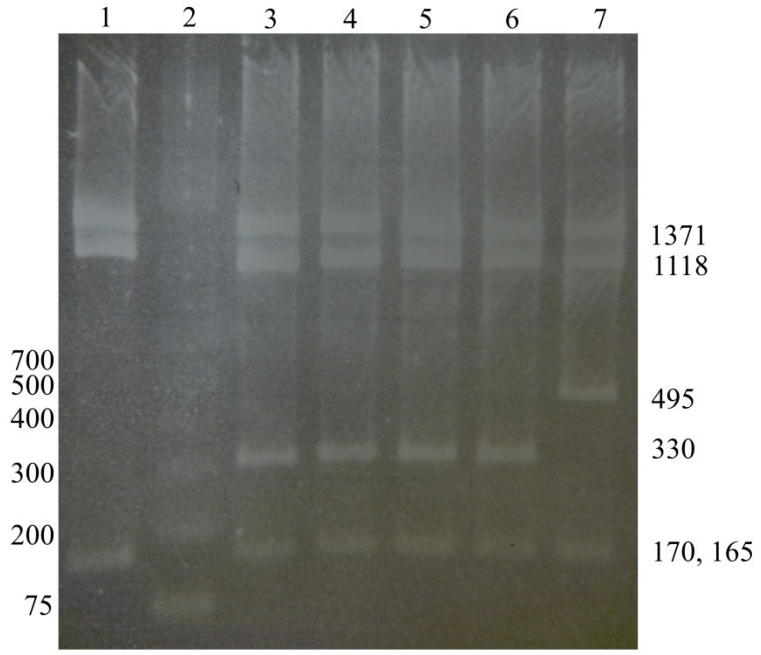

Figure 6.1. Sample results demonstrating a successful doubling of an elastin-like polypeptide (ELP) L_{10} insert to L_{20}. 20. Plasmids were digested with *PflM*I and *Bgl*I for 1 h and then run on a 2% agarose gel before being stained with ethidium bromide. This digest should yield 170, 1118 and 1371 bp bands from the vector, plus an ELP band whose size will vary. In this instance, the L10 gene was 165 bp long, the L20 gene was 330 bp, and the L_{30} gene was 495 bp. Lane 1 is a positive control digest of pUC19-L10, Lane 2 is the molecular weight ladder, and Lanes 3–7 are clones from the RDL reaction concatemerizing L_{10} to L_{20}. Based on the increase in band sizes, Lanes 3–6 contain the genes for L_{20}, while Lane 7 likely contains an L_{30} gene. Note that the 170 bp vector-derived fragment is clearly visible in Lanes 3–7 but overlaps the L_{10} gene in Lane 1. The L_{30} is the result of a double insertion of the ELP L_{10} gene into a single cloning vector. This is not an uncommon occurrence while performing RDL using the recommended molar ratios of insert to vector and may actually be beneficial in some cases.

Modification of the expression vector before insertion of the ELP gene is a necessary step of RDL (10). In order for the RDL strategy to generate complete repeats of an ELP gene, some of the DNA encoding for N- and C-terminal amino acids cannot be included in the original ELP oligonucleotide and must be added in the expression vector. This also allows for the introduction of various N- and C-terminal modifications without needing to redo the entire RDL procedure. Two *Sfi*I sites and a spacer of appropriate length need to be added to the pET-25b(+) vector so that the RDL-derived ELP gene can be inserted into the expression vector. This is a subtle but very significant departure from previous RDL methods (10). The *Sfi*I restriction enzyme is quite uncommon in its structure, and the majority of the literature on this enzyme states that efficient cleavage of DNA by *Sfi*I only occurs when 2 of its recognition sites are present and separated by roughly 200–300 bp (14–17). The *Sfi*I enzyme works by simultaneously cleaving at both recognition sites, which results in one compatible set of sticky ends in the vector. Some RDL literature suggests that a single *Sfi*I recognition site is sufficient (9,10); however, efficient and reproducible cleavage was only observed in our work when two appropriately spaced recognition sites were located in the same stretch of DNA. A vector with a single *Sfi*I site was only cleaved with ~10% efficiency, whereas a vector with two *Sfi*I sites and a spacer had a cleavage efficiency of ~100%. Using a vector with a single *Sfi*I site and doping the digest reaction with a short double-stranded DNA oligonucleotide also containing an *Sfi*I cut site did not significantly improve vector linearization in our experience. The modification sequence we designed contained the DNA for the N- and C-terminal

amino acids of the ELP gene, the two *Sfi*I restriction sites and their spacer, a tobacco etch virus protease recognition site, and a polyhistidine tag.

ELPs were expressed by a conventional IPTG induction method. There are other protocols that suggest uninduced expression yields more ELP (18); however, we have found that IPTG induction of these constructs and a 24 h expression period dramatically increased expression yields. Numerous parameters were tested, including expression time, OD_{600} at time of induction, incubation temperature, IPTG concentration, and uninduced expression. The expression conditions described here represent those that worked well for the corresponding constructs; however, they may not be ideal for the expression of other ELPs, and some sequence specific optimization may be required.

In most circumstances, standard Tris-glycine SDS-PAGE was sufficient unless small ELPs such as L_{20} were being produced. In this case, Tris-tricine electrophoresis allowed for superior resolution of the low molecular weight products. The tricine SDS-PAGE method has been modified in order to scale down the gel sizes for a Bio-Rad Mini-Protein Tetra Cell system (see protocol in Supplementary Material) (19). In all cases, gels were negatively stained with $CuCl_2$ (20) as some literature suggests conventional Coomassie staining does not work on ELPs (21).

Denaturing nickel affinity chromatography was the first method used to purify the ELPs. It was chosen because it can act as a pre-concentration step for poorly expressed ELPs and also because the use of urea helps to ensure that

individual ELPs, as well as any inclusion bodies, are fully solubilized. Especially with very hydrophobic ELPs, there is a chance their transition temperature is below room temperature and that they would end up being inadvertently removed from solution when centrifuging away insoluble cellular contaminants. If the ELPs are poorly expressed, their low concentration could potentially cause the mass aggregation temperature to be prohibitively high, thus making an exclusively ITC-based purification impossible. We found that an overnight binding of the crude cell lysate to the nickel affinity column beads is crucial to recovering large amounts of ELP. In other ELP purification protocols polyethyleneimine is used to remove DNA; however, it is not necessary for denaturing nickel affinity chromatography, and in our experience, polyethyleneimine actually precipitated the hydrophobic ELPs as well as the DNA. Other ELP constructs may elute at different imidazole concentrations, so gradient elutions may need to be optimized for ELP constructs not used in this study. Figure 6.2 illustrates the elution of a leucine-containing ELP and the reversible cloudiness that corresponds to eluents containing significant amounts of the protein.

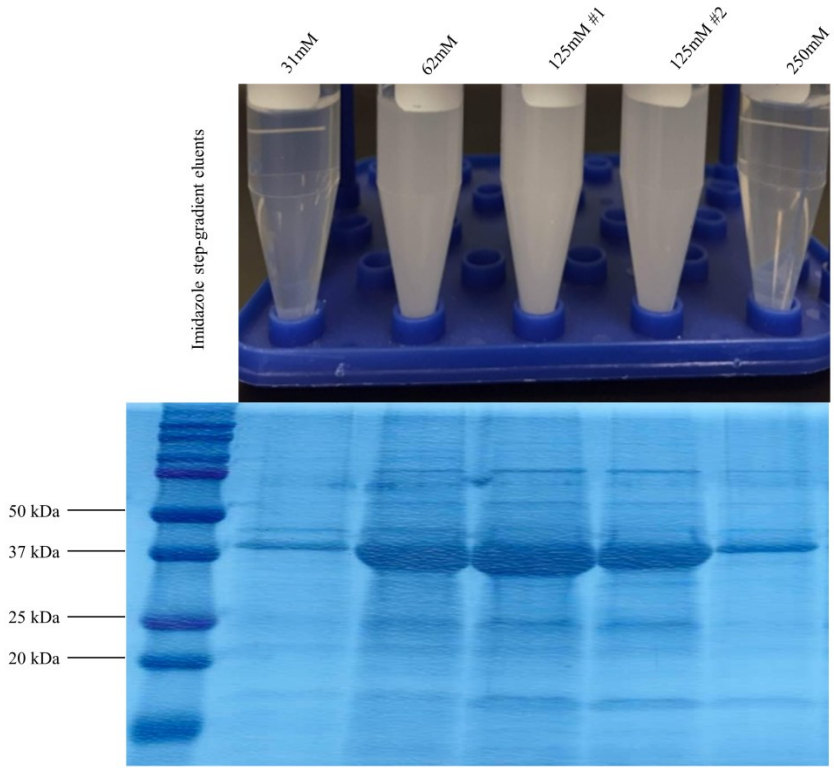

Figure 6.2. Demonstration of the concentration effects for elastin-like polypeptide (ELP) L_{80}–containing metal-affinity eluents. The sample tubes represent various imidazole step-gradient eluents from a purification of ELP L_{80} from the Ni-NTA column left at room temperature for a few minutes. From left to right, the tubes and their corresponding lanes on a $CuCl_2$-stained 12% SDS-PAGE gel are the 31 mM, 62 mM, 125 mM #1, 125 mM #2, and 250 mM imidazole eluents in 25 mM Tris, 50mM NaCl, pH 8.0. This ELP has a molecular weight of 39.7 kDa; 125 mM #1 and 125 mM #2 refer to sequential fractions of the same eluent. Sample volumes of 15 µL were loaded onto the SDS-PAGE gel. The cloudiness was easily reversed simply by placing the tubes at 4°C for a few minutes.

ITC was then used to purify the ELPs from any contaminating proteins left over from the metal affinity chromatography. This is a common method for purifying ELPs, and it is readily employed throughout the literature. ITC will only work, however, if the ELPs are sufficiently concentrated so that they can undergo a phase transition under reasonable conditions and they are not so hydrophobic as to have a mass aggregation temperature below the freezing point of water. For our

hydrophobic proteins, the transition temperatures can fall below room temperature and as such, supplementary NaCl and heated centrifugation were not always necessary. Because of the immobilized metal affinity chromatography, only one round of ITC was necessary to fully purify the ELPs. Figure 6.3 shows the affinity chromatography eluents and their subsequent purification using only one round of ITC. Determining the appropriate conditions for purifying an ELP using ITC may require some optimization. Mass spectrometry was carried out on the purified ELPs, and we found that most leucine-containing ELPs did not elicit a strong signal. L_{40}, however, did respond well, and its measured molecular weight was 21,155 Da, which matches with the expected molecular weight of 21,125, within the margin-of-error of the spectrometer. Because all of the leucine-containing ELPs were derived from the same DNA sequence, this result suggests there are no reasons to doubt the identity of the other ELPs.

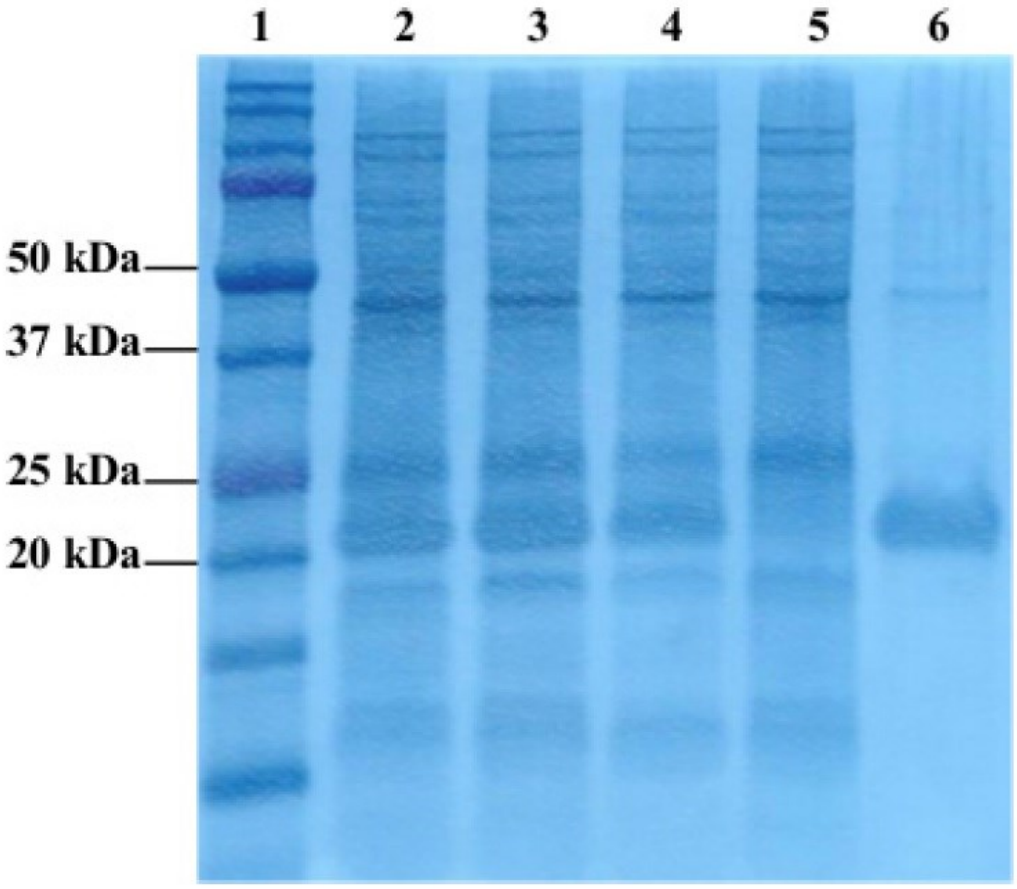

Figure 6.3. Polyacrylamide gel demonstrating the results of metal-affinity and inverse temperature cycling (ITC) purification of elastin-like polypeptide (ELP) L_{40}. Lane 1 was loaded with 5 μL of the molecular weight ladder. Lanes 2–4 were loaded with 15 μL samples of eluents from the metal-affinity purification eluted with 62 mM imdiazole (Lane 2) and 125 mM imidazole (Lanes 3 and 4) and showing the ELP band at 21 kDa. Lane 5 shows the impurities from 15 μL eluent collected after the hot spin in the ITC procedure, and Lane 6 was loaded with 15 μL of the final purified ELP sample after the cold spin and shows the ELP primarily as a monomer but with a small amount of dimer as well. Samples were run on a Tris-tricine gel and stained with $CuCl_2$.

Existing ITC purification approaches depend on triggering an ELP phase transition in the *E. coli* cellular lysate. This requires the solubility, transition temperature, and concentration of the ELP to fall within a certain range of values for a successful transition to be possible. For ELPs with a small number of repeats, and thus a high transition temperature, this approach may not be feasible.

Additionally, constructs with strongly hydrophobic guest amino acids may have transition temperatures near or below the freezing point of water and, as such, the ITC-only approach may not be viable. In this case, the ELP may be inadvertently removed from the cell lysate when it undergoes centrifugation to remove the insoluble cell debris from the soluble fraction. The result could be the same if the ELPs are overexpressed and end up in inclusion bodies. Preliminary purifications of the leucine-containing ELPs using conventional non-denaturing tip sonication and ITC-only purifications yielded minimal amounts of protein. As such, a new purification approach was necessary.

The advantage of our method is that it is applicable to a wider range of ELP constructs than ITC-only purification procedures. The protocol uses denaturing metal affinity chromatography as the first step in purification. This ensures the ELPs are fully soluble upon cell lysis, in case they have very low transition temperatures or are expressed as inclusion bodies. Should there be an additional, chaotrope-sensitive domain appended to the ELP, non-denaturing metal affinity chromatography may be an acceptable substitute. The chromatography can also be used to concentrate the ELPs in order to lower their transition temperature to more reasonable levels should they be poorly expressed or have high transition temperatures at moderate concentrations. For instance, this hybrid method was used to successfully purify a conventional hydrophilic ELP construct in our lab that was so poorly expressed (0.35 mg per liter of cells) that standard ITC-only purification failed because the phase transition could not be triggered due to such a low ELP concentration. The chromatography was key to

successful purification because it allowed us to significantly pre-concentrate the ELP before attempting ITC. Our hybrid purification approach has been used to successfully purify as much as 660 mg of marginally soluble, short ELPs per liter of cells. While this value varied depending on the specific length of the construct, observed yields ranged 250–660 mg/L. These results are a significant improvement over our in-house attempts to apply conventional ITC-only purification methods to this class of ELPs as well as previously reported yields of comparable marginally soluble, short ELPs that produced roughly 10 and 35 mg per liter of cells, respectively (12,13). The first purification step serves to remove a large number of contaminating proteins that would otherwise be carried over into the subsequent ITC step. These contaminating proteins typically would require multiple rounds of ITC to be removed, but by employing affinity chromatography first, a pure product can be obtained after one round of ITC. Furthermore, by using a small polyhistidine tag for the affinity purification, rather than a larger multi-kilodalton partner such as MBP or glutathione S-transferase, it may not be necessary to remove the affinity tag. This reduces the amount of sample preparation and eliminates potential complications if the ELP complexes with its purification partner after the two are cleaved from one another.

Our new protocol is designed to improve the overall efficiency of the RDL DNA concatemerization process by using a combination of denaturing metal affinity chromatography and ITC to purify ELPs that would otherwise be unpurifiable using an ITC-only procedure. It does not require the use of large solubility or affinity partners and only requires a short polyhistidine tag, which

may not necessarily need to be removed depending on the downstream applications for which the ELPs will be used. This protocol is designed specifically to expand upon ITC-based purifications to allow for the rapid purification of constructs that are: (i) poorly-expressed; (ii) expressed in inclusion bodies or as ELP aggregates; (iii) short constructs with high transition temperatures; and/or (iv) ELPs with strongly hydrophobic guest amino acids.

6.5. Author contributions

M.S.B. and L.D.U. contributed to the conception of the study. M.S.B. and A.K.A. contributed to the development, analysis, and execution of the experiments. M.S.B., A.K.A., and L.D.U. wrote and edited the manuscript.

6.6. Acknowledgments

The authors would like to acknowledge Wayne Materi, Valentyna Semenchenko, Angela Marilyn Brigley, and Catherine de Guzman for their advice and technical assistance. This work was supported by the Natural Sciences and Engineering Research Council of Canada Discovery grant #RES0011279. M.S.B. was supported by the Alberta Innovates Technology Futures graduate student scholarship in nanotechnology #200801440. A.K.A. was the recipient of the Ministry of Higher Education and King Saud University Scholarship, Saudi Arabia.

6.7. Competing interests

The authors declare no competing interests.

6.8. Correspondence

Address correspondence to Markian S. Bahniuk: Department of Biomedical Engineering, 1098 Research Transition Facility, 8308-114 Street, University of Alberta, Edmonton, Alberta, Canada T6G 2V2, E-mail: mbahniuk@ualberta.ca; or Larry D. Unsworth, Department of Chemical and Materials Engineering, University of Alberta, 13-390 - Donadeo Innovation Centre for Engineering (ICE), 9211 - 116 Street, Edmonton, Alberta, Canada T6G 1H9, E-mail: larry.unsworth@ualberta.ca

6.9. References

1. Urry, D.W. 1988. Entropic elastic processes in protein mechanisms. I. Elastic structure due to an inverse temperature transition and elasticity due to internal chain dynamics. J. Protein Chem 7:1-34.

2. Urry, D.W., C.H. Luan, T.M. Parker, D.C. Gowda, K.U. Prasad, M.C. Reid, and A. Safavy. 1991. Temperature of polypeptide inverse temperature transition depends on mean residue hydrophobicity. J. Am. Chem. Soc 113:4346-4348.

3. Urry, D.W., T.L. Trapane, and K.U. Prasad. 1985. Phase-structure transitions of the elastin polypentapeptide-water system within the framework of composition-temperature studies. Biopolymers 24:2345-2356.

4. Ge, X., D.S.C. Yang, K. Trabbic-carlson, B. Kim, A. Chilkoti, H. Hall, and N. Carolina. 2005. Self-Cleavable Stimulus Responsive Tags for Protein Purification without Chromatography. J. Am. Chem. Soc 127:11228-11229.

5. Cole, M.A., N.H. Voelcker, H. Thissen, and H.J. Griesser. 2009. Stimuli-responsive inter faces and systems for the control of protein–surface and cell–surface interactions. Biomaterials 30:1827-1850.

6. Chilkoti, A., M.R. Dreher, and D.E. Meyer. 2002. Design of thermally responsive, recombinant polypeptide carriers for targeted drug delivery. Adv Drug Deliv Rev 54:1093-1111.

7. Bidwell, G.L., A.N. Davis, I. Fokt, W. Priebe, and D. Raucher. 2007. A thermally targeted elastin-like polypeptide-doxorubicin conjugate overcomes drug resistance. Invest. New Drugs 25:313-326.

8. Urry, D.W., T.M. Parker, M.C. Reid, and D.C. Gowda. 1991. Biocompatibility of the bioelastic materials, poly(GVGVP) and its γ-irradiation cross-linked matrix: summary of generic biological test results. J. Bioact. Compat. Polym 6:263-282.

9. Meyer, D.E., and A. Chilkoti. 1999. Purification of recombinant proteins by fusion with thermally-responsive polypeptides. Nat. Biotechnol 17:1112-1115.

10. Meyer, D.E., and A. Chilkoti. 2002. Genetically encoded synthesis of protein-based polymers with precisely specified molecular weight and sequence by recursive directional ligation: examples from the elastin-like polypeptide system. Biomacromolecules 3:357-367.

11. Urry, D.W., D.C. Gowda, T.M. Parker, C.H. Luan, M.C. Reid, C.M. Harris, A. Pattanaik, and R.D. Harris. 1992. Hydrophobicity scale for proteins based on inverse temperature transitions. Biopolymers 32:1243-1250.

12. Bataille, L., W. Dieryck, A. Hocquellet, C. Cabanne, K. Bathany, S. Lecommandoux, B. Garbay, and E. Garanger. 2015. Expression and purification of short hydrophobic elastin-like polypeptides with maltose-binding protein as a solubility tag. Protein Expr. Purif 110:165-171.

13. Bataille, L., W. Dieryck, A. Hocquellet, C. Cabanne, K. Bathany, S. Lecommandoux, B. Garbay, and E. Garanger. 2016. Recombinant Production and Purification of Short Hydrophobic Elastin-Like Polypeptides with Low Transition Temperatures. Protein Expr Purif 121:81-87.

14. Wentzell, L.M., T.J. Nobbs, and S.E. Halford. 1995. *Sfi*I restriction endonuclease makes a four-strand DNA break at two copies of its recognition sequence. J. Mol. Biol 248:581-595.

15. Nobbs, T.J., M.D. Szczelkun, L.M. Wentzell, and S.E. Halford. 1998. DNA excision by the *Sfi* I restriction endonuclease. J. Mol. Biol 281:419-432.

16. Wentzell, L.M., and S.E. Halford. 1998. DNA looping by the *Sfi* I restriction endonuclease. J. Mol. Biol 281:433-444.

17. Williams, S.A., and S.E. Halford. 2001. I endonuclease activity is strongly influenced by the non-specific sequence in the middle of its recognition site. Nucleic Acids Res 29:1476-1483.

18. Chow, D.C., M.R. Dreher, K. Trabbic-Carlson, and A. Chilkoti. 2006. Ultra-high expression of a thermally responsive recombinant fusion protein in *E. coli*. Biotechnol Prog 22:638-646.

19. Schägger, H. 2006. Tricine – SDS-PAGE. Nat Protoc 1:16-22.

20. Lee, C., A. Levin, and D. Branton. 1987. Copper staining: a five-minute protein stain for sodium dodecyl sulfate-polyacrylamide gels. Anal. Biochem 166:308-312.

21. McPherson, D.T., J. Xu, and D.W. Urry. 1996. Product purification by reversible phase transition following *Escherichia coli* expression of genes encoding up to 251 repeats of the elastomeric pentapeptide GVGVP. Protein Expr Purif 7:51-57.

7. Self-Assembly/Disassembly Hysteresis of Nanoparticles Composed of Marginally Soluble, Short Elastin-Like Polypeptides

7.1. Abstract

Elastin-like polypeptides (ELPs) are a fascinating biomaterial that has undergone copious development for a variety of therapeutic applications including as a nanoscale drug delivery vehicle. The systematic examination of leucine-containing ELPs endeavours to expand existing knowledge about fundamental assembly-disassembly behaviours to increasingly hydrophobic sequences. It was observed that these marginally soluble, short ELPs tend to behave consistently with previous observations related to assembly-related ELP phase transitions but deviated in their disassembly. It was found that chain length, concentration and overall sequence hydrophobicity may influence the irreversible formation of sub-micron particles as well as the formation of multi-micron scale, colloidally unstable aggregates. Amino acid composition affected surface charge and packing density of the particles. Particle stability upon dilution was found to vary depending upon chain length and hydrophobicity, with particles composed of longer and/or more hydrophobic ELPs being more resistant to disassembly upon isothermal dilution. Taken together, these results suggest marginally soluble ELPs may self-assemble but not disassemble as expected and that parameters including particle size, zeta potential and dilution resistance would benefit from further systematic evaluations. This information has the potential to reveal novel preparation methods capable of expanding the utility of all existing ELP-based biomaterials.

Keywords: elastin-like polypeptides, hysteresis, dynamic light scattering, inverse temperature transition, dilution stability

7.2. Introduction

Elastin-like polypeptides (ELPs) are a fascinating biomaterial resulting from the fusion of the fields of biology, biochemistry and engineering. Based upon a highly repetitive sequence derived from mammalian elastin, ELPs are a versatile, customizable, stimuli-responsive biopolymer capable of self-assembling into a variety of architectures (1). The most common ELP is composed of any number of repeats of the pentapeptide sequence valine-proline-glycine-X-glycine (VPGXG) where X can be any amino acid except proline (2). This sequence can undergo a reversible phase transition in response to environmental stimuli and self-assemble into nano or micron-scale structures. There are a variety of stimuli capable of triggering this assembly including temperature, salt concentration, pH, light and the binding of a ligand, though temperature is the most commonly employed (3, 4). The sequence and architecture of the ELP construct itself contributes substantially to the exact conditions required to trigger the phase transition, resulting in a flexible and programmable platform technology (5-8). It is in part due to the relative ease of modification of the ELP family that it is a system under vigorous development for a wide variety of applications. ELPs are being developed for recombinant protein purification, tissue engineering and nanoscale targeted drug delivery (9-11). There are numerous reviews in the literature detailing the myriad of ways in which ELPs are being engineered for specific applications (11-17).

Despite the widespread development of ELP-based biomaterials, the behaviour of ELPs is still not fully understood. For instance, the mechanism responsible for the reversible phase transition of ELPs is still an area of active investigation. The most recent models suggest that ELPs are intrinsically disordered and capable of momentarily adopting local beta-turn and polyproline structures both below and above their transition temperatures and that sudden decreased backbone solvation may cause ELP aggregation without affecting the structural fluidity of the individual ELP chains (18-24). Some systematic studies have been carried out examining the effects of guest amino acid, chain length, concentration and pH on the transition temperature of ELPs but the scopes of these studies have been limited either by the limited fidelity of early ELP synthetic techniques or by a focus on a narrow range of ELP constructs and particle characteristics (5, 25-33). While this information may be somewhat useful for designing a construct for a specific temperature or pH trigger using the studied characteristics, these models are still limited in scope and there are other key parameters for which there is no systematic understanding.

Two properties of critical importance to the successful transition of ELP biomaterials to clinical applications like drug delivery include controlling particle size and zeta potential (34). These parameters are key factors in determining their biological fate and therapeutic efficacy, though no systematic observations have been made on how ELP sequence affects these parameters (34, 35). Another factor critical to the success of ELPs as a delivery vehicle is their stability upon dilution (36). Concentration has been shown to affect transition conditions and as

clinical administration usually involves diluting these materials within the blood compartment, it is important to understand their disassembly conditions. Other poorly understood aspects of ELP behaviour include whether existing trends in amino acid content, chain length and concentration effects on ELP T_t apply to increasingly hydrophobic constructs, the role of temperature treatment profiles in assembly characteristics, as well as a generalized understanding of ELP behaviour upon cooling.

This study begins to address these unknown parameters while simultaneously expanding upon the existing body of knowledge regarding systematically-studied behaviour of ELPs. The effects of chain length, amino acid chemistry and protein concentration were re-examined using a novel suite of short, highly hydrophobic ELPs developed by our group (7). ELPs composed of 20, 40, 80 or 160 pentapeptide repeats with leucine in the guest amino acid position, as well as a valine-containing 40-mer control, were studied across a range of concentrations and temperatures using dynamic light scattering, zeta-potential and transmission electron microscopy. ELP particle stability upon isothermal dilution was also investigated. The systematic approach undertaken herein allowed for the deconvolution of the effects concentration, guest amino acid chemistry and chain length have on assembly, disassembly and particle characteristics such as size, stability and ELP behaviour as well as advancing the body of evidence supporting clinical therapeutic use of ELPs.

7.3. Materials and Methods

7.3.1. ELP Synthesis

ELPs were synthesized according to Bahniuk *et al* (7). Briefly, the initial ELP genes were purchased through Integrated DNA Technologies (Coralville, IA, USA) and were concatemerized together in a pUC-19 cloning vector (Bio Basic, Ontario, Canada) using a modified recursive directional ligation procedure. The restriction enzymes PflMI and BglI (New England Biolabs, Ipswich, MA, USA) were used to create ELP inserts and vectors which were recombined multiple times to form ELP genes of various lengths. Additional digestions, gel purifications and dephosphorylation reactions were employed to ensure a minimum number of *Escherichia coli* (*E. coli*) XL10-Gold (Agilent Technologies, Santa Clara, CA, USA) needed to be screened.

ELP genes were inserted into a pET-25b(+) expression vector containing the N and C-terminal sequences for the ELP genes as well as a tobacco etch virus protease cut site and polyhistidine tag. The expression vector also contained two SfiI (New England Biolabs, Ipswich, MA, USA) restriction enzyme recognition sites with a spacer sequence in order to facilitate efficient vector linearization before ELP gene insertion. As with the concatemerization, additional restriction digests, gel purifications and dephosphorylation reactions ensured the cloning was as efficient as possible. DNA sequencing was carried out at the Molecular Biology Service Unit at the University of Alberta to confirm the ELP genes were

correct then the expression plasmids were transformed into OneTouch *E. coli* BL21 (DE3) (Invitrogen, Carlsbad, Ca, USA).

ELP expression was performed by growing the *E. coli* in Terrific Broth (Thermo Fisher Scientific, Waltham, MA, USA) at 37°C containing 100 μg/mL ampicillin (Thermo Fisher Scientific) and 10 mM L-proline (Sigma-Aldrich, St. Louis, MO, USA) and inducing expression with 2 mM isopropyl βD-1-thiogalactopraniside (Thermo Fisher Scientific) once the OD_{600} of the culture reached 0.8. Upon induction, the cells were left to grow at 37°C, 225 rpm for 24 hours. Cells were pelleted and frozen in liquid nitrogen before being subjected to denaturing metal-affinity chromatography purification. Buffered 8M urea was used to lyse the cells and fully solubilize any ELP before binding them to nickel beads at 4°C. After extensive washing the ELPs were eluted using a buffered imidazole step gradient. ELP-containing eluents were subjected to one round of inverse temperature cycling to complete the purification. When necessary, solid NaCl up to 1.5M and/or temperatures of 37°C were employed to trigger the phase transition of the ELPs. Exact conditions depended greatly on the construct and its concentration upon expression. Polyacrylamide gel electrophoresis was used to confirm the success of the purifications and sample concentrations were quantified using UV absorbance at 280 nm.

7.3.2. ELP Temperature Trend DLS Measurements

ELP concentrations were normalized by mass in part to control the number of pentameric ELP subunits between samples and also due to technical

limitations at both high and low molarities. The lower molarity limit for each ELP sample was dictated by the 0.01 mg/mL minimum sensitivity of the DLS instrument. Given the breadth of ELP lengths studied herein, this meant that the lowest reliably measurable molarity for L20 would be much higher than that of L160. Additionally, attempts to match the highest molarities of shorter constructs using longer ELPs were impeded by the requisite high mass concentrations and difficulties associated with concentrating ELPs to those levels and the resulting instability of the protein solutions, even at low temperatures.

Thermal behavior of five ELP constructs (V40, L20, L40, L80 and L160) at concentrations of 0.05, 0.1, 0.5, and 1.0 mg/mL was studied using dynamic light scattering (DLS) (Malvern Zetasizer Nano ZS, Malvern Instruments Ltd, Malvern UK). Frozen ELP aliquots were thawed and diluted on ice with PBS pH 7.4 to the desired concentration. 100 μL of sample was placed in a 40 μL minimum volume DLS cuvette and kept cold on ice until measurement. ELP samples were equilibrated within the zetasizer at 5°C before starting measurements. Samples were heated from 5°C to 50°C and subsequently cooled back to 5°C. Size was measured at 5°C intervals. A two minute interval at each measurement temperature was programmed to allow for thermal equilibration of the sample. Two measurements, each with >10 subruns were recorded at each temperature during heating and cooling. L20 at 0.5 and 1.0 mg/mL samples were sonicated on ice for thirty minutes prior to the temperature trend measurements to ensure that no particles carried over from the concentrated stock solution or had inadvertently formed during sample preparation. Absorbance, refractive index and

viscosity of the PBS and ELP were calculated using Malvern's zetasizer software 7.03. Protein analysis mode was used for all measurements. Measurement settings were automatically optimized at each temperature interval. Unless otherwise stated, all DLS data represents the peak position of the distribution of particle sizes. All aggregate distributions had polydispersity index (PDI) values <0.2 unless the samples were actively undergoing a substantial change in particle diameter or the sample had been affected by particle precipitation.

7.3.3. ELP Zeta Potential Measurements

Zeta potential of five ELP constructs (V40, L20, L40, L80, and L160) at concentrations of 0.05, 0.1, 0.5, and 1.0 mg/mL was determined using a Malvern Zetasizer Nano ZS. All measurements were performed at 5 and 37°C. Frozen ELP aliquots were thawed in water then placed on ice immediately after thawing. ELPs were diluted with cold PBS pH 7.4 to make two 50 μL aliquots of each concentration. Note that L20 samples at 0.5 and 1.0 mg/mL were sonicated on ice before use as explained previously. All samples were kept on ice until use and ELP solutions, PBS buffer and sample cuvettes were equilibrated at 5 or 37°C as needed before measurements were taken. A 40V electrical potential was used to measure all samples. Three measurements of each sample were taken to ensure reproducibility. Each measurement had a minimum of 10 subruns, with a maximum of 60 subruns at 37°C and 100 subruns at 5°C. The diffusion barrier technique, details of which are available on the Malvern website, was used for all measurements. 35 μL of ELP was loaded into the bottom of a folded capillary zeta cell (Malvern Instruments Ltd, Malvern UK) already filled with PBS. The

sample was then loaded in the instrument and measured immediately to minimize diffusion of the ELP. Absorbance, refractive index, viscosity and dielectric constant of the PBS and ELPs were calculated using Malvern's zetasizer software 7.03.

7.3.4. ELP Dilution DLS Measurements

Nanoparticle size upon dilution of all ELP constructs (V40, L20, L40, L80, and L160) was measured using DLS (Malvern Zetasizer Nano ZS, Malvern Instruments Ltd, Malvern UK). Frozen ELP aliquots were thawed and diluted on ice with PBS pH 7.4 to a starting concentration of 1.0 mg/mL. 100 μL was pipetted into a 40 μL minimum volume DLS cuvette and allowed to equilibrate for 20 minutes at 37°C in the zetasizer. Five repeats were collected, each with >10 subruns used to collect the overall data. This ELP solution was then diluted to 0.5 mg/mL in the DLS cuvette with PBS (isotonic) pH 7.4 kept at 37°C (isothermal) in a heat block. The sample was then allowed to equilibrate at 37°C for 10 minutes before taking 5 measurements. The sample was subsequently diluted to 0.10 mg/mL and then 0.05 mg/mL using this process, taking five measurements at each concentration and allowing 10 minutes between dilutions. L20 was sonicated on ice for 30 minutes before measurement in order to ensure no nanoparticles were carried over from the concentrated stock solution or inadvertently formed during sample preparation. Absorbance, refractive index, and viscosity of the PBS and ELP were calculated using Malvern's Zetasizer Software 7.03.

7.3.5. Transmission Electron Microscopy

Transmission electron microscopy (TEM) was carried out at the Cell Imaging Center at the University of Alberta. Samples for TEM were prepared as they were for temperature trend DLS measurements. The samples were heated in a Mastercycler gradient thermocycler (Eppendorf, Hamburg, Germany) under conditions identical to those during the temperature trend. 400 mesh carbon-coated copper grids (Ted Pella, Redding, Ca, USA) were subjected to glow discharge in a Pelco easiGlow™ system (Ted Pella, Redding, Ca, USA) at 0.4 mBar, 15 mAmp and positive polarity for 45 seconds. 10 μL samples were immediately placed on charged grids for three minute incubations on an appropriately warmed heatblock (VWR International, Radnor, Pennsylvania, USA), before two rounds of washing in pre-warmed ultrapure MilliQ water (EMD Millipore, Etobicoke, Ontario, Canada) on the same heated surface. Samples were then directly taken for TEM imaging on a Hitachi H-7650 TEM using a 60 kV accelerating voltage. Images were acquired using a 16 megapixel EMCCD camera (Advanced Microscopy Techniques) and processed using the AMT Image Capture Engine software version 602.576.

7.3.6. Statistical Methods

An unpaired Student's *t*-test was used to evaluate the significance of differences between various results. The minimum level of significance was set to $\alpha = 0.05$.

7.4. Results

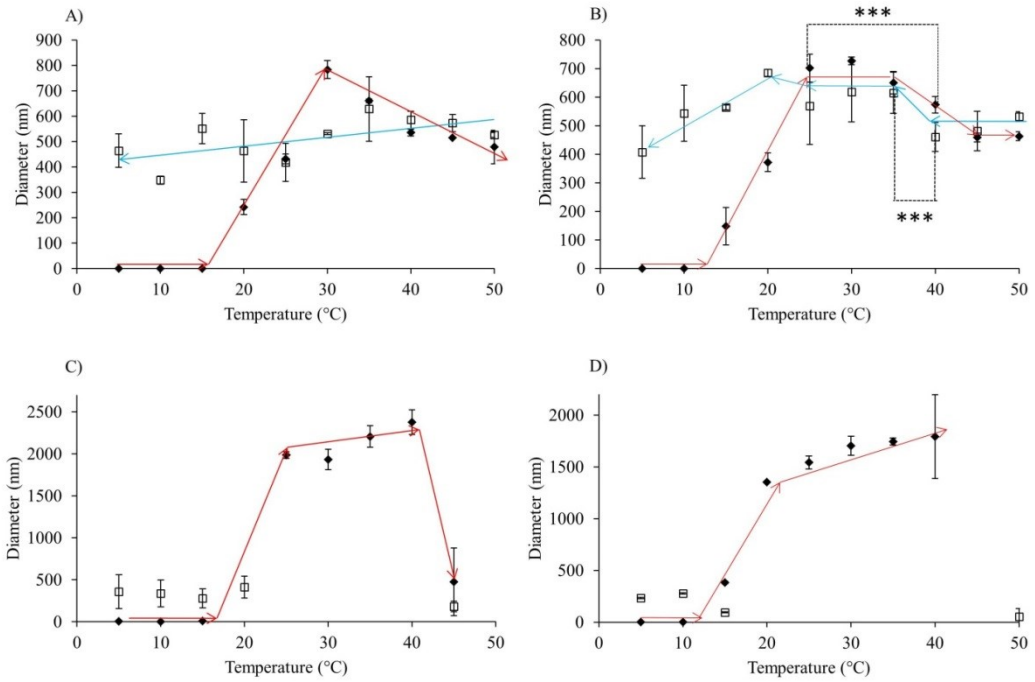

Figure 7.1. ELP L20 diameters as measured using DLS in 1X PBS pH 7.4, upon heating (♦) and cooling (□). Solution temperature was altered in 5°C increments with a 2 minute equilibration period prior to taking readings. ELP solution concentrations were A) 0.05, B) 0.10, C) 0.50 and D) 1.0 mg/mL. Missing temperature points were considered unreliable and removed. TEM was used in these instances to analyze particle diameters. Trend lines are presented only to guide the eye; each data point represents the average ± SD, n≥10. * represents a $p<0.05$, ** represents a $p<0.005$ and *** represents a $p<0.0001$.

The assembly and disassembly of ELP constructs formed from L20 for a variety of conditions are summarized in Figure 7.1. Figure 7.1a summarizes L20 results at a concentration of 0.05 mg/mL exposed to an increase in solution temperature from 5 to 50°C, which was then decreased back to 5°C. Upon heating, the diameter suddenly increased from ~1 to ~240 nm at 20°C. Aggregate size continued to increase to 780 nm as the temperature was raised to 30°C, after

which the L20 diameter decreased to 478 nm as the temperature increased to 50°C. Upon cooling, the diameter of the L20 aggregate fluctuated somewhat between 350 and 630 nm but did not return to the original <10nm size. The L20 at 0.10 mg/mL (Figure 7.1b) showed a similar behaviour to that of 0.05 mg/mL, except the temperature at which the sudden change in size occurred was 15°C as opposed to 20°C. The maximal diameter was again observed at 30°C with a statistically significant decrease in size upon further increase in temperature. Cooling the sample generally reversed the trend seen upon heating from 25 to 50°C. Further cooling saw the particle size decrease but not return to the pre-heated state.

Increasing the concentration of L20 from 0.10 to 0.50 mg/mL changed the ELP behaviour considerably. Upon heating to 20°C a drastic increase in particle size was observed (Figure 7.1c), with results that were beyond the range of the DLS instrument (>10 μm). Diameters at higher temperature suggested a particle size in the 2 μm range before decreasing to below 500 nm at 45°C. Visual examination of the DLS cuvette after reaching 50°C showed precipitation had occurred during the course of the temperature-dependent measurements. Cooling the sample down to 5°C did not result in a resolubilization of the precipitated ELPs; supported by the fact that DLS results showed particle diameters did not decrease to <10 nm. The numerical values for L20 diameters at and above the size shift temperature for the heating as well as the entire cooling may have been affected by the settling of larger particles and the upper sensitivity of the instrument. As such, the data from Panel C should only be interpreted to show

that L20 at 0.50 mg/mL had a size shift at 20°C after which very large aggregates formed and the ELP suspension became unstable. Cooling the sample back to 5°C did not result in aggregate dissolution. The L20, 1.0 mg/mL system showed a large change in particle size at 15°C and upon further heating, micron sized aggregates formed that, like the 0.50 mg/mL sample, grew too large to be reliably measured using DLS (Figure 7.1d). This sample also displayed instability and precipitated protein was observed after heating to 40°C and this remained even after cooling back to 5°C. As such, the data obtained from heating at 45 and 50°C and the subsequent cooling profile may have been affected by the sample instability.

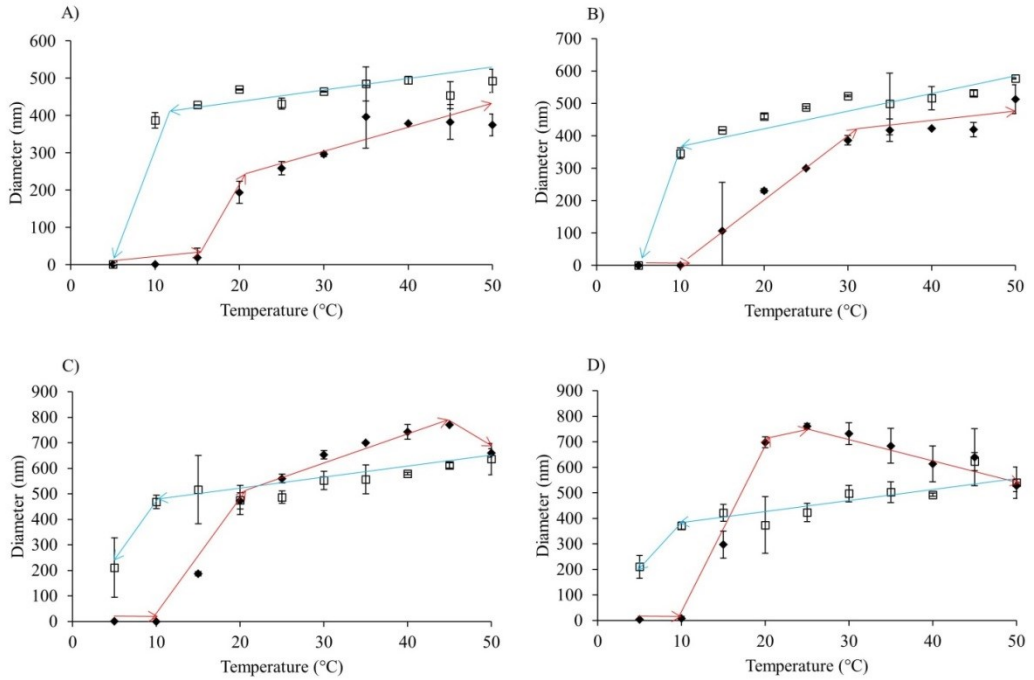

Figure 7.2. ELP L40 diameters as measured using DLS in 1X PBS pH 7.4, upon heating (♦) and cooling (□). Solution temperature was altered in 5°C increments with a 2 minute equilibration period prior to taking readings. ELP solution concentrations were A) 0.05, B) 0.10, C) 0.50 and D) 1.0 mg/mL. Trend lines are presented only to guide the eye; each data point represents the average ± SD, n≥10.

The behaviour of ELP L40 at various temperatures and concentrations is summarized in Figure 7.2. The lowest ELP concentration, 0.05 mg/mL showed that the particle size drastically changed from approximately 1 to 200 nm at 20°C (Figure 7.2a). Upon further heating, the diameter increased to about 375 nm. As the sample was subsequently cooled, the diameter of the L40 particles stayed relatively stable until cooled to 5°C, at which point the ELP aggregates returned to the pre-heated sample sizes. The size of the particles as they were cooled was

slightly higher than the diameters observed while the sample was being heated. Similarly, ELPs at 0.10 mg/mL began aggregating at 15°C and the particle diameter grew steadily with increasing temperature until 30°C, at which point the size stabilized around 400 nm. At 50°C the size increased to approximately 500 nm and the diameter decreased slightly but steadily during the cooling treatment. Once the sample reached 5°C again, the L40 particles appeared to have completely returned to their pre-heated state. L40 ELPs at 0.50 mg/mL showed a change in particle diameter at 15°C (Figure 7.2c). In this case the particle diameter increased steadily, reaching a maximum of ~770 nm when the temperature reached 45°C. Beyond this point and throughout the majority of the cooling treatment the L40 diameter decreased steadily until the sample reached 5°C when the size decreased sharply, but did not reach a value small enough to indicate a complete return to pre-heated size for the ELPs. At 1.0 mg/mL L40 underwent a transition in particle size at 15°C which saw the diameter sharply increase to about 750 nm at 25°C before steadily decreasing in diameter as the temperature increased to 50°C. Cooling the sample back down continued the trend of a steadily decreasing particle diameter. At 5°C the size of the L40 decreased sharply from ~350 to 200 nm, a behaviour which was also observed for the L40 at 0.50 mg/mL.

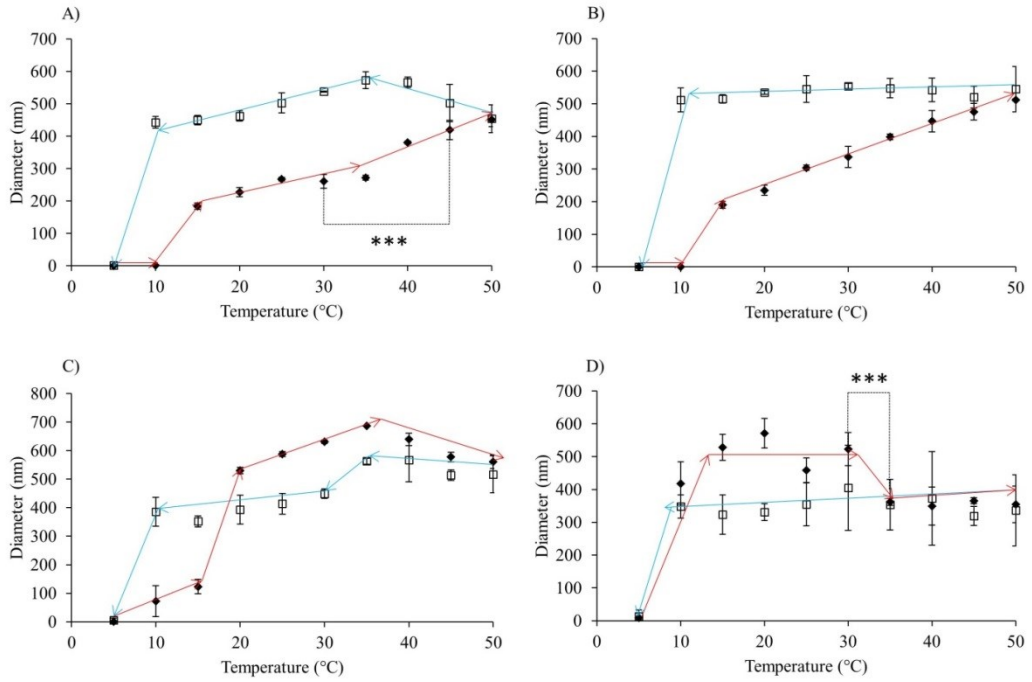

Figure 7.3. ELP L80 diameters as measured using DLS in 1X PBS pH 7.4, upon heating (♦) and cooling (□). Solution temperature was altered in 5°C increments with a 2 minute equilibration period prior to taking readings. ELP solution concentrations were A) 0.05, B) 0.10, C) 0.50 and D) 1.0 mg/mL. Trend lines are presented only to guide the eye; each data point represents the average ± SD, n≥10. * represents a $p<0.05$, ** represents a $p<0.005$ and *** represents a $p<0.0001$.

ELP L80, at a solution concentration 0.05 mg/mL, showed a transition in diameter when heated to 15°C (Figure 7.3a), from 15-35°C the size of the particles remained ~240 nm. As the sample was heated further, the ELPs underwent a statistically significant increase in size to about 420 nm. Interestingly, as the sample was then cooled back down to 5°C, the particle diameter increased to values larger than those seen during the heat treatment, averaging ~440 nm until disassembly was observed at 5°C. Increasing the

concentration to 0.10 mg/mL did not result in vastly different behaviour compared to 0.05 mg/mL (Figure 7.3b). A similar change in diameter at 15°C was observed with the particle diameter increased steadily to a maximum of roughly 500 nm at 50°C. Upon being cooled the particle size remained consistent with the maximal size observed during heating until it returned to its pre-heated size at 5°C. At 0.50 mg/mL, L80 diameter increased at 10°C and remained at a diameter of ~100 nm until the sample temperature reached 20°C (Figure 7.3c). At this point the diameter sharply increased to more than 500 nm, a range in which the particles remained for the rest of the heat treatment. As this sample was cooled, the particle size fell within the range of 400-500 nm. As seen with the previous L80 samples, this sample also fully returned to its pre-heated size when the temperature reached 5°C. Finally, at 1.0 mg/mL a transition in diameter occurred at 10°C (Figure 7.3d). Upon reaching this temperature, the particle size underwent a dramatic increase from less than 10 nm to more than 450 nm. The diameter stayed in this range until it was heated to 35°C, at which point they shrank to about 350 nm-a statistically significant decrease in size. As the samples were cooled, there was minimal variation in the size of the L80 until 5°C when the particles returned to their pre-heated state.

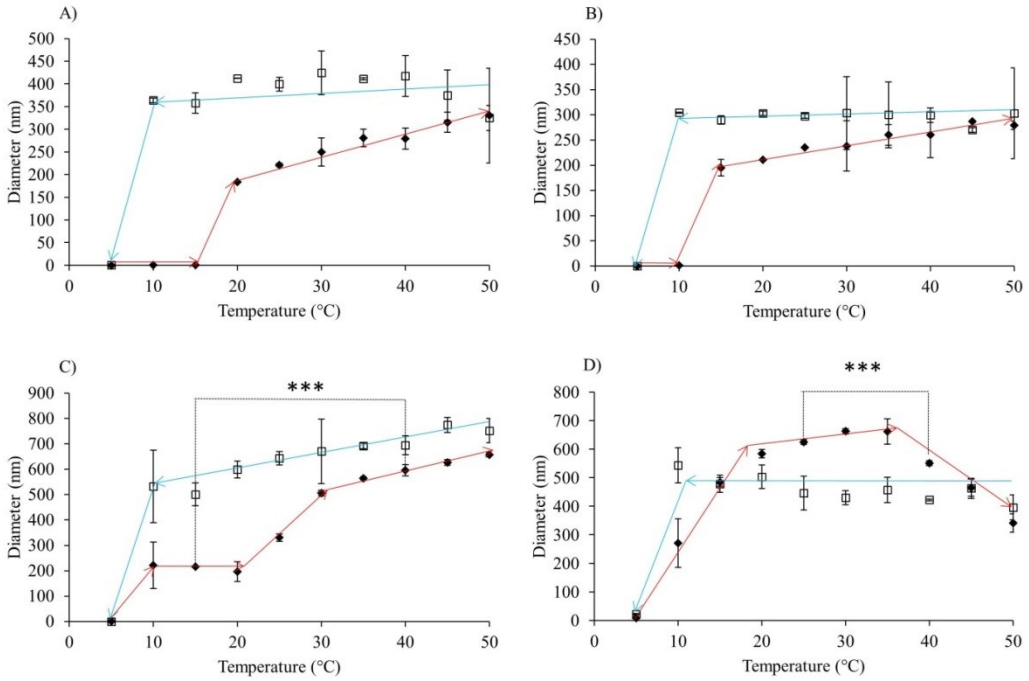

Figure 7.4. ELP L160 diameters as measured using DLS in 1X PBS pH 7.4, upon heating (♦) and cooling (□). Solution temperature was altered in 5°C increments with a 2 minute equilibration period prior to taking readings. ELP solution concentrations were A) 0.05, B) 0.10, C) 0.50 and D) 1.0 mg/mL. Trend lines are presented only to guide the eye; each data point represents the average ± SD, n≥10. * represents a $p<0.05$, ** represents a $p<0.005$ and *** represents a $p<0.0001$.

The results of altering solution temperature and ELP concentration on L160 are shown in Figure 7.4. At the lowest concentration, 0.05 mg/mL, the system underwent a transition in diameter at 20°C, where its diameter increased from ~1 to ~160 nm (Figure 7.4a). As the temperature increased, particle size increased steadily to a maximum of ~330 nm. Upon being cooled, the particle diameter did not fluctuate significantly until complete disassembly of the system at 5°C. When at 0.10 mg/mL the ELPs assembled at 15°C, with particles at ~200

nm that increased to ~300 nm upon further heating (Figure 7.4b). As the sample was cooled back down to 5°C, the size of the particles remained constant until complete dissolution was observed at 5°C. The 0.50 mg/mL solution of ELP L160 transitioned when heated to 10°C to form particles ~200 nm in diameter (Figure 7.4c). This size was maintained until heated to 25°C where the diameter began to increase significantly but steadily, to a maximum of 650 nm at 50°C. Statistical analysis of the diameters at 15°C and 40°C indicated a significant increase in size upon heating with a $p<0.0001$. Upon cooling the particle diameter decreased smoothly to a minimum of about 500 nm before completely returning to their pre-heated state at 5°C. Finally, a concentration of 1.0 mg/mL showed a size transition at 10°C (Figure 7.4d). When heated to this temperature the particle diameter increased to about 250 nm and continued to grow to a maximum of ~660 nm at 35°C. Further heating of the sample led to a statistically significant ($p<0.0001$) decrease in size to ~550 nm at 40°C, a trend which continued to a final diameter of 340 nm at 50°C. Cooling the L160 solution resulted in a moderate and steady increase in size from 400 nm at 50°C to ~540 nm at 10°C. At 5°C the size decreased precipitously, as seen in other cases where the ELP aggregates returned to their pre-heated state.

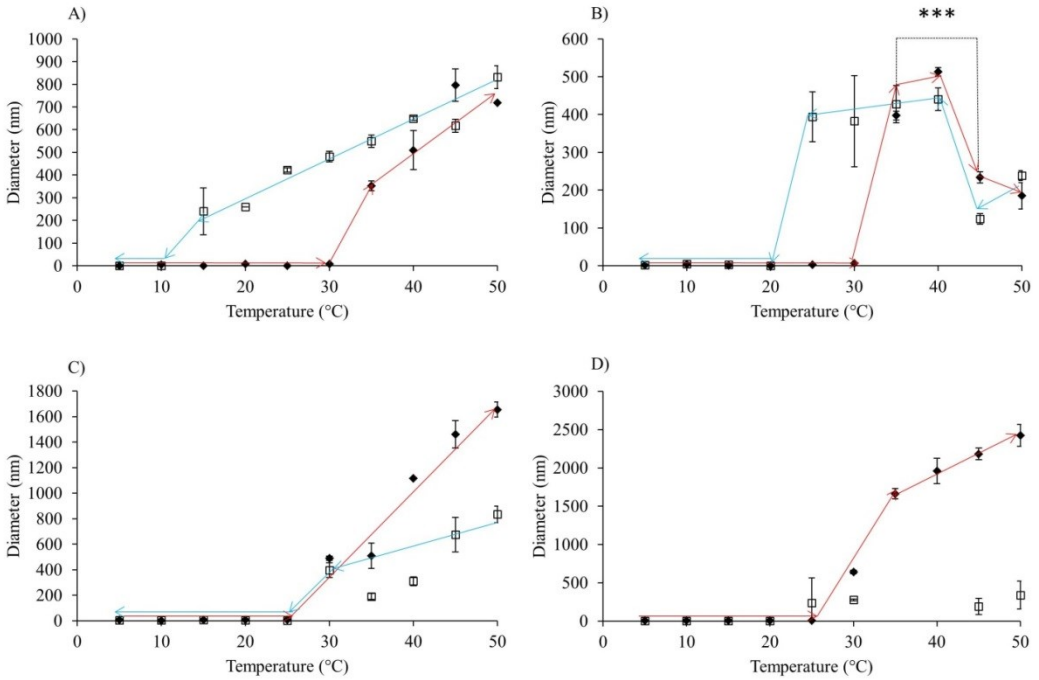

Figure 7.5. ELP V40 diameters as measured using DLS in 1X PBS pH 7.4, upon heating (♦) and cooling (□). Solution temperature was altered in 5°C increments with a 2 minute equilibration period prior to taking readings. ELP solution concentrations were A) 0.05, B) 0.10, C) 0.50 and D) 1.0 mg/mL. Missing temperature points were considered unreliable and removed. TEM was used in these instances to analyze particle diameters. Trend lines are presented only to guide the eye; each data point represents the average ± SD, n≥10. * represents a $p<0.05$, ** represents a $p<0.005$ and *** represents a $p<0.0001$.

ELP V40 assembly as a function of temperature and concentration is shown in Figure 7.5. At 0.05 mg/mL this construct underwent a sudden size transition at 35°C and the size of the particles increased with temperature without reaching a plateau (Figure 7.5a). The opposite trend was observed when the sample was cooled, with a complete return to the pre-heated size observed at 10°C and an apparent hysteresis of 25°C. Similar to the 0.05 mg/mL results, the 0.10 mg/mL sample underwent a temperature-triggered increase in diameter at 35°C to

~400 nm (Figure 7.5b). Once heated to 45°C a statistically significant reduction in diameter to ~200 nm occurred. This behaviour was also observed in reverse when the sample was cooled, with the diameter increasing as the temperature was decreased to 40°C and a complete return to pre-heated sizes was seen at 20°C. At a concentration of 0.50 mg/mL V40 began to display unusual behaviour (Figure 7.5c). It transitioned at a temperature of 30°C, but the initial particle size at that temperature was already 500 nm. As the temperature increased the diameter rose into the micron range. Visual observations made on V40 samples after heating to 50°C showed the presence of some precipitation in the bottom of the DLS cuvette. Once the sample was cooled back to 5°C, no precipitated material was visible in the bottom of the cuvette. This is consistent with the particle diameter for V40 decreasing to <10 nm as the sample was cooled. It may be possible however that the diameters recorded during the cooling phase and potentially the dissolution temperature may have been affected by sample instability. This potential instability was further observed when the concentration of V40 was increased to 1.0 mg/mL (Figure 7.5d). Like at 0.50 mg/mL, this sample transitioned at 30°C with an initial particle size of more than 500 nm. The diameter rose to more than 2 microns at 50°C; again, precipitate was observed after the heating was completed but no insoluble protein was visible upon cooling down to 5°C. It may be possible that the V40 diameters upon cooling and putative dissolution temperature may have been influenced by sample instability.

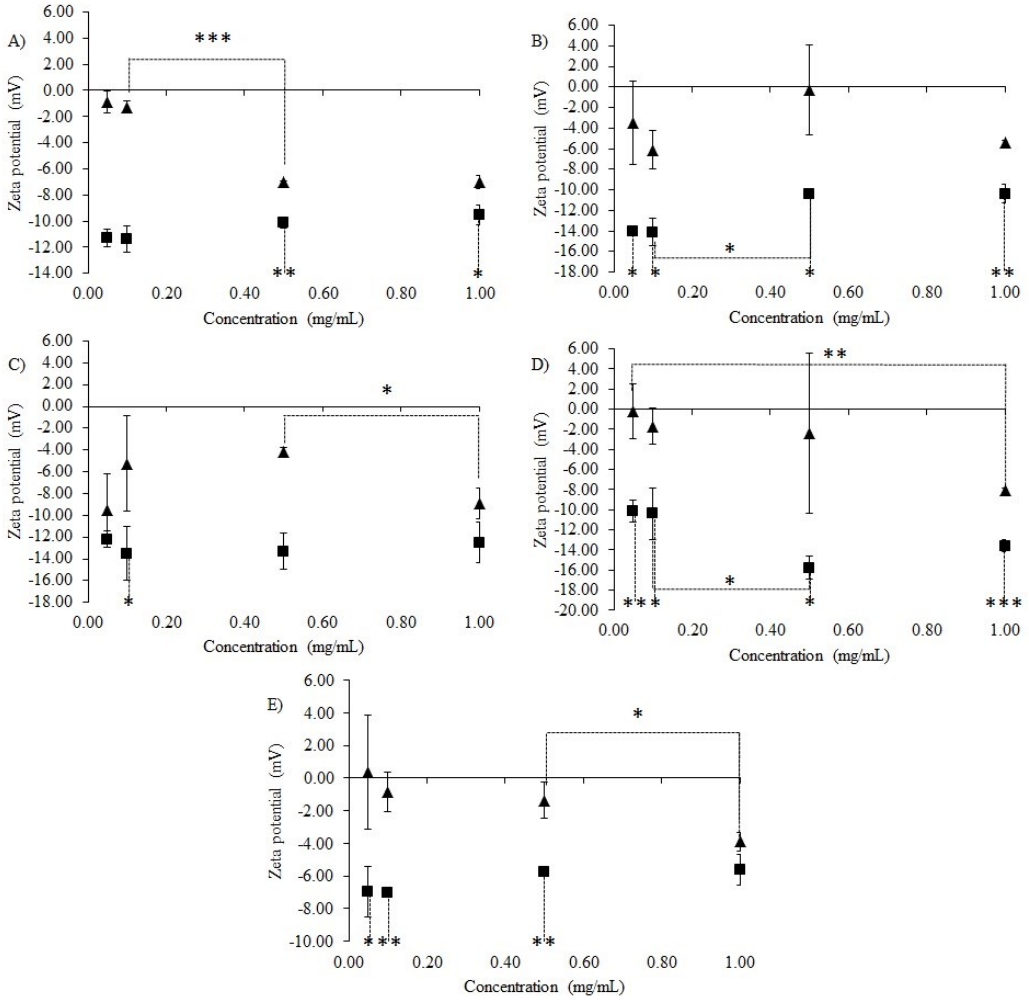

Figure 7.6. ELP surface charge as measured by zeta potential in 1X PBS pH 7.4, below and above their respective transition temperatures. The constructs are ordered as follows: A) L20, B) L40, C) L80, D) L160 and E) V40. Measurements taken at 5°C are represented by ▲ while those at 37°C are represented by ■. Reported values represent the mean ± standard deviation with an n=3. * represents $p<0.05$, ** represents a $p<0.005$ and *** represents a $p<0.0001$.

The effect of ELP concentration and sample temperature on zeta potential was also investigated (Figure 7.6). The behaviour of ELP L20 can be split into two groups-low concentration samples (0.05 an 0.10 mg/mL) and high concentration samples (0.50 and 1.0 mg/mL). The low concentration samples had a charge of less that -2mV when below their assembly temperature and charges of

-11 mV at 37°C. The high concentration samples had a statistically significantly larger charge below their transition at -7 mV but at 37°C had charges in the same range as the low concentration samples at ~10 mV. The change in charge upon heating the high concentration samples to 37°C was found to be statistically significant for both 0.50 mg/mL ($p<0.005$) and 1.0 mg/mL ($p<0.05$). Like L20, the low concentration L40 samples (0.05 and 0.10 mg/mL) showed similar charges below and above their assembly temperatures, at about -4.5 and -14 mV, respectively (Figure 7.6b). Heating these samples from 5 to 37°C resulted in a statistically significant increase in charge in both cases ($p<0.05$). At 0.50 mg/mL and 5°C the L40 was found to have almost no net charge, while at 37°C had a charge of -10 mV, a statistically significant change ($p<0.05$). The highest concentration, 1.0 mg/mL, had a stronger charge when disassembled (-5mV) and underwent a statistically significant ($p<0.005$) increase in charge at 37°C to a value comparable to that of the 0.50 mg/mL sample. ELP L80 showed similar behaviours between the 0.05 mg/mL and 1.0 mg/mL samples (Figure 7.6c). In both cases the potential at 5°C was roughly -9 mV and -12 mV at 37°C. The intermediate concentration samples also had similar characteristics to one another with charges of roughly -5 and -14 mV at 5 and 37°C, respectively. The increase in charge upon heating 0.10 mg/mL samples was found to be statistically significant ($p<0.05$). ELP L160 samples at 0.05, 0.10 and 0.50 mg/mL all had similar charges at 5°C, in the range of 0 to -2 mV (Figure 7.6d). The 1.0 mg/mL sample was significantly more charged at the same temperature, with a charge of -8 mV. At 37°C the 0.05 and 0.10 mg/mL samples underwent significant changes

in zeta potential values to around -10 mV ($p<0.005$ for 0.05 mg/mL and $p<0.05$ for 0.10 mg/mL) while the 0.50 and 1.0 mg/mL samples possessed greater potentials at -16 and -14 mV, significant changes from the 5°C values ($p<0.05$ for 0.50 mg/mL and $p<0.0001$ for 1.0 mg/mL). ELP V40 showed some similarities to L160 with the 0.05, 0.10 and 0.50 mg/mL samples at 5°C again falling in the range of 0 to -2 mV (Figure 7.6e). The 1.0 mg/mL sample once again had a significantly larger zeta potential, though only at -4 mV. At 37°C regardless of concentration, all V40 samples had similar zeta potentials around -6.5 mV, changes which were significant compared to the corresponding 5°C values for all but the 1.0 mg/mL sample ($p<0.05$ for 0.05 mg/mL, $p<0.005$ for 0.10 mg/mL and $p<0.005$ for 0.5 mg/mL).

Generally speaking, when a charge was observed, all ELPs were negative. This is consistent with the average charge of an individual ELP chain being slightly negative. In all cases increasing the temperature from 5°C to 37°C, that is, from below to above T_t for each ELP system resulted in an increase of the magnitude of the zeta potential decrease in the total surface charge of each sample regardless of concentration. This change in zeta potential was found to be statistically significant in many cases with the exceptions of L80 and V40 at 1.0 mg/mL. Concentration likely affected the zeta potential for soluble ELPs, where three of the five constructs tested showed an increasing negative charge. At 37°C there did not appear to be any discernable relationship between ELP concentration and the zeta potential magnitude.

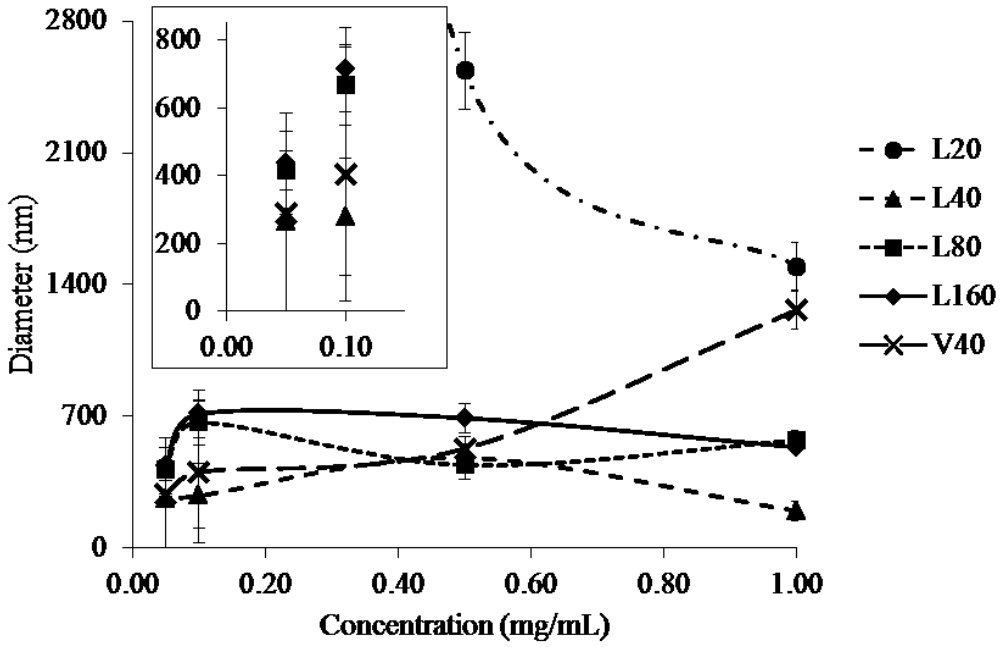

Figure 7.7. ELP diameters in 1X PBS pH 7.4 at 37°C as measured using DLS upon dilution from 1.0 mg/mL down to 0.50, 0.10 then 0.05 mg/mL in sequence, using prewarmed buffer. L20 is represented by ● with a dash-dot line, L40 by▲ and a dashed line, L80 by ■ and a square dot line, L160 by ♦ and a solid line and V40 by **x** with a long-dashed line**.** The inset graph is an expanded view of the data points at 0.10 and 0.05 mg/mL. Missing temperature points were larger than the operational range of the instrument. Trend lines are presented only to guide the eye. Values represent the mean ± standard deviation with an n≥10.

ELP particle size and stability as a function of dilution was evaluated by diluting 1.0 mg/mL ELP solutions at 37°C and monitoring particle diameters using DLS. A comparison of the results for each ELP system is given in Figure 7.7. ELP L20 displayed some unexpected behaviour when subjected to dilution. At 1.0 mg/mL and 37°C, L20 had an initial particle diameter of 1.5 μm that increased to 2.5 μm upon dilution to 0.50 mg/mL. Further dilution saw the sizes increase beyond the point where they could be accurately measured with the instrument. Diluting the initial 1.0 mg/mL sample to 0.05 mg/mL did not result in

resolubilization as precipitated protein was clearly visible at the end of the dilution testing. ELP L40 had an initial diameter of ~200 nm at 1.0 mg/mL, which increased to ~480 nm when diluted two-fold. Particle size decreased to ~265 nm for both 0.10 and 0.05 mg/mL. However, the accompanying PDI values increased from <0.1 to 0.4 and 1.0 upon dilution to 0.10 and 0.05 mg/mL, respectively, which may imply the particle stability was weakened. L80 showed an initial diameter of ~570 nm at 1.0 mg/mL that varied moderately over the course of the dilutions to ~440, 670 and 415 nm at 0.50, 0.10 and 0.05 mg/mL, respectively. L160 displayed similar behaviour to L80, with a 1.0 mg/mL diameter of ~540 nm that, upon dilution, fluctuated to 690, 710 and finally 440 nm as it was diluted to 0.50, 0.10 and 0.05 mg/mL, respectively. Unlike L40, the PDI values for L80 and L160 never exceeded 0.12, a value low enough to imply minimal polydispersity and not large enough to suggest possible perturbation of the ELP particle assemblies. ELP V40 formed particles with diameters of ~1.3 μm at 1.0 mg/mL. This value decreased significantly to 540 nm when the sample was diluted to 0.50 mg/mL ($p<0.0001$), a trend which continued with values of 400 nm at 0.10 mg/mL and finally 300 nm at 0.05 mg/mL.

Overall the majority of the constructs tended to decrease in diameter as they were diluted from 1.0 to 0.05 mg/mL, the extent of which varied depending on the construct. Only L20 appeared to form larger, irreversibly precipitated particles as the sample became more dilute. Complete particle breakdown was not observed for any system as no diameters below 10 nm were observed; though the

PDI for L40 became large enough to suggest some instability in that system upon a 20-fold dilution.

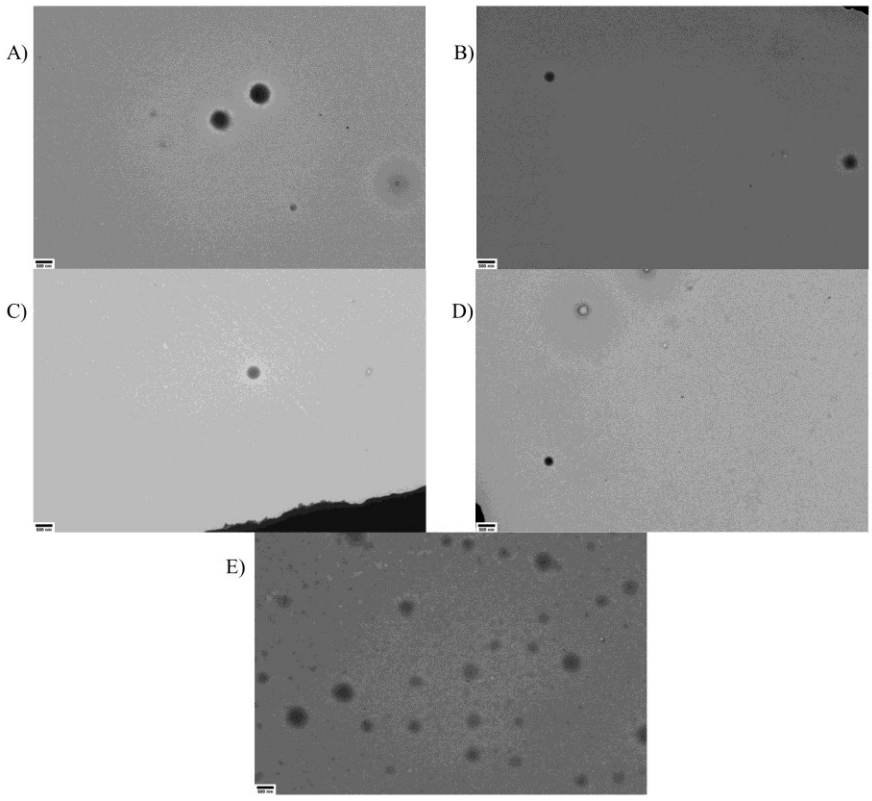

Figure 7.8. Representative TEM images of A) L20, B) L40, C) L80, D) L160 and E) V40 at 0.10 mg/mL after being heated to 35°C using the identical temperature trend heating profile used for DLS analysis. All images are at 5000X magnification with a 500 nm scale bar.

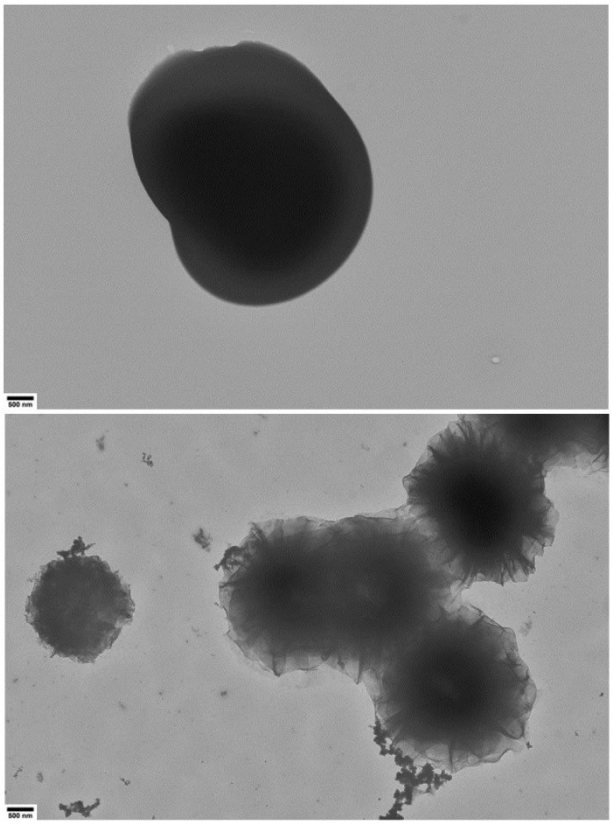

Figure 7.9. Representative TEM images of L20 (top) and V40 (bottom) at 1.0 mg/mL after being heated to 50°C using the identical temperature trend heating profile used for DLS analysis. All images are at 5000X magnification with a 500 nm scale bar.

Transmission electron microscopy was carried out as a secondary assessment of ELP particle morphology and diameter. Each construct was examined at 0.10 mg/mL after heating in a manner consistent with previously discussed variable-temperature DLS experiments up to 35°C. These conditions were chosen as all constructs were stable throughout their heating and cooling at this concentration and the temperature is in the range of biological significance. Additional samples were prepared for L20 and V40 at 1.0 mg/mL after heating to 50°C in order to visualize the structures formed during precipitation.

ELP L20 TEM results are shown in Figures 7.8 and 7.9. The lower concentration sample showed particles which were spherical, well dispersed and electron dense. There were many particles visible on each grid and the sizes matched the average measured by DLS, though some heterogeneity in particle diameter was observed. At 1.0 mg/mL there were significantly fewer particles visible on the TEM grids, each with a diameter in the 2-10 micron range. TEM images of ELPs L40, L80 and L160 are all shown in Figure 7.8. These three constructs all presented as electron dense, well-dispersed spheres. There were many particles visible for each construct on TEM grids, though more were visible for shorter chain ELPs. The sizes measured by TEM generally matched the results from the DLS at 0.10 mg/mL and 35°C, with L160 tending to be ~20% larger when viewed by TEM than by DLS.

ELP V40 particles at 0.10 mg/mL and 35°C (Figure 7.8) or 1.0 mg/mL and 50°C (Figure 7.9) were similar to the L-series: spherical structures were observed though they did not appear as electron dense as the L-series. At 0.10 mg/mL and 35°C, the diameters of the V40 particles generally matched those measured with DLS, though the deviations from the mean size appeared larger for the TEM samples. This may be because the standard deviation value reported by the DLS instrument only represents the variance in the mean diameter over multiple measurements, rather than the total width of each measured size distribution. The lower overall charge of V40 particles may have also played a role in that their structures may have been stabilized less by the oppositely charged EM grid than the L-series and, consequently, may have been prone to

greater variation in their size once sampled on the EM grid. At 1.0 mg/mL and 50°C, the V40 structures on the TEM showed the lowest electron density of any sample and the structures resembled spheres that possibly were formed from lamellae of protein. Regardless of formation mechanisms these structures were unlike all other samples.

Sample (mg/mL)	T_t heating (°C)	T_t cooling (°C)	Hysteresis (Δ°C)	Zeta Potential (5°C, mV)	Zeta Potential (37°C, mV)	Notes
L20 0.05	20	N/A	20+	-0.882 ± 0.8	-11.3 ± 0.6	No disassembly observed
L20 0.10	15	N/A	15+	-1.27 ± 0.4^{***a}	-11.4 ± 1.0	No disassembly observed
L20 0.50	20	N/A	20+	-7.04 ± 0.1^{***a}	-10.1 ± 0.4	Not all diameters quantifiable
L20 1.0	15	N/A	15+	-7.04± 0.5	-9.52 ± 0.8	Not all diameters quantifiable
L40 0.05	20	5	15	-3.47 ± 4.0	-14.0 ± 0.5	
L40 0.10	15	5	10	-6.10 ± 1.9	-14.1 ± 1.4^{*b}	
L40 0.50	15	N/A	15+	-0.233 ± 4.4	-10.4 ± 0.2^{*b}	No disassembly observed
L40 1.0	15	N/A	15+	-5.38 ± 0.2	-10.4 ± 0.9	No disassembly observed
L80 0.05	15	5	10	-9.53 ± 3.4	-12.2 ± 0.8	
L80 0.10	15	5	10	-5.25 ± 4.4	-13.5 ± 2.5	
L80 0.50	10	5	5	-4.22 ± 0.5^{*c}	-13.3 ± 1.6	
L80 1.0	10	5	5	-8.89 ± 1.4^{*c}	-12.5 ± 1.9	
L160 0.05	15	5	10	-0.242 ± 2.8^{**d}	-10.2 ± 1.1	
L160 0.10	10	5	5	-1.71 ± 1.8	-10.4 ± 2.6^{*e}	
L160 0.50	10	5	5	-2.37 ± 8.0	-15.8 ± 1.1^{*e}	
L160 1.0	10	5	5	-8.06 ± 0.2^{**d}	-13.6 ± 0.6	
V40 0.05	35	10	25	0.344 ± 3.5	-6.94 ± 1.6	
V40 0.10	35	20	15	-0.834 ± 1.2	-7.00 ± 0.14	
V40 0.50	30	25	5	-1.37 ± 1.1^{*f}	-5.73 ± 0.3	Not all diameters quantifiable
V40 1.0	30	25	5	-3.90 ± 0.6^{*f}	-5.61 ± 0.9	Not all diameters quantifiable

Table 7.1. Summaries of ELP assembly and disassembly behaviour upon heating and cooling as observed with DLS in 1X PBS pH 7.4 with heating and cooling in 5°C increments. Zeta potential values represent the mean ± standard deviation with an n=3.Asterisks denote statistical significance with * representing $p<0.05$, ** representing a $p<0.005$ and *** representing a $p<0.0001$. The letters a-f denote the pairs of data compared together in order to evaluate statistical significance.

7.5. Discussion

As explained in the materials and methods section, mass concentration was used to normalize the amount of ELP in each sample due in part due to

technical limitations. While this allowed for equivalent amounts of ELP pentamers to be present in samples of the same mass concentration, this does not take into account the effect of molarity. As such, considerations of molarity may be used to explain some of the observed behaviours when mass concentration cannot.

With only 20 repeats of the VPGLG amino acid sequence, the L20 ELP is the shortest construct examined with the relatively hydrophobic leucine in the guest amino acid position. Generally speaking, the concentration of L20 did affect the size of the particles formed above the transition temperatures. At a concentration of 0.05 or 0.10 mg/mL, particle size reached a maximum of approximately 650 nm during heating before decreasing to about 500 nm in diameter. At 0.10 mg/mL this decrease in particle diameter while heating as well as the reverse during cooling were found to be statistically significant ($p<0.0001$). Increasing the L20 concentration to 0.50 or 1.0 mg/mL resulted in the formation of micron-scale aggregates which were not stable in solution and did not resolubilize upon cooling. The ELP concentration may have some effect on the transition temperature as it varied from 15 to 20°C depending on the sample conditions, but there was no clear trend with this data set, possibly due to the 5°C temperature resolution of the DLS program. L20 particle dissolution was not observed at any of the tested concentrations which implies the system exhibits some considerable hysteresis, in the range of 15-20°C, though it cannot be fully quantified. The diameters of these particles were consistent across DLS and TEM samples. That L20, regardless of concentration, particle size or stability, did not

disassemble seriously challenges the fundamental assumption that all ELP phase changes are reversible and that they fully disassemble upon cooling. The irreversible precipitation of L20 was also observed when examining the dilution stability, so the initial concentration-based precipitation is not reversed by sample dilution. This is unlike observations made in this study for V40 under an identical dilution treatment, nor is it consistent with turbidimetric analysis of dilutions performed on particles composed of repeats of ELP exons 20-24 (28). This property of irreversible precipitation was also seen during routine L20 purifications. Inverse temperature cycling-based purifications of L20 using standard procedures resulted in permanently precipitated samples when ELP concentrations were >0.40 mg/mL. Additionally, stock solutions of L20 at these high concentrations were found to contain micron-sized aggregates immediately upon thawing (data not shown). These irreversible precipitates could only be successfully resolubilized by minimizing the time they were heated above their T_t during purification and subjecting samples to bath sonication on ice. There is no evidence to suggest that surface charge plays a role in the formation of large L20 aggregates, as zeta-potential values for the system above its transition temperature were all in the range of -10.5 mV.

Increasing the ELP length from 20 to 40 repeats lead to some differences in the ELP temperature response and assembly behaviour. The concentration of L40 was shown to affect the size of the particles both in the heating and cooling phases. During the heating phase the average particle sizes increased from ~350 to 650 nm as the ELP concentration increased while during cooling the average

size remained in the 400-450 nm range over the range of the tested concentrations. At no point were micron-sized particles observed. This can also be inferred by comparing the particle size measurements at 50°C. For L40 the diameters for both heating and cooling are in good agreement, unlike cases when the sample underwent precipitation (i.e. L20 and V40). The T_t was also affected by the ELP concentration. At 0.05 mg/mL the L40 underwent its transition at 20°C but at 0.10 to 1.0 mg/mL the ELPs transitioned at 15°C. Hysteresis of the assembly/disassembly transition temperature was observed for all samples. As the 0.50 and 1.0 mg/mL samples did not fully disassemble upon cooling, a numerical value cannot be determined. For the 0.05 and 0.10 mg/mL samples the values for hysteresis were ~15 and 10°C, respectively. As the more concentrated samples did not disassemble, there may be a concentration-dependence for the dissolution of the L40 system. Particle diameters measured using TEM agreed with DLS results for identical conditions. The zeta potential for L40 when heated above its T_t displayed some concentration dependence, with lower concentration samples having stronger charges. Dilution stability testing did not decisively show particle breakup, though increasing PDI values at 0.05 and 0.10 mg/mL dilutions suggest instability upon further dilution may be possible. This instability upon dilution is not consistent with the behaviour of any of the other ELPs tested herein. While studies of ELP particle stability upon dilution are severely lacking in the literature, Osborne *et al.* reported that an ELP construct composed of repeats of ELP exons 20-24 demonstrated particle dissolution upon dilution using turbidimetric methods, though the degree of dilution was not reported (28). ELP

L40 behaviour upon dilution appears to fall between the results reported by Osborne and those made here using related L-series constructs.

L80 constructs self-assembled when heated to 10-15°C to form 200-600 nm diameter particles, with both the T_t and particle size dependent upon ELP concentration. Lower concentrations generally resulted in smaller particles, though heating a 1.0 mg/mL solution to greater than 35°C resulted in a statistically significant ($p<0.0001$) decrease in particle size from ~500 to ~320 nm. Upon cooling, the particle diameters tended to remain steady and upon reaching 5°C every tested concentration of L80 was shown to fully disassemble. Concentration dependence was observed for the L80 transition temperature during assembly but not disassembly. At 0.05 and 0.10 mg/mL the T_t was 15°C and at higher concentrations the T_t decreased to 10°C. Hysteresis was observed under all sample conditions except for 1.0 mg/mL, with a value ranging from 5-10°C. Surface charge and dilution stability data suggest this was a stable construct in general, with no tendency to precipitate or destabilize upon dilution. TEM results confirm the sizes determined using other methods in that L80 presents as a spherical, electron dense particle that was well dispersed and not prone to aggregation.

ELP L160 was the largest tested construct (77 kDa) and in general, the concentration of L160 appears to have some effect on the diameter of the particles formed upon heating. Samples with lower concentrations of ELPs formed smaller diameter particles upon heating, with average diameters in the 250-300 nm range for 0.05 and 0.10 mg/mL samples and diameters in the 500-600 nm range for

more concentrated samples. This same trend can be observed for the particle sizes when the samples were being cooled. As with other constructs, some statistically significant ($p<0.0001$) decrease in particle diameter was observed for the 1.0 mg/mL sample upon heating above 35°C. At a concentration of 0.50 mg/mL, L160 formed particles upon heating to 10°C. The particle diameter remained consistent at ~200 nm until the sample temperature reached 25°C, whereupon the particle diameters steadily increased to a maximum of ~625 nm. Cooling the L160 samples back to 5°C resulted in very little variation in particle diameter until disassembly was observed at 5°C for all ELP concentrations. Unlike other ELP constructs, each of the L160 samples did show complete disassembly upon cooling in a concentration independent manner. Concentration clearly affected the assembly T_t for this system. Transition temperatures ranged from 10-20°C with more concentrated samples having lower transitions. Hysteresis was observed at 0.05 and 0.10 mg/mL and the value of the hysteresis ranged from 5-10°C. The zeta potential values for this construct above its T_t ranged from -10 to -16 mV which suggests these particles should be colloidally stable. This was the only construct to show a greater zeta potential value at 37°C as the concentration of L160 was increased. Additionally, diluting a sample of L160 particles from 1.0 to 0.05 mg/mL did not result in any meaningful fluctuations of diameter or large standard deviations indicative of decreased particle stability. Electron microscopy was consistent with the observations made with other techniques in that the particles at 35°C and 0.10 mg/mL roughly matched the DLS observations and resulted in the formation of spherical, electron dense and well-dispersed

structures. Previous studies suggested the uniform intensity observed for all L-series ELPs indicated the formation of a micelle-like structure (37).

ELP V40 underwent a phase transition upon heating to 30-35°C, with higher concentration samples requiring less heating to elicit a response. Once above their transition temperature, V40 formed particles ranging in size from 200 nm to microns in diameter. TEM images suggested that the V40 was not as electron dense as leucine-containing ELPs, which may indicate that guest amino acid hydrophobicity influences packing density. Previous studies have shown that the packing density of assembled ELP above their T_t can be influenced by the phase transition of individual blocks in a block copolymer ELP, solution salt concentration and the distribution of hydrophilic and hydrophobic guest amino acids throughout a multiblock copolymer (27, 38, 39). The results herein suggest that the role of guest amino acid hydrophobicity in ELP homopolymers may be another avenue by which to engineer the packing density of ELP particles for the needs of specific applications. While there was no clear relationship between ELP concentration and diameter for this system, it was evident that at concentrations of 0.50 and 1.0 mg/mL very large aggregates were formed quickly and precipitation was observed once the samples had been heated to 50°C. This is consistent with the disagreement between sample diameters at 50°C during heating and cooling. While this precipitation matches the behaviour for L20, unlike L20 the V40 precipitates resolubilized upon cooling to 5°C and visible settling was no longer apparent. That this construct readily resolubilized was consistent with its observed behaviour during purification. Inverse temperature cycling procedures were able

to precipitate and resolubilize the V40 normally, just like L40, L80 and L160. At 0.05 mg/mL the V40 particle size appeared to continually increase as the sample was heated and the reverse was observed upon cooling. Of all the V40 samples tested, 0.10 mg/mL most resembled the leucine-containing ELPs during its temperature trend. Upon assembly this sample formed structures 400-500 nm in diameter which significantly ($p<0.0001$) decreased in size to ~175 nm upon heating to 45°C. As also observed at 0.05 mg/mL, this behaviour was reversed during sample cooling. It appeared that regardless of sample concentration or particle size and solubility, cooling V40 down to as low as 5°C resulted in complete ELP resolubilization, though large hysteresis values were observed for 0.10 mg/mL and especially 0.05 mg/mL V40. Compared to the leucine-containing ELPs, V40 had lower overall zeta potential values. Above its transition temperature, V40 only had a zeta potential of about -6.5 mV which did not vary in conjunction with sample concentration. This charge value is low enough that sample precipitation would not be unexpected though precipitation was only observed for the more concentrated samples during the up to 3 hour sample testing periods. As with L20 it appears that surface charge is not the only factor that contributes to the development of micron-scale aggregates and subsequent precipitation of ELPs. V40 also demonstrated further unusual behaviour relative to other tested constructs when its stability upon dilution was examined. This construct started off with a diameter of just over 1 micron at 1.0 mg/mL and steadily decreased in size with dilution to a final size of about 300 nm at 0.05 mg/mL, with the first dilution producing a significant decrease in particle

diameter ($p<0.0001$). Further dilution may result in observations consistent with previously examined ELPs (28). No other construct demonstrated such a large decrease in diameter. Interestingly, unlike the L20 which precipitated during this procedure, the dilution of V40 appeared to have reversed the growth of the aggregates and prevented their precipitation as no visible settling was observed for this construct. This may be related to the ease with which precipitated V40 can be resolubilized simply by cooling but L20 cannot.

Systematic analysis of ELPs at various concentrations allows for the deconvolution of the effect various parameters have on ELP behaviour in a broader context. Concentration has been shown to influence the formation and disassembly of particles in response to temperature changes. For instance, the degree of hysteresis observed for tested ELPs becomes larger as the ELP concentration decreased (Table 7.1). The zeta potential of ELPs at 5°C, that is below their transition temperatures, displayed some tendency to increase in magnitude as the sample concentration increased and this was particularly evident at 1.0 mg/mL. This pattern was not observed for the same ELPs at temperatures above their assembly points. At 37°C, three of the constructs did not exhibit any variation in charge (L20, L80, and V40), L160 increased with concentration and L40 decreased in zeta potential as concentration increased. Examining the five tested ELP constructs, based on solution concentration, lead to two distinct groups of behaviours: ELPs which were prone to precipitation (L20 and V40) and ELPs which did not precipitate (L40, L80 and L160). The ELPs which did precipitate demonstrated a previously described transition temperature shift in association

with concentration, where a higher concentration resulted in a lower T_t. This group of ELPs also showed a concentration-dependant precipitation where at ELP concentrations below 0.50 mg/mL particles of greater than 1 micron in diameter did not form, nor was precipitation observed either visually or suggested through the DLS results. TEM results were used to confirm the formation of micron-scale aggregates for samples at 1.0 mg/mL and submicron particles at 0.10 mg/mL when the samples were heated above their T_t. Regardless of sample preparation, all particles were roughly spherical. L20 was electron dense and well dispersed, while V40 appeared less dense. Concentration was not observed to independently influence either the tendency or temperature at which L20 and V40 disassembled nor did there appear to be a concentration-dependent particle size at concentrations where precipitation did not occur. The subset of ELP constructs that did not precipitate (L40, L80 and L160) had a variety of responses dependent upon concentration. As observed previously, as the sample concentration increased, the T_t of this subset of ELPs decreased (5, 30, 32). The disassembly of these constructs did not appear to vary based on sample concentration and was observed at 5°C for all samples. Generally speaking, more concentrated samples tended to form larger diameter constructs and this relationship was more pronounced while the samples were heated rather than when they were being cooled. Concentrated ELP solutions also tended to show size profiles upon heating with more dynamic behaviour: regions where the size plateaued or increased at varying rates. For L80 and L160 this even resulted in statistically significant decreases in the particle diameters at concentrations of 1.0 mg/mL.

TEM confirmed the DLS measurements at 0.10 mg/mL and 35^{o}C and spherical, well dispersed and electron dense particles were observed for all of the non-precipitating constructs.

By comparing the responses of L20, L40, L80 and L160 at equivalent mass concentrations, the effect of chain length for hydrophobic, short ELPs was elucidated. Consistent with previous reports in the literature, transition temperatures decreased with longer chain lengths, holding all other parameters constant (5). One of the most interesting results was that chain length may affect the size and stability of particles formed in solution and that the relationship between chain length and particle size is inverse. Longer ELPs were found to form smaller diameter particles when, given identical mass concentrations, there were equal amounts of ELP pentapeptide sequences between samples. The relationship between ELP chain length and particle diameter and the role of the quantity of ELP pentapeptides compared to the number of ELP molecules has never been explored in the literature previously. Longer ELPs appeared to more readily disassemble upon cooling compared to the shorter constructs, with L20 resolubilization not observed under any of the current tested conditions, limited by the lower mass sensitivity of the DLS instrument. The lack of observable L20 resolubilization herein may be explained by the relatively high molarity of the L20 samples compared to the longer ELP constructs. Some hysteresis was present during sample cooling, with larger discrepancies between assembly and disassembly temperatures for the shorter ELPs. The dilution stability results suggested that longer ELPs tended to retain their size better than shorter ones,

though the precipitation of L20 during the dilution test limits the range of lengths that could be successfully tested in this manner. There were no discernable relationships between ELP chain length and surface charge, regardless of sample temperature, nor did there appear to be a correlation between length and ELP behaviour in response to cooling. All construct diameters remained stable until cooled to 5°C. L20 was found to form larger particles in general and, at high concentrations, micron-scale structures which precipitated out of solution. L40, L80 and L160, composed of identical but longer sequences, consistently formed particles with sub-micron diameters without any solution stability issues over the course of the 3 hour measurements. TEM observations were consistent with sizes measured using DLS and support the notion that chain length showed an inverse relationship with particle size for the leucine-containing ELPs.

A comparison of the responses of L40 and V40 can be used to extrapolate generalizations regarding the influence of guest amino acid residues. Clearly the more hydrophilic V40 had a higher T_t than the L40. This is generally in agreement with predictions described in previous literature, though there are some variations due to the different lengths of ELPs tested (31). V40 was also observed to form significantly larger particles upon heating compared to L40. So much so that the V40 even precipitated at 0.50 and 1.0 mg/mL while the L40 formed sub-micron particles with no observed stability issues during the ~3 hour temperature trend testing. At concentrations where precipitation was not a concern, L40 tended to present as more consistently-sized particles while being heated. While being cooled, V40 sizes resembled those measured during the corresponding

heating size trends while L40 particles had a relatively steady diameter with an abrupt change in size at ~5°C. V40 also appeared to have larger hysteresis values than L40 when precipitation was not observed, with differences as large as 25°C for V40 but only 15°C for L40. There was no clear relationship between particle size and guest amino acid residue observed. Zeta potential of assembled particles, that is at 37°C, did appear to be affected by the guest amino acid with the more hydrophobic L40 displaying a stronger negative charge at all concentrations compared to V40. TEM analysis revealed that the V40 construct was less electron dense that L40 which implies that a greater hydrophobicity may result in tighter packing of ELP chains (27).

The systematic analysis of a family of ELPs with varying guest amino acid hydrophobicity and/or chain length at several equivalent concentrations over a range of temperatures allowed for the deconvolution of the influence these various sample parameters have upon particle assembly behaviour and characteristics. This information can be broadly applied to the design of all future ELP-based materials and also can be used to expand the utility of existing ELP constructs. This novel family of hydrophobic ELPs behaved consistently with previously reported observations regarding the effects of guest amino acid chemistry, chain length and concentration on ELP assembly transition temperatures. The disassembly and hysteresis behaviour of this family of ELPs challenges the generalization that VPGXG-type ELPs disassemble and resolubilize upon cooling. Systematic experimentation revealed that chain length, concentration and guest amino acid hydrophobicity may all influence this

irreversible assembly. The surface charge of the systems was shown to be influenced by the solubility state of the ELPs as controlled by temperature and also by the guest amino acid hydrophobicity. More hydrophobic guest resides may result in a greater density of ELP molecules per particle, as suggested by the electron densities seen in TEM. The size of the ELP particles was influenced by sample concentration, with higher concentrations associated with larger particles and, in some cases, micron-scale aggregate formation and precipitation. More concentrated samples also showed more dynamic diameters upon heating, with samples at 1.0 mg/mL showing significant decreases in diameter with heating. Chain length also played a role with shorter chain lengths resulting in larger particles overall and greater tendencies for precipitation. ELP precipitation was observed for two separate constructs and potentially influenced by both guest amino acid hydrophobicity and chain length. More hydrophobic guest amino acids may allow for greater stability for shorter ELP sequences and may also result in a less reversible particle formation and/or precipitation depending on sample concentration. Hysteresis was observed in all samples and, due to its relationship with the T_t, varied with ELP concentration. Additionally, hysteresis was found to be more pronounced overall for constructs with shorter chain lengths. These short ELPs also were not found to disassemble as reliably as their longer counterparts, with sample concentration also influencing measurable resolubilization. Novel dilution stability testing suggested that pre-formed ELP particles composed of longer chain lengths were more stable when subjected to isothermal and isotonic dilution. Guest amino acid chemistry may also affect

dilution stability with more hydrophobic residues showing smaller variations in diameter.

The roles of temperature and concentration on ELP behaviour have not been systematically analyzed and the results reported herein, in addition to the design guidelines presented above, suggest that existing ELP constructs may be used to form particles of varying diameters, depending upon solution conditions and temperature treatments. This may be a resourceful and cost-effective way of expanding upon the utility of individual ELP constructs without resorting to further sequence modifications.

7.6. Conclusion

In this study, leucine-containing ELPs composed of 20, 40, 80 or 160 repeats of the VPGLG sequence as well as a 40 repeat valine-containing construct were evaluated for their assembly, disassembly, particle, charge and dilution stability characteristics. These experiments were performed at four distinct concentrations in order to deconvolute the role of sample concentration. Additional analysis allowed for the elucidation of the roles of guest amino acid chemistry and chain length on ELP behaviours.

Leucine-containing ELPs showed assembly transition temperatures dependent upon sample concentration and chain length consistent with other more hydrophilic constructs studied in the literature. Chain length was found to have an inverse relationship with particle diameter, with L20, the shortest construct, forming micron-scale aggregates and precipitating out of solution at high

concentrations. This behaviour was also observed for the valine-containing V40 construct despite it being twice the length of L20. The guest amino acid chemistry was found to potentially influence the zeta potential, with more hydrophobic constructs showing greater charge and electron densities suggesting a corresponding effect on packing density. Temperature-mediated disassembly behaviour was also found to vary with chain length whereby the shortest constructs tended to resist disassembly upon cooling as low as 5°C. L40 demonstrated that sample concentration also played a role in disassembly resistance, as more concentrated samples did not completely resolubilize, while less concentrated samples did fully disassemble. No resistance to disassembly was observed in the valine-containing construct. Dilution-mediated disassembly testing indicated that pre-formed ELP particles could be subjected to isothermal and isotonic dilution up to 20-fold their original concentration.

7.7. Acknowledgements

The authors would like to acknowledge the technical assistance provided by Lavina Hsiao Wei Ng and Owais Khalid for dynamic light scattering, as well as Woo Jung Cho and the Cell Imaging Center at the University of Alberta for equipment access, training and technical expertise. This work was supported by the Natural Sciences and Engineering Research Council of Canada Discovery grant #RES0011279. MSB was supported by Alberta Innovates Technology Futures Graduate Student Scholarship in Nanotechnology #200801440. AKA was the recipient of the Ministry of Higher Education and King Saud University Scholarship, Saudi Arabia. SVE was the recipient of a Natural Sciences and

Engineering Research Council of Canada Undergraduate Student Research Award.

7.8. References

1. Urry DW. Entropic elastic processes in protein mechanisms. I. Elastic structure due to an inverse temperature transition and elasticity due to internal chain dynamics. Journal of protein chemistry. 1988;7(1):1-34.

2. Urry DW, Luan CH, Parker TM, Gowda DC, Prasad KU, Reid MC, et al. Temperature of polypeptide inverse temperature transition depends on mean residue hydrophobicity. Journal of the American Chemical Society. 1991;113(11):4346-8.

3. Urry D, Long M, Cox B, Ohnishi T, Mitchell L, Jacobs M. The synthetic polypentapeptide of elastin coacervates and forms filamentous aggregates. Biochimica et Biophysica Acta (BBA)-Protein Structure. 1974;371(2):597-602.

4. Puiggalí J, Franco L, J. del Valle L. Smart systems related to polypeptide sequences. AIMS Materials Science. 2016;3(1):289-323.

5. Meyer DE, Chilkoti A. Quantification of the Effects of Chain Length and Concentration on the Thermal Behavior of Elastin-like Polypeptides. Biomacromolecules. 2004;5:846-51.

6. Cho Y, Zhang Y, Christensen T, Sagle LB, Chilkoti A, Cremer PS. Effects of Hofmeister anions on the phase transition temperature of elastin-like polypeptides. J Phys Chem B. 2008;112(44):13765-71.

7. Bahniuk MS, Alshememry AK, Unsworth LD. High-yield recombinant expression and purification of marginally soluble, short elastin-like polypeptides. BioTechniques. 2016;61(6):297.

8. Meyer DE, Chilkoti A. Genetically Encoded Synthesis of Protein-Based Polymers with Precisely Specified Molecular Weight and Sequence by Recursive Directional Ligation: Examples from the Elastin-like Polypeptide System. Biomacromolecules. 2002:357-67.

9. Meyer DE, Chilkoti A. Purification of recombinant proteins by fusion with thermally-responsive polypeptides. Nature Biotechnology. 1999;17.

10. McHale MK, Setton LA, Chilkoti A. Synthesis and in vitro evaluation of enzymatically cross-linked elastin-like polypeptide gels for cartilaginous tissue repair. Tissue engineering. 2005;11(11-12):1768-79.

11. MacEwan SR, Chilkoti A. Applications of elastin-like polypeptides in drug delivery. Journal of controlled release : official journal of the Controlled Release Society. 2014;190:314-30.

12. Rodriguez-Cabello JC, Arias FJ, Rodrigo MA, Girotti A. Elastin-like polypeptides in drug delivery. Adv Drug Deliv Rev. 2016;97:85-100.

13. Smits FCM, Buddingh BC, van Eldijk MB, van Hest JCM. Elastin-Like Polypeptide Based Nanoparticles: Design Rationale Toward Nanomedicine. Macromolecular Bioscience. 2015;15(1):36-51.

14. Navon Y, Bitton R. Elastin-Like Peptides (ELPs) - Building Blocks for Stimuli-Responsive Self-Assembled Materials. Israel Journal of Chemistry. 2016;56(8):581-9.

15. Saxena R, Nanjan MJ. Elastin-like polypeptides and their applications in anticancer drug delivery systems: a review. Drug Deliv. 2015;22(2):156-67.

16. Yeboah A, Cohen RI, Rabolli C, Yarmush ML, Berthiaume F. Elastin-like polypeptides: A strategic fusion partner for biologics. Biotechnol Bioeng. 2016;113(8):1617-27.

17. Kowalczyk T, Hnatuszko-Konka K, Gerszberg A, Kononowicz AK. Elastin-like polypeptides as a promising family of genetically-engineered protein based polymers. World J Microbiol Biotechnol. 2014;30(8):2141-52.

18. Yao XL, Hong M. Structure distribution in an elastin-mimetic peptide (VPGVG)3 investigated by solid-state NMR. Journal of the American Chemical Society. 2004;126(13):4199-210.

19. Hong M, Isailovic D, McMillan R, Conticello V. Structure of an elastin-mimetic polypeptide by solid-state NMR chemical shift analysis. Biopolymers. 2003;70(2):158-68.

20. Li NK, Garcia Quiroz F, Hall CK, Chilkoti A, Yingling YG. Molecular description of the LCST behavior of an elastin-like polypeptide. Biomacromolecules. 2014;15(10):3522-30.

21. Reichheld SE, Muiznieks LD, Keeley FW, Sharpe S. Direct observation of structure and dynamics during phase separation of an elastomeric protein. Proceedings of the National Academy of Sciences. 2017:201701877.

22. Rauscher S, Baud S, Miao M, Keeley FW, Pomes R. Proline and glycine control protein self-organization into elastomeric or amyloid fibrils. Structure. 2006;14(11):1667-76.

23. Kumashiro KK, Ohgo K, Elliott DW, Kagawa TF, Niemczura WP. Backbone motion in elastin's hydrophobic domains as detected by 2H NMR spectroscopy. Biopolymers. 2012;97(11):882-8.

24. Muiznieks LD, Keeley FW. Proline periodicity modulates the self-assembly properties of elastin-like polypeptides. Journal of Biological Chemistry. 2010;285(51):39779-89.

25. Fujita Y, Mie M, Kobatake E. Construction of nanoscale protein particle using temperature-sensitive elastin-like peptide and polyaspartic acid chain. Biomaterials. 2009;30:3450-7.

26. Ghoorchian A, Vandemark K, Freeman K, Kambow S, Holland NB, Streletzky KA. Size and shape characterization of thermoreversible micelles of three-armed star elastin-like polypeptides. The Journal of Physical Chemistry B. 2013;117(29):8865-74.

27. MacEwan SR, Weitzhandler I, Hoffmann I, Genzer J, Gradzielski M, Chilkoti A. Phase Behavior and Self-Assembly of Perfectly Sequence-Defined and Monodisperse Multiblock Copolypeptides. Biomacromolecules. 2017;18(2):599-609.

28. Osborne JL, Farmer R, Woodhouse KA. Self-assembled elastin-like polypeptide particles. Acta Biomater. 2008;4(1):49-57.

29. Nicolini C, Ravindra R, Ludolph B, Winter R. Characterization of the Temperature- and Pressure-Induced Inverse and Reentrant Transition of the Minimum Elastin-Like Polypeptide GVG(VPGVG) by DSC, PPC, CD, and FT-IR Spectroscopy. Biophysical Journal. 2004;86(March).

30. McDaniel JR, Radford DC, Chilkoti A. A unified model for de novo design of elastin-like polypeptides with tunable inverse transition temperatures. Biomacromolecules. 2013;14(8):2866-72.

31. Urry DW, Gowda DC, Parker TM, Luan CH, Reid MC, Harris CM, et al. Hydrophobicity scale for proteins based on inverse temperature transitions. Biopolymers. 1992;32(9):1243-50.

32. Girotti A, Reguera J, Arias FJ, Alonso M, Testera AM, Rodríguez-Cabello JC. Influence of the Molecular Weight on the Inverse Temperature Transition of a Model Genetically Engineered Elastin-like pH-Responsive Polymer. Macromolecules. 2004;37(9):3396-400.

33. MacKay JA, Callahan DJ, FitzGerald KN, Chilkoti A. Quantitative model of the phase behavior of recombinant pH-responsive elastin-like polypeptides. Biomacromolecules. 2010;11(11):2873-9.

34. Lundqvist M, Stigler J, Elia G, Lynch I, Cedervall T, Dawson KA. Nanoparticle size and surface properties determine the protein corona with possible implications for biological impacts. Proc Natl Acad Sci U S A. 2008;105(38):14265-70.

35. Verma A, Stellacci F. Effect of surface properties on nanoparticle–cell interactions. Small. 2010;6(1):12-21.

36. MacKay JA, Chen M, McDaniel JR, Liu W, Simnick AJ, Chilkoti A. Self-assembling chimeric polypeptide-doxorubicin conjugate nanoparticles that abolish tumours after a single injection. Nature materials. 2009;8(12):993-9.

37. Dreher MR, Simnick AJ, Fischer K, Smith RJ, Patel A, Schmidt M, et al. Temperature triggered self-assembly of polypeptides into multivalent spherical micelles. Journal of the American Chemical Society. 2008;130:687-94.

38. Sallach RE, Wei M, Biswas N, Conticello VP, Lecommandoux S, Dluhy RA, et al. Micelle density regulated by a reversible switch of protein secondary structure. Journal of the American Chemical Society. 2006;128(36):12014-9.

39. Serrano V, Liu W, Franzen S. An infrared spectroscopic study of the conformational transition of elastin-like polypeptides. Biophysical journal. 2007;93(7):2429-35.

8. The Effect of Physiochemical Properties of Elastin-Like Polypeptide Nanoparticles on Human Plasma Protein Adsorption

8.1. Abstract

Elastin-like polypeptides (ELPs) are being developed for numerous biomedical applications. There is only limited understanding of the biomaterial biocompatibility, with conflicting results in the literature. As protein adsorption is the fate determining event for blood-contacting biomaterials, an understanding of this complex series of events indicates the blood-biocompatibility of ELP-based biomaterials as well as a better fundamental understanding of the protein adsorption phenomenon. The aim of this study is to elucidate the blood-biocompatibility ELP nanoparticles through examining the adsorbed proteome from platelet-poor human plasma as a function of nanoparticle diameter, ELP guest amino acid and chain length. The adsorbed proteomes were found to contain extremely large proportions of albumin but also large amounts of immunoglobulin G and activated complement factor 3. Variations in the compositions of the proteomes across the ten nanoparticle systems involved plasminogen, fibronectin, activated fibrinogen as well as coagulation modulating antithrombin and alpha$_2$ macroglobulin. Plasma clotting experiments showed these nanoparticles slightly inhibited normal blood clotting, with shorter and/or more hydrophilic constructs displaying greater variances from the control than longer or more hydrophobic constructs. Taken together, these results indicate that ELP nanoparticles may stimulate a host immune response despite the large amounts of passivating albumin found adsorbed to the surface.

Keywords: Elastin-like polypeptides, protein adsorption, biocompatibility, blood clotting, Western blotting, human plasma

8.2. Introduction

Elastin-like polypeptides (ELPs) are an excellent example of a platform molecule capable of programmable, stimulus-responsive self-assembly (1). Derived from the extracellular matrix protein elastin, ELPs are an uncharged, highly repetitive biopolymer capable of reversible self-assembly in response to various environmental stimuli (2). The most prevalent ELPs are composed of any number of repeating valine-proline-glycine-X-glycine (VPGXG) amino acid sequences, where X can be any amino acid except proline (3). The specific amino acid in the "guest amino acid" X position, as well as the total number of repeats of the pentapeptide sequence, influences the environmental conditions under which ELPs undergo coacervation; allowing them to be engineered to assemble under very specific conditions (4). Some of these environmental stimuli include temperature, salt concentration, pH, light and the binding of specific ligands (5). Engineering a specific ELP sequence and appending various biofunctional moieties is a relatively straightforward process, given that detailed protocols exist for the recombinant production of ELPs (6-9). Given that ELPs are a unique, tunable, self-assembling platform technology capable of being adapted with numerous complex biofunctions, it should be no surprise that ELPs are undergoing rampant development for numerous applications including particulate and hydrogel drug delivery, biosensing, tissue engineering and recombinant protein purification (10-18).

Favourable biocompatibility is critical for clinical applications of biomaterials and there is limited data to prove this is the case for all ELP-based materials. Although there are many instances where ELPs have been successfully employed as tissue scaffolds that is not sufficient evidence that the material is biocompatible; cell culture conditions are insufficiently complex as to simulate a host environment (19-23). One of the most comprehensive studies of ELP biocompatibility involved evaluating a crosslinked VPGVG-based ELP matrix with a series of generic biocompatibility tests recommended by the American Society for Testing of Materials for medical and surgical materials and devices. Tested included the Ames mutagenicity test, acute systemic toxicity, intracutaneous toxicity, system antigenicity, dermal sensitization, pyrogenicity and *in vitro* hemolysis (24). The results of this testing indicated good biocompatibility, though given the aforementioned flexibility of the ELP platform, it may not be correct to assume this extends to all ELP materials. A subsequent study comparing a VPGVG-based construct to one with a 3:1 ratio of valine to phenylalanine in the guest amino acid position indicated that this alteration to the guest amino acid chemistry caused inflammation and fibrous encapsulation of the implant (25). An ELP block copolymer with valine or glutamic acid in the guest position along with alanine or isoleucine substitutions in the first or third positions of the pentapeptide was not found to elicit any deleterious host response and the implant was stable for over a year (26). Microparticles composed of repeats of VPAVG were found to stimulate inflammation and monocyte cell infiltration when used for ocular applications

(27). These seemingly conflicting results indicate that the biocompatibility of ELP-based biomaterials requires further study.

Immediately upon implantation, the biomaterial is exposed to thousands of individual components which make up blood-the primary medium at the interface of the host and biomaterial. Within seconds, proteins found in the blood begin to adsorb to the surface of the biomaterial (28). This adsorption is a complex and dynamic event which may directly impact the overall host response to the material (29). As the adsorption of protein from plasma to the biomaterial surface is the initial host response event, a wealth of insight may be gleaned from examining the content of the adsorbed protein corona. Studies have shown that this corona of adsorbed proteins can dictate a range of host responses to the biomaterial including inflammation, biodistribution, toxicity and immune recognition (30-32). Identifying the types and relative amounts of proteins found adsorbed to ELP nanoparticle surfaces will help to evaluate the material biocompatibility for plasma-contacting applications and systematic variations within the ELP sequences, like hydrophobicity, chain length and particle diameter will yield fundamental level information regarding how protein biomaterial design in general can influence host response.

ELPs are uniquely suited to understanding the molecular level properties of materials and their effect on plasma protein adsorption. The precise control over molecular level attributes (ie. amino acid composition, chain length, etc) through to nanoparticle properties (size, charge, etc) provides a unique ability to understand protein adsorption at the biomaterial-blood interface. Moreover, that

the amino-acid level chemical variations may be performed independently of morphological variations and *vice versa* allows for the deconvolution of the influence of these various properties on protein adsorption; information which is useful for the development of all protein-based biomaterials. That plasminogen, for instance, was found in moderately large amounts adsorbed only to 200 nm L80 nanoparticles suggests that both nanoparticle size and ELP chain length influence the adsorption of this fibrinolytic protein. Similarly, fibronectin was found in moderately high levels exclusively on 500 nm L40 which implies that the adsorption of this protein can be modulated by particle diameter, chain length and amino acid hydrophobicity.

This study will characterize particles made of leucine-containing ELPs with 20, 40, 80 or 160 repeats as well as a valine-containing construct with 40 repeats. Each ELP protein will be used to form ~200 and ~500 nm particles which will first undergo physical characterization with dynamic light scattering, zeta potential and transmission electron microscopy. These samples were incubated with platelet poor human plasma and the adsorbed proteome examined using gel electrophoresis, colloidal gold stain and Western blotting. A plasma recalcification turbidimetric assay shows how the presence of ELP nanoparticles affects blot clotting. The results provide insight into the biocompatibility of ELP nanoparticles and what role chain length, guest amino acid hydrophobicity and particle diameter may play in plasma protein adsorption and blood clotting.

8.3. Materials and Methods

8.3.1. ELP Synthesis

ELP synthesis was conducted as detailed elsewhere (6). Briefly, ELP genes were synthesized by Integrated DNA technologies (Coralville, IA, USA) then cloned into a pUC-19 cloning vector (Bio Basic, Ontario, Canada), concatemerized up to four times using a recursive directional ligation scheme which employed the restriction enzymes PflMI and BglI (New England Biolabs, Ipswich, MA, USA) to create compatible inserts and vectors. Multiple digestion reactions, agarose gel purifications vector dephosphorylations and post-ligation digests were employed to maximize the rate of successful ELP concatemerization. Ligation products were cloned into *Escherichia coli* (*E. coli*) XL10-Gold (Agilent Technologies, Santa Clara, CA, USA).

After concatemerization, ELP genes were ligated into a modified pET-25b(+) expression vector (EMD Millipore, Etobicoke, Ontario, Canada). The modifications included N and C-terminal caps for the ELP sequence, a tobacco etch virus protease cleavage site, polyhistidine tag as well as two SfiI restriction enzyme (New England Biolabs, Ipswich, MA, USA) recognition sites with a spacer sequence in between them. Similar to the concatemerization reactions, supplementary digests, purifications, dephosphorylations and post-ligation digests were employed to ensure the cloning reaction was as efficient as possible. DNA sequencing was performed at the Molecular Biology Service Unit at the University of Alberta to confirm ELP DNA sequence fidelity.

ELP expression was undertaken by first transforming OneTouch *E. coli* BL21 (DE3) (Invitrogen, Carlsbad, Ca, USA) with the ELP-containing expression vectors. Cells were then grown in Terrific Broth (Thermo Fisher Scientific, Waltham, MA, USA) at 37°C containing 100 µg/mL ampicillin (Thermo Fisher Scientific) and 10 mM L-proline (Sigma-Aldrich, St. Louis, MO, USA). Once the bacterial cultures reached an OD_{600} of 0.8, expression was induced by the addition of isopropyl βD-1-thiogalactopraniside (Thermo Fisher Scientific) to a final concentration of 2 mM and cells were incubated at 37°C, 225 rpm for 24 hours. Cells were collected by centrifugation and flash frozen in liquid nitrogen before undergoing denaturing metal-affinity chromatography. Buffered 8M urea (ThermoFisher, Waltham, Massachusetts, USA) was used to lyse the cells and solubilize ELPs before polyhistidine-containing proteins were bound to nickel beads. The column underwent extensive washing before elution using a buffered imidazole step gradient (Sigma-Aldrich, St. Louis, Missouri, USA). ELP purification was completed by performing one round of inverse temperature cycling using temperature ranges of 4-37°C and up to 1.5 M NaCl (ThermoFisher, Waltham, Massachusetts, USA) as necessary to trigger phase transitions. Polyacrylamide gel electrophoresis was used to verify ELP purity and sample concentrations were measured with UV absorbance at 280 nm.

8.3.2. DLS Measurements

Particle size as a function of thermal incubation time at 37°C was measured using dynamic light scattering (DLS, Malvern Zetasizer Nano ZS, Malvern Instruments Ltd, Malvern UK). ELP aliquots were diluted to final

concentrations using chilled 1X PBS pH 7.4 on ice. 100 µL samples were placed in 40 µL cuvettes and kept on ice until being placed into a preheated 37°C zetasizer. Measurements were taken immediately upon sample insertion and continued for ~30 minutes. Instrument settings were automatically optimized periodically throughout the measurement period resulting in diameter measurements at discrete time points. Absorbance, viscosity and refractive index values were calculated using the included software, with protein analysis mode used for all measurements. Unless otherwise stated, all DLS data represents the peak position of the particle size distributions. Polydispersity (PDI) values for all measured diameters were found to be <0.15.

8.3.3. Zeta Potential Measurements

The zeta potential values for 200 and 500 nm ELP nanoparticles were determined using a Malvern Zetasizer Nano ZS. All measurements were performed at 37°C. ELP samples were thawed and diluted on ice using chilled 1X PBS pH 7.4. Sample solutions were incubated at 37°C for the time necessary for their diameters to reach 200 or 500 nm then immediately measured using the diffusion barrier sampling technique with PBS serving as the barrier solution. Three measurements were taken for each sample with a 40 V electrical potential with 12-60 subruns sampled per measurement. Dielectric constant, refractive index, absorbance and viscosity of the buffer and protein were calculated using the included software package.

8.3.4. Transmission Electron Microscopy

Transmission electron microscopy (TEM) was performed at the Cell Imaging Center on the University of Alberta campus. 400 mesh carbon-coated copper grids (Ted Pella, Redding, Ca, USA) underwent a glow discharge treatment in a Pelco easiGlow™ system (Ted Pella, Redding, Ca, USA) at 0.4 mBar, 15 mAmp and positive polarity for 45 seconds. Samples for TEM were prepared by diluting and incubating L40 and V40 ELP solutions in an identical fashion as they were for DLS measurements. After the appropriate 37°C incubations, 10 µL aliquots were immediately placed on the sample grids, themselves on a 37°C surface, for three minutes. The grids were then rinsed with 37°C ultrapure MilliQ water (EMD Millipore, Etobicoke, Ontario, Canada). Samples were then immediately imaged using a Hitachi H-7650 TEM at a 60 kV accelerating voltage. Images were acquired using a 16 megapixel EMCCD camera (Advanced Microscopy Techniques) and processed using the AMT Image Capture Engine software version 602.576.

8.3.5. ELP Nanoparticle Plasma Incubation and Total Protein Assay

Platelet poor human plasma was procured through the Research Division of Canadian Blood Services and aliquoted and kept at -80°C until used. As per Canadian Blood Services policy, samples had been pooled to preserve donor anonymity and donors had provided informed consent. ELP nanoparticle solutions were prepared in 1X PBS pH 7.4 by incubating samples at 37°C at concentrations and time periods determined using DLS. 200 µL of the ELP nanoparticle

solutions were combined with 1.8 mL of 37°C platelet-poor human plasma and incubated at 37°C with rocking agitation for 2 hours. Afterwards samples were centrifuged at 37°C, 20000 x g for 10 minutes to pellet the nanoparticles and adsorbed proteome and the soluble phase was replaced with 1 mL of 37°C PBS. The nanoparticles were then incubated at 37°C for 30 minutes with rocking in order to remove loosely bound proteins. This wash procedure was performed twice in total, with the final nanoparticle pellet resuspended in 100 μL of 10% sodium dodecyl sulfate (SDS) (ThermoFisher, Waltham, Massachusetts) in PBS. In order to elute the adsorbed proteome and disassemble and resolubilize the nanoparticles, the solution was incubated at 37°C with rocking for 2 hours.

The microplate protocol of the detergent compatible (DC) Protein Assay (Bio-Rad, Hercules, CA) was used to quantify the adsorbed proteome. Standard curves were generated using bovine serum albumin (BSA) in 10% SDS in PBS at concentrations from 0.2 to 1.5 mg/mL. Each sample and standard was tested in triplicate by measuring the absorbance at 750 nm using a Synergy H1 plate reader (Biotek Instruments Inc., Winooski, VT) and reported as the average and standard deviation.

8.3.6. SDS-PAGE and Western Blotting

The adsorbed proteome was analyzed using denaturing SDS-polyacrylamide gel electrophoresis (SDS-PAGE) and Western blotting techniques as described previously (33-35). To compare the results between various nanoparticle samples, a constant amount of protein (30 μg) was run on each

electrophoresis gel. To ensure complete sample denaturation and reduction, a denaturing sample buffer containing SDS and 0.5 M β-mercaptoethanol (Bioshop Canada Inc., Burlington, ON) was added and then each sample was heated at 95°C for 5 minutes. Samples were then run on 12% denaturing polyacrylamide gels and transferred onto 0.2 μm Immuno-Blot polyvinylidene difluoride (PVDF) membranes (Bio-Rad, Hercules, CA) using standard methods. All consumable had been purchased from Bio-Rad and used without further purification. Each membrane was divided into 25 strips, with two used for colloidal gold non-specific protein stain and the remaining 23 used for Western blotting for 23 individual plasma proteins. The primary and secondary antibodies were used without further purification at 1:1000 dilution. An additional Western blot was performed on all nanoparticle proteomes against albumin at 1:5000 dilution of each antibody. Western blotting results were visualized using horseradish peroxidase (HRP)-functionalized secondary antibodies and 350 μL of TMB-stabilized HRP substrate (Promega, Madison, WI) per membrane strip. The time allowed for the colour development reaction was kept consistent between Western blot to allow for meaningful comparisons of results between blots. Immediately after the colour developing reaching was quenched in water the strips were dried, re-assembled and digitized.

8.3.7. Plasma Recalcification Turbidimetric Assay

In order to evaluate clot formation in the presence of ELP nanoparticles, a previously described plasma recalcification turbidimetric assay was used (35, 36). A Synergy H1 plate reader was set to 37°C and programmed to automatically read

the turbidity at 405 nm each minute for an hour. 25 μL of 200 or 500 nm ELP nanoparticles in PBS were added to 100 μL of 37°C platelet-poor plasma in a 96-well multiwall plate. 100 μL of 25 μM $CaCl_2$ (EMD Millipore, Etobicoke, Ontario) or PBS was added to each sample well immediately before placing the plate in the plate reader. Each sample clot reaction was repeated five times and the results were reported as average and standard deviation after background turbidity was eliminated and each sample baseline was artificially set to zero absorbance.

8.3.8. Statistical Analysis

An unpaired Student's *t*-test was used to evaluate the significance of differences between various results. The minimum level of significance was set to $\alpha = 0.05$.

8.4. Results

8.4.1. ELP Nanoparticle Physical Characterization

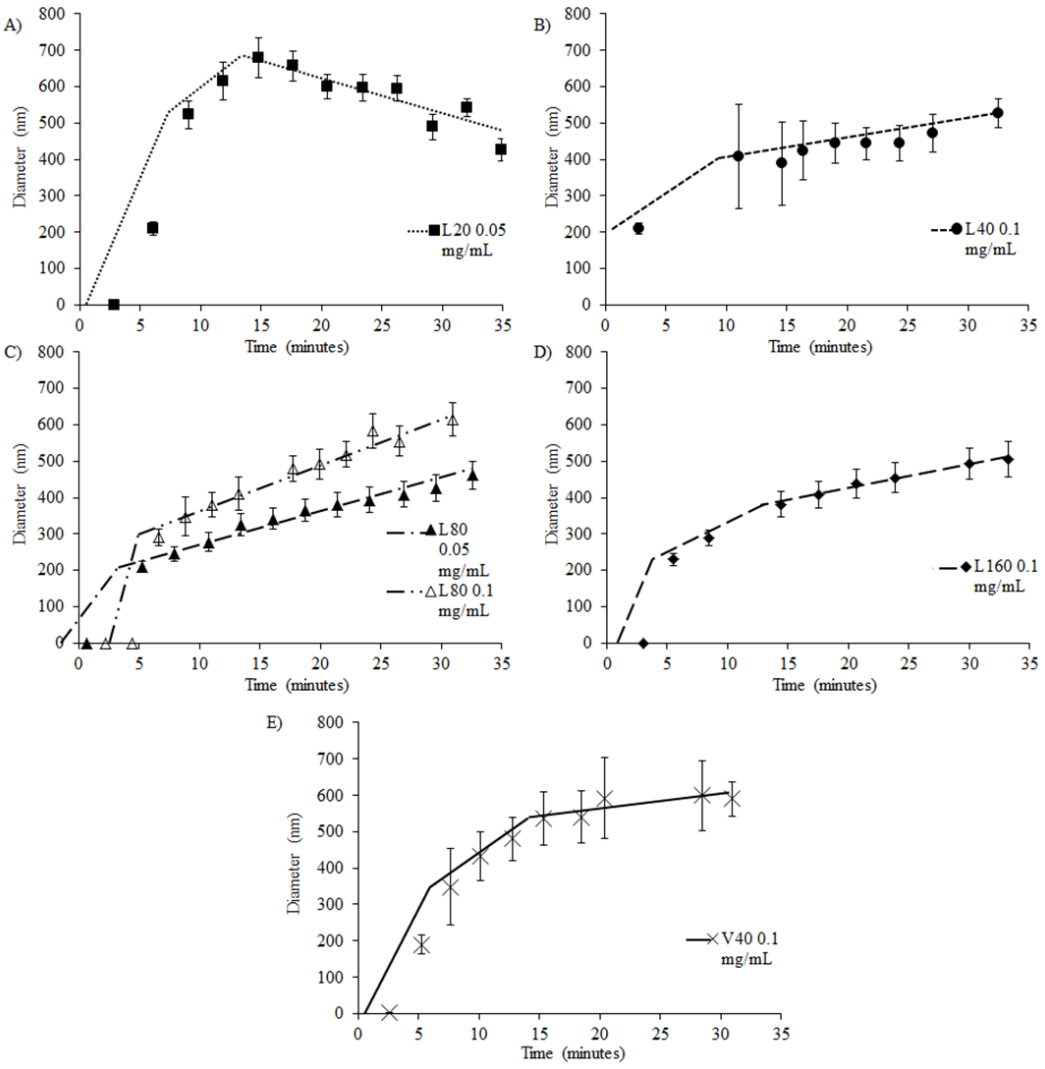

Figure 8.1. ELP A) L20, B) L40, C) L80, D) L160 and E) V40 diameters as measured using DLS in 1X PBS pH 7.4 as a function of incubation time at 37°C. L20 is represented by ■ and a square dot line, L40 by ● with a dashed line, L80 at 0.05 mg/mL by ▲ and a dash-dot line, L80 at 0.10 mg/mL by Δ with a dash-dot-dot line, L160 by ♦ and a dot-dash-dash line and V40 by X with a solid line. DLS subruns were taken continuously, with discrete measurements reported a their corresponding incubation times. Any clearly unreliable measurements were removed. Trend lines are presented only to guide the eye; each data point represents the average ± SD, n≥12.

The changes in ELP L20, L40, L80, L160 and V40 diameters as a function of incubation time at 37°C in 1X PBS pH 7.4 are illustrated in Figure 8.1. L20, at a concentration of 0.05 mg/mL, underwent a large change in diameter from <10 nm to ~510 nm in less than 10 minutes. The particle diameter peaked at a value of ~670 nm at 15 minutes before steadily decreasing to ~400 nm after 35 minutes, a significant decrease in diameter ($p<0.0001$). At the time of the first measurement, ~3 minutes after incubating the sample at 37°C, ELP L40 at 0.10 mg/mL was found to have already formed particles with a diameter of ~200 nm. This sharp increase in diameter continued for a total of ~10 minutes, to a size of ~400 nm before the rate of change in diameter slowed, with a final value of ~500 nm after ~32 minutes of incubation at 37°C. L80 was evaluated first at a concentration of 0.10 mg/mL and was found to drastically increase in diameter from <10 to ~300 nm after ~6 minutes of incubation at 37°C. From ~6-30 minutes of incubation the diameter continued to increase, though at a much lower rate, to a final value of ~600 nm. L80 was also tested at 0.05 mg/mL in order to find a condition under which ~200 nm particles would form. At this lower concentration the L80 diameter profile strongly resembled that of the larger concentration sample though the sizes were all smaller. The initial large diameter change reached a value of ~200 nm, after which the growth rate decreased and reached a final value of ~400 nm. As observed with most other samples, the diameter of ELP L160 increased sharply after ~5 minutes at 37°C, rising from <10 nm to ~200 nm. As the incubation period continued, the diameter continued to increase to a final value of ~450 nm after ~33 minutes at 37°C. The particle size for V40 increased

considerably after ~7 minutes of incubation to a value of ~350 nm. The size continued to increase strongly for a total of ~15 minutes to ~500 nm before the values appeared to plateau, with a final measurement at 30 minutes showing diameters of ~550 nm. Temporal resolution for all incubations times was considered to be ± 10 seconds.

System	Concentration (mg/mL)	Time at 37°C (min:sec)	Diameter (nm)	Zeta potential (mV)
L20-200	0.05	6:10	209 ± 18	-9.4 ± 0.4
L20-500	0.05	9:00	522 ± 39	-9.9 ± 0.7
L40-200	0.10	2:50	210 ± 15	-8 ± 5
L40-500	0.10	27:10	473 ± 52	-7 ± 5
L80-200	0.05	6:40	211 ± 15	-8 ± 2
L80-500	0.10	19:50	492 ± 40	-9 ± 1
L160-200	0.10	5:30	230 ± 17	-8 ± 2
L160-500	0.10	30:10	492 ± 42	-6 ± 1
V40-200	0.10	5:10	190 ± 26	-7.2 ± 0.7
V40-500	0.10	12:50	480 ± 60	-7.5 ± 0.6

Table 8.1. Summaries of 200 and 500 nm ELP nanoparticle incubation times at 37°C in 1X PBS pH 7.4, diameters and zeta potentials. Incubation times are considered to be ± 10 seconds. Particle diameters represent the mean ± standard deviation with an $n \geq 12$ while the zeta potential values repesent the mean ± standard deviation with an n=3.

From the results of the ELP particle diameter as a function of 37°C incubation, time points were found for each construct which would yield nanoparticles with 200 and 500 nm diameters. The chosen concentrations, incubation periods and resulting diameters are summarized in Table 8.1. A concentration of 0.05 mg/mL was required for ELP L20 because samples at 0.10 mg/mL did not form particles with diameters less than 500 nm (data not shown). Similarly, 200 and 500 nm L80 nanoparticles needed to be formed from 0.05 and

0.10 mg/mL solutions, respectively, because neither solution yielded both particle sizes upon incubation at 37°C. L40, L160 and V40 samples at concentrations of 0.10 mg/mL were found to form both 200 and 500 nm particles. L40 was found to form 200 nm particles the quickest, requiring only 2 minutes and 45 seconds at 37°C, while L20 formed 500 nm particles after only 9 minutes at 37°C. L20 also had the lowest total incubation time for both nanoparticle sizes, with V40 times also much lower than the longer L-series constructs. Zeta potential values in Table 8.1 were collected in a separate series of tests using the incubation times derived from Figure 8.1. All of the measured values are negative, consistent with the aggregation of individual, slightly negative ELP chains with values in the range of -6 to -10 mV. Previous zeta potential measurements of these marginally soluble ELPs at a temperature of 5°C and otherwise equivalent conditions show that upon incubation at 37°C, the magnitude of the zeta potential for each sample increased in conjunction with the aggregation of individual ELP chains by ~3-8 mV.

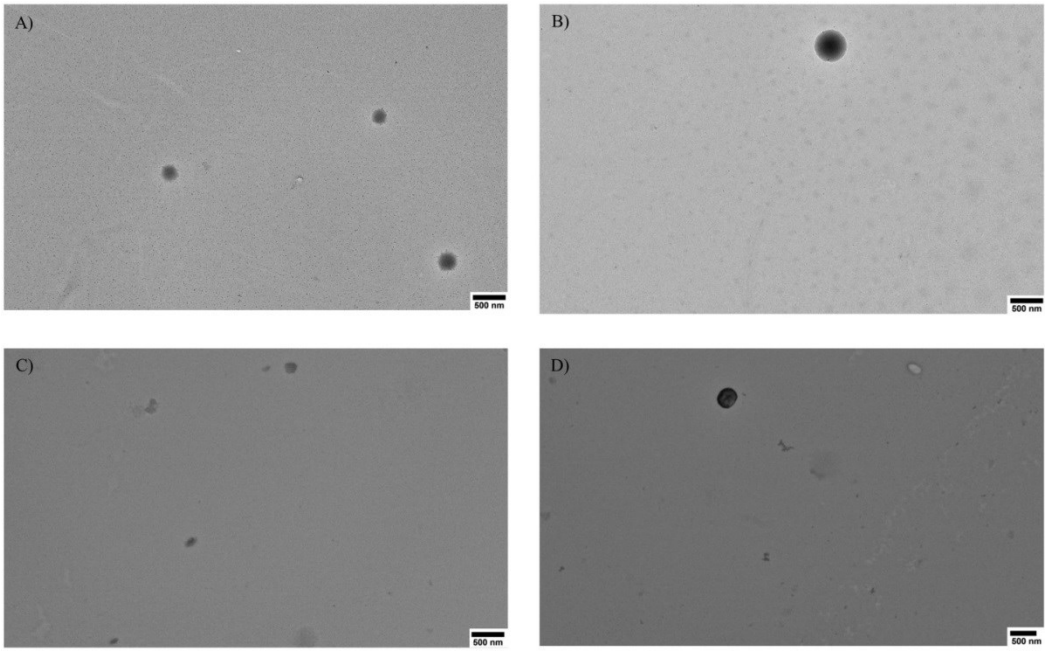

Figure 8.2. Representative TEM images of A) L20-200 nm, B) L20-500 nm, C) V40-200 nm and D) V40-500 nm. All images are at 5000X magnification with a 500 nm scale bar.

Transmission electron microscopy was performed as an alternate assessment of ELP particle diameter and morphology. L20 and V40 200 and 500 nm particles were prepared as described for DLS and zeta-potential. Figure 8.2A and 2B are representative samples for 200 and 500 nm L20 nanoparticles, respectively. In both instances the particles were well dispersed, spherical and electron dense. Many particles were visible on each TEM grid and the sizes were in agreement with those measured by DLS. Representative images for 200 and 500 nm preparations of V40, Figures 8.2C and 8.2D respectively, reveal that these nanoparticles were also well dispersed with diameters matching those measured by DLS. The spherical morphologies and electron densities for the V40-derived nanoparticles were not as regular as those observed for L40.

8.4.2. Adsorbed Proteome Characterization

System	Concentration of Adsorbed Protein (μg/μL)	Total Protein Processed on Western Blot (μg)	Total Protein Processed on Gold Stain (μg)
L20-200	0.49 ± 0.05*[a]	30 ± 3	1.5 ± 0.2
L20-500	0.37 ± 0.01*[a]	30 ± 0.8	1.5 ± 0.04
L40-200	0.24 ± 0.02*[b]	30 ± 3	1.5 ± 0.2
L40-500	0.22 ± 0.03**[c]	30 ± 4	1.5 ± 0.2
L80-200	0.31 ± 0.05	30 ± 5	1.5 ± 0.3
L80-500	0.41 ± 0.01	30 ± 0.7	1.5 ± 0.04
L160-200	0.34 ± 0.03	30 ± 3	1.5 ± 0.2
L160-500	0.30 ± 0.02	30 ± 2	1.5 ± 0.1
V40-200	0.38 ± 0.08*[b]	30 ± 6	1.5 ± 0.3
V40-500	0.35 ± 0.03**[c]	30 ± 3	1.5 ± 0.2

Table 8.2. Amounts of adsorbed and processed protein determined using the DC protein assay. Adsorbed protein values represent the mean ± standard deviation with an n=3. Asterisks denote statistical significance with * representing $p<0.05$ and ** representing a $p<0.005$. The letters a-c denote the pairs of data compared together in order to evaluate statistical significance.

Plasma protein	Fragment size (kDa)	Fragment name	System									
			L20 200	L20 500	L40 200	L40 500	L80 200	L80 500	L160 200	L160 500	V40 200	V40 500
Albumin	66		12+	12+	12+	12+	12+	12+	12+	12+	12+	12+
C3	42	Activation	12	12	12	10	11	9	11	9	9	10
	70	β	12	12	12	12	12	12	12	12	12	12
	115	α	11	11	6	3	10	8	9	4	8	7
	187	Whole	8	11	7	6	11	8	9	1	8	9
IgG	27	Light Chain	12	12	12	12	12	12	12	12	12	12
	55	Heavy Chain	12	12	11	12	12	12	12	12	12	12
$Alpha_1$ antitrypsin	47		12	12	12	12	12	12	12	12	12	12
Fibrinogen	48	γ	11	11	11	12	11	12	12	12	12	12
	56	β	12	12	11	11	10	12	12	11	11	12
	68	α	12	12	12	12	12	12	12	12	12	12
	< 48	Cleavage	5	0	0	0	0	2	2	0	0	3
Vitronectin	54		1	4	2	2	2	1	2	1	2	2
Fibronectin	259		0	0	0	9	0	2	0	0	0	0
Prothrombin	70		8	1	1	1	3	6	2	2	2	7
Antithrombin	53		10	5	8	9	10	11	8	3	10	10
Plasminogen	91		0	0	1	1	8	1	0	0	2	1
Transferrin	77		12	12	12	12	12	12	12	12	12	12
$Alpha_2$ macroglobulin	163		8	4	10	9	10	6	8	7	10	10

Table 8.3. Relative intensities for Western blots of plasma proteins adsorbed to all ELP nanoparticles. 0 indicates no band was present, 12 indicates maximal band intensity, with intermediate values indicated intermediate intensities. The + notation indicates samples which were processed with 1:5000 dilution primary and secondary antibodies, as opposed to the 1:1000 dilution used in the standard procedure.

Plasma protein	Fragment size (kDa)	Fragment name	System L20 200	L40 200	L80 200	L160 200	V40 200
Albumin	66		12+	12+	12+	12+	12+
C3	42	Activation	12	12	11	11	9
	70	β	12	12	12	12	12
	115	α	11	6	10	9	8
	187	Whole	8	7	11	9	8
IgG	27	Light Chain	12	12	12	12	12
	55	Heavy Chain	12	11	12	12	12
$Alpha_1$ antitrypsin	47		12	12	12	12	12
Fibrinogen	48	γ	11	11	11	12	12
	56	β	12	11	10	12	11
	68	α	12	12	12	12	12
	< 48	Cleavage	5	0	0	2	0
Vitronectin	54		1	2	2	2	2
Fibronectin	259		0	0	0	0	0
Prothrombin	70		8	1	3	2	2
Antithrombin	53		10	8	10	8	10
Plasminogen	91		0	1	8	0	2
Transferrin	77		12	12	12	12	12
$Alpha_2$ macroglobulin	163		8	10	10	8	10

Table 8.4. Relative intensities for Western blots of plasma proteins adsorbed to 200 nm ELP nanoparticles. 0 indicates no band was present, 12 indicates maximal band intensity, with intermediate values indicated intermediate intensities. The + notation indicates samples which were processed with 1:5000 dilution primary and secondary antibodies, as opposed to the 1:1000 dilution used in the standard procedure.

Plasma protein	Fragment size (kDa)	Fragment name	System L20 500	L40 500	L80 500	L160 500	V40 500
Albumin	66		12+	12+	12+	12+	12+
C3	42	Activation	12	10	9	9	10
	70	β	12	12	12	12	12
	115	α	11	3	8	4	7
	187	Whole	11	6	8	1	9
IgG	27	Light Chain	12	12	12	12	12
	55	Heavy Chain	12	12	12	12	12
$Alpha_1$ antitrypsin	47		12	12	12	12	12
Fibrinogen	48	γ	11	12	12	12	12
	56	β	12	11	12	11	12
	68	α	12	12	12	12	12
	< 48	Cleavage	0	0	2	0	3
Vitronectin	54		4	2	1	1	2
Fibronectin	259		0	9	2	0	0
Prothrombin	70		1	1	6	2	7
Antithrombin	53		5	9	11	3	10
Plasminogen	91		0	1	1	0	1
Transferrin	77		12	12	12	12	12
$Alpha_2$ macroglobulin	163		4	9	6	7	10

Table 8.5. Relative intensities for Western blots of plasma proteins adsorbed to 500 nm ELP nanoparticles. 0 indicates no band was present, 12 indicates maximal band intensity, with intermediate values indicated intermediate intensities. The + notation indicates samples which were processed with 1:5000 dilution primary and secondary antibodies, as opposed to the 1:1000 dilution used in the standard procedure.

Plasma protein	Fragment size (kDa)	Fragment name	System L40 200	L40 500	V40 200	V40 500
Albumin	66		12+	12+	12+	12+
C3	42	Activation	12	10	9	10
	70	β	12	12	12	12
	115	α	6	3	8	7
	187	Whole	7	6	8	9
IgG	27	Light Chain	12	12	12	12
	55	Heavy Chain	11	12	12	12
$Alpha_1$ antitrypsin	47		12	12	12	12
Fibrinogen	48	γ	11	12	12	12
	56	β	11	11	11	12
	68	α	12	12	12	12
	< 48	Cleavage	0	0	0	3
Vitronectin	54		2	2	2	2
Fibronectin	259		0	9	0	0
Prothrombin	70		1	1	2	7
Antithrombin	53		8	9	10	10
Plasminogen	91		1	1	2	1
Transferrin	77		12	12	12	12
$Alpha_2$ macroglobulin	163		10	9	10	10

Table 8.6. Relative intensities for Western blots of plasma proteins adsorbed to 40-mer repeat ELP nanoparticles. 0 indicates no band was present, 12 indicates maximal band intensity, with intermediate values indicated intermediate intensities. The + notation indicates samples which were processed with 1:5000 dilution primary and secondary antibodies, as opposed to the 1:1000 dilution used in the standard procedure.

In order to begin assessing ELP nanoparticle biocompatibility *via* plasma protein adsorption, 200 and 500 nm particles of ELPs L20, L40, L80, L160 and V40 were incubated with platelet poor human plasma at 37°C for 2 hours. Loosely bound proteins were removed *via* two rounds of washing and a 10% SDS in PBS solution was used to elute the bound proteome from the nanoparticle

surfaces and resolubilize the ELPs present in the sample. As such, the samples analyzed by protein assay and Western blotting contained both the adsorbed plasma proteome and ELP proteins. Preliminary results demonstrated no reactivity between ELPs and the DC protein assay, owing to their near complete lack of reactive tyrosine and tryptophan amino acids and no cross-reactivity was observed between any anti-plasma protein antibodies and ELPs (data not shown). The concentrations of the final adsorbed proteomes, as quantified by the DC protein assay, are reported in Table 8.2.

The use of highly specific Western blotting not only allowed for the identification of various adsorbed proteins and their relative intensities, but the lack of signal reliably confirms the lack of corresponding proteins in the adsorbed samples. The sensitivity of the method, with its multiple signal intensifying steps, is unlikely to fail to detect proteins for which there are primary antibodies. In order to identify individual proteins from the adsorbed proteome, SDS-PAGE and Western blotting analysis were used where direct comparisons of specific protein band strengths between blots are able to be done due to the constant amount of protein (30 μg) and consistent colour-developing reaction times used. When all adsorbed proteomes were run together on one gel and stained with colloidal gold, in order to best allow for comparisons to the Western blotting results, the amount of protein run for each sample was reduced proportionally with the width of the gel well (from 60 mm to 3 mm). The variations in binding affinities between different primary antibodies does not allow for direct comparisons of band intensities between different individual proteins. While Western blotting methods

are capable of detecting individual proteins with high selectivity and sensitivity, they cannot provide information regarding protein conformation. This technical limitation is noteworthy as the conformation, or change therein, of a protein has been shown to result in additional cellular reactions in certain circumstances (37). Table 8.3 summarizes the Western blot band intensity data for all ELP nanoparticle systems, with Tables 8.4, 8.5 and 8.6 focusing on band intensities from 200 nm particles, 500 nm particles and particles composed of 40-mer ELPs, respectively. Band intensities were quantified using a 13-step greyscale where a value of zero indicates no band was present, a value of 12 indicates a complete black band and intermediate values indicate intermediate intensities. The + symbol, when appended after an intensity score, indicates the primary and secondary antibodies were used at a 1:5000 dilution rather than the standard 1:1000. This additional dilution was found to be necessary when testing for the presence of albumin, as the normal 1:1000 dilutions resulted in rapidly developing non-specific banding throughout the membrane.

All eluted proteome samples were run together on an SDS-PAGE gel and non-specifically stained with colloidal gold in order to assess the proteome composition *via* the protein banding patterns (data not shown). This non-specific visualization method revealed strong similarities in protein composition between all ELP eluents. Each sample showed very strong banding at ~66, and ~25 kDa, at least partially consistent with albumin and the light chain of IgG. A strong band at ~45 kDa could be the C3 activation fragment and/or $alpha_1$ antitrypsin. Moderately strong bands were observed between 50-66 kDa, sizes associated with

fibrinogen and IgG, among other plasma proteins. A strong signal at 75-80 kDa was also observed across all samples and may be at least partially due to the presence of transferrin and C3β. All ELP eluents also had similar moderate banding patterns between 25-37 kDa. One notable difference was the presence of strong protein bands at ~22 kDa for the L40 samples, with little to no corresponding intensities amongst the other samples.

8.4.3. Plasma Clotting in the Presence of ELP Nanoparticles

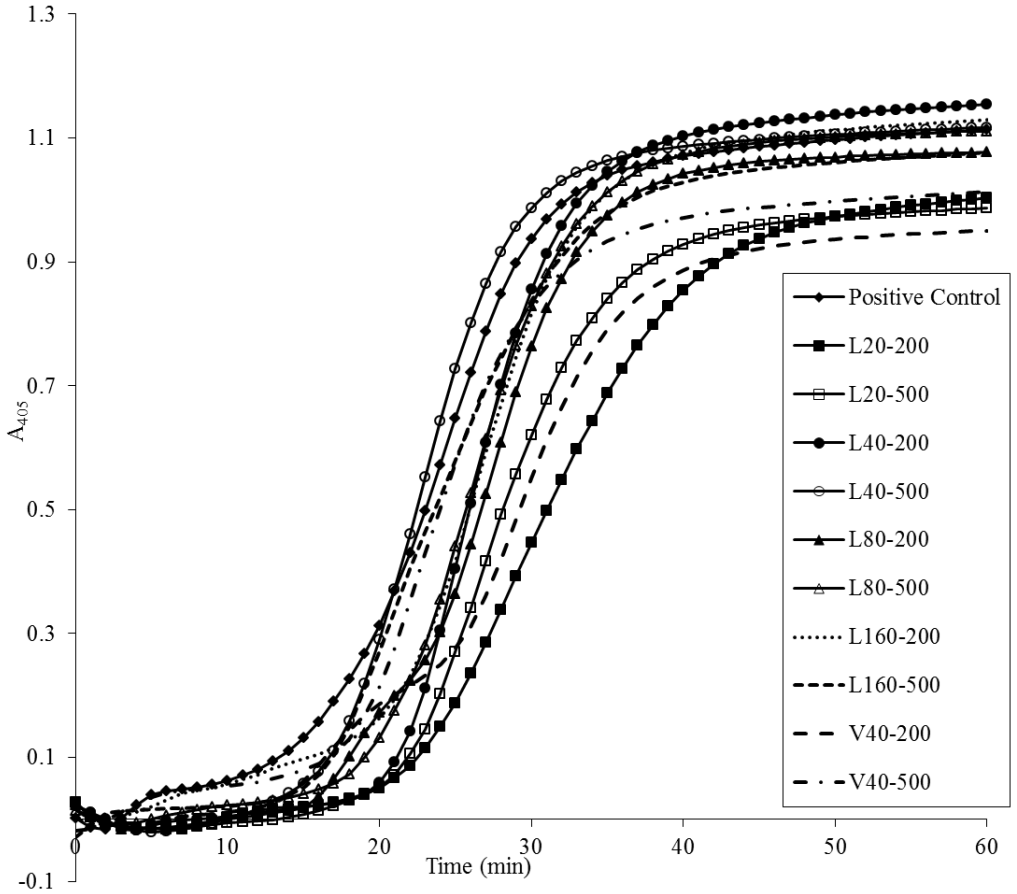

Figure 8.3. Background and baseline corrected average clot formation in platelet poor human plasma over time in the presence of all ELP nanoparticles. The absorbance profiles represent the plasma only control (♦), L20-200 nm (■), L20-500 nm (□), L40-200 nm (●), L40-500 nm (○), L80-200 nm (▲), L80-500 nm (Δ), L160-200 nm (square dot line), L160-500 nm (short dash line), V40-200 nm

(long dash line) and V40-500 nm (dash-dot line) after correcting for background absorbance and artificially setting time 0 values to zero absorbance. Values represent an average of n≥5 with error considered to be ± 10%.

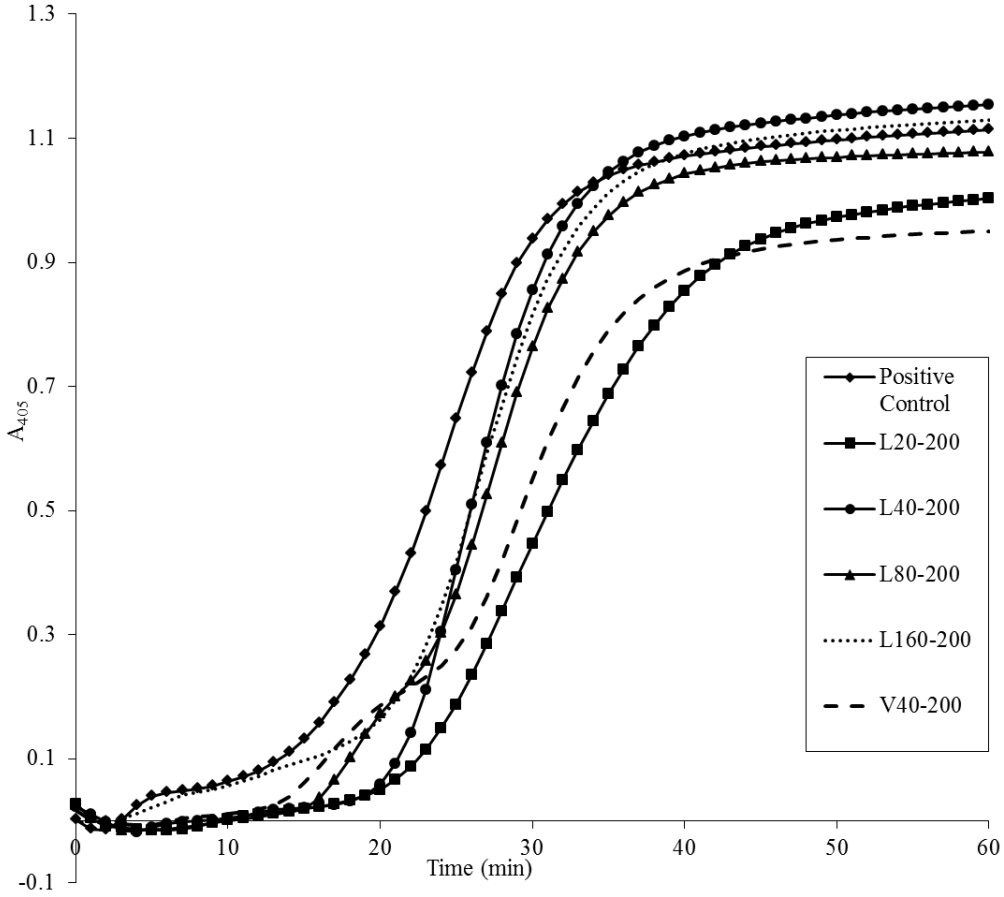

Figure 8.4. Background and baseline corrected average clot formation in platelet poor human plasma over time in the presence of 200 nm ELP nanoparticles. The absorbance profiles represent the plasma only control (♦), L20-200 nm (■), L40-200 nm (●), L80-200 nm (▲), L160-200 nm (square dot line) and V40-200 nm (long dash line) after correcting for background absorbance and artificially setting time 0 values to zero absorbance. Values represent an average of n≥5 with error considered to be ± 10%.

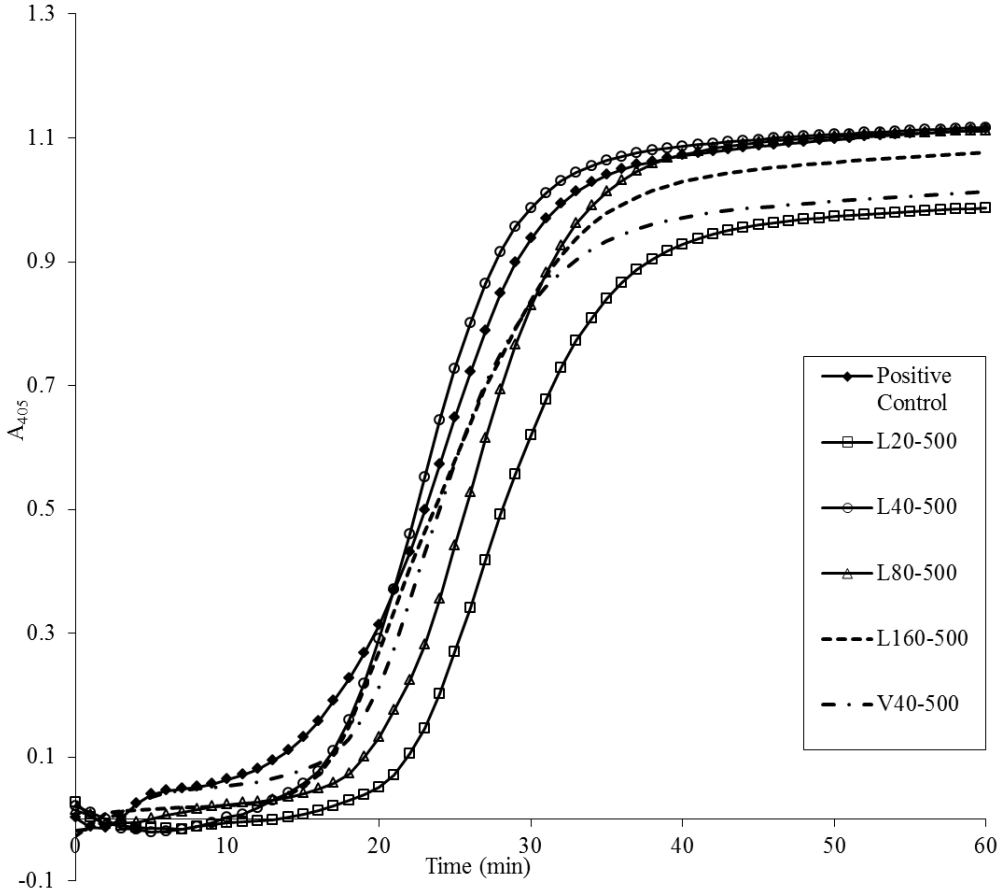

Figure 8.5. Background and baseline corrected average clot formation in platelet poor human plasma over time in the presence of 500 nm ELP nanoparticles. The absorbance profiles represent the plasma only control (♦), L20-500 nm (□), L40-500 nm (○), L80-500 nm (Δ), L160-500 nm (short dash line), and V40-500 nm (dash-dot line) after correcting for background absorbance and artificially setting time 0 values to zero absorbance. Values represent an average of n≥5 with error considered to be ± 10%.

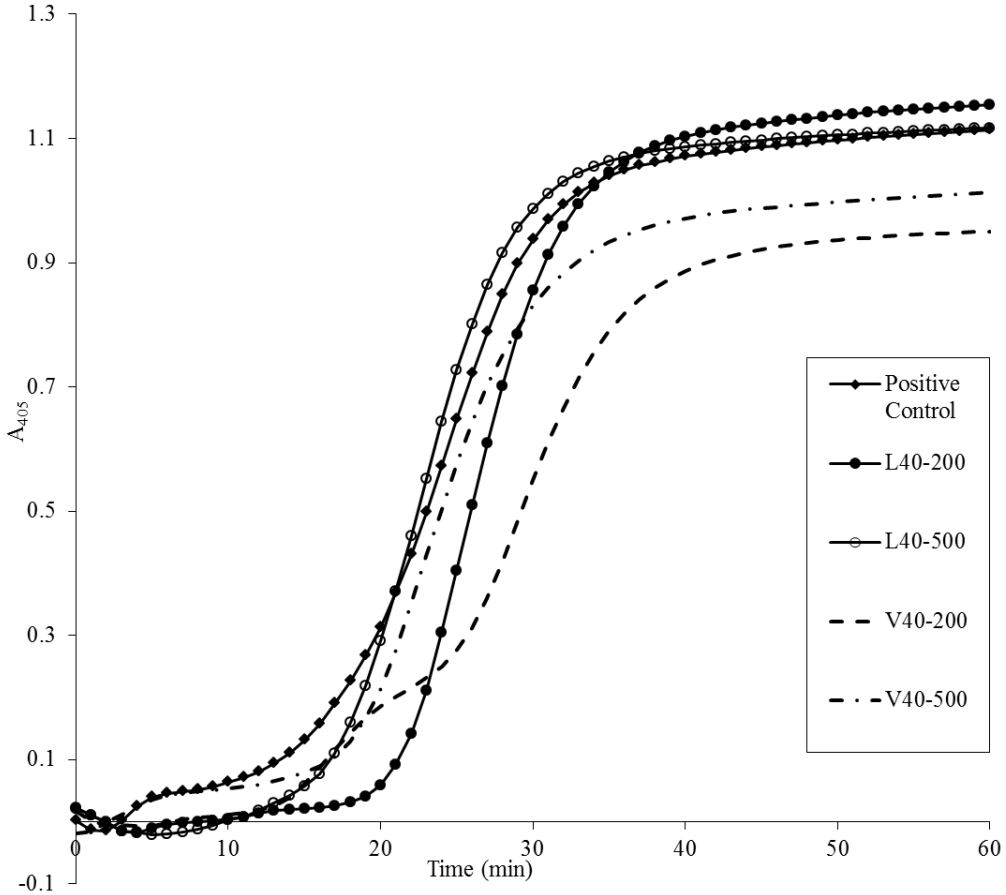

Figure 8.6. Background and baseline corrected average clot formation in platelet poor human plasma over time in the presence of 40-mer repeat ELP nanoparticles. The absorbance profiles represent the plasma only control (♦), L40-200 nm (●), L40-500 nm (○), V40-200 nm (long dash line) and V40-500 nm (dash-dot line) after correcting for background absorbance and artificially setting time 0 values to zero absorbance. Values represent an average of n≥5 with error considered to be ± 10%.

A human plasma recalcification turbidimetric assay was performed in order to examine what effect the presence of ELP nanoparticles may have on blood clotting. Nanoparticles in 1X PBS at pH 7.4 were incubated with recalcified human plasma at 37°C for one hour and the solution turbidity monitored continuously. A positive control sample containing 1X PBS in place of the

nanoparticle solution was run alongside in order to directly compare clotting times. Negative controls for each ELP-containing sample, with PBS in place of the calcium solution, were used to account for any baseline turbidity not caused by the clot reaction. The absorbance at 405 nm was monitored in order to ascertain the rate and intensity of the turbidity change associated with clotting. Figure 8.3 shows the results from the control sample as well as all ELP nanoparticle samples, with Figures 8.4, 8.5 and 8.6 showing the control sample along with either 200 or 500 nm particles or with all ELP nanoparticles made with 40-mer ELPs. The reported results were corrected for any background turbidity and were all artificially baseline corrected so that all samples had an absorbance at 405 nm of zero at the beginning of the assay. Each clot reaction or control was repeated five times and the average values were reported. The overall profiles for each sample and the control show some general similarities, with the clot reactions vigorously increasing the sample turbidities about ~20 minutes into the assay and beginning to plateau after ~40 minutes. There are, however, some differences between the control and ELP-containing samples. All ELP-containing clotting reactions underwent a sharp increase in turbidity later than the control, with delays as large as ~8 minutes for L20-200 and L20-500 samples. L160-200 and V40-500 were the only samples to show an uptick in turbidity alongside the control at ~5 minutes, with similar upticks occurring after ~18 minutes for L80-200 and V40-200. Additionally, all L20 and V40-containing samples had lower final absorbance values than the control and longer L-series ELPs.

8.5. Discussion

ELPs are well known as a flexible platform for biomaterial engineering. The environmental conditions under which ELPs will self-assemble can be controlled *via* the guest amino acid chemistry and overall chain length, recombinant methods allow for the trivial insertion of numerous bioactive moieties and ELPs themselves can be used in a variety of applications including nanoparticulate and hydrogel drug delivery systems, tissue scaffolding, environmental sensing and recombinant protein purification. Another relatively unexplored aspect of ELP platform flexibility involves how various particulate architectures can be obtained from a single construct, given careful sample preparation. For instance, Osborne, Farmer and Woodhouse used crosslinking and solvent additives like DMSO and PEG to investigate particles composed of hydrophobic and cross-linking elastin domains (38). They found that glutaraldehyde crosslinking stabilized the ELP particles and that poly(ethylene glycol) was able to reduce the mean particle size and stabilize the resulting structures without the addition of glutaraldehyde.

8.5.1. ELP Nanoparticle Physical Characterization

The principle of sample preparation affecting particle size is exploited herein in order to produce ELP nanoparticles of two size classes, 200 and 500 nm, from the same ELP protein sequence. It was found that each of the five tested ELP sequences, L20, L40, L80, L160 and V40, were capable of forming particles of both diameters simply by controlling the protein concentration and incubation period above their transition temperatures. Experiments using physiologically

relevant solution (1X PBS pH 7.4) and temperature (37°C) conditions and ELP concentrations of 0.10 mg/mL demonstrated that these conditions were favourable for the formation of both 200 and 500 nm particles for L40, L160 and V40 ELPs as well as 500 nm particles using L80. A concentration of 0.05 mg/mL was required in order for L80 to form 200 nm particles and for L20 to form 200 and 500 nm particles. The changes in particle diameter as a function of incubation time, as illustrated in Figure 8.1, indicate that all of the tested samples underwent a large increase in diameter, from <10 nm to ~200 nm or more, during the first 2-7 minutes of incubation at 37°C. Some variation in particle dynamics was observed with further incubation. The particle diameter dynamics of L20 stood out amongst all other tested samples, as this was the only construct where the diameter increased then began to decrease over the tested incubation period. All other samples showed continued growth of their diameters at reduced rates relative to the initial assembly event, with some sample diameters reaching plateaus. The L80 construct was unique amongst the five tested ELP constructs as two different protein concentrations were necessary in order to obtain both 200 and 500 nm particles.

Comparing nanoparticle development provides insight into the role of ELP concentration in the resulting particle sizes. Both L80 samples underwent particle formation at similar times and the overall diameter profiles follow similar slopes, but clearly lower initial ELP concentrations yield consistently smaller particles, consistent with previously observations examining L-series ELPs at concentrations from 0.05-1.0 mg/mL. This was also observed with L20 at 0.10

mg/mL, with initial particle diameters immediately exceeding 500 nm (data not shown). Comparing the behaviours of L40 and V40 allows for the delineation of the role of guest amino acid chemistry. Both samples exhibited similar size growth profiles, though the V40 diameter increased to ~520 nm before beginning to plateau. That the L40 sample diameter began to plateau at ~380 nm suggests that, with all other conditions held constant, more hydrophobic guest amino acid residues may yield smaller-diameter particles. This may be related to differences in the packing densities of ELP nanoparticles, as shown with TEM where L40 particles had a more uniform electron density compared to V40. Comparing the diameter development profiles for L20 and L80 at 0.05 mg/mL indicates that the ELP chain length can affect particle diameter and its change over time during isothermal incubation. In this case it appears that longer chains result in steadier growth of smaller particles, with no decrease over the ~30 minute time frame. At the end of the experiment the diameters of both systems were comparable. The profiles for L40, L80 and L160 all at 0.10 mg/mL also provide an opportunity to assess the role of ELP chain length. The particle diameters during the first ~15 minutes indicate an inverse relationship between size and chain length, with the L40 generally forming the largest and L160 the smallest. As the incubation period extended, the L40 and L160 samples followed very similar trajectories, each plateauing at similar times with similar sizes. L80 diameters continued to increase at a greater rate, reaching a final diameter of ~570 nm.

Once the nanoparticle preparation conditions were chosen and sizes verified by TEM, the zeta potential values for each system were measured. It was

found that despite variations in particle diameter, ELP concentration, chain length and/or guest amino acid hydrophobicity, the zeta potential values measured in 1X PBS pH 7.4 at 37°C for all constructs were all found to be in the range of -6 to -10 mV. This implies that factors common to all of the tested ELP constructs likely had a stronger influence on the zeta potential than variable characteristics like the guest amino acid or total chain length.

8.5.2. Adsorbed Proteome Quantitation and Identification

DC protein assay tests on ELP-only control samples did not elicit any meaningful responses when evaluated using a standard BSA standard curve. This was not surprising given that the ELP constructs were severely lacking in amino acid chemistries which react strongly with the DC protein assay and allowed for a measurement of the concentration of the adsorbed proteome without needing to compensate for the presence of ELPs in the samples. Overall, the concentrations of the adsorbed proteome are low, approaching the lower limit of the DC protein assay without any sample dilution. These results are unexpected given the hydrophobicity of all ELPs, particularly leucine-containing constructs. Recent studies show the role of hydrophobicity, while influencing the adsorbed protein corona, does not always behave in a consistent manner (39). Studies have shown that coating polystyrene nanoparticles with either transferrin or hydrophobin proteins lead to reduced protein corona formation (40, 41). The amount of protein adsorbed to the ELP nanoparticles was at least an order of magnitude lower than that found on the surface of thermogelling polymer hydrogels and was in the range of values found for protein adsorption to clinically-employed bioactive

glass 45S5 (33, 35). Given that the zeta potential values for each of the nanoparticle systems were in the same narrow range of values, it is unlikely that any variations in the amount of adsorbed protein between samples was influenced by differences in particle charge. Generally speaking, more protein was found adsorbed to the 200 nm particles than the corresponding 500 nm particles, with the L20 system showing a statistically significant difference ($p<0.05$). The only sample which did not follow this trend was L80, where the 500 nm samples adsorbed more protein, though this may be due to the 500 nm sample (0.10 mg/mL) having twice the ELP concentration of the 200 nm sample (0.05 mg/mL). That the 200 nm particles generally adsorbed more protein than their corresponding 500 nm constructs is not unusual given that, when the amount of ELP was held constant, smaller particles should have a greater surface area for potential adsorption events.

There was no clear correlation between ELP chain length and amount of adsorbed proteome when comparing L20, L40, L80 and L160. While the L20-derived samples adsorbed the most protein despite their lower ELP concentration, the next shortest construct (L40) adsorbed the least. ELP guest amino acid chemistry was found to play a role in the extent of protein adsorption, with the more hydrophobic L40 adsorbing significantly less protein that the corresponding V40 construct at both 200 nm ($p<0.05$) and 500 nm ($p<0.005$) size classes. These results are counter-intuitive, as biomaterial non-fouling strategies generally revolve around the use of highly hydrated polymers such as poly(ethylene glycol) or zwitterionic polybetaines (42, 43).

Albumin is a protein found in high concentrations in plasma and its presence on biomaterial surfaces is generally considered innocuous-so much so that surface passivation strategies have been developed using the protein (44). Given its ubiquity, the detection of albumin on ELP nanoparticle surfaces is not unexpected. Previous studies have found large amounts of the protein on other biomaterial surfaces including clinically-employed bioactive glass 45S5, though these previous albumin intensities were never so high that the primary and secondary antibodies needed to be further diluted from 1:1000 to 1:5000 in order to avoid non-specific banding (33-35). Other studies using amorphous silica, β-cyclodextrin, cellulose or polylactic-*co*-glycolic acid nanoparticles have shown serum albumin as a less prominent component of protein coronas, with variations based upon particle physical characteristics (45, 46). That albumin was found to be such a large component of the adsorbed proteome may help to explain why ELP-derived materials are generally considered biocompatible. Widespread albumin binding to hydrophobic entities has been shown to act as a dysopsonin and increase nanoparticle circulation in blood as well as hydrophobic drug half-life (47, 48). However, some studies have shown that denatured albumin can cause platelet adsorption and activation as well as increased phagocytic response (32, 49). While Western blotting cannot determine the conformation of the adsorbed albumin, the potential for negative reactions as a function of adsorbed albumin must be recognized

Complement represents a protein-based component of innate immunity. Activation of complement can result in inflammation, cell lysis, opsonisation and

an increased adaptive immune response (50). Complement component 3 (C3) is a key molecule in all three of the complement activation pathways, particularly the alternative pathway, which is the most relevant activation pathway for host-biomaterial interactions (51). Complement activation *via* the alternative pathway begins by the activated C3b portion of C3 interacting with complement Factor B. Cleavage of Factor B by Factor D results in the formation of C3bBb convertase- an enzyme which will generate more C3b in a self-propagating loop (52). C3 can appear on denaturing SDS-PAGE as up to four distinct bands: a 187 kDa whole C3, a 115 kDa α chain, a 70 kDa β chain and potentially a 42 kDa activation fragment. Intensity values from Tables 8.3-8.6 indicate that all four bands were detected in the adsorbed proteomes of all ten ELP nanoparticle samples. Intensity values for the whole and α chain showed considerable variability, while levels of the β chain and activation fragment only ranged from high to very high. That each of the ELP nanoparticle systems, regardless of particle diameter, chain length or guest amino acid chemistry is capable of strongly activating complement is a serious concern for all ELP-based biomaterials.

Transferrin is another plasma protein associated with innate immunity. While generally well known for its role in iron transport, studies have demonstrated that transferrin can activate macrophages (53, 54). Studies using transferrin as a coating on polystyrene nanoparticles observed that the presence of this protein lead to decreased nonspecific protein adsorption from human plasma solutions (40). This protein was found adsorbed to all ELP nanoparticles at very

high levels and as such, suggests that ELP nanoparticles may activate macrophage cells and/or act to supress nonspecific protein corona formation.

Immunoglobulin G (IgG) is the most common variant of the immunoglobulin family, a class of proteins found prominently in plasma. Immunoglobulins play a central role in adaptive immunity by binding to antigens and recruiting macrophage cells (55). IgG also plays a role in complement by initiating the classical complement activation pathway (56). Both the light and heavy chains of IgG were found in very large amounts across all ELP nanoparticle samples. IgG has been found previously in moderate levels on amorphous silica nanoparticles as well as low levels on various curcumin preparations composed of β-cyclodextrin, cellulose or dendrimers (45, 46). The levels of IgG on ELP nanoparticles in concert with the high levels of C3 activation and transferrin, further strengthens the possibility that ELP-based nanoparticles could stimulate an immune response.

Fibrinogen is another prominent protein component of plasma. Upon activation by thrombin, this protein is a major component of blood clots. The activation of fibrinogen can be detected on SDS-PAGE by the presence of bands with molecular weights below 48 kDa. These bands would be detected in addition to the usual three bands of fibrinogen: α, β and γ with molecular weights of 68, 56 and 48 kDa, respectively. Each of these three standard fibrinogen chains was detected for each ELP nanoparticle system in very high levels. Additionally, four nanoparticle samples contained fibrinogen cleavage fragments in low to moderate levels in their adsorbed proteomes: L20-200, L80-500, L160-200 and V40-500.

Even the presence of adsorbed at 5 ng/cm^2 fibrinogen, if denatured sufficiently, can lead to the activation of platelets (57-59); that it is found in high levels for all constructs in addition to the detection cleavage fragments for four samples suggests the ELP nanoparticles may exhibit procoagulant activity. Previous studies of ELPs composed of repeats of tropoelastin exons 20-24 have shown that, when used as a surface coating, they reduce fibrinogen adsorption and may also affect the conformation of the adsorbed fibrinogen, resulting in varying levels of platelet activation (60-62). While there are significant differences in the sequences of the ELPs tested herein, as well as the assembly/disassembly states of the constructs, further studies of fibrinogen adsorption to ELP-based materials is warranted.

Prothrombin is the inactive precursor to the potent coagulation enzyme thrombin. This precursor was found in low levels for most ELP nanoparticle constructs. L20-200, L80-500 and V40-500 were found to have moderately high levels of the protein adsorbed to their surface. That these specific samples were three of the four for which fibrinogen cleavage was detected suggests that there may be a correlation between the extent of prothrombin adsorption and fibrinogen activation. Studies using silica nanoparticles have demonstrated that nanoparticle size can significantly affect the adsorption of prothrombin (63).

Antithrombin is a powerful serine protease inhibitor and is known to inactivate various enzymes in the coagulation cascade, most notably thrombin (64). Antithrombin was found to adsorb to all ELP nanoparticles in moderately-high to high levels except for L20-500 and L160-500, where they were found to

adsorb in moderate and low levels, respectively. The presence of this protein may help to shift the coagulation balance in response to these materials back toward neutral or anti-coagulant levels, depending on the proportion of other coagulation or fibrinolytic factors.

Plasminogen is the inactive precursor of plasmin, a serine protease which is capable of dissolving fibrin clots. It was found to adsorb in low levels to ELP nanoparticles L40-200, L40-500, L80-500, V40-200 and V40-500. Interestingly, it was also found in moderately high levels on L80-200. Its presence in the adsorbed proteome indicates potential fibrinolytic activity, something actively sought in the development of other biomaterial surfaces (65, 66).

Fibronectin, vitronectin and fibrinogen are plasma proteins capable of facilitating cell attachment and activation to material surfaces (67, 68). In addition to the high levels of fibrinogen found adsorbed to all ELP samples, low levels of vitronectin were also found in the adsorbed proteome of all ELP nanoparticles. This protein has been found to make up a large proportion of the protein corona found on silica nanoparticles incubated in 10% human plasma (45). Fibronectin was only found in low levels on L80-500 and moderately high levels on L40-500. This suggests that there may be some substantial protein-modulated cell activity from macrophages, leukocytes and platelets amongst other cell types. Cell binding and activation may be of particular concern for the two samples to which all three cell binding proteins adsorbed.

Alpha$_1$ antitrypsin is a serine protease inhibitor responsible for modulating enzymes associated with inflammation, most notable neutrophil elastase (69). This plasma protein was found in very high levels adsorbed to all ELP nanoparticles and may protect these particles from degradation by elastase. This is of critical importance because elastase is one of only two endopeptidases shown to be able to degrade soluble ELPs and the only one capable of digesting ELPs once they have formed particles (70). This protein has previously been found to adsorb to polystyrene nanoparticles with a variety of surface functionalization (71).

Alpha$_2$ macroglobulin is another protease inhibitor found in plasma. Unlike alpha$_1$ antitrypsin, alpha$_2$ macroglobulin is capable of inhibiting the activity of a very large number of proteases from numerous catalytic classes. This protein has been found to be a major component of the adsorbed proteome of amorphous silica nanoparticles (45). Most relevant to the discussion of biomaterial adsorption is that both thrombin and plasmin may be inhibited by alpha$_2$ macroglobulin (72). This broad-spectrum protease was found adsorbed to all ELP nanoparticle systems in moderately low to moderately high intensities. Given the large number of enzymes it can act upon, determining the consequences of alpha$_2$ macroglobulin adsorption would require analysis beyond Western blotting.

Inasmuch as the presence of adsorbed proteins may yield information as to the host response to biomaterials, so too does the absence of proteins provide useful information. Of the 23 plasma proteins which were scanned for using

Western blotting, only 12 were found adsorbed to some or all of the ELP nanoparticles. The total lack of kininogen, prekallikrein as well as Factors XI and XII implies that any coagulation activation due to the presence of ELP nanoparticles would not occur *via* the contact activation pathway. The absence of Proteins S and C in all adsorbed proteomes suggests a limited fibrinolytic host response to ELP nanoparticles.

Given the careful ELP sequence design and sample preparation, it is possible to deconvolute the effects of nanoparticle diameter, ELP chain length and gust amino acid hydrophobicity on human plasma protein adsorption. Fibrinogen cleavage was shown to be dependent upon nanoparticle diameter, with only one size class each of L20, L80, L160 and L160 containing fibrinongen cleavage products in their proteomes. Fibronectin was found on 500 nm L40 and L80 but not the corresponding 200 nm samples. There were also many instances where the intensity of a specific protein differed greatly between 200 and 500 nm particles composed of the same ELP protein including prothrombin for L20 and V40, antithrombin for L20 and L160, plasminogen for L80 and alpha$_2$ macroglobulin for L20 and L80. These results are consistent with previous reports using polymeric or inorganic nanoparticles, wherein differences in particle size resulted in large variations on the quantities of specific proteins comprising the adsorbed corona (63, 71). Adsorbed proteome content and intensity was also found to vary as a function of ELP chain length, with whole and α chains of C3, fibrinogen cleavage fragments, fibronectin, prothrombin, antithrombin and plasminogen all showing considerable variation amongst the L-series ELPs. While these proteins

all varied between the L-series of ELPs, there was no discernable correlation between protein presence/absence nor intensity as a function of chain length. Guest amino acid hydrophobicity was also found to affect fibrinogen cleavage as well as the extent of prothrombin and fibronectin adsorption. While some variance in content and intensity of the adsorbed proteomes was observed between ELP nanoparticles, instances where variations in particle size, chain length or hydrophobicity did not affect protein adsorption substantially. This was the case for albumin, C3, IgG, alpha$_1$ antitrypsin, fibrinogen, vitronectin and transferrin. In these instances it is likely that the adsorption of these proteins is due to factors which were constant among all ELP nanoparticles including surface charge, polarity or the conserved residues throughout the ELP sequences.

8.5.3. ELP Nanoparticle Effect on Plasma Clotting

The plasma recalcification turbidimetric assay results demonstrate that ELP nanoparticles elicit a range of moderately inhibitory effects on human plasma clotting. This is consistent with previous studies using tropoelastin exon-derived ELPs that demonstrated these materials did not elicit pro-coagulant responses and, when used to coat polymeric surfaces, reduced platelet activation (60-62, 73). While the turbidimetric profiles of each sample generally reflect that of the control, there are differences in the timing of the onset and plateau points of the clotting reaction and final endpoint values which imply that the presence of ELP nanoparticle may affect blood clotting. The largest perturbations were observed for the L20 and V40 constructs at both 200 and 500 nm diameters. The V40-200 containing sample displayed large delays in clot reaction initiation and

plateau though this was not the case for V40-500. Both samples also showed decreased endpoint values relative to the control sample. Both L20 samples showed the largest delay in the onset of clotting and were two of the three samples with the largest delays in the reaction reaching plateau and lowest endpoint turbidities. As the L-series ELP chain length increased, the degree of clot perturbation tended to decrease. 200 nm L40 particles delayed the onset of the clot reaction but did not affect the plateau. 500 nm particles of the same construct had minimal impact on the clot reaction. L80 and L160 ELPs prompted some delay in the onset of clotting, with longer ELPs stimulating shorted delays. L40, L80 and L160 clot reactions all had final turbidity values similar to that of the control sample. From the L-series clot results, it is clear that increased chain length decreased the type and degree of clot reaction perturbation. When comparing nanoparticle size classes, the samples containing 200 nm particles tended to delay the onset of clotting more frequently than the corresponding 500 nm particles. Comparing V40 and L40 results allowed for speculation on the role of guest amino acid hydrophobicity. The clotting results suggest the more hydrophilic V40 constructs tend to significantly depress the final overall absorbance for both the 200 nm ($p<0.0001$) and 500 nm ($p<0.05$) size classes. Variations in the adsorbed proteome between ELP nanoparticle systems would influence their respective clotting responses. Western blotting revealed the presence of both pro- and anti-coagulant proteins on all samples and the clotting assay revealed the nanoparticles to be moderately inhibitory. As such, it is possible that the adsorbed $alpha_2$ macroglobulin inhibited pro-coagulant enzymes

to a greater extent that anti-coagulant enzymes and that antithrombin and plasminogen had a more pronounced effect on the clot reaction than fibrinogen and prothrombin. Variations in the quantities of these proteins, as assessed by Western blot band intensities, could account for some of the variance between samples. The conformation of adsorbed fibrinogen may have also played a role, consistent with previous findings where various ELP surface coatings prompted different conformations of adsorbed fibrinogen, depending upon the stiffness of the ELP layer (62).

8.6. Conclusion

ELPs L20, L40, L80, L160 and V40 were found to form 200 or 500 nm particles in 1X PBS pH 7.4 after ~3-30 minutes incubation at 37°C. ELP solution concentration was found to affect particle size, with increased concentrations yielding larger particles. 0.05 or 0.10 mg/mL ELP solutions were found capable of forming 200 or 500 nm particles from each of the five ELP sequences. DLS and TEM images were in good agreement regarding the particle diameters. Zeta potential measurements revealed charges in the range of -6 to -10 mV across all ten nanoparticle systems. After a two hour incubation in platelet-poor human plasma, ~0.2-0.5 mg/mL of adsorbed protein was found to elute from the nanoparticle surfaces, amounts similar to previous proteomes adsorbed to clinically employed bioactive glass. Denaturing SDS-PAGE and colloidal gold staining indicated that the adsorbed proteomes from all samples had very similar banding patterns with the heaviest banding at ~66 kDa. Western blotting showed that all ELP nanoparticle proteomes contained 8 of the 23 plasma proteins that

were screened for, with various samples containing additional plasma proteins. Copious amounts of albumin were detected in the adsorbed samples, with quantities so high that primary and secondary Western blotting antibodies needed to be diluted an additional 5-fold beyond the standard procedure. High levels of activated C3, IgG and transferrin in all adsorbed proteomes suggest that all ELP nanoparticles may elicit an immune response regardless of guest amino acid chemistry, chain length or particle diameter. Consistently large amounts of fibrinogen and alpha$_1$ antitrypsin were also detected across all samples. A plasma recalcification turbidimetric assay demonstrated that ELP nanoparticles generally had a moderately inhibitory effect on clotting, with ~2-8 minute delays in the onset and plateau relative to the control. In addition to the largest of the kinetic delays, endpoint intensities were found to be lower for the shortest tested construct, L20, as well as the hydrophilic V40. In general, the longer the chain length, the more the clotting reaction resembled the control sample. Hydrophobic L40 was also found to resemble the control sample more than the V40. Given the largely favourable clot responses in combination with very large amounts of adsorbed albumin, it is possible that these ELP nanoparticle systems may not prompt significant deleterious host responses, though high amounts of IgG and activated C3 regardless of ELP sequence, length or particle diameter may imply that conserved elements across all samples may prompt an immune response to these materials.

8.7. Acknowledgements

The authors would like to acknowledge the technical assistance provided by Scott Elgersma for dynamic light scattering and zeta potential, as well as Woo Jung Cho and the Cell Imaging Center at the University of Alberta for TEM access, training and technical expertise. This work was supported by the Natural Sciences and Engineering Research Council of Canada Discovery grant #RES0011279. MSB was supported by Alberta Innovates Technology Futures Graduate Student Scholarship in Nanotechnology #200801440. AKA was the recipient of the Ministry of Higher Education and King Saud University Scholarship, Saudi Arabia.

8.8. References

1. Callahan DJ, Liu W, Li X, Dreher MR, Hassouneh W, Kim M, et al. Triple stimulus-responsive polypeptide nanoparticles that enhance intratumoral spatial distribution. Nano Lett. 2012;12(4):2165-70.

2. Urry DW. Entropic elastic processes in protein mechanisms. I. Elastic structure due to an inverse temperature transition and elasticity due to internal chain dynamics. Journal of protein chemistry. 1988;7(1):1-34.

3. Urry DW, Gowda DC, Parker TM, Luan CH, Reid MC, Harris CM, et al. Hydrophobicity scale for proteins based on inverse temperature transitions. Biopolymers. 1992;32(9):1243-50.

4. Chilkoti A, Dreher MR, Meyer DE. Design of thermally responsive, recombinant polypeptide carriers for targeted drug delivery. Cancer. 2002;54:1093-111.

5. Puiggalí J, Franco L, J. del Valle L. Smart systems related to polypeptide sequences. AIMS Materials Science. 2016;3(1):289-323.

6. Bahniuk MS, Alshememry AK, Unsworth LD. High-yield recombinant expression and purification of marginally soluble, short elastin-like polypeptides. BioTechniques. 2016;61(6):297.

7. Meyer DE, Chilkoti A. Genetically Encoded Synthesis of Protein-Based Polymers with Precisely Specified Molecular Weight and Sequence by Recursive Directional Ligation: Examples from the Elastin-like Polypeptide System. Biomacromolecules. 2002:357-67.

8. Meyer DE, Chilkoti A. Purification of recombinant proteins by fusion with thermally-responsive polypeptides. Nature Biotechnology. 1999;17(November).

9. Bataille L, Dieryck W, Hocquellet A, Cabanne C, Bathany K, Lecommandoux S, et al. Recombinant Production and Purification of Short Hydrophobic Elastin-Like Polypeptides with Low Transition Temperatures. Protein Expression and Purification. 2016.

10. Lin M, Rose-John S, Grötzinger J, Conrad U, Scheller J. Functional expression of a biologically active fragment of soluble gp130 as an ELP-fusion protein in transgenic plants: purification via inverse transition cycling. Biochemical Journal. 2006;398(3):577-83.

11. Yeboah A, Cohen RI, Rabolli C, Yarmush ML, Berthiaume F. Elastin-like polypeptides: A strategic fusion partner for biologics. Biotechnol Bioeng. 2016;113(8):1617-27.

12. Sarangthem V, Cho Ea, Bae SM, Singh TD, Kim SJ, Kim S, et al. Construction and application of elastin like polypeptide containing IL-4 receptor targeting peptide. PLoS ONE. 2013;8(12):1-12.

13. Shi P, Aluri S, Lin YA, Shah M, Edman M, Dhandhukia J, et al. Elastin-based protein polymer nanoparticles carrying drug at both corona and core suppress tumor growth in vivo. Journal of Controlled Release. 2013;171(3):330-8.

14. Meyer DE, Kong GA, Dewhirst MW, Zalutsky MR, Chilkoti A. Targeting a Genetically Engineered Elastin-like Polypeptide to Solid Tumors by Local Hyperthermia 1. In Vitro. 2001;42745:1548-54.

15. Koetting MC, Peters JT, Steichen SD, Peppas NA. Stimulus-responsive hydrogels: Theory, modern advances, and applications. Materials Science and Engineering: R: Reports. 2015;93:1-49.

16. Rodriguez-Cabello JC, Pina MJ, Ibanez-Fonseca A, Fernandez-Colino A, Arias FJ. Nanotechnological Approaches to Therapeutic Delivery Using Elastin-Like Recombinamers. Bioconjug Chem. 2015;26(7):1252-65.

17. Wang W, Jashnani A, Aluri SR, Gustafson JA, Hsueh PY, Yarber F, et al. A thermo-responsive protein treatment for dry eyes. J Control Release. 2015;199:156-67.

18. Heilshorn S. Endothelial cell adhesion to the fibronectin CS5 domain in artificial extracellular matrix proteins. Biomaterials. 2003;24(23):4245-52.

19. Urry DW. Protein elasticity based on conformations of sequential polypeptides: the biological elastic fiber. Journal of protein chemistry. 1984;3(5-6):403-36.

20. Yigit S, Dinjaski N, Kaplan DL. Fibrous proteins: At the crossroads of genetic engineering and biotechnological applications. Biotechnol Bioeng. 2016;113(5):913-29.

21. Desai MS, Lee SW. Protein-based functional nanomaterial design for bioengineering applications. Wiley Interdiscip Rev Nanomed Nanobiotechnol. 2015;7(1):69-97.

22. Kowalczyk T, Hnatuszko-Konka K, Gerszberg A, Kononowicz AK. Elastin-like polypeptides as a promising family of genetically-engineered protein based polymers. World J Microbiol Biotechnol. 2014;30(8):2141-52.

23. Nettles DL, Chilkoti A, Setton LA. Applications of elastin-like polypeptides in tissue engineering. Adv Drug Deliv Rev. 2010;62(15):1479-85.

24. Urry DW, Parker TM, Reid MC, Gowda DC. Biocompatibility of the Bioelastic Materials, Poly(GVGVP) and Its γ-Irradiation Cross-Linked Matrix: Summary of Generic Biological Test Results. Journal of Bioactive and Compatible Polymers. 1991;6(3):263-82.

25. Elsas FJ, Gowda DC, Urry DW. Synthetic polypeptide sleeve for strabismus surgery. Journal of pediatric ophthalmology and strabismus. 1992;29(5):284-6.

26. Sallach RE, Cui W, Balderrama F, Martinez AW, Wen J, Haller Ca, et al. Long-term biostability of self-assembling protein polymers in the absence of covalent crosslinking. Biomaterials. 2010;31(4):779-91.

27. Rincon AC, Molina-Martinez IT, de Las Heras B, Alonso M, Bailez C, Rodriguez-Cabello JC, et al. Biocompatibility of elastin-like polymer poly(VPAVG) microparticles: in vitro and in vivo studies. J Biomed Mater Res A. 2006;78(2):343-51.

28. Horbett TA. Chapter II.1.2 - Adsorbed Proteins on Biomaterials A2 - Ratner, Buddy D. In: Hoffman AS, Schoen FJ, Lemons JE, editors. Biomaterials Science (Third Edition): Academic Press; 2013. p. 394-408.

29. Vroman L, Adams A, Fischer G, Munoz P. Interaction of high molecular weight kininogen, factor XII, and fibrinogen in plasma at interfaces. Blood. 1980;55(1):156-9.

30. Schleh C, Rothen-Rutishauser B, Kreyling WG. The influence of pulmonary surfactant on nanoparticulate drug delivery systems. European journal of pharmaceutics and biopharmaceutics. 2011;77(3):350-2.

31. Deng ZJ, Liang M, Monteiro M, Toth I, Minchin RF. Nanoparticle-induced unfolding of fibrinogen promotes Mac-1 receptor activation and inflammation. Nature nanotechnology. 2011;6(1):39-44.

32. Mortimer GM, Butcher NJ, Musumeci AW, Deng ZJ, Martin DJ, Minchin RF. Cryptic epitopes of albumin determine mononuclear phagocyte system clearance of nanomaterials. ACS nano. 2014;8(4):3357-66.

33. Bahniuk MS, Pirayesh H, Singh HD, Nychka Ja, Unsworth LD. Bioactive glass 45S5 powders: effect of synthesis route and resultant surface chemistry and crystallinity on protein adsorption from human plasma. Biointerphases. 2012;7(1-4):1-5.

34. Yogasundaram H, Bahniuk MS, Singh H-D, Aliabadi HM, Uludağ H, Unsworth LD. BSA Nanoparticles for siRNA Delivery: Coating Effects on Nanoparticle Properties, Plasma Protein Adsorption, and In Vitro siRNA Delivery. International journal of biomaterials. 2012;2012:584060-.

35. Nikouei NS, Vakili MR, Bahniuk MS, Unsworth L, Akbari A, Wu J, et al. Thermoreversible hydrogels based on triblock copolymers of poly(ethylene glycol) and carboxyl functionalized poly(ε-caprolactone): The effect of carboxyl group substitution on the transition temperature and biocompatibility in plasma. Acta biomaterialia. 2014;12:81-92.

36. Abraham S, So A, Unsworth LD. Poly(carboxybetaine methacrylamide)-modified nanoparticles: a model system for studying the effect of chain chemistry on film properties, adsorbed protein conformation, and clot formation kinetics. Biomacromolecules. 2011;12(10):3567-80.

37. Tsai WB, Grunkemeier JM, Horbett TA. Variations in the ability of adsorbed fibrinogen to mediate platelet adhesion to polystyrene-based materials: A multivariate statistical analysis of antibody binding to the platelet binding sites of fibrinogen. Journal of Biomedical Materials Research Part A. 2003;67(4):1255-68.

38. Osborne JL, Farmer R, Woodhouse KA. Self-assembled elastin-like polypeptide particles. Acta Biomater. 2008;4(1):49-57.

39. Nel AE, Mädler L, Velegol D, Xia T, Hoek EM, Somasundaran P, et al. Understanding biophysicochemical interactions at the nano–bio interface. Nature materials. 2009;8(7):543-57.

40. Pitek AS, O'Connell D, Mahon E, Monopoli MP, Bombelli FB, Dawson KA. Transferrin coated nanoparticles: study of the bionano interface in human plasma. PloS one. 2012;7(7):e40685.

41. Grunér M, Kauscher U, Linder M, Monopoli M. An environmental route of exposure affects the formation of nanoparticle coronas in blood plasma. Journal of proteomics. 2016;137:52-8.

42. Ostuni E, Chapman RG, Holmlin RE, Takayama S, Whitesides GM. A survey of structure− property relationships of surfaces that resist the adsorption of protein. Langmuir. 2001;17(18):5605-20.

43. Binazadeh M, Kabiri M, Unsworth LD. Poly (ethylene glycol) and Poly (carboxy betaine) based nonfouling architectures: Review and current efforts. Proteins at Interfaces III State of the Art: ACS Publications; 2012. p. 621-43.

44. Lyman D, Klein KG, Brash J, Fritzinger B, Andrade J, Bonomo F. Platelet interaction with protein-coated surfaces: an approach to thrombo-resistant surfaces. Platelet Adhesion and Aggregation in Thrombosis: Countermeasures. 1970.

45. Fedeli C, Segat D, Tavano R, Bubacco L, De Franceschi G, de Laureto PP, et al. The functional dissection of the plasma corona of SiO 2-NPs spots histidine rich glycoprotein as a major player able to hamper nanoparticle capture by macrophages. Nanoscale. 2015;7(42):17710-28.

46. Yallapu MM, Ebeling MC, Chauhan N, Jaggi M, Chauhan SC. Interaction of curcumin nanoformulations with human plasma proteins and erythrocytes. International journal of nanomedicine. 2011;6:2779.

47. Aggarwal P, Hall JB, McLeland CB, Dobrovolskaia MA, McNeil SE. Nanoparticle interaction with plasma proteins as it relates to particle biodistribution, biocompatibility and therapeutic efficacy. Advanced drug delivery reviews. 2009;61(6):428-37.

48. Sleep D, Cameron J, Evans LR. Albumin as a versatile platform for drug half-life extension. Biochimica et Biophysica Acta (BBA)-General Subjects. 2013;1830(12):5526-34.

49. Sivaraman B, Latour Ra. The adherence of platelets to adsorbed albumin by receptor-mediated recognition of binding sites exposed by adsorption-induced unfolding. Biomaterials. 2010;31(6):1036-44.

50. Molina H. Complement and immunity. Rheumatic Disease Clinics of North America. 2004;30(1):1-18.

51. Andersson J, Ekdahl KN, Lambris JD, Nilsson B. Binding of C3 fragments on top of adsorbed plasma proteins during complement activation on a model biomaterial surface. Biomaterials. 2005;26(13):1477-85.

52. Nilsson B, Ekdahl KN. The tick-over theory revisited: is C3 a contact-activated protein? Immunobiology. 2012;217(11):1106-10.

53. Moos T, Morgan EH. Transferrin and transferrin receptor function in brain barrier systems. Cellular and molecular neurobiology. 2000;20(1):77-95.

54. Stafford JL, Belosevic M. Transferrin and the innate immune response of fish: identification of a novel mechanism of macrophage activation. Developmental and comparative immunology. 2003;27(6-7):539-54.

55. Anderson JM, Rodriguez A, Chang DT. Foreign body reaction to biomaterials. Seminars in immunology. 2008;20(2):86-100.

56. Abbas AK. Cellular and molecular immunology. In: Lichtman AH, Pillai S, editors. 6th ed. ed. Philadelphia :: Saunders Elsevier; 2007.

57. Mosesson MW. Fibrinogen and fibrin structure and functions. Journal of thrombosis and haemostasis : JTH. 2005;3(8):1894-904.

58. Massa TM, Yang ML, Ho JYC, Brash JL, Santerre JP. Fibrinogen surface distribution correlates to platelet adhesion pattern on fluorinated surface-modified polyetherurethane. Biomaterials. 2005;26(35):7367-76.

59. Unsworth LD, Sheardown H, Brash JL. Polyethylene oxide surfaces of variable chain density by chemisorption of PEO-thiol on gold: Adsorption of proteins from plasma studied by radiolabelling and immunoblotting. Biomaterials. 2005;26(30):5927-33.

60. Srokowski E, Blit P, McClung W, Brash J, Santerre J, Woodhouse K. Platelet adhesion and fibrinogen accretion on a family of elastin-like polypeptides. Journal of Biomaterials Science, Polymer Edition. 2011;22(1-3):41-57.

61. Blit PH, McClung WG, Brash JL, Woodhouse Ka, Santerre JP. Platelet inhibition and endothelial cell adhesion on elastin-like polypeptide surface modified materials. Biomaterials. 2011;32(25):5790-800.

62. Srokowski EM, Woodhouse Ka. Evaluation of the bulk platelet response and fibrinogen interaction to elastin-like polypeptide coatings. Journal of Biomedical Materials Research - Part A. 2014;102(2):540-51.

63. Tenzer S, Docter D, Rosfa S, Wlodarski A, Kuharev Jr, Rekik A, et al. Nanoparticle size is a critical physicochemical determinant of the human blood plasma corona: a comprehensive quantitative proteomic analysis. ACS nano. 2011;5(9):7155-67.

64. Davie EW, D P, Kulman JD. An Overview of the Structure and Function of Thrombin. Seminars In Thrombosis And Hemostasis. 2006;32(suppl 1):3-15.

65. McClung W, Clapper D, Hu S-P, Brash J. Lysine-derivatized polyurethane as a clot lysing surface: conversion of adsorbed plasminogen to plasmin and clot lysis in vitro. Biomaterials. 2001;22(13):1919-24.

66. McClung WG, Clapper DL, Hu SP, Brash JL. Adsorption of plasminogen from human plasma to lysine-containing surfaces. Journal of biomedical materials research. 2000;49(3):409-14.

67. Gresele P, Page C, Fuster V, Vermylen J. Platelets in Thrombotic and Non-Thrombotic Disorders. Transfusion Medicine. 2003;13(1):57-8.

68. Rubel C, Fernández GC, Dran G, Bompadre MB, Isturiz MA, Palermo MS. Fibrinogen promotes neutrophil activation and delays apoptosis. The Journal of Immunology. 2001;166(3):2002-10.

69. Stoller JK, Aboussouan LS. α1-antitrypsin deficiency. The Lancet. 2005;365(9478):2225-36.

70. Shah M, Hsueh P-Y, Sun G, Chang HY, Janib SM, MacKay JA. Biodegradation of elastin-like polypeptide nanoparticles. Protein science : a publication of the Protein Society. 2012;21(6):743-50.

71. Lundqvist M, Stigler J, Elia G, Lynch I, Cedervall T, Dawson KA. Nanoparticle size and surface properties determine the protein corona with possible implications for biological impacts. Proc Natl Acad Sci U S A. 2008;105(38):14265-70.

72. De Boer J, Creasey A, Chang A, Abbink J, Roem D, Eerenberg A, et al. Alpha-2-macroglobulin functions as an inhibitor of fibrinolytic, clotting, and

neutrophilic proteinases in sepsis: studies using a baboon model. Infection and immunity. 1993;61(12):5035-43.

73. Woodhouse KA, Klement P, Chen V, Gorbet MB, Keeley FW, Stahl R, et al. Investigation of recombinant human elastin polypeptides as non-thrombogenic coatings. Biomaterials. 2004;25(19):4543-53.

9. Hydrophobic Elastin-Like Polypeptide Nanoparticles: Adsorbed Proteome and Effects on Macrophage Cell Viability and Phagocytosis

9.1. Abstract

While the development of elastin-like polypeptides (ELPs) for a variety of biomedical applications is widespread, assessments of their biocompatibility, information critical for their clinical deployment, are limited. Studies insofar have utilized only a narrow cross section of the wide variety of ELP sequences reported in the literature and have not spanned the breadth of applications for which they are being developed. As macrophages can limit the efficacy of nanoparticle-based delivery systems and further activate immune responses, insight into this cellular response reveals early immune biocompatibility of ELP nanoparticles. This study will examine the macrophage response to ELP nanoparticles as mediated by the adsorbed protein corona as a function of ELP guest amino acid, chain length and nanoparticle diameter. The breadth of proteins found adsorbed to ELP nanoparticle surface was found to vary, with hydrophilic nanoparticles adsorbing a narrower variety than the hydrophobic constructs. Diameter was also found to play a role, with smaller diameter hydrophobic particles adsorbing a wider range of proteins. Macrophage cell viability was unaffected by the presence of ELP nanoparticles, and their phagocytic capabilities were unimpeded except when incubated with a 500 nm valine-containing 40-mer. This nanoparticle was found to significantly decrease the phagocytic capacity of macrophage cells relative to the control and to a corresponding 500 nm leucine-containing 40-mer. Nanoparticle size and the proportion and conformation of opsonin to dysopsonin proteins likely influenced this outcome. Taken together, these results suggest that, while most of the tested constructs do not elicit or impair macrophage

phagocytosis, certain combinations of ELP sequence and particle size can result in an adsorbed protein corona which leads to an immune response.

Keywords: Elastin-like polypeptides, biocompatibility, nanoparticle protein corona, cell viability, macrophage phagocytosis

9.2. Introduction

Elastin-like polypeptides (ELPs) are a family of protein biopolymers currently experiencing vigorous development as an engineered biomaterial. The highly repetitive, generally uncharged amino acid sequences which characterize this protein family were developed after studies of the mammalian extracellular matrix protein elastin (1). The most common ELP sequence is composed of any number of repeats of the pentapeptide valine-proline-glycine-X-glycine (VPGXG) where the "guest amino acid" X is valine in native elastin, but can be any amino acid with the exception of proline (2). What makes this and other related ELP sequences distinctive and desirable for biomaterial development is that it can undergo a rapid and reversible lower critical solution temperature self-assembly in response to changes in solution conditions, most commonly temperature (3). Both the chemistry of the guest amino acid and the number of repeats of the pentapeptide sequence affect the conditions wherein ELPs will undergo self-assembly. Generally, hydrophobic guest amino acids lower the transition temperature and fewer ELP repeats raise the transition temperature (4, 5). That ELPs are protein based and produced using recombinant methods also means the addition of bioactive moieties such as ligand binding sites, crosslinking domains,

cell signalling sequences and/or enzyme-cleavage sequences is relatively straightforward (6, 7). The flexibility in the sequence and programmable environmental response of ELPs ultimately results in a tunable platform which is being engineered for a variety of applications including tissue engineering, hydrogel-based delivery, recombinant protein purification and nanoparticle drug delivery (8-13).

While ELPs, as a platform for a variety of biomaterials, are undergoing rigorous application-driven development, the evaluation of their biocompatibility, critical for successful clinical applications, is lacking. The most frequently cited study examined the biocompatibility of a crosslinked matrix of ELP composed of 100-200 repeats of $(VPGVG)_n$. A series of tests recommended by the American Society for the Testing of Materials for medical and surgical materials were performed, including mutagenicity, acute and intracutaneous toxicity, systemic antigenicity, pyrogenicity and hemolysis, after which the material was shown to have favourable biocompatibility (14). $(VPAVG)_n$ microparticles have been tested for intraocular injection and while no acute inflammatory response was observed upon injection into the rabbit hind paw, some intraocular inflammation was observed (15). A similar study was carried out wherein scleral insertion of crosslinked sleeves composed of $(VPGVG)_n$ or $[(VPGVG)_3\ (VPGFG)]_n$ revealed the guest amino acid chemistry affected the host response, with the phenylalanine-containing ELP sleeve causing inflammation and the formation of a fibrous membrane (16). Given the flexibility of the ELP platform, these results, while informative, may not be applicable for all ELPs. The utility of these results is

further reduced given that biocompatibility of a material is related to the intended application. For instance, ocular injection biocompatibility results may not translate into favourable biocompatibility for tissue scaffolding applications or nanoparticle drug delivery.

The biocompatibility of nanoparticles, for instance, has been shown to be dictated by the corona of plasma proteins which adsorb to their surface immediately upon implantation (17-19). The composition of this adsorbed protein corona can be influenced by nanoparticle physical properties including the size, surface charge and hydrophobicity of the material (20-22). As such, the interplay between the nanoparticle, adsorbed corona and host response, including innate immunity and macrophages, is of critical importance for the evaluation of biocompatibility (23, 24). Macrophages are efficient and motile phagocytic scavenging cells that are found in all vertebrates and are located in multiple tissues. Their primary role is phagocytizing materials such as pathogens and other non-self proteins and cells that require removal. Detection is accomplished through pathogen-associated molecular patterns (25). Macrophages also play key roles in chemokine signaling to recruit other immune cells to an infection and are important as antigen presenters to T cells of the adaptive immune system (26). RAW 264.7 is a murine macrophage cell line commonly used to study various innate effector functions such phagocytosis, lysis of antibody-coated targets, cytokine release and lysozyme secretion (26). RAW 264.7 cells also bear receptors for immunoglobulin and complement (25). Therefore, RAW 264.7 cells have all the characteristics of normal macrophages. Given their important role in

multiple aspects of the innate and adaptive immune systems, and as first responders to invaders at locations that connect the external and internal environments, RAW 264.7 macrophages are ideal immune cells with which to examine potential host response to ELP nanoparticle exposure.

This study will use ELP nanoparticles of either 200 or 500 nm diameters formed from ELP protein sequences made up of 20, 40, 80 or 160 repeats of a leucine-containing construct or a 40-mer valine-containing sequence. The adsorbed protein coronae found on 200 and 500 nm leucine and valine 40-mer samples will be identified using proteometric mass spectroscopy. 200 and 500 nm particles of each of the five ELP sequences will be incubated with RAW 264.7 cells and the cell viability will be investigated using the Annexin V/propridium iodide cell assay. The total proportion of cellular phagocytic activity as well as the mean uptake per cell will be assayed by monitoring their uptake of fluorescent *Escherichia coli* cells. The results will provide insight into the biocompatibility of ELP nanoparticles while delineating the role of ELP particle size, chain length and guest amino acid hydrophobicity on the content of the adsorbed protein corona and macrophage viability and phagocytosis response.

9.3. Materials and Methods

9.3.1. ELP Synthesis and Nanoparticle Preparation

ELP proteins composed of 20, 40, 80 or 160 repeats of a leucine-containing pentapeptide as well as a valine-containing 40-mer were synthesized,

purified and quantified using recombinant methods with *Escherichia coli* (*E. coli*) as previously described (7). 200 and 500 nm diameter particles composed from each of the five ELP constructs were prepared by incubation at 0.05 or 0.10 mg/mL at 37°C for ~3-30 minutes and characterized by dynamic light scattering and transmission electron microscopy as described in Chapter 8.

9.3.2. Nanoparticle Protein Adsorption

500 μL of each of the ten ELP nanoparticle samples in Dulbecco's Minimal Essential Medium (DMEM) with Earle's balanced salt solution (Sigma-Aldrich, Canada) supplemented with 1 % 2 mM L-glutamine, 1% penicillin/streptomycin, and 10 % heat-inactivated FBS were incubated at 37°C with rocking for 2 hours. Loosely bound proteins were removed by centrifuging the samples at 37°C for 2 minutes, aspirating the soluble phase and resuspending the pellets in 500 μL of 37°C Tris buffered saline, pH 7.4. This wash procedure was performed twice, after which the pellets were frozen at -20°C until proteomic analysis.

9.3.3. Proteomic Analysis

The samples received were incubated with 0.5 μg of dithiothreitol at 37°C for 30 min, then with 2.5 μg of iodoacetamide at 37°C for 30min, then with 0.4 μg of trypsin at 37C for at least 2 hours before peptide clean up using C18 stage tip (27). The cleaned peptides were run on Agilent Qtof 6550 connected to an Agilent 1200 capillary HPLC. The peptides were separated over a 2500mm x 2.1mm C18 column at 100 μl/min using water/acetonitrile/formic acid gradients.

Raw data was searched using Byonic v2.7.7 against the Uniprot Bos Taurus protein database, with tryptic peptide specificity, and 10 ppm and 20 ppm mass error tolerances for precursors and fragments, respectively (28). Oxidized methionine as well as deamidated glutamine and asparagine were treated as potential modifications. Only proteins with a log(prob) score or -2 or lower were considered identified..

9.3.4. RAW 264.7 cell line culture conditions

RAW 264.7 cells were grown to confluence at 37 °C with 5% CO_2 in culture media consisting of DMEM with Earle's balanced salt solution (Sigma-Aldrich, Canada) supplemented with 1% 2 mM L-glutamine, 1% penicillin/streptomycin, and 10% heat-inactivated FBS. Cells were passed every third day by harvesting cells in a harvest buffer medium (1.5 mM EDTA, 135 mM NaCl, 20 mM HEPES, 5 mM KCl, pH 7.4) at 37^{o}C with 5 % CO_2 for 10 minutes, followed by pipetting to detach cells from cell culture plate (BD Biosciences, Mississauga, Canada). Cells were seeded into new flasks at a sub-cultivation ratio of 1:10.

9.3.5. GFP-Escherichia coli bacteria

Green fluorescent protein (GFP)-expressing *E. coli* were cultured by streaking frozen cells onto an ampicillin (Amp)-containing Luria broth (LB) agar plate (1% Bacto-agar (BD), 0.5% yeast extract, 85.55 mM NaCl, 5% ampicillin

pH 7) using a heat-sterilized sterilized inoculating loop, and incubated overnight at 37^{o}C. Single isolated colonies were then used to inoculate 5 mL of LB-Amp solution. The culture was grown overnight in a shaker at 37^{o}C.

9.3.6. Examination RAW 264.7 cell viability following exposure to ELPs

The Annexin V/ PI apoptosis assay was used to measure the effects of ELPs on cell viability. Annexin V-FITC binds to damaged membranes undergoing early to late apoptosis, while the fluorescent molecule, propridium iodide (PI) penetrates damaged plasma membranes of necrotic and/or late apoptotic cells and intercalates with nucleic acids to enhance its fluorescence. Thus, the balance of fluorescence between Annex V-FITC and PI provides a quantitative measure of cells that are i) viable, ii) early apoptotic, iii) late apoptotic and iv) necrotic. To perform the assay, cells were grown to confluence over 3 days in DMEM and then harvested as above and enumerated with Trypan Blue staining solution (Sigma Aldrich, Canada) on a haemocytometer to ensure cell cultures had >95% viable cells and to determine cell concentration. Following enumeration, cells were re-suspended in fresh culture media and seeded in 24-well flat-bottom culture plates (Corning Costar, USA) at 2.5 x 10^5 cells per well. Cells were incubated for 1 h at 37°C to allow for cell attachment to wells, followed by a 2 h exposure to each ELP construct (L20, L40, L80, L160 and V40) at two nanoparticle diameters (200 and 500 nm). The ELPs were suspended in 1X

phosphate buffered saline (PBS; 2.7 mM KCl, 1.5 mM KH_2PO_4, 136.9 mM 148 NaCl, 15.2 mM Na2HPO4; pH 7.0). Vehicle (equivalent PBS volume), positive (1 % ethanol) and negative (culture media) control treatments were also included.

Following exposure, cell culture media with nanoparticles was removed from wells and cells were washed twice with 1X PBS, harvested as above, and transferred to 5 mL polystyrene tubes (Corning Science, Canada) containing 3 mL of PBS supplemented with 0.5 % fetal bovine serum (FBS) (Sigma, Canada) (herein known as PBS-FBS). Cells were centrifuged at 400 x *g* for 7 minutes to pellet cells. The supernatant was decanted and the cell pellet gently disrupted and resuspended in 1 mL of 1x Annexin V binding buffer (BD Biosciences, Canada). Cells were then centrifuged at 400 x *g* for 7 minutes, followed by decanting supernatant and gently disrupting cell pellet. 5 µL of Annexin V-FITC and 4 µL of 1:10 diluted PI (2 µg/mL) were added to each tube and incubated at room temperature in the dark for 15 minutes. Following incubation, an additional 500 µL of Annexin V binding buffer was added to each tube to wash excess Annexin V and PI and the cells were centrifuged at 400 x *g* for 7 minutes. The supernatant was decanted and cells were resuspended in 500 µL of Annexin V binding buffer and analyzed by flow cytometry (compensated for spectral overlap) for indications of cell death by monitoring for proportional increases in Annexin V-FITC and PI fluorescence, and for changes in cell profile outputs, relative to unexposed controls.

9.3.7. Examination RAW 264.7 phagocytic capacity following exposure to ELPs

Flow cytometry (Beckman Coulter Quanta SC, Mississauga, Canada) was used to measure the effects of ELPs on the phagocytic capacity of RAW 264.7 to internalize GFP-*E. coli*. To perform the assay, $2.5x10^5$ cells per well were seeded into 24-well flat bottom culture plate (Costar) and incubated for 1 h at 37°C to allow for cell attachment to wells, followed by a 2 h exposure to ELP constructs as described above. Vehicle (equivalent PBS volume) and negative (culture media) control treatments were also included. Following exposure, ELPs were removed from wells and cells were washed three times with 1X PBS by gentle rocking, and then incubated for 2 h at 37^oC with PBS-suspended GFP-*E. coli* at a multiplicity of infection (MOI) of 10:1 (*E. coli* to cell, $2.5x10^6$ cells/well) to stimulate phagocytosis. Following phagocytosis, non-internalized *E. coli* were aspirated from wells and the cells were washed three times by gently rocking with PBS and then mechanically detached from the culture plate using warmed harvest buffer. Harvested cell samples were transferred to corresponding 1.5 mL centrifuge tubes and GFP-*E.coli* fluorescence in each sample was determined using the FL2 channel on the flow cytometer. Phagocytic activity was reported in two ways. First, as the percentage of RAW 264.7 cells that had phagocytized GFP-*E. coli* (i.e. phagocytic-positive cells), and second, as the mean fluorescence intensity (MFI) of the phagocytic-positive cells. Percent phagocytosis is a measure of whether a cell has successfully internalized a GFP-*E. coli*, while MFI

is a proxy measure of the phagocytic index (i.e. the number of GFP-*E. coli* that have been consumed per cell).

9.3.8. Statistics

Statistical analysis was performed using Graphpad Prism 6.0 Statistical Software. To investigate effects of ELPs on proportional changes in cell viability, a one-way analysis of variance (ANOVA) with a pairwise Tukey multiple comparison test was performed for comparisons between ELP nanoparticle diameter (i.e. 200 vs. 500 nm) within each cell death category (i.e., viable, early apoptosis, late apoptosis or necrosis) for each ELP construct (i.e. L20, L40, L60, L80, L160 and V40). Similar one-way ANOVA analysis was performed for comparisons between ELP constructs, within each cell death category for constructs of either identical guest amino acid or chain length. To analyze the effects of ELPs on phagocytosis, a one-way ANOVA with a Tukey multiple comparison test was performed for comparisons between ELP nanoparticle diameter (i.e. 200 vs. 500 nm) within an ELP construct (i.e. L20, L40, L60, L80, L160 and V40). Background fluorescence was subtracted from raw phagocytic values, which were normalized to vehicle controls. Similar one-way ANOVA comparisons, plus unpaired t tests, were made between ELP constructs of either identical guest amino acid or chain length. Background fluorescence was subtracted from raw phagocytic values, which were normalized to unexposed control for each ELP construct. For both cell viability and phagocytosis, a

probability of $p < 0.05$ was considered significant. Data values are presented as mean ± standard error on the mean (SEM).

9.4. Results

9.4.1. Proteometric Identification of ELP Nanoparticle Protein Coronae

L40-200	L40-500
Serum albumin	Fetuin-A
Fetuin-A	Serum albumin
Alpha 1 antiproteinase	Alpha 1 antiproteinase
Inter-alpha-trypsin inhibitor heavy chain H2	Fibulin-1
Alpha-1B-glycoprotein	Apolipoprotein A-I
Apolipoprotein A-I	Hemoglobin fetal subunit beta
Fetuin-B	Hemoglobin subunit alpha
Hemoglobin subunit alpha	Apolipoprotein A-II
Alpha-2-macroglobulin	Kininogen-1
Vitamin D-binding protein	Serotransferrin
Fibulin-1	Pancreatic elastase inhibitor
Alpha-fetoprotein	Fibulin-3
Inter-alpha-trypsin inhibitor heavy chain H4	
Hemoglobin fetal subunit beta	
Apolipoprotein A-II	
Complement C3	
Kininogen-1	
Hemopexin	
Plasminogen	
Alpha-2-antiplasmin	
Complement factor B	
Pancreatic elastase inhibitor	
Beta-2-glycoprotein 1	
Prothrombin	
Platelet factor 4	
Apolipoprotein E	
Angiotensin	
Alpha-1-acid glycoprotein	
Serpin A3-5	
Trypsin inhibitor	

Table 9.1. Adsorbed FBS proteins found on L40 nanoparticle surfaces. Proteins were identified using the Byonic™ software package and are ranked in decreasing

order of the absolute value of the log base 10 protein p-value to a minimum value of 2.

V40-200	V40-500
Serum albumin	Serum albumin
Alpha 1 antiproteinase	Alpha 1 antiproteinase
Fetuin-A	Fetuin-A
Hemoglobin subunit alpha	Hemoglobin subunit alpha
Apolipoprotein A-II	Apolipoprotein A-II
Guanylate binding protein 5	Fetuin-B
C4b-binding protein alpha-like	Vitamin D-binding protein
	Serotransferrin

Table 9.2. Adsorbed FBS proteins found on V40 nanoparticle surfaces. Proteins were identified using the Byonic™ software package and are ranked in decreasing order of the absolute value of the log base 10 protein p-value to a minimum value of 2.

Proteins found adsorbed to ELP nanoparticle surfaces and identified using mass spectroscopy were ordered based upon the likelihood of the protein spectrum matches arising due simply to random chance (protein p-value), with the highest confidence proteins listed first and a lower p-value cut off of 1%. Across all four of the tested samples, the three highest ranked proteins were serum albumin, fetuin-A and alpha 1 antiproteinase (also known as $alpha_1$ antitrypsin). Hemoglobin and apolipoproteins A-I and A-II are also found across all ELP nanoparticle samples.

The proteome adsorbed to 200 nm L40 was found to be composed of a wide variety of additional proteins including complement proteins C3 and factor B, coagulation and fibrinolysis associated proteins alpha-2-macroglobulin,

kininogen-1, plasminogen, alpha-2-antiplasmin, prothrombin and platelet factor 4. Transport-associated proteins including vitamin D binding protein fibulin-1, hemopexin, apolipoprotein E and alph-1-acid glycoprotein were also identified as components of the L40-200 proteome along with protease inhibitors such as serpin A3-5, trypsin inhibitor and pancreatic elastase inhibitor.

In contrast to the 200 nm L40 particles, the 500 nm particles were found to have an adsorbed proteome composed of considerably fewer proteins. Most of the proteins found on the L40-500 sample were also present on the L40-200, with the exception of serotransferrin.

The proteomes associated with ELP V40-based nanoparticles were found to be composed of a narrower range of proteins than either L40 system. In addition to the albumin, fetuin-A, alpha-1-antiproteinase, hemoglobin and apolipoprotein A-II found adsorbed to all samples, V40-200 adsorbed two unique proteins, guanylate binding protein 5 and C4b-binding protein, while V40-500 was found to adsorb fetuin-b, vitamin D-binding protein and serotransferrin; all of which were also detected on L40 samples.

9.4.2. Cell Viability

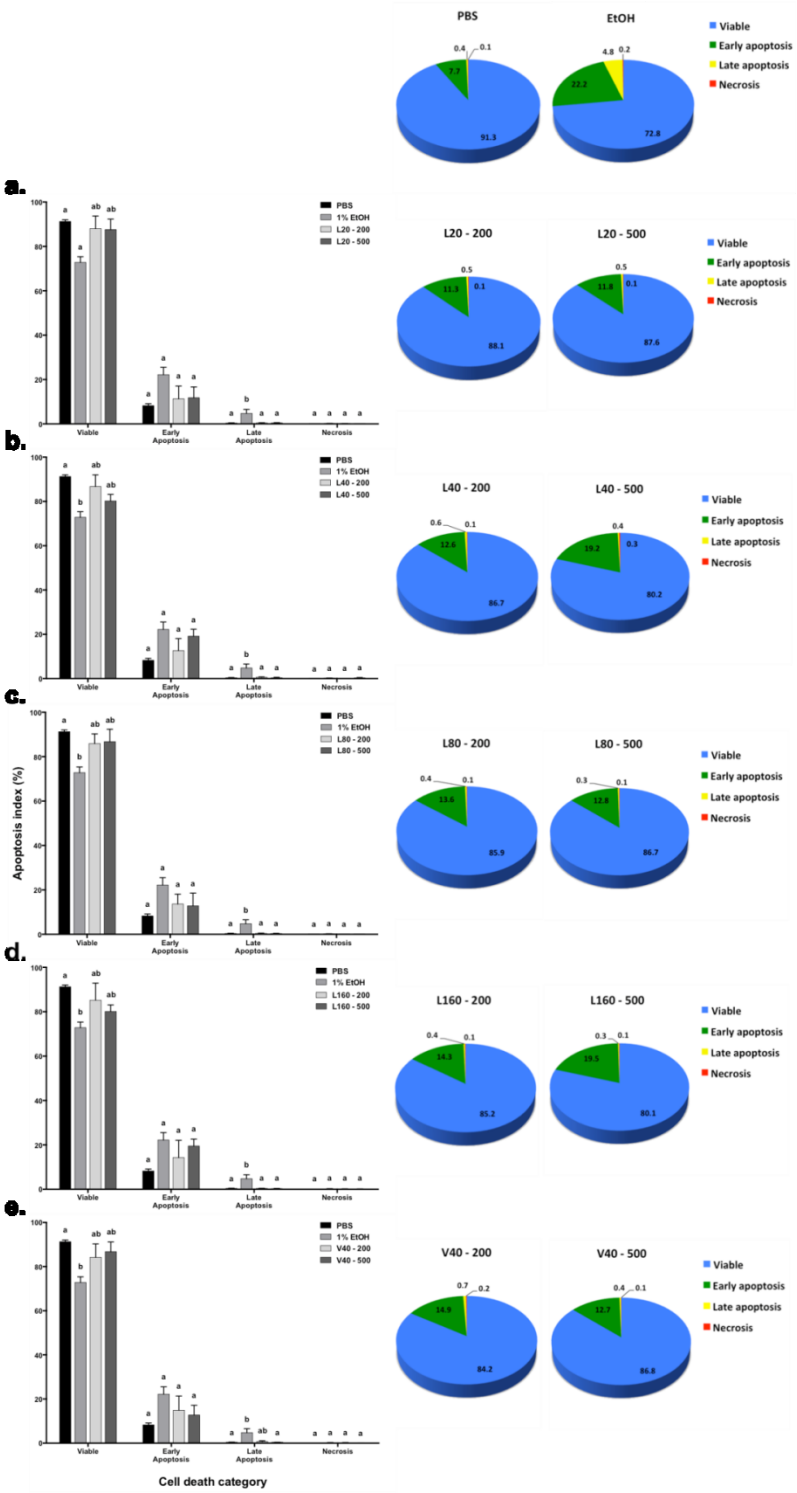

Figure 9.1. Relative RAW 264.7 cell apoptosis results following a 2 h in vitro exposure to PBS (negative control), ethanol (positive control), or to 200 or 500 nm elastin-like polypeptide (ELP) NP constructs (a. L20, b. L40, c. L80 d. L160, e. V40). Cell viability is measured as proportional changes in FITC-Annexin V

and propridium iodide fluorescence in a cell population as measured by flow cytometry. Cell death is proportioned into: viable, early apoptosis, late apoptosis and necrosis cell death categories as a histogram or into pie charts for each exposure. Data are means ± SEM, n = 3 independent experiments. Different lower-case letters denote significant differences (ANOVA, $p < 0.05$) between cell death categories for a given ELP NP, followed by a Tukey multiple comparison test.

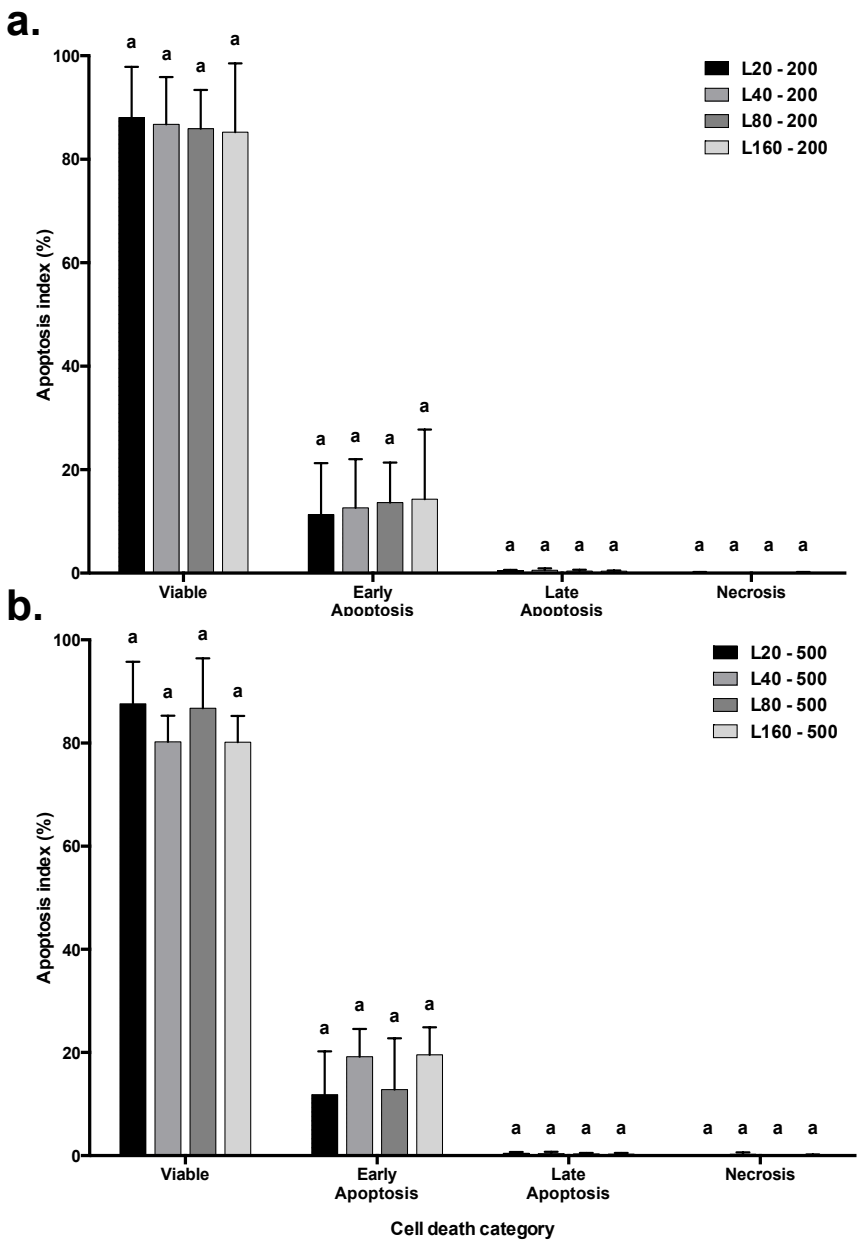

Figure 9.2. Relative RAW 264.7 cell apoptosis following a 2 h in vitro exposure to 200 nm (a) or 500 nm (b) elastin-like polypeptide (ELP) NP constructs (L20, L40, L80, L160). Cell viability is measured as proportional changes in FITC-Annexin V and propridium iodide fluorescence in a cell population as measured by flow cytometry. Cell death is proportioned in to: viable, early apoptosis, late apoptosis and necrosis cell death categories as a histogram for each exposure. Data are means ± SEM, n = 3 independent experiments. Different lower-case letters denote significant differences (ANOVA, $p < 0.05$) between cell death categories for a given ELP NP, followed by a Tukey multiple comparison test.

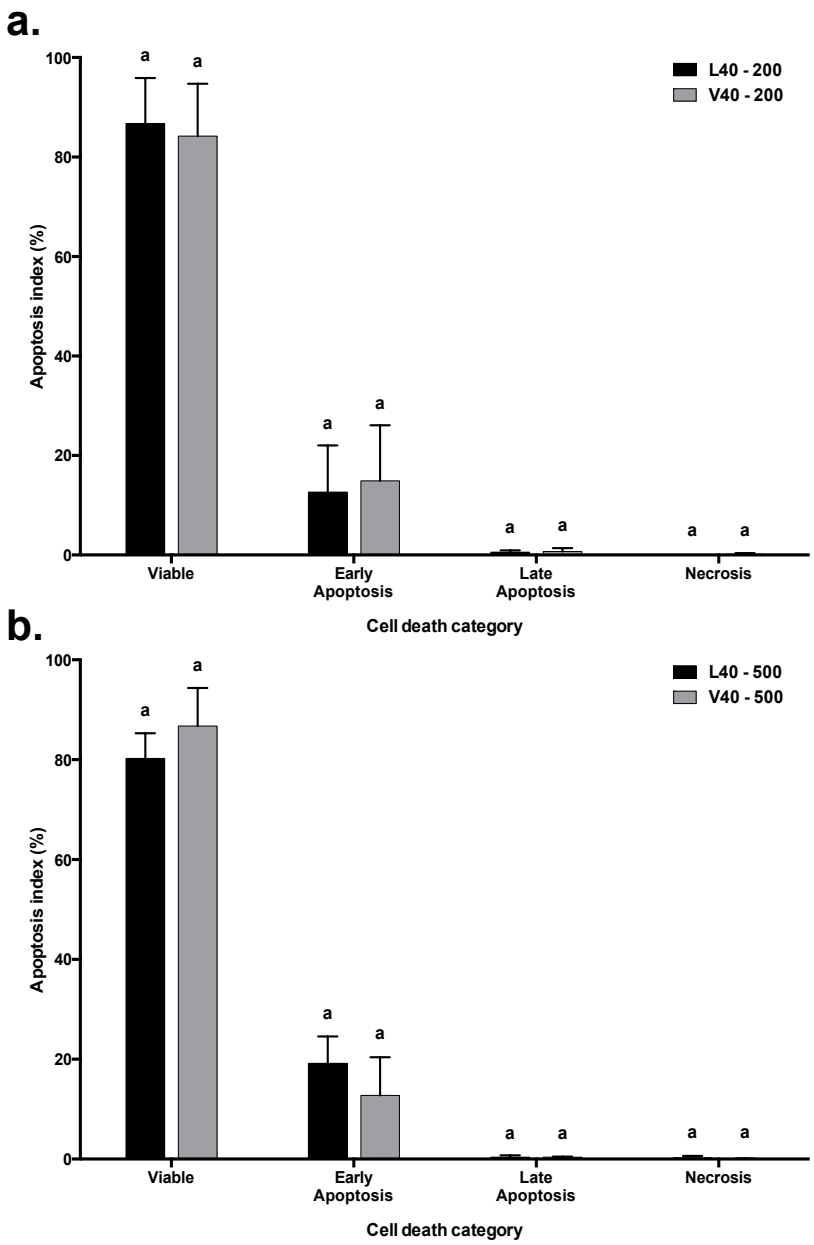

Figure 9.3. Relative RAW 264.7 cell apoptosis following a 2 h in vitro exposure to 200 nm (a) or 500 nm (b) elastin-like polypeptide (ELP) NP constructs (L40 and V40). Cell viability is measured as proportional changes in FITC-Annexin V and propridium iodide fluorescence in a cell population as measured by flow cytometry. Cell death is proportioned in to: viable, early apoptosis, late apoptosis and necrosis cell death categories as a histogram for each exposure. Data are means ± SEM, n = 3 independent experiments. Different lower-case letters denote significant differences (ANOVA, $p < 0.05$) between cell death categories for a given ELP NP, followed by a Tukey multiple comparison test.

Exposure to 1% EtOH (positive control) significantly increased the proportion of early apoptotic cells (22.2 ± 3.35 %) and late apoptotic cells (4.8 ± 1.78 %) and decreased the proportion of viable cells (72.8 ± 2.53 %) when compared to vehicle control in Figure 9.1. RAW 264.7 cell viability was not affected following a 2 h exposure to all ELP constructs and results were statistically similar to vehicle controls (PBS; Viable: 91.3 ± 0.66 %, Early apoptosis: 7.7 ± 0.75 %, Late apoptosis: 0.4 ± 0.10 %, Necrosis: 0.1 ± 0.0 %) when either chain lengths (Figure 9.2) or constructs of identical chain lengths but varying guest amino acid hydrophobicity were compared (Figure 9.3).

9.4.3. Cell Phagocytosis

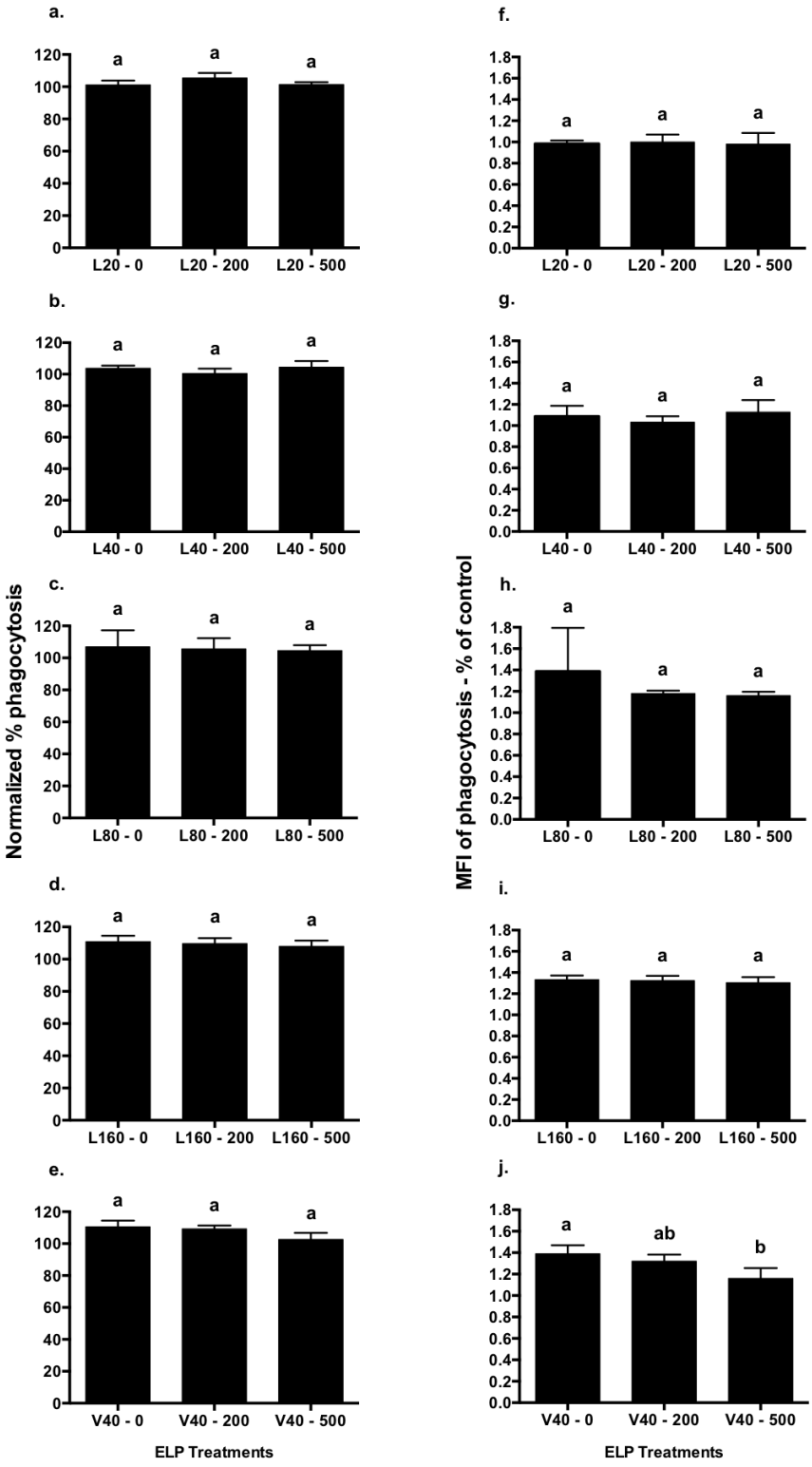

Figure 9.4. Normalized results of RAW 264.7 cell phagocytosis of GFP-*E. coli* (10:1 multiplicity of infection) following a 2 h *in vitro* exposure to either vehicle control (0) or to 200 nm or 500 nm elastin-like polypeptide (ELP) NP constructs (L20, L40, L80, L160, V40). Phagocytosis is a measure of GFP fluorescence of a cell population using flow cytometry and is presented as % phagocytosis (a, b, c, d, e), which is a measure of the percent of the population that has successfully internalized GFP-*E. coli*, and mean fluorescent intensity (MFI) of phagocytosis (f, g, h, i, j), which is an estimation of the phagocytic index (i.e. the number of GFP-*E. coli* that have been consumed per cell). Data are means ± SEM, n = 3 independent experiments. Different lower-case letters denote significant differences (ANOVA, $p < 0.05$) between ELP NP sizes for a given ELP, followed by a Tukey multiple comparison test.

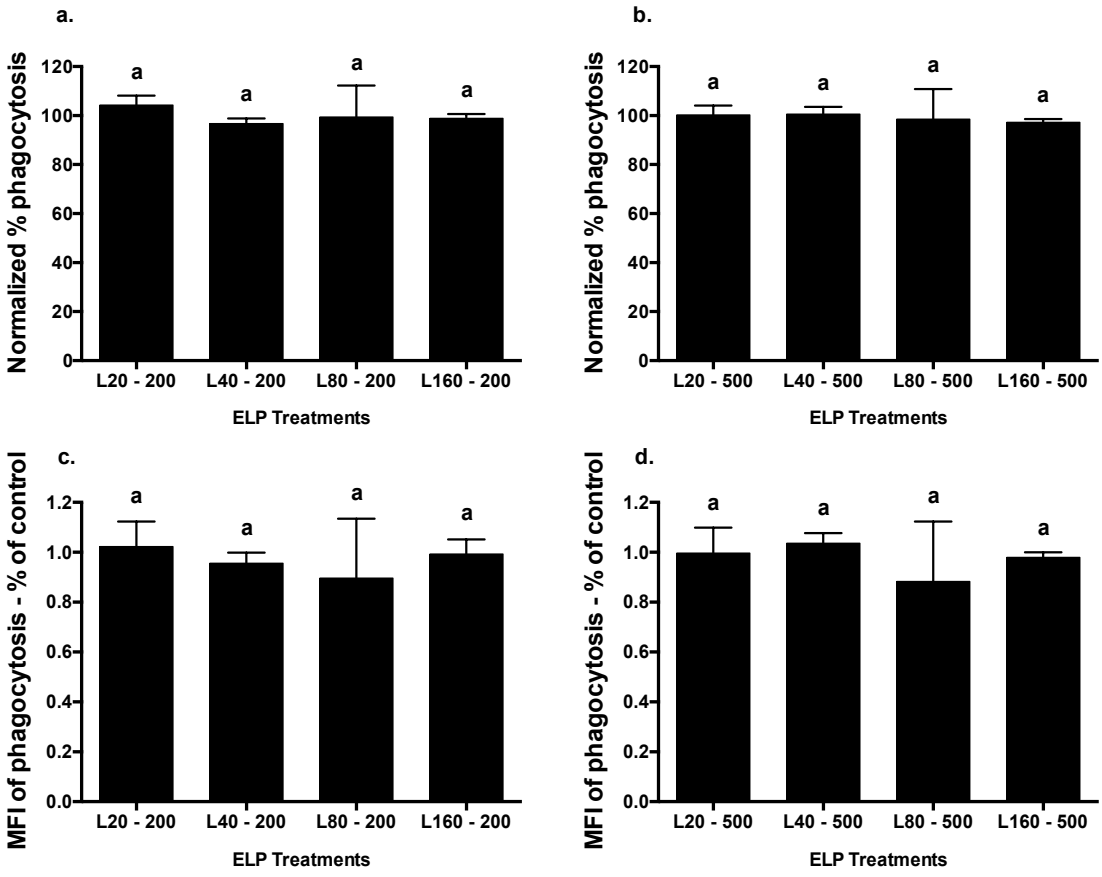

Figure 9.5. Normalized results of RAW 264.7 cell phagocytosis of GFP-*E. coli* (10:1 multiplicity of infection) following a 2 h in vitro exposure to 200 nm (a, c) or 500 nm (b, d) elastin-like polypeptide (ELP) NP constructs (L20, L40, L80, L160). Phagocytosis values are a measure of GFP fluorescence of a cell population using flow cytometry. Results compare ELP constructs at one size and

are presented as % phagocytosis (a, b), which is a measure of the percent of the population that has successfully internalized GFP-*E. coli*, and mean fluorescence intensity (MFI) of phagocytosis (c, d), which is an estimation of the phagocytic index (i.e. the number of GFP-*E. coli* that have been consumed per cell). Different lower-case letters denote significant differences (ANOVA, $p < 0.05$) between ELP nanoparticles at a given ELP size (200 nm or 500 nm), followed by a Tukey multiple comparison test.

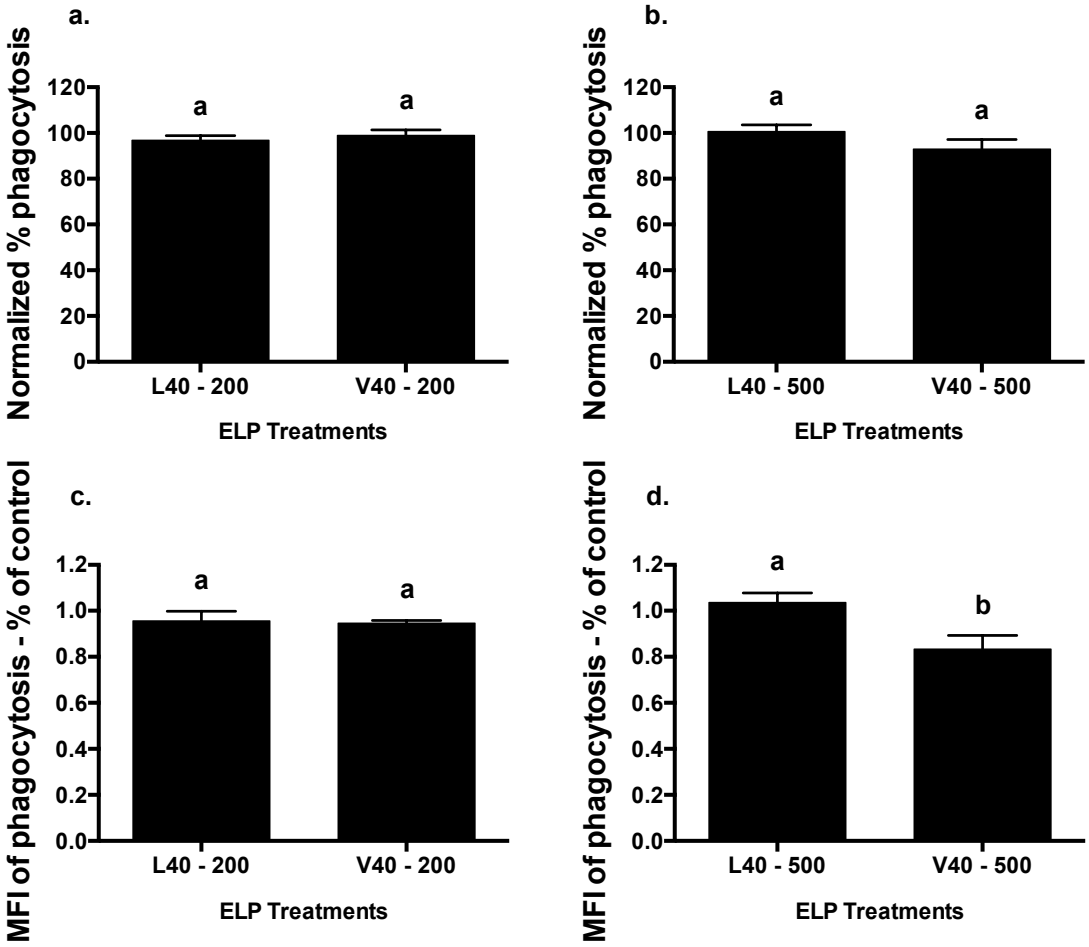

Figure 9.6. Normalized results of RAW 264.7 cell phagocytosis of GFP-*E. coli* (10:1 multiplicity of infection) following a 2 h *in vitro* exposure to 200 nm (a, c) or 500 nm (b, d) elastin-like polypeptide (ELP) NP constructs (L40, V40). Phagocytosis values are a measure of GFP fluorescence of a cell population using flow cytometry. Results compare ELP constructs at one size and are presented as % phagocytosis (a, b), which is a measure of the percent of the population that has successfully internalized GFP-*E. coli*, and mean fluorescence intensity (MFI) of phagocytosis (c, d), which is an estimation of the phagocytic index (i.e. the number of GFP-*E. coli* that have been consumed per cell). Different lower-case

letters denote significant differences (unpaired t test, $p < 0.05$) between ELP nanoparticles at a given ELP size (200 nm or 500 nm).

The phagocytic capacity (i.e. % phagocytosis) of RAW 264.7 cells, like the cell viability, was also not significantly affected from pre-exposure to all ELP NP constructs, when compared to control cells. Aside from a significant decrease in normalized MFI for V40 500 nm (0.83 ± 0.035) when compared to control (V40-0; 1.39 ± 0.045) (Figure 9.4) and to L40 500 nm (1.03 ± 0.023) (Figure 9.6), the MFI for all other ELP nanoparticles was also not significantly affected from prior exposure.

9.5. Discussion

The adsorption of proteins onto nanoparticle surfaces is a complex series of events, with numerous particle characteristics shown to influence the breadth and quantity of the adsorbed proteome including the type of material used, particle size/curvature, surface hydrophobicity and charge (29-33). The use of 200 and 500 nm particles composed of either ELP L40 or V40 allowed for the delineation of the effects of hydrophobicity and size/curvature on protein adsorption from a complex media onto protein nanoparticles. As the materials used for the composition of the various nanoparticles are all proteins with very similar or identical amino acid sequences, the role of material influence on protein adsorption is minimized. The same can be said for surface charge effects as

previous zeta potential measurements of these particles in 1X PBS pH 7.4 yielded values of -7 to -8 mV.

Comparing the results of the proteometric analysis of these protein-based nanoparticles to other similar studies in the literature provides some intriguing insights into how the material choice may affect the adsorbed proteome. While literature studying the adsorption of proteins from complex solutions onto protein-derived nanoparticles is limited, there have been numerous studies employing nanoparticles composed of other materials as reviewed by Karmali *et al.* (29). Studies using non-protein nanoparticles have identified adsorbed protein coronae composed of 50 to 300 separate proteins (20, 22, 34). That the ELP nanoparticles tested herein adsorbed corona composed of significantly smaller variety of proteins is noteworthy, though not unexpected given that recent studies have shown that coating inorganic nanoparticles with protein can decrease the variety of the adsorbed proteome and limit protein adsorption in general. This has been demonstrated using polystyrene nanoparticles coated with transferrin as well as sulfonated and carboxylated polystyrene nanoparticles treated with fungus-derived hydrophobin proteins (35, 36).

While the proteometric analysis performed herein cannot speak to the quantities of the adsorbed proteins, the results clearly demonstrate that a greater variety of proteins were identified adsorbed to the more hydrophobic L40-derived nanoparticles, with 30, 12, 7 and 8 individual PSMs for L40-200, L40-500, V40-200 and V40-500, respectively. While keeping particle diameter constant, increasing the hydrophobicity of the ELP guest amino acid by changing it from

valine to leucine increased the number of identified proteins from 7 to 30 and 8 to 12 for 200 and 500 nm particles, respectively. These results are consistent with previous studies using polymer or latex nanoparticles with varying hydrophobicities whereby a greater variety of proteins were found adsorbed to the more hydrophobic particles (32, 37).

Some insight into the role of nanoparticle size/curvature can be inferred by comparing the compositions of the protein corona of 200 and 500 nm particles of ELPs L40 or V40. Particle diameter has been shown to affect the adsorbed corona previously in the literature (20, 22, 30, 38). Studies have even gone so far to suggest that smaller particles, given their higher curvature may have protein corona which are enriched with smaller proteins, though this is not observed throughout the literature (22, 39, 40). The ELP nanoparticle datasets clearly indicated an increased variety of proteins for L40-derived 200 nm particles compared to the 500 nm samples. The majority of the proteins which were identified in the corona of the 500 nm particles were also present on the 200 nm samples with the exceptions of serotransferrin and fibulin-3. As such, the observation can be made that decreasing the diameter of L40-derived nanoparticles from 500 to 200 nm generally resulted in an expanded variety of adsorbed proteins, rather than a completely different proteome composition. No clear molecular-weight related relationship exists for the proteome of L40-200 as multiple proteins with molecular weights >100 kDa were identified including alpha-2-macroglobulin, complement C3 and interalpha-trypsin inhibitor heavy chain H2.

The differences in the proteomes of V40 nanoparticles are not as clear as they were for L40. This implies that the role of ELP nanoparticle size in protein adsorption from complex media may not be wholly independent from the influence of particle hydrophobicity. In previous studies of non-protein nanoparticle systems, similar results were observed whereby when two mechanisms of interaction between media and material were identified, hydrophobicity was always included (29). The variations in the adsorbed proteomes of 200 and 500 nm V40-derived nanoparticles were limited. The five most likely proteins for each construct were identical, with only the least likely two or three proteins differing between samples.

As phagocytic cells, macrophages actively interact with foreign particles and pathogens that have penetrated inside an organism. Therefore, internalized nanoparticles become key targets for macrophages, which increase the potential for toxicity from this interaction. Moreover, given that nanoparticles, such as ELPs, likely contain a biomolecular corona of immune activating blood proteins, the chances for adverse effects from this interaction are further increased.

Previous biocompatibility studies have shown cell death from metal-based nanoparticles is attributed to oxidative stress from the generation of reactive oxygen species (ROS) when nanoparticles act as catalysts (41). Free radical toxicity is a common mechanism by which many types of nanoparticles can affect cell health, and excessive ROS products can initiate cellular apoptosis by causing excessive damage or changes to the cytoplasmic and/or inner mitochondrial membranes (42, 43). Mitochondrial destabilization results in the loss of

mitochondrial transmembrane potential and the downstream activation of the proteolytic caspase cascade that leads to the execution pathway and the final death of the cell (44). The lack of apoptotic or necrotic indices following short-term exposure suggests that the ELP constructs were not acutely toxic to RAW 264.7 cells and were not activating cytotoxic caspase cascades. These results are consistent with previous studies wherein fibroblast cell viability was unaffected by the presence of silk ELPs and murine peritoneal macrophages were not affected by the presence of VPAVG microparticles (15, 45). While the number of ELP biocompatibility studies in the literature are lacking, that ELPs are undergoing vigorous development for tissue engineering also implies that these materials generally do not present a significant impediment to cell viability (46-49).

Research on the effects of nanoparticles on tissue-derived macrophages (e.g. lungs, kidneys, cell lines, etc.) has focused largely on their capacity to internalize various types of nanoparticles, as well as the potential for apoptosis and oxidative stress, and the inflammatory consequences of in vitro and in vivo exposures. In general, data has shown that macrophages readily internalize various types of nanoparticles, both in vivo and in vitro, and oxidative stress and apoptosis is particle-type dependent (50-55). While these areas of research are important to understanding effects on the innate immune system, what has not been explored to a great extent are the effects of nanoparticles on the phagocytic capacity of macrophages to consume pathogens, a key immunological endpoint. Bruneau *et al.* recently showed that ambient exposure of trout to Ag nanoparticles

decreased kidney-isolated macrophages from consuming phagocytic beads (56). Ede *et al.* also showed decreased phagocytosis of fluorescent beads by a phagocytic rat mast cell line (RBL-2H3) when pre-exposed to rosette carbon nanotubes and Jovanović has shown comparable disturbances in pathogen phagocytosis in fathead minnow neutrophils, another type of phagocyte (57, 58). The lack of changes to the phagocytic capacity of RAW 264.7 cells when pre-exposed to all ELPs except for V40-500 generally supports the cytotoxicity findings that ELPs are likely highly compatible with cells. These findings are especially relevant given the phagocytic nature of macrophages compared to other cell types, and their increased opportunity to interact and be damaged by foreign nanoparticles. Immunological studies of ELP biomaterials are limited and the results of which are not clear. Rooney found that ELP coated Mylar™ both reduced and increased leukocyte response, depending on the tested biomarker (59). A study using ELP fusion proteins as DNA condensing biopolymers were successful in masking the DNA from an immune response in Balc/c immunocompetent mice (60). VPAVG microparticles were found to elicit some fibroblastic response after intraocular injection (15). Silk-ELP hydrogels and elastin-derived peptides, the result of trauma to native elastin, have both been shown to enhance macrophage migration (45, 61).

The inconsistency in cellular responses to ELP materials in the literature was reflected in the phagocytosis results reported herein, given that the MFI of the RAW 264.7 cells was significantly depressed after exposure to V40-500 samples relative to the control and L40-500. While the proportion of macrophage cells

actively internalizing *E. coli* was not affected, the capacity of those cells to uptake the bacteria was reduced. If the V40-500 nanoparticles were being internalized by the macrophage cells, those particles may occupy the cytosolic space which would otherwise be occupied by *E. coli* (62). It is well established that particle size will affect phagocytosis, with 500 nm particles being more prone to uptake compared to 200 nm particles (54, 63, 64). Particle size on its own does not, however, explain the lack of response to L40-500 nm particles. The adsorbed protein corona on particle surfaces is known to strongly affect the biological response to the material (20, 38, 65, 66). Of the proteins identified in the V40-500 protein corona, two immediately stand out as immunomodulatory. Serotransferrin has been shown to activate macrophage in fish and fetuin has also been shown to promote endocytosis in a dose dependant manner (67-69). While these proteins were detected on both V40 and L40 500 nm particles, the mass spectroscopy technique does not provide any information regarding protein conformation or absolute quantities of individual proteins. As such the relative proportions of these immunomodulatory proteins both to the bulk proteome and to dysopsonins like albumin may be responsible for the differing cellular responses (65, 70, 71).

9.6. Conclusion

ELP nanoparticles made from L40 or V40 ELP sequences at 200 or 500 nm particle diameters, after incubation in complete DMEM, were shown to contain noticeable differences in the composition of their respective adsorbed proteomes. While serum albumin, alpha 1 antiproteinase, fetuin-A and hemoglobin subunit alpha were found to adsorb to all samples, 2 to 25 other

positively identified proteins were found across the various nanoparticles. It is noteworthy that the overall number of individual protein sequences was found to be quite low when compared to the 50-300 proteins identified adsorbed to inorganic or polymeric nanoparticles in previous studies. The more hydrophobic leucine-containing samples were found to adsorb a greater variety of proteins than the valine constructs. The 200 nm L40 was found to adsorb a larger variety of proteins from solution when compared to the L40-500 sample. Particle diameter was found to play a clear role for the hydrophobic samples more than the hydrophilic, suggesting that there may be more than one main interaction mechanism between the solution proteins and ELP nanoparticles. Ten nanoparticle samples were used for RAW 264.7 cell viability and phagocytosis testin: 200 and 500 nm particles each of L20, L40, L80, L160 and V40. None of these nanoparticles were found to significantly impact cell viability as assessed by either Annexin V or propridium iodide. The proportion of these macrophage cells actively uptaking *E. coli* after being incubated with the ten ELP nanoparticles did not vary from control samples. The mean fluorescence intensity, a measure of how many *E. coli* the RAW 264.7 cells were internalizing was found to be significantly decreased after incubation with V40-500 relative to the control sample and L40-500. The proportions and conformations of opsonin and dysopsonin proteins, in addition to particle size may be responsible for the different macrophage responses. Further studies would be useful for a deeper understanding of the biological response to ELP nanoparticles. Given that V40 and L40-derived 500 nm particles are of very similar composition and yet yielded

noticeable variations in their adsorbed proteomes and phagocytic responses suggests that this system may also be of use for fundamental studies on protein adsorption to protein nanoparticles and the biological consequences therein. This information is critical for the future development of all protein-based biomaterials.

9.7. References

1. Urry DW. Entropic elastic processes in protein mechanisms. I. Elastic structure due to an inverse temperature transition and elasticity due to internal chain dynamics. Journal of protein chemistry. 1988;7(1):1-34.

2. Urry D, Long M, Cox B, Ohnishi T, Mitchell L, Jacobs M. The synthetic polypentapeptide of elastin coacervates and forms filamentous aggregates. Biochimica et Biophysica Acta (BBA)-Protein Structure. 1974;371(2):597-602.

3. Urry DW. Physical Chemistry of Biological Free Energy Transduction As Demonstrated by Elastic Protein-Based Polymers. The Journal of Physical Chemistry B. 1997;101(51):11007-28.

4. Urry DW, Gowda DC, Parker TM, Luan CH, Reid MC, Harris CM, et al. Hydrophobicity scale for proteins based on inverse temperature transitions. Biopolymers. 1992;32(9):1243-50.

5. Chilkoti A, Dreher MR, Meyer DE. Design of thermally responsive, recombinant polypeptide carriers for targeted drug delivery. Cancer. 2002;54:1093-111.

6. Meyer DE, Chilkoti A. Genetically Encoded Synthesis of Protein-Based Polymers with Precisely Specified Molecular Weight and Sequence by Recursive Directional Ligation: Examples from the Elastin-like Polypeptide System. Biomacromolecules. 2002:357-67.

7. Bahniuk MS, Alshememry AK, Unsworth LD. High-yield recombinant expression and purification of marginally soluble, short elastin-like polypeptides. BioTechniques. 2016;61(6):297.

8. Hu F, Ke T, Li X, Mao PH, Jin X, Hui FL, et al. Expression and purification of an antimicrobial peptide by fusion with elastin-like polypeptides in Escherichia coli. Applied biochemistry and biotechnology. 2010;160(8):2377-87.

9. Dreher MR, Simnick AJ, Fischer K, Smith RJ, Patel A, Schmidt M, et al. Temperature triggered self-assembly of polypeptides into multivalent spherical micelles. Journal of the American Chemical Society. 2008;130(2):687-94.

10. Meyer DE, Kong GA, Dewhirst MW, Zalutsky MR, Chilkoti A. Targeting a Genetically Engineered Elastin-like Polypeptide to Solid Tumors by Local Hyperthermia 1. In Vitro. 2001;42745:1548-54.

11. Rodriguez-Cabello JC, Pina MJ, Ibanez-Fonseca A, Fernandez-Colino A, Arias FJ. Nanotechnological Approaches to Therapeutic Delivery Using Elastin-Like Recombinamers. Bioconjug Chem. 2015;26(7):1252-65.

12. Lim DW, Nettles DL, Setton La, Chilkoti A. In situ cross-linking of elastin-like polypeptide block copolymers for tissue repair. Biomacromolecules. 2008;9(1):222-30.

13. Heilshorn SC, Liu JC, Tirrell DA. Cell-binding domain context affects cell behavior on engineered proteins. Biomacromolecules. 2005;6(1):318-23.

14. Urry DW, Parker TM, Reid MC, Gowda DC. Biocompatibility of the Bioelastic Materials, Poly(GVGVP) and Its γ-Irradiation Cross-Linked Matrix: Summary of Generic Biological Test Results. Journal of Bioactive and Compatible Polymers. 1991;6(3):263-82.

15. Rincon AC, Molina-Martinez IT, de Las Heras B, Alonso M, Bailez C, Rodriguez-Cabello JC, et al. Biocompatibility of elastin-like polymer

poly(VPAVG) microparticles: in vitro and in vivo studies. J Biomed Mater Res A. 2006;78(2):343-51.

16. Elsas FJ, Gowda DC, Urry DW. Synthetic polypeptide sleeve for strabismus surgery. Journal of pediatric ophthalmology and strabismus. 1992;29(5):284-6.

17. Schleh C, Rothen-Rutishauser B, Kreyling WG. The influence of pulmonary surfactant on nanoparticulate drug delivery systems. European journal of pharmaceutics and biopharmaceutics. 2011;77(3):350-2.

18. Deng ZJ, Liang M, Monteiro M, Toth I, Minchin RF. Nanoparticle-induced unfolding of fibrinogen promotes Mac-1 receptor activation and inflammation. Nature nanotechnology. 2011;6(1):39-44.

19. Lesniak A, Fenaroli F, Monopoli MP, Åberg C, Dawson KA, Salvati A. Effects of the presence or absence of a protein corona on silica nanoparticle uptake and impact on cells. ACS nano. 2012;6(7):5845-57.

20. Lundqvist M, Stigler J, Elia G, Lynch I, Cedervall T, Dawson KA. Nanoparticle size and surface properties determine the protein corona with possible implications for biological impacts. Proc Natl Acad Sci U S A. 2008;105(38):14265-70.

21. Wolfram J, Yang Y, Shen J, Moten A, Chen C, Shen H, et al. The nano-plasma interface: implications of the protein corona. Colloids and Surfaces B: Biointerfaces. 2014;124:17-24.

22. Tenzer S, Docter D, Rosfa S, Wlodarski A, Kuharev Jr, Rekik A, et al. Nanoparticle size is a critical physicochemical determinant of the human blood

plasma corona: a comprehensive quantitative proteomic analysis. ACS nano. 2011;5(9):7155-67.

23. Hsu M, Juliano R. Interactions of liposomes with the reticuloendothelial system: II. Nonspecific and receptor-mediated uptake of liposomes by mouse peritoneal macrophages. Biochimica et Biophysica Acta (BBA)-Molecular Cell Research. 1982;720(4):411-9.

24. Harashima H, Sakata K, Funato K, Kiwada H. Enhanced hepatic uptake of liposomes through complement activation depending on the size of liposomes. Pharmaceutical research. 1994;11(3):402-6.

25. Raschke W, Baird S, Ralph P, Nakoinz I. Functional macrophage cell lines transformed by Abelson leukemia virus. Cell. 1978;15(1):261-7.

26. Ralph P, Nakoinz I. Antibody-dependent killing of erythrocyte and tumor targets by macrophage-related cell lines: enhancement by PPD and LPS. The Journal of Immunology. 1977;119(3):950-4.

27. Ishihama Y, Rappsilber J, Andersen JS, Mann M. Microcolumns with self-assembled particle frits for proteomics. Journal of chromatography A. 2002;979(1):233-9.

28. Bern M, Kil YJ, Becker C. Byonic: advanced peptide and protein identification software. Current protocols in bioinformatics. 2012:13.20. 1-13.20. 14.

29. Karmali PP, Simberg D. Interactions of nanoparticles with plasma proteins: implication on clearance and toxicity of drug delivery systems. Expert Opinion on Drug Delivery. 2011;8(3):343-57.

30. Pedersen MB, Zhou X, Larsen EKU, Sørensen US, Kjems J, Nygaard JV, et al. Curvature of synthetic and natural surfaces is an important target feature in classical pathway complement activation. The journal of immunology. 2010;184(4):1931-45.

31. Geys J, Nemmar A, Verbeken E, Smolders E, Ratoi M, Hoylaerts MF, et al. Acute toxicity and prothrombotic effects of quantum dots: impact of surface charge. Environmental health perspectives. 2008;116(12):1607.

32. Gessner A, Waicz R, Lieske A, Paulke B-R, Mäder K, Müller R. Nanoparticles with decreasing surface hydrophobicities: influence on plasma protein adsorption. International journal of pharmaceutics. 2000;196(2):245-9.

33. Gessner A, Lieske A, Paulke BR, Müller RH. Influence of surface charge density on protein adsorption on polymeric nanoparticles: analysis by two-dimensional electrophoresis. European journal of pharmaceutics and biopharmaceutics. 2002;54(2):165-70.

34. Lai W, Wang Q, Li L, Hu Z, Chen J, Fang Q. Interaction of gold and silver nanoparticles with human plasma: Analysis of protein corona reveals specific binding patterns. Colloids and Surfaces B: Biointerfaces. 2017;152:317-25.

35. Pitek AS, O'Connell D, Mahon E, Monopoli MP, Bombelli FB, Dawson KA. Transferrin coated nanoparticles: study of the bionano interface in human plasma. PloS one. 2012;7(7):e40685.

36. Grunér M, Kauscher U, Linder M, Monopoli M. An environmental route of exposure affects the formation of nanoparticle coronas in blood plasma. Journal of proteomics. 2016;137:52-8.

37. Cedervall T, Lynch I, Foy M, Berggård T, Donnelly SC, Cagney G, et al. Detailed identification of plasma proteins adsorbed on copolymer nanoparticles. Angewandte Chemie International Edition. 2007;46(30):5754-6.

38. Lynch I, Cedervall T, Lundqvist M, Cabaleiro-Lago C, Linse S, Dawson KA. The nanoparticle–protein complex as a biological entity; a complex fluids and surface science challenge for the 21st century. Advances in colloid and interface science. 2007;134:167-74.

39. Verma A, Stellacci F. Effect of surface properties on nanoparticle–cell interactions. Small. 2010;6(1):12-21.

40. Mahmoudi M, Lynch I, Ejtehadi MR, Monopoli MP, Bombelli FB, Laurent S. Protein− nanoparticle interactions: opportunities and challenges. Chemical reviews. 2011;111(9):5610-37.

41. Wilkinson K, Ekstrand-Hammarström B, Ahlinder L, Guldevall K, Pazik R, Kępiński L, et al. Visualization of custom-tailored iron oxide nanoparticles chemistry, uptake, and toxicity. Nanoscale. 2012;4(23):7383-93.

42. AshaRani P, Low Kah Mun G, Hande MP, Valiyaveettil S. Cytotoxicity and genotoxicity of silver nanoparticles in human cells. ACS nano. 2008;3(2):279-90.

43. Sharma V, Anderson D, Dhawan A. Zinc oxide nanoparticles induce oxidative DNA damage and ROS-triggered mitochondria mediated apoptosis in human liver cells (HepG2). Apoptosis. 2012;17(8):852-70.

44. Elmore S. Apoptosis: a review of programmed cell death. Toxicologic pathology. 2007;35(4):495-516.

45. Ozaki C, Somamoto S, Kawabata S, Tabata Y. Effect of an artificial silk elastin-like protein on the migration and collagen production of mouse fibroblasts. Journal of Biomaterials Science, Polymer Edition. 2014;25(12):1266-77.

46. Lin CY, Liu JC. Modular protein domains: an engineering approach toward functional biomaterials. Curr Opin Biotechnol. 2016;40:56-63.

47. Desai MS, Lee SW. Protein-based functional nanomaterial design for bioengineering applications. Wiley Interdiscip Rev Nanomed Nanobiotechnol. 2015;7(1):69-97.

48. Lim DW, Nettles DL, Setton La, Chilkoti A. Rapid Cross-Linking of Elastin-like Polypeptides with (Hydroxymethyl) phosphines in Aqueous Solution. Biomacromolecules. 2007;8:1463-70.

49. Heilshorn S. Endothelial cell adhesion to the fibronectin CS5 domain in artificial extracellular matrix proteins. Biomaterials. 2003;24(23):4245-52.

50. Bartneck M, Keul HA, Zwadlo-Klarwasser G, Groll Jr. Phagocytosis independent extracellular nanoparticle clearance by human immune cells. Nano letters. 2009;10(1):59-63.

51. Rojas JM, Sanz-Ortega L, Mulens-Arias V, Gutiérrez L, Pérez-Yagüe S, Barber DF. Superparamagnetic iron oxide nanoparticle uptake alters M2

macrophage phenotype, iron metabolism, migration and invasion. Nanomedicine: Nanotechnology, Biology and Medicine. 2016;12(4):1127-38.

52. Sabareeswaran A, Ansar EB, Varma PRVH, Mohanan PV, Kumary TV. Effect of surface-modified superparamagnetic iron oxide nanoparticles (SPIONS) on mast cell infiltration: An acute in vivo study. Nanomedicine: Nanotechnology, Biology and Medicine. 2016;12(6):1523-33.

53. Senoh H, Kano H, Suzuki M, Ohnishi M, Kondo H, Takanobu K, et al. Comparison of single or multiple intratracheal administration for pulmonary toxic responses of nickel oxide nanoparticles in rats. Journal of occupational health. 2017;59(2):112-21.

54. Kettler K, Giannakou C, de Jong WH, Hendriks AJ, Krystek P. Uptake of silver nanoparticles by monocytic THP-1 cells depends on particle size and presence of serum proteins. Journal of Nanoparticle Research. 2016;18(9).

55. Seiffert J, Buckley A, Leo B, Martin NG, Zhu J, Dai R, et al. Pulmonary effects of inhalation of spark-generated silver nanoparticles in Brown-Norway and Sprague–Dawley rats. Respiratory research. 2016;17(1):85.

56. Bruneau A, Turcotte P, Pilote M, Gagné F, Gagnon C. Fate of silver nanoparticles in wastewater and immunotoxic effects on rainbow trout. Aquatic Toxicology. 2016;174:70-81.

57. Ede JD, Ortega VA, Boyle D, Beingessner RL, Hemraz UD, Fenniri H, et al. The effects of rosette nanotubes with different functionalizations on channel catfish (Ictalurus punctatus) lymphocyte viability and receptor function. Environmental Science: Nano. 2016;3(3):578-92.

58. Jovanović B, Palić D. Immunotoxicology of non-functionalized engineered nanoparticles in aquatic organisms with special emphasis on fish—Review of current knowledge, gap identification, and call for further research. Aquatic toxicology. 2012;118:141-51.

59. Rooney M, Woodhouse K. Decreased tissue factor expression with increased CD11b upregulation on elastin-based biomaterial coatings. Biomaterials Science. 2014;2(10):1377-83.

60. Nouri FS, Wang X, Chen X, Hatefi A. Reducing the visibility of the vector/DNA nanocomplexes to the immune system by elastin-like peptides. Pharmaceutical research. 2015;32(9):3018.

61. Dale MA, Xiong W, Carson JS, Suh MK, Karpisek AD, Meisinger TM, et al. Elastin-derived peptides promote abdominal aortic aneurysm formation by modulating M1/M2 macrophage polarization. The Journal of Immunology. 2016;196(11):4536-43.

62. Simon SI, Schmid-Schönbein G. Biophysical aspects of microsphere engulfment by human neutrophils. Biophysical journal. 1988;53(2):163-73.

63. Tabata Y, Ikada Y. Effect of the size and surface charge of polymer microspheres on their phagocytosis by macrophage. Biomaterials. 1988;9(4):356-62.

64. Champion JA, Walker A, Mitragotri S. Role of particle size in phagocytosis of polymeric microspheres. Pharmaceutical research. 2008;25(8):1815-21.

65. Aggarwal P, Hall JB, McLeland CB, Dobrovolskaia MA, McNeil SE. Nanoparticle interaction with plasma proteins as it relates to particle biodistribution, biocompatibility and therapeutic efficacy. Advanced drug delivery reviews. 2009;61(6):428-37.

66. Tenzer S, Docter D, Kuharev J, Musyanovych A, Fetz V, Hecht R, et al. Rapid formation of plasma protein corona critically affects nanoparticle pathophysiology. Nature nanotechnology. 2013;8(10):772-81.

67. Stafford JL, Belosevic M. Transferrin and the innate immune response of fish: identification of a novel mechanism of macrophage activation. Developmental and comparative immunology. 2003;27(6-7):539-54.

68. Wang H, Zhang M, Bianchi M, Sherry B, Sama A, Tracey KJ. Fetuin (α2-HS-glycoprotein) opsonizes cationic macrophagedeactivating molecules. Proceedings of the National Academy of Sciences. 1998;95(24):14429-34.

69. Jersmann HP, Dransfield I. Fetuin/α2-HS glycoprotein enhances phagocytosis of apoptotic cells and macropinocytosis by human macrophages. Clinical Science. 2003;105(3):273-8.

70. Dobrovolskaia MA, Patri AK, Zheng J, Clogston JD, Ayub N, Aggarwal P, et al. Interaction of colloidal gold nanoparticles with human blood: effects on particle size and analysis of plasma protein binding profiles. Nanomedicine: Nanotechnology, Biology and Medicine. 2009;5(2):106-17.

71. Vyner MC, Amsden BG. Polymer chain flexibility-induced differences in fetuin A adsorption and its implications on cell attachment and proliferation. Acta Biomater. 2016;31:89-98.

10. Conclusions

10.1. Major Conclusions

The central goal of this thesis was to better understand the host response to biomaterials, with biocompatibility being a parameter critical for the successful deployment of any biomaterial. Our current understanding of biomaterial biocompatibility is limited in part due to the breadth of biomaterials engineered for various biomedical applications. Furthermore, the host response to a biomaterial is not elicited by the material surface properties, but the layer of adsorbed proteins which instantaneously coat the biomaterial surface. That there are a myriad of proteins which may be involved serves to further obfuscate our understanding of the issue of host response and biocompatibility. In order to further our understanding of protein adsorption, this thesis has evaluated the ramifications of molecular-level modifications to biomaterials on protein adsorption from human plasma using Western blotting.

The first biomaterial which was examined was a thermogelling ABA block polymer composed of poly(caprolactone) polymer in the A position and poly(ethylene glycol) in the central block. This polymer underwent a gelation when heated to physiological temperatures and could be used for in situ hydrogel delivery of therapeutics. This material was then reduced in order to modify the material to have either 30 or 54% carboxylation in the lateral polymer blocks. Protein adsorption studies found that carboxylation did not affect the amount of albumin, transferrin or Complement Factor 3 (C3) adsorbed to the material though 30% carboxylation did prevent the adsorption of fibrinogen, $alpha_1$ antitrypsin, prothrombin and antithrombin when compared to the 54% hydrogel. This 54%

carboxylation was found to completely eliminate the adsorption of immunoglobulin G (IgG) observed on the 30% sample. Plasma clotting revealed that both polymer hydrogels stimulated a stronger clotting response than observed in the control, with the 54% sample causing a statistically significant decrease in the final clot endpoint. Overall the study showed that the 54% carboxylated sample may elicit less of a deleterious host response than the 30% sample.

Osseointegrative bioactive glass 45S5 was tested to determine how different material manufacturing methods and crystallinities affected the composition of the adsorbed proteome. As this material has been used clinically for decades, the composition of the proteome would also yield insight into the adsorbed proteins associated with a biocompatible material. Melt-derived amorphous and crystalline 45S5 as well as a sol-gel form of the material were all tested using human plasma. The concentration of the adsorbed proteome on all samples was found to be very low, below the lower sensitivity of standard protein assays, prompting the use of an innovative colloidal gold nanoparticle-based assay. Immunoblotting showed a greater variety of plasma proteins adsorbed to the sol-gel derived glass, including transferrin, fibrinogen and IgG. Albumin was the only protein detected in moderate to high levels across all samples. Crystallization of melt-cast bioactive glass eliminated the activation of C3 and almost completely eliminated the adsorption of any C3 along with $alpha_1$ antitrypsin. This also led to an increase in albumin adsorption. Taken together, these results showed that using a sol-gel manufacturing method, while significantly increasing the material and porosity and surface area, also increased

the protein adsorption and potential for deleterious host responses. Crystallization was found to decrease the potential for deleterious host response.

Poly(acrylic acid)-functionalized metal oxide nanoparticles were examined for the role of the metal oxide core on protein adsorption and stimulation of phagocytosis. TiO_2, CeO_2, Fe_2O_3 and ZnO-containing particles along with a hollow capsule sample were all found to adsorb large amounts of albumin and transferrin as well as moderate to high levels of fibrinogen, IgG and C3 as well as low to moderately-high amounts of C3 activation. Fibronectin, Factor XI and beta-lipoprotein were found to exhibit some specificity by only adsorbing strongly to one of the nanoparticle samples. Each of the nanoparticles was shown to inhibit normal plasma clotting, with the ZnO sample completely eliminating the clot response. Phagocytosis was enhanced in two immune cell lines by the presence of an adsorbed protein corona.

A protocol for the recombinant synthesis of a novel family of temperature-responsive self-assembling elastin-like polypeptides (ELPs) was developed. The novel ELP sequences featured hydrophobic leucine amino acids and a moderately low number of repeating units. Modifications to standard concatemerization procedures increased the success rate of DNA ligation and transformation from ~2% to >95%. One of the key changes involved doubling the number of cleavage sites for a specific restriction enzyme in order to increase its efficiency. Given that this was the most hydrophobic homopolymer of ELPs produced recombinantly to date, a new protein purification procedure needed to be developed as reversible temperature cycling methods commonly employed for standard ELPs did not

yield any appreciable product. Denaturing metal affinity chromatography was critical to ensuring the ELP was fully solubilized before a primary separation from the cellular milieu. Final ELP yields were found to be 10-20 fold greater than reported yields for comparable hydrophobic ELPs.

As leucine-containing ELPs were novel constructs, with previously studied protein sequences typically comprising of significantly more hydrophilic amino acids, the temperature modulated self-assembly behaviour was examined. Samples were produced in such a way as to isolate the role of amino acid hydrophobicity and chain length and protein concentration was also controlled. Dynamic light scattering and transmission electron microscopy revealed that, among other findings, micron-sized, unstable particles formed for large concentrations of ELP of either 20 repeats of a leucine-containing sequence or 40 repeats of a valine-containing sequence. More hydrophobic sequences resulted in smaller particles, as did longer ELP chains. These longer chains also conferred greater particle stability upon dilution. Large hysteresis values were observed for hydrophobic ELPs, with some irreversible assembly observed as a function of protein concentration, hydrophobicity and chain length.

Once an understanding of the assembly and disassembly of leucine-containing ELPs was gleaned, the information was used to develop 200 and 500 nm particles composed of one of four leucine-ELPs or a valine control sample and the plasma protein adsorption was examined. The choice of samples and preparation methods allowed for the delineation of the effects of protein hydrophobicity and chain length as well as particle diameter. Low levels of

adsorbed plasma proteins were detected, almost below the sensitivity of the standard protein assay kit. A number of proteins were detected in high levels across all samples including activated C3, IgG, fibrinogen, transferrin and alpha$_1$ antitrypsin. Extremely high levels of albumin were also detected and required an additional 5-fold dilution of both primary and secondary antibodies in order to avoid any non-specific Western blotting signals. Varying levels of fibrinogen cleavage fragments, alpha$_2$ macroglobulin, plasminogen and prothrombin were also detected across all samples. Plasma clotting was not found to be strongly affected by the presence of ELP nanoparticles, though particles composed of either 20 repeats of the leucine sequence or 40 of the valine did significantly affect the onset of the clot reaction onset as well as the final intensity value.

Protein adsorption to 200 and 500 nm ELP particles was further examined by mass spectroscopy and macrophage phagocytosis. Both sequence hydrophobicity and particle size were found to affect the adsorbed protein fingerprint, with hydrophobic sequences adsorbing a greater variety of protein. Particle size was found to strongly influence the corona for hydrophobic particles, with a greater variety found on the 200 nm particles, though the effect was not noticeable for the valine-containing construct. None of the ELP nanoparticles were found to adversely affect macrophage cell viability. 500 nm valine-containing ELP particles were found to significantly decrease phagocytic capacity of the macrophages but not the proportion of active cells. This was thought to be a result of the large particle size in combination with the proportions of adsorbed opsonin and dysopsonin proteins which adsorbed to the particle surfaces.

10.2. Future Outlook

These findings have revealed numerous instances wherein chemical modifications to biomaterials can greatly impact the content of the adsorbed proteome. Examples include: the carboxylation of thermogelling polymers, which resulted in the complete elimination of fibrinogen, $alpha_1$ antitrypsin and/or IgG, variations of metal oxide species in poly(acrylic acid) nanoparticles controlling adsorption of fibronectin and Factor XI and ELP nanoparticle size, chain length or hydrophobicity directing the adsorption of $alpha_2$ macroglobulin, plasminogen and prothrombin in addition to fibrinogen activation. In each of these cases valuable information regarding biocompatibility as dictated by the adsorbed protein corona can be obtained in two methods. The forces dictating the adsorption of proteins to each of these surfaces can be examined in greater detail to learn how to direct the adsorption process. Additionally, the above samples may be used to evaluate downstream responses as a function of the levels of the identified proteins like cell signalling and recruitment, phagocytsis, adaptive immune response, particle transport, circulatory half-life and hepatic clearance.

Furthermore, information regarding host responses to protein-based materials specifically is lacking. ELPs are an intriguing material with which to glean more insight about this process. As variability may be introduced in the guest amino acid position, overall chain length and at the protein termini with relative ease, ELPs represent a flexible platform with which to probe amino acid-

level effects on protein adsorption. Furthermore, careful sample preparation can yield particles with near-identical physical characteristics but containing fundamental-level variations in the protein sequences. This would be invaluable in delineating the amino acid level effects of protein adsorption, as chemical modifications to biomaterials often alters physical properties as well. That identical ELP sequences may be adapted to various device forms, such as particles, coatings, hydrogels and matricies would also determine morphological implications on protein adsorption.

11. References

Chapter 1

1. Horbett TA. Chapter II.1.2 - Adsorbed Proteins on Biomaterials A2 - Ratner, Buddy D. In: Hoffman AS, Schoen FJ, Lemons JE, editors. Biomaterials Science (Third Edition): Academic Press; 2013. p. 394-408.

2. Vroman L. Effect of Adsorbed Proteins on the Wettability of Hydrophilic and Hydrophobic Solids. Nature. 1962;196(4853):476-7.

3. Vroman L, Adams A, Fischer G, Munoz P. Interaction of high molecular weight kininogen, factor XII, and fibrinogen in plasma at interfaces. Blood. 1980;55(1):156-9.

4. Abbas AK. Cellular and molecular immunology. In: Lichtman AH, Pillai S, editors. 6th ed. ed. Philadelphia :: Saunders Elsevier; 2007.

5. Medzhitov R, Janeway Jr C. Innate immunity. New England Journal of Medicine. 2000;343(5):338-44.

6. Medzhitov R. Recognition of microorganisms and activation of the immune response. Nature. 2007;449(7164):819-26.

7. Anderson JM, Rodriguez A, Chang DT. Foreign body reaction to biomaterials. Seminars in immunology. 2008;20(2):86-100.

8. Bonvini RF. Inflammatory response post-myocardial infarction and reperfusion: a new therapeutic target? European Heart Journal Supplements. 2005;7(Suppl I):I27-I36.

9. Hamad OA, Ekdahl KN, Nilsson B, editors. Non-proteolytically activated C3 promotes binding of activated platelets and platelet-derived microparticles to leukocytes via CD11b/CD18. Immunobiology; 2012.

10. Hamad OA, Nilsson PH, Wouters D, Lambris JD, Ekdahl KN, Nilsson B. Complement component C3 binds to activated normal platelets without preceding proteolytic activation and promotes binding to complement receptor 1. The journal of immunology. 2010;184(5):2686-92.

11. Klos A, Tenner AJ, Johswich K-O, Ager RR, Reis ES, Köhl J. The role of the anaphylatoxins in health and disease. Molecular immunology. 2009;46(14):2753-66.

12. Walport MJ. Complement. First of two parts. The New England journal of medicine. 2001;344(14):1058-66.

13. Wong N, Kojima M, Dobo J, Ambrus G, Sim R. Activities of the MBL-associated serine proteases (MASPs) and their regulation by natural inhibitors. Molecular immunology. 1999;36(13):853-61.

14. Matsushita M. The lectin pathway of the complement system. Microbiology and immunology. 1996;40(12):887-93.

15. Andersson J, Ekdahl KN, Lambris JD, Nilsson B. Binding of C3 fragments on top of adsorbed plasma proteins during complement activation on a model biomaterial surface. Biomaterials. 2005;26(13):1477-85.

16. Craddock PR, Fehr J, Brigham KL, Kronenberg RS, Jacob HS. Complement and leukocyte-mediated pulmonary dysfunction in hemodialysis. New England Journal of Medicine. 1977;296(14):769-74.

17. Fitch JC, Rollins S, Matis L, Alford B, Aranki S, Collard CD, et al. Pharmacology and biological efficacy of a recombinant, humanized, single-chain

antibody C5 complement inhibitor in patients undergoing coronary artery bypass graft surgery with cardiopulmonary bypass. Circulation. 1999;100(25):2499-506.

18. Haverich A, Shernan SK, Levy JH, Chen JC, Carrier M, Taylor KM, et al. Pexelizumab reduces death and myocardial infarction in higher risk cardiac surgical patients. The Annals of thoracic surgery. 2006;82(2):486-92.

19. Gemmell CH, Black JP, Yeo EL, Sefton MV. Material-induced up-regulation of leukocyte CD11b during whole blood contact: Material differences and a role for complement. Journal of Biomedical Materials Research Part A. 1996;32(1):29-35.

20. Tang L, Liu L, Elwing HB. Complement activation and inflammation triggered by model biomaterial surfaces. Journal of biomedical materials research. 1998;41:333-40.

21. Salvador-Morales C, Flahaut E, Sim E, Sloan J, Green ML, Sim RB. Complement activation and protein adsorption by carbon nanotubes. Molecular immunology. 2006;43(3):193-201.

22. Ricklin D, Lambris JD. Complement in immune and inflammatory disorders: therapeutic interventions. The Journal of Immunology. 2013;190(8):3839-47.

23. Tillou X, Poirier N, Le Bas-Bernardet S, Hervouet J, Minault D, Renaudin K, et al. Recombinant human C1-inhibitor prevents acute antibody-mediated rejection in alloimmunized baboons. Kidney international. 2010;78(2):152-9.

24. Andersson J, Larsson R, Richter R, Ekdahl KN, Nilsson B. Binding of a model regulator of complement activation (RCA) to a biomaterial surface:

surface-bound factor H inhibits complement activation. Biomaterials. 2001;22(17):2435-43.

25. Andersson J, Bexborn F, Klinth J, Nilsson B, Ekdahl KN. Surface-attached PEO in the form of activated pluronic with immobilized factor H reduces both coagulation and complement activation in a whole-blood model. Journal of Biomedical Materials Research Part A. 2006;76(1):25-34.

26. Wu Y-Q, Qu H, Sfyroera G, Tzekou A, Kay BK, Nilsson B, et al. Protection of nonself surfaces from complement attack by factor H-binding peptides: implications for therapeutic medicine. The Journal of Immunology. 2011;186(7):4269-77.

27. Bahniuk MS, Pirayesh H, Singh HD, Nychka Ja, Unsworth LD. Bioactive glass 45S5 powders: effect of synthesis route and resultant surface chemistry and crystallinity on protein adsorption from human plasma. Biointerphases. 2012;7(1-4):41-.

28. Nikouei NS, Vakili MR, Bahniuk MS, Unsworth L, Akbari A, Wu J, et al. Thermoreversible hydrogels based on triblock copolymers of poly(ethylene glycol) and carboxyl functionalized poly(ε-caprolactone): The effect of carboxyl group substitution on the transition temperature and biocompatibility in plasma. Acta biomaterialia. 2014;12:81-92.

29. Vyner MC, Liu L, Sheardown HD, Amsden BG. The effect of elastomer chain flexibility on protein adsorption. Biomaterials. 2013;34(37):9287-94.

30. Vuoriluoto M, Orelma H, Zhu B, Johansson LS, Rojas OJ. Control of Protein Affinity of Bioactive Nanocellulose and Passivation Using Engineered Block and Random Copolymers. ACS Appl Mater Interfaces. 2016;8(8):5668-78.

31. Ryu KE, Rhim H, Park CW, Chun HJ, Hong SH, Kim JJ, et al. Plasma protein adsorption to anion substituted poly (vinyl alcohol) membranes. Macromolecular research. 2003;11(6):451-7.

32. Kurosawa S, Kamo N, Aizawa H, Muratsugu M. Adsorption of 125I-labeled immunoglobulin G, its F(ab')2 and Fc fragments onto plasma-polymerized films. Biosens Bioelectron. 2007;22(11):2598-603.

33. Neuffer MC, McDivitt J, Rose D, King K. Hemostatic dressings for the first responder: a review. Military medicine. 2004;169(9):716.

34. Waner M, editor Novel hemostatic alternatives in reconstructive surgery. Seminars in hematology; 2004: Elsevier.

35. Banerjee R, Nageswari K, Puniyani R. Hematological aspects of biocompatibility-review article. Journal of biomaterials applications. 1997;12(1):57-76.

36. Kumar A, Kar S, Fay WP. Thrombosis, physical activity, and acute coronary syndromes. J Appl Physiol (1985). 2011;111(2):599-605.

37. Griep MA, Fujikawa K, Nelsestuen GL. Possible basis for the apparent surface selectivity of the contact activation of human blood coagulation factor XII. Biochemistry. 1986;25(21):6688-94.

38. Zhuo R, Miller R, Bussard KM, Siedlecki CA, Vogler EA. Procoagulant stimulus processing by the intrinsic pathway of blood plasma coagulation. Biomaterials. 2005;26(16):2965-73.

39. Renné T, Pozgajová M, Grüner S, Schuh K, Pauer H-U, Burfeind P, et al. Defective thrombus formation in mice lacking coagulation factor XII. Journal of Experimental Medicine. 2005;202(2):271-81.

40. Vogler EA, Siedlecki CA. Contact activation of blood-plasma coagulation. Biomaterials. 2009;30(10):1857-69.

41. de Maat S, Maas C. Factor XII: form determines function. J Thromb Haemost. 2016;14(8):1498-506.

42. Gorbet MB, Sefton MV. Biomaterial-associated thrombosis: roles of coagulation factors, complement, platelets and leukocytes. Biomaterials. 2004;25(26):5681-703.

43. Hemostasis and thrombosis : practical guidelines in clinical management. In: Roberts HR, Saba HI, editors.

44. Ziats NP, Pankowsky D, Tierney B, Ratnoff O, Anderson JM. Adsorption of Hageman factor (factor XII) and other human plasma proteins to biomedical polymers. The Journal of laboratory and clinical medicine. 1990;116(5):687-96.

45. Mulzer SR, Brash JL. Identification of plasma proteins adsorbed to hemodialyzers during clinical use. Journal of biomedical materials research. 1989;23(12):1483-504.

46. Yau JW, Stafford AR, Liao P, Fredenburgh JC, Roberts R, Weitz JI. Mechanism of catheter thrombosis: comparison of the antithrombotic activities of

fondaparinux, enoxaparin, and heparin in vitro and in vivo. Blood. 2011;118(25):6667-74.

47. Larsson M, Rayzman V, Nolte MW, Nickel KF, Björkqvist J, Jämsä A, et al. A factor XIIa inhibitory antibody provides thromboprotection in extracorporeal circulation without increasing bleeding risk. Science translational medicine. 2014;6(222):222ra17-ra17.

48. Elam J-H, Nygren H. Adsorption of coagulation proteins from whole blood on to polymer materials: relation to platelet activation. Biomaterials. 1992;13(1):3-8.

49. Van der Kamp K, Van Oeveren W. Factor XII fragment and kallikrein generation in plasma during incubation with biomaterials. Journal of Biomedical Materials Research Part A. 1994;28(3):349-52.

50. Lee JH, Lee HB, Andrade JD. Blood compatibility of polyethylene oxide surfaces. Progress in Polymer Science. 1995;20(6):1043-79.

51. Park K, Mosher DF, Cooper SL. Acute surface-induced thrombosis in the canine ex vivo model: Importance of protein composition of the initial monolayer and platelet activation. Journal of Biomedical Materials Research Part A. 1986;20(5):589-612.

52. Eberhart R, Munro M, Frautschi J, Lubin M, Clubb F, Miller C, et al. Influence of Endogenous Albumin Binding on Blood-Material Interactionsa. Annals of the New York Academy of Sciences. 1987;516(1):78-95.

53. Yeh H-Y, Lin J-C. Bioactivity and platelet adhesion study of a human thrombomodulin-immobilized nitinol surface. Journal of Biomaterials Science, Polymer Edition. 2009;20(5-6):807-19.

54. Jaffer IH, Fredenburgh JC, Hirsh J, Weitz JI. Medical device-induced thrombosis: what causes it and how can we prevent it? J Thromb Haemost. 2015;13 Suppl 1:S72-81.

55. Tang L, Jennings TA, Eaton JW. Mast cells mediate acute inflammatory responses to implanted biomaterials. Proceedings of the National Academy of Sciences. 1998;95(15):8841-6.

56. Sivaraman B, Latour Ra. The adherence of platelets to adsorbed albumin by receptor-mediated recognition of binding sites exposed by adsorption-induced unfolding. Biomaterials. 2010;31(6):1036-44.

57. Gresele P, Page C, Fuster V, Vermylen J. Platelets in Thrombotic and Non-Thrombotic Disorders. Transfusion Medicine. 2003;13(1):57-8.

58. Shen M, Horbett TA. The effects of surface chemistry and adsorbed proteins on monocyte/macrophage adhesion to chemically modified polystyrene surfaces. Journal of biomedical materials research. 2001;57(3):336-45.

59. Shen M, Martinson L, Wagner MS, Castner DG, Ratner BD, Horbett TA. PEO-like plasma polymerized tetraglyme surface interactions with leukocytes and proteins: in vitro and in vivo studies. Journal of Biomaterials Science, Polymer Edition. 2002;13(4):367-90.

60. Kondo A, Oku S, Murakami F, Higashitani K. Conformational changes in protein molecules upon adsorption on ultrafine particles. Colloids and Surfaces B: Biointerfaces. 1993;1(3):197-201.

61. Karlsson M, Mårtensson L-G, Jonsson B-H, Carlsson U. Adsorption of human carbonic anhydrase II variants to silica nanoparticles occur stepwise: binding is followed by successive conformational changes to a molten-globule-like state. Langmuir. 2000;16(22):8470-9.

62. Abraham S, So A, Unsworth LD. Poly(carboxybetaine methacrylamide)-modified nanoparticles: a model system for studying the effect of chain chemistry on film properties, adsorbed protein conformation, and clot formation kinetics. Biomacromolecules. 2011;12(10):3567-80.

63. Tsai WB, Grunkemeier JM, Horbett TA. Variations in the ability of adsorbed fibrinogen to mediate platelet adhesion to polystyrene-based materials: A multivariate statistical analysis of antibody binding to the platelet binding sites of fibrinogen. Journal of Biomedical Materials Research Part A. 2003;67(4):1255-68.

64. Sivaraman B, Latour RA. The relationship between platelet adhesion on surfaces and the structure versus the amount of adsorbed fibrinogen. Biomaterials. 2010;31(5):832-9.

65. Forsyth CB, Solovjov DA, Ugarova TP, Plow EF. Integrin αMβ2-mediated cell migration to fibrinogen and its recognition peptides. The Journal of experimental medicine. 2001;193(10):1123-34.

66. Bacakova L, Filova E, Parizek M, Ruml T, Svorcik V. Modulation of cell adhesion, proliferation and differentiation on materials designed for body implants. Biotechnol Adv. 2011;29(6):739-67.

67. Di Cio S, Gautrot JE. Cell sensing of physical properties at the nanoscale: Mechanisms and control of cell adhesion and phenotype. Acta Biomater. 2016;30:26-48.

68. Hoffman AS. Stimuli-responsive polymers: Biomedical applications and challenges for clinical translation. Advanced drug delivery reviews. 2013;65(1):10-6.

69. Ruel-Gariepy E, Leroux J-C. In situ-forming hydrogels—review of temperature-sensitive systems. European Journal of Pharmaceutics and Biopharmaceutics. 2004;58(2):409-26.

70. Loh XJ, Li J. Biodegradable thermosensitive copolymer hydrogels for drug delivery. Expert Opinion on Therapeutic Patents. 2007;17(8):965-77.

71. Moon HJ, Park MH, Joo MK, Jeong B. Temperature-responsive compounds as in situ gelling biomedical materials. Chemical Society Reviews. 2012;41(14):4860-83.

72. Dou QQ, Liow SS, Ye E, Lakshminarayanan R, Loh XJ. Biodegradable thermogelling polymers: working towards clinical applications. Adv Healthc Mater. 2014;3(7):977-88.

73. Hench LL, Splinter RJ, Allen WC, Greenlee TK. Bonding mechanisms at the interface of ceramic prosthetic materials. Journal of Biomedical Materials Research. 1971;5(6):117-41.

74. Hench LL, Paschall Ha. Direct chemical bond of bioactive glass-ceramic materials to bone and muscle. Journal of biomedical materials research. 1973;7(3):25-42.

75. Xynos ID, Edgar aJ, Buttery LD, Hench LL, Polak JM. Ionic products of bioactive glass dissolution increase proliferation of human osteoblasts and induce insulin-like growth factor II mRNA expression and protein synthesis. Biochemical and biophysical research communications. 2000;276(2):461-5.

76. Gough JE, Notingher I, Hench LL. Osteoblast attachment and mineralized nodule formation on rough and smooth 45S5 bioactive glass monoliths. Journal of biomedical materials research Part A. 2004;68(4):640-50.

77. Christodoulou I, Buttery LDK, Saravanapavan P, Tai G, Hench LL, Polak JM. Dose- and time-dependent effect of bioactive gel-glass ionic-dissolution products on human fetal osteoblast-specific gene expression. Journal of biomedical materials research Part B, Applied biomaterials. 2005;74(1):529-37.

78. Christodoulou I, Buttery LDK, Tai G, Hench LL, Polak JM. Characterization of human fetal osteoblasts by microarray analysis following stimulation with 58S bioactive gel-glass ionic dissolution products. Journal of biomedical materials research Part B, Applied biomaterials. 2006;77(2):431-46.

79. Hench LL. Bioceramics. Journal of the American Ceramic Society. 1998;81(7):1705-28.

80. Peitl Filho O, Latorre GP, Hench L. Effect of crystallization on apatite-layer formation of bioactive glass 45%. J Biomed Mater Res. 1996;30:509-14.

81. Peitl O, Dutra E, Hench LL. Highly bioactive P 2 O 5 ± Na 2 O ± CaO ± SiO 2 glass-ceramics. Time. 2001;292.

82. Lefebvre L, Gremillard L, Chevalier J, Bernache-Assollant D, editors. Sintering Behavior of 45S5 Bioglass®. Key Engineering Materials; 2008: Trans Tech Publ.

83. Lefebvre L, Chevalier J, Gremillard L, Zenati R, Thollet G, Bernache-Assolant D, et al. Structural transformations of bioactive glass 45S5 with thermal treatments. Acta Materialia. 2007;55(10):3305-13.

84. El-Ghannam A, Ducheyne P, Shapiro IM. Formation of surface reaction products on bioactive glass and their effects on the expression of the osteoblastic phenotype and the deposition of mineralized extracellular matrix. Biomaterials. 1997;18(4):295-303.

85. Wilson J, Pigott GH, Schoen FJ, Hench LL. Toxicology and biocompatibility of bioglasses. Journal of biomedical materials research. 1981;15(6):805-17.

86. Vrouwenvelder W, Groot C. Histological and biochemical evaluation of osteoblasts cultured on bioactive glass, hydroxylapatite, titanium alloy, and stainless steel. Journal of biomedical. 1993;27:465-75.

87. Matsuda T, Yamauchi K, Ito G. The influence of bioglass on the growth of fibroblasts. Journal of biomedical materials research. 1987;21(4):499-507.

88. Kokubo T, Kushitani H, Sakka S, Kitsugi T, Yamamuro T. Solutions able to reproduce in vivo surface-structure changes in bioactive glass-ceramic A-W3. Journal of Biomedical Materials Research. 1990;24(6):721-34.

89. Lai DY. Toward toxicity testing of nanomaterials in the 21st century: a paradigm for moving forward. Wiley Interdisciplinary Reviews: Nanomedicine and Nanobiotechnology. 2012;4(1):1-15.

90. Suri SS, Fenniri H, Singh B. Nanotechnology-based drug delivery systems. Journal of occupational medicine and toxicology. 2007;2(1):16.

91. Nanotechnology and drug delivery. In: Arias JL, editor.

92. Couvreur P, Vauthier C. Nanotechnology: intelligent design to treat complex disease. Pharmaceutical research. 2006;23(7):1417-50.

93. Sahoo SK, Labhasetwar V. Nanotech approaches to drug delivery and imaging. Drug discovery today. 2003;8(24):1112-20.

94. Ortega VA, Ede JD, Boyle D, Stafford JL, Goss GG. Polymer-Coated Metal-Oxide Nanoparticles Inhibit IgE Receptor Binding, Cellular Signaling, and Degranulation in a Mast Cell-like Cell Line. Advanced Science. 2015;2(11).

95. Wiench K, Wohlleben W, Hisgen V, Radke K, Salinas E, Zok S, et al. Acute and chronic effects of nano-and non-nano-scale TiO 2 and ZnO particles on mobility and reproduction of the freshwater invertebrate Daphnia magna. Chemosphere. 2009;76(10):1356-65.

96. Molnar RM, Bodnar M, Hartmann JF, Borbely J. Preparation and characterization of poly (acrylic acid)-based nanoparticles. Colloid and Polymer Science. 2009;287(6):739-44.

97. Urry DW. Entropic elastic processes in protein mechanisms. I. Elastic structure due to an inverse temperature transition and elasticity due to internal chain dynamics. Journal of protein chemistry. 1988;7:1-34.

98. Daamen WF, Veerkamp JH, Van Hest JCM, Van Kuppevelt TH. Elastin as a biomaterial for tissue engineering. Biomaterials. 2007;28(30):4378-98.

99. Mithieux SM, Weiss AS. Elastin. Advances in protein chemistry. 2005;70:437-61.

100. Bax DV, Rodgers UR, Bilek MM, Weiss AS. Cell adhesion to tropoelastin is mediated via the C-terminal GRKRK motif and integrin αVβ3. Journal of biological chemistry. 2009;284(42):28616-23.

101. Robinet A, Fahem A, Cauchard J-H, Huet E, Vincent L, Lorimier S, et al. Elastin-derived peptides enhance angiogenesis by promoting endothelial cell migration and tubulogenesis through upregulation of MT1-MMP. Journal of cell science. 2005;118(2):343-56.

102. De Vries HJ, Middelkoop E, Mekkes JR, Dutrieux RP, Wildevuur CH, Westerhof W. Dermal regeneration in native non-cross-linked collagen sponges with different extracellular matrix molecules. Wound Repair and Regeneration. 1994;2(1):37-47.

103. Urry D, Long M, Cox B, Ohnishi T, Mitchell L, Jacobs M. The synthetic polypentapeptide of elastin coacervates and forms filamentous aggregates. Biochimica et Biophysica Acta (BBA)-Protein Structure. 1974;371(2):597-602.

104. Urry DW, Gowda DC, Parker TM, Luan CH, Reid MC, Harris CM, et al. Hydrophobicity scale for proteins based on inverse temperature transitions. Biopolymers. 1992;32:1243-50.

105. Vrhovski B, Jensen S, Weiss AS. Coacervation characteristics of recombinant human tropoelastin. European Journal of Biochemistry. 1997;250(1):92-8.

106. Urry DW, Trapane TL, Long MM, Prasad KU. Test of the librational entropy mechanism of elasticity of the polypentapeptide of elastin. Effect of introducing a methyl group at residue 5. Journal of the Chemical Society, Faraday Transactions 1: Physical Chemistry in Condensed Phases. 1983;79(4):853-68.

107. Urry DW, Luan CH, Parker TM, Gowda DC, Prasad KU, Reid MC, et al. Temperature of polypeptide inverse temperature transition depends on mean residue hydrophobicity. Journal of the American Chemical Society. 1991;113(11):4346-8.

108. Reguera J, Calvo B. Thermal Behavior and Kinetic Analysis of the Chain Unfolding and Refolding and of the Concomitant Nonpolar Solvation and Desolvation of Two Elastin-like Polymers. Macromolecules. 2003:8470-6.

109. Girotti A, Fernandez-Colino A, Lopez IM, Rodriguez-Cabello JC, Arias FJ. Elastin-like recombinamers: biosynthetic strategies and biotechnological applications. Biotechnol J. 2011;6(10):1174-86.

110. Chilkoti A, Dreher MR, Meyer DE. Design of thermally responsive, recombinant polypeptide carriers for targeted drug delivery. Cancer. 2002;54:1093-111.

111. Cho Y, Zhang Y, Christensen T, Sagle LB, Chilkoti A, Cremer PS. Effects of Hofmeister anions on the phase transition temperature of elastin-like polypeptides. J Phys Chem B. 2008;112(44):13765-71.

112. McDaniel JR, Radford DC, Chilkoti A. A unified model for de novo design of elastin-like polypeptides with tunable inverse transition temperatures. Biomacromolecules. 2013;14(8):2866-72.

113. Navon Y, Bitton R. Elastin-Like Peptides (ELPs) - Building Blocks for Stimuli-Responsive Self-Assembled Materials. Israel Journal of Chemistry. 2016;56(8):581-9.

114. Puiggalí J, Franco L, J. del Valle L. Smart systems related to polypeptide sequences. AIMS Materials Science. 2016;3(1):289-323.

115. Meyer DE, Chilkoti A. Genetically Encoded Synthesis of Protein-Based Polymers with Precisely Specified Molecular Weight and Sequence by Recursive Directional Ligation: Examples from the Elastin-like Polypeptide System. Biomacromolecules. 2002:357-67.

116. Meyer DE, Chilkoti A. Purification of recombinant proteins by fusion with thermally-responsive polypeptides. Nature Biotechnology. 1999;17(November).

117. Meyer DE, Trabbic-Carlson K, Chilkoti a. Protein purification by fusion with an environmentally responsive elastin-like polypeptide: effect of polypeptide length on the purification of thioredoxin. Biotechnology progress. 2001;17(4):720-8.

118. Hu F, Ke T, Li X, Mao PH, Jin X, Hui FL, et al. Expression and purification of an antimicrobial peptide by fusion with elastin-like polypeptides in Escherichia coli. Applied biochemistry and biotechnology. 2010;160(8):2377-87.

119. Lin M, Rose-John S, Grötzinger J, Conrad U, Scheller J. Functional expression of a biologically active fragment of soluble gp130 as an ELP-fusion

protein in transgenic plants: purification via inverse transition cycling. Biochemical Journal. 2006;398(3):577-83.

120. Yeboah A, Cohen RI, Rabolli C, Yarmush ML, Berthiaume F. Elastin-like polypeptides: A strategic fusion partner for biologics. Biotechnol Bioeng. 2016;113(8):1617-27.

121. Li NK, Garcia Quiroz F, Hall CK, Chilkoti A, Yingling YG. Molecular description of the LCST behavior of an elastin-like polypeptide. Biomacromolecules. 2014;15(10):3522-30.

122. Hong M, Isailovic D, McMillan R, Conticello V. Structure of an elastin-mimetic polypeptide by solid-state NMR chemical shift analysis. Biopolymers. 2003;70(2):158-68.

123. Yao X, Hong M. Structure distribution in an elastin-mimetic peptide (VPGVG) 3 investigated by solid-state NMR. Journal of the American Chemical Society. 2004;126(13):4199-210.

124. Rauscher S, Baud S, Miao M, Keeley FW, Pomes R. Proline and glycine control protein self-organization into elastomeric or amyloid fibrils. Structure. 2006 Nov 30;14(11):1667-76.

125. Muiznieks LD, Keeley FW. Proline periodicity modulates the self-assembly properties of elastin-like polypeptides. Journal of Biological Chemistry. 2010 Dec 17;285(51):39779-89.

126. Kumashiro KK, Ohgo K, Elliott DW, Kagawa TF, Niemczura WP. Backbone motion in elastin's hydrophobic domains as detected by 2H NMR spectroscopy. Biopolymers. 2012 Nov 1;97(11):882-8.

127. Reichheld SE, Muiznieks LD, Keeley FW, Sharpe S. Direct observation of structure and dynamics during phase separation of an elastomeric protein. Proceedings of the National Academy of Sciences. 2017 May 15:201701877.

128. MacEwan SR, Chilkoti A. Applications of elastin-like polypeptides in drug delivery. Journal of controlled release : official journal of the Controlled Release Society. 2014;190:314-30.

129. Rodriguez-Cabello JC, Pina MJ, Ibanez-Fonseca A, Fernandez-Colino A, Arias FJ. Nanotechnological Approaches to Therapeutic Delivery Using Elastin-Like Recombinamers. Bioconjug Chem. 2015;26(7):1252-65.

130. Rodriguez-Cabello JC, Arias FJ, Rodrigo MA, Girotti A. Elastin-like polypeptides in drug delivery. Adv Drug Deliv Rev. 2016;97:85-100.

131. Saxena R, Nanjan MJ. Elastin-like polypeptides and their applications in anticancer drug delivery systems: a review. Drug Deliv. 2015;22(2):156-67.

132. Herrera Estrada LP, Champion JA. Protein nanoparticles for therapeutic protein delivery. Biomater Sci. 2015;3(6):787-99.

133. Germershaus O, Lühmann T, Rybak JC, Ritzer J, Meinel L. Application of natural and semi-synthetic polymers for the delivery of sensitive drugs. International Materials Reviews. 2014;60(2):101-31.

134. Ryu JS, Raucher D. Elastin-like polypeptide for improved drug delivery for anticancer therapy: preclinical studies and future applications. Expert Opin Drug Deliv. 2015;12(4):653-67.

135. Price R, Poursaid A, Ghandehari H. Controlled release from recombinant polymers. J Control Release. 2014;190:304-13.

136. Massodi I, Bidwell GL, 3rd, Raucher D. Evaluation of cell penetrating peptides fused to elastin-like polypeptide for drug delivery. J Control Release. 2005;108(2-3):396-408.

137. Sarangthem V, Cho Ea, Bae SM, Singh TD, Kim SJ, Kim S, et al. Construction and application of elastin like polypeptide containing IL-4 receptor targeting peptide. PLoS ONE. 2013;8(12):1-12.

138. Dreher MR, Simnick AJ, Fischer K, Smith RJ, Patel A, Schmidt M, et al. Temperature triggered self-assembly of polypeptides into multivalent spherical micelles. Journal of the American Chemical Society. 2008;130(2):687-94.

139. Shi P, Aluri S, Lin YA, Shah M, Edman M, Dhandhukia J, et al. Elastin-based protein polymer nanoparticles carrying drug at both corona and core suppress tumor growth in vivo. Journal of Controlled Release. 2013;171(3):330-8.

140. MacKay JA, Chen M, McDaniel JR, Liu W, Simnick AJ, Chilkoti A. Self-assembling chimeric polypeptide-doxorubicin conjugate nanoparticles that abolish tumours after a single injection. Nature materials. 2009;8(12):993-9.

141. Meyer DE, Kong GA, Dewhirst MW, Zalutsky MR, Chilkoti A. Targeting a Genetically Engineered Elastin-like Polypeptide to Solid Tumors by Local Hyperthermia 1. In Vitro. 2001;42745:1548-54.

142. Meyer DE, Shin B, Kong G, Dewhirst M, Chilkoti A. Drug targeting using thermally responsive polymers and local hyperthermia. Journal of controlled release. 2001;74(1):213-24.

143. Park SM, Cha JM, Nam J, Kim MS, Park S-J, Park ES, et al. Formulation optimization and in vivo proof-of-concept study of thermosensitive liposomes

balanced by phospholipid, elastin-like polypeptide, and cholesterol. PloS one. 2014;9(7):e103116.

144. Han W, MacEwan SR, Chilkoti A, López GP. Bio-inspired synthesis of hybrid silica nanoparticles templated from elastin-like polypeptide micelles. Nanoscale. 2015;7(28):12038-44.

145. Costa RR, Castro E, Arias FJ, Rodríguez-Cabello JC, Mano JoF. Multifunctional compartmentalized capsules with a hierarchical organization from the nano to the macro scales. Biomacromolecules. 2013;14(7):2403-10.

146. Koetting MC, Peters JT, Steichen SD, Peppas NA. Stimulus-responsive hydrogels: Theory, modern advances, and applications. Materials Science and Engineering: R: Reports. 2015;93:1-49.

147. Adams SB, Jr., Shamji MF, Nettles DL, Hwang P, Setton LA. Sustained release of antibiotics from injectable and thermally responsive polypeptide depots. J Biomed Mater Res B Appl Biomater. 2009;90(1):67-74.

148. Wang W, Jashnani A, Aluri SR, Gustafson JA, Hsueh PY, Yarber F, et al. A thermo-responsive protein treatment for dry eyes. J Control Release. 2015;199:156-67.

149. Lim DW, Nettles DL, Setton La, Chilkoti A. Rapid Cross-Linking of Elastin-like Polypeptides with (Hydroxymethyl) phosphines in Aqueous Solution Rapid Cross-Linking of Elastin-like Polypeptides with (Hydroxymethyl) phosphines in Aqueous Solution. Construction. 2007:1463-70.

150. Nettles DL, Kitaoka K, Hanson NA, Flahiff CM, Mata BA, Hsu EW, et al. In situ crosslinking elastin-like polypeptide gels for application to articular

cartilage repair in a goat osteochondral defect model. Tissue Eng Part A. 2008;14(7):1133-40.

151. Heilshorn S. Endothelial cell adhesion to the fibronectin CS5 domain in artificial extracellular matrix proteins. Biomaterials. 2003;24(23):4245-52.

152. Heilshorn SC, Liu JC, Tirrell DA. Cell-binding domain context affects cell behavior on engineered proteins. Biomacromolecules. 2005;6(1):318-23.

153. Hsueh YS, Savitha S, Sadhasivam S, Lin FH, Shieh MJ. Design and synthesis of elastin-like polypeptides for an ideal nerve conduit in peripheral nerve regeneration. Mater Sci Eng C Mater Biol Appl. 2014;38:119-26.

154. Yigit S, Dinjaski N, Kaplan DL. Fibrous proteins: At the crossroads of genetic engineering and biotechnological applications. Biotechnol Bioeng. 2016;113(5):913-29.

155. Urry DW, Parker TM, Reid MC, Gowda DC. Biocompatibility of the Bioelastic Materials, Poly(GVGVP) and Its γ-Irradiation Cross-Linked Matrix: Summary of Generic Biological Test Results. Journal of Bioactive and Compatible Polymers. 1991;6(3):263-82.

156. Wood S, Lemons J, Prasad K, Urry D. In vitro calcification and in vivo biocompatibility of the cross-linked polypentapeptide of elastin. Journal of biomedical materials research. 1986;20(3):315-35.

157. Rincon AC, Molina-Martinez IT, de Las Heras B, Alonso M, Bailez C, Rodriguez-Cabello JC, et al. Biocompatibility of elastin-like polymer poly(VPAVG) microparticles: in vitro and in vivo studies. J Biomed Mater Res A. 2006;78(2):343-51.

158. Elsas FJ, Gowda DC, Urry DW. Synthetic polypeptide sleeve for strabismus surgery. Journal of pediatric ophthalmology and strabismus. 1992;29(5):284-6.

159. Sallach RE, Cui W, Balderrama F, Martinez AW, Wen J, Haller Ca, et al. Long-term biostability of self-assembling protein polymers in the absence of covalent crosslinking. Biomaterials. 2010;31(4):779-91.

Chapter 2

1. Unsworth LD, Sheardown H, Brash JL. Polyethylene oxide surfaces of variable chain density by chemisorption of PEO-thiol on gold: adsorption of proteins from plasma studied by radiolabelling and immunoblotting. Biomaterials. 2005 Oct 31;26(30):5927-33.

2. Kim HR, Andrieux K, Gil S, Taverna M, Chacun H, Desmaële D, Taran F, Georgin D, Couvreur P. Translocation of poly (ethylene glycol-co-hexadecyl) cyanoacrylate nanoparticles into rat brain endothelial cells: role of apolipoproteins in receptor-mediated endocytosis. Biomacromolecules. 2007 Mar 12;8(3):793-9.

3. McClung WG, Babcock DE, Brash JL. Fibrinolytic properties of lysine-derivatized polyethylene in contact with flowing whole blood (Chandler loop model). Journal of Biomedical Materials Research Part A. 2007 Jun 1;81(3):644-51.

4. Bahniuk MS, Alshememry AK, Unsworth LD. High-yield recombinant expression and purification of marginally soluble, short elastin-like polypeptides. BioTechniques. 2016 Dec;61(6):297-304.

Chapter 3

1. Hoffman AS. Stimuli-responsive polymers: biomedical applications and challenges for clinical translation. Adv Drug Deliv Rev 2012;65:10–6

2. Li Z, Zhang Z, Liu KL, Ni X, Li J. Biodegradable hyperbranched amphiphilic polyurethane multiblock copolymers consisting of poly (propylene glycol), poly (ethylene glycol), and polycaprolactone as in situ thermogels. Biomacromolecules 2012;13:3977–89

3. Ruel-Gariepy E, Leroux J-C. In situ-forming hydrogels – review of temperature-sensitive systems. Eur J Pharm Biopharm 2004;58:409–26

4. Rathi RC, Zentner GM. Biodegradable low molecular weight triblock poly (lactide-co-glycolide) polyethylene glycol copolymers having reverse thermal gelation properties. U.S. Patent No. 6,004,573, 21 December 1999

5. Shim MS, Lee HT, Shim WS, Park I, Lee H, Chang T, et al. Poly (D, L-lactic acid- co-glycolic acid)-b-poly (ethylene glycol)-b-poly (D, L-lactic acid-co-glycolic acid) triblock copolymer and thermoreversible phase transition in water. J Biomed Mater Res 2002;61:188–96

6. Loh XJ, Li J. Biodegradable thermosensitive copolymer hydrogels for drug delivery. Expert Opin 2007;17:3977–89

7. Zentner GM, Rathi R, Shih C, McRea JC, Seo M-H, Oh H, et al. Biodegradable block copolymers for delivery of proteins and water-insoluble drugs. J Control Release 2001;72:203–15

8. Yin HB, Gong CY, Shi S, Liu XY, Wei YQ, Qian ZY. Toxicity evaluation of biodegradable and thermosensitive PEG-PCL-PEG hydrogel as a potential in situ sustained ophthalmic drug delivery system. J Biomed Mater Res B Appl Biomater 2010;92:129–37

9. Gong C, Shi S, Dong P, Kan B, Gou M, Wang X, et al. Synthesis and characterization of PEG-PCL-PEG thermosensitive hydrogel. Int J Pharm 2009;365:89–99

10. Ni PY, Fan M, Qian ZY, Luo JC, Gong CY, Fu SZ, et al. Synthesis and characterization of injectable, thermosensitive, and biocompatible acellular bone matrix/poly (ethylene glycol)-poly (ε-caprolactone)-poly (ethylene

glycol) hydrogel composite. J Biomed Mater Res, Part A 2012;100:171–9

11. Jiang ZQ, Deng XM, Hao JY. Novel thermogelling poly (ε -caprolactone-co-lactide)-poly (ethylene glycol)-poly (ε -caprolactone-co-lactide) aqueous solutions. Chin Chem Lett 2007;18:747–9

12. Bae SJ, Joo MK, Jeong Y, Kim SW, Lee W-K, Sohn YS, et al. Gelation behavior of poly (ethylene glycol) and polycaprolactone triblock and multiblock copolymer aqueous solutions. Macromolecules 2006;39:4873–9

13. Bae SJ, Suh JM, Sohn YS, Bae YH, Kim SW, Jeong B. Thermogelling poly (caprolactone-b-ethylene glycol-b-caprolactone) aqueous solutions. Macromolecules 2005;38:5260–5

14. Gong C, Shi S, Wu L, Gou M, Yin Q, Guo Q, et al. Biodegradable in situ gel-forming controlled drug delivery system based on thermosensitive PCL-PEG-PCL hydrogel. Part 2: sol-gel-sol transition and drug delivery behavior. Acta Biomater 2009;5:3358–70

15. Mahmud A, Xiong XB, Lavasanifar A. Novel self-associating poly (ethylene oxide)-block-poly (ε -caprolactone) block copolymers with functional side groups on the polyester block for drug delivery. Macromolecules 2006;39:9419–28

16. Safaei Nikouei N, Lavasanifar A. Characterization of the thermo- and pH-responsive assembly of triblock copolymers based on poly(ethylene glycol) and functionalized poly(ε -caprolactone). Acta Biomater 2011;7:3708–18

17. Brash JL. Exploiting the current paradigm of blood material interactions for the rational design of blood-compatible materials. J Biomater Sci Polym Ed

2000;11:1135–46

18. Loh XJ, Tan YX, Li Z, Teo LS, Goh SH, Li J. Biodegradable thermogelling poly(ester urethane) s consisting of poly (lactic acid) – thermodynamics of micellization and hydrolytic degradation. Biomaterials 2008;29:2164–72

19. Bahniuk MS, Pirayesh H, Singh HD, Nychka JA, Unsworth LD. Bioactive glass 45S5 powders: effect of synthesis route and resultant surface chemistry and

crystallinity on protein adsorption from human plasma. Biointerphases 2012;7:1–15

20. Abraham S, So A, Unsworth LD. Poly(carboxybetaine methacrylamide)-

modified nanoparticles: a model system for studying the effect of chain chemistry on film properties, adsorbed protein conformation, and clot formation kinetics. Biomacromolecules 2011;12:3567–80

21. Cheng Y, He C, Ding J, Xiao C, Zhuang X, Chen X. Thermosensitive hydrogels based on polypeptides for localized and sustained delivery of anticancer drugs. Biomaterials 2013;34(38):10338–47

22. Hou Y, Matthews AR, Smitherman AM, Bulick AS, Hahn MS, Hou H, et al. Thermoresponsive nanocomposite hydrogels with cell-releasing behavior. Biomaterials 2008;29:3175–84

23. Liu YY, Shao YH, Lu J. Preparation, properties and controlled release behaviors of pH-induced thermosensitive amphiphilic gels. Biomaterials 2006;27:4016–24

24. Wang Q, Li L, Jiang S. Effects of a PPO-PEO-PPO triblock copolymer on micellization and gelation of a PEO-PPO-PEO triblock copolymer in aqueous solution. Langmuir 2005;21:9068–75

25. Sivaraman B, Latour RA. The adherence of platelets to adsorbed albumin by receptor-mediated recognition of binding sites exposed by adsorption-induced unfolding. Biomaterials 2010;31:1036–44

26. Takeuchi Y, Tsujimoto T, Uyama H. Thermogelation of amphiphilic poly (asparagine) derivatives. Polym Adv Technol 2011;22:620–6

27. Wojciechowski P, Ten Hove P, Brash JL. Phenomenology and mechanism of the transient adsorption of fibrinogen from plasma (Vroman effect). J Colloid Interface Sci 1986;111:455–65

28. Molina H. Complement and immunity. Rheum Dis Clin North Am 2004;30:1–18

29. Tang L, Liu L, Elwing HB. Complement activation and inflammation triggered by model biomaterial surfaces. J Biomed Mater Res 1998;41:333–40

30. Unsworth LD, Sheardown H, Brash JL. Polyethylene oxide surfaces of variable chain density by chemisorption of PEO-thiol on gold: adsorption of proteins from plasma studied by radiolabelling and immunoblotting. Biomaterials

2005;26:5927–33

31. Gettins PGW. Serpin structure, mechanism, and function. Chem Rev 2002;102:4751–804

32. Moos T, Morgan EH. Transferrin and transferrin receptor function in brain barrier systems. Cell Mol Neurobiol 2000;20:77–95

33. Stafford JL, Belosevic M. Transferrin and the innate immune response of fish: identification of a novel mechanism of macrophage activation. Dev Comp

Immunol 2003;27:539–54

34. Mosesson MW. Fibrinogen and fibrin structure and functions. J Thromb Hemost 2005;3:1894–904

35. Massa TM, Yang ML, Ho JYC, Brash JL, Santerre JP. Fibrinogen surface

distribution correlates to platelet adhesion pattern on fluorinated surface-modified polyetherurethane. Biomaterials 2005;26:7367–76

36. Tang L, Eaton JW. Natural responses to unnatural materials: a molecular mechanism for foreign body reactions. Mol Med 1999;5:351

37. El-Ghannam A, Ducheyne P. Shapiro, I.M. Effect of serum proteins on

osteoblast adhesion to surface-modified bioactive glass and hydroxyapatite. J Orthop Res 1999;17:340–5

Chapter 4

1. Hench LL, Splinter RJ, Allen WC, Greenlee TK. Bonding mechanisms at the interface of ceramic prosthetic materials. Journal of Biomedical Materials Research Part A. 1971 Nov 1;5(6):117-41.

2. Hench LL, Paschall HA. Direct chemical bond of bioactive glass-ceramic materials to bone and muscle. Journal of Biomedical Materials Research Part A. 1973 May 1;7(3):25-42.

3. Sarkisov PD, Mikhailenko NY, Khavala VM. Biological activity of glass-and sitall-based materials. Glass and ceramics. 1993 Sep 1;50(9):372-9.

4. Hench LL. Bioactive materials: the potential for tissue regeneration. Journal of Biomedical Materials Research Part A. 1998 Sep 15;41(4):511-8.

5. Xynos ID, Hukkanen MV, Batten JJ, Buttery LD, Hench LL, Polak JM. Bioglass® 45S5 stimulates osteoblast turnover and enhances bone formation in vitro: implications and applications for bone tissue engineering. Calcified Tissue International. 2000 Oct 24;67(4):321-9.

6. Gough JE, Notingher I, Hench LL. Osteoblast attachment and mineralized nodule formation on rough and smooth 45S5 bioactive glass monoliths. Journal of Biomedical Materials Research Part A. 2004 Mar 15;68(4):640-50.

7. Christodoulou I, Buttery LD, Saravanapavan P, Tai G, Hench LL, Polak JM. Dose-and time-dependent effect of bioactive gel-glass ionic-dissolution products on human fetal osteoblast-specific gene expression. Journal of Biomedical Materials Research Part B: Applied Biomaterials. 2005 Jul 1;74(1):529-37.

8. Christodoulou I, Buttery LD, Tai G, Hench LL, Polak JM. Characterization of human fetal osteoblasts by microarray analysis following stimulation with 58S bioactive gel-glass ionic dissolution products. Journal of Biomedical Materials Research Part B: Applied Biomaterials. 2006 May 1;77(2):431-46.

9. Hench LL Bioceramics. Journal of the American Ceramic Society. 1998 Jul 1;81:1705–1728

10. Greenlee TK, Beckham CA, Crebo AR, Malmorg JC. Glass ceramic bone implants. A light microscopic study. Journal of Biomedical Materials Research Part A. 1972 May 1;6(3):235-44.

11. Peitl Filho O, Latorre GP, Hench L. Effect of crystallization on apatite-layer formation of bioactive glass 45%. J Biomed Mater Res. 1996;30:509-14.

12. Peitl O, Zanotto ED, Hench LL. Highly bioactive P 2 O 5–Na 2 O–CaO–SiO 2 glass-ceramics. Journal of Non-Crystalline Solids. 2001 Nov 30;292(1):115-26.

13. Kokubo T, Takadama H. How useful is SBF in predicting in vivo bone bioactivity?. Biomaterials. 2006 May 31;27(15):2907-15.

14. Hench LL, Jones JR, Sepulveda P. Bioactive materials for tissue engineering scaffolds. In Future strategies for tissue and organ replacement 2002 (pp. 3-24).

15. Lefebvre L, Gremillard L, Chevalier J, Bernache-Assollant D. Sintering Behavior of 45S5 Bioglass®. InKey Engineering Materials 2008 (Vol. 361, pp. 265-268). Trans Tech Publications.

16. Lefebvre L, Chevalier J, Gremillard L, Zenati R, Thollet G, Bernache-Assolant D, Govin A. Structural transformations of bioactive glass 45S5 with thermal treatments. Acta Materialia. 2007 Jun 30;55(10):3305-13.

17. Nychka JA, Mazur SL, Kashyap S, Li D, Yang F. Dissolution of bioactive glasses: The effects of crystallinity coupled with stress. JOM Journal of the Minerals, Metals and Materials Society. 2009 Sep 1;61(9):45-51.

18. Chen QZ, Thompson ID, Boccaccini AR. 45S5 Bioglass®-derived glass–ceramic scaffolds for bone tissue engineering. Biomaterials. 2006 Apr 30;27(11):2414-25.

19. Li R, Clark AE, Hench LL. An investigation of bioactive glass powders by sol-gel processing. Journal of Applied Biomaterials. 1991 Dec 1;2(4):231-9.

20. Jones JR, Sepulveda P, Hench LL. Dose-dependent behavior of bioactive glass dissolution. Journal of Biomedical Materials Research Part A. 2001 Jan 1;58(6):720-6.

21. Pirayesh H. Effects manufacturing method on surface mineralization of bioactive glasses.

22. Kokubo T, Kushitani H, Sakka S, Kitsugi T, Yamamuro T. Solutions able to reproduce in vivo surface-structure changes in bioactive glass-ceramic A-W3. Journal of Biomedical Materials Research Part A. 1990 Jun 1;24(6):721-34.

23. El-Ghannam A, Ducheyne P, Shapiro IM. Formation of surface reaction products on bioactive glass and their effects on the expression of the osteoblastic phenotype and the deposition of mineralized extracellular matrix. Biomaterials. 1997 Jan 1;18(4):295-303.

24. Wilson J, Pigott GH, Schoen FJ, Hench LL. Toxicology and biocompatibility of bioglasses. Journal of Biomedical Materials Research Part A. 1981 Nov 1;15(6):805-17.

25. Vrouwenvelder WC, Groot CG, De Groot K. Behaviour of fetal rat osteoblasts cultured in vitro on bioactive glass and nonreactive glasses. Biomaterials. 1992 Jan 1;13(6):382-92.

26. Matsuda T, Yamauchi K, Ito G. The influence of bioglass on the growth of fibroblasts. Journal of Biomedical Materials Research Part A. 1987 Apr 1;21(4):499-507.

27. Vrouwenvelder WC, Groot CG, De Groot K. Histological and biochemical evaluation of osteoblasts cultured on bioactive glass, hydroxylapatite, titanium

alloy, and stainless steel. Journal of Biomedical Materials Research Part A. 1993 Apr 1;27(4):465-75.

28. Brash JL. Exploiting the current paradigm of blood–material interactions for the rational design of blood-compatible materials. Journal of Biomaterials Science, Polymer Edition. 2000 Jan 1;11(11):1135-46.

29. Kaufmann EA, Ducheyne P, Radin S, Bonnell DA, Composto R. Initial events at the bioactive glass surface in contact with protein-containing solutions. Journal of Biomedical Materials Research Part A. 2000 Dec 15;52(4):825-30.

30. Buchanan LA, El-Ghannam A. Effect of bioactive glass crystallization on the conformation and bioactivity of adsorbed proteins. Journal of Biomedical Materials Research Part A. 2010 May 1;93(2):537-46.

31. Singh HD, Wang G, Uludağ H, Unsworth LD. Poly-L-lysine-coated albumin nanoparticles: stability, mechanism for increasing in vitro enzymatic resilience, and siRNA release characteristics. Acta biomaterialia. 2010 Nov 30;6(11):4277-84.

32. Taylor JA, Lancaster GM, Ignatiev A, Rabalais JW. Interactions of ion beams with surfaces. Reactions of nitrogen with silicon and its oxides. The Journal of Chemical Physics. 1978 Feb 15;68(4):1776-84.

33. Kim HR, Andrieux K, Gil S, Taverna M, Chacun H, Desmaële D, Taran F, Georgin D, Couvreur P. Translocation of poly (ethylene glycol-co-hexadecyl)

cyanoacrylate nanoparticles into rat brain endothelial cells: role of apolipoproteins in receptor-mediated endocytosis. Biomacromolecules. 2007 Mar 12;8(3):793-9.

34. Unsworth LD, Sheardown H, Brash JL. Polyethylene oxide surfaces of variable chain density by chemisorption of PEO-thiol on gold: adsorption of proteins from plasma studied by radiolabelling and immunoblotting. Biomaterials. 2005 Oct 31;26(30):5927-33.

35. Chen QZ, Rezwan K, Armitage D, Nazhat SN, Boccaccini AR. The surface functionalization of 45S5 Bioglass®-based glass-ceramic scaffolds and its impact on bioactivity. Journal of Materials Science: Materials in Medicine. 2006 Nov 1;17(11):979-87.

36. NIST (2003) X-ray Photoelectron spectroscopy database (database on the Internet) (cited November 2010). Available from: http://srdata.nist.gov/xps/

37. Hench LL. Bioceramics: from concept to clinic. Journal of the american ceramic society. 1991 Jul 1;74(7):1487-510.

38. Cros A, Saoudi R, Hollinger G, Hewett CA, Lau SS. An x-ray photoemission spectroscopy investigation of oxides grown on Au x Si1− x layers. Journal of Applied Physics. 1990 Feb 15;67(4):1826-30.

39. Aoyama T, Sugii T, Ito T. Determination of band line-up in β-SiC/Si heterojunction for Si-HBT's. Applied surface science. 1990 Jan 1;41:584-6.

40. Sivaraman B, Latour RA. The adherence of platelets to adsorbed albumin by receptor-mediated recognition of binding sites exposed by adsorption-induced unfolding. Biomaterials. 2010 Feb 28;31(6):1036-44.

41. El-Ghannam A, Hamazawy E, Yehia A. Effect of thermal treatment on bioactive glass microstructure, corrosion behavior, ζ potential, and protein adsorption. Journal of Biomedical Materials Research Part A. 2001 Jun 5;55(3):387-95.

42. Mladenovic Z, Sahlin-Platt A, Bengtsson Å, Ransjö M, Shchukarev A. Surface characterization of bone graft substitute materials conditioned in cell culture medium. Surface and Interface Analysis. 2010 Jun 1;42(6-7):452-6.

43. Cerruti M, Bianchi CL, Bonino F, Damin A, Perardi A, Morterra C. Surface modifications of bioglass immersed in TRIS-buffered solution. A multitechnical spectroscopic study. The Journal of Physical Chemistry B. 2005 Aug 4;109(30):14496-505.

44. Peitl Filho O, Latorre GP, Hench L. Effect of crystallization on apatite-layer formation of bioactive glass 45%. J Biomed Mater Res. 1996;30:509-14.

45. Anitua E, Andia I, Ardanza B, Nurden P, Nurden AT. Autologous platelets as a source of proteins for healing and tissue regeneration. Thrombosis and haemostasis. 2004 Jan 1;91(1):4-15.

46. Molina H. Complement and immunity. Rheumatic Disease Clinics of North America. 2004 Feb 29;30(1):1-8.

47. Tang L, Liu L, Elwing HB. Complement activation and inflammation triggered by model biomaterial surfaces. Journal of Biomedical Materials Research Part A. 1998 Aug 1;41(2):333-40.

48. Clark AE, Hench LL, Paschall HA. The influence of surface chemistry on implant interface histology: a theoretical basis for implant materials selection. Journal of Biomedical Materials Research Part A. 1976 Mar 1;10(2):161-74.

49. Gettins PG. Serpin structure, mechanism, and function. Chemical reviews. 2002 Dec 11;102(12):4751-804.

50. Mosesson MW. Fibrinogen and fibrin structure and functions. Journal of Thrombosis and Haemostasis. 2005 Aug 1;3(8):1894-904.

51. Massa TM, Yang ML, Ho JY, Brash JL, Santerre JP. Fibrinogen surface distribution correlates to platelet adhesion pattern on fluorinated surface-modified polyetherurethane. Biomaterials. 2005 Dec 31;26(35):7367-76.

52. Tang L, Eaton JW. Natural responses to unnatural materials: A molecular mechanism for foreign body reactions. Molecular medicine. 1999 Jun;5(6):351.

53. Moos T, Morgan EH. Transferrin and transferrin receptor function in brain barrier systems. Cellular and molecular neurobiology. 2000 Feb 1;20(1):77-95.

54. Davie EW, Kulman JD. An overview of the structure and function of thrombin. In Seminars in thrombosis and hemostasis 2006 Feb (Vol. 32, No. S 1, pp. 003-015). Copyright© 2006 by Thieme Medical Publishers, Inc., 333 Seventh Avenue, New York, NY 10001, USA..

55. El-Ghannam A, Ducheyne P, Shapiro IM. Effect of serum proteins on osteoblast adhesion to surface-modified bioactive glass and hydroxyapatite. Journal of orthopaedic research. 1999 May 1;17(3):340-5.

Chapter 5

1. Walkey CD, Olsen JB, Song F, Liu R, Guo H, Olsen DWH, et al. Protein corona fingerprinting predicts the cellular interaction of gold and silver nanoparticles. ACS nano. 2014;8(3):2439-55.

2. Lee YK, Choi EJ, Webster TJ, Kim SH, Khang D. Effect of the protein corona on nanoparticles for modulating cytotoxicity and immunotoxicity. Int J Nanomedicine. 2015;10:97-113.

3. Casals E, Pfaller T, Duschl A, Oostingh GJ, Puntes VF. Hardening of the nanoparticle–protein corona in metal (Au, Ag) and oxide (Fe3O4, CoO, and CeO2) nanoparticles. Small. 2011;7(24):3479-86.

4. Maiorano G, Sabella S, Sorce B, Brunetti V, Malvindi MA, Cingolani R, et al. Effects of cell culture media on the dynamic formation of protein− nanoparticle complexes and influence on the cellular response. ACS nano. 2010;4(12):7481-91.

5. Colman RW. Are hemostasis and thrombosis two sides of the same coin? Journal of Experimental Medicine. 2006;203(3):493-5.

6. Pondman KM, Tsolaki AG, Paudyal B, Shamji MH, Switzer A, Pathan AA, et al. Complement deposition on nanoparticles can modulate immune responses by macrophage, B and T cells. Journal of biomedical nanotechnology. 2016;12(1):197-216.

7. Reddy ST, van der Vlies AJ, Simeoni E, Angeli V, Randolph GJ, O'Neil CP, et al. Exploiting lymphatic transport and complement activation in nanoparticle vaccines. Nature biotechnology. 2007;25(10):1159-64.

8. Deng ZJ, Mortimer G, Schiller T, Musumeci A, Martin D, Minchin RF. Differential plasma protein binding to metal oxide nanoparticles. Nanotechnology. 2009;20(45):455101.

9. Gordy MA, Pila EA, Hanington PC. The role of fibrinogen-related proteins in the gastropod immune response. Fish & shellfish immunology. 2015;46(1):39-49.

10. Couleau N, Techer D, Pagnout C, Jomini S, Foucaud L, Laval-Gilly P, et al. Hemocyte responses of Dreissena polymorpha following a short-term in vivo exposure to titanium dioxide nanoparticles: preliminary investigations. Science of the Total Environment. 2012;438:490-7.

11. Gagné F, Auclair J, Turcotte P, Fournier M, Gagnon C, Sauvé S, et al. Ecotoxicity of CdTe quantum dots to freshwater mussels: impacts on immune system, oxidative stress and genotoxicity. Aquatic toxicology. 2008;86(3):333-40.

12. Lillico DM, Zwozdesky MA, Pemberton JG, Deutscher JM, Jones LO, Chang JP, et al. Teleost leukocyte immune-type receptors activate distinct phagocytic modes for target acquisition and engulfment. Journal of leukocyte biology. 2015;98(2):235-48.

13. Yogasundaram H, Bahniuk MS, Singh H-D, Aliabadi HM, Uludağ H, Unsworth LD. BSA Nanoparticles for siRNA Delivery: Coating Effects on Nanoparticle Properties, Plasma Protein Adsorption, and In Vitro siRNA Delivery. International journal of biomaterials. 2012;2012:584060-.

14. Bahniuk MS, Pirayesh H, Singh HD, Nychka JA, Unsworth LD. Bioactive glass 45S5 powders: effect of synthesis route and resultant surface chemistry and crystallinity on protein adsorption from human plasma. Biointerphases. 2012;7(1-4):1-5.

15. Nikouei NS, Vakili MR, Bahniuk MS, Unsworth L, Akbari A, Wu J, et al. Thermoreversible hydrogels based on triblock copolymers of poly(ethylene glycol) and carboxyl functionalized poly(ε-caprolactone): The effect of carboxyl group substitution on the transition temperature and biocompatibility in plasma. Acta biomaterialia. 2014;12:81-92.

16. Abraham S, So A, Unsworth LD. Poly(carboxybetaine methacrylamide)-modified nanoparticles: a model system for studying the effect of chain chemistry on film properties, adsorbed protein conformation, and clot formation kinetics. Biomacromolecules. 2011;12(10):3567-80.

17. Sivaraman B, Latour Ra. The adherence of platelets to adsorbed albumin by receptor-mediated recognition of binding sites exposed by adsorption-induced unfolding. Biomaterials. 2010;31(6):1036-44.

18. Anderson J, Bonfield T, Ziats N. Protein adsorption and cellular adhesion and activation on biomedical polymers. The International journal of artificial organs. 1990;13(6):375-82.

19. Collier T, Anderson J. Protein and surface effects on monocyte and macrophage adhesion, maturation, and survival. Journal of Biomedical Materials Research Part A. 2002;60(3):487-96.

20. Wojciechowski P, Ten Hove P, Brash JL. Phenomenology and mechanism of the transient adsorption of fibrinogen from plasma (Vroman effect). Journal of Colloid and Interface Science. 1986;111(2):455-65.

21. Cedervall T, Lynch I, Lindman S, Berggård T, Thulin E, Nilsson H, et al. Understanding the nanoparticle–protein corona using methods to quantify exchange rates and affinities of proteins for nanoparticles. Proceedings of the National Academy of Sciences. 2007;104(7):2050-5.

22. Lu J, Stewart AJ, Sadler PJ, Pinheiro TJ, Blindauer CA. Albumin as a zinc carrier: properties of its high-affinity zinc-binding site. Portland Press Limited; 2008.

23. Farrugia A. Albumin usage in clinical medicine: tradition or therapeutic? Transfusion medicine reviews. 2010;24(1):53-63.

24. Lyman D, Klein KG, Brash J, Fritzinger B, Andrade J, Bonomo F. Platelet interaction with protein-coated surfaces: an approach to thrombo-resistant surfaces. Platelet Adhesion and Aggregation in Thrombosis: Countermeasures. 1970.

25. Cornelius R, Macri J, Cornelius K, Brash J. Interactions of Apolipoproteins AI, AII, B and HDL, LDL, VLDL with Polyurethane and Polyurethane-PEO Surfaces. Langmuir. 2015;31(44):12087-95.

26. Cornelius RM, Macri J, Cornelius KM, Brash JL. Lipoprotein interactions with a polyurethane and a polyethylene oxide-modified polyurethane at the plasma–material interface. Biointerphases. 2016;11(2):029810.

27. Macfarlane R. An enzyme cascade in the blood clotting mechanism and its function as a biochemical amplifier. Nature. 1964;202(4931):498-9.

28. Davie EW, Ratnoff OD. Waterfall sequence for intrinsic blood clotting. Science. 1964;145(3638):1310-2.

29. Romney G, Glick M. An updated concept of coagulation with clinical implications. The Journal of the American Dental Association. 2009;140(5):567-74.

30. Hoffman M. Remodeling the blood coagulation cascade. Journal of thrombosis and thrombolysis. 2003;16(1):17-20.

31. Proença-Ferreira R, Franco-Penteado CF, Traina F, Saad ST, Costa FF, Conran N. Increased adhesive properties of platelets in sickle cell disease: roles for αIIbβ3-mediated ligand binding, diminished cAMP signalling and increased phosphodiesterase 3A activity. British journal of haematology. 2010;149(2):280-8.

32. Kelly PM, Åberg C, Polo E, O'connell A, Cookman J, Fallon J, et al. Mapping protein binding sites on the biomolecular corona of nanoparticles. Nature nanotechnology. 2015;10(5):472-9.

33. Vogt C, Pernemalm M, Kohonen P, Laurent S, Hultenby K, Vahter M, et al. Proteomics analysis reveals distinct corona composition on magnetic nanoparticles with different surface coatings: Implications for interactions with primary human macrophages. PloS one. 2015;10(10):e0129008.

34. Landgraf L, Christner C, Storck W, Schick I, Krumbein I, Dähring H, et al. A plasma protein corona enhances the biocompatibility of Au@ Fe 3 O 4 Janus particles. Biomaterials. 2015;68:77-88.

35. Mosesson MW. Fibrinogen and fibrin structure and functions. Journal of thrombosis and haemostasis : JTH. 2005;3(8):1894-904.

36. Tang L, Eaton JW. Natural responses to unnatural materials: A molecular mechanism for foreign body reactions. Molecular Medicine. 1999;5(6):351-.

37. Massa TM, Yang ML, Ho JYC, Brash JL, Santerre JP. Fibrinogen surface distribution correlates to platelet adhesion pattern on fluorinated surface-modified polyetherurethane. Biomaterials. 2005;26(35):7367-76.

38. Gresele P, Page C, Fuster V, Vermylen J. Platelets in Thrombotic and Non-Thrombotic Disorders. Transfusion Medicine. 2003;13(1):57-8.

39. Davie EW, D P, Kulman JD. An Overview of the Structure and Function of Thrombin. Seminars In Thrombosis And Hemostasis. 2006;32(suppl 1):3-15.

40. Changa D. The binding of free calcium ions in aqueous solution using chelating agents, phosphates and poly (acrylic acid). Journal of the American Oil Chemists' Society. 1983;60(3):618-22.

41. Kuila D, Blay GA, Borjas RE, Hughes S, Maddox P, Rice K, et al. Polyacrylic acid (poly-A) as a chelant and dispersant. Journal of applied polymer science. 1999;73(7):1097-115.

42. Wang Q, Prigiobbe V, Huh C, Bryant SL. Alkaline Earth Element Adsorption onto PAA-Coated Magnetic Nanoparticles. Energies. 2017;10(2):223.

43. Molina H. Complement and immunity. Rheumatic Disease Clinics of North America. 2004;30(1):1-18.

44. Janeway Jr CA, Medzhitov R. Innate immune recognition. Annual review of immunology. 2002;20(1):197-216.

45. Medzhitov R, Janeway C, editors. Innate immune induction of the adaptive immune response. Cold Spring Harbor symposia on quantitative biology; 1999: Cold Spring Harbor Laboratory Press.

46. Iwasaki A, Medzhitov R. Control of adaptive immunity by the innate immune system. Nature immunology. 2015;16(4):343-53.

47. Holmskov U, Thiel S, Jensenius JC. Collectins and ficolins: humoral lectins of the innate immune defense. Annual review of immunology. 2003;21(1):547-78.

48. Endo Y, Takahashi M, Fujita T. Lectin complement system and pattern recognition. Immunobiology. 2006;211(4):283-93.

49. Andersson J, Ekdahl KN, Lambris JD, Nilsson B. Binding of C3 fragments on top of adsorbed plasma proteins during complement activation on a model biomaterial surface. Biomaterials. 2005;26(13):1477-85.

50. Engberg AE, Rosengren-Holmberg JP, Chen H, Nilsson B, Lambris JD, Nicholls IA, et al. Blood protein-polymer adsorption: Implications for understanding complement-mediated hemoincompatibility. Journal of Biomedical Materials Research Part A. 2011;97(1):74-84.

51. Chen F, Wang G, Griffin JI, Brenneman B, Banda NK, Holers VM, et al. Complement proteins bind to nanoparticle protein corona and undergo dynamic exchange in vivo. Nature nanotechnology. 2017;12(4):387-93.

52. Klapper Y, Hamad OA, Teramura Y, Leneweit G, Nienhaus GU, Ricklin D, et al. Mediation of a non-proteolytic activation of complement component C3 by phospholipid vesicles. Biomaterials. 2014;35(11):3688-96.

53. Binnemars-Postma KA, ten Hoopen HW, Storm G, Prakash J. Differential uptake of nanoparticles by human M1 and M2 polarized macrophages: protein corona as a critical determinant. Nanomedicine. 2016;11(22):2889-902.

54. Inturi S, Wang G, Chen F, Banda NK, Holers VM, Wu L, et al. Modulatory role of surface coating of superparamagnetic iron oxide nanoworms in complement opsonization and leukocyte uptake. ACS nano. 2015;9(11):10758-68.

55. Ekstrand-Hammarström B, Hong J, Davoodpour P, Sandholm K, Ekdahl KN, Bucht A, et al. TiO 2 nanoparticles tested in a novel screening whole human blood model of toxicity trigger adverse activation of the kallikrein system at low concentrations. Biomaterials. 2015;51:58-68.

56. Hamad OA, Nilsson PH, Wouters D, Lambris JD, Ekdahl KN, Nilsson B. Complement component C3 binds to activated normal platelets without preceding proteolytic activation and promotes binding to complement receptor 1. The journal of immunology. 2010;184(5):2686-92.

57. Anderson JM, Rodriguez A, Chang DT. Foreign body reaction to biomaterials. Seminars in immunology. 2008;20(2):86-100.

58. Abbas AK. Cellular and molecular immunology. In: Lichtman AH, Pillai S, editors. 6th ed. ed. Philadelphia :: Saunders Elsevier; 2007.

59. Unsworth LD, Sheardown H, Brash JL. Polyethylene oxide surfaces of variable chain density by chemisorption of PEO-thiol on gold: Adsorption of

proteins from plasma studied by radiolabelling and immunoblotting. Biomaterials. 2005;26(30):5927-33.

60. Scherbart AM, Langer J, Bushmelev A, van Berlo D, Haberzettl P, van Schooten F-J, et al. Contrasting macrophage activation by fine and ultrafine titanium dioxide particles is associated with different uptake mechanisms. Particle and fibre toxicology. 2011;8(1):31.

61. Moos T, Morgan EH. Transferrin and transferrin receptor function in brain barrier systems. Cellular and molecular neurobiology. 2000;20(1):77-95.

62. Stafford JL, Belosevic M. Transferrin and the innate immune response of fish: identification of a novel mechanism of macrophage activation. Developmental and comparative immunology. 2003;27(6-7):539-54.

63. Ortega V, Katzenback B, Stafford J, Belosevic M, Goss G. Effects of polymer-coated metal oxide nanoparticles on goldfish (Carassius auratus L.) neutrophil viability and function. Nanotoxicology. 2015;9(1):23-33.

Chapter 6

1. Urry, D.W. 1988. Entropic elastic processes in protein mechanisms. I. Elastic structure due to an inverse temperature transition and elasticity due to internal chain dynamics. J. Protein Chem 7:1-34.

2. Urry, D.W., C.H. Luan, T.M. Parker, D.C. Gowda, K.U. Prasad, M.C. Reid, and A. Safavy. 1991. Temperature of polypeptide inverse temperature transition depends on mean residue hydrophobicity. J. Am. Chem. Soc 113:4346-4348.

3. Urry, D.W., T.L. Trapane, and K.U. Prasad. 1985. Phase-structure transitions of the elastin polypentapeptide-water system within the framework of composition-temperature studies. Biopolymers 24:2345-2356.

4. Ge, X., D.S.C. Yang, K. Trabbic-carlson, B. Kim, A. Chilkoti, H. Hall, and N. Carolina. 2005. Self-Cleavable Stimulus Responsive Tags for Protein Purification without Chromatography. J. Am. Chem. Soc 127:11228-11229.

5. Cole, M.A., N.H. Voelcker, H. Thissen, and H.J. Griesser. 2009. Stimuli-responsive inter faces and systems for the control of protein–surface and cell–surface interactions. Biomaterials 30:1827-1850.

6. Chilkoti, A., M.R. Dreher, and D.E. Meyer. 2002. Design of thermally responsive, recombinant polypeptide carriers for targeted drug delivery. Adv Drug Deliv Rev 54:1093-1111.

7. Bidwell, G.L., A.N. Davis, I. Fokt, W. Priebe, and D. Raucher. 2007. A thermally targeted elastin-like polypeptide-doxorubicin conjugate overcomes drug resistance. Invest. New Drugs 25:313-326.

8. Urry, D.W., T.M. Parker, M.C. Reid, and D.C. Gowda. 1991. Biocompatibility of the bioelastic materials, poly(GVGVP) and its γ-irradiation cross-linked matrix: summary of generic biological test results. J. Bioact. Compat. Polym 6:263-282.

9. Meyer, D.E., and A. Chilkoti. 1999. Purification of recombinant proteins by fusion with thermally-responsive polypeptides. Nat. Biotechnol 17:1112-1115.

10. Meyer, D.E., and A. Chilkoti. 2002. Genetically encoded synthesis of protein-based polymers with precisely specified molecular weight and sequence by recursive directional ligation: examples from the elastin-like polypeptide system. Biomacromolecules 3:357-367.

11. Urry, D.W., D.C. Gowda, T.M. Parker, C.H. Luan, M.C. Reid, C.M. Harris, A. Pattanaik, and R.D. Harris. 1992. Hydrophobicity scale for proteins based on inverse temperature transitions. Biopolymers 32:1243-1250.

12. Bataille, L., W. Dieryck, A. Hocquellet, C. Cabanne, K. Bathany, S. Lecommandoux, B. Garbay, and E. Garanger. 2015. Expression and purification of short hydrophobic elastin-like polypeptides with maltose-binding protein as a solubility tag. Protein Expr. Purif 110:165-171.

13. Bataille, L., W. Dieryck, A. Hocquellet, C. Cabanne, K. Bathany, S. Lecommandoux, B. Garbay, and E. Garanger. 2016. Recombinant Production and Purification of Short Hydrophobic Elastin-Like Polypeptides with Low Transition Temperatures. Protein Expr Purif 121:81-87.

14. Wentzell, L.M., T.J. Nobbs, and S.E. Halford. 1995. *Sfi*I restriction endonuclease makes a four-strand DNA break at two copies of its recognition sequence. J. Mol. Biol 248:581-595.

15. Nobbs, T.J., M.D. Szczelkun, L.M. Wentzell, and S.E. Halford. 1998. DNA excision by the *Sfi* I restriction endonuclease. J. Mol. Biol 281:419-432.

16. Wentzell, L.M., and S.E. Halford. 1998. DNA looping by the *Sfi* I restriction endonuclease. J. Mol. Biol 281:433-444.

17. Williams, S.A., and S.E. Halford. 2001. I endonuclease activity is strongly influenced by the non-specific sequence in the middle of its recognition site. Nucleic Acids Res 29:1476-1483.

18. Chow, D.C., M.R. Dreher, K. Trabbic-Carlson, and A. Chilkoti. 2006. Ultra-high expression of a thermally responsive recombinant fusion protein in *E. coli*. Biotechnol Prog 22:638-646.

19. Schägger, H. 2006. Tricine – SDS-PAGE. Nat Protoc 1:16-22.

20. Lee, C., A. Levin, and D. Branton. 1987. Copper staining: a five-minute protein stain for sodium dodecyl sulfate-polyacrylamide gels. Anal. Biochem 166:308-312.

21. McPherson, D.T., J. Xu, and D.W. Urry. 1996. Product purification by reversible phase transition following *Escherichia coli* expression of genes encoding up to 251 repeats of the elastomeric pentapeptide GVGVP. Protein Expr Purif 7:51-57.

Chapter 7

1. Urry DW. Entropic elastic processes in protein mechanisms. I. Elastic structure due to an inverse temperature transition and elasticity due to internal chain dynamics. Journal of protein chemistry. 1988;7(1):1-34.

2. Urry DW, Luan CH, Parker TM, Gowda DC, Prasad KU, Reid MC, et al. Temperature of polypeptide inverse temperature transition depends on mean residue hydrophobicity. Journal of the American Chemical Society. 1991;113(11):4346-8.

3. Urry D, Long M, Cox B, Ohnishi T, Mitchell L, Jacobs M. The synthetic polypentapeptide of elastin coacervates and forms filamentous aggregates. Biochimica et Biophysica Acta (BBA)-Protein Structure. 1974;371(2):597-602.

4. Puiggalí J, Franco L, J. del Valle L. Smart systems related to polypeptide sequences. AIMS Materials Science. 2016;3(1):289-323.

5. Meyer DE, Chilkoti A. Quantification of the Effects of Chain Length and Concentration on the Thermal Behavior of Elastin-like Polypeptides. Biomacromolecules. 2004;5:846-51.

6. Cho Y, Zhang Y, Christensen T, Sagle LB, Chilkoti A, Cremer PS. Effects of Hofmeister anions on the phase transition temperature of elastin-like polypeptides. J Phys Chem B. 2008;112(44):13765-71.

7. Bahniuk MS, Alshememry AK, Unsworth LD. High-yield recombinant expression and purification of marginally soluble, short elastin-like polypeptides. BioTechniques. 2016;61(6):297.

8. Meyer DE, Chilkoti A. Genetically Encoded Synthesis of Protein-Based Polymers with Precisely Specified Molecular Weight and Sequence by Recursive Directional Ligation: Examples from the Elastin-like Polypeptide System. Biomacromolecules. 2002:357-67.

9. Meyer DE, Chilkoti A. Purification of recombinant proteins by fusion with thermally-responsive polypeptides. Nature Biotechnology. 1999;17.

10. McHale MK, Setton LA, Chilkoti A. Synthesis and in vitro evaluation of enzymatically cross-linked elastin-like polypeptide gels for cartilaginous tissue repair. Tissue engineering. 2005;11(11-12):1768-79.

11. MacEwan SR, Chilkoti A. Applications of elastin-like polypeptides in drug delivery. Journal of controlled release : official journal of the Controlled Release Society. 2014;190:314-30.

12. Rodriguez-Cabello JC, Arias FJ, Rodrigo MA, Girotti A. Elastin-like polypeptides in drug delivery. Adv Drug Deliv Rev. 2016;97:85-100.

13. Smits FCM, Buddingh BC, van Eldijk MB, van Hest JCM. Elastin-Like Polypeptide Based Nanoparticles: Design Rationale Toward Nanomedicine. Macromolecular Bioscience. 2015;15(1):36-51.

14. Navon Y, Bitton R. Elastin-Like Peptides (ELPs) - Building Blocks for Stimuli-Responsive Self-Assembled Materials. Israel Journal of Chemistry. 2016;56(8):581-9.

15. Saxena R, Nanjan MJ. Elastin-like polypeptides and their applications in anticancer drug delivery systems: a review. Drug Deliv. 2015;22(2):156-67.

16. Yeboah A, Cohen RI, Rabolli C, Yarmush ML, Berthiaume F. Elastin-like polypeptides: A strategic fusion partner for biologics. Biotechnol Bioeng. 2016;113(8):1617-27.

17. Kowalczyk T, Hnatuszko-Konka K, Gerszberg A, Kononowicz AK. Elastin-like polypeptides as a promising family of genetically-engineered protein based polymers. World J Microbiol Biotechnol. 2014;30(8):2141-52.

1. Urry DW. Entropic elastic processes in protein mechanisms. I. Elastic structure due to an inverse temperature transition and elasticity due to internal chain dynamics. Journal of protein chemistry. 1988;7(1):1-34.

2. Urry DW, Luan CH, Parker TM, Gowda DC, Prasad KU, Reid MC, et al. Temperature of polypeptide inverse temperature transition depends on mean residue hydrophobicity. Journal of the American Chemical Society. 1991;113(11):4346-8.

3. Urry D, Long M, Cox B, Ohnishi T, Mitchell L, Jacobs M. The synthetic polypentapeptide of elastin coacervates and forms filamentous aggregates. Biochimica et Biophysica Acta (BBA)-Protein Structure. 1974;371(2):597-602.

4. Puiggalí J, Franco L, J. del Valle L. Smart systems related to polypeptide sequences. AIMS Materials Science. 2016;3(1):289-323.

5. Meyer DE, Chilkoti A. Quantification of the Effects of Chain Length and Concentration on the Thermal Behavior of Elastin-like Polypeptides. Biomacromolecules. 2004;5:846-51.

6. Cho Y, Zhang Y, Christensen T, Sagle LB, Chilkoti A, Cremer PS. Effects of Hofmeister anions on the phase transition temperature of elastin-like polypeptides. J Phys Chem B. 2008;112(44):13765-71.

7. Bahniuk MS, Alshememry AK, Unsworth LD. High-yield recombinant expression and purification of marginally soluble, short elastin-like polypeptides. BioTechniques. 2016;61(6):297.

8. Meyer DE, Chilkoti A. Genetically Encoded Synthesis of Protein-Based Polymers with Precisely Specified Molecular Weight and Sequence by Recursive Directional Ligation: Examples from the Elastin-like Polypeptide System. Biomacromolecules. 2002:357-67.

9. Meyer DE, Chilkoti A. Purification of recombinant proteins by fusion with thermally-responsive polypeptides. Nature Biotechnology. 1999;17.

10. McHale MK, Setton LA, Chilkoti A. Synthesis and in vitro evaluation of enzymatically cross-linked elastin-like polypeptide gels for cartilaginous tissue repair. Tissue engineering. 2005;11(11-12):1768-79.

11. MacEwan SR, Chilkoti A. Applications of elastin-like polypeptides in drug delivery. Journal of controlled release : official journal of the Controlled Release Society. 2014;190:314-30.

12. Rodriguez-Cabello JC, Arias FJ, Rodrigo MA, Girotti A. Elastin-like polypeptides in drug delivery. Adv Drug Deliv Rev. 2016;97:85-100.

13. Smits FCM, Buddingh BC, van Eldijk MB, van Hest JCM. Elastin-Like Polypeptide Based Nanoparticles: Design Rationale Toward Nanomedicine. Macromolecular Bioscience. 2015;15(1):36-51.

14. Navon Y, Bitton R. Elastin-Like Peptides (ELPs) - Building Blocks for Stimuli-Responsive Self-Assembled Materials. Israel Journal of Chemistry. 2016;56(8):581-9.

15. Saxena R, Nanjan MJ. Elastin-like polypeptides and their applications in anticancer drug delivery systems: a review. Drug Deliv. 2015;22(2):156-67.

16. Yeboah A, Cohen RI, Rabolli C, Yarmush ML, Berthiaume F. Elastin-like polypeptides: A strategic fusion partner for biologics. Biotechnol Bioeng. 2016;113(8):1617-27.

17. Kowalczyk T, Hnatuszko-Konka K, Gerszberg A, Kononowicz AK. Elastin-like polypeptides as a promising family of genetically-engineered protein based polymers. World J Microbiol Biotechnol. 2014;30(8):2141-52.

18. Yao XL, Hong M. Structure distribution in an elastin-mimetic peptide (VPGVG)3 investigated by solid-state NMR. Journal of the American Chemical Society. 2004;126(13):4199-210.

19. Hong M, Isailovic D, McMillan R, Conticello V. Structure of an elastin-mimetic polypeptide by solid-state NMR chemical shift analysis. Biopolymers. 2003;70(2):158-68.

20. Li NK, Garcia Quiroz F, Hall CK, Chilkoti A, Yingling YG. Molecular description of the LCST behavior of an elastin-like polypeptide. Biomacromolecules. 2014;15(10):3522-30.

21. Reichheld SE, Muiznieks LD, Keeley FW, Sharpe S. Direct observation of structure and dynamics during phase separation of an elastomeric protein. Proceedings of the National Academy of Sciences. 2017:201701877.

22. Rauscher S, Baud S, Miao M, Keeley FW, Pomes R. Proline and glycine control protein self-organization into elastomeric or amyloid fibrils. Structure. 2006;14(11):1667-76.

23. Kumashiro KK, Ohgo K, Elliott DW, Kagawa TF, Niemczura WP. Backbone motion in elastin's hydrophobic domains as detected by 2H NMR spectroscopy. Biopolymers. 2012;97(11):882-8.

24. Muiznieks LD, Keeley FW. Proline periodicity modulates the self-assembly properties of elastin-like polypeptides. Journal of Biological Chemistry. 2010;285(51):39779-89.

25. Fujita Y, Mie M, Kobatake E. Construction of nanoscale protein particle using temperature-sensitive elastin-like peptide and polyaspartic acid chain. Biomaterials. 2009;30:3450-7.

26. Ghoorchian A, Vandemark K, Freeman K, Kambow S, Holland NB, Streletzky KA. Size and shape characterization of thermoreversible micelles of three-armed star elastin-like polypeptides. The Journal of Physical Chemistry B. 2013;117(29):8865-74.

27. MacEwan SR, Weitzhandler I, Hoffmann I, Genzer J, Gradzielski M, Chilkoti A. Phase Behavior and Self-Assembly of Perfectly Sequence-Defined and Monodisperse Multiblock Copolypeptides. Biomacromolecules. 2017;18(2):599-609.

28. Osborne JL, Farmer R, Woodhouse KA. Self-assembled elastin-like polypeptide particles. Acta Biomater. 2008;4(1):49-57.

29. Nicolini C, Ravindra R, Ludolph B, Winter R. Characterization of the Temperature- and Pressure-Induced Inverse and Reentrant Transition of the Minimum Elastin-Like Polypeptide GVG(VPGVG) by DSC, PPC, CD, and FT-IR Spectroscopy. Biophysical Journal. 2004;86(March).

30. McDaniel JR, Radford DC, Chilkoti A. A unified model for de novo design of elastin-like polypeptides with tunable inverse transition temperatures. Biomacromolecules. 2013;14(8):2866-72.

31. Urry DW, Gowda DC, Parker TM, Luan CH, Reid MC, Harris CM, et al. Hydrophobicity scale for proteins based on inverse temperature transitions. Biopolymers. 1992;32(9):1243-50.

32. Girotti A, Reguera J, Arias FJ, Alonso M, Testera AM, Rodríguez-Cabello JC. Influence of the Molecular Weight on the Inverse Temperature Transition of a Model Genetically Engineered Elastin-like pH-Responsive Polymer. Macromolecules. 2004;37(9):3396-400.

33. MacKay JA, Callahan DJ, FitzGerald KN, Chilkoti A. Quantitative model of the phase behavior of recombinant pH-responsive elastin-like polypeptides. Biomacromolecules. 2010;11(11):2873-9.

34. Lundqvist M, Stigler J, Elia G, Lynch I, Cedervall T, Dawson KA. Nanoparticle size and surface properties determine the protein corona with possible implications for biological impacts. Proc Natl Acad Sci U S A. 2008;105(38):14265-70.

35. Verma A, Stellacci F. Effect of surface properties on nanoparticle–cell interactions. Small. 2010;6(1):12-21.

36. MacKay JA, Chen M, McDaniel JR, Liu W, Simnick AJ, Chilkoti A. Self-assembling chimeric polypeptide-doxorubicin conjugate nanoparticles that abolish tumours after a single injection. Nature materials. 2009;8(12):993-9.

37. Dreher MR, Simnick AJ, Fischer K, Smith RJ, Patel A, Schmidt M, et al. Temperature triggered self-assembly of polypeptides into multivalent spherical micelles. Journal of the American Chemical Society. 2008;130:687-94.

38. Sallach RE, Wei M, Biswas N, Conticello VP, Lecommandoux S, Dluhy RA, et al. Micelle density regulated by a reversible switch of protein secondary structure. Journal of the American Chemical Society. 2006;128(36):12014-9.

39. Serrano V, Liu W, Franzen S. An infrared spectroscopic study of the conformational transition of elastin-like polypeptides. Biophysical journal. 2007;93(7):2429-35.

Chapter 8

1. Callahan DJ, Liu W, Li X, Dreher MR, Hassouneh W, Kim M, et al. Triple stimulus-responsive polypeptide nanoparticles that enhance intratumoral spatial distribution. Nano Lett. 2012;12(4):2165-70.

2. Urry DW. Entropic elastic processes in protein mechanisms. I. Elastic structure due to an inverse temperature transition and elasticity due to internal chain dynamics. Journal of protein chemistry. 1988;7(1):1-34.

3. Urry DW, Gowda DC, Parker TM, Luan CH, Reid MC, Harris CM, et al. Hydrophobicity scale for proteins based on inverse temperature transitions. Biopolymers. 1992;32(9):1243-50.

4. Chilkoti A, Dreher MR, Meyer DE. Design of thermally responsive, recombinant polypeptide carriers for targeted drug delivery. Cancer. 2002;54:1093-111.

5. Puiggalí J, Franco L, J. del Valle L. Smart systems related to polypeptide sequences. AIMS Materials Science. 2016;3(1):289-323.

6. Bahniuk MS, Alshememry AK, Unsworth LD. High-yield recombinant expression and purification of marginally soluble, short elastin-like polypeptides. BioTechniques. 2016;61(6):297.

7. Meyer DE, Chilkoti A. Genetically Encoded Synthesis of Protein-Based Polymers with Precisely Specified Molecular Weight and Sequence by Recursive Directional Ligation: Examples from the Elastin-like Polypeptide System. Biomacromolecules. 2002:357-67.

8. Meyer DE, Chilkoti A. Purification of recombinant proteins by fusion with thermally-responsive polypeptides. Nature Biotechnology. 1999;17(November).

9. Bataille L, Dieryck W, Hocquellet A, Cabanne C, Bathany K, Lecommandoux S, et al. Recombinant Production and Purification of Short Hydrophobic Elastin-Like Polypeptides with Low Transition Temperatures. Protein Expression and Purification. 2016.

10. Lin M, Rose-John S, Grötzinger J, Conrad U, Scheller J. Functional expression of a biologically active fragment of soluble gp130 as an ELP-fusion protein in transgenic plants: purification via inverse transition cycling. Biochemical Journal. 2006;398(3):577-83.

11. Yeboah A, Cohen RI, Rabolli C, Yarmush ML, Berthiaume F. Elastin-like polypeptides: A strategic fusion partner for biologics. Biotechnol Bioeng. 2016;113(8):1617-27.

12. Sarangthem V, Cho Ea, Bae SM, Singh TD, Kim SJ, Kim S, et al. Construction and application of elastin like polypeptide containing IL-4 receptor targeting peptide. PLoS ONE. 2013;8(12):1-12.

13. Shi P, Aluri S, Lin YA, Shah M, Edman M, Dhandhukia J, et al. Elastin-based protein polymer nanoparticles carrying drug at both corona and core suppress tumor growth in vivo. Journal of Controlled Release. 2013;171(3):330-8.

14. Meyer DE, Kong GA, Dewhirst MW, Zalutsky MR, Chilkoti A. Targeting a Genetically Engineered Elastin-like Polypeptide to Solid Tumors by Local Hyperthermia 1. In Vitro. 2001;42745:1548-54.

15. Koetting MC, Peters JT, Steichen SD, Peppas NA. Stimulus-responsive hydrogels: Theory, modern advances, and applications. Materials Science and Engineering: R: Reports. 2015;93:1-49.

16. Rodriguez-Cabello JC, Pina MJ, Ibanez-Fonseca A, Fernandez-Colino A, Arias FJ. Nanotechnological Approaches to Therapeutic Delivery Using Elastin-Like Recombinamers. Bioconjug Chem. 2015;26(7):1252-65.

17. Wang W, Jashnani A, Aluri SR, Gustafson JA, Hsueh PY, Yarber F, et al. A thermo-responsive protein treatment for dry eyes. J Control Release. 2015;199:156-67.

18. Heilshorn S. Endothelial cell adhesion to the fibronectin CS5 domain in artificial extracellular matrix proteins. Biomaterials. 2003;24(23):4245-52.

19. Urry DW. Protein elasticity based on conformations of sequential polypeptides: the biological elastic fiber. Journal of protein chemistry. 1984;3(5-6):403-36.

20. Yigit S, Dinjaski N, Kaplan DL. Fibrous proteins: At the crossroads of genetic engineering and biotechnological applications. Biotechnol Bioeng. 2016;113(5):913-29.

21. Desai MS, Lee SW. Protein-based functional nanomaterial design for bioengineering applications. Wiley Interdiscip Rev Nanomed Nanobiotechnol. 2015;7(1):69-97.

22. Kowalczyk T, Hnatuszko-Konka K, Gerszberg A, Kononowicz AK. Elastin-like polypeptides as a promising family of genetically-engineered protein based polymers. World J Microbiol Biotechnol. 2014;30(8):2141-52.

23. Nettles DL, Chilkoti A, Setton LA. Applications of elastin-like polypeptides in tissue engineering. Adv Drug Deliv Rev. 2010;62(15):1479-85.

24. Urry DW, Parker TM, Reid MC, Gowda DC. Biocompatibility of the Bioelastic Materials, Poly(GVGVP) and Its γ-Irradiation Cross-Linked Matrix: Summary of Generic Biological Test Results. Journal of Bioactive and Compatible Polymers. 1991;6(3):263-82.

25. Elsas FJ, Gowda DC, Urry DW. Synthetic polypeptide sleeve for strabismus surgery. Journal of pediatric ophthalmology and strabismus. 1992;29(5):284-6.

26. Sallach RE, Cui W, Balderrama F, Martinez AW, Wen J, Haller Ca, et al. Long-term biostability of self-assembling protein polymers in the absence of covalent crosslinking. Biomaterials. 2010;31(4):779-91.

27. Rincon AC, Molina-Martinez IT, de Las Heras B, Alonso M, Bailez C, Rodriguez-Cabello JC, et al. Biocompatibility of elastin-like polymer poly(VPAVG) microparticles: in vitro and in vivo studies. J Biomed Mater Res A. 2006;78(2):343-51.

28. Horbett TA. Chapter II.1.2 - Adsorbed Proteins on Biomaterials A2 - Ratner, Buddy D. In: Hoffman AS, Schoen FJ, Lemons JE, editors. Biomaterials Science (Third Edition): Academic Press; 2013. p. 394-408.

29. Vroman L, Adams A, Fischer G, Munoz P. Interaction of high molecular weight kininogen, factor XII, and fibrinogen in plasma at interfaces. Blood. 1980;55(1):156-9.

30. Schleh C, Rothen-Rutishauser B, Kreyling WG. The influence of pulmonary surfactant on nanoparticulate drug delivery systems. European journal of pharmaceutics and biopharmaceutics. 2011;77(3):350-2.

31. Deng ZJ, Liang M, Monteiro M, Toth I, Minchin RF. Nanoparticle-induced unfolding of fibrinogen promotes Mac-1 receptor activation and inflammation. Nature nanotechnology. 2011;6(1):39-44.

32. Mortimer GM, Butcher NJ, Musumeci AW, Deng ZJ, Martin DJ, Minchin RF. Cryptic epitopes of albumin determine mononuclear phagocyte system clearance of nanomaterials. ACS nano. 2014;8(4):3357-66.

33. Bahniuk MS, Pirayesh H, Singh HD, Nychka Ja, Unsworth LD. Bioactive glass 45S5 powders: effect of synthesis route and resultant surface chemistry and crystallinity on protein adsorption from human plasma. Biointerphases. 2012;7(1-4):1-5.

34. Yogasundaram H, Bahniuk MS, Singh H-D, Aliabadi HM, Uludağ H, Unsworth LD. BSA Nanoparticles for siRNA Delivery: Coating Effects on Nanoparticle Properties, Plasma Protein Adsorption, and In Vitro siRNA Delivery. International journal of biomaterials. 2012;2012:584060-.

35. Nikouei NS, Vakili MR, Bahniuk MS, Unsworth L, Akbari A, Wu J, et al. Thermoreversible hydrogels based on triblock copolymers of poly(ethylene glycol) and carboxyl functionalized poly(ε-caprolactone): The effect of carboxyl group substitution on the transition temperature and biocompatibility in plasma. Acta biomaterialia. 2014;12:81-92.

36. Abraham S, So A, Unsworth LD. Poly(carboxybetaine methacrylamide)-modified nanoparticles: a model system for studying the effect of chain chemistry on film properties, adsorbed protein conformation, and clot formation kinetics. Biomacromolecules. 2011;12(10):3567-80.

37. Tsai WB, Grunkemeier JM, Horbett TA. Variations in the ability of adsorbed fibrinogen to mediate platelet adhesion to polystyrene-based materials: A multivariate statistical analysis of antibody binding to the platelet binding sites of fibrinogen. Journal of Biomedical Materials Research Part A. 2003;67(4):1255-68.

38. Osborne JL, Farmer R, Woodhouse KA. Self-assembled elastin-like polypeptide particles. Acta Biomater. 2008;4(1):49-57.

39. Nel AE, Mädler L, Velegol D, Xia T, Hoek EM, Somasundaran P, et al. Understanding biophysicochemical interactions at the nano–bio interface. Nature materials. 2009;8(7):543-57.

40. Pitek AS, O'Connell D, Mahon E, Monopoli MP, Bombelli FB, Dawson KA. Transferrin coated nanoparticles: study of the bionano interface in human plasma. PloS one. 2012;7(7):e40685.

41. Grunér M, Kauscher U, Linder M, Monopoli M. An environmental route of exposure affects the formation of nanoparticle coronas in blood plasma. Journal of proteomics. 2016;137:52-8.

42. Ostuni E, Chapman RG, Holmlin RE, Takayama S, Whitesides GM. A survey of structure− property relationships of surfaces that resist the adsorption of protein. Langmuir. 2001;17(18):5605-20.

43. Binazadeh M, Kabiri M, Unsworth LD. Poly (ethylene glycol) and Poly (carboxy betaine) based nonfouling architectures: Review and current efforts. Proteins at Interfaces III State of the Art: ACS Publications; 2012. p. 621-43.

44. Lyman D, Klein KG, Brash J, Fritzinger B, Andrade J, Bonomo F. Platelet interaction with protein-coated surfaces: an approach to thrombo-resistant surfaces. Platelet Adhesion and Aggregation in Thrombosis: Countermeasures. 1970.

45. Fedeli C, Segat D, Tavano R, Bubacco L, De Franceschi G, de Laureto PP, et al. The functional dissection of the plasma corona of SiO 2-NPs spots histidine rich glycoprotein as a major player able to hamper nanoparticle capture by macrophages. Nanoscale. 2015;7(42):17710-28.

46. Yallapu MM, Ebeling MC, Chauhan N, Jaggi M, Chauhan SC. Interaction of curcumin nanoformulations with human plasma proteins and erythrocytes. International journal of nanomedicine. 2011;6:2779.

47. Aggarwal P, Hall JB, McLeland CB, Dobrovolskaia MA, McNeil SE. Nanoparticle interaction with plasma proteins as it relates to particle biodistribution, biocompatibility and therapeutic efficacy. Advanced drug delivery reviews. 2009;61(6):428-37.

48. Sleep D, Cameron J, Evans LR. Albumin as a versatile platform for drug half-life extension. Biochimica et Biophysica Acta (BBA)-General Subjects. 2013;1830(12):5526-34.

49. Sivaraman B, Latour Ra. The adherence of platelets to adsorbed albumin by receptor-mediated recognition of binding sites exposed by adsorption-induced unfolding. Biomaterials. 2010;31(6):1036-44.

50. Molina H. Complement and immunity. Rheumatic Disease Clinics of North America. 2004;30(1):1-18.

51. Andersson J, Ekdahl KN, Lambris JD, Nilsson B. Binding of C3 fragments on top of adsorbed plasma proteins during complement activation on a model biomaterial surface. Biomaterials. 2005;26(13):1477-85.

52. Nilsson B, Ekdahl KN. The tick-over theory revisited: is C3 a contact-activated protein? Immunobiology. 2012;217(11):1106-10.

53. Moos T, Morgan EH. Transferrin and transferrin receptor function in brain barrier systems. Cellular and molecular neurobiology. 2000;20(1):77-95.

54. Stafford JL, Belosevic M. Transferrin and the innate immune response of fish: identification of a novel mechanism of macrophage activation. Developmental and comparative immunology. 2003;27(6-7):539-54.

55. Anderson JM, Rodriguez A, Chang DT. Foreign body reaction to biomaterials. Seminars in immunology. 2008;20(2):86-100.

56. Abbas AK. Cellular and molecular immunology. In: Lichtman AH, Pillai S, editors. 6th ed. ed. Philadelphia :: Saunders Elsevier; 2007.

57. Mosesson MW. Fibrinogen and fibrin structure and functions. Journal of thrombosis and haemostasis : JTH. 2005;3(8):1894-904.

58. Massa TM, Yang ML, Ho JYC, Brash JL, Santerre JP. Fibrinogen surface distribution correlates to platelet adhesion pattern on fluorinated surface-modified polyetherurethane. Biomaterials. 2005;26(35):7367-76.

59. Unsworth LD, Sheardown H, Brash JL. Polyethylene oxide surfaces of variable chain density by chemisorption of PEO-thiol on gold: Adsorption of proteins from plasma studied by radiolabelling and immunoblotting. Biomaterials. 2005;26(30):5927-33.

60. Srokowski E, Blit P, McClung W, Brash J, Santerre J, Woodhouse K. Platelet adhesion and fibrinogen accretion on a family of elastin-like polypeptides. Journal of Biomaterials Science, Polymer Edition. 2011;22(1-3):41-57.

61. Blit PH, McClung WG, Brash JL, Woodhouse Ka, Santerre JP. Platelet inhibition and endothelial cell adhesion on elastin-like polypeptide surface modified materials. Biomaterials. 2011;32(25):5790-800.

62. Srokowski EM, Woodhouse Ka. Evaluation of the bulk platelet response and fibrinogen interaction to elastin-like polypeptide coatings. Journal of Biomedical Materials Research - Part A. 2014;102(2):540-51.

63. Tenzer S, Docter D, Rosfa S, Wlodarski A, Kuharev Jr, Rekik A, et al. Nanoparticle size is a critical physicochemical determinant of the human blood plasma corona: a comprehensive quantitative proteomic analysis. ACS nano. 2011;5(9):7155-67.

64. Davie EW, D P, Kulman JD. An Overview of the Structure and Function of Thrombin. Seminars In Thrombosis And Hemostasis. 2006;32(suppl 1):3-15.

65. McClung W, Clapper D, Hu S-P, Brash J. Lysine-derivatized polyurethane as a clot lysing surface: conversion of adsorbed plasminogen to plasmin and clot lysis in vitro. Biomaterials. 2001;22(13):1919-24.

66. McClung WG, Clapper DL, Hu SP, Brash JL. Adsorption of plasminogen from human plasma to lysine-containing surfaces. Journal of biomedical materials research. 2000;49(3):409-14.

67. Gresele P, Page C, Fuster V, Vermylen J. Platelets in Thrombotic and Non-Thrombotic Disorders. Transfusion Medicine. 2003;13(1):57-8.

68. Rubel C, Fernández GC, Dran G, Bompadre MB, Isturiz MA, Palermo MS. Fibrinogen promotes neutrophil activation and delays apoptosis. The Journal of Immunology. 2001;166(3):2002-10.

69. Stoller JK, Aboussouan LS. α1-antitrypsin deficiency. The Lancet. 2005;365(9478):2225-36.

70. Shah M, Hsueh P-Y, Sun G, Chang HY, Janib SM, MacKay JA. Biodegradation of elastin-like polypeptide nanoparticles. Protein science : a publication of the Protein Society. 2012;21(6):743-50.

71. Lundqvist M, Stigler J, Elia G, Lynch I, Cedervall T, Dawson KA. Nanoparticle size and surface properties determine the protein corona with possible implications for biological impacts. Proc Natl Acad Sci U S A. 2008;105(38):14265-70.

72. De Boer J, Creasey A, Chang A, Abbink J, Roem D, Eerenberg A, et al. Alpha-2-macroglobulin functions as an inhibitor of fibrinolytic, clotting, and neutrophilic proteinases in sepsis: studies using a baboon model. Infection and immunity. 1993;61(12):5035-43.

73. Woodhouse KA, Klement P, Chen V, Gorbet MB, Keeley FW, Stahl R, et al. Investigation of recombinant human elastin polypeptides as non-thrombogenic coatings. Biomaterials. 2004;25(19):4543-53.

Chapter 9

1. Urry DW. Entropic elastic processes in protein mechanisms. I. Elastic structure due to an inverse temperature transition and elasticity due to internal chain dynamics. Journal of protein chemistry. 1988;7(1):1-34.

2. Urry D, Long M, Cox B, Ohnishi T, Mitchell L, Jacobs M. The synthetic polypentapeptide of elastin coacervates and forms filamentous aggregates. Biochimica et Biophysica Acta (BBA)-Protein Structure. 1974;371(2):597-602.

3. Urry DW. Physical Chemistry of Biological Free Energy Transduction As Demonstrated by Elastic Protein-Based Polymers. The Journal of Physical Chemistry B. 1997;101(51):11007-28.

4. Urry DW, Gowda DC, Parker TM, Luan CH, Reid MC, Harris CM, et al. Hydrophobicity scale for proteins based on inverse temperature transitions. Biopolymers. 1992;32(9):1243-50.

5. Chilkoti A, Dreher MR, Meyer DE. Design of thermally responsive, recombinant polypeptide carriers for targeted drug delivery. Cancer. 2002;54:1093-111.

6. Meyer DE, Chilkoti A. Genetically Encoded Synthesis of Protein-Based Polymers with Precisely Specified Molecular Weight and Sequence by Recursive Directional Ligation: Examples from the Elastin-like Polypeptide System. Biomacromolecules. 2002:357-67.

7. Bahniuk MS, Alshememry AK, Unsworth LD. High-yield recombinant expression and purification of marginally soluble, short elastin-like polypeptides. BioTechniques. 2016;61(6):297.

8. Hu F, Ke T, Li X, Mao PH, Jin X, Hui FL, et al. Expression and purification of an antimicrobial peptide by fusion with elastin-like polypeptides in Escherichia coli. Applied biochemistry and biotechnology. 2010;160(8):2377-87.

9. Dreher MR, Simnick AJ, Fischer K, Smith RJ, Patel A, Schmidt M, et al. Temperature triggered self-assembly of polypeptides into multivalent spherical micelles. Journal of the American Chemical Society. 2008;130(2):687-94.

10. Meyer DE, Kong GA, Dewhirst MW, Zalutsky MR, Chilkoti A. Targeting a Genetically Engineered Elastin-like Polypeptide to Solid Tumors by Local Hyperthermia 1. In Vitro. 2001;42745:1548-54.

11. Rodriguez-Cabello JC, Pina MJ, Ibanez-Fonseca A, Fernandez-Colino A, Arias FJ. Nanotechnological Approaches to Therapeutic Delivery Using Elastin-Like Recombinamers. Bioconjug Chem. 2015;26(7):1252-65.

12. Lim DW, Nettles DL, Setton La, Chilkoti A. In situ cross-linking of elastin-like polypeptide block copolymers for tissue repair. Biomacromolecules. 2008;9(1):222-30.

13. Heilshorn SC, Liu JC, Tirrell DA. Cell-binding domain context affects cell behavior on engineered proteins. Biomacromolecules. 2005;6(1):318-23.

14. Urry DW, Parker TM, Reid MC, Gowda DC. Biocompatibility of the Bioelastic Materials, Poly(GVGVP) and Its γ-Irradiation Cross-Linked Matrix: Summary of Generic Biological Test Results. Journal of Bioactive and Compatible Polymers. 1991;6(3):263-82.

15. Rincon AC, Molina-Martinez IT, de Las Heras B, Alonso M, Bailez C, Rodriguez-Cabello JC, et al. Biocompatibility of elastin-like polymer poly(VPAVG) microparticles: in vitro and in vivo studies. J Biomed Mater Res A. 2006;78(2):343-51.

16. Elsas FJ, Gowda DC, Urry DW. Synthetic polypeptide sleeve for strabismus surgery. Journal of pediatric ophthalmology and strabismus. 1992;29(5):284-6.

17. Schleh C, Rothen-Rutishauser B, Kreyling WG. The influence of pulmonary surfactant on nanoparticulate drug delivery systems. European journal of pharmaceutics and biopharmaceutics. 2011;77(3):350-2.

18. Deng ZJ, Liang M, Monteiro M, Toth I, Minchin RF. Nanoparticle-induced unfolding of fibrinogen promotes Mac-1 receptor activation and inflammation. Nature nanotechnology. 2011;6(1):39-44.

19. Lesniak A, Fenaroli F, Monopoli MP, Åberg C, Dawson KA, Salvati A. Effects of the presence or absence of a protein corona on silica nanoparticle uptake and impact on cells. ACS nano. 2012;6(7):5845-57.

20. Lundqvist M, Stigler J, Elia G, Lynch I, Cedervall T, Dawson KA. Nanoparticle size and surface properties determine the protein corona with possible implications for biological impacts. Proc Natl Acad Sci U S A. 2008;105(38):14265-70.

21. Wolfram J, Yang Y, Shen J, Moten A, Chen C, Shen H, et al. The nano-plasma interface: implications of the protein corona. Colloids and Surfaces B: Biointerfaces. 2014;124:17-24.

22. Tenzer S, Docter D, Rosfa S, Wlodarski A, Kuharev Jr, Rekik A, et al. Nanoparticle size is a critical physicochemical determinant of the human blood plasma corona: a comprehensive quantitative proteomic analysis. ACS nano. 2011;5(9):7155-67.

23. Hsu M, Juliano R. Interactions of liposomes with the reticuloendothelial system: II. Nonspecific and receptor-mediated uptake of liposomes by mouse

peritoneal macrophages. Biochimica et Biophysica Acta (BBA)-Molecular Cell Research. 1982;720(4):411-9.

24. Harashima H, Sakata K, Funato K, Kiwada H. Enhanced hepatic uptake of liposomes through complement activation depending on the size of liposomes. Pharmaceutical research. 1994;11(3):402-6.

25. Raschke W, Baird S, Ralph P, Nakoinz I. Functional macrophage cell lines transformed by Abelson leukemia virus. Cell. 1978;15(1):261-7.

26. Ralph P, Nakoinz I. Antibody-dependent killing of erythrocyte and tumor targets by macrophage-related cell lines: enhancement by PPD and LPS. The Journal of Immunology. 1977;119(3):950-4.

27. Ishihama Y, Rappsilber J, Andersen JS, Mann M. Microcolumns with self-assembled particle frits for proteomics. Journal of chromatography A. 2002;979(1):233-9.

28. Bern M, Kil YJ, Becker C. Byonic: advanced peptide and protein identification software. Current protocols in bioinformatics. 2012:13.20. 1-13.20. 14.

29. Karmali PP, Simberg D. Interactions of nanoparticles with plasma proteins: implication on clearance and toxicity of drug delivery systems. Expert Opinion on Drug Delivery. 2011;8(3):343-57.

30. Pedersen MB, Zhou X, Larsen EKU, Sørensen US, Kjems J, Nygaard JV, et al. Curvature of synthetic and natural surfaces is an important target feature in classical pathway complement activation. The journal of immunology. 2010;184(4):1931-45.

31. Geys J, Nemmar A, Verbeken E, Smolders E, Ratoi M, Hoylaerts MF, et al. Acute toxicity and prothrombotic effects of quantum dots: impact of surface charge. Environmental health perspectives. 2008;116(12):1607.

32. Gessner A, Waicz R, Lieske A, Paulke B-R, Mäder K, Müller R. Nanoparticles with decreasing surface hydrophobicities: influence on plasma protein adsorption. International journal of pharmaceutics. 2000;196(2):245-9.

33. Gessner A, Lieske A, Paulke BR, Müller RH. Influence of surface charge density on protein adsorption on polymeric nanoparticles: analysis by two-dimensional electrophoresis. European journal of pharmaceutics and biopharmaceutics. 2002;54(2):165-70.

34. Lai W, Wang Q, Li L, Hu Z, Chen J, Fang Q. Interaction of gold and silver nanoparticles with human plasma: Analysis of protein corona reveals specific binding patterns. Colloids and Surfaces B: Biointerfaces. 2017;152:317-25.

35. Pitek AS, O'Connell D, Mahon E, Monopoli MP, Bombelli FB, Dawson KA. Transferrin coated nanoparticles: study of the bionano interface in human plasma. PloS one. 2012;7(7):e40685.

36. Grunér M, Kauscher U, Linder M, Monopoli M. An environmental route of exposure affects the formation of nanoparticle coronas in blood plasma. Journal of proteomics. 2016;137:52-8.

37. Cedervall T, Lynch I, Foy M, Berggård T, Donnelly SC, Cagney G, et al. Detailed identification of plasma proteins adsorbed on copolymer nanoparticles. Angewandte Chemie International Edition. 2007;46(30):5754-6.

38. Lynch I, Cedervall T, Lundqvist M, Cabaleiro-Lago C, Linse S, Dawson KA. The nanoparticle–protein complex as a biological entity; a complex fluids and surface science challenge for the 21st century. Advances in colloid and interface science. 2007;134:167-74.

39. Verma A, Stellacci F. Effect of surface properties on nanoparticle–cell interactions. Small. 2010;6(1):12-21.

40. Mahmoudi M, Lynch I, Ejtehadi MR, Monopoli MP, Bombelli FB, Laurent S. Protein− nanoparticle interactions: opportunities and challenges. Chemical reviews. 2011;111(9):5610-37.

41. Wilkinson K, Ekstrand-Hammarström B, Ahlinder L, Guldevall K, Pazik R, Kępiński L, et al. Visualization of custom-tailored iron oxide nanoparticles chemistry, uptake, and toxicity. Nanoscale. 2012;4(23):7383-93.

42. AshaRani P, Low Kah Mun G, Hande MP, Valiyaveettil S. Cytotoxicity and genotoxicity of silver nanoparticles in human cells. ACS nano. 2008;3(2):279-90.

43. Sharma V, Anderson D, Dhawan A. Zinc oxide nanoparticles induce oxidative DNA damage and ROS-triggered mitochondria mediated apoptosis in human liver cells (HepG2). Apoptosis. 2012;17(8):852-70.

44. Elmore S. Apoptosis: a review of programmed cell death. Toxicologic pathology. 2007;35(4):495-516.

45. Ozaki C, Somamoto S, Kawabata S, Tabata Y. Effect of an artificial silk elastin-like protein on the migration and collagen production of mouse fibroblasts. Journal of Biomaterials Science, Polymer Edition. 2014;25(12):1266-77.

46. Lin CY, Liu JC. Modular protein domains: an engineering approach toward functional biomaterials. Curr Opin Biotechnol. 2016;40:56-63.

47. Desai MS, Lee SW. Protein-based functional nanomaterial design for bioengineering applications. Wiley Interdiscip Rev Nanomed Nanobiotechnol. 2015;7(1):69-97.

48. Lim DW, Nettles DL, Setton La, Chilkoti A. Rapid Cross-Linking of Elastin-like Polypeptides with (Hydroxymethyl) phosphines in Aqueous Solution. Biomacromolecules. 2007;8:1463-70.

49. Heilshorn S. Endothelial cell adhesion to the fibronectin CS5 domain in artificial extracellular matrix proteins. Biomaterials. 2003;24(23):4245-52.

50. Bartneck M, Keul HA, Zwadlo-Klarwasser G, Groll Jr. Phagocytosis independent extracellular nanoparticle clearance by human immune cells. Nano letters. 2009;10(1):59-63.

51. Rojas JM, Sanz-Ortega L, Mulens-Arias V, Gutiérrez L, Pérez-Yagüe S, Barber DF. Superparamagnetic iron oxide nanoparticle uptake alters M2 macrophage phenotype, iron metabolism, migration and invasion. Nanomedicine: Nanotechnology, Biology and Medicine. 2016;12(4):1127-38.

52. Sabareeswaran A, Ansar EB, Varma PRVH, Mohanan PV, Kumary TV. Effect of surface-modified superparamagnetic iron oxide nanoparticles (SPIONS) on mast cell infiltration: An acute in vivo study. Nanomedicine: Nanotechnology, Biology and Medicine. 2016;12(6):1523-33.

53. Senoh H, Kano H, Suzuki M, Ohnishi M, Kondo H, Takanobu K, et al. Comparison of single or multiple intratracheal administration for pulmonary toxic

responses of nickel oxide nanoparticles in rats. Journal of occupational health. 2017;59(2):112-21.

54. Kettler K, Giannakou C, de Jong WH, Hendriks AJ, Krystek P. Uptake of silver nanoparticles by monocytic THP-1 cells depends on particle size and presence of serum proteins. Journal of Nanoparticle Research. 2016;18(9).

55. Seiffert J, Buckley A, Leo B, Martin NG, Zhu J, Dai R, et al. Pulmonary effects of inhalation of spark-generated silver nanoparticles in Brown-Norway and Sprague–Dawley rats. Respiratory research. 2016;17(1):85.

56. Bruneau A, Turcotte P, Pilote M, Gagné F, Gagnon C. Fate of silver nanoparticles in wastewater and immunotoxic effects on rainbow trout. Aquatic Toxicology. 2016;174:70-81.

57. Ede JD, Ortega VA, Boyle D, Beingessner RL, Hemraz UD, Fenniri H, et al. The effects of rosette nanotubes with different functionalizations on channel catfish (Ictalurus punctatus) lymphocyte viability and receptor function. Environmental Science: Nano. 2016;3(3):578-92.

58. Jovanović B, Palić D. Immunotoxicology of non-functionalized engineered nanoparticles in aquatic organisms with special emphasis on fish—Review of current knowledge, gap identification, and call for further research. Aquatic toxicology. 2012;118:141-51.

59. Rooney M, Woodhouse K. Decreased tissue factor expression with increased CD11b upregulation on elastin-based biomaterial coatings. Biomaterials Science. 2014;2(10):1377-83.

60. Nouri FS, Wang X, Chen X, Hatefi A. Reducing the visibility of the vector/DNA nanocomplexes to the immune system by elastin-like peptides. Pharmaceutical research. 2015;32(9):3018.

61. Dale MA, Xiong W, Carson JS, Suh MK, Karpisek AD, Meisinger TM, et al. Elastin-derived peptides promote abdominal aortic aneurysm formation by modulating M1/M2 macrophage polarization. The Journal of Immunology. 2016;196(11):4536-43.

62. Simon SI, Schmid-Schönbein G. Biophysical aspects of microsphere engulfment by human neutrophils. Biophysical journal. 1988;53(2):163-73.

63. Tabata Y, Ikada Y. Effect of the size and surface charge of polymer microspheres on their phagocytosis by macrophage. Biomaterials. 1988;9(4):356-62.

64. Champion JA, Walker A, Mitragotri S. Role of particle size in phagocytosis of polymeric microspheres. Pharmaceutical research. 2008;25(8):1815-21.

65. Aggarwal P, Hall JB, McLeland CB, Dobrovolskaia MA, McNeil SE. Nanoparticle interaction with plasma proteins as it relates to particle biodistribution, biocompatibility and therapeutic efficacy. Advanced drug delivery reviews. 2009;61(6):428-37.

66. Tenzer S, Docter D, Kuharev J, Musyanovych A, Fetz V, Hecht R, et al. Rapid formation of plasma protein corona critically affects nanoparticle pathophysiology. Nature nanotechnology. 2013;8(10):772-81.

67. Stafford JL, Belosevic M. Transferrin and the innate immune response of fish: identification of a novel mechanism of macrophage activation. Developmental and comparative immunology. 2003;27(6-7):539-54.

68. Wang H, Zhang M, Bianchi M, Sherry B, Sama A, Tracey KJ. Fetuin (α2-HS-glycoprotein) opsonizes cationic macrophagedeactivating molecules. Proceedings of the National Academy of Sciences. 1998;95(24):14429-34.

69. Jersmann HP, Dransfield I. Fetuin/α2-HS glycoprotein enhances phagocytosis of apoptotic cells and macropinocytosis by human macrophages. Clinical Science. 2003;105(3):273-8.

70. Dobrovolskaia MA, Patri AK, Zheng J, Clogston JD, Ayub N, Aggarwal P, et al. Interaction of colloidal gold nanoparticles with human blood: effects on particle size and analysis of plasma protein binding profiles. Nanomedicine: Nanotechnology, Biology and Medicine. 2009;5(2):106-17.

71. Vyner MC, Amsden BG. Polymer chain flexibility-induced differences in fetuin A adsorption and its implications on cell attachment and proliferation. Acta Biomater. 2016;31:89-98.

Appendix 1

A Detailed and High-Yield Protocol for the Concatemerization, Expression and Purification of Marginally Soluble, Short Elastin-Like Polypeptides

Published as a supplementary protocol to "Bahniuk MS, Alshememry AK, Unsworth LD. High-yield recombinant expression and purification of marginally soluble, short elastin-like polypeptides. BioTechniques. 2016 Dec;61(6):297-304."

A Detailed and High-Yield Protocol for the Concatemerization, Expression and Purification of Marginally Soluble, Short Elastin-Like Polypeptides

PROTOCOL FOR:
High-yield recombinant expression and purification of marginally soluble, short elastin-like polypeptides

Markian S. Bahniuk[1,2,¶,*], Abdullah K. Alshememry[2,3,¶], Larry D. Unsworth[1,2,4,*]
1 Department of Biomedical Engineering, University of Alberta, Edmonton, Alberta, Canada
2 National Institute for Nanotechnology, National Research Council, Edmonton, Alberta, Canada
3 Faculty of Pharmacy and Pharmaceutical Sciences, University of Alberta, Edmonton, Alberta, Canada
4 Department of Chemical & Materials Engineering, University of Alberta, Edmonton, Alberta, Canada
¶ These authors contributed equally to the manuscript.
** Corresponding Authors*

BioTechniques, Vol. 61, No. 6, December 2016, pp. 297–304

LEGEND

⇨ ***ATTENTION***

* ***HINT***

REST

REAGENTS

Synthetic DNA encoding for a short repeat of ELPs (Integrated DNA Technologies, Coralville, Iowa, USA)

XL10 Gold competent *Escherichia coli* cells (Agilent Technologies, Santa Clara, California, USA)

Ampicillin (ThermoFisher, Waltham, Massachusetts, USA)

Agarose for plates and electrophoresis gels (EMD Millipore, Etobicoke, Ontario, Canada)

Bacto-tryptone (BD Biosciences, San Jose, California, USA)

Yeast extract (BD Biosciences, San Jose, California, USA)

Glycerol (EMD Millipore, Etobicoke, Ontario, Canada)

NaCl (ThermoFisher, Waltham, Massachusetts, USA)

KCl (ThermoFisher, Waltham, Massachusetts, USA)

$MgSO_4$ (ThermoFisher, Waltham, Massachusetts, USA)

Glucose (ThermoFisher, Waltham, Massachusetts, USA)

Plasmid miniprep kit (Qiagen, Toronto, Ontario, Canada)

MinElute gel extraction kit (Qiagen, Toronto, Ontario, Canada)

EcoRI (New England Biolabs, Ipswich, Massachusetts, USA)

HinDIII (New England Biolabs, Ipswich, Massachusetts, USA)

NdeI (New England Biolabs, Ipswich, Massachusetts, USA)

BamHI (New England Biolabs, Ipswich, Massachusetts, USA)

BglI (New England Biolabs, Ipswich, Massachusetts, USA)

PflMI (New England Biolabs, Ipswich, Massachusetts, USA)

SfiI (New England Biolabs, Ipswich, Massachusetts, USA)

pUC19 cloning vector (Bio Basic, Markham, Ontario, Canada)

T4 DNA ligase enzyme (Invitrogen, Carlsbad, California, USA)

Ligase buffer (Invitrogen, Carlsbad, California, USA)

Antarctic phosphatase (New England Biolabs, Ipswich, Massachusetts, USA)

OneTouch BL21(DE3) competent *Escherichia coli* cells (Invitrogen, Carlsbad, California, USA)

Glacial Acetic Acid (Sigma-Aldrich, St. Louis, Missouri, USA)

Tris-base (Invitrogen, Carlsbad, California, USA)

Ethylenediaminetetraacetic acid (EDTA) (ThermoFisher, Waltham, Massachusetts, USA)

Ethidium bromide (Sigma-Aldrich, St. Louis, Missouri, USA)

pET-25b(+) expression vector (EMD Millipore, Etobicoke, Ontario, Canada)

Terrific broth rich media (TB) (ThermoFisher, Waltham, Massachusetts, USA)

L-proline (Sigma-Aldrich, St. Louis, Missouri, USA)

Isopropyl β-D-1-thiogalactopyranoside (IPTG) (ThermoFisher, Waltham, Massachusetts, USA)

Copper chloride (Sigma-Aldrich, St. Louis, Missouri, USA)

40% Acrylamide:Bis Acrylamide, 29:1 Solution (Bio-Rad Laboratories, Hercules, California, United States)

Sodium dodecyl sulfate (SDS) (ThermoFisher, Waltham, Massachusetts, USA)

Ammonium persulfate (APS) (Bio-Rad Laboratories, Hercules, California, United States)

Tetramethylethylenediamine (TEMED) (EMD Millipore, Etobicoke, Ontario, Canada)

Tricine (ThermoFisher, Waltham, Massachusetts, USA)

Ammonium acetate (VWR International, Radnor, Pennsylvania, USA)

Glycine (Bio-Rad Laboratories, Hercules, California, United States)

Precision Plus Protein™ Dual Color Standards (Bio-Rad Laboratories, Hercules, California, United States)

Methanol (Sigma-Aldrich, St. Louis, Missouri, USA)

Urea (ThermoFisher, Waltham, Massachusetts, USA)

Imidazole (Sigma-Aldrich, St. Louis, Missouri, USA)

NaH_2PO_4 (EMD Millipore, Etobicoke, Ontario, Canada)

NaOH (ThermoFisher, Waltham, Massachusetts, USA)

REAGENT SETUP

Ligase buffer needs to be thoroughly mixed, aliquoted, stored frozen and used only once. Great care must be taken to thaw the ligase buffer at room temperature and mix very thoroughly to ensure any precipitants are fully resolubilized.

500 mM and 1 M Proline stock solutions are made and aliquoted to 1 mL and 10 mL, respectively and then stored frozen and used once.

Urea solutions need to be filtered and made fresh to avoid the risk of them carbamylating the ELP samples.

PROCEDURE

DESIGN AND INITIAL PROCESSING OF A NEW ELP GENE

1. Order a gene coding for 10 repeats of VPGLG (L_{10}) from a DNA synthesis company. Note that due to its length, the L_{10} was provided in the pIDTblue plasmid. The exact sequence of this gene is detailed in Supplementary Figure 1.

⇨ ***ATTENTION*** : The protocol will refer to the doubling of L_{10} to L_{20} and the expression of L_{20} simply as examples. This protocol is applicable to all ELP sequences.

2. Transform the pIDTblue-L_{10} plasmid into XL10 Gold *Escherichia coli* (*E. coli*). Begin by thawing an aliquot of competent cells on ice for 20 minutes. Add 2

µL of 0.5 ng/µL plasmid to the competent cells and stir gently with a pipette tip. Incubate the cells on ice for 30 minutes, then 42°C for exactly 30 seconds, and then back on ice for 2 minutes. Add 900 µL of super optimal broth with catabolite repression (SOC) media to the cell aliquots and incubate at 37°C with 225 rpm rotation for one hour. Hold the microcentrifuge tubes horizontally in the shaking incubator to allow for better mixing. After this recovery period, plate various volumes of the cell solution on LB agar plates supplemented with 100 µg/mL ampicillin and grow overnight at 37°C.

3. Roughly 16 hours later remove the plates from heat and store at 4°C for use in the afternoon. Pick individual colonies and grow them up in 5mL liquid cultures of LB broth and 100 µg/mL ampicillin at 37°C and 225 rpm overnight.

4. About 16 hours later remove the liquid cultures from the incubator and use a portion of the liquid culture to make glycerol stocks by combining 1mL of the resulting bacterial solution with 450 µL of sterile 80% glycerol. This can be kept at -80°C and used multiple times to generate new liquid cultures as needed.

REST: **Once a glycerol stock is made, this is often a convenient pause point. These stocks can be stable for years with proper storage. This type of rest point occurs multiple times in this protocol.**

5. Process the remaining liquid culture using a miniprep kit to yield a solution of purified pIDTblue-L_{10} plasmid. Measure the purity and concentration of this

solution using a spectrophotometer, ideally one designed to use low sample volumes such as a NanoDrop. If yields are low, larger initial volumes of liquid culture can be used.

 ***REST:*** **Purified DNA can be frozen at -20°C for weeks without any deleterious effects. There are multiple places throughout this protocol where this rest point may be applied.**

6. Extract the L_{10} gene from the purified plasmid by double digesting with EcoRI and HinDIII. Add 0.5 µL of each 20 U/µL enzyme to 2-3 µg of DNA in the manufacturer-recommended buffer in a final reaction volume of 20 µL and incubate at 37°C for 2 hours. Purify the gene by running the digest on a 2% agarose gel using Tris-acetate-EDTA running buffer then separate the 196 base pair (bp) band using a gel extraction kit. Kits designed to use a minimal amount of elution solution such as the Qiagen MinElute kit are recommended as they minimize sample dilution. Ethidium bromide is used to visualize sample bands in DNA gels though other options are available.

* ***HINT*****: For all restriction enzyme digest reactions, be sure to add the enzyme(s) last and gently mix the final solution to ensure complete dispersion of the enzyme(s).**

7. Prepare a pUC-19 cloning vector for the newly purified L_{10} gene. Digest 1.5-2.0 µg of the plasmid with 0.5 µL each of 20 U/µL EcoRI and HinDIII like with the pIDTblue-L_{10} plasmid and purify by running the digest on 1% agarose gel and extracting the 2635 bp linearized plasmid using a gel extraction kit.

8. Ligate the L_{10} sequence into the pUC19 vector by combining 20 fmol of insert with 10 fmol of vector, heat the DNA mixture at 65°C for 5 minutes to ensure the sticky ends are fully available, then add ligase buffer from a fresh aliquot as well as 0.5 µL of 1 U/µL T4 DNA ligase enzyme and ultrapure water to reach a final reaction volume of 10 µL. Incubate the ligase reaction at 16°C for 20 minutes. In order to reduce the number of incorrect background colonies, add 0.5 µL of 20 U/µL BamHI enzyme after the ligation reaction and incubate at 37°C for 10 minutes.

9. Add 2 µL of the ligase reaction to 100 µL of chemically competent XL10 gold *E. coli* and transform as described above. Grow up multiple transformed colonies in liquid culture and purify with a miniprep kit as mentioned previously.

10. Confirm correct insertion of L_{10} into pUC19 by isolating plasmid DNA from multiple transformed colonies then digesting both pIDTblue-L_{10} and putative pUC19-L_{10} plasmids with BglI and NdeI. Add 0.5 µL of 10 U/µL BglI and 0.5 µL of 20 U/µL NdeI enzymes to about 750 ng of DNA, in supplier-recommended buffer conditions for a final reaction volume of 20 µL and incubate at 37°C for 1 hour. When run on an agarose gel, a successful pUC19-L_{10} vector will result in plasmid fragments of 67, 334, 1051 and 1379 bp. An unmodified pUC19 would

digest in to fragments of 62, 1056 and 1568 bp. pIDTblue-L_{10} would show a banding pattern of 178, 212, 1276 and 1436 bp.

RECURSIVE DIRECTIONAL LIGATION (RDL)

11. Prepare the pUC19-L_{10} vector for RDL by digesting 1.5-2.0 µg of it with 0.5 µL of 10 U/µL PflMI restriction enzyme in the recommended buffer conditions with a final volume of 20 µL for 4 hours at 37°C. The L_{10} insert is prepared in the same fashion except that the DNA is digested with both 10 U/µL PflMI and 10 U/µL BglI.

12. Purify the vector using a 1% agarose gel electrophoresis followed by a gel extraction. A correct vector digest yields one band on the DNA gel corresponding to the size of the vector as opposed to an uncut vector which will run smaller than its actual length.

13. Redigest the purified linear vector with PflMI as described above to minimize the amount of uncut vector present in the sample. No agarose gel purification or extraction is necessary after this second restriction digest.

14. To abate the amount of vector reclosure during the upcoming ligation reaction, the vector DNA can be dephosphorylated so that it cannot be ligated closed on itself. Treat the twice-digested vector with Antarctic phosphatase. Add 2.3 µL of the provided 10X buffer to the 20 µL digest reaction along with 1 µL of

the 5U/μL phosphatase enzyme. Incubate this reaction at 37°C for one hour then 65°C for 5 minutes to inactivate the phosphatase.

15. Purify and extract the insert similarly to the vector, but using a 2% gel. The insert digest contains multiple fragments, with bands of 170, 1118 and 1371 bp corresponding to vector fragments. In the case of L_{10}, the DNA fragment of interest had a molecular weight of 165 bp. Do not dephosphorylate the insert.

16. Ligate the linearized and dephosphorylated pUC19-L_{10} with the L_{10} gene insert using an insert:vector ratio of 50:10 fmol. We have found that this ratio does allow for the occasional double insertion which may be useful in some RDL situations. Heat the DNA mixtures at 65°C for 5 minutes to ensure the sticky ends of the sequences were open for ligation to one another. Afterwards, add ligase buffer from a freshly thawed aliquot in addition to 0.5 μL of 1U/μL T4 DNA ligase and ultrapure water to bring the reaction to a final volume of 10 μL. Allow the ligation reaction to proceed for 20 minutes at 16°C.

17. Use the ligation reaction to transform 100 μL of XL10-gold cells as described in step 2 in the "Initial Processing of a New ELP Gene" section.

18. In addition to the ligation reaction above, control reactions can be set up periodically to assess the number of vector-only transformations that may otherwise obscure the correct clones resulting from RDL. One of these controls involved replacing the insert and ligase with water to estimate how much of the pUC19-L_{10} remained uncut through the vector preparation procedure. Another

control only replaces the insert with water to examine the degree of vector reclosure in the ligation reaction.

19. Grow up some of the resulting bacterial colonies in 5 mL liquid cultures with 100 μg/mL ampicillin at 37°C and 225 rpm overnight and collect the plasmids using a miniprep kit. In order to screen the DNA for correct oligomerization of the L_{10} gene into L_{20}, digest roughly 750 ng of the plasmids with 0.5 μL each of 10 U/μL PflMI and BglI in a final reaction volume of 20 μL at 37°C for one hour then separate the fragments by 2% agarose electrophoresis. A successful RDL reaction resulting in L_{20} is illustrated by an apparent doubling of the length of the ELP gene from 165 to 330 bp. This result is illustrated in Figure 1.

20. Once correct clones have been identified, glycerol stocks can be made of them as described in Step 4 of the "Initial Processing of a New ELP Gene" section.

21. From this point on the RDL procedure can be repeated using the pUC19-L_{20} for further concatemerization.

EXPRESSION VECTOR MODIFICATION

22. Digest roughly 2 μg of expression plasmid pET-25b(+) with 0.5 μL each of 20 U/μL EcoRI and NdeI in EcoR1 buffer in a final reaction volume of 20 μL at 37°C for 4 hours. The digest can be confirmed by running a portion on a 0.8% agarose gel. This plasmid digestion does not require purification due to a post-ligation restriction digest detailed below.

23. Our modifying sequence was of sufficient length that it could only be obtained as part of a plasmid and is referred to as pIDT-mod. As such, upon its receipt it should be first transformed into XL10-Gold cells as detailed in Step 2 of the "Initial Processing of a New ELP Gene" section. The sequence of the expression vector modifier is given in Supplementary Figure 2.

24. Grow up a successfully transformed colony of pIDT-mod in 5mL of LB with 100 μg/mL ampicillin at 37°C and 225 rpm overnight and extract and purify the plasmid using a Qiagen miniprep kit.

25. Digest approximately 4 μg of the purified pIDT plasmid using 0.5 μL each of 20 U/μL EcoRI and NdeI in EcoR1 buffer in a final reaction volume of 20 μL at 37°C for 4 hours.

26. Separate the digest reactions on a 2% agarose gel and collect the 293 bp band using a gel extraction kit.

27. Combine the linearized vector and insert at a 20:10 fmol insert:vector ratio and heat at 65°C for 5 minutes. Use 0.5 μL of 1U/μL T4 DNA ligase, ligase buffer and ultrapure water to a final volume of 10 μL. Allow the ligation reaction to proceed at 16°C for 20 minutes. After the ligation, add 0.5 μL of 20 U/μL BamHI and incubate the solution at 37°C for 10 minutes. This "killer cut" serves to cleave only DNA with the original undesired EcoRI to NdeI sequence present in pET-25b(+). This effectively eliminates the generation of *E. coli* colonies containing the original vector, as any remaining pET-25b(+) will be linearized

and thus will not be able to transform *E. coli* whereas the modified expression vector lacks a BamHI cut site and will remain circular.

28. Use 2 µL of the ligation reaction to transform 100 µL of XL10-gold cells as described previously in step 2 of the "Initial Processing of a New ELP Gene" section.

29. To screen for correct expression vector modification, perform BamHI and SfiI single digest reactions. Collect plasmid from the previous transformation by growing up individual colonies in 5mL liquid culture with 100 µg/mL ampicillin at 37°C and 225 rpm overnight and collect the plasmids using a miniprep kit. Digest about 500ng of plasmid using either 0.5 µL of 20 U/µL BamHI at 37°C or by 0.5 µL of 20 U/µL SfiI at 50°C in the manufacturer-recommended buffer for 1 hour. BamHI will not cut the correctly modified plasmid and SfiI should linearize the majority of it. For the original pET-25b(+), the opposite is true.

⇨ ***ATTENTION***: SfiI digests must be carried out at the non-standard reaction temperature of 50°C. The enzymatic activity at 37°C is greatly reduced. This applies to all SfiI reactions in the protocol.

CLONING AN ELP GENE INTO A MODIFIED EXPRESSION VECTOR

30. Digest 1.5-2.0 µg of the modified expression vector with 0.5 µL of 20 U/µL SfiI enzyme in the recommended buffer up to a final volume of 20 µL for 4 hours

at 50°C. Note that this enzyme requires a non-standard incubation temperature for full activity. This reaction can be done multiple times in parallel to increase the final yield of the linearized plasmid.

31. Run the digest reaction on a 0.8% agarose gel to separate the linearized vector from the undigested vector and SfiI recognition site spacer sequence. Extract the 5530 bp band representing the linearized modified expression using a gel extraction kit.

32. Redigest the extracted DNA with SfiI again using the same conditions as Step 30. No agarose gel electrophoresis or extraction is necessary after this second digest. This additional digest step will significantly decrease the likelihood of getting incorrect clones after transformation with the ELP gene.

33. Dephosphorylate the doubly-digested vector using Antarctic phosphatase to significantly reduce the likelihood of reclosed vector clones. 2.3 μL of the 10X dephosphorylation buffer is added to the 20 μL SfiI digest reaction along with 1 μL of the 5 U/μL phosphatase enzyme. Incubate this reaction at 37°C for one hour then 65°C for 5 minutes in order to inactivate the phosphatase.

34. Prepare the ELP insert by first digesting about 4 μg of the pUC-L_{20} plasmid with 0.5 μL each of 10 U/μL PflMI and BglI using manufacturer-recommended buffer conditions in a final reaction volume of 20 μL at 37°C for 4 hours. This reaction can be done multiple times in parallel to increase final yields.

35. Purify the ELP insert by running the digest reaction on a 2% agarose gel. This gel percentage may change depending on the size of the ELP gene. The digestion

will yield multiple bands. Bands of 170m 118 and 1371 bp are fragments of the pUC vector and should not be isolated. The L_{20} gene will present as a band at 330 bp. Collect this band from the gel using a gel extraction kit.

36. Ligate the ELP L_{20} gene and modified expression vector together using a 50:10 fmol ratio. The ligation and transformation procedure is identical to that of steps 16 and 17 of the "Recursive Directional Ligation" procedure above except that between the ligation and transformation steps include a killer cut using SfiI. Add 0.5 µL of 20 U/µL SfiI enzyme to the ligation reaction and incubate at 50°C for 10 minutes to reduce the number of vector-only colonies. This killer cut will linearize remaining modified expression vector plasmids which would otherwise result in false positive transformants.

37. Screen the colonies produced by the ligation and transformation procedure by NdeI and EcoRI double digest. Begin by growing the colonies in 5 mL LB with 100 µg/mL ampicillin overnight at 37°C and 225 rpm. Extract the DNA using a miniprep kit. Digest about 750 ng of each plasmid with 0.5 µL each of 20 U/µL NdeI and EcoRI in the manufacturer recommended buffer and a final reaction volume of 20 µL at 37°C for 1 hour.

38. Run the resulting DNA fragments using agarose gel electrophoresis. For the L_{20} gene the DNA fragment that would confirm successful ligation would be 407 bp. A 2% agarose gel would be appropriate for these conditions. Longer ELP constructs would result in larger bands which may require a lower percentage agarose gel. The other DNA fragment that is generated is 5453 bp in length. If a

colony contains a modified expression vector (*ie*. an empty vector clone) then an NdeI and EcoRI double digest will result in bands of 293 and 5453 bp.

TRANSFORMING *E. coli* BL21(DE3) WITH AN ELP EXPRESSION PLASMID

39. Thaw one 50 µL aliquot of OneTouch BL21 (DE3) *E. coli* cells on ice for 20 minutes. Meanwhile, dilute a solution of purified ELP expression plasmid to 10 ng/µL. After the cells are thawed, add 2 µL of this plasmid solution to and stir gently using the pipette tip. Thaw the cells on ice for 20 minutes before adding the DNA. Incubate the cells and DNA on ice for a minimum of 30 minutes then heat shock at 42°C for exactly 30 second. Leave the cells on ice for 2 minutes to recover then add 900 µL of SOC media and incubate the cells at 37°C and 225 rpm for one hour. Plate various volumes of the cell solution on LB plates containing 100 µg/mL ampicillin and grown overnight at 37°C.

40. The next morning remove the plates from the heat and leave at 4°C. Grow liquid cultures using 5mL of LB with 100 µg/mL ampicillin at 37°C and 225 rpm overnight, purify the plasmid using a Qiagen miniprep kit and send the resulting DNA for sequencing. Use standard T7 promoter and terminator primers for Sanger sequencing. Given the highly repetitive and GC-rich DNA sequences of the ELP gene, the PCR reaction may require modifications to work properly. The sequencing reactions and any necessary adjustments in the PCR reaction were addressed by the Molecular Biology Service Unit at the University of Alberta.

41. Once correct clones have been identified, glycerol stocks can be made up as in Step 4 of the "Initial Processing" section.

ELP EXPRESSION

42. In the afternoon, prepare a starter culture of 50 mL of terrific broth media (TB) containing 50 µL of 100 mg/mL ampicillin (100 µg/mL final concentration) and 1 mL of 500 mM proline (10 mM final concentration) by adding filter sterilized ampicillin and proline to autoclaved and cooled TB. Inoculate from previous glycerol stock using sterile disposable inoculating loop.

43. Incubate in a shaking incubator at 37°C, 225 rpm for ~16 hours.

44. The next morning use the starter culture to inoculate 1 L of rich TB media supplemented with 10 mL of 1 M proline (10 mM proline final concentration) and 1 mL of 100 mg/mL ampicillin (100 µg/mL final concentration) by adding filter sterilized ampicillin and proline to autoclaved and cooled TB. Then incubate at 37°C to an optical density at 600nm (OD_{600}) of 0.8.

45. Induce cell expression using 1 mL of 2 M Isopropyl β-D-1-thiogalactopyranoside (IPTG) (2 mM final concentration) then incubate at 37°C, 225 rpm for 24 hours.

46. Collect cell pellet by centrifugation at 3000 g at 4°C, for 20 mins. Discard the supernatant and weigh the wet pellet then store it at -80°C until further use.

REST: **The bacterial pellets can remain frozen for a few months with no side effects.**

DENATURING POLYACRYLAMIDE GEL ELECTROPHORESIS (SDS-PAGE)

47. To make the 20% separating gel layer, mix 5 mL of 3M Tris, 0.4% SDS, pH 8.45 with 7.6 mL of 40% acrylamide (acrylamide/bis-acrylamide 29:1 ratio). Also add 3 g of glycerol then add 12.4 mL of Milli-Q water. Ensure the glycerol is well-mixed by inverting the tube several times. Just before pouring the gel add 50 µL of 10% ammonium persulfate and 20 µL of tetramethylethylenediamine (TEMED). Then immediately pour the mixture in the casting frame and allow it to solidify for 45 minutes. These volumes are sufficient to produce four gels using the Bio-Rad Mini-Protean Tetra Cell system and may need to be adjusted for other gel equipment.

48. To make the 5% stacking gel layer, mix 1.25 mL of 3M Tris, 0.4% SDS, pH 8.45 with 625 µL of 40% acrylamide (acrylamide/bis-acrylamide 29:1 ratio). Then add 3.1 mL of Milli-Q distilled water. Invert the tube several times to ensure even mixing. Immediately before casting the stacking gel add 23 µL of 10% ammonium persulfate and 10 µL of TEMED. Then immediately pour the mixture in the casting frame and allow it to solidify for 45 minutes.

49. Once the gel has run to completion (typically the gel is stopped when the sample dye runs off the bottom of the gel) transfer the gel to a container and wash with an excess of MilliQ water twice for 5 minutes each with rocking.

50. Incubate the gel for 10 minutes in 50-100 mL of 0.19M Tris, 0.1% SDS buffer at pH 8.8 with rocking.

51. After discarding the buffer, pour 50 mL of 0.3M $CuCl_2$ on the gel and incubate for 10 minutes with rocking.

52. Dispose of the copper solution then wash the gel again with an excess of MilliQ water twice for 5 minutes each.

METAL AFFINITY CHROMATOGRAPHY

53. Prepare a fresh and filter sterilized denaturing lysis solution (8 M urea, 10 mM Tris, 115 mM monosodium phosphate, pH 8.0) and denaturing washing solution (8 M urea, 10 mM Tris, 115 mM monosodium phosphate, pH 6.3).

* ***HINT*: Keep these solutions warm in order to increase the dissolution rate of the solid urea.**

54. Thaw the cell pellets by immersing them in water at room temperature.

55. Add 25 mL of lysis buffer ensuring complete resuspension of the pelleted *E. coli*.

56. Incubate the lysis reaction at room temperature with rocking for 1 hour. Then incubate at 4°C for 30 minutes with rocking to allow time for any ELPs to fully solubilize.

57. During incubation period, equilibrate a 1.5 mL Ni-NTA column by washing with 1.5 column volumes of MilliQ water followed by washing with 1.5 column volumes of denaturing lysis solution.

58. Transfer solution of lysed cells to an appropriate centrifuge tube and spin at 20 000 g, 4°C for 30 min.

59. Decant the crude soluble lysate into a new tube then filter sterilize it to remove any small insoluble particles. Remove and save a 50 µL sample for SDS-PAGE analysis.

60. Transfer the nickel beads into the soluble lysate tube.

61. Incubate the lysate and nickel beads at 4°C with rotation or rocking overnight.

⇨ ***ATTENTION***: It is critical to allow the beads and soluble cell lysate to bind overnight. Shorter incubation times will significantly lower the final ELP yield.

62. Start the next day by making the buffered imidazole solutions (31 mM, 62 mM, 125 mM, 250 mM, 500 mM, 2 M) using 25 mM Tris, 50 mM NaCl buffer at pH 8.0.

63. Ideally in a 4°C cold room, transfer the soluble lysate and column material mixture back into the nickel column being careful to recollect as much of the column material as possible.

64. Add three column volume of denaturing wash solution and keep the flow through for SDS-PAGE analysis. This should be done at room temperature to avoid urea crystallization in the wash solution. This wash should be repeated a total of two times.

65. Move the column back into the cold room (if applicable) and repeat the same wash procedure three times using 25 mM Tris, 50 mM NaCl buffer at pH 8.0. This serves to both wash the protein on the column and remove the urea from the previous lysis and wash solutions.

66. Begin the elution by adding two column volumes of 31 mM buffered imidazole and collect the flow through. Repeat the elution step using progressively higher imidazole concentrations such as 62 mM, 125 mM, 250 mM, 500 mM and 2 M. This is most useful when first processing an unfamiliar ELP. Once it is known what imidazole concentration(s) elute the ELP, the gradient approach may not be necessary.

✻ ***HINT*: Once the threshold for ELP elution is found, multiple elutions can be made at the same imidazole concentration to minimize the amount of imidazole in the ELP sample.**

67. After elution samples are collected, keep them at 4°C until further purified using ITC. Sample eluents processed on SDS-PAGE can be seen in Figures 2 and 3.

⇨ ***ATTENTION*: Some ELP constructs may not be stable in solution at 4°C for long periods of time.**

INVERSE TEMPERATURE CYCLING (ITC)

68. Run the nickel chromatography eluents on SDS-PAGE and choose those with relatively strong ELP bands for ITC purification. Depending on the construct, simply warming the various eluents to 37°C may cause those containing ELP to turn cloudy. While this is a convenient alternative, running eluents on SDS-PAGE is a much better method of identifying ELP-containing eluents but will require more time. This may be unfavourable for solution-unstable constructs.

69. Before combining the eluents, save 50 µL from each for SDS-PAGE analysis.

70. Combine ELP-containing eluents then induce the ELP transition by incubating the solution at 37°C water bath for 15 minutes. Again, depending on the ELP

construct being produced, a higher temperature and/or supplementary NaCl may be necessary to trigger the ELP phase transition. This may require some experimentation for new constructs. Figures 2 and 4 illustrate the visual change that may be observed for ELPs undergoing assembly.

71. Transfer samples from the water bath to a pre-warmed centrifuge and immediately spin them down at 20,000g at 37°C for 15 minutes. Collect the soluble fraction and replace it with equivalent volume of pre-chilled phosphate-buffered saline (PBS) pH 7.4. Lower volumes could be used if concentrating the sample is desired.

* ***HINT:*** **The ELP pellet may not be visible in all cases.**

72. Resuspend the ELP pellets using bath sonication on ice for 30 minutes to ensure maximal pellet resuspension and ELP resolubilization.

73. After sonication, transfer samples immediately to a pre-chilled centrifuge and spin them down at 20 000 g at 4°C for 15 min. Transfer the ELP-containing supernatant to a clean tube and then resuspend any remaining pellet in pre-chilled PBS. It can be useful to screen the final pellet on SDS-PAGE to see if any ELP was not solubilized or if any contaminating protein carried over.

* ***HINT:*** **It may be possible in some circumstances to recover more ELP from the sample tube by repeating the resuspension step. However, any additional ELP will likely be significantly more dilute than the first resuspension.**

74. Run samples on SDS-PAGE to assess their purity. If one round of ITC isn't sufficient, repeat a second round of ITC. If the ELPs were concentrated during the first round of ITC, the temperature and amount of NaCl necessary to trigger the phase transition may be decreased. Note: Since the phase transition can triggered at room temperature for some ELP constructs, samples should be kept in ice as often as possible. Sample results demonstrating a successful ITC purification can be seen in Figure 3.

75. Determine the ELP product concentrations based on their absorbance at 280 nm. Dilute the ELP solutions as necessary to ensure they will not become cloudy during the absorbance measurement. The Beer-Lambert law can be used to convert absorbance at 280 nm to protein concentration in conjunction with an extinction coefficient calculated using the ProtParam tool from ExPASy. Note that other conventional protein quantification methods may not be applicable to ELPs due to the assays being dependent upon side chain chemistries. ELPs have significantly fewer reactive side chains than common standard curve proteins such

as bovine serum albumin or immunoglobulin G so these methods would significantly underestimate the concentration of ELP solutions.

76. Aliquot samples into small volumes then immediately flash freeze them with liquid nitrogen then store at -80 °C.

FIGURES

Supplementary Figure 1. Sequence of an elastin-like polypeptide gene encoding $(VPGLG)_{10}$.

This sequence is used as the basis for recursive directional ligation (RDL) showing all the relevant restriction enzyme cut sites necessary for cloning and gene concatemerization.

Supplementary Figure 2. Sequence of the expression vector modifying DNA sequence.

This DNA sequence shows the relevant restriction enzyme sites for modification of the expression vector and insertion of the ELP gene. Note that the DNA sequence between the two SfiI cut sites is purified away and does not end up in the final ELP gene but is vital for efficient SfiI cleavage.

RECIPIES

Super Optimal Broth with Catabolite Repression (SOC) (100 mL)

Ingredient	Volume	Final Concentration
Tryptone	2 g	2% (w/v)
Yeast Extract	0.5 g	0.5% (w/v)

NaCl	0.05 g	10 mM
250 mM KCl	1 mL	2 mM
ddH_2O	98 mL	N/A

Adjust pH to 7.0

Add dd H_2O to a final volume of 100mL

Autoclave and allow to cool to less than 50°C

Add sterilized $MgCl_2$ and glucose

1 M $MgCl_2$	1 mL	10 mM
2 M glucose	1 mL	20 mM

Terrific Broth (TB) (1 L)

**The sterile potassium phosphate solution must be added after the rest of the media has been autoclaved*

Tryptone	12 g	1.2% (w/v)
Yeast Extract	24 g	2.4% (w/v)
Glycerol	4 mL	0.4% (v/v)

Add ddH_2O to a final volume of 900 mL

Autoclave and allow to cool

Add 100 mL of potassium phosphate solution

Potassium phosphate solution for TB (100 mL)

K_2HPO_4	12.5 g	0.72 M
KH_2PO_4	2.3 g	0.17 M

Dissolve in ddH_2O to a final volume of 100 mL and autoclave

Copper Staining Buffer for SDS-PAGE (1 L)

Tris base	23.0 g	0.19M

Tris acid	29.9 g	0.19M
10% SDS	10 mL	0.1% (w/v)

Use either tris base or acid-not both

Add ddH_2O to a final volume of ~990 mL

Adjust solution pH to 8.8

Add ddH_2O to a final volume of 1 L

<u>10% Sodium Dodecyl Sulfate (SDS) (100 mL)</u>

SDS	10 g	10% (w/v)

Add ddH_2O to a final volume of 100 mL

<u>Denaturing Lysis Solution (125 mL)</u>

* *The urea will dissolve much faster if the solution is heated*

Urea	60.1 g	8 M
$NaH_2PO_4 \cdot H_2O$	1.73 g	100 mM
Tris base	0.15 g	10 mM

Add ~80mL H_2O

Adjust pH to 8.0

Add H_2O to a final volume of 125 mL

Filter sterilize

<u>Denaturing Wash Solution (125 mL)</u>

* *The urea will dissolve much faster if the solution is heated*

Urea	60.1 g	8 M

$NaH_2PO_4 \cdot H_2O$	1.73 g	100 mM
Tris base	0.15 g	10 mM

Add ~80mL H_2O

Adjust pH to 6.3

Add H_2O to a final volume of 125 mL

Filter sterilize

<u>25 mM Tris, 50 mM NaCl Buffer (200 mL)</u>

Tris base	606 mg	25 mM
NaCl	584 mg	50 mM

Add dd H_2O to a final volume of ~190 mL

Adjust pH to 8.0

Add dd H_2O to a final volume of 200 mL

Filter sterilize

TROUBLESHOOTING

-Inefficient restriction enzyme cleavages:

Prepare DNA using XL10 Gold *E. coli* or non-methylating cell lines such as GM2929.

Prepare multiple parallel digests to increase the total amount of digested DNA.

-Insufficient amounts of purified DNA after agarose gel extractions:

Ensure gel extraction kit and procedure is working properly.

Perform multiple parallel digests and serially elute the products with the extraction kit.

-No colonies after cloning:

Ensure correct antibiotics were used on the agarose plates.

Double check DNA molar ratios are correct.

Check that only the vector DNA was dephosphorylated.

Make sure the phosphatase enzyme is deactivated completely.

Confirm transformation procedure is working.

Confirm ligase enzyme and buffer are working.

-Many colonies after cloning but few or none contain the insert of interest:

Confirm vector DNA has been linearized correctly.

Ensure phosphatase enzyme is working properly.

Ensure DNA molar ratios are correct.

-No or poor expression levels:

Confirm DNA sequence is correct.

Ensure ELP is not in the insoluble cell lysate and unintentionally discarded before purification.

Vary expression conditions including induction, OD_{600}, expression time and expression temperature to optimize ELP expression levels.

-Poor metal-affinity purification results:

Confirm ELP expression.

Ensure matrix is clean and/or charged.

Increase binding time.

Consult the QIAexpressionist manual for further suggestions.

-Additional ELP is present in the urea washes:

Nickel column may be saturated. Consider using a larger column volume.

Add ~3 mM imidazole to lysis and wash buffers to reduce nonspecific binding.

-Incomplete resolubilization of purified ELP during the ITC procedure:

Proper temp for cold spin

ELP may be too concentrated. Dilute before heating to trigger phase transition.

-ELP separates out of solution despite storing at 4°C:

Store flash frozen immediately upon purification.

Dilute ELP to lower concentration before storage at 4°C.

-Sample for A_{280} measurements turn cloudy:

Dilute sample further before taking measurements.

EQUIPMENT

DNA electrophoresis tank (VWR International, Radnor, Pennsylvania, USA)

UVP ChemDocIt T52 gel imaging system (UVP, Upland, California, USA)

Shaking incubator for liquid cell culture (New Brunswick Scientific, Edison, New Jersey, USA)

Variable temperature heat block/water bath (VWR International, Radnor, Pennsylvania, USA)

Pipettors for handling down to 0.5µL liquid volumes and disposable tips (VWR International, Radnor, Pennsylvania, USA)

Nanodrop spectrophotometer (ThermoFisher, Waltham, Massachusetts, USA)

MilliQ lab water system (EMD Millipore, Etobicoke, Ontario, Canada)

BioMate 3 UV spectrophotometer (ThermoFisher, Waltham, Massachusetts, USA)

Temperature-controlled high-speed centrifuge (Eppendorf, Hamburg, Germany)

Ni-NTA Superflow Columns (Qiagen, Toronto, Ontario, Canada)

Thermo Barnstead Labquake™ Tube Shaker/Rotators (ThermoFisher, Waltham, Massachusetts, USA)

Rapid-flow filters (ThermoFisher, Waltham, Massachusetts, USA)

Water bath (ThermoFisher, Waltham, Massachusetts, USA)

Branson 2800 Ultrasonic Cleaner (Branson Ultrasonics, Danbury, Connecticut, United States)

Mini-PROTEAN® Tetra Cell (Bio-Rad Laboratories, Hercules, California, United States)

EQUIPMENT SETUP

Before use, drain the storage solution from the nickel-NTA columns then was them two times with twice the column volume of ultrapure water, then twice with twice the column volume of denaturing wash buffer.

Wash nickel columns after use by incubating them with 0.5 M NaOH for 30 min, then drain the column and add the storage solution and keep at 4°C.

During the ITC procedure, pre-heating and pre-chilling the centrifuge in advance is essential to ensure the centrifuge reaches the appropriate temperature.

Appendix 2

BSA Nanoparticles for siRNA Delivery: Coating Effects on Nanoparticle Properties, Plasma Protein Adsorption, and In Vitro siRNA Delivery

Published as "Yogasundaram H, Bahniuk MS, Singh HD, Aliabadi HM, Uludağ H, Unsworth LD. BSA nanoparticles for siRNA delivery: coating effects on nanoparticle properties, plasma protein adsorption, and in vitro siRNA delivery. International journal of biomaterials. 2012 Aug 7;2012."

Abstract

Developing vehicles for the delivery of therapeutic molecules, like siRNA, is an area of active research. Nanoparticles composed of bovine serum albumin, stabilized via the adsorption of poly-L-lysine (PLL), have been shown to be potentially inert drug-delivery vehicles. With the primary goal of reducing nonspecific protein adsorption, the effect of using comb-type structures of poly(ethylene glycol) (1 kDa, PEG) units conjugated to PLL (4.2 and 24 kDa) on BSA-NP properties, apparent siRNA release rate, cell viability, and cell uptake were evaluated. PEGylated PLL coatings resulted in NPs with ζ-potentials close to neutral. Incubation with platelet-poor plasma showed the composition of the adsorbed proteome was similar for all systems. siRNA was effectively encapsulated and released in a sustained manner from all NPs. With 4.2 kDa PLL, cellular uptake was not affected by the presence of PEG, but PEG coating inhibited uptake with 24 kDa PLL NPs. Moreover, 24 kDa PLL systems were cytotoxic and this cytotoxicity was diminished upon PEG incorporation. The overall results identified a BSA-NP coating structure that provided effective siRNA encapsulation while reducing ζ-potential, protein adsorption, and cytotoxicity, necessary attributes for in vivo application of drug-delivery vehicles.

1. Introduction

Short interfering RNA (siRNA) is extremely promising for the therapeutic treatment of a myriad of diseases; however, its clinical application has hitherto been hindered by an apparent inability to control its delivery. The use of NP based drug delivery vehicles presents several advantages over conventional delivery stratagems, including the fact that they may be used for precise tissue targeting, remain in blood for a prolonged time, and be immediately injected into the systemic circulation. Furthermore, favorable tissue responses have been observed for decreasing particle sizes [1] and a multitude of covalent and noncovalent modifications of NP surfaces can be achieved, aspects that facilitate the design of more effective carriers. In particular, BSA-based NPs have many advantageous qualities [2]: presence of a hydrophobic core facilitating delivery of hydrophobic drugs, a natural abundance in plasma, relative stability and inertness in biochemical pathways, availability, and a relatively benign in vivo biological fate [3]. Unlike NPs fabricated from synthetic polymers, it is thought that the natural protein removal mechanisms will result in a reduced overall toxicity related to the application of BSA NPs [3]. That said, an important step in facilitating the localization of these NPs at the site of interest involves both decreasing their removal from the circulation (i.e., decreasing opsonization) as well as ensuring that any targeting moiety remains able to interact with the cellular site of interest. Inhibiting nonspecific protein adsorption will then be central to both of these effects. A common strategy for preventing protein adsorption at the tissue-material interface is to incorporate end-tethered PEG to the surfaces of biomaterials. It has been well established that the presence of end-tethered PEG

can prevent particulate aggregation, reduce interactions with plasma proteins [4], minimize reticuloendothelial system clearance, and prolong blood circulation time of a host of NPs [5–7].

PEGylation of surfaces has been shown to impede nonspecific protein adsorption [8], where both the presence and conformation of end-tethered PEG play a critical role [9, 10]. It is noteworthy that not only is the amount of plasma protein adsorbed at the tissue-biomaterial interface important in obfuscating an engineered surface but also the composition of the protein layer itself is critical, as this may ultimately direct host responses. NP opsonization has been correlated to surface properties, including hydrophilicity, roughness, ζ-potential, and surface chemistry [11]. Recent results [12] have shown that systemic administration of BSA NPs, stabilized with polyethyleneimine-graft-PEG with bisphosphonic acid attached for bone targeting, showed no beneficial effects associated with the polymer coating. Although the reason for this result was not fully elucidated, it was postulated that the biodistribution of the NPs may be affected by the presence of the adsorbed protein corona to the PEG modified NPs; it is hoped that further analyzing the adsorbed protein composition to these PEG modified BSA NPs may clarify this point. Other previous work [13] has looked specifically at the use of positively charged poly-L-lysine(PLL) as a coating polymer that stabilizes the NP used for the apparent release of siRNA from BSA NPs. It was observed that, for low concentrations of PLL, varying the size of the PLL used for coating resulted in minimal effect on the net release of siRNA from the NPs. In further work [14],

the release of a model drug from BSA NPs could be controlled from ~5 to 90% over 14 days, depending on the nature of coating designed to display differential stability against endogenous enzymes.

In this study, we continued the development of BSA NPs by exploring the role of PEG coating by employing comblike structures of PEG-conjugated PLLs and compared systems stabilized via unmodified PLL. Specifically, PLLs of 4.2 and 24 kDa were utilized to understand the effect molecular weight may have on critical issues related to NP stabilization, siRNA encapsulation and passive release kinetics, plasma protein adsorption, cytotoxicity, and cellular incorporation. Conjugates of PLLs with 1 kDa PEG were synthesized so as to determine if any direct effect on NP stabilization as well as siRNA encapsulation and passive release kinetics might be altered. The cellular uptake of the NPs and the plasma protein adsorption profile were assessed, investigating the role of PEG coating on these features. Our results identified specific types of BSA NPs that provided adequate siRNA release and cellular uptake with relatively low amounts of protein adsorption and cytotoxicity.

2. Materials and Methods

BSA and HBr salt of PLLs of different MWs (4.2 and 24 kDa) were purchased from Sigma-Aldrich (St. Louis, MO, USA) and used without further purification. The sodium dodecyl sulfate (SDS) was obtained from J. T. Baker (Phillipsburg,

NJ, USA). FAM-labelled siRNA (double stranded, 21 base pairs) was purchased from Ambion Inc. (Austin, TX, USA). EDTA/trypsin (10X; Invitrogen, Carlsbad, CA, USA) was diluted 1 : 10 with Hank's Buffered Salt Solution (HBSS; Invitrogen) to 0.05 g/L concentration before use. Dulbecco's Modified Eagle Medium (DMEM; high glucose), and penicillin/streptomycin (10000 U/mL/10 mg/mL) solution were obtained from Invitrogen. Fetal bovine serum (FBS) was from PAA Laboratories (Etobicoke, Ontario, Canada). Sodium phosphate, monobasic, monohydrate sodium phosphate, and sodium chloride laboratory-grade reagents were purchased from EMD Chemical Inc. (Darmstadt, Germany). Ethanol was purchased from Fischer Scientific (Ottawa, Ontario, Canada). The N-hydroxysuccinimide ester of 1 kDa (mPEG-NHS) was obtained from Creative PEG works, NC, USA. The 3,3′,5,5′-tetramethylbenzidine substrate (TMBS) was obtained from Promega (Madison, WI, USA). The dialysis tubing of various MW cutoffs was obtained from Spectrum Laboratories Inc. (Rancho Dominguez, CA, USA).

2.1. PEG Conjugation to PLL

Previously reported methods were used to conjugate PLL to 1 kDa PEG [15]. Briefly, PLL was dissolved in 0.1 M phosphate buffer (PB, pH 7.4) to a final concentration of 2.4 mg/mL. mPEG-NHS was diluted to 18 mM using 0.1 M PB, added to the PLL solution, and reacted for 3 hrs at room temperature. Solution was dialyzed 2 days against MilliQ (18 Ω) water, at 4°C; MilliQ water being

changed twice a day. Dialysate containing 4.2 and 24 kDa PLL was freeze-dried and used to reconstitute the polymer solutions at desired concentrations.

2.2. NP Preparation

BSA NPs were formed via a coacervation method as detailed elsewhere [13]. Briefly, 250 μL of 10 mg/mL BSA in water was added dropwise to an equal volume of 10 mM NaCl in water at room temperature. After 15 min stirring (600 rpm, room temperature), ethanol was added dropwise to a final volume ratio of 6 : 1, ethanol to BSA solution. The mixture was stirred for 3 hrs to form NPs. To stabilize formed NPs, native PLLs (0.3 mg/mL) or PEG-conjugated PLLs (0.3 mg PLL equivalents/mL) in deionized water were introduced dropwise to the equal volume of NPs suspension under constant stirring. Stirring was continued for 1 hr at room temperature to ensure time for the PLL and PEG-PLL conjugates to adsorb to the BSA NP surface. Suspensions of coated NPs were dialyzed against ddH2O for 3 days (12 hrs between solution replacements). Where indicated, the amount of coating on the surface was determined by using the FITC-labeled PLL or PEG-PLL. The polymer labeling was achieved by incubating 10 μL of 0.1 mM FITC solution (in DMSO) with 1 mL of PLL or PEG-PLL (2 mg/mL in 100 mM phosphate buffer, pH = 7.4) for 1 hr at room temperature. Ethanol (9 mL) was then added to this solution. The solution then was centrifuged at room temperature (3000 rpm) for 15 minutes, and the supernatant, with unconjugated FITC, was removed. The pellet formed during this

process was further washed with 5 mL of ethanol and centrifuged at 3000 rpm for 15 min [13]. The solids obtained were air-dried under vacuum for 5 hrs and stored in the dark at 4°C until used. The coating of FITC-labeled polymer was determined using fluorescence measurements. The coated NPs suspension was then diluted with phosphate buffer (pH = 7.4) by 100% and centrifuged (15,000 rpm, 1 hr) and fluorescence (λ_{EX}: 485 nm; λ_{EM}: 527 nm) of the supernatant was analyzed using a multiwall plate reader (Thermo Labsystems, Franklin, MA, USA). A calibration curve generated was used to calculate the coating efficiency as (1 – FITC-polymer$_{supernatant}$/(FITC-polymer$_{supernatant}$ + FITC-polymer$_{pellet}$)) x 100%.

2.3. Particle Sizing and ζ-Potential

Mean particle size of the coated and uncoated NPs were determined using dynamic light scattering (Zetasizer 3000 HS, Malvern Instruments Ltd., UK) with a 633 nm He-Ne laser at a scattering angle of 90°. Uncoated BSA NPs were used directly for the measurements while the coated BSA NPs were diluted 1 : 2 with PB (10 mM, pH 7.4). Intensity measurements were used to determine the NP size. The ζ-potential of the NPs was determined by measuring their electrophoretic mobility using the same instrument at 25°C.

2.4. Plasma Incubation and Elution

Human blood plasma was obtained from Canadian Blood Services, where Canadian Blood Services obtained written informed consent from all volunteers for the collection and distribution of human blood products for research purposes. Human blood products were then shipped to our lab and used following research ethics procedures as approved by the University of Alberta Research Ethics Board (Institutional), Canadian Blood Services Research Ethics Board (Federal), and the National Research Council of Canada Research Ethics Board (Federal). NP solutions (500 μL) were combined with an equal volume of undiluted human plasma and incubated at room temperature for 2 hrs with gentle rocking. The samples were then centrifuged at 13000 rpm for 10 minutes and the supernatants discarded. Pellets were resolubilized in 1 mL of 0.15 M phosphate buffered saline (PBS; pH 7.4) for 30 minutes and the procedure was repeated two times. These samples were spun down and pellets were solubilized in 2% w/v SDS in 0.15 M PBS for one hr, with rocking at room temperature in order to elute adsorbed plasma proteins. To separate the NPs from the eluted plasma proteins, the samples were centrifuged at 13000 rpm for 10 minutes and the supernatants collected and characterized using SDS-PAGE and immunoblotting analysis.

2.5. SDS-PAGE and Immunoblotting

Reduced SDS-PAGE and immunoblotting techniques were used to evaluate and to identify eluted proteins as described previously [9]. All electrophoretic apparatus were purchased from Bio-Rad (Hercules, CA). Briefly, samples were

separated on 12% SDS-PAGE gels and then transferred onto a 0.2 μm immunoblot PVDF membrane. The membrane was cut into strips for total protein staining using colloidal gold (Bio-Rad) and for immunoblotting. Primary and secondary antibodies (see Table S1 in Supplementary Materials available online at http://dx.doi.org/10.1155/2012/584060) were used without further purification at concentrations of 1 : 1000. To visualize protein-antibody complexes, 350 μL of stabilized TMBS substrate was incubated with membrane strips for 10 minutes at room temperature, with rocking. The colour-developing reaction was then quenched for 10 minutes using 2 mL of MilliQ water.

2.6. Preparation of siRNA Loaded BSA NPs and Release Studies

The coacervation technique previously described was employed to prepare BSA NPs encapsulating siRNA. Briefly, 500 μL of aqueous solution of BSA (10 mg/mL) was added to an equal volume of 10 mM NaCl solution under stirring (600 rpm) in glass vials. The stirring was continued for 15 minutes at room temperature. To achieve siRNA encapsulation, siRNA solution (20 μL of 0.15 mg/mL) was added to this binary solution and stirred at 600 rpm for 1 hr at room temperature. The siRNA (scrambled) used for encapsulation was either unlabeled or labeled with FAM. NPs were then formed by adding ethanol dropwise (final volume ratio of ethanol to starting BSA solution = 6). Stirring was continued for 3 hrs at room temperature after the complete addition of ethanol. To coat these siRNA loaded BSA NPs with PLL's, 500 μL of an aqueous polymer

solution was added dropwise to an equal volume of BSA NPs suspension under constant shaking of 500 rpm. Shaking was continued for 1 hr.

To obtain encapsulation efficiency, NPs containing FAM-labeled siRNA were centrifuged at 15000 rpm for 30 minutes. The FAM-labeled siRNA in the supernatant and pellet were determined using a plate reader (λ_{EX}: 485 nm, λ_{EM}: 527 nm) and a calibration curve based on known concentrations of FAM-labeled siRNA. The encapsulation efficiency was calculated as (FAM-siRNA$_{pellet}$/(FAM-siRNA$_{pellet}$ + FAM-siRNA$_{supernatant}$)) × 100%. FAM-labeled siRNA was also used to study the apparent release kinetics of siRNA from BSA NPs coated with different polymers. Polymer concentration of 0.3 mg/mL was used to coat BSA NPs and release values were normalized to 0% for day 0, as described previously [13]. The suspensions were incubated at 37°C in PBS under shaking and aliquots were taken at predetermined time points and centrifuged at 15000 rpm for 30 minutes. The siRNA in the supernatant and pellet were determined using a calibration curve.

2.7. Cell Uptake Studies

To assess cellular uptake of NPs, human breast cancer MDA-231 cells were used. Two sets of NPs were prepared for cell uptake; (i) uncoated and coated BSA NPs with no siRNA, and (ii) uncoated and coated BSA NPs loaded with FAM-labeled siRNA. The siRNA encapsulation was achieved as described above, except that

20 µL of siRNA solution (0.15 mg/mL) was used for FAM-labeled siRNA encapsulation. 1000µL of aqueous polymer solution was added to 2000 µL of BSA NPs suspension (final concentration: 0.3 mg/mL) under shaking for 1 hr to achieve coating. The suspensions were then dialyzed against DMEM for 24 hrs with two changes in dialysis solution.

For uptake, a monolayer of MDA-MB-231 cells were seeded in 24-well plates and allowed to attach for 24 hrs to reach ~50% confluency (see [16] for culture conditions on the cells). The medium was replaced with 500 µL of fresh DMEM with 10% FBS and 1% antibiotics (penicillin/streptomycin). Then, 500 µL of NP suspension in DMEM was added to the cells (in triplicate) and the cells were incubated for 24 hrs at 37°C in a humidified atmosphere of 95% air/5% CO2. After the incubation period, cells were washed with HBSS (×2) and trypsinized. A 3.7% formaldehyde solution was added to suspended cells and the siRNA uptake was quantified by a Beckman Coulter QUANTA SC flow cytometer using the FL1 channel to detect cell-associated fluorescence. The percentage of cells showing FAM-fluorescence and the mean fluorescence in total cell population were determined. Calibration was performed by gating with the negative control (i.e., "No Treatment") group such that the autofluorescent cell population represented 1-2% of the total cell population.

3. Results and Discussion

The nature of the NP coating, in addition to its role in NP stabilization, is expected to control the apparent release of the encapsulated therapeutic agents whilst creating an interface that inhibits nonspecific protein adsorption. In addition to this, it is desirable to evaluate if PEGylation of the PLL based NP coating affects cytotoxicity and/or the cellular uptake of siRNA. Towards this end, NPs were coated with 4.2 and 24 kDa PLLs and PEG conjugates of the same. The use of PLL was considered advantageous as compared to previously employed PEI since the latter is synthetic, highly cytotoxic to mammalian cells, and undergoes an ill-defined degradation pattern. Unlike chemical crosslinkers, such as glutaraldehyde, the coating approach employed is thought to be a more bioacceptable means to stabilize the particles and further provides a convenient means of surface control. After characterization of the NP features, protein adsorption, composition of adsorbed protein layer, apparent siRNA release, cytotoxicity, and cellular uptake of siRNA were assessed.

3.1. PEG-PLL Conjugation

Conjugation of mPEG-NHS to PLL was demonstrated through the addition of varying quantities of PEG and subsequent NMR analysis after dialysis to determine the resulting PEG:PLL molar ratio. The maximum conjugation ratio of PEG : PLL was determined to be ~26 and 150 for 4.2 and 24 kDa PLL systems, respectively (results not shown). On average, this translated into the incorporation of ~6 PEG per 1 kDa of PLL for both 4.2 and 24 kDa systems. However, given

that the PDI of the PLL and PEG polymer was not one, these values are considered on average.

3.2. NP Characterization

The amount of PLL or PEG-PLL incorporated into the coating used to stabilize the NPs was determined so as to evaluate the effect of the presence of PEG upon ζ-potential and resulting NP size. It was evident that unmodified PLLs, regardless of size, incorporated similar mass amounts into the NP coating layer of ~0.1 mg PLL per mg BSA (Table 1). Although, it is evident that on a mole basis there would be more molecules of 4.2 kDa PLL adsorbed than 24 kDa systems, PLL adsorption is largely driven by electrostatic forces so the amount of PLL needed to occupy the charges on the surface of the NP was similar, regardless of individual chain lengths. Moreover, this amount of PLL in the coating layer agreed with previously published results for similar systems [13]. However, PEGylated 4.2 and 24 kDa PLL systems showed an adsorbed amount of PEG-PLL at 16 ± 6 and 7 ± 3 μg conjugate per mg BSA, respectively. An order of magnitude decrease in adsorbed mass was seen in the stabilizing layer upon PLL PEGylation. It is likely that this significant decrease in adsorbed mass was due to steric hindrances imposed by preadsorbed PEG conjugates that prevented other PEG-PLLs from reaching the interface or from the screening of PLL charges that would reduce the driving force for PEG-PLL incorporation into the film.

Differences observed between 4.2 and 24 kDa PEG-PLL coatings suggest that the smaller polymer conjugate may better fill the surface of the NP.

	Coated amount (mg conjugate/mg BSA)	ζ-Potential (mV)	Diameter (nm)
Uncoated	—	−10.1 ± 0.4	255 ± 30
4.2 kDa PLL	0.12 ± 0.03	10.1 ± 0.5	350 ± 90
24 kDa PLL	0.10 ± 0.02	20.4 ± 0.5	310 ± 30
4.2 kDa PEG-PLL	0.016 ± 0.006	1.8 ± 0.3	220 ± 26 (14%) 880 ± 100 (86%)
24 kDa PEG-PLL	0.007 ± 0.003	7.8 ± 0.9	845 ± 140

Table 1: Selected characteristics of prepared NPs: (i) efficiency of PLL and PEG-PLL coating on BSA NPs, (ii) ζ-potential, and (iii) average size (average ± standard deviation). Note that the NPs from 4.2 kDa PLL-PEG coating gave two size populations with relative ratios of 14% and 86%.

Mean particle sizes and ζ-potentials for PLL-coated NPs were similar to previously reported values (Table 1) [13]. NPs formed with 4.2 and 24 kDa PLLs yielded statistically similar average particle sizes of ~350 and 310 nm, respectively; results similar to previously reported values for PLL coated BSA NPs [13]. Upon using PEG-PLL for stabilizing the BSA NPs, the diameter of the NPs increased dramatically. For 4.2 kDa PEG-PLL systems a bimodal distribution in particle diameter was observed, where ~14 and 86% of the NP population had diameters of ~220 and 880 nm, respectively. Systems composed of 24 kDa PEG-PLL systems had an average diameter of ~845 nm. While the difference between systems using different PLL MWs was negligible, it is obvious that the

differences observed upon incorporation of PEG were not. This large difference may be a direct result of the steric hindrances imposed by adsorbed PEG-PLL leading to lower amount of conjugate being incorporated into the stabilizing coating. With less conjugated PEG-PLL filling the surface, a larger NP may form.

The ζ-potentials of all four types of NPs were positive, suggesting sufficient PLL or PEG-PLL adsorbed to offset the inherent negative ζ-potential of the BSA NP. The ζ-potential for the 4.2 and 24 kDa PLL systems were ~10 and 20 mV, respectively. The ζ-potentials for similar systems were found to plateau, with respect to increasing PLL concentration, around these values, suggesting that the NP surfaces were nearly saturated [13]. The PEG-PLL coating instead appeared to reduce the ζ-potential, as the 4.2 and 24 kDa PEG-PLL constructs had ζ-potentials of ~1.8 and 7.8 mV, respectively. Low average ζ-potentials for the PEG-PLL coated NPs seemed to suggest the presence of PEG, as PEG should result in a less charged surface as well as possibly screening ζ-potentials. It is interesting that there was a higher ζ-potential for the 24 versus 4.2 kDa PEG-PLL system given that the 4.2 kDa system adsorbed more PEG-PLL material. It may be that the more 4.2 kDa PEG-PLL molecules result in a more compressed PEG layer that shields the ζ-potentials of the PLL and thus lower the ζ-potential. Whereas the 24 kDa PEG-PLL film has more flexible PEG chains (i.e., mushroom regime) that may allow for more of the ζ-potential to be measured. The literature has shown that PEI-PEG systems observed a ζ-potential plateau at ~14 mV, which was greater than that observed herein [12]. A weak positive charge (ζ-potential <

+5 mV) has been suggested for minimally adsorbing surfaces [17, 18] and PEG-coated NPs prepared in this study fulfill this feature, and surface PEGs could further improve the stability for such low ζ-potential NPs. Moreover, this low ζ-potential may also mediate NP aggregation; however, previous studies have shown that NP sizes are highly dependent on coating properties [13].

3.3. Protein Adsorption to NP Systems

The adsorption of proteins at the NP-blood interface is crucial to several important aspects of drug delivery, where a decrease in the amount of adsorbed protein may lead to an increase in the effectiveness of incorporating tethered targeting molecules on the NP surface. Moreover, decreasing protein adsorption may lead to increased circulation times by decreasing opsonization and potential host responses to the NP. Thus, in order to understand how the differences in the coating affects both nonspecific protein adsorption as well as the composition of the adsorbed layer, 4.2 and 24 kDa PLL and PEGylated versions of these PLLs were evaluated using platelet poor plasma adsorption, where adsorbed proteins were eluted from the surface using a 2% SDS incubation. As there is no way to accurately control the total surface area of NPs in solution, or to accurately estimate it, conducting a total protein analysis would not be indicative of the amount of adsorbed protein per surface area. Moreover, as it has been shown previously that 4.2 and 24 kDa PLL systems do not leak more than 1% of the

BSA incorporated into the formed NPs within 2 hrs, all eluted proteins are most likely from adsorbed protein [13].

Since immunoblot analysis is qualitative for detecting protein levels, and more informative for determining protein presence, equal volumes of eluted protein solution were loaded (50 µL), being a commonly employed technique. The results of the immunoblot analysis for the adsorbed plasma proteins on NPs are summarized in Table 2. The presence of high levels of fibrinogen and fibrinogen fragments suggests active coagulation in all samples except for the 24 kDa PLL NPs. It is possible that fibrinogen might have been less easily eluted from these surfaces. Adsorbed fibrinogen has previously been shown to activate platelets and induce the accumulation of phagocytes [19, 20].

	Fragment size (kDa)	Fragment name	System			
			4.2 PLL	24 PLL	4.2 PEG-PLL	24 PEG-PLL
Fibrinogen	48	γ	***	**	**	***
	56	β	***	**	***	***
	68	α	***	***	***	***
	<48	Cleavage	*	0	*	**
Albumin	66		***	***	***	***
C3	42	Activation	**	*	**	**
	70	β	*	**	**	**
	115	α	0	0	0	0
Apolipoprotein A-1	27		0+	0+	0	0
Plasminogen	25		0	0	0	0
	60		0+	*	0	0

Table 2: BSA NP plasma adsorption conditions and results as evaluated with immunoblots. Plasma proteins eluted with 1.0 mL of 2% SDS in PBS; 0 indicates zero band intensity, while 0+ indicates trace band intensity and ***indicates highest intensity bands. Proteins shown in Table 1 but absent from this table were not observed in immunoblotting (zero band intensity throughout).

High intensity bands for human serum BSA were observed for all formulations. BSA adsorption in these systems is not unusual as the surfaces were formed with polymers that bind avidly to BSA. BSA is an unreactive protein that displays anticell adhesion and provides "passivation" properties, so that the presence of BSA in such great quantities on all of the NP systems is promising from a biocompatibility standpoint [21, 22].

Complement activation is a response against foreign surfaces with important implications for biocompatibility of administered agents [23]. Complement activation pathways are triggered by a variety of stimuli but ultimately serve to cause opsonization through the activation of C3 [24]. C3 is composed of α (115 kDa) and β (70 kDa) peptide chains. If complement is activated and the C3 cleaved, a 42-kDa fragment is created. The 42 kDa C3 fragment and the 70-kDa β-fragment were both present in relatively significant quantities on all NP systems. The presence of the 42-kDa C3 fragment indicated complement activation. PLL-coated NPs appeared to adsorb less 70 kDa C3. While this may be the case, it is important to consider that 70 kDa C3 may simply be less readily eluted from these surfaces than the others. The 115-kDa α C3 fragment was not

observed on any of the systems. It is possible that the NPs did generate this fragment, but it did not adsorb to the NP surfaces.

Trace levels of apolipoprotein A-1 were found on both PLL-coated NP systems, while none was observed on PEG-PLL coated NPs. The presence of apolipoprotein A-1 implies anti-inflammatory activity. The literature states that HDLs such as apolipoprotein A-1 are also capable of endothelial protection, including the control of cell proliferation, the inhibition of apoptosis, the modulation of the secretory functions, the regulation of coagulation, fibrinolysis, and platelet adhesion, and the inhibition of inflammatory processes. Similar to the apolipoprotein A-1 case, 60 kDa plasminogen was found in moderate quantities on the 24 kDa PLL system, with minor amounts in 4.2 kDa PLL coated NPs and none on PEG-PLL coated NPs. This data suggests that PEG can effectively block plasminogen adsorption in these NP systems. Plasminogen binding is likely to be facilitated due to the epsilon amines of the PLL chains [25]. The presence of surface-localized plasminogen may actually enhance the biocompatibility characteristics of the NPs, as it is the precursor for plasmin, which has the potential for clot dissolution [25]. Further studies are needed to discern if the surface-adsorbed plasminogen indeed can be converted to plasmin within blood while localized to the NP surface.

In addition to these five proteins, sixteen other proteins were screened without detection, even in trace amounts, for any of the NP formulations. These fifteen include high molecular weight kininogen (HMWK), low molecular weight kininogen (LMWK), factor I, fibronectin, -antitrypsin, thrombin, prothrombin, protein C, vitronectin, protein S, prekallikrein, antithrombin, immunoglobulin G (IgG), factor XII, factor XI, and -macroglobulin. The lack of the contact phase coagulation proteins of the intrinsic clotting cascade, prekallikrein, HMWK, factor XI and factor XII (Table 2) implied that the NPs should not be procoagulant. HMWK has been shown to both enhance biocompatibility through its anticell adhesion properties, as well as to hinder it by acting as a cofactor for the contact phase of coagulation; therefore, it is unclear whether the presence of this protein on the surfaces is desirable [26, 27]. Further along the cascade, the absence of prothrombin and thrombin reinforces the inference that the systems are noncoagulant [28]. Fibrinogen was detected in significant quantities (Table 2), so the absence of thrombin is especially important to prevent fibrin formation.

The anticoagulation pathway was also monitored via the immunoblots. Protein C, a significant component of anticoagulation, was not observed in significant quantities. Protein S, a cofactor for Protein C, and vitronectin, an indirect inhibitor of plasminogen conversion to plasmin, were also not detected, indicating that the proteins controlling anticoagulation were not present. Two proteins involved in both coagulation and anticoagulation pathways, α_2-macroglobulin and antithrombin, were investigated, but not detected again. Antithrombin is an

uncharged serine protease inhibitor that is responsible for limiting irregular clotting [28]. Due to the absence of thrombin, the absence of α_2-macroglobulin is inconsequential for the coagulation pathway. α_2-Macroglobulin inhibits plasmin in the anticoagulation pathway, but was not detected. Antithrombin, which has a variety of targets in both the coagulation and anticoagulation pathways, was not observed in any of the NP systems.

The absence of other proteins not involved in clotting or fibrinolysis cascades is informative. Lack of IgG adsorption suggests a lack of reactivity by the circulating antibodies and no subsequent stimulation of the immune response. The lack of IgG also indicates that the possible complement activation seen (based on the presence of C3 fragments; Table 2) occurs via the alternative pathway only. The α_1-antitrypsin is an important serine proteases in the body [29]. α_1-Antitrypsin has a charge of −12 at a pH of 7.0, so its adsorption to the positively charged NPs would be expected. However, it was not detected in the immunoblot analysis. It is possible that other negatively charged proteins are preferentially adsorbed to the surface of the NPs, neutralizing its charge.

3.4. siRNA Encapsulation Efficiency and Release

siRNA encapsulation as a function of coating conditions was explored (Figure 1). Respective encapsulation efficiencies ranged from 16 ± 2% to 53± 7% for uncoated and 4.2 kDa PEG-PLL coated NPs. Statistically significant differences

in encapsulation efficiency from uncoated NPs were observed for NPs with 4.2 kDa PLL ($P < 0.005$), 4.2 kDa PEG-PLL ($P < 0.05$), and 24 kDa PEG-PLL ($P < 0.05$). In almost all cases, the use of a coating increased the encapsulation efficiency. Previous studies have shown that when PEI was used to stabilize poly(D,L-lactide-co-glycolide) NPs, the encapsulation efficiency increased from ~43–80% [30]. The cationic polymers presumably sequester the siRNA from freely diffusing during the fabrication process and help to retain the therapeutic agent within the NPs. Using PEG-substituted PLL for coating resulted in increased encapsulation efficiency for both 4.2 and 24 kDa PLL systems. Furthermore, the 4.2 kDa PLL systems, with or without PEG, exhibited nearly double the encapsulation efficiencies of their corresponding 24 kDa PLL systems (Figure 1). Excluding the 24 kDa PLL systems (which did not give statistical significance from uncoated NPs), these results demonstrate that encapsulation efficiency can be controlled through varying PLL size and the incorporation of PEGylated PLL moieties.

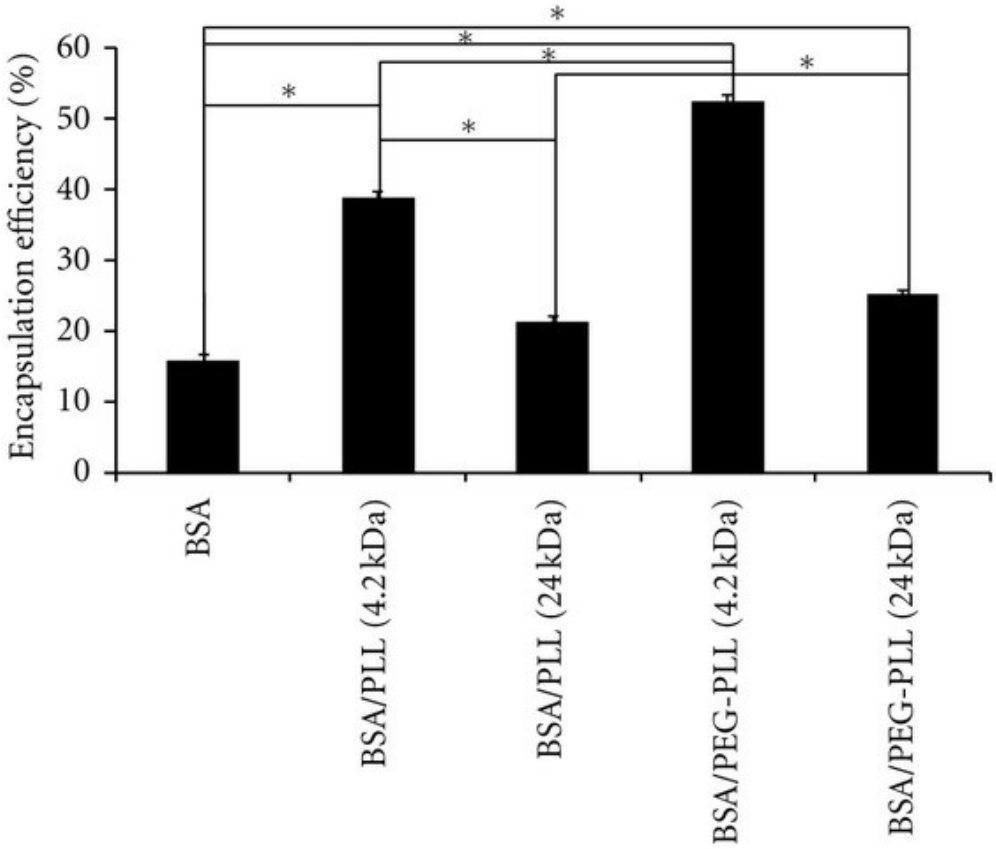

Figure 1: Encapsulation efficiencies of siRNA in various NPs. The value in parentheses represents the molecular weight of the PLL in kDa. For statistical comparison via double-sided t-tests, one asterisk (*) represents and data represent average ±1 SD, n > 5.

The siRNA release from the NPs coated with PLL and PEG-PLL conjugates was monitored over 7 days (Figure 2). It should be noticed that all systems studied had a minimal burst effect, which may suggest the incorporation of the siRNA within the NPs studied. The highest release was observed in the 4.2 kDa PLL coated NPs, which had a Day 7 release of 93 ± 1%, while the lowest release was observed in the 24 kDa PLL coated NPs, with a Day 7 release of 33 ± 1%. Despite

the similar adsorbed mass incorporated into the stabilizing layer for both 4.2 and 24 kDa PLLs, the release profile of siRNA was drastically different. This may be an indication that the 24 kDa PLL coatings form a more stable NP which may impede both the breakup of the NP and/or the diffusive release of siRNA. However, previous work in our lab has shown that 4.2 and 24 kDa PLL stabilized NPs yield similar stabilities at the 0.3 mg/mL condition [13]; thus, is it likely that the differences observed are most likely due to an increase in resistance to diffusive forces leading to a slower release profile for the 24 kDa PLL systems.

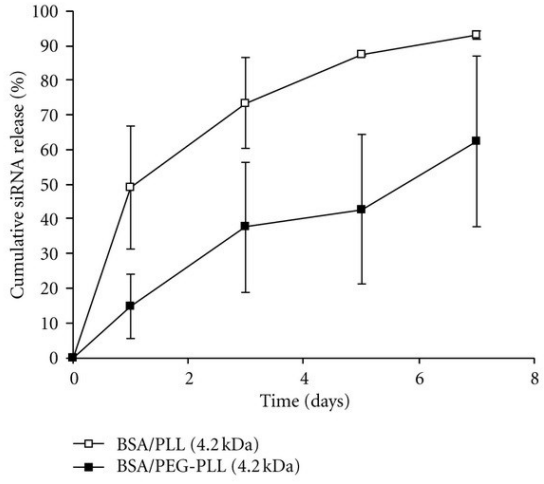

(a)

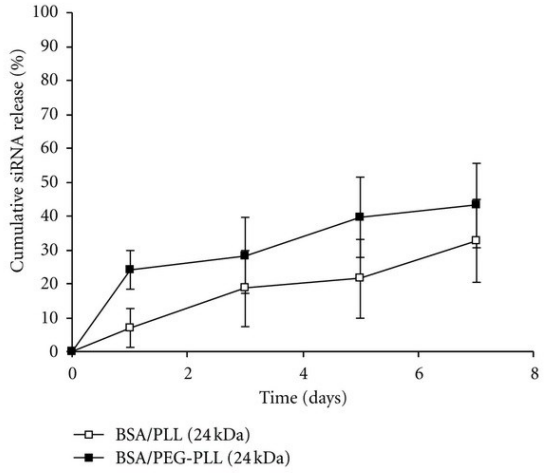

(b)

Figure 2: Cumulative siRNA release profile for 4.2 kDa (a) and 24 kDa (b) PLL-based coatings, over seven days. Trend lines are provided as a guide to the eye only. Data points represent an average ±1 SD, $n \geq 3$.

Interestingly, the effect of incorporating PEG into the NP coating had a different effect upon siRNA release for 4.2 and 24 kDa PLL systems. After 7 days it was observed that 4.2 kDa coated NPs showed a decrease in siRNA release from 93 ± 1% to 62 ± 25 % ($P < 0.05$) upon incorporating PEG, whereas for 24 kDa an

increased release from 33 ± 1% to 43 ± 12% occurred upon PEG presence; the latter trend was not statistically significant. These data may coincide with the discussion regarding the density of the PEG-PLL layers highlighted by the ζ-potential studies. Namely, that the 4.2 kDa PLL layer adsorbed more PEG-PLL than the 24 kDa system, yet had a lower net charge that may suggest a denser PEG layer that shielded some of the 4.2 kDa PLL charge. Thus, it is probable that the large 24 kDa PEG-PLL conjugate was not as able to fill the surface an impede passive siRNA release as compared to the 4.2 kDa conjugate. Taken together, these results indicated that, based upon the presence/absence of PEG and the size of PLL, siRNA release from BSA NPs can be controlled over a range of ~20% to 90% over 7 days. Previously, mPEG-PGLA-PLL coated NPs [31] yielded a similar release profile, including ~85% release after 7 days. Related in vivo work using solid lipid NPs [32] had similar release profiles except for the fact that they observed an initial burst release of ~20% that was not observed herein. Through modifying NP creation parameters in this lipid study, the overall release could be varied from ~70–90% over a period of 7 days. An experiment involving PLGA-PLL NPs (with adsorbed PEG to improve circulation time) found a plateau in the release profile at ~55% after 7 days [33].

3.5. Cellular Uptake

siRNA uptake was investigated in order to ascertain the delivery potential of the NPs as a function of coating properties. Flow cytometry was used to detect siRNA

uptake based on NPs containing FAM-labeled siRNA, as well as the cell counts from the cultures exposed to the NPs. The latter is representative of cell survival upon incubation with the NPs containing no siRNA or FAM-labeled siRNA (Figure 3). Uncoated NPs and NPs coated with 4.2 kDa PLL had similar cell counts, irrespective of the presence or absence of encapsulated siRNA. Coating with 24 kDa PLL caused a dramatic drop in cell numbers, clearly indicating the toxicity of this type of coating irrespective of the presence or absence of encapsulated siRNA (Figure 3). After coating with PEG-substituted PLLs, there was little toxicity for the 24 kDa PLL for blank NPs and siRNA-containing NPs >20-fold increase in toxicity. With 4 kDa PLL, using PEG-substituted PLL gave better cells counts in the absence of siRNA but somehow reduced cell counts in the presence of siRNA ($P < 0.05$ between the two groups). No other system showed such a difference with and without siRNA (based on paired t-test). The encapsulated siRNA was nonspecific and was not expected on its own to cause cell toxicity. It is possible that it might have resulted in nonspecific effects once inside the cells since the molecule is highly charged and it might interact with cationic molecules critical for cell survival (such as histones, etc.), ultimately disrupting the normal cellular physiology. This issue needs to be further explored in future studies.

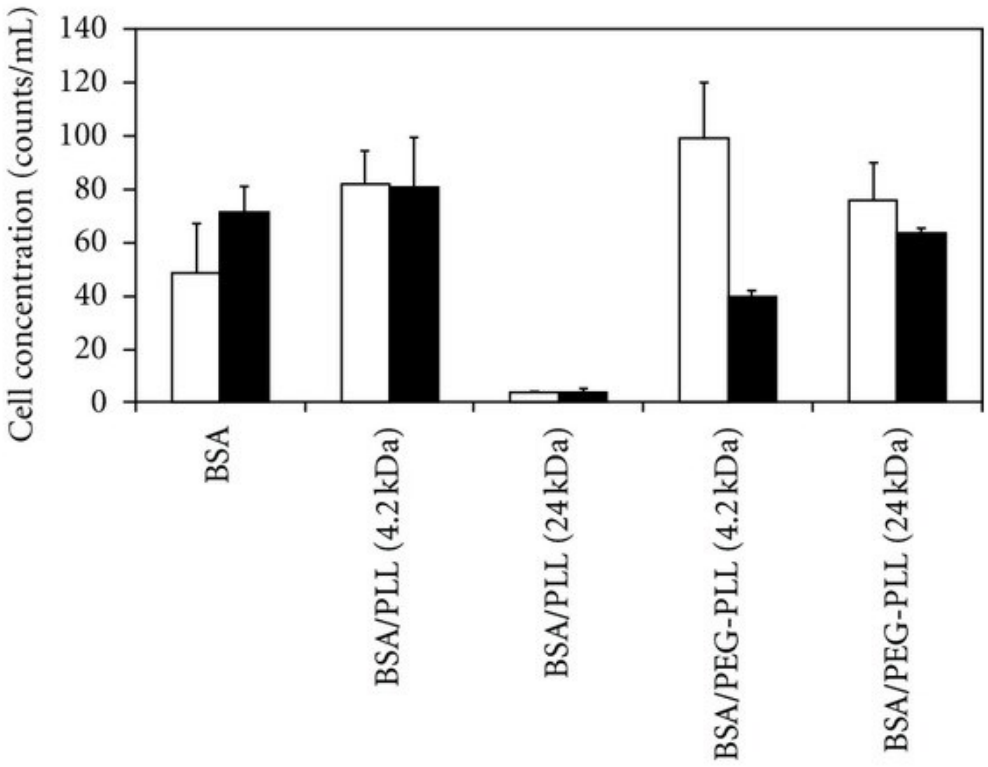

Figure 3: Cell concentrations after exposure to blank NPs (□) and FAM-siRNA-containing NPs (■). The value in parentheses represents the molecular weight of the PLL in kDa. The NPs coated in PEG-PLL (4 kDa) and containing FAM-siRNA showed the greatest cell concentrations. Data represent average ±1 SD, n > 5.

The siRNA uptake is summarized in Figure 4 as the mean uptake (Figure 4(a)) or the percentage of cells positive for siRNA (Figure 4(b)). The mean fluorescence of the cells exposed to NPs without FAM-siRNA was not statistically different among the NPs (as expected), and represented the background readings (i.e., normal autofluorescence). Compared to uncoated NPs, cells exposed to coated NPs containing FAM-siRNA all had greater fluorescence than the background ($P < 0.01$ for NPs coated with 4 kDa PLL, 24 kDa PLL and 4 kDa PEG-PLL), except the NPs coated with 24 kDa PEG-PLL. The latter did not show any evidence of

increased uptake based on mean fluorescence of the cells. Although it is unknown why modification of the 24 kDa PLL NPs with PEG resulted in an insignificant amount of uptake (compared to controls), it is possible that the large average diameter of ~800 nm may prohibit cellular uptake. It was clear that the NPs coated with 24 kDa PLL had the highest cellular delivery of FAM-labeled siRNA. This was consistent with toxicity results that indicated highest toxicity (i.e., cell interaction) with this type of NPs. While the presence of PEG did not affect uptake with 4.2 kDa PLL, an apparent dramatic effect of PEG was evident with the 24 kDa PLL. The protein-repellent properties of PEG presumably prevented binding to cell surfaces, which is critical for internalization and siRNA uptake. This result was also in line with toxicity results, where the cells displayed much more tolerance to 24 kDa PEG-PLL coated NPs.

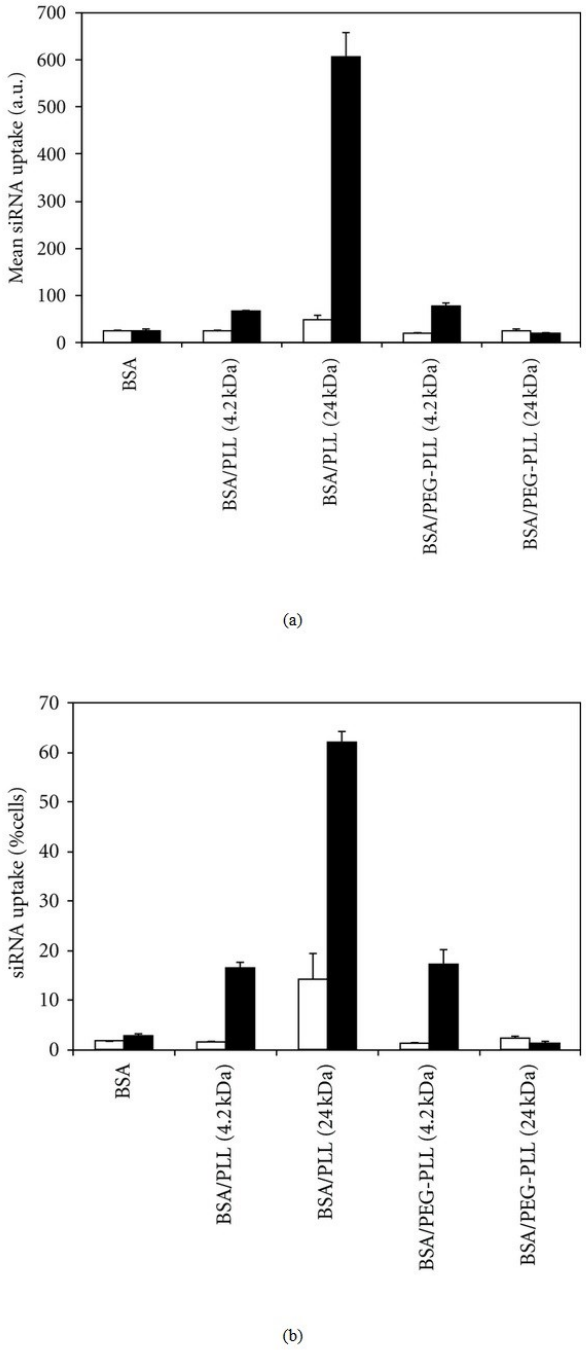

Figure 4: Data summarizing the mean uptake and percent cellular uptake of labeled and unlabeled siRNA. (a) Mean (+1 SD) FAM fluorescence of the cells exposed to NPs without siRNA (□) and with siRNA (■). BSA NPs coated with 24 kDa PLL showed the greatest cellular uptake. (b) Mean (+1 SD) siRNA-positive cells when the cells were exposed to NPs without siRNA (□) and with siRNA (■). BSA NPs coated with 24 kDa PLL showed the greatest value of siRNA-positive cell population. The value in parentheses represents the molecular weight of the PLL in kDa.

Figure 4(b) summarizes that uptake of BSA NPs among the cell population exposed to the NPs. Note that the uptake was minimal in the absence of coating (i.e., pure BSA NPs) and for NPs containing no FAM-labeled siRNA, which served as the background control (1–3% siRNA-positive cell population). The only exception to this observation was the NPs coated with the 24 kDa PLL; a high percentage of cells (14.4%) became auto-fluorescent that yielded significantly high proportion of "apparently" siRNA-positive cells. We previously made such an observation when NPs imparted certain toxicity on the cells [34]. For example, when cells are exposed to blank NPs with no reporter genes such as GFP, they display GFP-like fluorescence (with similar excitation/emission characteristics to FAM) even in the absence of a reporter gene. It is not surprising that the most toxic formulation in this study behaved in this way as well.

With NPs coated by 4.2 kDa PLL and 4.2 kDa PEG-PLL, ~16 and 17% of the cells, respectively, yielded siRNA-positive cells, clearly indicating the beneficial effect of this coating on the cellular delivery of the NPs. With NPs coated by 24 kDa PLL, 62.2% of the cells yielded siRNA-positive cells, but using the same MW PLL with PEG substitution abolished the uptake totals (note the lack of difference in cell uptake for between siRNA-positive and siRNA-negative NPs). Considering the auto-fluorescence obtained in the cells exposed the 24 kDa PLL coated NPs, we expect the uptake to be closer to ~48% in this case. PEG

obviously plays a significant role in this case, preventing the uptake of the NPs. This is in line with previous protein adsorption results, which indicated relatively less binding of plasma proteins to the NPs. It must be noted that the uptake values reported among the cell population should be considered as a relative measure to compare different NP formulations and not taken at absolute values. It is possible to significantly alter the measured values depending on the siRNA loading in NPs; with higher fluorescing NPs, higher rates of uptake could be obtained for the same formulations.

4. Conclusions

The stabilizing coating used on BSA NPs was expected to have significant implications on the physical characteristics of the formed NPs, blood plasma interactions, siRNA encapsulation, and cellular uptake. It was observed that the use of PEG increased average NP size and polymer coating on the NPs. In addition, PEG coatings were found to decrease nonspecific protein adsorption from human plasma as well as decrease the cytotoxicity of certain NPs (i.e., ones coated with highly toxic 24 kDa PLL). This result was likely not due to size, but rather attributed to inherently higher toxicity of the high MW PLL. Although an extensive array of adsorbed proteins was found on the NP surfaces, proteins for both passivating the NPs as well as activating the foreign body reactions were noted. The benefit of a PEGylated NPs was not clear in this respect and further evaluation (in vitro or in vivo) will be necessary to fully reveal the

biocompatibility of the NPs. For the NPs coated with 4.2 kDa PLL, PEG also increased the siRNA encapsulation efficiency, maintained a similar cellular uptake, and delayed siRNA release over a period of 7 days. These desirable results suggest that NP engineering could be possible by controlling PLL size and the use of PEG to prevent the removal from the bloodstream without hindering the efficiency of drug delivery. It is thought that the fundamental knowledge acquired in this study will further the design of coating strategies for controlling the formation and biological interactions of BSA NPs in circulation for the express purpose of delivering drugs via systemic administration.

Abbreviations

BSA: Bovine serum BSA

FAM: 5-Carboxyfluorescein

MW: Molecular weight

NP: Nanoparticle

PEG: Poly(ethylene glycol)

PLL: Poly-L-lysine

siRNA: Short interfering RNA.

Authors' Contribution

H. Yogasundaram and M. S. Bahniuk are equally contributed.

Acknowledgments

This work was supported by Discovery Grants provided to Hasan Uludağ and Larry David Unsworth by the Natural Sciences and Engineering Research Council of Canada (NSERC), and an operating grant provided to Larry David Unsworth by the National Research Council-National Institute of Nanotechnology (NRC-NINT). The authors thank Chemical and Materials Engineering Department (University of Alberta, Canada) for the infrastructure and personnel support.

References

1. H. Harashima, K. Sakata, K. Funato, and H. Kiwada, "Enhanced hepatic uptake of liposomes through complement activation depending on the size of liposomes," Pharmaceutical Research, vol. 11, no. 3, pp. 402–406, 1994.
2. C. Weber, J. Kreuter, and K. Langer, "Desolvation process and surface characteristics of HSA-nanoparticles," International Journal of Pharmaceutics, vol. 196, no. 2, pp. 197–200, 2000.
3. G. Wang and H. Uludag, "Recent developments in nanoparticle-based drug delivery and targeting systems with emphasis on protein-based

nanoparticles," Expert Opinion on Drug Delivery, vol. 5, no. 5, pp. 499–515, 2008.

4. L. D. Unsworth, H. Sheardown, and J. L. Brash, "Protein-resistant polyethylene oxide-grafted surfaces: chain density-dependent multiple mechanisms of action," Langmuir, vol. 24, no. 5, pp. 1924–1929, 2008.
5. K. S. Soppimath, T. M. Aminabhavi, A. R. Kulkarni, and W. E. Rudzinski, "Biodegradable polymeric nanoparticles as drug delivery devices," Journal of Controlled Release, vol. 70, no. 1-2, pp. 1–20, 2001.
6. J. Milton Harris and R. B. Chess, "Effect of pegylation on pharmaceuticals," Nature Reviews Drug Discovery, vol. 2, no. 3, pp. 214–221, 2003.
7. D. E. Owens and N. A. Peppas, "Opsonization, biodistribution, and pharmacokinetics of polymeric nanoparticles," International Journal of Pharmaceutics, vol. 307, no. 1, pp. 93–102, 2006.
8. P. Kingshott, H. Thissen, and H. J. Griesser, "Effects of cloud-point grafting, chain length, and density of PEG layers on competitive adsorption of ocular proteins," Biomaterials, vol. 23, no. 9, pp. 2043–2056, 2002.
9. L. D. Unsworth, H. Sheardown, and J. L. Brash, "Polyethylene oxide surfaces of variable chain density by chemisorption of PEO-thiol on gold: adsorption of proteins from plasma studied by radiolabelling and immunoblotting," Biomaterials, vol. 26, no. 30, pp. 5927–5933, 2005.

10. L. D. Unsworth, H. Sheardown, and J. L. Brash, “Protein resistance of surfaces prepared by sorption of end-thiolated poly(ethylene glycol) to gold: effect of surface chain density,” Langmuir, vol. 21, no. 3, pp. 1036–1041, 2005.
11. M. Bonomini, B. Pavone, V. Sirolli et al., “Proteomics characterization of protein adsorption onto hemodialysis membranes,” Journal of Proteome Research, vol. 5, no. 10, pp. 2666–2674, 2006.
12. G. Wang, C. Kucharski, X. Y. Lin, and H. Uludağ, “Bisphosphonate-coated BSA nanoparticles lack bone targeting after systemic administration,” Journal of Drug Targeting, vol. 18, no. 8, pp. 611–626, 2010.
13. H. D. Singh, G. Wang, H. Uludağ, and L. D. Unsworth, “Poly-L-lysine-coated albumin nanoparticles: stability, mechanism for increasing in vitro enzymatic resilience, and siRNA release characteristics,” Acta Biomaterialia, vol. 6, no. 11, pp. 4277–4284, 2010.
14. H. D. Singh, I. Bushnak, and L. D. Unsworth, “Engineered peptides with enzymatically cleavable domains for controlling the release of model protein drug from “soft” nanoparticles,” Acta Biomaterialia, vol. 8, no. 2, pp. 636–645, 2012.
15. S. Zhang, J. E. Wright, N. Ozber, and H. Uludağ, “The interaction of cationic polymers and their bisphosphonate derivatives with hydroxyapatite,” Macromolecular Bioscience, vol. 7, no. 5, pp. 656–670, 2007.

16. H. M. Aliabadi, B. Landry, P. Mahdipoor, and H. Uludağ, “Induction of apoptosis by survivin silencing through siRNA delivery in a human breast cancer cell line,” Molecular Pharmaceutics, vol. 8, no. 5, pp. 1821–1830, 2011.
17. N. Cao, D. Cheng, S. Zou, H. Ai, J. Gao, and X. Shuai, “The synergistic effect of hierarchical assemblies of siRNA and chemotherapeutic drugs co-delivered into hepatic cancer cells,” Biomaterials, vol. 32, no. 8, pp. 2222–2232, 2011.
18. A. J. Convertine, D. S. W. Benoit, C. L. Duvall, A. S. Hoffman, and P. S. Stayton, “Development of a novel endosomolytic diblock copolymer for siRNA delivery,” Journal of Controlled Release, vol. 133, no. 3, pp. 221–229, 2009.
19. T. M. Massa, M. L. Yang, J. Y. C. Ho, J. L. Brash, and J. P. Santerre, “Fibrinogen surface distribution correlates to platelet adhesion pattern on fluorinated surface-modified polyetherurethane,” Biomaterials, vol. 26, no. 35, pp. 7367–7376, 2005.
20. L. Tang and J. W. Eaton, “Natural responses to unnatural materials: a molecular mechanism for foreign body reactions,” Molecular Medicine, vol. 5, no. 6, pp. 351–358, 1999.
21. G. A. Skarja, R. L. Kinlough-Rathbone, D. W. Perry, F. Rubens, and J. L. Brash, “A cone-and-plate device for the investigation of platelet biomaterial interactions,” Journal of Biomedical Materials Research, vol. 34, no. 4, pp. 427–438, 1997.

22. S. Thakurta and A. Subramanian, “Evaluation of in situ albumin binding surfaces: a study of protein adsorption and platelet adhesion,” Journal of Materials Science: Materials in Medicine, vol. 22, no. 1, pp. 137–149, 2011.
23. L. Tang, L. Liu, and H. B. Elwing, “Complement activation and inflammation triggered by model biomaterial surfaces,” Journal of Biomedical Materials Research, vol. 41, no. 2, pp. 333–340, 1998.
24. H. Molina, “Complement and immunity,” Rheumatic Disease Clinics of North America, vol. 30, no. 1, pp. 1–18, 2004.
25. J. L. Brash, “Exploiting the current paradigm of blood-material interactions for the rational design of blood-compatible materials,” Journal of Biomaterials Science, Polymer Edition, vol. 11, no. 11, pp. 1135–1146, 2000.
26. S. Asakura, R. W. Hurley, K. Skorstengaard, I. Ohkubo, and D. F. Mosher, “Inhibition of cell adhesion by high molecular weight kininogen,” Journal of Cell Biology, vol. 116, no. 2, pp. 465–476, 1992.
27. R. G. Flemming, R. A. Proctor, and S. L. Cooper, “Bacterial adhesion to functionalized polyurethanes,” Journal of Biomaterials Science, Polymer Edition, vol. 10, no. 6, pp. 679–697, 1999.
28. E. W. Davie and J. D. Kulman, “An overview of the structure and function of thrombin,” Seminars in Thrombosis and Hemostasis, vol. 32, no. 1, pp. 3–15, 2006.

29. P. G. W. Gettins, “Serpin structure, mechanism, and function,” Chemical Reviews, vol. 102, no. 12, pp. 4751–4803, 2002.

30. Y. Patil and J. Panyam, “Polymeric nanoparticles for siRNA delivery and gene silencing,” International Journal of Pharmaceutics, vol. 367, no. 1-2, pp. 195–203, 2009.

31. J. Du, Y. Sun, Q. S. Shi, et al., “Biodegradable nanoparticles of mPEG-PLGA-PLL Triblock Copolymers as Novel Non-Viral Vectors for Improving siRNA Delivery and Gene Silencing,” International Journal of Molecular Sciences, vol. 13, no. 1, pp. 516–533, 2012.

32. T. Lobovkina, G. B. Jacobson, E. Gonzalez-Gonzalez, et al., “In vivo sustained release of siRNA from solid lipid nanoparticles,” ACS Nano, vol. 5, no. 12, pp. 9977–9983, 2011.

33. J. Zhou, T. R. Patel, M. Fu, J. P. Bertram, and W. M. Saltzman, “Octa-functional PLGA nanoparticles for targeted and efficient siRNA delivery to tumors,” Biomaterials, vol. 33, no. 2, pp. 583–591, 2011

34. M. Abbasi, H. Uludağ, V. Incani, C. Y. M. Hsu, and A. Jeffery, “Further investigation of lipid-substituted poly(L-lysine) polymers for transfection of human skin fibroblasts,” Biomacromolecules, vol. 9, no. 6, pp. 1618–1630, 2008.